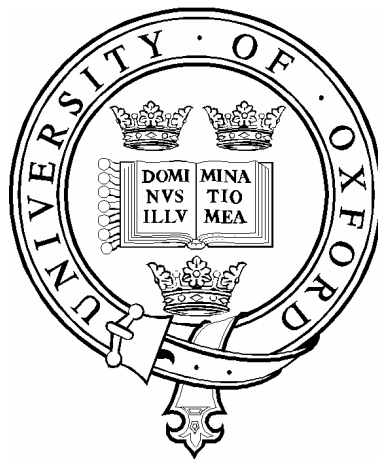


MODEL TESTING OF FOUNDATIONS FOR
OFFSHORE WIND TURBINES

by

Felipe Alberto Villalobos Jara



A thesis submitted for the degree of
Doctor of Philosophy
at the University of Oxford

Keble College, Michaelmas Term 2006

ABSTRACT

Model testing of foundations for offshore wind turbines

A thesis submitted for the degree of Doctor of Philosophy

Felipe Alberto Villalobos Jara
Keble College, Oxford
Michaelmas Term 2006

Suction caissons are a new foundation option for offshore wind turbines. This thesis is focussed on the behaviour of suction caisson foundations in sand and in clay during installation, and under subsequent vertical and combined moment-lateral loadings. The research is based on extensive experimental work carried out using model scaled caissons. The analysis of the results allowed the determination of parameters for hyperplasticity models. Model caissons were vertically loaded in loose and dense sands to study in service states and plastic behaviour. Bearing capacity increased with the length of the caisson skirt. The bearing capacity formulation showed that the angle of friction mobilised was close to the critical state value for loose sands and close to those of peak values due to dilation for dense sands. The vertical load increased, though at a lower rate than during initial penetration, after large plastic displacements occurred. A hardening law formulation including this observed behaviour is suggested. In sand the installation of caissons by suction showed a drastic reduction in the net vertical load required to penetrate the caisson into the ground compared with that required to install caissons by pushing. This occurred due to the hydraulic gradients created by the suction. The theoretical formulations of the yield surface and flow rule were calibrated from the results of moment loading tests under low constant vertical loads. The fact that caissons exhibit moment capacity under tension loads was considered in the yield surface formulation. Results from symmetric and non symmetric cyclic moment loading tests showed that Masing's rules were obeyed. Fully drained conditions, partially drained and undrained conditions were studied. Caisson rotation velocities scaled in the laboratory to represent those in the field induced undrained response for relevant periods of wave loading, a wide range of seabed permeabilities and prototype caisson dimensions. Under undrained conditions and low constant vertical loads the moment capacity of suction caissons was very small. Under partially drained conditions the moment capacity decreased with the increase of excess pore pressure. In clay, vertical cyclic loading around a mean vertical load of zero showed that in the short term the negative excess pore pressures generated during suction installation reduced vertical displacements. The yield surface and the flow rule were determined from moment swipe and constant vertical load tests. The moment capacity was found to depend on the ratio between the preload V_o and the ultimate bearing capacity V_u . Gapping response was observed during cyclic moment loading tests, but starting at smaller normalised rotations than in the field. The hysteresis loop shape obtained during gapping cannot be reproduced by means of the Masing's rules.

ACKNOWLEDGEMENTS

I would like to thank Professor Houlsby for offering me the Research Assistance post, without which my research would not have been possible. I am also in debt to Professor Houlsby for his patience in reading my thesis and for giving me useful comments. I am also grateful to Dr Byrne for allowing me the use of the computer programs to control the VMH loading rig. Similarly, I would like to thank Dr Byrne for reading my thesis and for giving me valuable contributions. I would also express my gratitude to Professor Sills for allowing me the use of equipment of the environmental soil mechanics laboratory and encouraging me during my research.

I am grateful to the Department of Trade and Industry and the Engineering and Physical Sciences Research Council for funding this research as part of the larger DTI Future Energy Solutions project. I would like to acknowledge engineers in SLP Engineering Ltd, Shell Renewables Ltd, Fugro Ltd, Garrad Hassan, and HR Wallingford for interesting discussions in meetings as part of the DTI research project.

I want to thank to the laboratory technicians Bob, Chris and Clive for their help. I am grateful to the researchers in Room 11 and in the soil mechanics laboratory Kaori Kuribayashi, Gwyn Lintern, Gert Bartholomeeussen, John Pickhaver, Nick Melin, Giang Nguyen, Suched Likitlersuang, KK, Jackie Sim, Paul Bonnet, Mattia Rovere, Mobin Ojaghi, Anthony Comer, Ed Hazell and Phil Price for their camaraderie reflected in chats and activities in and out of work. Many thanks to Peter for interesting conversations about cultures, art and artists.

I shared the days in Oxford with many new friends. Salvador Venegas, Dolores Sanchez, Matthew Niblett, Berny Sèbe and Tom Brennan from Keble College. Richard Campbell, David Cocks, Misha and Rebecca from the Walking Club. Mario, Serguei and Rosana from the Mexican Society. Jeff, Olivia, Ross, Mikhail, Thomas and Yoshi from Merton College. Oliver Bleskie, Sanjeev Krishna, Kulviar and Bobby Jones from Magdalen College. And my friends Josh, Justin, Simon and Victor for good football games.

I want to especially thank my *petite amie* Claire for accompanying me along this journey. I also met new compatriot friends Yerko, Nicole, Javier, Catalina, Francisco, Meredith, Jaime and Jo, with whom I enjoyed delicious meals and wines as well as yaps. I met friends Matt, Fabiola and Phil in London, Ingo in Hannover, and Miguel Pereira in Hamburg with whom I had wonderful moments. I want to express my gratitude to Professor Verdugo who showed constant interest in my research as well as Mr Barrera. My friends and colleagues Pato and Diego have always been in contact with good sense of humour. Infinite thankfulness to my family, especially my cousin Hugo and my mother who send me more email 'letters' than anybody else.

LIST OF SYMBOLS

A	caisson lid cross area
A	strip flat footing area = BL
A	shear modulus material constant
B	strip footing width
B_c	cohesion component of bearing capacity
B_q	surcharge component of bearing capacity
B_γ	weight component of bearing capacity
C	settlement service state formulation constant
C_c	coefficient of curvature
C_D	drag coefficient
C_M	inertia coefficient
C_s	shape factor
C_t	thixotropy strength ratio
C_u	coefficient of uniformity
D	depth
D_f	fluid depth
D_s	grain size
D_{10}	average grain diameter of the 10% passing
DOF	degree of freedom
E	Young's modulus
F	dimensionless flow factor
F	frictional force
F_D	drag force
F_M	inertia force
F_T	thrust force
G	shear modulus
G_s	soil specific gravity
H	horizontal load
H_s	significant wave height
K	absolute permeability
K	lateral earth pressure coefficient
K	$K_P - K_A$
K_A, K_P	Krynine active and passive pressure coefficients
K_i	foundation stiffness $i = v, m, h$
K_i	theoretical foundation stiffness coefficients for $i = V, M, MH, H$
L	wave length
L	strip footing length
L	caisson skirt length
$L/2R$	caisson aspect ratio
LL	liquid limit
LRP	load reference point
$M/2R$	moment load
$M/2RH$	load ratio
M_o	constrained modulus
N_c	cohesion bearing capacity factor
N_q	surcharge bearing capacity factor
N_F	number of flow channels
N_H	number of pressure drops
N_γ	weight bearing capacity factor

NC	normally consolidated
OC	over consolidated
OCR	overconsolidation ratio
PL	plastic limit
PPT	pore pressure transducer
Q	soil mineralogy parameter
Q	deviatoric load
R	radius
$2R$	diameter
$2R\theta$	rotational displacement
R_d	relative density
R_n	normalised roughness
R_{max}	maximum roughness
S	suction force
S_t	sensitivity
T	wave period
T	total shear vane torque
T	temperature
T_v	dimensionless time factor during consolidation
V'	buoyant or submerged vertical load
V_c	contact vertical load
V_m	mean vertical load
V_o	maximum vertical load experienced by the foundation
V_t	drained tension load
V_u	ultimate bearing capacity load
W	submerged weight of the caisson, soil plug and water column
Z	stress distribution function
a	load-settlement curve initial slope
a	pore pressure factor
a	factor of depth below the caisson
a_1	pore pressure factor for $k_f = 1$
$a_{V_1}, a_{V_2}, a_M, a_H$	association factors
b	peak vertical load parameter
c	cohesion
c	post-bearing capacity failure parameter
c_D	drag coefficient
c_M	inertia coefficient
c_T	thrust coefficient
c_v, c_h	coefficient of vertical and horizontal consolidation
c_0, c_1, c_2	pressure factor equation parameters
d	vane diameter
d	distance between LRP and another point of load application
d	dissipation function
d_q, d_γ	depth factors
d_w	water depth
e	eccentricity
f_o, f_i	outside and inside soil arching variation
f_p	post peak load parameter

g	acceleration of gravity
h	vane length
h	caisson penetration
\dot{h}	caisson penetration velocity
h_c	contact penetration
h_f	head difference
h_i	yield surface intersection with horizontal load axis
h_o	horizontal load dimension of yield surface
h_{om}	horizontal load dimension of yield surface at the metacentre
h_p	caisson self-weight penetration
h_{pe}	estimated caisson self-weight penetration
h_t	penetration at maximum tension load
i	hydraulic gradient
i_c	critical hydraulic gradient
k	coefficient of permeability
k_a, k_p	Rankine active and passive lateral earth pressure coefficients
k_f	permeability ratio
k_i	theoretical dimensionless stiffness coefficients for $i = v, m, mh, h$
m	constant of soil arching extension
m_i	yield surface intersection with moment load axis
m_o	moment load dimension of yield surface
m_{om}	moment load dimension of yield surface at the metacentre
n	exponent of shear modulus function
p'	mean effective stress
p_a	atmospheric pressure
p_{cav}	cavitation pressure
q	steady flow rate
q	radial displacement
\dot{q}	radial displacement increment
q_c	cone resistance
s	spacing between caissons in a multiple caisson foundation
s	suction
s_u	undrained shear strength
t	time
t	caisson skirt wall thickness
$t/2R$	thickness ratio
t_o	yield surface tension parameter
t_p	time of full caisson penetration
t_s	time of caisson penetration under suction assistance
u	horizontal displacement
u'	excess pore pressure
v	caisson velocity
v_n	non-dimensional footing velocity
v_1	wind far upstream velocity

w	water content
w	vertical displacement
w_s	vertical displacement at lowest softening load
w_t	total vertical displacement
y	yield surface
z_m	depth of the metacentre
Λ	critical state parameter
Θ	vane rotation
Ω	rotor speed
α	adhesion factor
α	maximum yield surface dimension
α_i	internal variable and plastic displacement for $i = V, M, H$
$\dot{\alpha}_i$	plastic displacement increment for $i = V, M, H, Q$
β_1, β_2	yield surface curvature parameters
γ	soil unit weight
γ'	buoyant soil unit weight
γ_d	dry soil unit weight
γ_f	fluid unit weight
γ_w	water unit weight
δ	interface angle of friction
θ	spiral fan angle
θ	soil arching angle
θ	caisson rotation
κ	unloading-reloading slope in $v - \ln p'$ plane
λ	blade tip speed ratio
λ	slope of normal compression line in $v - \ln p'$ plane
λ	multiplier in the flow rule formulation
μ_d	dynamic viscosity
μ_k	kinematic viscosity
ν	Poisson's ratio
ρ	shear strength gradient
ρ_a	air density
ρ_f	fluid density
ρ_w	water density
σ'_{ij}	stress tensor
σ'_1, σ'_3	principal stresses
σ'_n	normal stress
σ'_r	radial stress
$\sigma'_{v_{seepage}}$	seepage vertical stress
σ'_v	vertical effective stress
$\Delta\sigma'_v$	consolidation vertical stress increment
σ'_{vo}	maximum vertical effective stress during consolidation
σ'_{vi}	vertical effective stress once $\Delta\sigma'_v$ is removed after swelling
τ	shear stress
v	specific volume
v_{cs}	critical state specific volume

ϕ'	angle of friction
ϕ'_{cs}	critical state angle of friction
ϕ'_{mob}	mobilised angle of friction
ϕ'_{peak}	peak angle of friction
χ	dissipative generalised load
$\bar{\chi}$	generalised load
ψ	wave number
ω	angular wave frequency
<i>crit</i>	critical
<i>e</i>	elastic
<i>f</i>	final
<i>h</i>	horizontal
<i>i</i>	initial
<i>i</i>	inside
<i>m</i>	mean
<i>max, min</i>	maximum, minimum
<i>mh, hm</i>	coupled
<i>o</i>	outside
<i>p</i>	plastic
<i>v</i>	vertical
<i>y</i>	yield
δ	increment
Δ	variation

Contents

Abstract	i
Acknowledgements	ii
List of symbols	ii
Contents	viii
1 INTRODUCTION	1
1.1 FOUNDATIONS FOR OFFSHORE WIND TURBINES	2
1.1.1 Motivation for the research project	2
1.1.2 The offshore wind energy industry	3
1.1.3 Environmental load of the wind	5
1.1.4 Environmental load of the waves and currents	6
1.1.5 Seabed materials at the UK sites proposed	8
1.1.6 Existing foundation options for offshore wind turbines	9
1.1.7 Suction caisson foundations	10
1.2 SHALLOW FOUNDATION RESEARCH	13
1.2.1 Elastic behaviour	13
1.2.2 Bearing capacity and plasticity models	14
1.2.3 Research on suction caisson foundations	18
1.2.4 A new theoretical approach	25
1.3 THE NEED FOR MORE RESEARCH	26
1.3.1 Research objectives	27
2 SOIL SPECIMENS AND APPARATUS	29
2.1 SOIL SPECIMENS MODELLED	29
2.1.1 Dogs Bay sand	30
2.1.2 White 14/25 Leighton Buzzard sand	30
2.1.3 Baskarp Cyclone sand	31
2.1.4 Redhill 110 sand	33
2.1.5 Speswhite kaolin clay	33
2.2 SAMPLE PREPARATION	37
2.2.1 Dry Dogs Bay and Leighton Buzzard sands	37
2.2.2 Oil-saturated Baskarp Cyclone sand	38
2.2.3 Water-saturated Redhill 110 sand	39
2.2.4 Friction angle of the cohesionless soils	39
2.2.5 Speswhite kaolin clay	40
2.3 MODEL SCALE CAISSONS	43
2.4 TESTING SITES AND BOUNDARY CONDITIONS	45
2.5 TESTING APPARATUS FOR MODEL FOOTINGS	48
2.5.1 The three-degree-of-freedom loading rig	48
2.5.2 The suction system	53

2.5.3	The reference point for loads and displacements	56
3	VERTICAL LOADING OF SKIRTED FOUNDATIONS IN SAND	58
3.1	INTRODUCTION	59
3.2	BEARING CAPACITY OF SHALLOW FOUNDATIONS	63
3.3	EXPERIMENTAL RESULTS	65
3.3.1	Loose sand samples	66
3.3.2	Dense sand samples	70
3.3.3	The axisymmetric bearing capacity coefficient N_q	71
3.3.4	The axisymmetric bearing capacity coefficient N_γ	73
3.3.5	Soil plug heave	74
3.4	HARDENING LAW	75
3.5	CONCLUSIONS	80
4	INSTALLATION OF SUCTION CAISSONS IN SAND	81
4.1	INTRODUCTION	81
4.2	THEORETICAL ANALYSIS	83
4.2.1	Pushing penetration	83
4.2.2	Non-linear stress distribution	86
4.2.3	Suction assisted penetration	87
4.2.4	Limits to suction assisted penetration	94
4.3	EXPERIMENTAL RESULTS	97
4.3.1	Pushing installation into loose and dry sand	97
4.3.2	Drained pullout tests	104
4.3.3	Pushing installation into dense saturated sand	105
4.3.4	Suction installation results in dense sand	108
4.4	CONCLUSIONS	120
5	MOMENT LOADING CAPACITY OF CAISSONS IN DRY SAND	122
5.1	A SIMPLE MODEL	122
5.2	THEORETICAL FRAMEWORK	125
5.2.1	Elasticity	126
5.2.2	Yield surface	128
5.2.3	Flow rule	130
5.3	EXPERIMENTAL RESULTS	131
5.3.1	Experimental procedures	131
5.3.2	Constant vertical load tests	132
5.4	ANALYSES OF THE RESULTS	139
5.4.1	Yield surface	139
5.4.2	Discussion	151
5.4.3	Flow rule	152
5.4.4	Validation	156
5.5	CYCLIC COMBINED LOADING TESTS	158
5.5.1	Introduction	158
5.5.2	Cyclic moment-rotation response	160
5.5.3	Non-symmetric moment loading tests	166
5.5.4	Cyclic vertical displacement response	168
5.6	CONCLUSIONS	172
5.6.1	Monotonic moment capacity	173

5.6.2	Cyclic moment capacity	174
6	MOMENT LOADING OF CAISSONS IN SATURATED SAND	175
6.1	EXPERIMENTS IN WATER-SATURATED SAND	176
6.1.1	Load paths	176
6.1.2	Response of caissons installed by pushing and by suction	180
6.1.3	Foundation stiffness	184
6.1.4	Yield surface and velocity vectors	185
6.1.5	Swipe tests of caissons installed by suction	188
6.1.6	Cyclic loading tests under constant vertical load	192
6.1.7	Cyclic swipe tests of suction caissons	200
6.2	EXPERIMENTS IN OIL-SATURATED SAND	205
6.2.1	Scaling laws in partially drained physical models	206
6.2.2	Moment loading tests	207
6.2.3	Yield points	213
6.2.4	Foundation stiffness	217
6.2.5	Vertical displacement	218
6.3	CONCLUSIONS	219
6.3.1	Experiments in water-saturated sand	219
6.3.2	Experiments in oil-saturated sand	220
7	SUCTION CAISSONS IN CLAY	222
7.1	INSTALLATION AND PULLOUT CAPACITY	223
7.1.1	Introduction	223
7.1.2	Penetration resistance	224
7.1.3	Pushing and suction installation test results	225
7.1.4	Pullout capacity	230
7.2	CYCLIC VERTICAL LOADING TESTS	233
7.2.1	Introduction	233
7.2.2	Results of cyclic loading around $V_m = V_c = 250$ N	235
7.2.3	Results of cyclic loading around $V_m = 0$ N	238
7.2.4	Comparison of displacements and excess pore pressure	241
7.2.5	Comparison of caisson foundation stiffness	243
7.3	MOMENT CAPACITY	244
7.3.1	Introduction	244
7.3.2	Swipe test results	246
7.3.3	Constant V' moment loading tests	251
7.3.4	Yield surface and flow vectors	256
7.3.5	Cyclic moment loading tests	258
7.4	CONCLUSIONS	265
7.4.1	Installation and pullout	265
7.4.2	Cyclic vertical loading	266
7.4.3	Moment loading	266
7.4.4	Discussion and recommendations	267
8	CONCLUSIONS	268
8.1	CONCLUDING REMARKS	268
8.1.1	Main findings	269
8.2	SUGGESTIONS FOR FURTHER RESEARCH	271

Chapter 1

INTRODUCTION

Abstract

The current renewable energy policy in the UK has motivated this research. This chapter starts describing the beginning and evolution of the now worldwide growing offshore wind energy industry. The particular characteristics of the environmental loads offshore, type of seabed soils and foundations commonly adopted are explained. The type of structure and loading regime establish new conditions from a civil engineering point of view. Suction caissons are introduced as an alternative foundation for offshore wind turbines. Suction caissons are currently an accepted alternative to pile foundations in applications for the oil and gas industry. However, this is not yet the case in applications for offshore wind turbines. A review of previous experimental and theoretical studies of shallow foundations is presented. A new theoretical approach referred to as hyperplasticity allows simpler and rigorous models to be constructed, which are suited for modelling monotonic, and more importantly, cyclic response of shallow foundations. However, little experimental research has been performed to calibrate and validate hyperplastic models. Therefore, experimental research is found to be essential to study the effects of different loading conditions, soil types and caisson geometries on the foundation response, interpreting the results within the hyperplasticity framework. It is concluded that the final objective of this research is to contribute to the design of suction caisson foundations for offshore wind turbines.

1.1 FOUNDATIONS FOR OFFSHORE WIND TURBINES

1.1.1 Motivation for the research project

The need for increased production of clean and sustainable energy in the near future has resulted in a search for alternatives to fossil fuels as sources of energy. Wind energy is one of the most promising options for electricity generation, with optimistic growth forecasts for the near future. The UK Government, in the Renewables Obligations (DTI, 2002), is implementing a renewable energy policy to reduce CO₂ emissions, with the target to supply from renewable sources 10% of the total electricity consumed in 2010, and according to the DTI (2003) 20% in 2020. Currently, seven offshore wind farms are operating along the UK coasts (Table 1.1). As part of the first round of offshore wind farm projects (*ca.* 630 turbines, totalling around 1700 MW) another 10 wind farms will be soon built and another 15 are announced to be built in the next ten years as part of the second round of projects (*ca.* 2000 turbines, totalling around 7100 MW). Given that, it is estimated that offshore wind energy will be capable of providing around 9% of the UK's electricity supply. However, if the 20% of electricity were supplied by offshore wind (using 3.5 MW turbines) another 3200 turbines might be necessary to achieve the remainder 11% target.

Within this context, a large research project was undertaken by an industry-university partnership with the aim of improving current design methods used for placing wind turbines offshore. At the University of Oxford the research has focused on the study of a novel foundation for offshore wind turbines. Information about the work at Oxford can be found in Houlby and Byrne (2000), Byrne *et al.* (2002), Byrne and Houlby (2003, 2006) and Villalobos *et al.* (2004b).

The design of foundations is based on a balanced proportion of theories and empiricism. A predominantly empirical approach is suitable when the type of foundation is familiar to

the geotechnical engineer due to previous experience. However, in the presence of a novel type of foundation such an approach may lead to too much risk. To employ a novel foundation in practice with confidence a complete investigation of its response under different likely loading conditions should be undertaken. This is the main motivation behind the work presented in this thesis. The reasons for studying novel foundations such as suction caissons for offshore wind turbines, are explained in sections §1.1.6 and §1.1.7.

1.1.2 The offshore wind energy industry

The use of wind as a source of energy dates from centuries ago. A milestone was reached in the 18th century when around 200000 windmills were rotating in Europe to grind corn or pump water. But in 1888 Charles Brush built the first wind turbine to generate electricity. Improvements in turbine efficiency led to the construction of thousands of *onshore* wind turbines particularly in California in the 1980's and in Germany in early 2000's. Protests by communities about the turbines' visual and noise 'contamination' brought support to the relatively new idea of harnessing the wind energy from *offshore*, where it is also more intense. In fact, Kühn (2002) shows that theoretically there is enough exploitable offshore wind resource to supply completely the electricity consumption in Europe. In 1998 the annual electricity consumption of the EU states was 2500 TWh, which according to Figure 1.1 could be obtained from wind farms located between 30 and 40 km from the shore with water depths between 20 and 30 m.

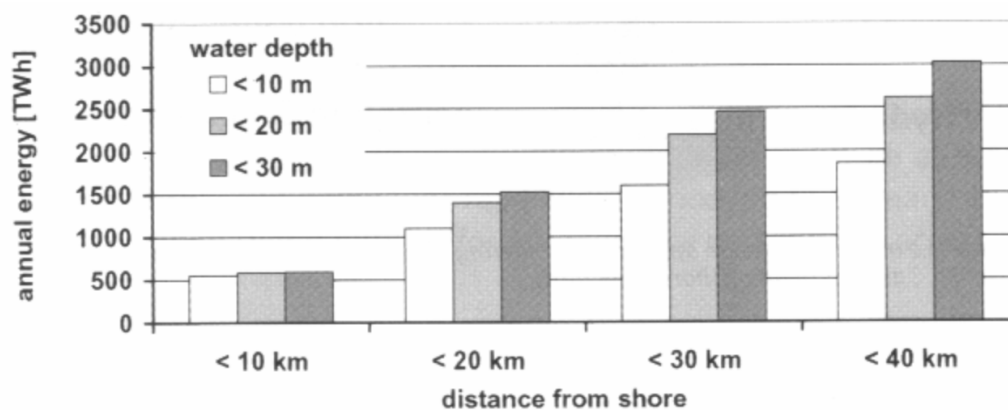


Figure 1.1: Estimated offshore wind energy potential in Europe (taken from Kühn, 2002)

In 1985 a row of 16 wind turbines were founded on an embankment pier in the harbour of

Ebeltoft, Denmark. However, it is considered that Nogersund in the Baltic sea, Sweden, became in 1991 the first operating *offshore* wind turbine. It was erected with a generation capacity of 220 kW, at 250 m from the shore and in 7 m water depth. Also in 1991 the world's first offshore wind farm was constructed at Vindeby, Denmark. Eleven turbines with a capacity of 450 kW each compose the wind farm with turbines resting on gravity base foundations 1.5 km from the shore and between 3 and 5 m water depth. A summary of the existing and about-to-be-completed offshore wind farms is presented in Table 1.1.

Table 1.1: Operating offshore wind farms in the world

Online	Wind Farm	Country	N ^o	MW	Foundation	do ¹ , km	wd ² , m
1991	Nogersund	S	1	0.2	mP	0.25	7
1991	Vindeby	DK	11	5	GB	1.5	3-5
1994	Medemblik (Lely)	NL	4	2	MP	0.75	5-10
1995	Tunø Knob	DK	10	5	GB	3-6	3-5
1996	Dronten	NL	19	11.4	MP	0.02	5
1997	Bockstigen	S	5	2.5	MP	3	6
2000	Blyth	UK	2	3.8	MP	0.8	6-11
2001	Middelgrunden	DK	20	40	GB	3	3-6
2001	Uttgrunden	S	7	10.5	MP	8	7-10
2001	Yttre Stengrund	S	5	10	MP	5	6-10
2002	Horns Rev	DK	80	160	MP	14-20	6-14
2003	Samsø	DK	10	23	MP	3.5	15-18
2003	Frederikshavn	DK	4	10.6	MP & SC	0.2	4
2003	Rødsand (Nysted)	DK	72	165	GB	6	6-9.5
2003	North Hoyle	UK	30	60	MP	7-8	10-20
2004	Scroby Sands	UK	30	60	MP	2.3	4-8
2004	Arklow Bank	IRL	7	25.2	MP	12	2-5
2004	Ems-Emden	D	1	4.5	CC	0.04	3
2005	Barrow	UK	30	90	MP	8	15-20
2005	Wilhelmhaven	D	1	4.5	SC	0.55	5
2005	Kentish Flats	UK	30	90	MP	8.5	5
2006	Breitling	D	1	2.5	CC	0.5	2
2006	Egmond	NL	36	108	MP	18	16-22
2007	Beatrice	UK	2	10	mP	25	45
2007	Lillgrund	S	48	110	GB	7	3
2007	Burbo	UK	25	90	MP	10	1-8

Total: 491 1104

¹ distance offshore, ² water depth; GB: gravity base, MP: monopile, mP: multiple piles, SC: suction caisson, CC: concrete cylinder

An estimation per country of the number of turbines and the capacity for the next few years is presented in Table 1.2. By comparison with the current situation there will be an increase by approximately 20 times in the number of turbines, which will generate 40 times more electricity. The future scenario is very promising. Germany and the UK

Table 1.2: Estimated future growing of turbine number and capacity in the world

Country	N°	MW	source
Belgium	60	300	www.offshorewindenergy.org/
China	40	200	<i>Windpower Monthly</i>
Denmark	130	400	www.windpower.org/
France	232	700	www.iwr.de/wind/offshore/
Germany	6122	27300	www.iwr.de/wind/offshore/
Ireland	433	1205	www.iwea.com/offshore/
Netherland	96	220	www.iwr.de/wind/offshore/
Polan	100	200	www.iwr.de/wind/offshore/
Spain	170	450	www.iwr.de/wind/offshore/
Sweden	630	2040	www.iwr.de/wind/offshore/
USA	519	1260	www.iwr.de/wind/offshore/
UK	2705	10151	www.bwea.com/
Total:	11237	44376	

are the countries with the most ambitious programmes (see for example the magazines *Windpower Monthly* and *Renewable Energy World* for updated information).

1.1.3 Environmental load of the wind

The wind velocity can be considered useful to harness energy if it is above 3 m/s (light wind), but full production (though varies with device) requires 12 m/s (strong wind). The wind to stop electricity generation is above 25 m/s (storm). The aerodynamic force generated by the wind on a turbine can be assumed proportional to the wind dynamic pressure $\frac{v_1^2 \rho_a}{2}$ multiplied by the rotor swept area πR^2 , where v_1 is the far upstream wind speed, ρ_a is the air density, and R is the rotor radius. Then the thrust force is giving by:

$$F_T = \frac{1}{2} \rho_a \pi R^2 v_1^2 c_T(\lambda) \quad (1.1)$$

where the thrust coefficient c_T accounts for the fact that the blades are rotating, therefore, it is a function of the tip speed ratio $\lambda = \frac{\Omega R}{v_1}$, where Ω is the rotor speed in rad/s. Assuming a generic 3.5 MW wind turbine, with a rotor speed of 15 rpm ($\frac{\pi}{2}$ rad/s), rotor radius of 60 m, and a wind speed $v_1 = 15$ m/s, results in $\lambda = 2\pi$. Thus, from Figure 1.2 the thrust coefficient is $c_T = 0.8$, and from equation (1.1), taking $\rho_a = 1.2$ kg/m³ (neglecting variation effects of altitude, air temperature, atmospheric pressure and relative humidity) the resulting thrust force on the hub is $F_T = 1.2$ MN. Note that for storm wind, say v_1

= 30 m/s, $c_T(\lambda = \pi)$ reduces to 0.3, resulting in an increase of F_T to 1.8 MN.

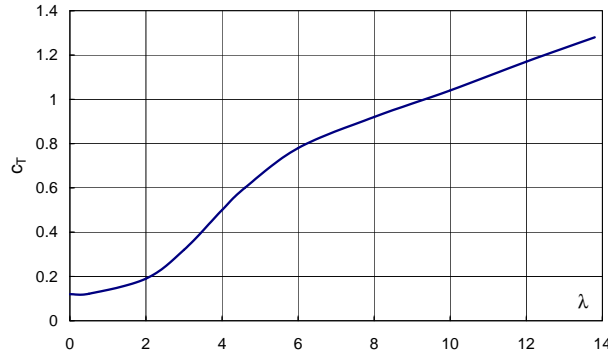


Figure 1.2: Thrust coefficient of a turbine as a function of the speed tip ratio (from Kühn, 2002)

Exact values will depend on the turbine design, nevertheless the above calculations are useful since they give the order of magnitude of the horizontal load applied at the hub level by the wind. More importantly note that the thrust force acts at a level that creates a very high moment at the foundation level (see Figure 1.6(a)).

1.1.4 Environmental load of the waves and currents

Waves induce vortices of water particles, which generate drag forces on obstacles. In addition, a fluid moving horizontally also generates pressures over obstacles. If a dominant extreme wave is idealized then hydrodynamic loads can be obtained from the drag and inertia forces applied on a submerged turbine tower as follows (Kühn, 2002):

$$F_D = \frac{C_D \rho_w (2R) H_s^2 \omega^2}{16\psi} \frac{\sinh(2\psi d_w) + 2\psi d_w}{\cosh(2\psi d_w) - 1} \quad (1.2)$$

$$F_M = \frac{\pi C_M \rho_w (2R)^2 H_s \omega^2}{8\psi} \quad (1.3)$$

where $C_D \approx 0.7$ and $C_M \approx 2$ are empirical coefficients for drag and inertia for smooth tubular sections, ρ_w is the water density, $2R$ is the tower diameter, H_s is the significant wave height, d_w is the water depth, $\omega = \frac{2\pi}{T}$ is the angular wave frequency and T is the wave period, and $\psi = \frac{2\pi}{L}$ is the ‘wave number’ with L being the wave length. The wave number can be obtained from:

$$\omega^2 = g\psi \tanh(\psi d_w) \quad (1.4)$$

in a deep water case $\omega^2 = g\psi$, where g is the acceleration of gravity. The drag force varies with time through a \cos^2 function whilst the inertia force varies with time through a sin function. Therefore, the total horizontal load H can be expressed by:

$$H = \max \{ F_D \cos^2(-\omega t) + F_M \sin(-\omega t) \} \quad \text{for} \quad -\frac{T}{4} \leq t \leq 0 \quad (1.5)$$

Figure 1.3 shows the kinematics and loads associated with a wave of 6.4 m height and 9.4 s period applied on a tower 3 m diameter and 10 m water depth. The bottom plot in Figure 1.3 shows that the maximum horizontal load is 0.45 MN and because the load acts at 10 m height, it results in a moment of 4.5 MNm on the foundation. Considering the following case: $2R = 6$ m, $d_w = 15$ m and an extreme wave $H_s = 12$ m and $T = 12$ s, results in a maximum drag force of 0.7 MN and a maximum inertial force of 2 MN. But because both loads are not in phase the maximum horizontal load is 2 MN, generating a moment of 30 MNm at seabed level.

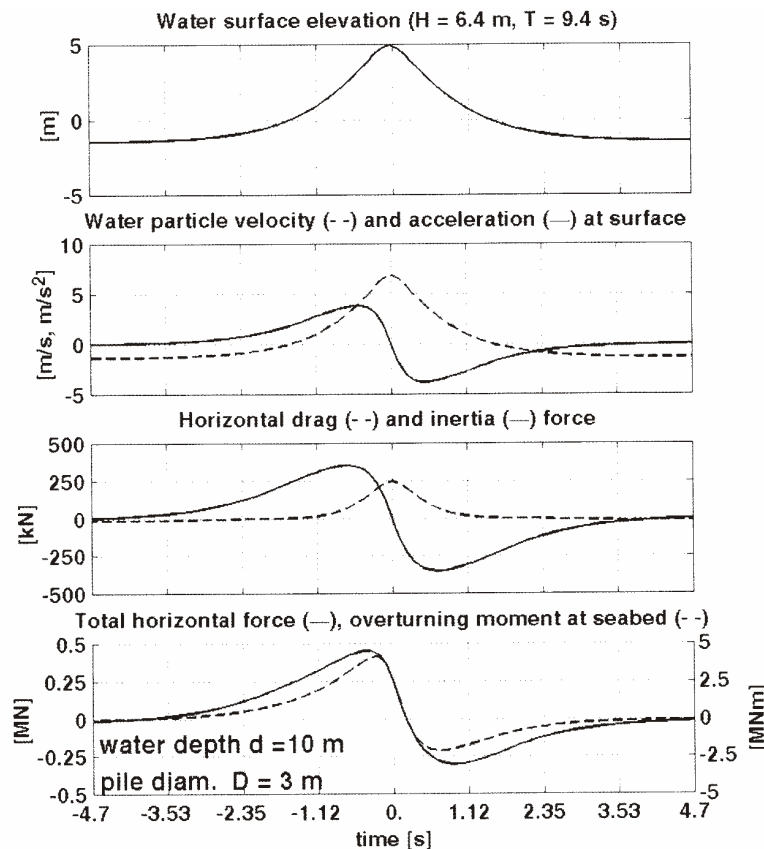


Figure 1.3: Kinematics and forces of an extreme wave in shallow water (from Kühn, 2002)

Shallow waters of 10 to 20 m can change dramatically with tidal range as in the Irish Sea

for example, where variations up to 8 m occur. Therefore, current induced forces should be included in the horizontal load. Apart from the horizontal load component, waves can induce an important vertical load component, pull and push during trough and crest respectively.

1.1.5 Seabed materials at the UK sites proposed

Table 1.3 gives a general description of the ground conditions in the UK sites proposed for the first round of wind farms. Figure 1.4(a) shows the seabed sediments in the Irish

Table 1.3: First round of wind farms in the United Kingdom

Area	Wind Farm	Site	Soil conditions sand over (clay over)	N°
Irish Sea	1 Robin Rigg	Solway Firth	medium & stiff clay	60
	2 Barrow†	Cumbria	medium & stiff clay	30
	3 North Hoyle†	North Wales	sand, bedrock & (bedrock)	30
	3 Rhyl Flats	North Wales	sand, medium & stiff clay	30
	4 Shell Flats	Lancashire	soft clay	90
	5 Burbo Bank	Liverpool Bay	sand, medium & stiff clay	30
Swansea Bay	Scaweather Sands	South Wales	(bedrock) & bedrock	30
Thames Estuary	Kentish Flats†	Kent	soft & stiff clay	30
	Gunfleet Sands	Essex	soft, medium & stiff clay	30
East Anglia / Skegness	Scroby Sands†	Norfolk	sand	30
	Cromer	Norfolk	medium clay & bedrock	30
	Inner Dowsing	Lincolnshire	medium clay & bedrock	30
	Lynn	Lincolnshire	medium clay & bedrock	30
Northeast	Teeside	Cleveland	bedrock & (bedrock)	30

†operating, N°: number of turbines

Sea and the sites of wind farms projected. There is mostly sand, corresponding to sand banks. These sand banks are underlain by clay, bedrock or simply sand continues deeper. However, there are also some sites with clay underlain by bedrock. A particular feature of the sand banks is their regular mobility caused by tides and currents. This phenomenon will cause sediment transport and scour, which will require a rip-rap or other form of protection around the suction caissons (HR Wallingford, 2004). This issue is not considered in this thesis.

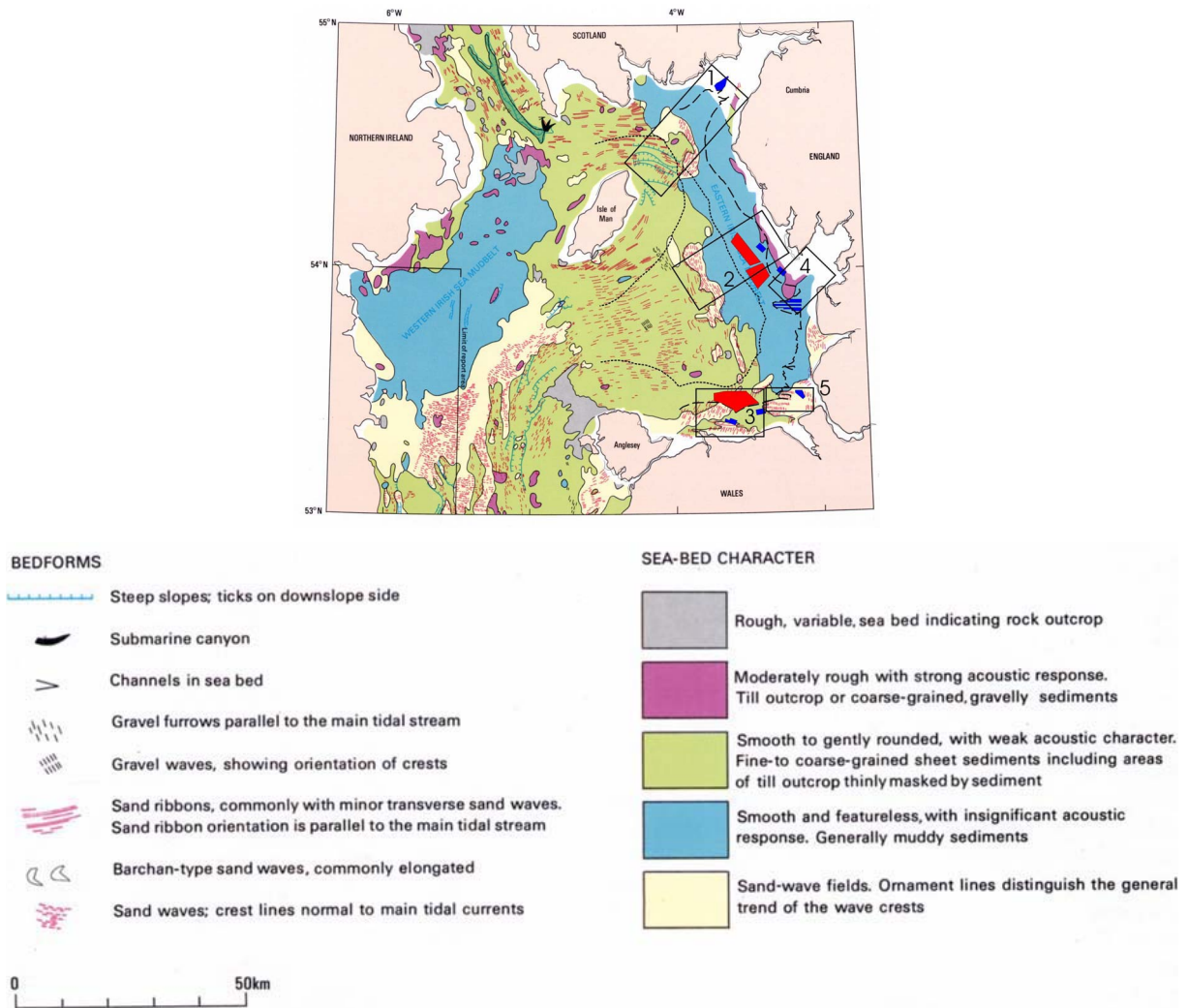


Figure 1.4: Seabed sediments in the Irish Sea, showing sites for offshore wind farm projects (British Geological Survey, 2004)

1.1.6 Existing foundation options for offshore wind turbines

According to Table 1.1 monopile foundations have dominated the offshore wind energy projects followed by gravity bases (see Figure 1.5(a)). It is important to realize that the increase of the turbine size above 3 MW implies larger loads acting on the turbine base, and hence, larger foundations. Indicative of this situation is the fact that the monopile diameters in the recent projects of Kentish Flats and Egmond are 4 m and 4.6 m respectively (Figure 1.5(b)), significantly larger than usual offshore driven piles. Moreover, the 5 MW world's largest wind turbine, the Beatrice offshore wind farm in the Moray Firth, Scotland, has been erected in 45 m water depth. The tower rests on jacket structures of 50 m height, which are founded on four piles (Figure 1.5(c)). Finally,

Figure 1.5(d) shows a very large reinforced concrete cylinder founded on piles for a 4.5 MW turbine project in Ems-Emden, Germany.

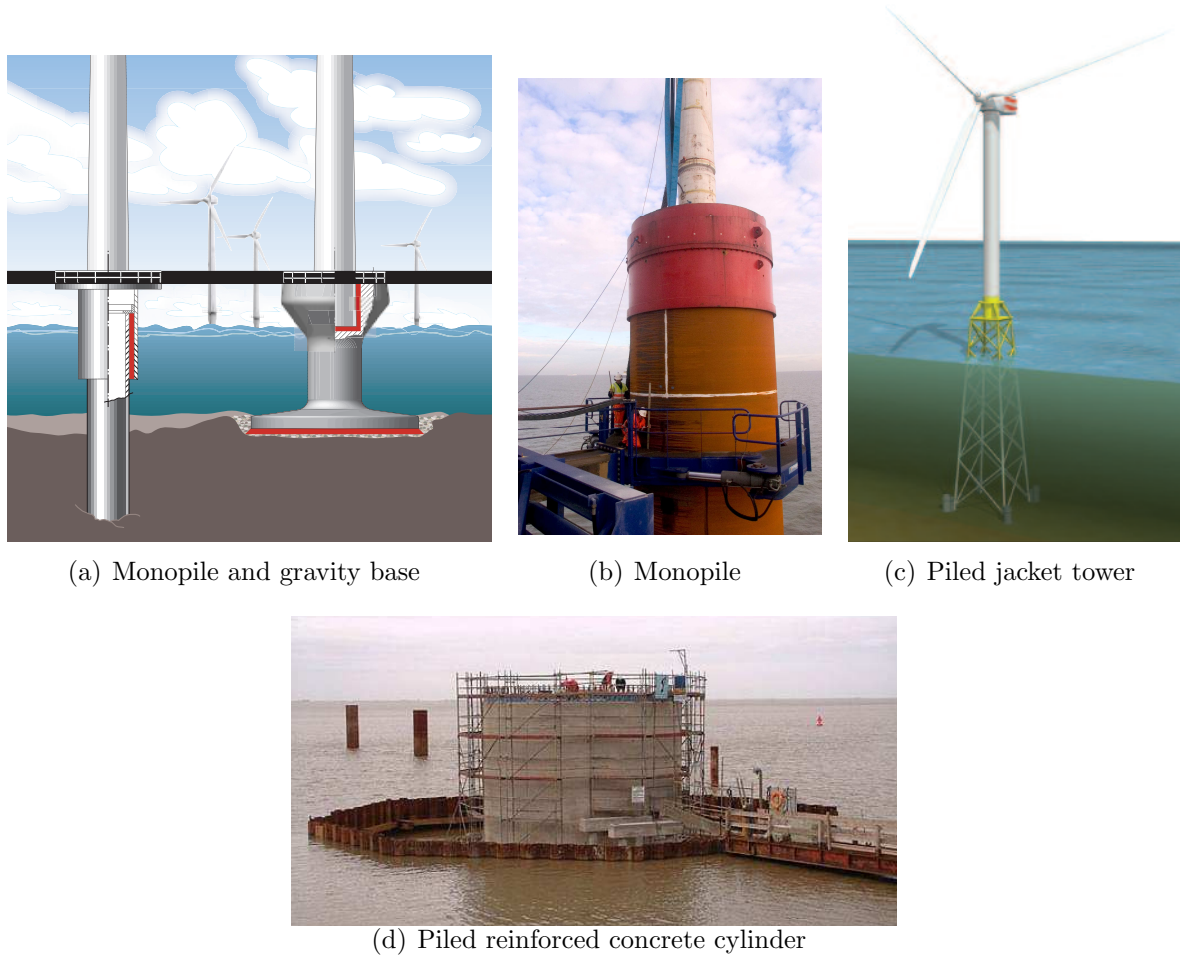


Figure 1.5: Existing foundation options for offshore wind turbines. Source: (a) www.densit.com, (b) www.kentishflats.co.uk, (c) www.beatrice.co.uk, and (d) www.enova.de

The existing foundation solutions adopted for large turbines seem to be cumbersome, time and resource consuming. As a result cheaper and simpler solutions are being sought by researchers and engineers. It has been proposed that suction caisson foundations, used previously as anchors in deep waters and as shallow foundations for oil rigs, might be a better alternative from the economic, technical and environmental point of view.

1.1.7 Suction caisson foundations

Suction caissons acquire the name from the fact that a *caisson* is a large water-tight box where the pressure inside differs from the atmospheric pressure. *Suction* corresponds to the negative pressure or underpressure applied inside the caisson to extract water and

in this way penetrate the caisson skirts into the ground. Because in shape they resemble an upside-down bucket, suction caissons have also been called suction buckets.

Suction caissons have demonstrated to be more efficient than piles, in terms of installation time in applications for the oil and gas industry (Andersen and Jostad, 1999). These issues acquire more importance in offshore applications where harsher weather conditions are prevalent. The efficiency in the installation of suction caissons relies on the use of pumps rather than large and heavy hammers used to drive piles, not to mention socketed and grouted piles, which require predrilled holes. Furthermore, suction caissons can be removed easily (by changing the suction to overpressure), making them more versatile and environmentally friendly, as compared with piled foundations.

Figures 1.6(a) and 1.6(b) show the two suction caisson configurations described by Houlsby and Byrne (2000) for offshore wind turbines. Figure 1.6(a) corresponds to a monopod suction caisson foundation, and Figure 1.6(b) depicts a multiple suction caisson foundation, tripod or tetrapod. Each configuration has a predominant loading system. In the first alternative the horizontal loads at the hub and at the wave-breaking level leads to a resultant overturning moment of 120 MNm which is transmitted directly to the foundation. Whilst in the second alternative the same moment is transferred through the lattice to the foundation as tensile and compressive vertical loads.

In the study of structure-foundation interaction problems attention should be paid to the substantial differences between for instance the jack-up problem and the wind turbine problem, as pointed out by Houlsby and Byrne (2000). Firstly, the water depth for oil and gas structures is much deeper than for wind turbines, in the order of 100 m for fixed structures and up to 2000 m for floating structures (Sparrevik, 2002). By contrast, the water depth at the sites designated by Crown Estates for the wind farm projects is between 10 m and 20 m. Secondly, the state of loading also differs since oil rigs are fairly heavy structures. Then gravity forces dominate over environmental forces. Conversely, offshore wind turbines are slender and light structures. Therefore, the environmental

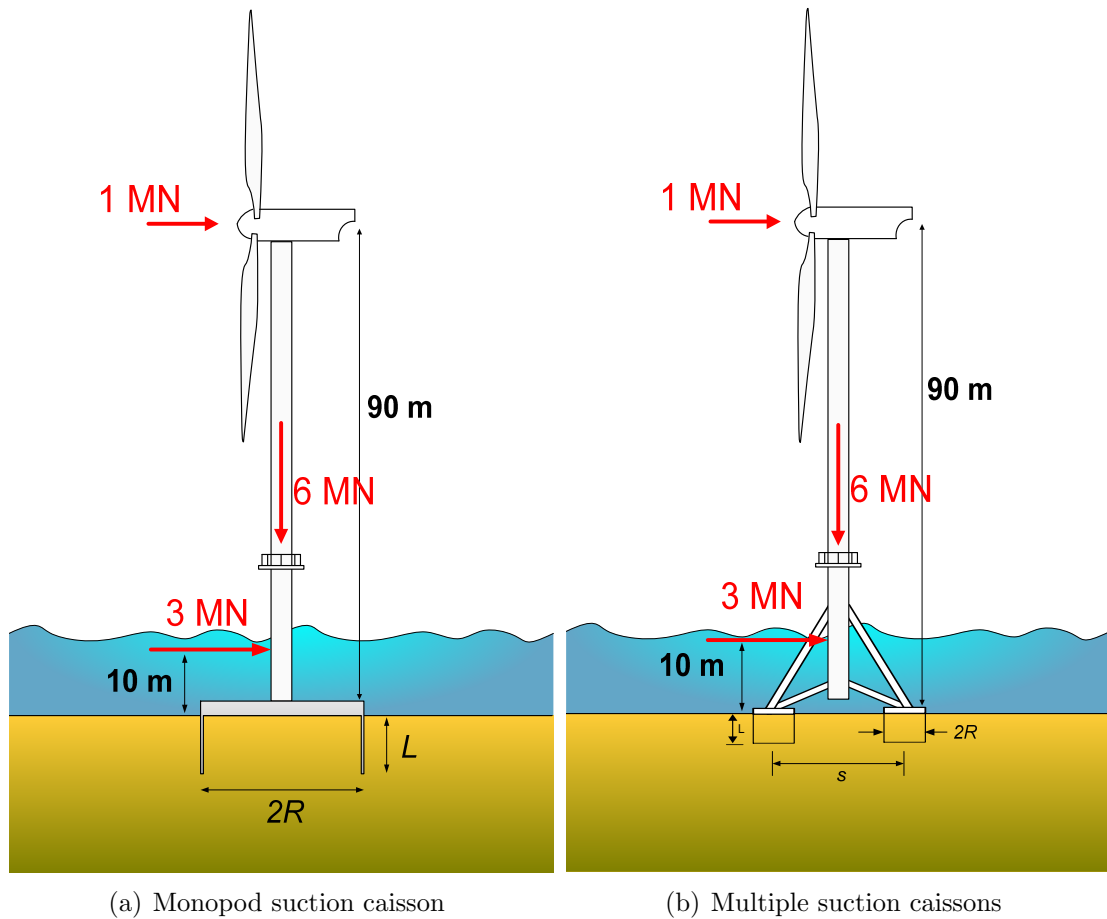


Figure 1.6: Typical loads and dimensions for a 3.5 MW turbine showing different foundations forces are much larger as a proportion of the gravity forces (Byrne and Houlsby, 2003). A comparison of typical extreme load values for a 3.5 MW wind turbine is shown in Figures 1.6(a) and 1.6(b).

It is important to highlight that the foundation cost has a strong influence on the total cost of offshore wind farm projects, typically being between 15% and 40% (Houlsby and Byrne, 2000). Feld *et al.* (1999) reported that the cost of the gravity base foundations at Vindeby and Tunø Knob represented 23% of the total costs of the wind farm. Feld *et al.* also determined that a tripod caisson reduces the footing steel by up to 34% in comparison with a tripod pile for the case of very hard clay (Rødsand), whereas for dense sand only 6% would be saved (Horns Rev). Moreover, Ibsen *et al.* (2003) indicated that in the Horns Rev project the foundation total costs comprised of 8% design, 46% steel and 46% installation. In addition, it was estimated that monopod suction caissons

can save up to 25% of steel compared with monopiles. However, an economic study carried out by Beresford (2003) contradicts the above estimate for the Kentish Flats and Solway Firth wind farm projects. Accounting only for the materials involved, Beresford (2003) determined that a monopile is the cheapest solution (*ca.* £80k) compared with: i) tetrapod piles (*ca.* £160k), ii) monopod caisson (*ca.* £400k in sand and *ca.* £300k in clay), and iii) tetrapod caissons (*ca.* £280k in sand and clay). However, the variable costs of installation can be easily equal or even higher than the fixed costs of materials and design. For instance, in the Scroby Sands project 30% of the foundation cost was equally split between fix and variable costs, without any unexpected delay owing to good weather. Variable costs were mostly controlled by the hire of a barge for £50k/day.

In October 2002 the first monopod suction caisson ($2R = 12$ m, $L = 6$ m) was installed into the sand of Frederikshavn. However, caisson foundations have not yet been installed offshore.

Finally, it is thought that a wind turbine could be completely assembled onshore and then transported and installed at once using suction caisson foundations. This possibility is an extraordinary advantage over the existing foundation options since it is an efficient use of time and resources.

1.2 SHALLOW FOUNDATION RESEARCH

1.2.1 Elastic behaviour

A compendium of linear-elastic solutions for flat, rigid footings resting on a homogeneous half space can be found in Poulos and Davis (1974), and a more instructive and pedagogic source in Davis and Selvadurai (1996). Bell (1991) and Ngo-Tran (1996) extended those solutions to the case of embedded footings. Using the scaled boundary finite element method Doherty and Deeks (2003) determine the solutions (stiffness coefficients) for *rigid caissons* embedded in non-homogeneous elastic soil. Subsequently, Doherty *et*

al. (2005) extend the analysis to caissons with *flexible skirts*. Elastic solutions are based on two soil parameters: the Poisson's ratio and the shear modulus. Whilst for the former values usually adopted are 0.5 for clays and 0.2 for sands, determination of the latter is not straightforward. From several resonant column tests conducted at small strain amplitudes reported by Hardin and Richart (1963) amongst others, it was found that the shear modulus varies with the specific volume and is a power function of the current level of stresses with exponent n . Mitchell and Soga (2005) present a summary of shear modulus functions for different type of soils with values of $n = 0.5 \pm 0.1$.

1.2.2 Bearing capacity and plasticity models

Methods of calculation based on Terzaghi (1943) bearing capacity formulation have been widely adopted in practice for the analysis of shallow foundations. This formulation superposes linearly the effects of soil cohesion, surcharge and weight. Meyerhof (1951), Brinch Hansen (1970) and Vesic (1975) developed methods that include factors to the original formulation to account for footing shape and depth; load inclination and eccentricity. Although these procedures of calculation are very similar, differences exist in the factor expressions. Furthermore, they are limited to the case of foundation collapse as a general shear failure, without providing information about previous or later stages of loading let alone footing displacements.

A different approach based on the concept of “yield” rather than “collapse” has been increasingly adopted by researchers. Houlsby and Byrne (2001) discuss the advantages of using a yield surface approach instead of the usual bearing capacity calculation approach. They point out that actually such an approach was initiated by Roscoe and Schofield in 1957 when envelopes of normalised forces were used to analyse the interaction between a steel frame and its foundations. So, the concept of force-resultant model was introduced by Roscoe and Schofield (1957), in which the structure response can be integrated with the foundation response and vice versa.

Embracing this concept Ticof (1977) carried out several series of load-controlled lateral loading tests on a flat, rough strip model footing resting on sand. He found that the data was well fitted by a symmetric parabolic envelope in the horizontal-vertical load $H - V$ plane, and an elliptical envelope in the moment-horizontal load $M - H$ plane. From these findings Butterfield and Ticof (1979) suggested a three dimensional “cigar shaped” yield surface in the $V - M - H$ space.

The cigar shaped yield surface was later verified by Georgiadis and Butterfield (1988) on dense, dry sand. Subsequently, Tan (1990) studied combined loading on saturated sand of conical and spudcan footings for applications to jack-up units in deep water. He established an analogy between the Cam Clay critical state model to analyse the response of soils in triaxial testing and the force-resultant model to analyse the combined loading of shallow foundations. Tan (1990) carried out “sideswipe” tests in the drum and beam centrifuges at Cambridge. A sideswipe test is defined as the application of horizontal displacement to a footing whilst keeping constant the vertical displacement, in analogy to an undrained triaxial test. Under certain conditions of foundation stiffness sideswipe events trace very closely the yield surface. Moreover, the concept of critical state in soils led to the concept of a parallel point or parallel line, which establishes the state of transition between settlement and uplift of a foundation. “Parallel” refers to the flow vectors being parallel to the H and M axis. Although, Tan proposed a non symmetrical yield surface and plastic potential, his study only included results in the $H - V$ plane, omitting moment and rotation from the analysis. Later Dean *et al.* (1992) continued Tan’s (1990) work introducing moment into the analysis.

Nova and Montrasio (1991) performed load-controlled tests using a system of weights and pulleys to apply combined loadings to a *strip footing* on a loose, silica sand. From the test results a work-hardening plasticity model with a non-associated flow rule was constructed within what it was referred to as a macro-element framework . This plasticity model consisted of: i) an empirical hardening law obtained from vertical load-penetration tests, ii) a yield surface, and iii) a plastic potential. Elastic analysis was considered in-

adequate in predicting displacements during combined loading according to Nova and Montrasio (1991). Further tests using a *circular footing* on a dense sand were analysed by Montrasio and Nova (1997), concluding that the shape of the yield surface was not affected by the circular footing shape, but the shape parameters introduced vary linearly with the foundation embedment.

Further experimental support for a “cigar shaped” yield surface composed of parabolas and ellipses was provided by Gottardi and Butterfield (1993, 1995) and Butterfield and Gottardi (1994). A step forward was undertaken by Martin (1994), who designed and constructed an advanced three-degree-of-freedom (3DOF) apparatus able to apply to a footing simultaneously vertical, rotational and horizontal displacements $(w, 2R\theta, u)$ and obtain the corresponding loads (V, M, H) . Martin conducted a comprehensive series of tests using spudcan footings on heavily overconsolidated Speswhite Kaolin clay. The testing programme included horizontal and rotational swipe events under various load ratios $\frac{M}{2RH}$ as well as moment and horizontal loading events under constant vertical load at different $\frac{M}{2RH}$ ratios. Martin concluded that the shape of the yield surface remained constant regardless of its expansion, the size of the yield surface increased with the footing penetration, and elastic behaviour occurred within the yield surface. Furthermore, a work-hardening plasticity formulation referred to as ‘Model B’ was developed, which was included in a structural analysis program suitable for the analysis of jack-up units. Overall, Martin’s (1994) work encapsulates the complete construction and application of a force-resultant model based on experimental data. Details of model B appear also in Houlsby and Martin (1992) and Martin and Houlsby (1999, 2000, 2001).

The effect of loading rate was investigated by Mangal (1999), who conducted using Martin’s 3DOF loading rig, *partially drained* loading tests using circular flat footings on a fine, oil-saturated sand. Mangal (1999) found in monotonic vertical loading tests (from velocities between 0.001 mm/s to 5 mm/s) that the initial foundation stiffness increased with rate. But after a penetration as small as $\frac{w}{2R} = 0.0003$ the stiffness reduced to values similar to those under drained conditions. From swipe tests with alternating slow and

rapid rates he found that the yield surface expands with rate. However, these experimental findings have not yet been interpreted within a rate dependent theoretical framework.

Using the 3DOF loading apparatus designed by Martin (1994), Gottardi *et al.* (1999) undertook a comprehensive programme of displacement-controlled tests using *circular flat footings* on dense sand with the purpose of developing work-hardening plasticity models. Based on the experimental results obtained by Gottardi *et al.* (1999) an extension of the modelling of spudcan footings for jack-ups on dense sands was carried out by Cassidy (1999) and Houlsby and Cassidy (2002). They developed a plastic potential function to define the flow rule. Association factors were introduced to account for strong non-associative response found in the experimental results. The constructed model, referred to as 'Model C', predicts the response of drained-monotonic combined loading. Based on experimental results reported Byrne and Houlsby (2001) using a flat footing on a crushable and very compressible carbonate sand, an extension of Model C was carried out by Cassidy *et al.* (2002). The implementation of a hardening law that is a function not only of the plastic vertical displacement, but also of the plastic horizontal and rotational displacements was found to improve the modelling.

Force-resultant models reduce the soil-footing interaction problem to the analysis of loads and displacements at one load reference point (LRP). Houlsby (2003) points out that changes of the LRP modify the moment, horizontal and vertical displacements, which in turn affect the value of the elastic stiffness coefficients and the parameter values of the yield surface. The reduction of the analysis to the LRP, ignoring the modelling of the soil, is a very useful simplification that allows the simulation of complex soil-footing interaction problems. Model B and Model C can successfully predict monotonic plastic behaviour. Force-resultant models have also been formulated for other geotechnical applications such as rock impacts and soil-pipe interaction (Nova and di Prisco, 2003). However, elasticity, loading rate effects and cyclic loading are not yet well modelled; the presence of localized stress effects, for instance the phenomena of liquefaction and scour can limit the applications of these models (Houlsby, 2003).

The extension of the yield surface formulation from planar loads to general loads, *i.e.* vertical load, two perpendicular moments, two perpendicular horizontal loads and torsional load, was proposed by Martin (1994). Houlsby (2003) extended model C to carry out a six-degree-of-freedom (6DOF) modelling of jack up foundations. Because of the necessity to verify experimentally 6DOF models, Byrne and Houlsby (2005) designed and constructed a spatial loading apparatus. Using the 6DOF apparatus, Bienen *et al.* (2006) report the results of spatial combined loading tests of a circular, rough flat footing on dry, loose sand. By means of horizontal, rotational and torsional swipe tests and radial displacement tests Bienen *et al.* assess the yield surface, the plastic potential and the hardening law. The parameter values of the yield surface agreed with the values obtained in previous 3DOF studies. The new yield surface parameter related with torsion was determined as well as the torsional association factor for the plastic potential. It was found that a higher degree of non-association was required to describe torsion. The proposed hardening law considered the contribution of the six plastic displacement components.

1.2.3 Research on suction caisson foundations

The search for improving anchorage systems for military submarine applications led to the idea that an inverted ‘cup’ subjected to vacuum might be a feasible solution (if not the only one) to the anchoring problem as considered by Goodman *et al.* in 1961. Suction installed skirted footings were not commercially used until 1980 (Senpere and Auvergne, 1982). However, it was in early nineties that extended use in mooring applications for floating production units took place. The first permanent suction caissons were installed in 1995, and nowadays there are more than 485 suction caissons installed worldwide (Andersen *et al.*, 2005). Although, Ibsen *et al.* (2003) report the suction assisted installation of a 12 m diameter caisson for a wind turbine in Frederikshavn, there is not yet an offshore installation for such an application. A summary of past laboratory research into suction caissons carried out around the world is presented in Table 1.4.

Senpere and Auvergne (1982) reported practical information related to suction pile installations in the North Sea. The soil conditions were a layer of five to six metres of dense sand overlying one or two metres of soft clay followed by stiff clay with caisson diameter $2R$ of 3.5 m, skirt length L of 9 m and skirt thickness t of 25 mm. For the Gullfaks C project Tjelta *et al.* (1986) presented field tests of a concrete suction caisson ($2R = 6.5$ m, $L = 22$ m and $t = 0.4$ m) installed into soft clay overlying medium dense sand layers and clayey sands at a very high suction level with a maximum of 500 kPa. However, the caisson penetration of the Gullfaks C platform was mostly due to self-weight with little suction. The Draupner E (formerly Europipe 16/11) and Sleipner T jacket projects demonstrated the feasibility of suction caissons penetrating very dense sands, which was initially verified in field tests ($2R = 1.5$ m, $L = 1.7$ m, $t = 12$ mm) and in laboratory tests ($2R = 550$ mm, $L = 300$ mm). These examples of successful installation of suction caissons demonstrated not only that the caisson skirt penetration into very dense sand is achievable, but also that suction caissons are an economically advantageous alternative to piled foundations (Tjelta, 1994, 1995).

Dyvik *et al.* (1993) reported the performance a series of static and cyclic loading tests on soft clay using large caissons intended to work as a cellular foundation for a tension leg platform TLP and floating structures. Andersen *et al.* (1993) showed that predictions (obtained from limit equilibrium and FE analysis) of pullout agreed very well with the experimental results, and upper limit predictions of cyclic vertical displacements were closer to the experimental results than lower limit predictions. As a result, suction caisson foundations have been preferred over piles and drag anchors for fixed and floating offshore platforms and in a wide range of other oil and gas facilities (Andersen and Jostad, 1999).

Aldwinckle (1994) carried out a study of the suction installation problem in sand, where the pore pressure variation was estimated during the penetration of the skirt. A *pressure factor* was introduced to account for the variation of pore pressure inside and outside the caisson, variation created by the hydraulic gradient caused by the suction. It was determined that the pressure factor diminishes exponentially with the skirt penetration

Table 1.4: Laboratory research on suction caissons (adapted from Byrne, 2000)

Reference	Soil ¹	Footing geometry $2R$ (L), mm	Loading ²	Test type ³
Goodman <i>et al.</i> , 1961	M, C, S	79 (99), 89 (188)	m V	installation
Brown & Nacci, 1971	S	254 (44.5)	m V	pullout
Helfrich <i>et al.</i> , 1976	S	415 (250)	m V	pullout
Wang <i>et al.</i> , 1977	S, M, C	111 (9.5, 55) 140 (13, 70) 200 (14.5, 82.6) 337 (35, 162)	m V	pullout
Larsen, 1989	S, C	104, 204, 305 (450)	m,c H	pullout
Steenen-Bach, 1992	S, C	48 (80, 96, 160) 65 (108, 130, 216) 80 (133, 160, 266)	m V	pullout
Clukey & Morrison, 1995	C	152.5 (305)	m,c V, V:H	100g pullout
Rao <i>et al.</i> , 1997	C	75 (75, 112.5, 150)	m V	pullout
Whittle <i>et al.</i> , 1998	C	50.8 (51)	m V	pullout
Randolph <i>et al.</i> , 1998	MCa	45 (106)	m,c H, V:H	120g
El-Gharbawy, 1998	C	125 (250) 100 (400, 600) 50 (600)	m,c V, V:H	pullout
Watson, 1999	C, MCa SCa	60 (25)	m,c V, H, m,c V:H	100g 150g
Allersma <i>et al.</i> , 1999	S, C	60 (67)	m H	150g
Allersma <i>et al.</i> , 1999b	S, C	60 (70)	m, c V	150g
Byrne, 2000	S	100 (16, 33, 66) 150 (50) 300 (100)	m, c V:M:H m, c V	dry sand oil saturated
Feld, 2001	S	200 (50, 100, 150, 200)	m V:M:H	pullout
House, 2002	C,MCa C	30, 40 (120), 46 (100) 10.4, 15.9, 37.2 (302.6) 40 (15), 32 (27), 25 (45) 22 (61), 19 (71)	m, c V m,c V:H	120g installation pullout
Byrne & Cassidy, 2002; Cassidy <i>et al.</i> , 2004	C	60 (15, 30, 60)	m, c V:M:H	100g
Rauch <i>et al.</i> , 2003	C	102 (910)	m V	installation
Chen & Randolph, 2004	C	30 (120)	m V	100g
Tran <i>et al.</i> , 2004, 2005	S	100 (100), 70, 80 (140) 60 (60), 70 (120)	m V	installation 100g
Kelly <i>et al.</i> , 2003, 2004, 2006a, 2006b	S, C	280 (180), 150, 200 (100) 150, 200 (100)	m, c V c V:M:H	pullout

¹ Sand, Clay, M as silt, and Calcareous; ² monotonic, cyclic, Vertical, Moment, and Horizontal;

³ experimental work at 1g, otherwise indicated

and increases with the permeability ratio, which is defined as the permeability of the soil inside the caisson divided by the permeability of the soil outside the caisson. The suction estimated by Aldwinckle (1994) agreed with experimental results obtained by Charles (1994). This work was continued by Houlsby and Byrne (2005b), who used theories for the analysis of open-ended piles, lateral earth pressure and bearing capacity to develop calculation procedures to design the installation of suction caissons.

The use of suction caissons for offshore wind turbines was mentioned as an alternative to gravity bases and piles by Ferguson (1998) and proposed by Houlsby and Byrne (2000) and Byrne (2000). One of the first studies of caissons for offshore wind turbines in sand was carried out by Feld (2001), who analysed the change in effective stresses (inside, outside and at the tip of the caisson skirt) due to the suction using a CPT approach. However, the tip resistance and the friction forces could not be related directly to CPT measurements of sleeve friction f_s and cone resistance q_c .

Byrne (2000) planned a testing programme in which the experimental results were interpreted within work-hardening plasticity models. To this end Byrne modified Martin's 3DOF apparatus to accommodate higher loads and wrote a computer program that enabled independent feedback control on each loading axis, using an updated data acquisition system. Results from horizontal swipe tests in dry sand under the same load ratio $\frac{M}{2RH}$ revealed that the induced rotation increases with the caisson aspect ratio $\frac{L}{2R}$, from zero for flat footings to a value close to the applied horizontal displacement $\frac{u}{2R}$ for $\frac{L}{2R} = 0.66$. Loads were normalised by V_u , the ultimate bearing capacity of a flat footing. The normalised lateral capacity was similar for flat footings and skirted footings regardless the aspect ratio ($0.16 \leq \frac{L}{2R} \leq 0.66$) for a normalised vertical load $\frac{V'}{V_u} \leq 0.08$. However, for $0.1 < \frac{V'}{V_u} \leq 0.21$ skirted footings had higher lateral capacity than flat footings. In moment swipe tests the applied rotation caused an increase of the horizontal displacements with $\frac{L}{2R}$. Nevertheless the moment capacity was practically independent of $\frac{L}{2R}$. Parameter values of the yield surface were determined for caissons, extending Gottardi *et al.*'s (1999) data for flat footings.

Byrne (2000) observed a striking result in cyclic vertical loading in very dense, oil-saturated sand, which was also found by Johnson (1999) for caissons and Mangal (1999) for flat footings, that little foundation stiffness degradation occurred. Furthermore, the loading rate had also little effect on the caisson response under high mean vertical loads ($V_m > 100$ N, $\frac{V'}{\gamma'(2R)^3} > 3$). As a consequence, it would be possible to deduce the transient

response studying only monotonic loading. Similar conclusions were drawn from cyclic moment loading tests under constant vertical load. In addition, the moment capacity was found to be a function of the constant vertical load. Moreover, hysteresis loops complied with Masing behaviour and Pyke's rules since backbone curves captured the cyclic response. From rapid pullout tests, it was observed that the tensile response became softer than in compression and the absolute maximum tensile capacity was reached at the cavitation limit of the pore fluid.

Kelly *et al.* (2003, 2004, 2006b) performed a testing programme to study the vertical response of multiple caisson foundations. The experiments made use of a model suction caisson in a pressure chamber. Two dense water-saturated sands were employed in addition to the operation of a computer-controlled hydraulic actuator which applies loads as high as 100 kN and allows vertical displacements as fast as 100 mm/s. Using a fine sand ($D_{10} = 0.075$ mm) multiple-amplitude cyclic loading tests at 1 Hz and a mean vertical load $V_m = 35$ kN (568 kPa), were performed with and without a pressure in the chamber of 200 kPa, which simulates 20 m of water depth. Results from these tests indicated that the pressure increases the excess pore pressure by exactly 200 kPa. As a consequence, the increase in water depth makes a caisson foundation under rapid pullout less vulnerable to cavitation. Moreover, the generated excess pore pressures $\Delta u'$ increased linearly with the applied vertical stresses $\Delta \sigma'_v$ at a ratio as small as $\frac{\Delta u'}{\Delta \sigma'_v} = 0.044$. No evidence of unloading stiffness degradation was observed in a test of 1000 cycles conducted at 35 kN \pm 15 kN. The *incremental displacement* per cycle decreased with the number of cycles becoming very small after 200 cycles, and half of the *cumulative displacement* occurred also in the first 200 cycles. Pullout tests conducted at 5 mm/s and 100 mm/s revealed that the tensile capacity increases substantially with the extraction rate as well as with the pressure. However, the extraction distance required to reach those highest tensile loads increases as well. These results were used to validate the calculation procedure proposed by Houlsby *et al.* (2005c) to predict tensile loads under different rates. However, cyclic load histories experienced by the caisson before pullout can reduce significantly the tensile response. Such cases are not covered by the theory of Houlsby *et al.* (2005c).

Using a much finer sand ($D_{10} = 0.007$ mm) Kelly *et al.* (2004, 2006b) found that as the frequency increases (0.1 Hz, 1 Hz and 10 Hz) the caisson net penetration decreases for relatively similar packages of ‘positive’ cyclic loads. Additionally, $\frac{\Delta u'}{\Delta \sigma'_v}$ increased with frequency but to much higher values, namely 0.14 for 0.1 Hz, 0.25 for 1 Hz and exponentially for 10 Hz. The increase in excess pore water pressure was not only caused by the higher loading rates, but also by the much lower sand permeability, at least three orders of magnitude lower. For the experimental conditions chosen (positive loads and dense sands) it was concluded that for serviceability loadings the design is controlled by the foundation stiffness rather than by the ultimate resistance.

Recently, there has been growing interest in studying the installation of caissons into sandy soils. Sanham (2003) finds that the penetration rate depends on the suction level and the caisson weight. Using caissons of aspect ratios 1 and 1.3 and loose sand he finds that for the same caisson weight the higher the suction the faster the penetration (from 0.03 mm/s to 0.66 mm/s). Conversely, the caisson weight did not influence the penetration rate. Tran *et al.* (2004) installed caissons at very high penetration rates, namely 0.3 mm/s and 6.5 mm/s. Surprisingly, piping failure did not occur. Despite the large amounts of flow generated by the extremely rapid penetrations, it was found that the soil plug heave was less than in slow penetration tests. It was suggested that most of the large upward flow generated occurred next to the skirt wall, disturbing substantially only the soil near the skirt. Results from mini-cone penetration tests carried out by Tran *et al.* (2005) before and after the suction installation gave evidence of relative density reductions from 91% to 50% (though around the centre and not next to the skirt), which in turn reduced the permeability to half.

Field trials have been less reported since they are more expensive than laboratory testing. Also, field trials are more complicated since there is less variation and accurate control over the soil and loading conditions. However, information from field trials represents an invaluable opportunity to compare laboratory results and calibrate models. For oil and

gas structure applications, ten field trials of suction caisson have been reported according to Byrne (2000). For wind turbine applications, Ibsen *et al.* (2003) described the installation and lateral loading trials of large scale suction caissons ($2R = 4$ m and 2 m, $\frac{L}{2R} = 1$) in Frederikshavn, site of the first installed prototype monopod caisson (section §1.1.7). Ibsen *et al.* mentioned that when critical suction was reached, piping in the sand adjacent to the skirt occurred, which halted irreversibly further penetration of the caisson.

Houlsby *et al.* (2005a, 2006) have reported two field trial programmes: at Bothkenar for clay and at Luce Bay for sand. The field trials were designed to install by suction large suction caissons and to subsequently apply monotonic and cyclic load paths. A hysteretic response was found from cyclic moment tests, evidence was found of gapping under large rotations and decay of the secant stiffness with the increase of rotation amplitude occurred. The tensile capacity obtained from pullout tests was limited by the capacity of the equipment. Kelly *et al.* (2006a) carried out tests to shadow the above field test results to study scale effects. Normalisation procedures were proposed for caisson stiffness and capacity. The derived scaling relationships performed better for small displacements rather than for large displacements.

Ibsen *et al.* (2005) reported the monitoring of deformations and pore pressures in the monopod caisson foundation in Frederikshavn. Measurements on the Vestas V90 3 MW turbine considered natural frequencies in operational mode, idling conditions, turbine without blades and nacelle. During operation the first mode of vibration was around 0.3 Hz (rotor excitation between 10 and 20 rpm) and the second mode between 0.5 and 1 Hz corresponded to the rotation of the blades. Knowledge of the excitation frequencies of the structure is fundamental, since the foundation design should avoid undesirable deformations due to resonance.

1.2.4 A new theoretical approach

Theoretical research based on finite element analysis and upper and lower bound theorems has been mostly dedicated to caissons in clayey soils. Those analysis as well as work-hardening plasticity models such as Model B and Model C have been limited to the modelling of monotonic behaviour. Although multiple yield surface models implemented within plasticity theory can cope with cyclic behaviour, these models become inevitably more complex with several parameters to determine. A new theory based on the work of Ziegler (1977, 1983) makes it possible to derive complete constitutive models from only two potential functions. Houlsby (1981) used this theory to derive plasticity models such as the modified Cam Clay model. The derived constitutive models automatically respect the first and second law of thermodynamics. This theory has been entitled *hyperplasticity* and has been further extended by Collins and Houlsby (1997) and Houlsby and Puzrin (2000). Hyperplasticity theory has been recently adopted by Nguyen-Sy (2006) to derive a model to analyse circular shallow foundations in three dimensions. Nguyen-Sy (2006) first validated the hyperplasticity model called ISIS, analysing monotonic loading of flat and spudcan footings on clay and sand to subsequently compare these results with results from Model B and Model C. This version of ISIS considered one yield surface, three dimensions and rate independence. To study cyclic behaviour a discretization of the continuous hyperplasticity model was performed, introducing a finite number (rather than infinite) of yield surfaces and mixed isotropic-kinematic hardening functions following Puzrin and Houlsby (2001, 2003). Isotropic hardening expands or contracts the current yield surface, whereas kinematic hardening translates the yield surface. An expression of the yield surface that can incorporate tensile capacity, which indeed suction caissons possess, was proposed by Nguyen-Sy and Houlsby (2005). The multiple-yield-surface model ISIS proved to be powerful in modelling Masing hysteretic behaviour of cyclically rotated caisson foundations.

1.3 THE NEED FOR MORE RESEARCH

Significant research has been recently devoted to the study of multiple caisson foundations (tripods and tetrapods), thanks to the work of Kelly *et al.* (2003, 2004, 2006b). Rather less attention has been paid to monopod caisson foundations. Investigation of tetrapod foundations has mainly concentrated on dense sands and positive cyclic vertical loadings. Additionally, the effect of suction installation has not yet been included. Moreover, transient loading of caissons in clay at low mean vertical loads, which includes negative cyclic loading, has not yet been covered by field or laboratory testing programmes. Furthermore, according to Table 1.4 the majority of the past laboratory work has covered ratios $\frac{V'}{\gamma'(2R)^3}$ greater than 1, whereas in the offshore wind problem that ratio is less than 1. Previous research considered principally high levels of V' compared with H and M , since applications were intended to be for heavy oil rigs.

Although preliminary studies provide valuable information, for instance Tran *et al.* (2004) describe effects of penetration rate caused by different suction levels applied, it is necessary to interpret experimental results within a theory able to capture the variables that influence the load-penetration response.

The studies of suction caissons have been limited to consider a sequence of different load paths. Some studies have disregarded completely the installation process. Moreover, the complete vertical loading response, including failure and post failure, has not yet been studied. Assessment of the effects of installation method, by pushing and by suction, on subsequent vertical and moment loading has not yet been considered. Although the tensile capacity has been extensively studied in sand, it has been neglected in the analysis of the yield surface; instead the yield surface for flat footings or spudcan footings has been adopted. Furthermore, since swipe tests involve only deviatoric displacements (rotational and horizontal) the studies of the flow rule have overlooked the vertical displacement variation.

No explanation has been given for the absence of loading rate effect in cyclic vertical loading tests. Interpretation of the excess pore pressures developed during the cycles is required, since it has been shown by Byrne (2000) that in dense sands pore pressure build up can cause a softer response without losing considerable strength, whereas in loose sands stiffness degradation is highly likely to occur. However, it is not known whether the developing of suction inside the caisson may impede any degradation or not.

Finally, Nguyen-Sy (2006) demonstrated that hyperplasticity is a powerful theory in the modelling of cyclic behaviour of shallow foundations. This thesis attempts to provide physical understanding by means of experimental results. The results will be interpreted using a theoretical model. This will allow the determination of parameter values within hyperplasticity models, and their subsequent validations. Comparisons with results obtained from tests with large scale caissons will be also pursued, in particular from the programme of testing performed by Houlsby *et al.* (2005a, 2006).

1.3.1 Research objectives

The objective of this thesis was to contribute to the construction of hyperplasticity models for the analysis of suction caisson foundations. This objective is aimed to the

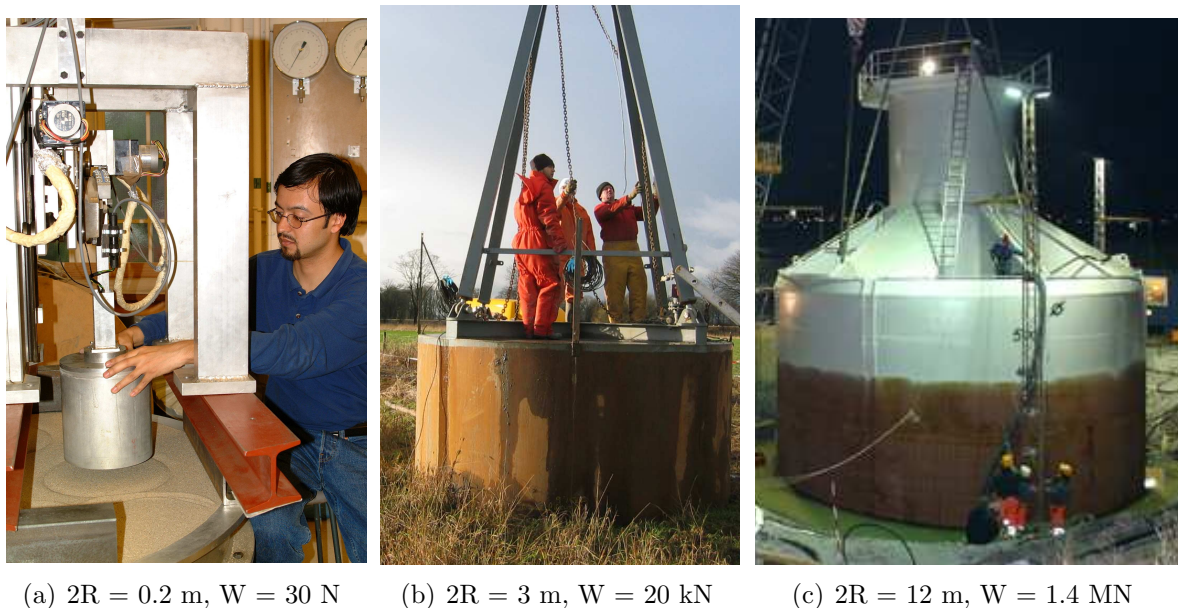


Figure 1.7: Caisson footings showing diameter $2R$ and weight W : (a) in the soil mechanics laboratory, (b) in the field site at Bothkennar, and (c) at Frederikshavn, taken from www.hornsrev.dk

development of design procedures for caisson foundations for offshore wind turbines. To accomplish this objective, it is necessary to extrapolate laboratory results not only to field trials, but obviously to prototype foundations. Figures 1.7(a), 1.7(b) and 1.7(c) illustrate three size and weight of caissons. The first corresponds to a model caisson tested in the laboratory that can be held with the hands. The second is a model caisson tested in the field that is easily moved with one crane. The third is a caisson foundation for an offshore wind turbine moved with three cranes.

In order to extrapolate the results from the laboratory to prototypes loads, displacements, pore pressure, stiffness, *etc.* will be normalised along this thesis using scaling expressions derived from dimensional analysis.

Chapter 2

SOIL SPECIMENS AND APPARATUS

Abstract

This chapter describes the main properties and characteristics of the soils used in the experiments. The preparation of soil specimens are also described. Descriptions of the model caissons designed are presented, and boundary conditions are explained. Finally, the loading apparatus is described.

2.1 SOIL SPECIMENS MODELLED

Two types of *dry* sand have been used in this investigation to study drained behaviour: Dogs Bay and White Leighton Buzzard. For the study of partially drained and undrained behaviour two other sands have been used in *fully saturated* conditions: Baskarp Cyclone and Redhill 110. A further series of undrained tests were carried out in the extensively used and studied Speswhite kaolin clay. Standard laboratory tests were deemed unnecessary since properties of these soils have been characterised in a number of previous experimental studies undertaken at the University of Oxford and elsewhere. The soil properties are summarised in Tables 2.1 and 2.3 for the sands and the clay respectively. Figure 2.1 shows the grading curves for the sands.

Table 2.1: Properties of the different sands used in the experiments

Property	Dogs Bay (Nutt, 1993)	Leighton Buzzard (Schnaid, 1990)	Baskarp Cyclone (Mangal, 1999; Byrne, 2000)	Redhill 110 (Kelly <i>et al.</i> , 2004)
Mineralogy	carbonate	silica	silica	silica
D_{10} : mm	0.11	0.63	0.018	0.08
D_{30} : mm	0.18	0.70	0.038	0.10
D_{50} : mm	0.24	0.80	0.058	0.12
D_{60} : mm	0.29	0.85	0.069	0.13
C_u	2.66	1.36	3.87	1.63
C_c	1.00	0.92	1.16	0.96
G_s	2.75	2.65	2.69	2.65
γ_{dmin} : kN/m ³	9.52	14.65	12.72	12.76
γ_{dmax} : kN/m ³	13.60	17.58	16.85	16.80
v_{min}	1.984	1.479	1.566	1.547
v_{max}	2.834	1.774	2.075	2.037
ϕ'_{cs} : (°)	40.3	33	32.5	36

2.1.1 Dogs Bay sand

This is a biogenic carbonate sand from the west coast of Ireland and as can be observed in Figure 2.2(a), consists of a large proportion of broken skeletal mollusc fragments in the form of plates, hollow globules and tubes with the carbonate content ranging from 87% to 92% (Evans, 1987). It is a problematic soil in the sense that its angular particles can lead to high initial specific volumes. Moreover, it is a brittle material that breaks easily under load; since it is uniformly graded the breakage of particles is maximised (Coop *et al.*, 2004). However, Nutt (1993) found that the influence of the breakage on the internal friction angle is negligible. Therefore, in this series of tests the grading curve was not checked after testing to assess breakage. In Figure 2.1 only the initial grading is depicted. For more details about this carbonate sand see Nutt (1993).

2.1.2 White 14/25 Leighton Buzzard sand

This is a very uniform silica sand that has been widely used in research. The solid grains have sub-angular to sub-rounded shapes, composed of mostly quartz minerals (Figure 2.2(b)). The sand used corresponds to the 0.6 - 1.18 mm fraction, which is often referred to as 14/25 because it passes between the British Standard No 14 and No 25 sieves. Further details on the mechanical properties of this sand can be found in Schnaid

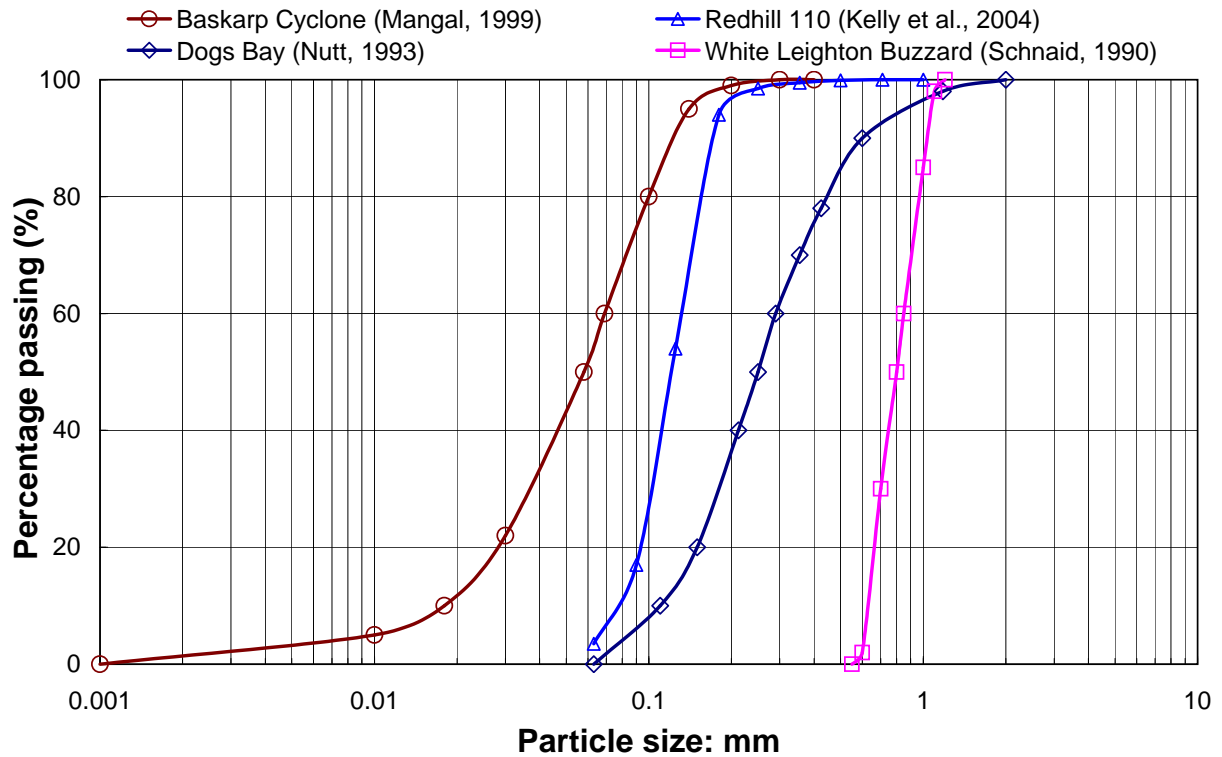


Figure 2.1: Particle size distribution curves for the cohesionless soils used in the experiments

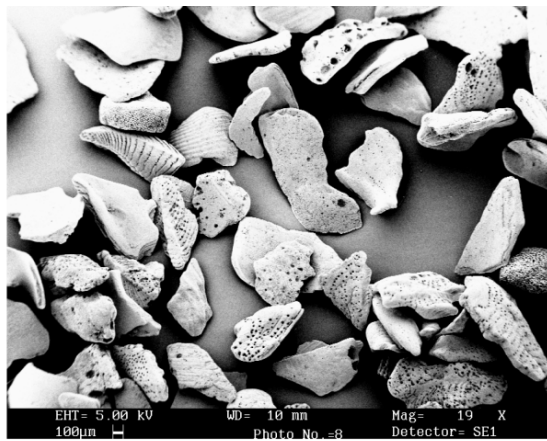
(1990).

2.1.3 Baskarp Cyclone sand

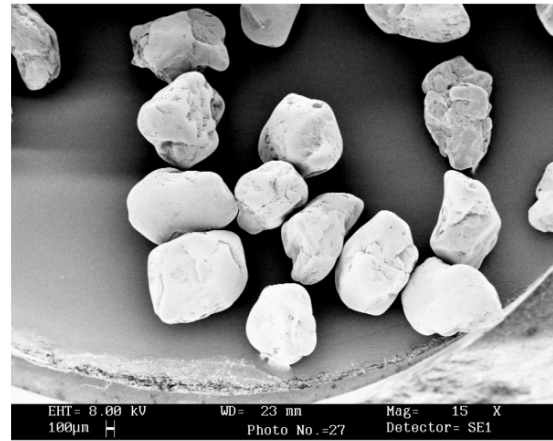
This sand comes from a Holocene deposit in the southwest of the lake Vättern, north of Jönköping, Sweden. The sand is very fine as a result of a cyclone separation system (AB Baskarpsand of Habo). The sand consists of 84% quartz and the grains are angular to sub-angular as can be observed in Figure 2.2(c). The election of this fine sand is based on the fact that the simulation of partially drained and undrained behaviour is possible. When the sand is saturated by silicon oil the drainage times of offshore foundations can be modelled appropriately in the laboratory. The silicon oil used had a kinematic viscosity of 100 centistoke, *i.e.* 100 times more viscous than water. The coefficient of permeability is defined by:

$$k = K \frac{\gamma_f}{\mu_d} = K \frac{g}{\mu_k} \quad (2.1)$$

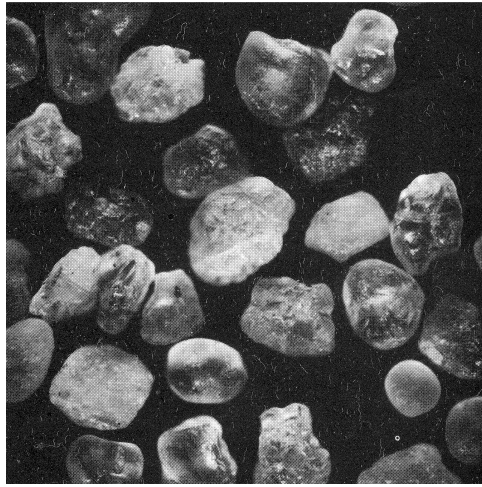
where K is the absolute permeability which indicates how *permeable* a porous material will be to *any* flowing fluid. The dynamic or absolute viscosity μ_d (Pa·s, Ns/m²), is related



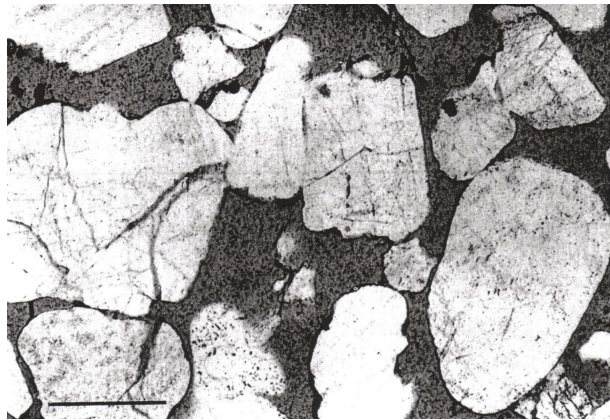
(a) Dogs Bay sand



(b) Leighton Buzzard sand



(c) Baskarp sand



(d) Redhill sand

Figure 2.2: Photographs taken by: (a) Bowman *et al.* (2001) (b) Sentenac *et al.* (2001), (c) Per Karmhagen of Askania AB (no scale bar provided), and (d) Richards and Barton (1999), (the scale bar is approximately 0.3 mm in length)

with the kinematic viscosity μ_k (m^2/s), by means of $\mu_k = \frac{\mu_d}{\rho_f}$. Then, the coefficient of permeability for a sand saturated with silicon oil k_{oil} , can be found by taking the proportion of the coefficient of permeability for water k_{water} , using (2.1) for the same temperature (25°C for example), which results in:

$$k_{oil} = \frac{\mu_{k_{water}}}{\mu_{k_{oil}}} k_{water} \quad (2.2)$$

The coefficient of permeability of the Baskarp Cyclone sand with a relative density of 80% and saturated with water is $8 \cdot 10^{-6}$ m/s (Mangal, 1999). For the case of saturation with oil, the values of kinematic viscosity μ_k , given in Table 2.2, and according to equation (2.2), k_{oil} is expected to be around hundred times lower than k_{water} , to be precise $\frac{k_{water}}{k_{oil}}$

= 111. However, Mangal suggested a $k_{oil} = 1.8 \cdot 10^{-7}$ m/s for the oil-saturated Baskarp Cyclone sand with a relative density of 80%, which is only 44 times lower than k_{water} . This disparity might be attributed to temperatures different to 25°C during permeability measurements.

Table 2.2: Silicon oil and water properties (after Mangal, 1999 and Byrne, 2000)

Property	oil	water
Kinematic viscosity, μ_k at 25°C, cs: mm ² /s	100	0.897
Specific gravity, G_s at 25°C	0.96	1
Bulk modulus, B (for $\epsilon < 1\%$): MPa	800	2200

2.1.4 Redhill 110 sand

Geologically this sand belongs to the Folkestone beds, which are marine shallow-water deposits of Cretaceous age. It was obtained from Redhill, one of the exposures around the Lower Greensand outcrop in the southeast of England. Commercially produced (WBB Minerals), Redhill 110 is a high silica sand with a total quartz content of 98.8%. Redhill 110 is a fine sand with angular grains, as observed in Figure 2.2(d), and has similar coefficient of uniformity and curvature to those of the Leighton Buzzard sand. The coefficient of permeability for a water-saturated sample was estimated by Kelly *et al.* (2004) to be $k = 1.5 \cdot 10^{-4}$ m/s. On one hand the high imperviousness of the oil-saturated Baskarp Cyclone sand specimens is appropriate in modelling transient response, but on the other hand it takes long time to complete, for instance a caisson installation by suction. To avoid difficult interpretation of test under non-dissipated pore pressures Baskarp Cyclone sand was replaced with the Redhill sand, which due to its larger coefficient of permeability allow drained conditions.

2.1.5 Speswhite kaolin clay

Speswhite kaolin clay has been used in numerous studies because its high permeability for a clay allows rapid consolidation of large specimens from reconstituted slurry. Characteristics taken from de Santa Maria (1988) and Martin (1994) are summarised in Table 2.3. It will be assumed here the shear strength distribution with depth proposed

Table 2.3: Representative Speswhite kaolin clay properties (after de Santa Maria, 1988 and Martin, 1994)

Property	Value
Specific gravity, G_s	2.61
Average effective unit weight, γ'	6.85 kN/m ³
Average moisture, w	50%
Liquid limit, LL	65%
Plastic limit, PL	34%
Coefficient of permeability, k ($p' = 200$ kPa)	$3 \cdot 10^{-9}$ m/s
Coefficient of consolidation, c_v ($p' = 200$ kPa)	0.3 mm ² /s

by Wroth (1984). The expression that Wroth (1984) postulates for this distribution is well supported by the results of undrained triaxial compression tests on isotropically consolidated specimens of reconstituted kaolin. Assuming that normally consolidated and overconsolidated specimens will reach the same *critical state point*, the shear strength can be written as:

$$s_u = \sigma'_v \left(\frac{s_u}{\sigma'_v} \right)_{nc} \text{OCR}^\Lambda \quad (2.3)$$

where $\left(\frac{s_u}{\sigma'_v} \right)_{nc}$ is the shear strength ratio for normally consolidated clays, $\sigma'_v = \gamma'z$ is the vertical stress, $\text{OCR} = \frac{\sigma'_{vo}}{\sigma'_{vi}}$ is the overconsolidation ratio with σ'_{vo} the maximum vertical stress in the consolidation process and σ'_{vi} the stress once the consolidation load has been removed. Λ is a parameter established in CSSM to indicate the relative slopes of the normal compression λ , and unloading-reloading κ lines for the soil.

$$\Lambda = \frac{\lambda - \kappa}{\lambda} \quad (2.4)$$

The consolidation procedure described below in §2.2.5 implies an OCR variation with depth of the form

$$\text{OCR} = \frac{\sigma'_{vo}}{\sigma'_{vi}} = \frac{\Delta\sigma'_v + \gamma'z}{\gamma'z} \quad (2.5)$$

where $\Delta\sigma'_v$ is the consolidation pressure. Thus, the shear strength gradient becomes

$$\frac{ds_u}{dz} = \gamma' \text{OCR}^\Lambda \left(\frac{s_u}{\sigma'_v} \right)_{nc} \left[1 - \frac{\Lambda}{\text{OCR}} \frac{\Delta\sigma'_v}{\gamma'z} \right] \quad (2.6)$$

The submerged unit weight of the clay specimen can be estimated from

$$\gamma' = \left(\frac{G_s - 1}{wG_s + 1} \right) \gamma_w \quad (2.7)$$

where G_s is the specific gravity. The water content w , can be expressed in terms of the undrained shear strength s_u , as shown in Figure 2.3, in which the group of data where $s_u < 20$ kPa corresponds to Martin (1994) and the data for $s_u > 20$ kPa to Smith (1993). The data referred to as stressed corresponds to vane tests on clay subjected to vertical and radial stresses in a 1 m diameter calibration chamber. The following relationships have been obtained from best fits of the results from vane shear tests performed by both authors.

$$w = 67.192 - 6.535 \ln s_u; \quad v = 2.754 - 0.171 \ln s_u \quad (2.8)$$

From the second expression in (2.8) an analogy with compression and critical state lines

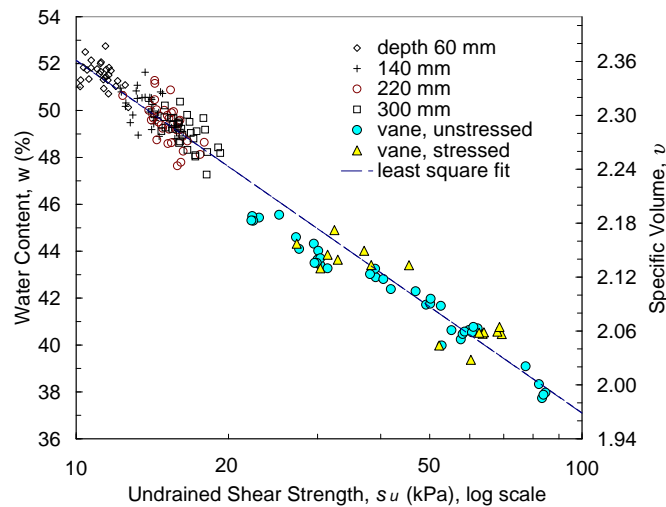


Figure 2.3: Undrained shear strengths and corresponding water content. Adapted from two series of shear vane tests: depth from 60 to 300 mm (Martin, 1994) and stressed and unstressed (Smith, 1993)

can be postulated in relation with the slope magnitude $\lambda = 0.171$ in the $v - \ln p'$ plane. In this investigation, the shear strength was measured at 25 mm and 125 mm depth with a shear vane apparatus mentioned later on in §2.2.5. Table 2.4 presents these results in the form of averaged s_u . To appreciate the idealized distribution of s_u with depth, Figures 2.4(a) and 2.4(b) illustrate the averaged values together with error bars. The

Table 2.4: Shear strength from shear vane tests and parameters for profile estimation

Tank (sample)	$s_{u_{25}}$ kPa	$s_{u_{125}}$ kPa	$\left(\frac{s_u}{\sigma'_v}\right)_{nc}$	Λ
1 ‡ (1)	4.6	7.3	0.19	0.70
2 (2)	5.1	8.1	0.21	0.70
2 ₂ (2)	4.6	7.3	0.19	0.70
2 ‡ (5)	5.7†	6.1†	0.23	0.71
3 (3)	6.7	10.2	0.26	0.70
3 ‡ (6)	4.5	8.4	0.22	0.70
4 (4)	8.8	13.2	0.35	0.70
4 ‡ (7)	6.3†	9.9†	0.22	0.73

‡specimen inverted, †back calculated

fluctuation is rather small and is hardly visible in some of the points. An explanation of the inverted specimens will be also found in §2.2.5. Figures 2.4(a) and 2.4(b) depict the strength profile estimated using (2.3) together with (2.5), (2.7). The values of $\left(\frac{s_u}{\sigma'_v}\right)_{nc}$

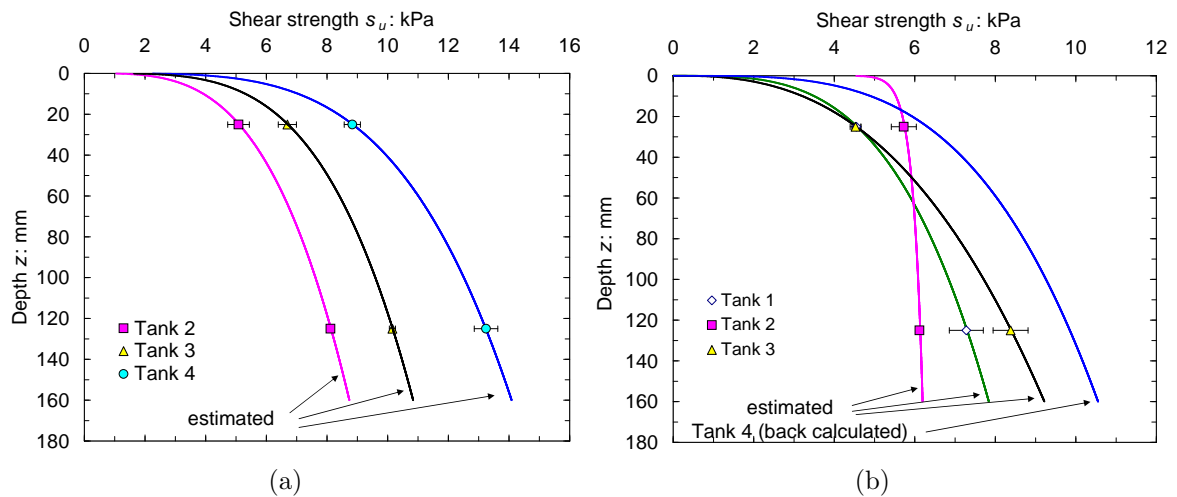


Figure 2.4: Vertical profiles of undrained shear strength (a) top of the sample (b) bottom of the sample (inverted)

and Λ were obtained from the best fit of (2.3) to the averaged experimental points of s_u . These profiles will be used in subsequent calculations, for instance, in the study of the vertical load required to install suction caissons.

2.2 SAMPLE PREPARATION

2.2.1 Dry Dogs Bay and Leighton Buzzard sands

The sand used during the testing was placed in a large aluminium tank with diameter 1100 mm and depth 250 mm. It had a rim at the top to which a loading apparatus and any other equipment could be attached as shown in Figure 2.10(a). A deeper sample of 400 mm was made possible by bolting on an additional 150 mm aluminium ring.

In the bearing capacity tests (Chapter 3), a total of five different relative densities were reached, four with the silica sand and one with the carbonate sand. Three loose samples of soil were prepared by carefully placing the sand into the tank from a scoop, keeping the drop height to a minimum. This method enables very loose sand samples to be prepared with relative densities of 26% for the Dogs Bay sand, and 40% and 47% for the Leighton Buzzard sand. For the denser samples only the Leighton Buzzard sand was used. A process of vibration was used until a high relative density ($R_d = 80\%$) was reached. This density was obtained after few minutes of vibration using a vibrating motor (Viking Vibrator CUB 52B, 5000 N force, 3000 rpm, rated output of 180 W, and motor mass of 13 Kg) attached underneath the tank. To control the sample density measurements of the sample thickness were carried out in several places on top of the sample, knowing a priori the weight of the sample. To obtain an even denser sample a surcharge (≈ 2 kPa) was placed on the sample in the form of lead weights (Lau, 1988). Attention was paid to not apply excessive vibration since this may induce non-uniformity of the sample, densifying more the top layer. Therefore, vibration was halted once no significant variation of the specimen thickness was measured.

A series of moment loading tests was carried out only in loose Leighton Buzzard samples following the preparation procedure above described. The mean relative density of the samples was 22%, values determined in each test are summarised in Tables 4.1 and 4.2. Densities were measured before testing by weighing the sand within the tank and determining the volume of the sample. The relative density was calculated assuming the values

of minimum and maximum specific volumes shown in Table 2.1, which were obtained by the authors shown in same table.

2.2.2 Oil-saturated Baskarp Cyclone sand

A watertight tank with a filter at the bottom, a drainage system and filled with 250 mm height of Baskarp Cyclone sand under a column of oil between 60 mm and 120 mm was used for partially drained and undrained testing (see Figure 2.13). Sample preparation followed the procedure suggested by Mangal (1999) and Byrne (2000). According to these procedures, firstly, the sample of oil-saturated sand was stirred with a device (stirrer) - developed by the above authors. The stirrer was attached to the tank rim and a rotating paddle was lowered at a very slow rate (0.1 - 0.03 mm/min) from the surface to 150 - 200 mm in depth. The paddle suspended the particles of soil allowing fluidisation of the sample and forming a homogeneous sample simultaneously. Putting the fluid containment tank shown in Figure 2.13 around 0.3 m above the fluid surface in the tank with the sample created a head which in turn applied an upward flow. In this way effective stresses were reduced. After five days of stirring, densification occurred by sedimentation of the fluidised particles in addition to vibration of the sample. The vibration was carried out using a vibrator motor attached underneath the tank. The vibration was applied in a range of 2 to 3 hours, which is a much longer period than that applied to dry sand. The fluid containment tank was located around 0.3 m below the fluid surface to create a hydraulic gradient, which resulted in a downwards flow. The vibration and the downward hydraulic gradient arrange the sand grains into a denser packing. The cone resistance q_c was estimated by driving a small cone penetrometer into the sample at a tested site. Mangal (1999) proposed an empirical expression of the relative density R_d (in %) related to q_c as follows:

$$R_d = \frac{1}{0.11} \ln \left(\frac{q_c}{0.044} \right) \quad q_c \text{ in kPa and at 75 mm penetration depth} \quad (2.9)$$

Using the small cone penetrometer relative densities of the three samples prepared were estimated as 64%, 74% and 80% respectively, which agreed with another estimate made

by extracting carefully a sample of a known volume for the first two samples. In the first sample vibration was not applied, hence the lower value of relative density measured.

2.2.3 Water-saturated Redhill 110 sand

As for the oil-saturated sand, a filter at the bottom together with drainage and a fluid containment tank were set up to aid sample preparation (see Figure 2.13). The sand samples of 250 mm height were saturated by upward percolation of the water inside the tank of diameter 1100 mm and depth 400 mm. Once fully saturated, samples were then densified by vibration with a motor underneath the tank under a small confining stress. A surcharge of 1.5 kPa over a circular plate on top of the sample was used to assist the densification. Above the sand surface a column of water of approximately 130 mm was maintained.

To prepare a new sample the process was repeated with the only difference that the fluid in the containment tank was pressurised from the compressor line to create an upward flow which fluidised the sample, instead of gravity used for saturation. The vibration of the tank with the sample in it was halted once a target density was reached. The density was determined by measuring the weight and the volume of the sample.

2.2.4 Friction angle of the cohesionless soils

To obtain an effective peak angle of friction ϕ'_{peak} , Bolton (1986) proposed an expression that accounts for the density or packing of the sand by means of the relative density R_d , and also for the level of stress at failure, p' . The relative density is given as:

$$R_d = \frac{\gamma_{dmax}}{\gamma_d} \frac{\gamma_d - \gamma_{dmin}}{\gamma_{dmax} - \gamma_{dmin}} = \frac{v_{max} - v}{v_{max} - v_{min}} \quad (2.10)$$

either in terms of γ_{dmax} , γ_{dmin} and γ_d (the maximum, minimum and current unit weights) or by using the maximum, minimum and current specific volume. The expression for the peak friction angle proposed by Bolton for plane strain and triaxial conditions respectively

is:

$$\begin{aligned}\phi'_{peak} - \phi'_{cs} &= 5[R_d(Q - \ln p') - 1] \\ \phi'_{peak} - \phi'_{cs} &= 3[R_d(Q - \ln p') - 1]\end{aligned}\tag{2.11}$$

where p' is in kPa. Equation (2.11) is plotted in Figure 2.5 for the four sands used, where the solid curves correspond to triaxial strain and the dashed lines to plane strain conditions. Values of the effective angle of friction at critical state ϕ'_{cs} , for triaxial conditions are given in Table 2.1. In addition, values of $Q = 10$ and 8 have been used for silica and carbonate sand respectively. Dilatancy has its greatest effect at low mean effective stresses. However, when mean effective stresses reduce below 150 kPa no appreciable effect on soil behaviour occurs. On this ground Bolton (1986) suggests that stress level effects are not significant below $p' = 150$ kPa ($\ln p' \approx 5$), then a compromise is to fix the value $\ln p' = 5$ in Equation (2.11).

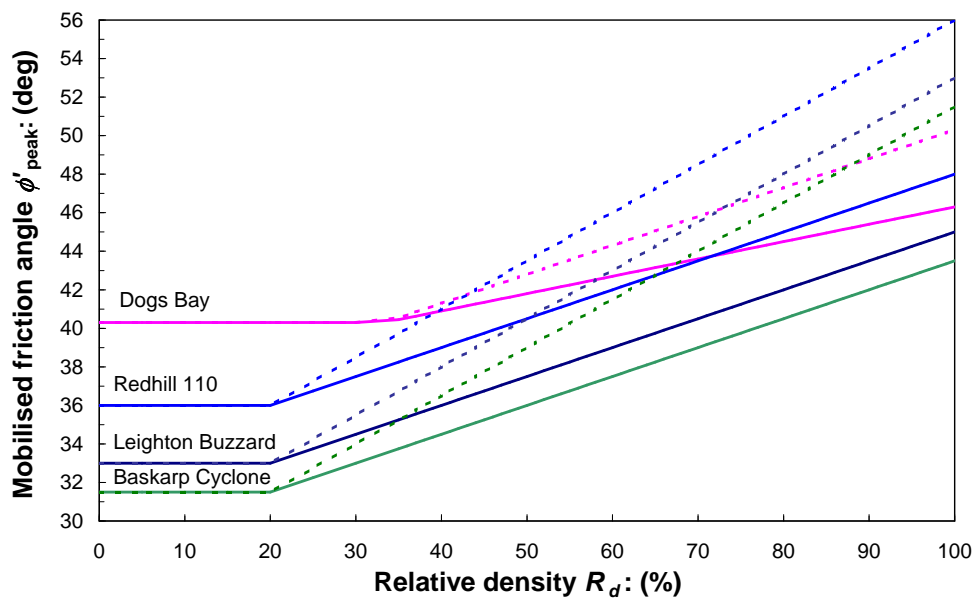


Figure 2.5: Variation of peak angles of shearing resistance ϕ'_{peak} , with relative density R_d , for the sands tested; solid curves for triaxial conditions and dashed curves for plane strain

2.2.5 Speswhite kaolin clay

The preparation of Speswhite kaolin clay specimens followed the method and procedures established since the one dimensional clay consolidation apparatus was designed and built by Gue (1984). This apparatus allows for the preparation of good quality homogeneous clay specimens with repeatable profiles of undrained shear strength and water

content with depth. Details of the design and operation of the apparatus are found in Gue (1984) and in de Santa Maria (1988). In preparing homogeneous kaolin slurry and subsequent consolidation of three specimens a similar sequence was followed to that described by Martin (1994). Briefly, a homogeneous material was obtained by mixing de-aired slurry at a moisture content of 120% in a ribbon blade mixer equipment with a vacuum pump. The slurry was pumped into cylindrical tanks of 450 mm diameter and 900 mm height. *Vyon* filters were then placed on top and the bottom of the specimens allowing drainage to atmospheric pressure during consolidation. Notwithstanding these similarities, a slightly different consolidation pressure path was applied, as can be observed in Figure 2.6. The

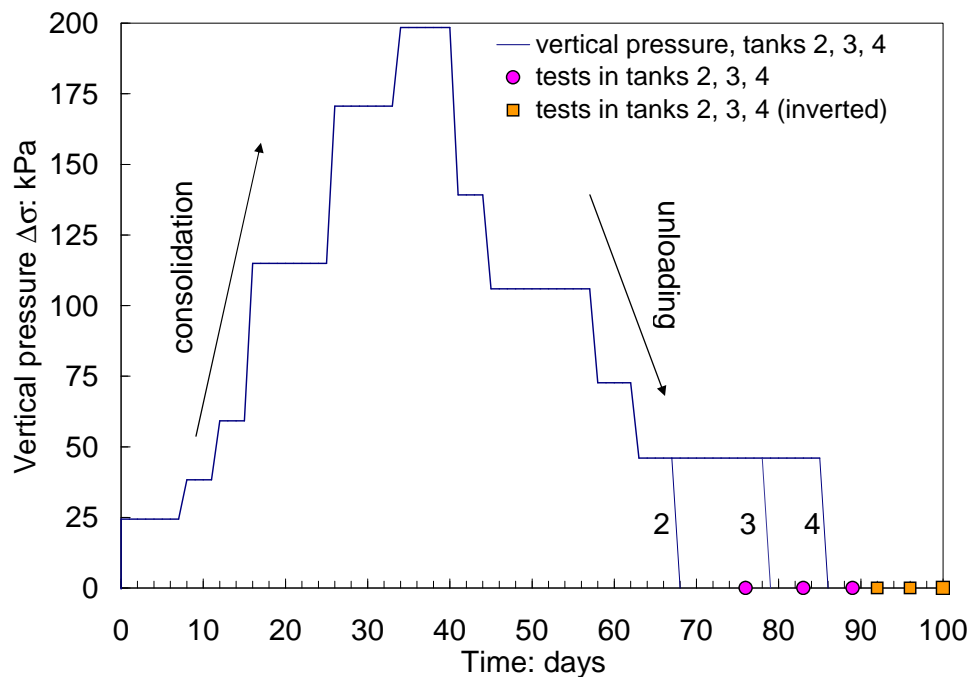


Figure 2.6: Speswhite kaolin clay consolidation and unloading pressures evolution with time for three tank (2, 3 and 4) showing in circles and squares the day of fully unloading and testing respectively

sequence of vertical pressure (25, 40, 60, 115, 170, 200, 140, 105, 70, 45, 0 kPa) allowed for a complete primary consolidation. The sequence of vertical consolidation pressures to reach 200 kPa took longer than the usual 3 or 4 weeks. At least 30 mm of space was allowed for filling with water the top of the sample. After fully unloading the sample a period of time elapsed to allow any negative pore water pressures developed in the swelling phase to dissipate. de Santa Maria (1988) carried out a “pushing up operation” allowing specimens to be extruded and cut after testing to remove the disturbed clay and

provide a second testing site. The square labels shown in Figure 2.6 represent a second series of tests carried out with the same specimens already prepared. However, these were not extruded and cut, but inverted and the undisturbed side of the specimens used instead.

The shear strength of each sample was measured using a shear vane apparatus shown in Figure 2.7(a). The apparatus is described by Bowden (1988) and subsequent modifications are described by Sills and Bartholomeeusen (2001). The vane diameter and length were $d = 12.65$ mm and $h = 30.3$ mm respectively (Figure 2.7(b)). The shear strength was calculated using the following equation:

$$s_u = \frac{T}{\frac{d^2 h}{2} + \frac{d^3}{2(n+3)}} \quad (2.12)$$

where the total torque $T = T_v + T_h$ is the contribution of the vertical and horizontal surfaces of the vane and is directly measured from the apparatus. The factor n was proposed by Wroth (1984) to include the effect of the shear stress distribution along the horizontal surface of the vane. Because of the lack of knowledge of an n value for the Speswhite kaolin clay, and to compensate for the friction along the extension rod and rate effects, it has been assumed equal to zero.

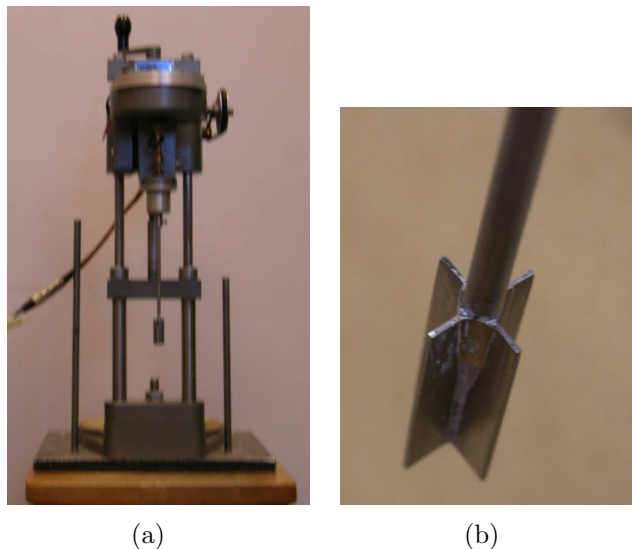


Figure 2.7: (a) Shear vane testing device, and (b) vane

2.3 MODEL SCALE CAISSONS

The model caissons used are listed in Table 2.5 with a capital letter denomination. This denomination will be repeatedly encountered along the thesis, for brevity, when referring to caissons tested. The geometry and geometrical parameters also appear in Table 2.5. The length L and radius R or diameter $2R$, correspond to the *inside* skirt depth and to the *outside* diameter $2R$ respectively. Later on, to be specific, the radius will be referred as R_i , R_o or R to refer to the inside, outside or average radius. Caissons can also be classified by defining the aspect ratio $L/2R$ and the thickness ratio $t/2R$. Table 2.6 shows values of the caisson stiffness coefficients following the calculation procedure suggested by Doherty *et al.* (2005). The vertical, rotational, horizontal, and coupled stiffness coefficients K_V , K_M , K_H , and K_{MH} were calculated to assess the flexibility of the caissons compared with infinitely rigid caissons K_∞ and caissons without skirt K_0 . In view of the results it is clear that the model caissons can be considered as practically infinitely rigid.

Table 2.5: Geometrical parameters of the model caissons tested

Caisson	A	B	C	D	E	F ₁₋₇
Diameter, $2R$: mm	293	203.4	200	150	150	50.9
Length of skirt, L : mm	146.5	203.5	100	150	100	†
Thickness of the skirt wall, t : mm	3.4	3.4	1.0	1.0	1.0	1.66
Aspect ratio, $L/2R$	0.5	1.0	0.5	1.0	0.67	†
Thickness ratio, $t/2R$	0.012	0.017	0.005	0.007	0.007	0.033

†Caissons F

Caisson	F_1	F_2	F_3	F_4	F_5	F_6	F_7
L : mm	0	13.3	26	38.7	51	76.9	102.1
$L/2R$	0	0.26	0.51	0.76	1	1.51	2.01

Photos of the caissons are given in Figures 2.8(a), 2.8(b), 2.8(c), 2.8(d), and 2.8(e). The skirts of caissons F₂₋₇ were fabricated from a brass tube, A and B from aluminium tubes and C, D and E from a corrosion resistant copper-aluminium alloy (duralumin or dural) plates. To account for the observation that, in general, a fine sand will mobilise more friction on a surface than a coarse sand, Uesugi and Kishida (1986) defined a normalised roughness $R_n = \frac{R_{max}}{D_{50}}$, where R_{max} is the maximum roughness (the height between the highest and lowest point of the surface profile). A smooth, intermediate and rough inter-

Table 2.6: Stiffness coefficients of the caissons ‡

Caisson	A	B	C	D	F ₃	F ₅
$K_{V\infty}$	10.26	16.47	10.26	16.47	10.26	16.47
K_V	10.25	16.43	10.24	16.38	10.26	16.44
K_{V0}	3.78	3.78	3.78	3.78	3.78	3.78
$K_{M\infty}$	16.70	68.44	16.70	68.44	16.70	68.44
K_M	16.54	67.17	16.39	65.58	16.62	67.74
K_{M0}	1.57	1.57	1.57	1.57	1.57	1.57
$K_{H\infty}$	9.81	17.18	9.81	17.18	9.81	17.18
K_H	9.74	16.89	9.66	16.58	9.78	17.01
K_{H0}	2.19	2.19	2.19	2.19	2.19	2.19
$K_{MH\infty}$	-7.69	-25.57	-7.69	-25.57	-7.69	-25.57
K_{MH}	-7.61	-25.14	-7.53	-24.55	-7.66	-25.35
K_{MH0}	-0.18	-0.18	-0.18	-0.18	-0.18	-0.18

‡assuming a caisson Young's modulus $E = 73$ GPa, sand shear modulus $G = G_R \left(\frac{z}{R}\right)^\alpha$, with $G_R = 1$ MPa and $\alpha = 0.5$

(a) Caissons F₇₋₂

(b) Caissons A and B



(c) Caisson A



(d) Caisson C



(e) Caisson D

Figure 2.8: Caisson models for dry sand samples: (a), (b); caissons for saturated soil samples showing the pore pressure transducer PPT and fluid valve: (c), (d), and (e)

face correspond to $R_n < 0.02$, $0.02 \leq R_n \leq 0.5$, and $R_n > 0.5$ respectively. Roughness was measured in the Metrology laboratory at the University of Oxford using a surface roughness machine (Taylor-Hobson Talysurf 4). A stylus tracks the surface profile through up and down movements which are followed by a strain gauged arm attached to it. From three measurements of roughness in different directions of the dural plate, R_{max} was con-

sidered to be in the order of $4 \mu\text{m}$. Then, smooth interfaces result for Dogs Bay and Leighton Buzzard sands ($R_n = 0.017, 0.005$), whilst intermediate interfaces with Baskarp Cyclone and Redhill sands ($R_n = 0.07, 0.03$). Although, no roughness measurements were made for the brass and aluminium tubes, from tactile and visual observations of the surfaces and the sands used it is unlikely that a rough interface could occur.

Caissons A, C, D and E were equipped with air and fluid valves, and also with a pore pressure transducer PPT. A *Vyon* filter was located in the opening of the fluid valve to avoid particles passing through, with the risk of clogging the pipe, especially at the last stages of the suction installation. These features and the set-up of the suction system set-up are shown in Figure 2.13.

2.4 TESTING SITES AND BOUNDARY CONDITIONS

The boundary conditions chosen for the vertical loading tests included a fully filled cylindrical bed of dry Leighton Buzzard or Dogs Bay sand 1100 mm in diameter and 250 mm high. The F_{1-7} caissons were located symmetrically in nine sites as depicted in Figure 2.9. This minimises the variation in soil characteristics across different tests, which is particularly important when carrying out parametric studies. The most unfavourable condition occurs when the distance available between two caissons is 97 mm. Disturbance of the surrounding soil increases with the soil level of packing. Because of the local or punching shear failure mechanism developed in loose cohesionless soils the extension of the mobilised volume of soil is reduce to not more than a diameter. Even for a hypothetical general shear failure mechanism in loose sand, the disturbance can occur within two diameters for the longest caisson ($\frac{L}{2R} = 2$), assuming rough contact, $\phi' = 34^\circ$, $\gamma_d = 15.7 \text{ kN/m}^3$ and surcharge of 1.57 kPa (using ABC program by Martin, 2003). However, for dense samples the soil volume at failure might extend beyond the two diameters available. The ABC program (Martin, 2003) computes a plastic region that extends three times the

diameter of a rough circular footing, assuming $\phi' = 44^\circ$, $\gamma_d = 17.2 \text{ kN/m}^3$ and a surcharge of 1.72 kPa. It is important to bear in mind that the use of collapse mechanisms based on rigid plasticity and fully associated flow probably overestimates the distances. To overcome boundary effects tests were carried out leaving a site in between, and completing the series with the last half of sites which would suffer somewhat the effect of previously disturbed neighbour sites. However, for longer caissons the failure tends to not open widely to the surface, showing the transition to a deep failure mechanism.

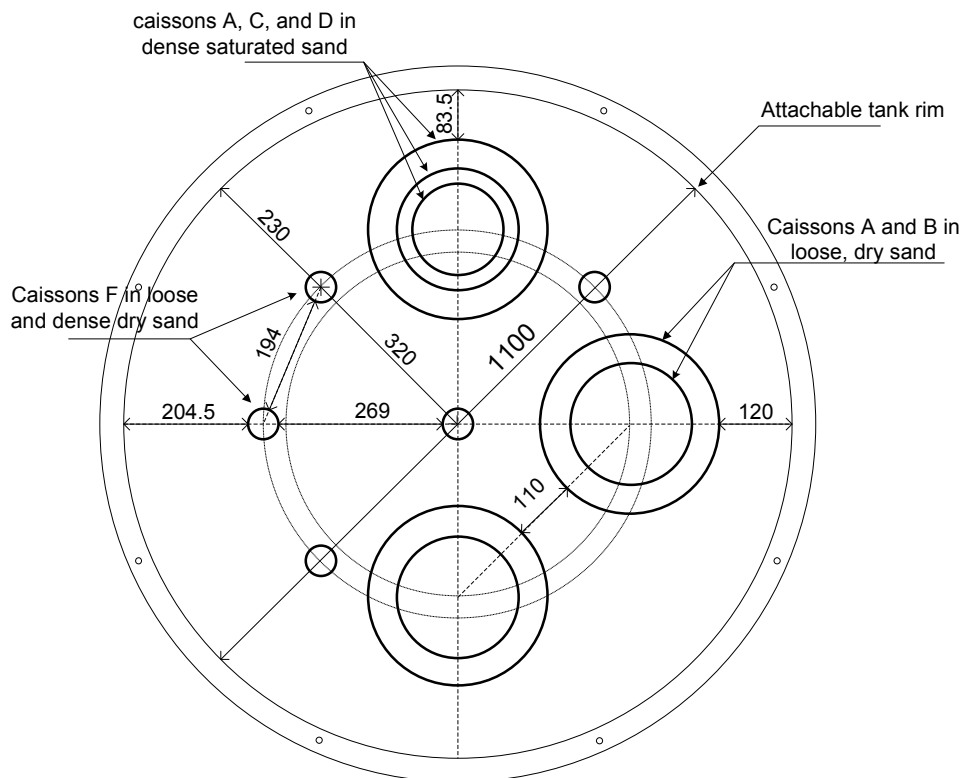


Figure 2.9: Plan view of the caisson's location inside the tank (dimensions in mm)

The use of caissons A and B for moment capacity tests constrains significantly the boundary conditions because of their larger size, as can be observed in Figure 2.9, in particular the distance to the bottom and wall of the tank is restricted. The former was solved by bolting on a ring of 150 mm thickness, as depicted in Figure 2.10(a), which increased the tank depth to 400 mm. The latter was mitigated incorporating spacers whose functions were to provide enough space between the ground surface and the loading apparatus to install these large caissons, and to switch the loading plane direction by 90° , so the caisson rotation acted on a larger volume of soil and not directly against the wall or towards the

centre, as seen in Figure 2.10(a). In principle, for a rotation or translation test in just one direction there would not have been interference, as long as a clockwise or anticlockwise sense is followed. However, for repetitive rotation tests interference between sites may occur. The maximum rotational displacement $2R\theta_{max}$ applied to the caissons is around 2 mm, inducing a maximum lateral displacement at the mudline level between $0.007L$ and $0.013L$ (caissons A and D). The disturbed extension at failure can be assessed in terms of the lateral earth pressure required to fully mobilise a wedge of soil. The disturbed extension at the ground surface is given by $L\tan(45^\circ - \phi'/2)$ and $L\tan(45^\circ + \phi'/2)$ according to the theoretical active and passive lateral earth pressure for smooth walls. The minimum lateral displacements of a rigid wall necessary to mobilise active and passive wedges are shown in Table 2.7. Bearing in mind that yield occurs previous to at least a fourth of $2R\theta_{max}$ (as it will be revealed in Chapters 5, 6 and 7), the lateral displacement ranges between $0.002L$ and $0.003L$. Then, according to Table 2.7 passive wedges can not be fully developed, nevertheless, active wedges can develop particularly in dense sands. Therefore, it is expected that in clays and loose sands side boundary effects are negligible with a remote possibility of appearing far after yield has occurred, hence at the end of moment loading tests. Conversely, boundary effects can occur in the form of active wedges in dense sands. Furthermore, because a smooth and rigid-walled tank was used boundary effects are mitigated since lower earth pressures are generated in case of an active wedge reaches the tank. In the following chapters comparisons among test results will assess whether side boundary effects take place or not.

Table 2.7: Minimum lateral displacement to produce active and passive state (taken from Sowers, 1979)

Soil	Active state	Passive state
Dense cohesionless	$0.0005L$	$0.005L$
Loose cohesionless	$0.002L$	$0.01L$
Stiff cohesive	$0.01L$	$0.02L$
Soft cohesive	$0.02L$	$0.04L$

The clay specimens were approximately 420 mm height, so the water depth available was 30 mm. Only one caisson (caisson D) was tested in the centre of each side of the specimens prepared in tanks 450 mm diameter and 450 mm of height.

2.5 TESTING APPARATUS FOR MODEL FOOTINGS

2.5.1 The three-degree-of-freedom loading rig

To develop plasticity models is necessary to establish: (a) the yield surface, (b) the hardening law, (c) a flow rule, and (d) the elastic behaviour. Along the thesis these four components will be explored as part of hyperplasticity models. To develop a theoretical models the experimental study of foundation response requires a loading device capable of applying complex load or displacement paths. To this end a three-degree-of-freedom loading rig has been in operation at the University of Oxford since 1992. The rig was designed and built by Martin in 1992 to test model spudcan footings on an overconsolidated clay (Martin, 1994). Subsequently, Mangal (1999) and Byrne (2000) adapted the loading rig for applications of larger loads to test model footings on much stiffer soils. The rig, shown in Figure 2.10(a), can apply any planar combination of vertical, rotational and horizontal displacements $(w, 2R\theta, u)$ to a footing by means of computer-controlled stepper motors. Therefore, offshore environmental loads can be represented. In Figure 2.10(a) the numbers show: **1**, **2** and **3** the long LVDTs for vertical, horizontal and rotational displacements; **4**, **5** and **6** the stepper motors for vertical, horizontal, and rotational moves; **7** the waterproof shaft with the ‘Cambridge’ *VMH* load cell inside; **8** the circular base plate to attach the footing; **9** the model caisson footing; **10** the reaction frame; **11** soil sample; **12** tank; **13** spacers, and **14** I-beams.

Displacement controlled tests can be performed by means of independent control of three stepper motors, allowing the exploration of softening behaviour. The independent control over the displacements $(w, 2R\theta, u)$ is accomplished by using separate bearing and motion systems. The vertical and horizontal motion is provided by linear sliding plates, whilst the rotational motion is guided by a rotary sliding ring. The arm supporting the model footing is attached directly to the rotary sliding ring, allowing rotation of the footing without the need for a fixed centre of rotation. The stepper motors drive the plates and

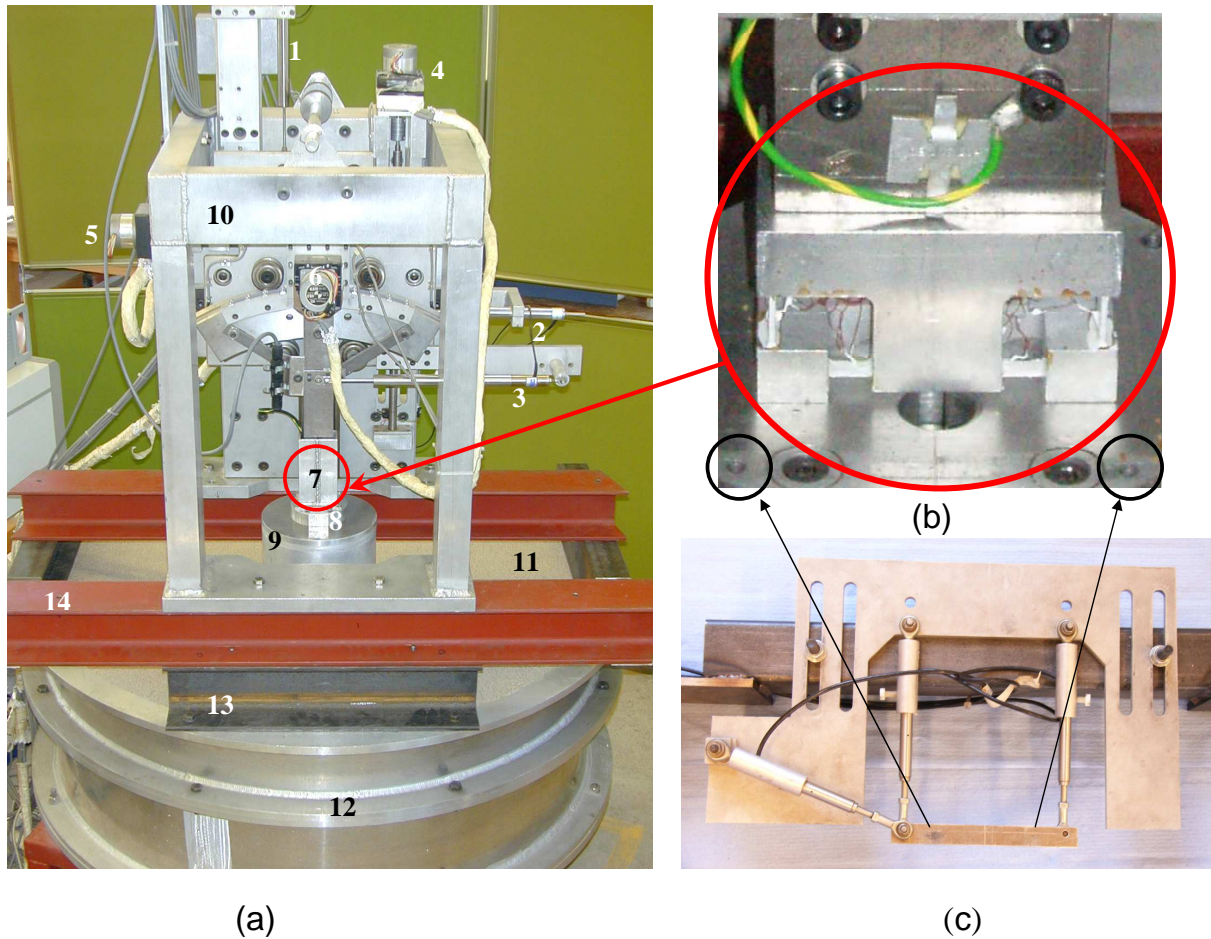


Figure 2.10: a) The three-degree-of-freedom *VMH* loading rig, (b) view of the ‘Cambridge’ *VMH* load cell, and (c) small LVDTs showing points of connection with base plate

ring with displacement ranges of $\Delta w = 300$ mm, $\Delta u = 50$ mm, and $\Delta\theta = 30^\circ$. Figure 2.10(b) shows the “Cambridge” load cell (Bransby, 1973) attached to the rig arm and to the footing through a base plate allowing measurements of the resultant planar loads (V, M, H). The *VMH* load cell is composed of two aluminium blocks jointed by a system of strain-gauged webs, with the gauges connected into Wheatstone bridge circuits. There are four vertical and four horizontal webs forming two vertical circuits and one horizontal circuit. Each circuit is powered by 10 Volt DC supply and the resulting signal is amplified and translated to load units using a calibration constant. The load cell was already calibrated at the start of the testing programme and the matrix obtained from the calibration that relates the measurements of the strain gages with the loads was obtained by Byrne (2000). This matrix was incorporated within the acquisition program (Byrne, 2000) and used throughout the testing programme. The load cell was calibrated for a load reference

point (LRP) 10 mm below the centre of the base plate to which the footing is attached (LRP is discussed in section §2.5.3). The calibration involved the use of a calibration apparatus in which a load V , M or H is varied at the LRP whilst keeping the other two constant. The moment was applied by increasing the eccentricity of a constant vertical load. The horizontal load was applied by a wire passing through a pulley and connected to hanging weights. The vertical load is increased by hanging weights. Further information about the load cell calibration can be found in Martin (1994), Mangal (1999), and Byrne (2000). The load cell webs are restricted to a maximum strain ϵ of 0.001, giving a workable range of loads (without factor of safety) as shown in Figure 2.11. For example, for low vertical loads and for a horizontal load of 400 N, the maximum moment is around 50 Nm.

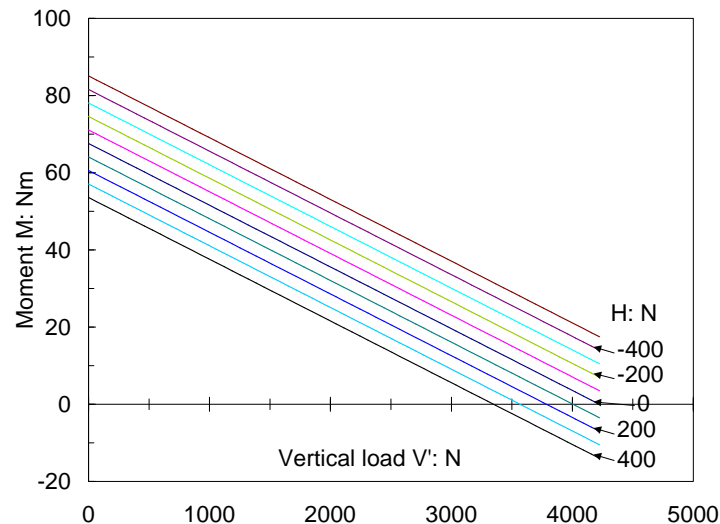


Figure 2.11: Load cell allowable loads (V , M , H) (Byrne, 2003)

To record footing displacements a system of three long range LVDTs was used. They were powered by a 5 Volts power supply and the resulting output signal was amplified and transformed to displacement units by means of calibration constants. As shown in Figure 2.10(a) the LVDTs follow the displacement of the sliding plates and the rotating arm of the loading rig from which the footing displacements can be deduced. This calculation is not strictly correct because the flexibility of the plates, ring, arm and any other component attached to the rig influences the real displacement of the footing. Therefore, correction due to rig flexibility is required. For the vertical loading tests presented

in Chapter 3, where $V_{max} \approx 500$ N, an additional LVDT measured directly the vertical displacement on the footing. Subsequent comparison of both recordings proved that differences were too small to represent a noticeable rig flexibility effect. Nevertheless, for combined loading tests when the moment is higher than 15 Nm and the horizontal load is higher than say 50 N, there is a need to account for the stiffness of the rig in the calculations of footing displacements. Thus, the footing displacements are corrected by adding to the long LVDT measurements the deformation suffered by the rig due to the loads, by means of a rig flexibility matrix [RFM].

$$\begin{Bmatrix} w \\ 2R\theta \\ u \end{Bmatrix}_{footing} = \begin{Bmatrix} w \\ 2R\theta \\ u \end{Bmatrix}_{rig} + [\text{RFM}] \begin{Bmatrix} V' \\ M/2R \\ H \end{Bmatrix} \quad (2.13)$$

Martin (1994) and Byrne (2000) determined this matrix for the rig. The cases of H less or larger than zero are treated separately. Adopting Byrne's matrix values,

$$[\text{RFM}] = \begin{Bmatrix} -5.09 \cdot 10^{-4} & 8.31 \cdot 10^{-4} & -1.60 \cdot 10^{-4} \\ -1.07 \cdot 10^{-4} & 3.83 \cdot 10^{-3} & -2.06 \cdot 10^{-3} \\ 8.92 \cdot 10^{-6} & -1.81 \cdot 10^{-3} & 2.61 \cdot 10^{-4} \end{Bmatrix} \quad \text{in mm/N for } H < 0$$

$$[\text{RFM}] = \begin{Bmatrix} -5.09 \cdot 10^{-4} & 8.31 \cdot 10^{-4} & 1.70 \cdot 10^{-6} \\ -1.07 \cdot 10^{-4} & 3.83 \cdot 10^{-3} & -2.06 \cdot 10^{-3} \\ 8.92 \cdot 10^{-6} & -1.81 \cdot 10^{-3} & 2.49 \cdot 10^{-4} \end{Bmatrix} \quad \text{in mm/N for } H > 0 \quad (2.14)$$

it is found that for any combinations of loads, where $V' > 500$ N, $M/2R > 50$ N, and $H > 50$ N, the corrections are of the order of 0.1 mm. Note that the two matrices in (2.14) differ only in the last column, which is associated with the horizontal load H .

Figure 2.10(c) shows a system of three short LVDTs designed by Byrne (2000) to obtain more refined displacement measurements. Although the short LVDTs offer a better resolution of the displacements $(w, 2R\theta, u)$, the stroke of each LVDT is limited to 10 mm. The small LVDTs were used mostly in cyclic tests where the long LVDTs provided a too

coarse resolution.

For footings in saturated soil, pore fluid pressure was measured using a PDCR 810 *Druck* pore pressure transducer PPT of ± 70 kPa range. The PPT was screwed to the top of the caisson lid and located in the plane of loading close to the caisson edge as shown in Figures 2.8(c), (d), and (e). A saturated *Vyon* filter protected the PPT strain-gauged diaphragm against direct contact with the soil.

The level of noise has a standard deviation for the loads of less than 0.5 N, for the long LVDTs between 6 μm and 30 μm , for the short LVDTs less than 2 μm , and for the PPT less than 50 Pa (Byrne, 2000). All displacements and loads were monitored and recorded using data-acquisition routines as well as being used within feedback control routines. All the electrical sensors were logged to a data-acquisition card located in a personal computer, with a maximum acquisition rate of 20 Hz. A MS Visual Basic 5.0 program written by Byrne (2000) allows the control of each of the three stepper motors independently. The control algorithm of a variable is a function of the *error* (between the current value and a specified value) and the *gain* to be determined to minimise the error. The gain depends strongly on the mean vertical load V_m , the range of loads (V' , M , H), and the soil stiffness. Choosing appropriate values of the gain is very important for the appropriate implementation of the sequences of footing moves with or without V' or *w hold subroutines*; *w hold subroutines* are relevant for swipe tests, whereas V hold subroutines are relevant for moment loading tests at constant V' . A modified V' hold subroutine is relevant for suction installation tests, where the timer in the hold subroutine within the program is disabled. Any vertical load V' targeted, such as the scaled submerged weight of the structure, can be kept constant throughout the suction installation by carefully adjusting the suction applied to the interior compartment of the caisson.

More complex moves are required to generate a load controlled feedback subroutine, for instance to carry out cyclic loading tests. Byrne (2000) developed an algorithm able to read and reproduce an input file with a specified load history. The option of gain change

becomes available during the test, which can accelerate the displacement rate in case the targeted load is not been reached. A load control subroutine implemented for cyclic vertical loading tests is discussed further in section §7.2. More information about the loading rig can be found in Martin (1994), Mangal (1999), and Byrne (2000). No change or modification of the apparatus and of the MS Visual Basic 5.0 program was considered necessary to carry out during the testing programme.

2.5.2 The suction system

The suction needed to install a caisson in the field is usually developed by large capacity pumps such as submersible Remotely Operated Vehicles (ROV). Figure 2.12 shows a pump used for suction pile installations. A scaled pump could therefore be used for suc-



Figure 2.12: Suction pump unit on top of a suction pile (taken from SPT Offshore, <http://www.suctionpile.com/pdf/SAPS001.pdf>)

tion installations in the laboratory. The first attempt reported in a letter by Goodman *et al.* (1961) proved that small pumps were suitable to install “cups”. Moreover, Wang *et al.* (1977) also used a pump and a small “medical aspirator” (peristaltic pump) for tests in clay. However, lately researchers have chosen other devices to generate suction such as those discussed at the ISOPE conference in 2001. There, House and Randolph (2001) and Kim *et al.* (2001) presented designs of computer controlled syringe pumps, which was implemented in centrifuges for the installation of suction caisson in clay and sand respectively. Using a suction pump and a depression vessel a suction percussive

technique was introduced by Allersma *et al.* (2001). The vessel is under suction through an crossover valve open to the pump. The valve is then close to the pump and open to the caisson compartment, applying instantaneously a large suction with short pulses. Once the pressure in the caisson and the vessel balances, the process is repeated until the caisson is fully penetrated. Allersma *et al.* (2001) pointed out that the main advantages of this technique over the gradual increase of the suction are: less likely to reach critical suction (piping), pump cavitation is avoided, and a better option to install caissons in layered soils and complicated seabeds is provided.

In the experimental work described here a simple and versatile water head difference method has been used. Sanham (2002) and Tran *et al.* (2004), among others, extensively used this method to study how different dead weights and flow rates affected the penetration under suction. The suction system developed is shown in Figure 2.13. Initially, tests were carried out to prove whether this method was suitable for a highly viscous fluid. This method was successful even for a caisson (not included in Table 2.5) with a thick skirt wall ($t = 3.4$ mm, and $R = L = 100$ mm), installed into a very dense oil-saturated Baskarp Cyclone sand sample ($R_d \approx 96\%$). Nonetheless, as calculations demonstrate, this caisson could be installed under a weight of $V' = 50$ N to achieve an initial self-weight penetration. Subsequent penetration was achieved under $V' = 50$ N by applying suction generated by a head difference. In particular, three variables were inspected, the reservoir pipe diameter (12.5 mm), a rough estimation of the head required (less than 400 mm) and the time necessary to install the caisson (between 1 and 4 hours).

A subsequent step was to connect a suction caisson to the *VMH* loading rig arm and to change the time subroutine within the control program, as explained in §2.5.1, to allow the suction installation of caissons. Once a suction caisson attached to the *VMH* loading rig was pushed into the ground between 15 to 30 mm with the bleed valve open (allowing the pressure inside the caisson to equilibrate with the pressure outside), the bleed valve was closed, and the fluid valve opened. Fluid in the caisson compartment was connected through a pipe to a reservoir, which was slowly lowered to increase the head difference h_f ,

between the inside and outside of the caisson. The head difference could be increased to a maximum of 300 mm (3 kPa), whilst the vertical load applied to the footing was kept constant using feedback control.

For water-saturated Redhill sand samples the reservoir was connected to the suction caissons by a pipe with an internal diameter of 6 mm, instead of the 12.5 mm for the oil-saturated sand. The pipe length was chosen to allow sufficient water flow with minimal head loss. The valve connected to the water reservoir was much more sensitive to any change, therefore, it had to be open or close with more subtleness than for the tests in oil-saturated sand. This procedure allowed caissons to be installed by suction in sand

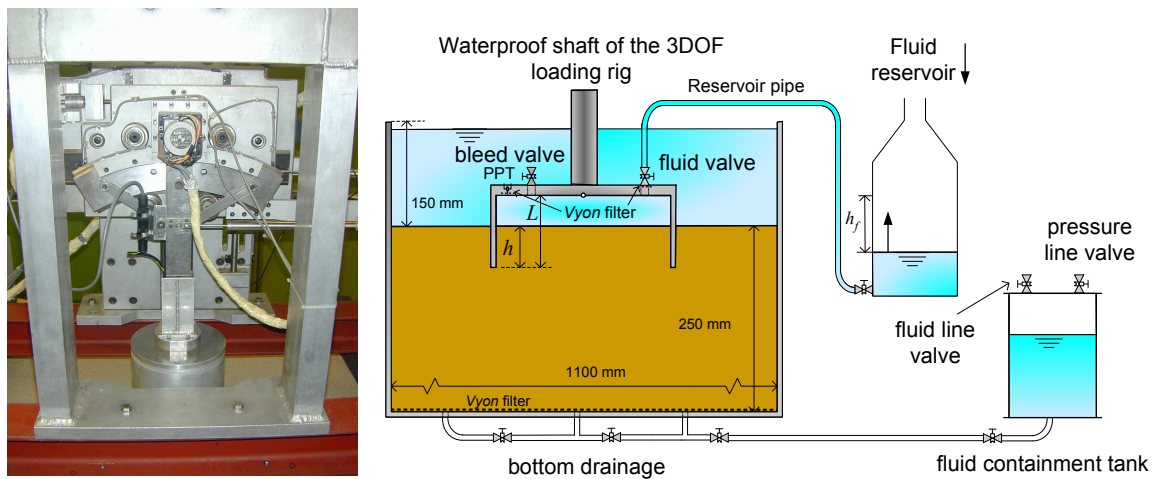


Figure 2.13: Diagram of the suction device

whilst connected to the loading rig. Once the suction phase was complete, it was possible to carry out combined loading tests similar to those carried out on the dry sand.

For installations in clay the suction was applied by using a vacuum pump, as previously reported by Rauch *et al.* (2003) for suction piles ($L/2R = 9$). The 1 atm vacuum line was connected to a system of containers and valves before to be attached to the caisson. The system ensured that no fluid could pass through to the vacuum line system and also allowed the operator to regulate and control the suction applied.

2.5.3 The reference point for loads and displacements

An idealised sequence of the installation is shown in Figure 2.14. It is an idealisation since it does not consider any rearrangement or remoulding of the soil surrounding the skirt caused by the caisson penetration. From the sequence in Figure 2.14 the convention

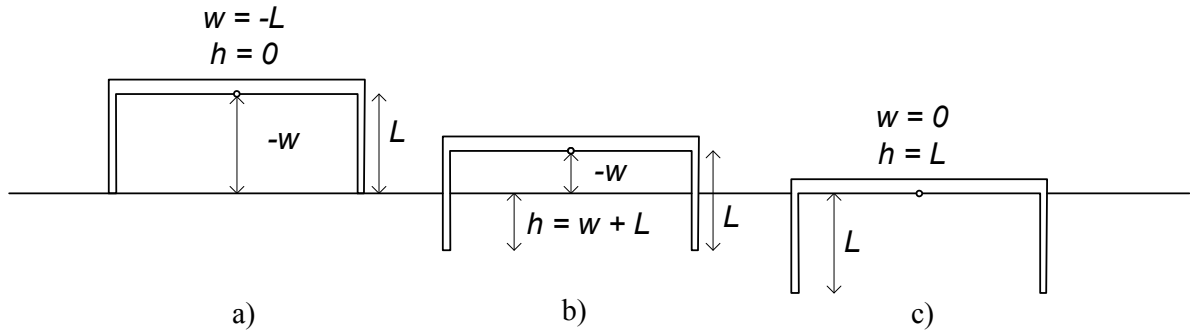


Figure 2.14: The vertical displacement during a caisson penetration in terms of w and h : (a) initial installation, (b) semi installed, and (c) fully installed

for caisson penetration is h and settlement is w once the caisson is installed, whilst vertical displacement will be generic, *i.e.* either h or w .

For loads and displacements the convention given by Butterfield *et al.* (1997) is assumed. Figure 2.15(a) illustrates this convention adopted for a fully installed suction caisson, where the combination of vertical, moment and horizontal loads (V' , $M/2R$, H) is associated with the respective set of vertical, rotational and horizontal displacements (w , $2R\theta$, u). Careful consideration must be given to the load reference point, particularly if it is different to that defined in Figure 2.15(a). Figure 2.15(b) illustrates the case of loads located by a structural engineer, for instance at a distance d above that according to Butterfield *et al.* (1997) or Figure 2.15(a). Although neither V' nor H modify their magnitudes or directions, for equivalent loads attention must be paid to the change in magnitude of the moment M , which becomes:

$$M' = M + d(H \cos \theta + V' \sin \theta) \quad (2.15)$$

where d is the distance between the load-application point and the load reference point chosen. Furthermore, as illustrated in Figure 2.15(c), the rotation θ in both positions is the same, but the horizontal displacement u , as well as the vertical displacement w ,

undergo the following modifications:

$$\begin{aligned} u' &= u - d \sin \theta \\ w' &= w + d \cos \theta \end{aligned} \tag{2.16}$$

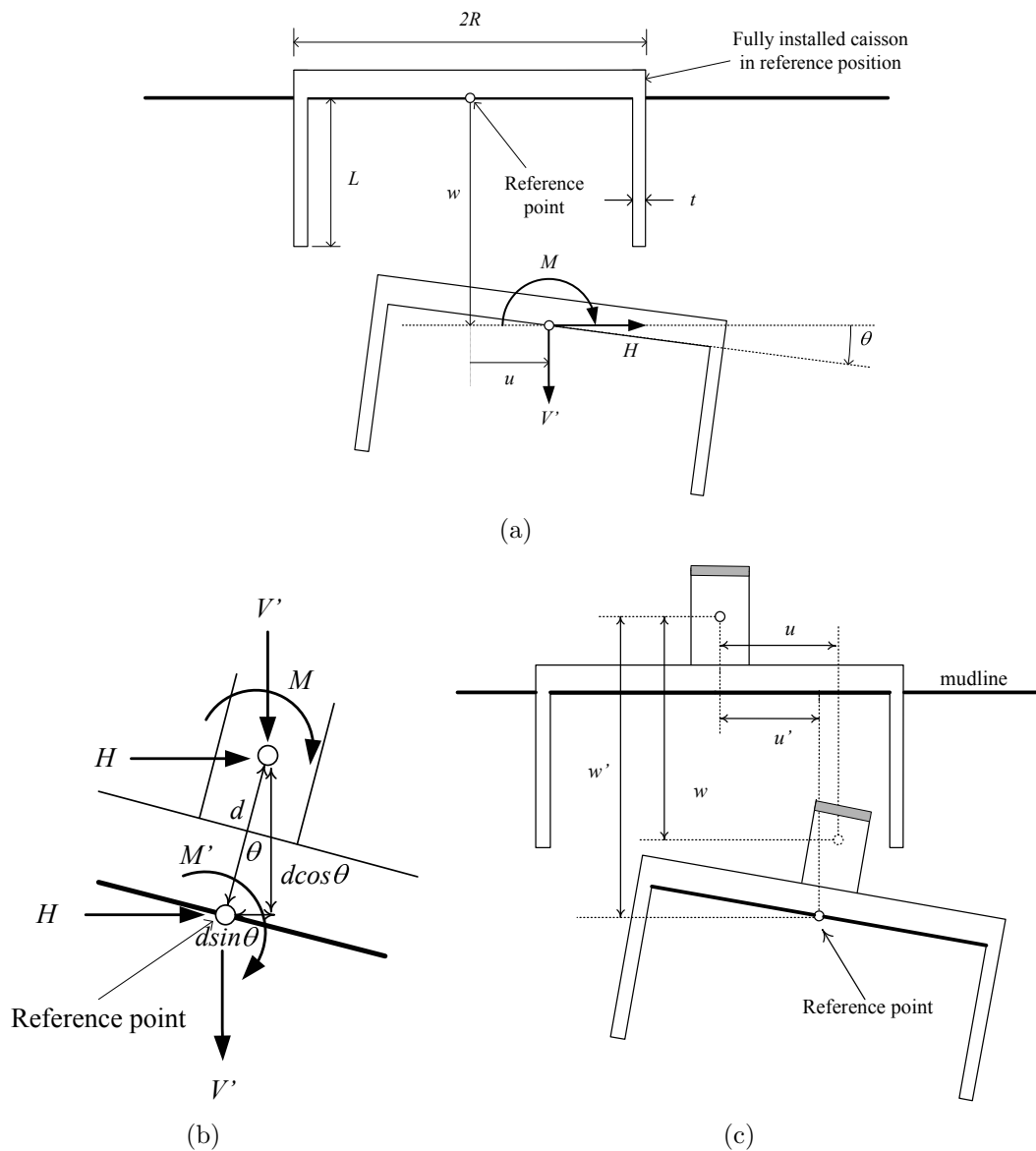


Figure 2.15: Coordinate system employed showing: (a) load and displacement components for a *VMH* combining loading, (b) loads applied to a certain point and the equivalent loads transferred to the reference point, and (c) displacements occurring in a certain point and the equivalent displacements transferred to the reference point

Chapter 3

VERTICAL LOADING OF SKIRTED FOUNDATIONS IN SAND

Abstract

The study of the relationship between the vertical load and the vertical displacement in soil-footing interaction problems is essential, not only from the vertical capacity point of view but, also to solve combined loading capacity problems. The bearing capacity formulation is used to analyse the failure of skirted footings tested under pure vertical load. It was found that bearing capacity increases with the length of the footing skirt. Axial symmetric bearing capacity factors for flat footings were used. The depth effect did not affect significantly the surcharge bearing capacity factor N_q for caisson aspect ratios below one. However, the weight bearing capacity factor N_γ increased considerably with the caisson aspect ratio. Finally, the development of a hardening law was pursued, proving that the use of a three term hyperbola gives a good agreement with experimental results in loose sand. For dense sands a formulation is proposed, which is able to reproduce hardening after peak and softening response.

3.1 INTRODUCTION

The investigation of the vertical capacity of skirted footings has two main objectives. The first is the determination of the ultimate bearing capacity under pure vertical load, and the second is the formulation of a hardening law for plasticity analysis. Although low vertical loads are expected owing to the light weight of wind turbines, as explained in Chapter 1, smaller caissons as part of tripod or tetrapod configurations can experience much larger vertical loads than in monopod caissons. Furthermore, in this study it was of particular interest to provide a complete insight into the different phases of loading that a skirted footing undergoes under the application of a monotonically increasing vertical load until failure and beyond.

A series of tests performed to investigate the load-penetration response of seven skirted footings on dry sand, covering loose and dense samples, is presented in Villalobos *et al.* (2003a). A preliminary analysis of these experimental results was carried out Byrne *et al.* (2003). Figure 3.1 shows two test results as examples where it is possible to define three phases in the $h - V'$ curves. The upper curve corresponds to caisson F_5 which is loaded into a dense sample of Leighton Buzzard sand. The lower curve corresponds to the same caisson, but in a very loose sample of Dogs Bay sand. Phase A represents the *installation* of the caisson, in which only the end bearing forces over the tip and the frictional forces along the external and internal walls of the caisson skirt are involved. Phase B corresponds to the development of the *bearing capacity* of the whole caisson, *i.e.* after the skirt wall inside the footing has fully penetrated the ground and simultaneously the caisson lid contacts the soil. The departure from phase A to B can be clearly observed in both curves, where dashed circles show the contact penetration h_c and the contact load V_c . Note that the onset of phase B differs, whilst for the caisson in a loose sample the *contact penetration*, occurred at a value close to the skirt length $h_c = L$, of 51 mm, for the caisson in the dense sample this occurred for h_c of 42 mm (though inside the caisson the skirt is embedded a depth L). This difference is caused by the formation of a soil plug which in dense sands raises above the mudline level during skirt penetration.

The penetration forces the dense packing of grains (low specific volume) around the skirt to rearrange. Due to the rearrangement grains shear each other to a level that dilates the sand, therefore, the initial low specific volume increases. Moreover, the phenomenon of dilatancy becomes more pronounced at low stresses. Subsequently, Figure 3.1 shows that in the dense sample *failure* can be recognised as a peak load is reached, whereas for the caisson in the loose sample the definition of failure is not straightforward. A dashed circle indicates a section where failure is assumed due to foundation stiffness reduction (definition and determination is presented in section §3.3.1). Finally, phase C defines *post failure* behaviour of the foundation where, despite previous failure, capacity increases as additional large penetration occurs. Note the complex response sequence after the peak load; further grains arrangements cause a short relaxation and softening followed by a final hardening.

The installation part (phase A) will be the subject of Chapter 4, whereas parts B and C are the theme of this chapter. However, measured heave caused by pushed installation has been included.

An initial interest in the study of bearing capacity was to assess the proximity of the vertical load required to install a caisson V_c , to the failure load. Despite the very different type of sands chosen, Figure 3.1 shows that in the dense sand the caisson failed at a load almost seven times V_c , and in the loose sand failure occurred at a load almost four times V_c .

Bearing capacity calculations of ‘rigid’ flat footings are based on the assumption of failure mechanisms. The same type of failure mechanisms may be assumed for skirted footings. But, the soil enclosed by the skirt acts as a flexible ‘cushion’ instead of being a rigid block. However, there are not as yet analytical solutions for this particular case, therefore, the bearing capacity has to be obtained from calculation procedures for rigid flat footings. Even though solutions for the flat footing problem, proposed by Terzaghi (1943), Meyerhof (1963), Brinch Hansen (1970) and Vesic (1975), are available in the majority of foundation engineering textbooks (Bowles, 1996; Craig, 1998; McCarthy, 1998; Tom-

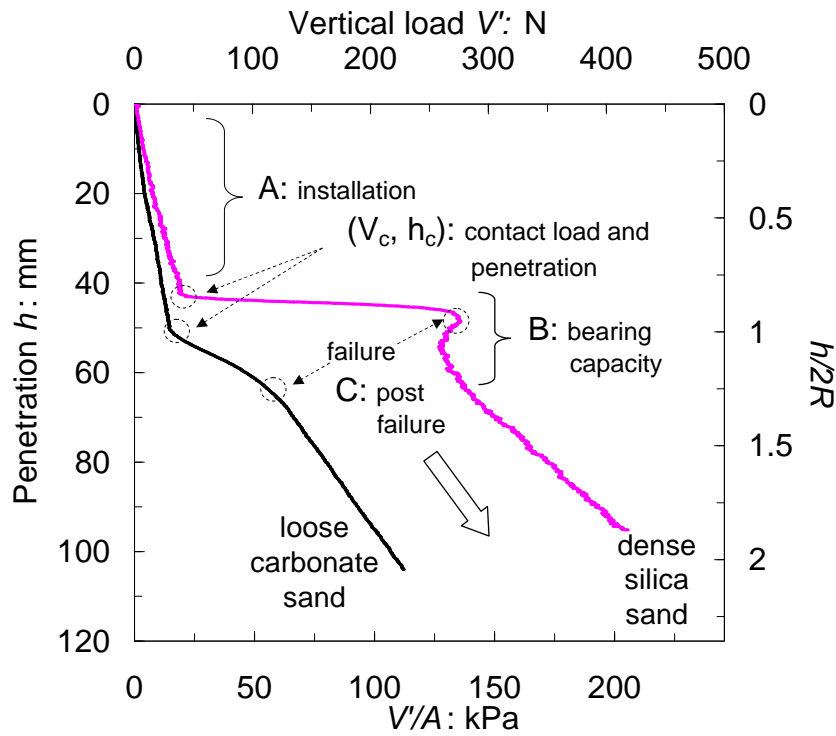


Figure 3.1: Measured vertical load-displacement curves of test FV55 in a $R_d = 88\%$ silica sand, and test FV65 in a $R_d = 26\%$ carbonate sand, using caisson model F_5 , $2R = L = 51$ mm and $\frac{L}{2R} = 1$

linson, 1999; Das, 2003) there are still unresolved issues. Using the stress characteristic method the bearing capacity problem in triaxial or plane conditions can be solved without the superposition of cohesive, surcharge and weight components (Bolton and Lau, 1993; Cassidy and Houlsby, 2002). Research is still in course to solve bearing capacity problems without the superposition effect (Ukritchon *et al.*, 2003; Zhu *et al.*, 2003; Kumar, 2003; Hjiatj *et al.*, 2004, 2005; Kobayashi, 2005; Osman and Bolton, 2005; Tsukamoto, 2005; Smith, 2005; Przewłócki, 2005; Lee *et al.*, 2005). Exact bearing capacity calculations are claimed to be achieved by means of the stress characteristic method using remeshing in the computer program ABC developed by Martin (2005). In addition, the validity of proposed empirical factors to account for footing shape, embedment, footing and load inclination are still being studied (Salgado *et al.*, 2004; Lee and Salgado, 2005; Zhu and Michalowski, 2005; Edwards *et al.*, 2005; Honjo and Amatya, 2005; Gourvenec *et al.*, 2006; Cerato and Lutenecker, 2006). Furthermore, the classical bearing capacity theory does not include calculation of settlements.

From preliminary calculations caissons taken as a rigid flat footing of depth $D = L$, can significantly increase the bearing capacity compared with the case when the skirt is ignored $D = L = 0$. However, there is still doubt whether the softening effect of the soil plug may modify significantly the bearing capacity. Therefore, research is needed to know how to assess the bearing capacity of skirted footings.

Returning to the second objective of this investigation, to solve the combined loading problem within the framework of plasticity theory as described in the introductory chapter, it is necessary to define a hardening law. In the study of the combined loading response of shallow foundations Martin (1994), Gottardi *et al.* (1999) and Houlsby and Cassidy (2002), have found that the hardening law relationship is mainly given by the vertical load penetration response. However, predictions of footing response have been improved when hardening becomes a function not only of the plastic vertical displacement, but also of the plastic rotational and plastic horizontal displacements (Houlsby and Byrne, 2001; Cassidy *et al.*, 2002). Bienen *et al.* (2006) extended the hardening law formulation including the six components of plastic displacement. Furthermore, one of the conclusions of Nguyen-Sy (2006) is that the value of the parameter V_o (interpreted as bearing capacity within plasticity models) has significant repercussions on the prediction of monotonic and cyclic combined loading response of suction caissons using hyperplasticity theory.

The present chapter will present experimental results from bearing capacity tests. A brief review of the bearing capacity formulation is given with the intention of showing the expressions later used in the analysis. Study of the hardening law is presented at the end of the chapter.

3.2 BEARING CAPACITY OF SHALLOW FOUNDATIONS

Theoretical and experimental research has been carried out for more than eighty years to resolve rigorously the bearing capacity of shallow foundations on sand. There are available solutions for flat strip and flat circular footings as well as for conical footings, but not yet for skirted footings. Since a flat footing is a particular case of a skirted footing with no skirt, the study of flat footings is a natural starting point for the subsequent study of skirted footings.

By means of a combination of lower and upper bound theorems and empiricism Terzaghi (1943) developed a general bearing capacity formulation which has been widely used in engineering practice. For a strip footing of width B and length L ($A = BL$) on a soil with angle of friction ϕ' , cohesion c , and surcharge σ'_v the bearing capacity V_o can be written as:

$$\frac{V_o}{A} = cN_c + \sigma'_v N_q + \frac{1}{2}\gamma'BN_\gamma \quad (3.1)$$

where N_c , N_q and N_γ are the bearing capacity factors. By analysing the punch of a strip metal tool on the surface of a metal mass (assumed cohesive but weightless), Prandtl (1920) determined the exact solution for N_c , which correspond to the first squared brackets in the following expression:

$$\frac{V_o}{A} = c \left[\cot \phi' \left\{ \tan^2 \left(\frac{\pi}{4} + \frac{\phi'}{2} \right) e^{\pi \tan \phi'} - 1 \right\} \right] + \sigma_v \left[\tan^2 \left(\frac{\pi}{4} + \frac{\phi'}{2} \right) e^{\pi \tan \phi'} \right] \quad (3.2)$$

The second squared brackets in (3.2) correspond to N_q , which was determined by Reissner (1924) from the analysis of a strip metal embedded in a metal mass (assumed frictional but cohesionless and weightless). In geotechnical engineering expression (3.2) has been adopted to solve bearing capacity problems, where N_c and N_q are expressed as:

$$N_c = (N_q - 1) \cot \phi' \quad (3.3)$$

$$N_q = \tan^2 \left(\frac{\pi}{4} + \frac{\phi'}{2} \right) e^{\pi \tan \phi'} \quad (3.4)$$

For a soil with weight there is not yet a unique formula for N_γ . Brinch Hansen (1970) among others, proposed the following formula for rough soil-footing contact:

$$N_\gamma = 1.5(N_q - 1) \tan \phi' \quad (3.5)$$

This simple semi-empirical expression is useful in the sense that it gives values which are close to the analytically calculated values by Bolton and Lau (1993), Cassidy and Houlsby (2002) and Martin (2005).

Terzaghi's formulation (3.1) has been subject to several adjustments, not just for the self-weight bearing capacity factor N_γ , but also for the inclusion of shape factors for footing geometries different from the strip case. Shape factors are no longer required for circular footings since values of N_q and N_γ are now available. Exact values of the axisymmetric N_q can be found in Bolton and Lau (1993).

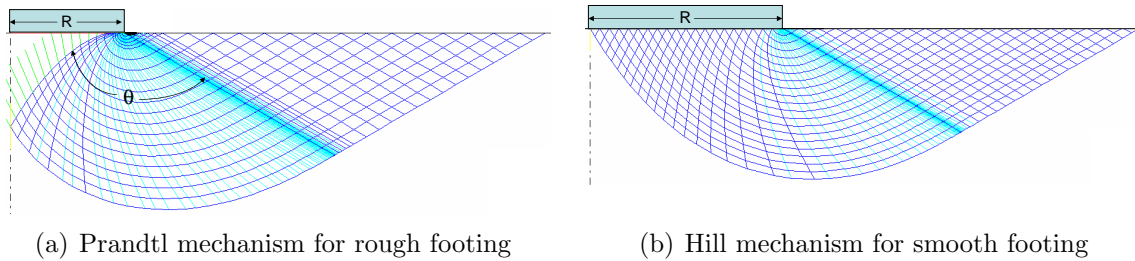


Figure 3.2: General shear failure mechanisms (Martin, 2005)

The development of a general shear failure mechanism is assumed as a condition *sine qua non* in bearing capacity analysis. In fact, Prandtl and Hill mechanisms of shear failure, shown in Figures 3.2(a) and 3.2(b), correspond to the case of general shear failure for rough and perfectly smooth footing-soil contact respectively. Alternatively, Vesic (1975) defined three possible symmetric failure mechanisms depending on the relative density R_d of the soil: general shear failure, local shear failure and punching failure. The bearing capacity analysis of skirted footings has the difficulty that the soil properties initially measured may change during installation since the rim of the skirt causes shearing of the soil

with a deep failure mechanism (Meyerhof, 1951). In addition, more significant changes are expected during phase B (Figure 3.1) where much higher loads develop. Consequently, the stress level increases considerably below the caisson lid leading to different consequences depending on the soil packing state. For a loose sand a contractile response induces an increase of the soil density and hence an increase of the angle of friction mobilised during failure. On the other hand, for a dense sand a dilative response during installation and before failure causes the angle of friction mobilised to reduce.

The bearing capacity of a caisson foundation can be calculated using bearing capacity theory as follows:

$$V_o = 2\pi R_o \int_0^h \tau_o dz + (\sigma'_v N_q + \gamma' R_o N_\gamma) A_o \quad (3.6)$$

where the subscript $_o$ identifies the radius, shear stress and area of the outside of the caisson as opposed to the inside, h is the caisson penetration, and N_q and N_γ are the bearing capacity factors for circular footings. The first term in (3.6) is the friction force which acts only on the outside skirt wall.

3.3 EXPERIMENTAL RESULTS

A total of 45 vertical loading tests using model scaled skirted footings were conducted. The skirted footings represent suction caisson foundations. The tests were performed using caissons F_{1-7} which were loaded with the *VMH* loading rig on sands of different mineralogies and densities (see Chapter 2 for description of the rig, model footings and soil samples used). The main series of tests, 36 in all, were carried out on a dry Leighton Buzzard sand at four different densities. A second set of tests, 9 in total, were carried out on a very loose dry Dogs Bay carbonate sand.

Displacement controlled tests were carried out under a constant velocity of penetration $\dot{h} = 0.05$ mm/s. In Table 3.1 each test is identified by two digits; the first indicates the sample number (or tank number) and the second the test number for that sample. The

tests are labelled from FV21 to FV59 for the Leighton Buzzard sand and from FV61 to FV69 for the Dogs Bay sand. The first tank series was a trial run. Each block in Table 3.1 corresponds to a caisson F with aspect ratio $\frac{L}{2R}$, tested in a soil with relative density R_d . V_c and h_c represent the soil-caisson lid *contact* load and penetration, as shown in Figure 3.1, where contact can also be understood as the end of installation. V_y and h_y represent the load and penetration at *yield*. The word yield is used in this particular loading condition to classify the foundation *failure* or collapse as indicated in Figure 3.1. Yield in a broader context is an irreversible phenomenon of deformation or displacement which can be present or not depending on the loading path applied.

Table 3.2 presents the values of the soil unit weight γ_d , specific volume v , and peak friction angle ϕ'_{peak} . The only parameter directly measured was γ_d , thereby the specific volume was obtained as $v = \frac{G_s \gamma_w}{\gamma_d}$, where $\gamma_w = 9.8 \text{ kN/m}^3$. The calculation method to determine ϕ'_{peak} was presented in section §2.2.4.

3.3.1 Loose sand samples

The series of tests on Dogs Bay sand and Leighton Buzzard sand are shown in Figures 3.3(a), 3.3(b) and 3.3(c). Similar load-displacement curves can be observed in the sense explained in Figure 3.1, *i.e.* phases A, B and C are present (except phase A for the flat footing). Yield loads V_y (circles) were determined as the intersection of two straight lines fitted to phase B and phase C respectively (determination of yield loads will be again touched on in Chapter 5). By superposing the theoretical bearing capacity curves obtained from a constant angle of friction ϕ' (equation (3.6)) on the experimental curves, the mobilised ϕ'_{mob} can be identified in Figures 3.3(a), 3.3(b) and 3.3(c). The friction outside the caisson was calculated by solving the integral for a linear distribution of stresses:

$$2\pi R_o \int_0^h \tau_o dz = \pi R_o \gamma_d (K \tan \delta)_o h^2 \quad (3.7)$$

For the range of ϕ'_{mob} values of the loose sands a lateral earth pressure coefficient $K \approx 2$ was adopted (see beginning of Chapter 4 for the expression of K used), and assuming a

Table 3.1: Summary of vertical loading tests

Caisson, $\frac{L}{2R}$	Test	R_d : %	V_c : N	h_c : mm	V_y : N	h_y : mm
F ₁ , 0	FV61	26			32	6.3
	FV27	40			18	3.0
	FV41	47	n.a.	n.a.	26	3.5
	FV31	83			118	4.0
	FV51	88			105	1.5
F ₂ , 0.26	FV62	26	7.3	13.1	64	28.0
	FV21	40	6.0	13.4	32	17.5
	FV49	47	5.2	12.0	44	16.4
	FV39	83	10.4	11.3	180	16.5
	FV52	88	14.8	10.7	153	13.0
F ₃ , 0.51	FV63	26	75	13.6	25.4	38.5
	FV22	40	52	30.5	10.5	23.4
	FV43	47	8.5	22.1	64	27.2
	FV33	83	19.2	20.6	236	30.0
	FV53	88	18.1	21.2	225	24.5
F ₄ , 0.76	FV64	26	21.3	39.1	96	54.5
	FV29	40	16.9	36.6	80	44
	FV44	47	16.4	33.7	82	41
	FV34	83	35.1	32.0	265	39
	FV59	88	32.8	31.1	275	35
F ₅ , 1	FV65	26	29.9	50.5	112	63.5
	FV24	40	27.1	48.6	90	57
	FV45	47	23.8	45.6	104	54.5
	FV58	88	50.0	42.8	335	50
	FV35	83	50.5	42.2	330	46
F ₆ , 1.51	FV66	26	40.0	76.2	154	95.5
	FV25	40	38.3	70.9	130	79.5
	FV46	47	42.1	69.8	155	78
	FV36	83	86.7	63.6	416	71
	FV56	88	69.9	64.2	415	69
F ₇ , 2.01	FV68	26	63.2	103.1	173	118
	FV26	40	67.0	97.8	170	107
	FV47	47	61.1	95.0	225	106.6
	FV37	83	136.1	86.0	450	98
	FV38	83	123.2	87.2	700	100
	FV57	88	129.4	87.0	560	92

skirt-soil interface angle of friction $\delta = 16^\circ$ results $(K \tan \delta)_o \approx 0.6$. Nevertheless, values of the outside friction (3.7) are practically negligible compared with the other terms in expression (3.6). Values of the exact bearing capacity factors (N_q from Bolton and Lau, 1993, and N_γ from Martin, 2005) were adopted considering a smooth soil-caisson contact according to section §2.3. The installation sequence shown in Figure 2.14, in which the

Table 3.2: Values used in bearing capacity calculations

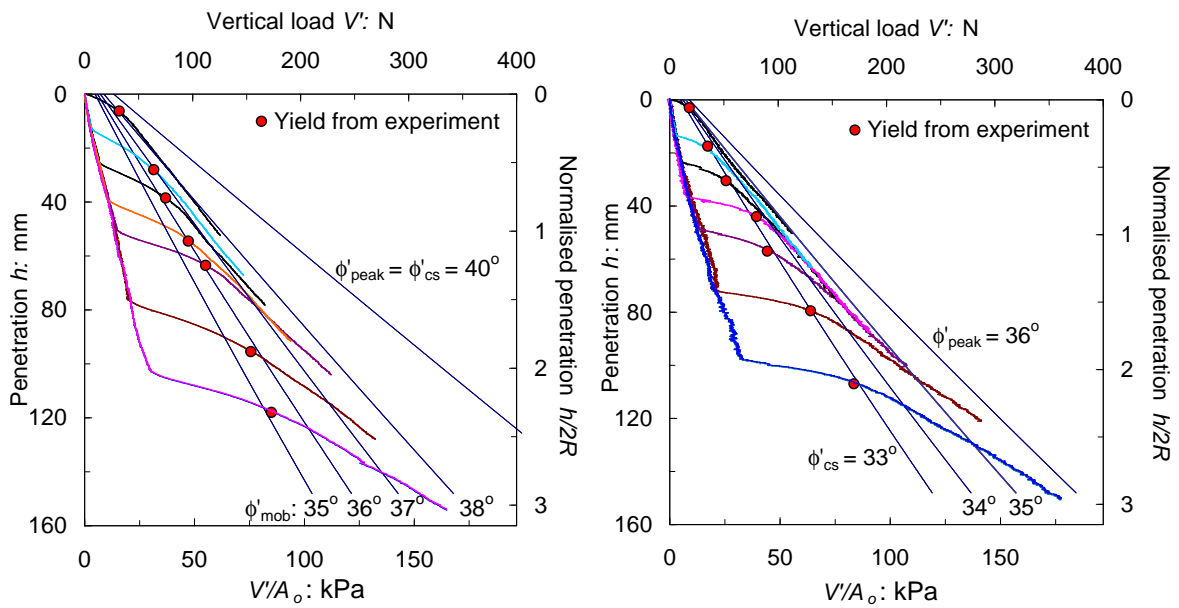
Sand	R_d : %	γ_d : kN/m ³	ν	ϕ'_{peak}
Dogs Bay	26	10.34	2.609	40.3
Leighton Buzzard	40	15.69	1.657	35.9
	47	15.89	1.636	36.9
	83	17.00	1.529	42.2
	88	17.16	1.515	43.5

soil inside the caisson rests at the same level of the soil outside the caisson, was practically true for the caissons installed into the very loose Dogs Bay sand. Conversely, in the loose Leighton Buzzard sand this was not the case due to soil plug heave (heave is further discussed in section §3.3.5).

Bearing capacity of caisson foundations is clearly overestimated if ϕ'_{peak} is used in the calculations. This overestimation increases with the aspect ratio $\frac{L}{2R}$. It is worth noting, however, that bearing capacity is reasonably well predicted for the flat footing using ϕ'_{peak} . Observing again Figure 3.3(a), yield occurs after a considerable settlement of the caisson. This considerable compression has been also reported for a calcareous sand from Western Australia by Byrne and Houlsby (2001) for tests with a flat footing of diameter 150 mm. After a settlement of almost half of the diameter they could not determine yield. It is possible that due to this high soil compressibility a critical state condition may not be reached. For instance, Nutt (1993) determined a value of $\phi' = 37.1^\circ$ from direct shear tests on a very loose Dogs Bay sand under $\sigma'_v = 40$ kPa. Luzziani and Coop (2002) and Coop *et al.* (2004) also determined that the critical state is reached for shear strains higher than 20% as observed in Figure 3.4. Therefore, in very loose sands since the punching shear mechanism prevents from the spread of failure surfaces (Vesić, 1975), ϕ'_{mob} is likely to not reach the value in critical state ϕ'_{cs} . Indeed, values between 35° and 38° are mobilised at yield according to Figure 3.3(a).

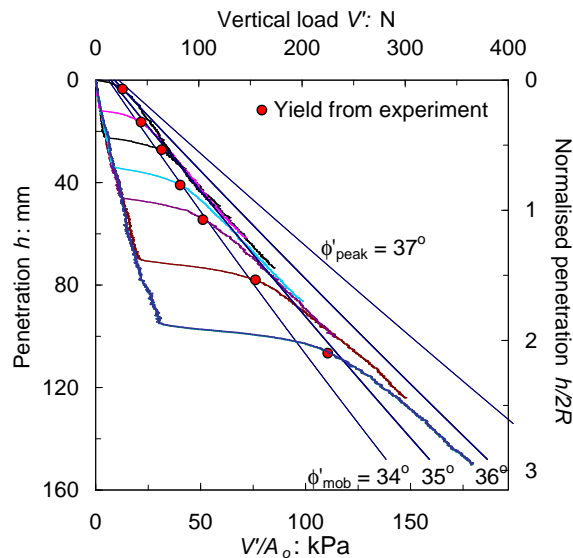
On the other hand, for the tests in silica sand, a local shear mechanism forms truncated failure surfaces, which can extend only along the spiral fan shown in Figure 3.2(b). As a consequence, the assumption of a ϕ'_{peak} in the calculations also overestimates bearing

capacity although not as much as for the calcareous sand. In fact, a clear critical state condition occurred at yield as can be observed in Figure 3.3(b) since a value of ϕ'_{cs} is mobilised. After yield ϕ'_{mob} increases due to compaction caused by further settlement, but yet ϕ'_{peak} is not reached. Figure 3.3(c) shows that soil dilation, though little, is restricted to develop only in the spiral fan and ϕ'_{mob} does not reach ϕ'_{peak} either. Therefore, to calculate bearing capacity of a caisson foundation in loose sand the *mobilised* angle of friction ϕ'_{mob} is unlikely to reach ϕ'_{peak} . It is important to know that the use of a single ϕ'



(a) Dogs Bay sand, $R_d = 26\%$

(b) Leighton Buzzard sand, $R_d = 40\%$



(c) Leighton Buzzard sand, $R_d = 47\%$

Figure 3.3: Measured vertical load-displacement curves and calculated bearing capacity for caissons with seven different $\frac{L}{2R}$

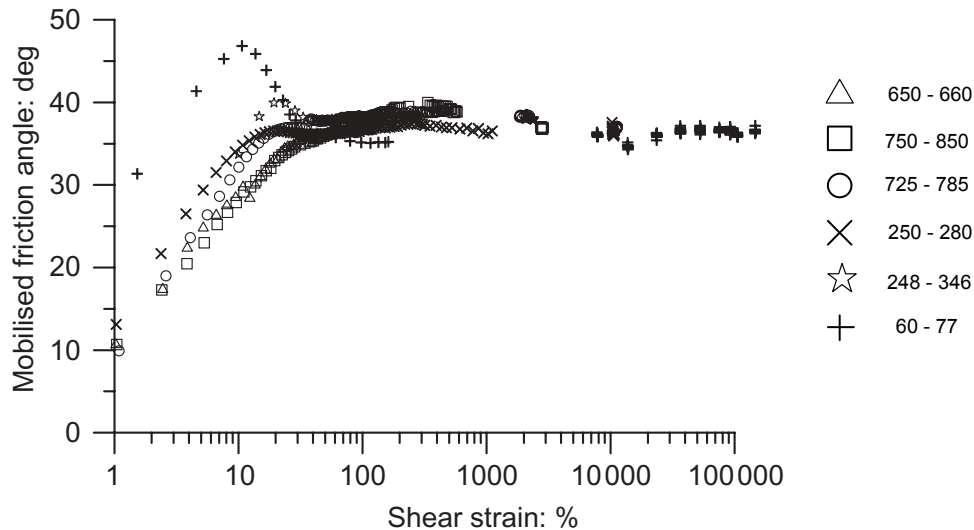


Figure 3.4: Mobilised angle of shear resistance with shear strain of Dogs Bay sand. Numbers next to symbols correspond to the net σ'_v during shearing (taken from Coop *et al.*, 2004)

should be treated as an attempt to represent an average value of the zones in failure.

3.3.2 Dense sand samples

The results of tests in dense sand are shown in Figures 3.5(a) and 3.5(b). In loose sample tests yield loads were found always at displacements $h_y > L$, whereas for dense samples $h_y \leq L$ (except in tests FV39 and FV33). It can be observed that a much higher increase of load with displacement leads to higher bearing capacity presented in the form of peaks. This peak load demonstrates that the soil dilated considerably as a consequence of shearing. Dilative behaviour was observed as heave of the soil surface around the caisson, which indicates the development of a general shear mechanism (see Figure 3.2(a) in Vesić, 1975). Because the tests were displacement controlled, it was possible to record beyond the peak a short load relaxation followed by a softening response that lasted until a settlement of around 20% of the diameter. The additional surcharge gained with subsequent settlement caused the final hardening response.

Since a general shear mechanism is expected to occur owing to the high values of R_d (Vesić, 1975), ϕ'_{peak} should be used. By superposing the theoretical curves on the experimental curves, it is observed that for flat footings bearing capacity calculation with

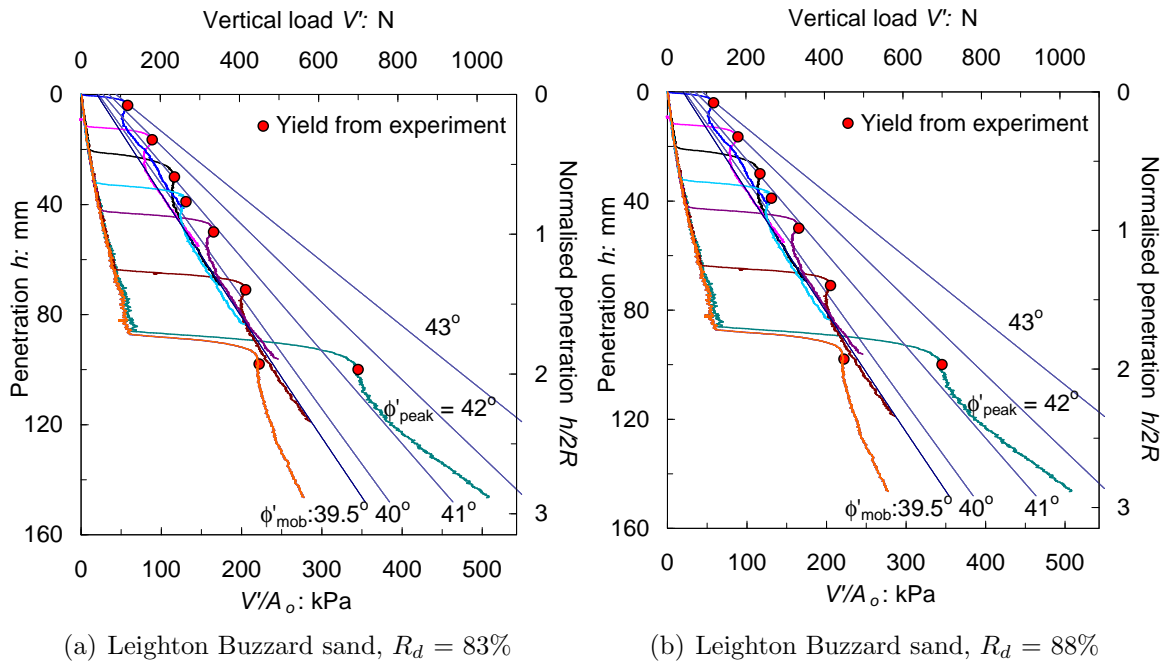


Figure 3.5: Measured vertical load-displacement curves and calculated bearing capacity for caissons with seven different $\frac{L}{2R}$

ϕ'_{peak} gives good predictions, nevertheless, for skirted footings the predictions are over-estimated. The discrepancy may be seen as not so significant, however, since the values of ϕ'_{mob} are high, one or two degrees can represent a big difference in bearing capacity. The reduction from ϕ'_{peak} to ϕ'_{mob} may be due to higher stresses developed with depth (increase in surcharge), which were not possible to account for in the calculation of ϕ'_{peak} . As a consequence, soil dilation was then restricted from developing completely. Alternatively, installation effects may reduce the initial soil strength. Although the soil plug is compressed during bearing capacity (phase B), there is irrecoverable deformation due to softening of the soil during installation caused by previous soil dilation in the plug, at the tip and next to the skirt outside the caisson. Soil dilation was reduced even more after yield, reaching a stage of strength where bearing capacity increases mobilising a lower ϕ'_{mob} between 39° and 40° .

3.3.3 The axisymmetric bearing capacity coefficient N_q

From the $h - V$ plots presented in Figures 3.3(a) to 3.5(b) it is clear that bearing capacity increases with settlement. Experimental data shown in Figure 3.6 confirms that N_q increases with $\frac{L}{2R}$ and R_d . The calculation of N_q was done along phase C, where

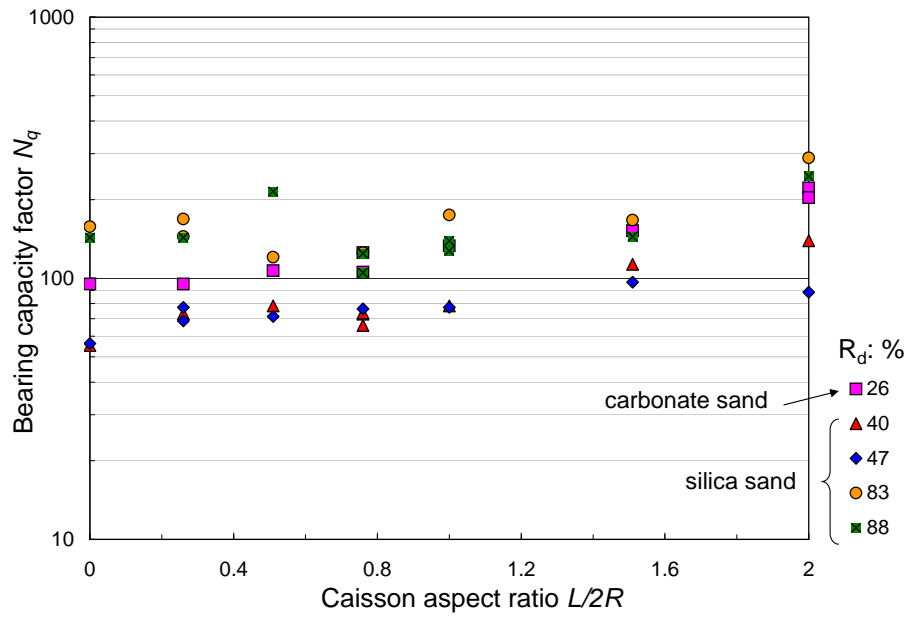


Figure 3.6: Experimental values of axisymmetric N_q

the component of surcharge is more predominant than self-weight. This occurs for large displacements when the footing has settled more than 20% of its diameter (plus h_c). The points plotted in Figure 3.6 were calculated from expression (3.1) using the following equation:

$$\frac{V'}{\pi R^2} = \gamma' w N_q + \frac{1}{2} \gamma' (2R) N_\gamma \quad (3.8)$$

where V' is the mobilised bearing capacity. For sufficiently large settlements the surcharge component predominates over the weight component, thus N_q can be expressed as:

$$N_q = \frac{1}{\gamma' \pi R^2} \frac{\Delta V'}{\Delta w} \quad \text{for } w > h_c + 0.4R \quad (3.9)$$

Despite the scatter it can be observed in Figure 3.6 that for aspect ratios less than one N_q is practically constant for a certain level of relative density, and for aspect ratios $1 < \frac{L}{2R} < 2$, N_q slightly increases.

Friction around the skirt wall was not considered in equation (3.9). To evaluate friction effects it will be assumed that the friction force per unit of penetration can be obtained by means of:

$$\Delta F = \gamma' (K \tan \delta) \pi 2R_o h \Delta h \quad (3.10)$$

where F is the friction force, $(K \tan \delta)$ is the coefficient of lateral earth pressure K multiplied by a friction coefficient $\tan \delta$, R_o is the exterior radius, and h is the penetration, *i.e.* $h = h_c + w$, where h_c is the contact penetration between the soil plug and the caisson lid. Expression (3.10) can also be derived as the increase in lateral earth pressure due to the extra settlement Δw as follows:

$$F + \Delta F = \gamma'(K \tan \delta)\pi 2R_o \left[\frac{1}{2}(h_c + \Delta w)^2 - \frac{\Delta w^2}{2} \right] = \gamma'(K \tan \delta)\pi 2R_o \left[\frac{1}{2}h_c^2 + h_c\Delta w \right] \quad (3.11)$$

Thus N_q is given by:

$$N_q = \frac{\Delta V'}{\Delta h} \frac{1}{\gamma' \pi R^2} - 2(K \tan \delta) \frac{h}{R} \approx \frac{\Delta V'}{\Delta h} \frac{1}{\gamma' \pi R^2} - \frac{h}{R} \quad (3.12)$$

The evaluation of the second term in (3.12) gives the reduction in the N_q value caused by the friction on the external skirt wall, which can be approximated to the penetration radius ratio $\frac{h}{R}$. Because of the small magnitude of $\frac{h}{R}$ the effect of friction can be neglected.

3.3.4 The axisymmetric bearing capacity coefficient N_γ

The values of N_γ were determined directly from the V_y loads in the $h - V$ curves, and the friction force F developed during installation δ was subtracted from V_y in the following

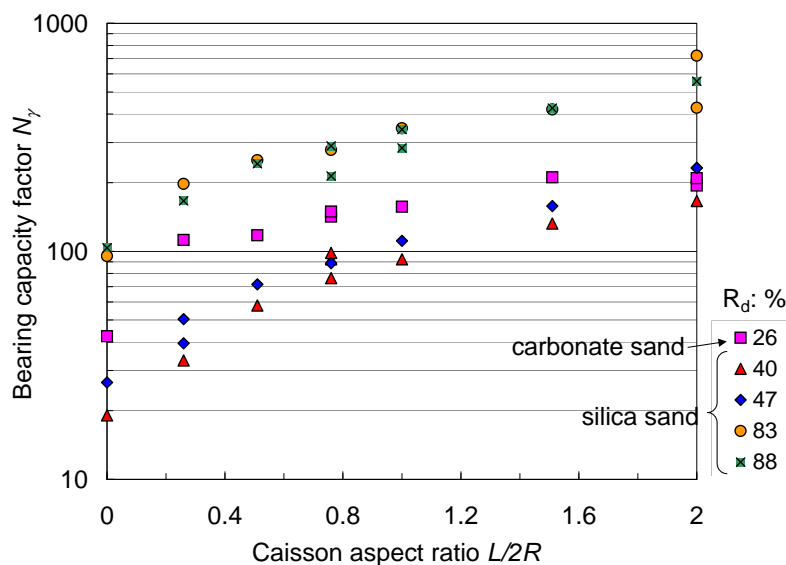


Figure 3.7: Experimental values of axisymmetric N_γ

form:

$$N_\gamma = \frac{V_y - F}{\gamma' \pi R^3} \quad (3.13)$$

A considerable increase of N_γ appears with relative density and with caisson aspect ratio. Since surcharge has not been accounted for in the N_γ analysis, it is clear that the N_γ increase is strongly related to the depth increase for a given relative density.

3.3.5 Soil plug heave

Heave of the soil-plug caused during installation is a concern because caisson design must be modified. It is necessary to evaluate the proportion of heave in order to include it in subsequent calculations.

Heave was determined as the subtraction of the penetration h_c to the skirt length L . Values of h_c are listed in Table 3.1 and heave is plotted in Figure 3.8(a) as a ratio of the diameter ($\frac{L-h_c}{2R}$) and in Figure 3.8(b) as ratio of the skirt length ($1 - \frac{h_c}{L}$). It is clearly observed that the onset of contact between the soil and caisson lid occurs always before full penetration L is completed ($h_c < L$), with the exception of tests in very loose carbonate sand. Caissons in dense silica sand generated a steady increase of heave with the aspect ratio, as shown in Figure 3.8(a). However, for loose samples there was a limit between $\frac{L}{2R} = 1.5$ and $\frac{L}{2R} = 2$. Figure 3.8(b) shows that heave had a maximum at $\frac{L}{2R} = 0.5$ reducing for other aspect ratios.

Heave can be calculated assuming that the soil displaced is equivalent to the volume of skirt wall penetrated.

$$h_{heave} = L - h_c = \left[\left(\frac{R}{R - 2t} \right)^2 - 1 \right] h_c \quad (3.14)$$

This simple equation offers a reasonable solution for the loosest silica sand as shown in Figure 3.8(a). For dense soils, it could be argued that the vertical stresses of the soil inside the caisson are higher than outside the caisson due to arching (Chapter 4). Consequently

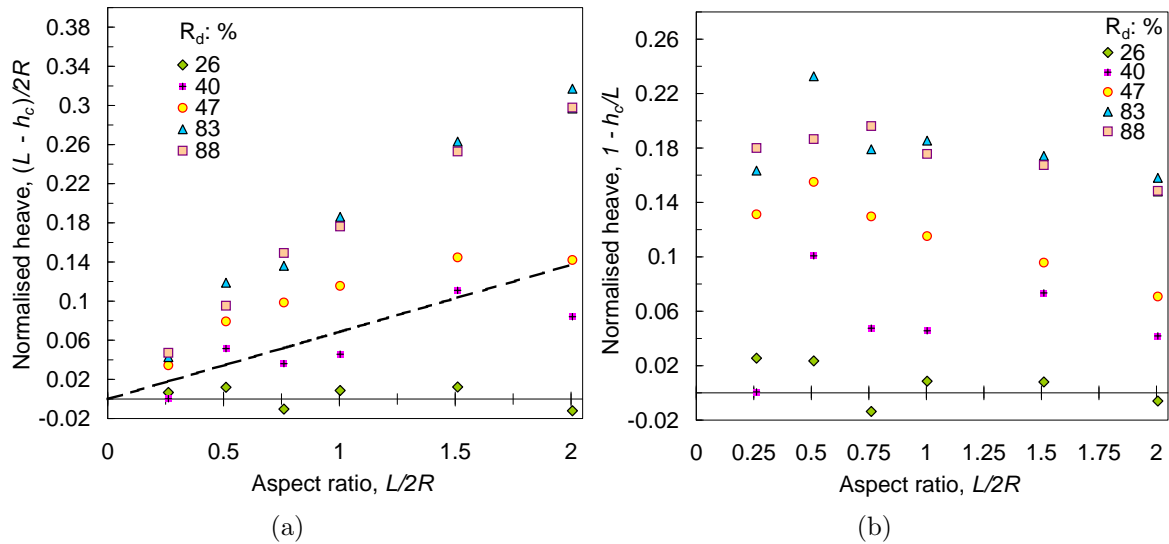


Figure 3.8: Heave found at the end of the installation for skirted footings pushed into the ground as a ratio of the (a) diameter, and the (b) length

the soil is removed completely outwards and the heave would be caused only by dilation of the sand. More importantly, dilation of dense sands can cause heave as high as 2.5 times that given by expression (3.14).

3.4 HARDENING LAW

As pointed out in the introduction, the determination of a hardening law is vital for the development of a hyperplasticity model to study the combined loading problem of caisson foundations. Construction of the hardening law requires modelling of the relationship between the vertical load and the vertical displacement. Looking at Figure 3.1, the part of the hardening law corresponding to phase B and C will be developed in the following. Phase A (installation) will be considered in Chapter 4.

Nova and Montrasio (1991) performed purely vertical load-controlled tests on loose sand. They removed the soil whilst the footing penetrated the ground to keep the surface at the same level as the footing base. Although an unrealistic procedure, it is useful in determining a clear maximum vertical load, which make modelling easier. An expression

suggested by Butterfield (1980) can be used to reproduce that response,

$$\frac{V'}{V_y} = 1 - e^{-\frac{aw}{V_y}} \quad (3.15)$$

where V_y is the asymptote of the curve (failure load) and a the initial slope of the load-settlement curve. Because the surcharge exists, especially for caissons, it is necessary to find an expression that is not forced to have a horizontal asymptote, but an inclined asymptote. de Santa Maria (1988) proposed a three-parameter hyperbola which is able to achieve an inclined asymptote.

$$V' = \frac{w}{\frac{1}{a} + \frac{w}{b+cw}} \quad (3.16)$$

Firstly, the parameter a is the initial slope of the curve which for a rigid circular foundation can be modelled as a static spring with a constant stiffness, K_V given by (Boussinesq, 1878):

$$a = K_V = \frac{4GR}{1-\nu} \quad (3.17)$$

where G and ν are the soil elastic shear modulus and the soil Poisson's ratio respectively.

Secondly, the parameter c can be deduced from the curve slope after failure (hardening in phase C), which is given by $\gamma' N_q \pi R^2$ for a geostatic vertical stress σ'_v distribution with depth (see equation (3.9)). Then c can be obtained from the curve slope during hardening and the elastic stiffness coefficient as follows:

$$c = \frac{\gamma' N_q \pi R^2 K_V}{K_V - \gamma' N_q \pi R^2} \quad (3.18)$$

Finally, the last parameter to predict the $w - V'$ response is b , which is related to the bearing capacity of a footing without surcharge, *i.e.* $\frac{1}{2} \gamma' N_\gamma (2R) \pi R^2$. Then the expression for b results in:

$$b = \frac{\gamma' N_\gamma \pi R^3 K_V}{K_V - \gamma' N_q \pi R^2} \quad (3.19)$$

Equation (3.19) has the same denominator as (3.18), and the numerator differs only in the exponent of R and the change of N_q by N_γ . Figure 3.9 depicts the measured and calculated $w - V'$ curves using (3.16) for a flat footing tested on loose sand. The calculated curves were fitted using the ‘Solver’ procedure within MS Excel to obtain the parameters a , b and c . The properties of the soil can be obtained using equations (3.17), (3.18) and (3.19), knowing *a priori* a , b and c from the tests.

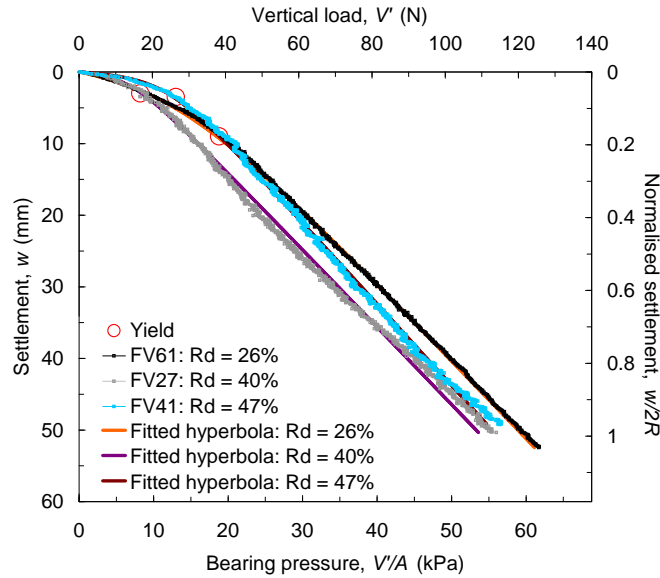


Figure 3.9: Experimental and calculated vertical load-displacement curves

$$G = a \frac{1 - \nu}{4R} \quad (3.20)$$

$$N_q = \frac{1}{\gamma' \pi R^2} \frac{ac}{a + c} \quad (3.21)$$

$$N_\gamma = \frac{1}{\gamma' \pi R^3} \frac{ab}{a + c} \quad (3.22)$$

$$w_y = \frac{b}{a + c} \quad (3.23)$$

Table 3.3 shows values of vertical stiffness K_V , shear moduli G , N_q , N_γ and settlement during yield w_y obtained using equations (3.20), (3.21) and (3.22). ν has been assumed to be equal to 0.2.

Equation (3.15) can be used as a first approximation of the $w - V'$ response in the

Table 3.3: Parameters fitted with a hyperbola for the loose sand test results

Test	K_V N/mm	G kPa	N_q	N_γ	$w_y/2R$ %
FV61	9.3	73	87	71	8.05
FV27	18.4	144	59	21	1.79
FV41	28.3	222	55	32	1.84

case of dense sand, but it is not able to predict beyond yield (V_y, w_y). Gottardi *et al.* (1999) introduced an empirical expression - used to fit the data of vertical loading tests performed on dense silica sand (yellow Leighton Buzzard sand), which can provide a fit after a peak yield. This expression is:

$$V' = \frac{K_V w^p}{1 + \left[\frac{K_V w_y}{V_y} - 2 \right] \frac{w^p}{w_y} + \left[\frac{w^p}{w_y} \right]^2} \quad (3.24)$$

where this time K_V is an initial plastic stiffness, w^p is the plastic component of the vertical displacement w , V_y and w_y are the peak value of the vertical load and vertical displacement. The use of plastic displacement refers to the fact that the elastic component must be subtracted from the total displacement. In practice the elastic component is very small compared with the plastic displacement, therefore, it can be neglected. Subsequently, Cassidy (1999) and Houlsby and Cassidy (2002) added the possibility of modifying the post-peak softening behaviour introducing a dimensionless constant f_p to 'lift' the curve avoiding V' becoming zero when w^p increases to large values. The expression is:

$$V' = \frac{K_V w^p + \frac{f_p}{1-f_p} \left[\frac{w^p}{w_y} \right]^2 V_y}{1 + \left[\frac{K_V w_y}{V_y} - 2 \right] \frac{w^p}{w_y} + \frac{1}{1-f_p} \left[\frac{w^p}{w_y} \right]^2} \quad w < 0.4R \quad (3.25)$$

Equation (3.25) equals (3.24) for $f_p = 0$. The experimental results presented here agree well with equations (3.24) or (3.25) until softening occurs. The hardening behaviour that appears after softening can not be well simulated. To include a peak response, softening and final hardening the following expression is proposed:

$$V' = \frac{aw + cw^3}{b^2 + w^2} \quad (3.26)$$

where a and c retain the same meaning as initial and final stiffness, but b is now related not only to the peak bearing capacity, but also to the minimum bearing capacity that occurs after the peak. The vertical displacement at peak is given by:

$$w_y = \sqrt{\frac{1}{2} \left(\frac{a}{c} - 3b^2 \right) - \frac{1}{2} \sqrt{\left(\frac{a}{c} - 3b^2 \right)^2 - \frac{4ab^2}{c}}} \quad (3.27)$$

and the vertical displacement at the end of softening and beginning of hardening is giving by:

$$w_s = \sqrt{\frac{1}{2} \left(\frac{a}{c} - 3b^2 \right) + \frac{1}{2} \sqrt{\left(\frac{a}{c} - 3b^2 \right)^2 - \frac{4ab^2}{c}}} \quad (3.28)$$

An iterative procedure is required to find b using equations (3.26) and (3.27) for $V' = V_y = \frac{1}{2} \gamma' N_\gamma (2R) \pi R^2$. Figure 3.10 shows an example of the improvement of the estimation of the $w - V'$ curve after peak and especially after the relaxation and softening. The further hardening is possible to reproduce using equation (3.26) in contrast with the expressions (3.24) by Gottardi *et al.* (1999) or (3.25) by Houlsby and Cassidy (2002) where the softening occurs *ad infinitum*.

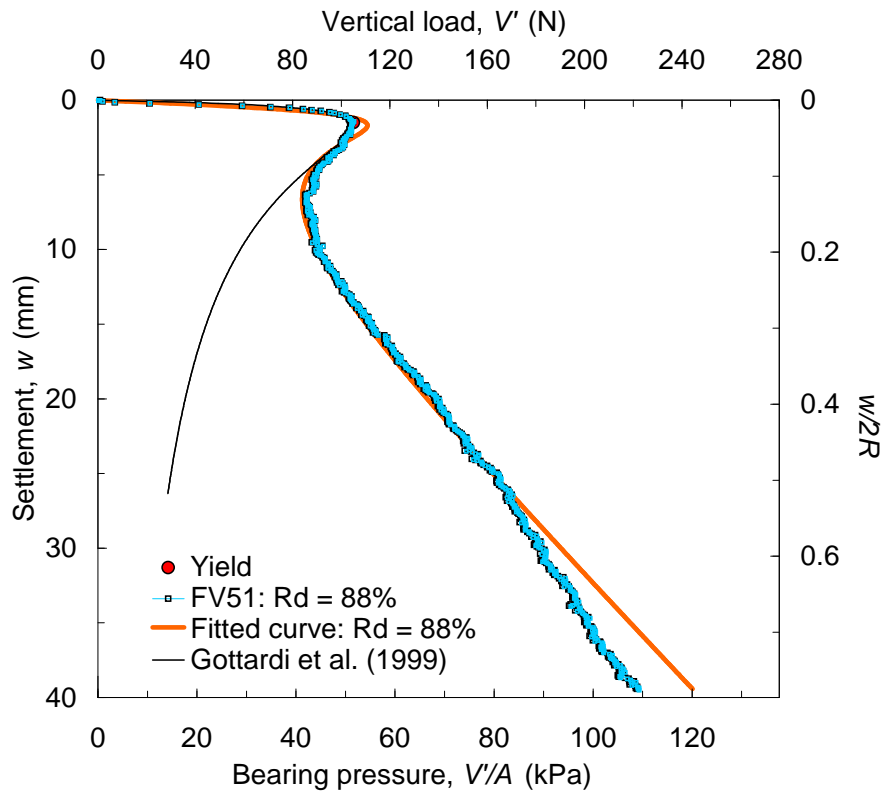


Figure 3.10: Experimental and theoretical vertical load-displacement curve for dense sand

3.5 CONCLUSIONS

Bearing capacity increases with the length of the caisson skirt. It was found that bearing capacity calculations of skirted footings require the choice of a mobilised angle of friction ϕ'_{mob} , because the use of a peak angle of friction ϕ'_{peak} leads to overestimations. In a very loose carbonate Dogs Bay sand critical state was not reached leading to values of ϕ'_{mob} less than ϕ'_{cs} , giving evidence of a punching failure mechanism. In the case of loose silica Leighton Buzzard sand, critical state was reached, hence $\phi'_{mob} = \phi'_{cs}$, which suggests the development of a local shear failure mechanism. In dense silica sand, dilation controlled the foundation response. The caisson installation (skirt penetration) formed a soil plug that rose inside the caisson above the mudline. This phenomenon is believed to reduce the ϕ'_{mob} below ϕ'_{peak} owing to progressive failure, since a general shear failure mechanism occurred.

Experimental values of N_q were obtained during the hardening response after failure. Increase of N_q with skirt length demonstrated the effect of surcharge. Experimental values of N_γ increased for $\frac{L}{2R} > 0$ reflecting the superposition effect of the surcharge.

A three term hyperbola proved to be a good hardening law expression for non-dilative sands. It was possible to interpret the physical meaning of the hyperbola parameters which allows for the determination of soil properties. For dilative sands expressions proposed by Gottardi *et al.* (1999) and by Cassidy and Houlsby (2002) were able to predict unlimited softening response. An expression capable to reproduce hardening observed after peak and softening is proposed.

Chapter 4

INSTALLATION OF SUCTION CAISSONS IN SAND

Abstract

This chapter is devoted to the study of the installation of caissons in sand by pushing and by suction. Experiments were planned and performed to assess the variables involved in the process of caisson installation. The experimental results are analysed based on the theory proposed by Houlsby and Byrne (2005b). Comparisons between measured and calculated results are extensively pursued. The use of suction reduces drastically the net vertical load required to install a caisson in dense sand due to the hydraulic gradients created by the suction. It was found that calculations of the required suction for installation of caissons were highly dependent on the permeability ratio used.

4.1 INTRODUCTION

Experiments using model caissons installed by pushing into dry sands were performed as part of testing programmes to study vertical loading response (Chapter 3) and moment loading response (Chapter 5). The analysis for estimating the penetration resistance of pushed caissons is based mostly on methods derived for driven open end piles. Although in suction caisson aspect ratios are significantly shorter than in piles, the analysis consid-

ers the same approach assessing friction on the skirt and bearing capacity at the tip.

The installation of a caisson by suction is possible due to the application of a differential pressure between the interior chamber of the caisson and the exterior at the same datum. In practice this differential pressure is obtained by pumping water out of the caisson, which may or may not be submerged. For a submerged caisson the external pressure is hydrostatic, *i.e.* it varies linearly with the fluid height above the caisson. This differential pressure creates a negative pressure relative to hydrostatic or *suction* that forces the caisson skirt to penetrate into the ground. There are several factors that need to be considered to make this method of installation successful, *e.g.* sealing between the soil and the caisson skirt wall, availability, magnitude and limits of the suction, weight of the structure, geometry of the caisson and verticality of the caisson.

Houlsby and Byrne (2005b) include the ‘arching effect’ or ‘silo effect’ in the analysis of suction caisson installation. Soil arching has been recognised in several geotechnical problems such as buried pipes, underground cavities (Terzaghi, 1943), retaining walls (Handy, 1985) and plugging in open ended piles (Randolph *et al.*, 1991; de Nicola and Randolph, 1997; Jardine *et al.*, 2005). From these studies it is well known that the distribution of stresses with depth may not be linear and may be much higher than the geostatic. It is important to verify and calibrate this feature in the theory. The importance of modelling accurately the load-penetration response of a suction caisson is not only fundamental to estimate the installation response, but also for further modelling of the combined loading response. Additionally, results from pushed installation tests need to be compared with results from suction installation tests, in terms of the net load required to install similar caissons into similar soils. Moreover, as it will be subsequently evident calculation of the suction relies undoubtedly on the predicted pushing penetration resistance.

A unique feature of this type of foundation is the installation process aided by suction. In consequence, analysis of the feasibility of suction application is important as well as the limits of the suction. These issues are covered by the theory (Houlsby and Byrne

(2005b) calculation procedure is referred throughout this chapter as ‘the theory’ unless the contrary is mentioned), but they need to be verified and calibrated against physical evidence. Normally not all the caisson skirt penetrates into the ground under the structure’s own weight. In light structures such as wind turbines, small penetration of the skirt into the ground will occur by own weight, approximately 10% or 20% of the skirt length L . However, this initial penetration is fundamental to create a seal capable of preventing the occurrence of an unconfined flow failure, *i.e.* piping failure. Once piping is developed erosion of the soil occurs, stopping the caisson penetration because of the drastic drop of the suction.

Houlsby and Byrne (2005b) found that predictions of the vertical load and the suction depend significantly on the value of the combined effect of lateral earth pressure K and friction coefficient $\tan\delta$, expressed as $K \tan \delta$. Although a range of values obtained from back calculated examples is given by Houlsby and Byrne (2005b), it is not yet clear how to chose a certain value from this range or more importantly how to calculate K for different conditions than the examples presented. Moreover, although the formulation to obtain expressions for non-linear stress distribution is presented, explicit expressions to obtain the vertical load and the suction are not shown by the above authors. This chapter progresses from the simple case of pushing installation in dry and loose sand, to pushing installation in saturated and dense sand to finally study the suction installation in dense sands.

4.2 THEORETICAL ANALYSIS

4.2.1 Pushing penetration

A general formulation to calculate the penetration load of caissons can be obtained considering skin friction and base resistance as for driven open ended piles. This formulation involves a shear stress distribution along the caisson skirt $\tau(z)$ and a normal stress distribution around the caisson tip σ'_{end} . Thus, the submerged load V' required to

penetrate a depth h the skirt of a circular caisson is given by:

$$V' = \underbrace{2\pi R_o \int_0^h \tau_o dz}_{F_o} + \underbrace{2\pi R_i \int_0^h \tau_i dz}_{F_i} + \underbrace{\int_{A_{rim}} \sigma'_{end} dA}_{B_c + B_q + B_\gamma} \quad (4.1)$$

where the subscripts o and i refer to *outside* and *inside* the caisson skirt wall respectively. Therefore, R_i and R_o are the inside and outside caisson radii; F_o and F_i represent the friction forces *inside* and *outside* the caisson skirt wall. The mobilised shear stress τ in the soil-skirt interface, called skin or shaft friction in pile analysis (Poulos and Davis, 1981; Fleming *et al.*, 1994; Tomlinson, 1999; Randolph, 2003; Jardine *et al.*, 2005), is given by the Coulomb failure criterion, which can be expressed as:

$$\tau = \sigma'_r \tan \delta = K \sigma'_v \tan \delta \quad (4.2)$$

where σ'_r is the radial (horizontal σ'_h or normal σ'_n stress), K is the coefficient of lateral earth pressure, which depends on the soil stress history next to the skirt wall, and $\tan \delta$ is the coefficient of friction of the soil-skirt interface with δ being the interface friction angle. Figure 4.1(a) shows that owing to friction on the skirt wall soil arching occurs and since by definition principal stresses act only on planes of zero shear stresses σ'_1 and σ'_3 rotate, hence $\theta \neq 90^\circ$. Taking force equilibrium on a triangular element and deducing $\sigma'_h - \sigma'_3 = \sigma'_1 - \sigma'_v$ from the Mohr circle shown in Figure 4.1(b), gives (Zeevaert, 1983; Handy, 1985; 2004):

$$K = K_A = \frac{\sigma'_h}{\sigma'_v} = \frac{\cos^2 \theta + k_a \sin^2 \theta}{\sin^2 \theta + k_a \cos^2 \theta} = \frac{1 - \sin^2 \phi}{1 + \sin^2 \phi} = \frac{\cos^2 \phi}{2 - \cos^2 \phi} \quad (4.3)$$

For a smooth wall $\theta = 90^\circ$, and (4.3) reduces to the Rankine active coefficient $k_a = \frac{1 - \sin \phi}{1 + \sin \phi}$. The Krynine active pressure coefficient K_A appears for fully mobilised friction at the wall replacing θ by $45^\circ - \frac{\phi}{2}$. For instance, K_A finds application in the case of caisson pullout, when the skirt wall is extracted from the ground. So, drained tension capacity can be

calculated as:

$$V'_t = \gamma'h^2(K_A \tan \delta)_o \pi R_o + \gamma'h^2(K_A \tan \delta)_i \pi R_i \approx \gamma'h^2 2\pi R K_A \tan \delta \quad (4.4)$$

It has been found in studies of wall friction in buried pipes that when K_A is high, $\tan \delta$ is low, keeping the product $K_A \tan \delta$ nearly constant with a theoretical maximum value of 0.193 (Handy, 2004). In the interest of analysing wall penetration into the ground the passive coefficient can be similarly deduced:

$$K = K_P = \frac{\sigma'_h}{\sigma'_v} = \frac{\cos^2 \theta + k_p \sin^2 \theta}{\sin^2 \theta + k_p \cos^2 \theta} = \frac{1 + \sin^2 \phi}{1 - \sin^2 \phi} = \frac{2 - \cos^2 \phi}{\cos^2 \phi} \quad (4.5)$$

Perfectly smooth walls ($\theta = 90^\circ$) reduce (4.5) to the Rankine passive coefficient $k_p = \frac{1 + \sin \phi}{1 - \sin \phi}$. The Krynine passive pressure coefficient K_P is deduced for walls with fully mobilised friction replacing θ by $45^\circ + \frac{\phi}{2}$.

The end bearing pressure σ'_{end} around the caisson rim will be calculated using the bearing capacity formulation in plane strains presented in Chapter 3, where B_c , B_q and B_γ correspond to the bearing capacity force components of cohesion, overburden and self weight respectively.

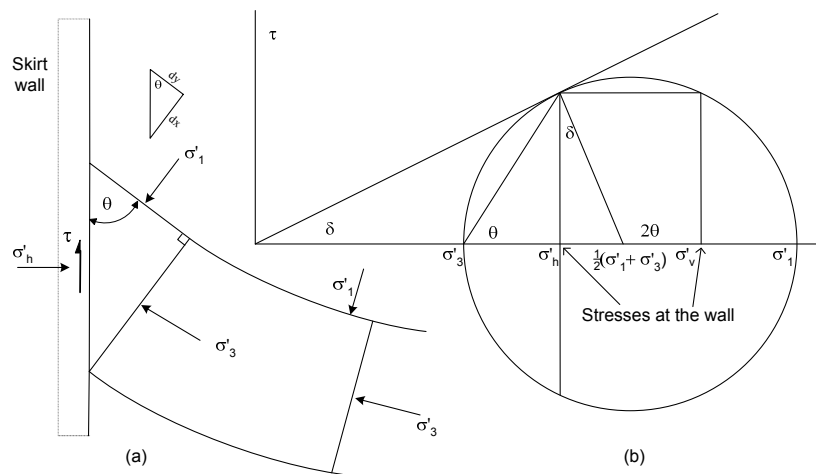


Figure 4.1: (a) Triangular soil element under force equilibrium showing arching trajectory defined by the minor principal stresses, and (b) Mohr circle showing stresses acting at the wall

4.2.2 Non-linear stress distribution

The vertical load V' required to penetrate a depth h the caisson skirt assuming a linear stress distribution $\sigma'_v = \gamma'z$, and assuming soil arching over the constant radii R_i and R_m (which results in an exponential stress distribution with depth) are covered in Houlsby and Byrne (2005b). An extension of this case considers the enhancement of stresses in a radius linearly varying with depth.

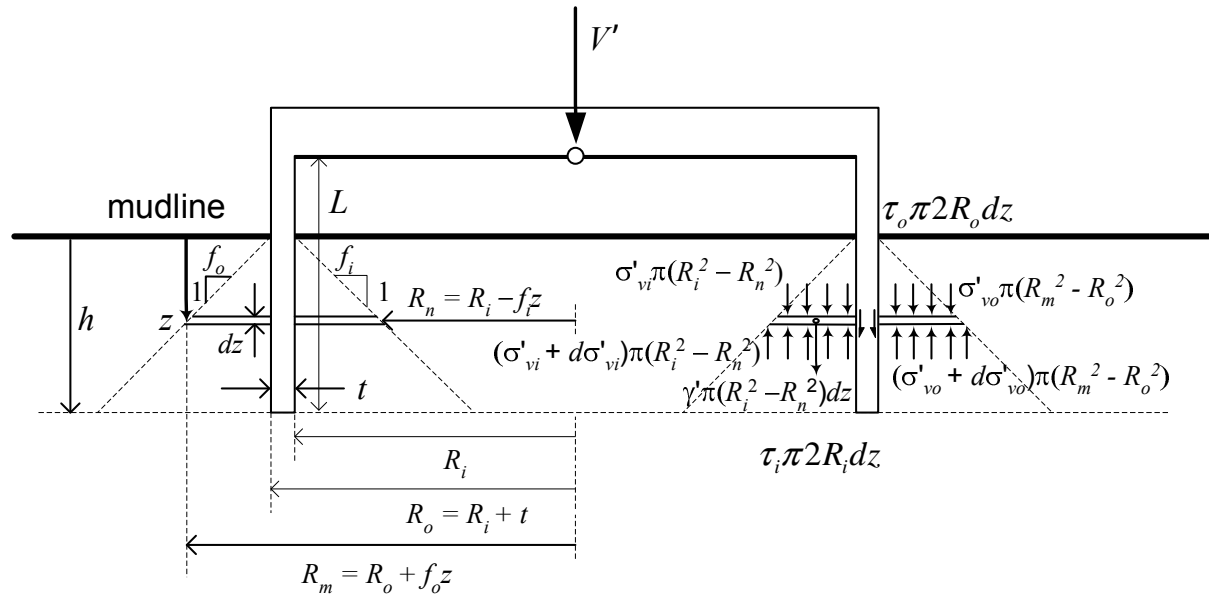


Figure 4.2: Outline of a suction caisson showing equilibrium of soil element dz

Figure 4.2 shows soil arching ‘varying’ linearly with depth inside the caisson as $R_i - R_n = f_i z$ and outside the caisson as $R_m - R_o = f_o z$, being f_i and f_o the respective constant rates of variation. Note the inverse contribution of arching, whilst inside the caisson R_n decreases with depth, outside the caisson R_m increases with depth. Equilibrium of the vertical forces acting on soil elements of thickness dz leads to the following ordinary differential equations ODE:

$$\frac{d\sigma'_{vi}}{dz} = f_i(z, \sigma'_{vi}) = \gamma' + \frac{\sigma'_{vi}}{Z_i(z)} \quad \frac{d\sigma'_{vo}}{dz} = f_o(z, \sigma'_{vo}) = \gamma' + \frac{\sigma'_{vo}}{Z_o(z)} \quad (4.6)$$

where Z_i and Z_o can be written as:

$$Z_i = \frac{R_i \left[1 - \left(1 - \frac{f_i z}{R_i} \right)^2 \right]}{2(K \tan \delta)_i} \quad Z_o = \frac{R_o \left[\left(1 + \frac{f_o z}{R_o} \right)^2 - 1 \right]}{2(K \tan \delta)_o} \quad (4.7)$$

Unfortunately there is not an analytical solution for (4.6). Nevertheless, these first order ODEs can be solved numerically using Euler or Runge-Kutta methods, in which each approximation for the unknown function is based on the previous value. A fourth order Runge-Kutta method was employed to solve (4.6) since it is more accurate and numerically stable than the Euler method. The iterative formula is given by:

$$\begin{aligned}
& \text{initial value of } \sigma'_v = 0 \text{ at } h = 0 \\
& \text{For } j = 0, 1, \dots, n - 1 \\
& k_1 = \Delta h f(h_j, \sigma_j) \\
& k_2 = \Delta h f\left(h_j + \frac{1}{2}\Delta h, \sigma_j + \frac{1}{2}k_1\right) \\
& k_3 = \Delta h f\left(h_j + \frac{1}{2}\Delta h, \sigma_j + \frac{1}{2}k_2\right) \\
& k_4 = \Delta h f(h_j + \Delta h, \sigma_j + k_3) \\
& \sigma_{j+1} = \sigma_j + \frac{1}{6}(k_1 + 2k_2 + 2k_3 + k_4)
\end{aligned} \tag{4.8}$$

where h is incremented by Δh , σ_j ($\equiv \sigma'_{vi_j} \equiv \sigma'_{vo_j}$) is incremented by a multiple of the parameters k_1, k_2, k_3 and k_4 preceding it, and $f(h, \sigma'_v)$ is the function on the right hand side of the ODE (4.6). The integration of (4.1) can be solved simultaneously changing the integrals for summations. The vertical load V' corresponding to a penetration depth h_j is obtained after each value of σ_{j+1} is solved, replaced in (4.2), sums are conducted to finally add the force terms as follows:

$$\begin{aligned}
V' = & \underbrace{2\pi R_o(K \tan \delta)_o \sum_{j=1}^n \sigma'_{vo_j} \Delta h}_{F_o} + \underbrace{2\pi R_i(K \tan \delta)_i \sum_{j=1}^n \sigma'_{vi_j} \Delta h}_{F_i} + \underbrace{\sigma'_{vi_n} 2N_q 2\pi R t}_{B_q} \\
& + \underbrace{\gamma' t N_\gamma 2\pi R t}_{B_\gamma} \quad \forall n \in \{1, \dots, N\} \quad \text{where } n = \frac{h}{\Delta h} \quad \text{and} \quad N = \frac{L}{\Delta h}
\end{aligned} \tag{4.9}$$

4.2.3 Suction assisted penetration

A schematic flow net is depicted in Figure 4.3, representing a suction caisson of $\frac{L}{2R} = 0.5$ and penetrating by suction half of its depth. The flow net has been constructed following procedures for plane strain conditions. For axial symmetric flow nets numerical

calculations are necessary (Aldwinkle, 1994). The suction or extraction of fluid from the caisson compartment creates a hydraulic gradient that makes interstitial fluid and fluid above the mudline to flow in the direction shown by the arrows in the figure. This flow occurs because of the presence of negative pressure differentials or negative relative heads between the fluid inside the caisson and the fluid in the soil voids. The flow direction is downwards outside the caisson and upwards inside the caisson. Horizontal flow occurs briefly as a transition from downwards to upwards flow. The flow channel next to the caisson's skirt wall drastically changes the flow direction, whereas for the other flow channels a smoother change occurs.

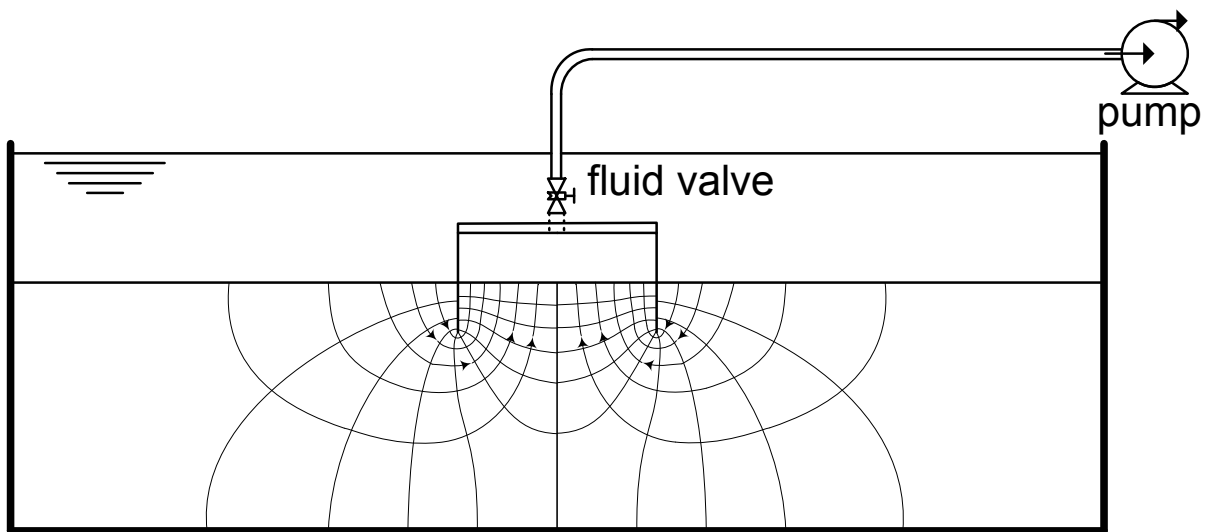


Figure 4.3: Seepage around a suction caisson during installation showing schematic flow net constructed using plane strain procedures

The flow direction caused by the suction influences the stresses and hence the soil strength and density. As a consequence, soil index and strength properties that are practically constant during a self-weight penetration can vary due to seepage created by the suction. The flow net sketched in Figure 4.3 considers a uniform permeability (vertical and radial). Alternatively, if seepage modifies the effective stresses then variation of the specific volume will occur; the coefficient of permeability (referred to as permeability onwards) can be substantially affected by the intensity of seepage because permeability is a function of the specific volume and hence of the soil unit weight.

If a flow net analysis is carried out to calculate flow rates or permeabilities if the pumping

rate is known, from Darcy's law the steady flow under the caisson can be written as:

$$q = 2\pi Rk \frac{s}{\gamma_f} \frac{N_F}{N_H} \quad (4.10)$$

where k is a uniform permeability, s is the suction or difference in total head between the first and last equipotential, γ_f is the fluid unit weight and N_F and N_H are the numbers of flow channels and equipotential drops, representing each the same total head loss. Houlsby and Byrne (2005b) extend the steady flow calculation when differences in permeability of the soil inside the caisson and outside the caisson occur.

$$q = 2Rk_o \frac{s}{\gamma_f} F \quad (4.11)$$

where k_o is the soil permeability outside the caisson and F is a dimensionless factor that accounts for the change in N_F and N_H as a function of $\frac{h}{2R}$ and the permeability ratio $k_f = \frac{k_i}{k_o}$, where k_i is the soil permeability inside the caisson. According to the flow net in Figure 4.3 $N_F = 6$, $N_H = 10$, $\frac{h}{2R} = 0.25$, and $k_f = 1$, resulting in $F = \frac{3\pi}{5} \approx 1.9$, which is slightly higher than the numerical calculations of $F = 1.6$ shown in Figure 4.4. This difference is due to the fact that the flow net was constructed following procedures for plane strain conditions and equations (4.10) and (4.11) and therefore F correspond to axial symmetric conditions. Note that F depends on the permeability ratio rather than on absolute values of permeability. This is an important point for the following analyses of the suction. In addition, no direct measurements of $\frac{k_i}{k_o}$ were possible. Figure 4.5 depicts a caisson being penetrated a depth h under the submerged weight V' and the application of suction s , which are counterbalanced by the shear stresses τ_i and τ_o as well as the end bearing stress at the tip σ'_{end} . The equilibrium of forces acting on the caisson established in (4.1) now includes the suction force sA_i resulting in:

$$V' + sA_i = 2\pi R_o \int_0^h \underbrace{\sigma'_{vo}}_{seepage} dz (K \tan \delta)_o + 2\pi R_i \int_0^h \underbrace{\sigma'_{vi}}_{seepage} dz (K \tan \delta)_i + \underbrace{(\sigma'_{vi})}_{seepage} N_q + \gamma' t N_\gamma) 2\pi R t \quad (4.12)$$

The suction s is added in equation (4.1) in the left hand side, capturing the assistance effect in the installation process. The flow net shown in Figure 4.3 illustrates how the hydraulic head varies along each flow channel. As a result, outside the caisson the downward flow increases the stresses, whereas inside the caisson the upward flow reduces the stresses.

Houlsby and Byrne (2005b) propose that the change of stresses due to seepage is proportional to the average hydraulic gradients inside and outside the caisson:

$$i_i = \frac{(1-a)s}{\gamma_f h}; \quad i_o = -\frac{as}{\gamma_f h} \quad (4.13)$$

where γ_f is the fluid unit weight and a is a pressure factor that represents the ratio between the excess pore fluid pressure at the tip of the caisson skirt and next to the base ($0 \leq a < 1$). Alternatively, the excess pore fluid pressures generated by the seepage regime become a function of the suction and the pressure factor as inside the caisson, and $-(1-a)s$ outside the caisson. Therefore, the effective vertical stresses in the soil inside and outside the caisson are modified by seepage according to:

$$\sigma'_{vi \text{ seepage}} = \left[1 - \frac{(1-a)s}{\gamma_f h} \right] \sigma'_{vi}; \quad \sigma'_{vo \text{ seepage}} = \left[1 + \frac{as}{\gamma_f h} \right] \sigma'_{vo} \quad (4.14)$$

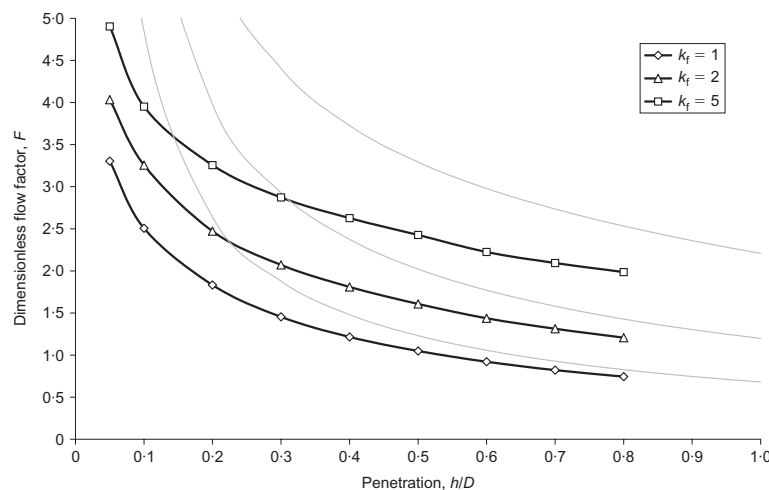


Figure 4.4: Variation of dimensionless flow parameter F . The faint lines correspond to the approximation $F = \frac{(1-a)\pi k_f}{4\left(\frac{h}{2R}\right)}$, with a a pressure factor to be introduced (taken from Houlsby and Byrne (2005b))

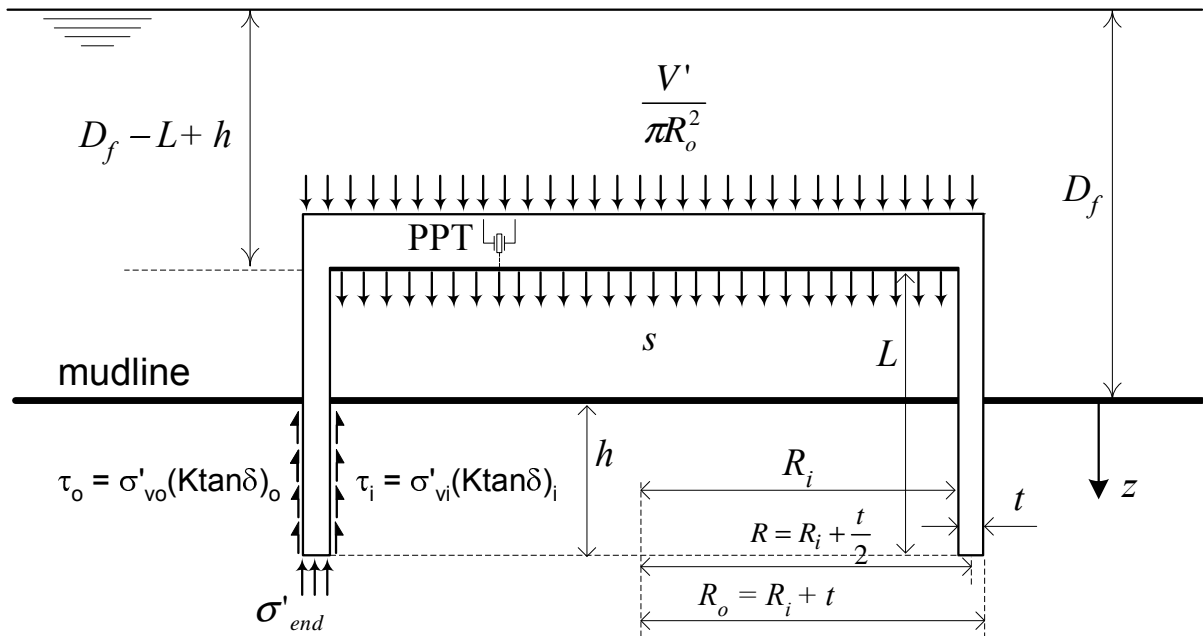


Figure 4.5: Vertical stresses on a suction caisson during installation

where σ'_{vo} and σ'_{vi} correspond to the case without seepage. The excess pore fluid pressure at the tip of the caisson can be obtained from inside or outside as follows:

$$u' = s - \sigma'_{vi} - \sigma'_{vi \text{ seepage}} = s - \frac{(1-a)s}{\gamma'h} \sigma'_{vi}; \quad u' = \sigma'_{vo} - \sigma'_{vo \text{ seepage}} = -\frac{as}{\gamma'h} \sigma'_{vo} \quad (4.15)$$

which reduces to the distribution $-as\frac{z}{h}$ with depth if $\sigma'_{vi} = \sigma'_{vo} = \gamma'z$ as assumed by Houlsby and Byrne (2005b). Replacing (4.14) in the respective σ'_{vi} and σ'_{vo} of expression (4.12) and assuming stresses linearly varying with depth leads to the following expression:

$$\begin{aligned} V' + sA_i &= 2\pi R_o \int_0^h (K \tan \delta)_o \left[1 + \frac{as}{\gamma'h} \right] \sigma'_{vo} dz \\ &+ 2\pi R_i \int_0^h (K \tan \delta)_i \left[1 - \frac{(1-a)s}{\gamma'h} \right] \sigma'_{vi} dz + \left\{ \left[1 - \frac{(1-a)s}{\gamma'h} \right] \sigma'_{vi} N_q + \gamma' t N_\gamma \right\} 2\pi R t \end{aligned} \quad (4.16)$$

It is worth pointing out that equation (4.16) reveals that the suction not only contributes as a driving force as in equation (4.12), but also contributes enormously in reducing the stresses at the caisson tip and inside the caisson skirt. Because of the reduced soil resistance at the caisson tip the skirt penetration is possible under a much lower net

vertical load. Solving the integrals results in:

$$V' + sA_i = \left[\gamma' + \frac{as}{h} \right] h^2 (K \tan \delta)_o \pi R_o + \left[\gamma' - \frac{(1-a)s}{h} \right] h^2 (K \tan \delta)_i \pi R_i + \\ + \left[\gamma' - \frac{(1-a)s}{h} \right] (hN_q + tN_\gamma) 2\pi Rt \quad (4.17)$$

Alternatively, the suction can be solved from expression (4.17) resulting in:

$$s = \frac{V' - [\gamma' h^2 (K \tan \delta)_o \pi R_o + \gamma' h^2 (K \tan \delta)_i \pi R_i + \gamma' h N_q 2\pi Rt + \gamma' t N_\gamma \pi Rt]}{ah(K \tan \delta)_o \pi R_o - (1-a)[h(K \tan \delta)_i \pi R_i + (N_q + \frac{t}{h} N_\gamma) 2\pi Rt] - A_i} \quad (4.18)$$

The bracketed expression in the numerator corresponds to the net force required to penetrate a caisson without suction ($F_i + F_o + B_q + B_\gamma$). Multiplying the numerator and the denominator of expression (4.18) by $\gamma' h$ leads to the introduction of the already known forces F_i , F_o , B_q and B_γ in the denominator. In this form a more compact equation for the suction required is obtained:

$$s = \frac{[V' - (F_i + F_o + B_q + B_\gamma)] \gamma' h}{aF_o - (1-a)(F_i + B_q + B_\gamma) - \gamma' h A_i} \quad (4.19)$$

The pressure factor a accounts for the variation of excess pore pressure with skirt depth. Aldwinkle (1994) carried out a numerical analysis using the finite element program IDEAS, whereby the seepage problem was solved by means of the heat transfer analogy. The analogies are: conductivity \equiv permeability, and temperature gradient \equiv pressure difference. It was assumed that the reduced 'pore pressure' at the tip was a times 'the suction' in the caisson compartment ($T = 0^\circ\text{C}$); at the same level but outside of the caisson the suction was zero ($T = 100^\circ\text{C}$). The a values obtained by Aldwinkle (1994) covered caisson aspect ratios $\frac{h}{2R} \leq 0.33$. Junaideen (2004) (cited by Houlsby and Byrne, 2005b) using almost the same mesh details verified and extended the values of a for $\frac{h}{2R} \leq 0.8$. If seepage provoked by the suction does not change the soil permeability ($k_f = 1$ in Figure 4.6), then the pressure factor a can be approximated by:

$$a = a_1 = c_0 - c_1 \left[1 - e^{-\frac{h}{c_2 2R}} \right] \quad (4.20)$$

with the values $c_0 = 0.45$, $c_1 = 0.36$, and $c_2 = 0.48$. Values of a at $h = 0$ are not important as this represents just the beginning of penetration before suction would be applied. The fact that seepage can change the soil buoyant unit weight implies also that the specific volume can change, and hence the permeability. The permeability k is found to be related to the specific volume v by means of the Kozeny-Carman equation for fully saturated porous media, which can be expressed as:

$$k = C_s D_s^2 \left(\frac{\gamma_f}{\mu_d} \right) \frac{(v-1)^3}{v} \quad (4.21)$$

where C_s is a shape factor equal to $\frac{1}{2}$ if full flow occurs through a tube, D_s can be interpreted as a representative grain size, normally taken as D_{10} ; μ_d and γ_f are the viscosity and unit weight of the fluid as described in Chapter 2. For a soil permeability ratio $k_f = \frac{k_i}{k_o}$ the pressure factor a is expressed by:

$$a = \frac{a_1 k_f}{(1 - a_1) + a_1 k_f} \quad (4.22)$$

Furthermore, the variation of a with h in (4.20) induces a variation in the calculated stresses in (4.14), and hence a variation in k_f . An attempt to include a reduction of only k_i in a soil annulus next to the caisson skirt wall will change the values of a as a function of the annulus dimensions (Aldwinkle (1994) used for example, one seventh of the radius). However, such a refinement in the analysis requires knowledge of how to evaluate the annulus dimensions. Since the suction calculation is very sensitive to a further research is necessary to find out the spatial distribution of the stresses around the caisson caused by seepage.

A general equation to determine the suction can be obtained arranging equation (4.16) in terms of s , as in equation (4.18) and also multiplying the numerator and denominator by $\gamma'h$ as in equation (4.19), resulting in:

$$s = \frac{(2\pi R_o \int_0^h \tau_o z dz + 2\pi R_i \int_0^h \tau_i z dz + (\sigma'_{vi} N_q + \gamma' t N_\gamma) A_{rim} - V') \gamma' h}{A_i \gamma' h - 2\pi R_o a \int_0^h \tau_o dz + (1-a)[2\pi R_i \int_0^h \tau_i dz + (\sigma'_{vi} N_q + \gamma' t N_\gamma) A_{rim}]} \quad (4.23)$$

It is worth pointing out that in (4.23) the integrals are the same as for the self-weight penetration. The expression of the suction for the case of exponential distribution of stresses can be obtained from equation (16) in Houlsby and Byrne (2005b). For the case of a non-linear stress distribution as described in section §4.2.2 the integrals in (4.23) become sums in a numerical calculation of stresses, then the suction can be obtained from:

$$s = \frac{\left(2\pi R_o \sum_{j=1}^n \tau_{o_j} h_j \Delta h + 2\pi R_i \sum_{j=1}^n \tau_{i_j} h_j \Delta h + h_j (\sigma'_{v i_j} N_q + \gamma' t N_\gamma) A_{rim} - V' h_j \right) \gamma'}{A_i \gamma' h_j - 2\pi R_o a \sum_{j=1}^n \tau_{o_j} \Delta h + (1-a) [2\pi R_i \sum_{j=1}^n \tau_{i_j} \Delta h + (\sigma'_{v i} N_q + \gamma' t N_\gamma) A_{rim}]}$$

$$\forall n \in \{1, \dots, N\} \quad \text{where} \quad n = \frac{h}{\Delta h} \quad \text{and} \quad N = \frac{L}{\Delta h}$$
(4.24)

4.2.4 Limits to suction assisted penetration

The assistance of suction to install a caisson is limited by the soil resistance. Exceeding a critical value of the suction induces a progressive and irreversible soil failure that consequently halts the caisson penetration. The critical hydraulic gradient i_c that causes a boiling or *piping* condition is given by (Terzaghi and Peck, 1967):

$$i_c = \frac{\gamma'}{\gamma_f}$$
(4.25)

A condition of zero effective vertical stress at the caisson tip may trigger and spread around the caisson creating also piping if the critical suction s_{crit} is reached. Clausen and Tjelta (1986) (cited by Feld, 2001) propose the following expression for the critical suction:

$$s_{crit} = \frac{\gamma' h}{1 - \frac{0.68}{1.46 \frac{h}{2R} + 1}}$$
(4.26)

Expression (4.26) was derived from numerical solutions of axial symmetric steady state flow for $\frac{h}{2R} < 0.5$. It can be observed in Figure 4.6 that the pressure factor implicitly suggested in (4.26) as $a = \frac{0.68}{1.46 \frac{h}{2R} + 1}$ follows a similar trend as in the formulation given in

(4.22), and indeed corresponds to $k_f \approx 2.5$. Additionally, the a expression of Clausen and Tjelta (1986) still is valid for $0.5 < \frac{h}{2R} < 1$. Replacing the critical hydraulic gradient

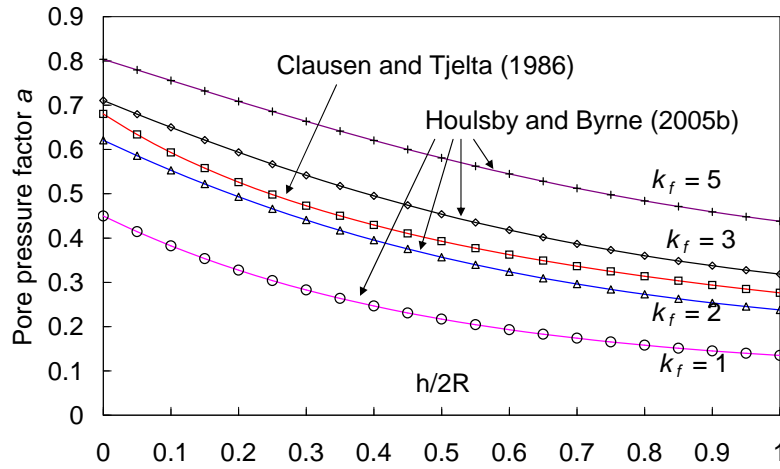


Figure 4.6: Variation of the pressure factor a with $\frac{h}{2R}$ comparing expressions by Clausen and Tjelta (1986) with Houlsby and Byrne (2005b)

(4.25) in (4.13) or alternatively making $\sigma'_{v \text{ seepage}} = 0$ in (4.14) a general expression can be obtained,

$$s_{crit} = \frac{\gamma' h}{1 - a} \quad (4.27)$$

In terms of the limit depth of penetration h_{crit} , expressions can be obtained replacing s_{crit} from equation (4.27) into s in equation (4.16). For example, for the particular case of a linear stress distribution, solving for h in equation (4.16) leads to:

$$h_{crit} = \frac{\gamma' A_i + \sqrt{(\gamma' A_i)^2 + 4\gamma'(1 - a)(K \tan \delta)_o \pi R_o V'}}{2\gamma'(K \tan \delta)_o \pi R_o} \quad (4.28)$$

In the unfavourable case of $V' = 0$ N, and assuming $R_i \approx R_o \approx R$, h_{crit} becomes equal to:

$$h_{crit} = \frac{R}{(K \tan \delta)_o} \quad (4.29)$$

For an usual value of $(K \tan \delta)_o \cong 0.5$, h_{crit} becomes equal to the caisson diameter $2R$. From equation (4.28) h_{crit} increases with V' and also with h since a diminishes with depth. If the exponential distribution of stresses $\sigma'_{v_o} = \gamma' Z_o \left(e^{\frac{z}{Z_o}} - 1 \right)$ (where $Z_o = \frac{R_o(m^2 - 1)}{2(K \tan \delta)_o}$ with $m > 1$ defining a constant extension of soil arching as a multiple of the radius mR_o) is

used in expression (4.16) the following equation results:

$$2\pi R_o(K \tan \delta)_o \gamma' Z_o^2 \left[e^{\frac{h}{Z_o}} - 1 - \frac{h}{Z_o} \right] - \gamma' A_i h - V'(1-a) = 0 \quad (4.30)$$

The solution for h_{crit} has to be found using a numerical method and iterating for h to obtain the variation of a with depth. If σ'_{v_o} is obtained numerically as in section §4.2.2, then the critical penetration depth is given by:

$$h = \frac{2\pi R_o(K \tan \delta)_o \sum_{j=1}^n \sigma'_{v_{o_j}} h_j \Delta h - V'(1-a)}{\gamma' A_i} \quad \forall n \in \{1, \dots, N\} \quad \text{where} \quad n = \frac{h}{\Delta h}$$

$$\text{and} \quad N = \frac{L}{\Delta h} \quad (4.31)$$

where h_{crit} is found when h coincides with the penetration h_j .

Another form to evaluate a limit to suction is by calculation of a reversed bearing capacity failure. This has been established for suction caissons in clay under uplift loading by Fuglsang and Steensen-Bach (1991) and employed by Deng and Carter (2000), Randolph and House (2002), House (2002) and Houlsby and Byrne (2005a). Whilst for caissons in clay the response relies on undrained conditions, in sand a fully drained condition is expected. The failure mechanism moves towards the inside of the caisson when the stresses outside the caisson overcome the stresses inside the caisson during suction installation. To avoid this type of failure the following condition must be verified:

$$\sigma'_{v_o} < N_q \sigma'_{v_i} \quad \forall \quad h \in (0, L] \quad (4.32)$$

substituting (4.14) into (4.32) for the linear and exponential stress distributions results in:

$$\frac{\left[1 - \frac{(1-a)s}{\gamma'h} \right] N_q}{\left[1 + \frac{as}{\gamma'h} \right]} > 1, \quad \frac{\left[1 - \frac{(1-a)s}{\gamma'h} \right] Z_i (e^{\frac{h}{Z_i}} - 1) N_q}{\left[1 + \frac{as}{\gamma'h} \right] Z_o (e^{\frac{h}{Z_o}} - 1)} > 1 \quad \forall \quad h \in (0, L] \quad (4.33)$$

where $Z_i = \frac{R_i}{2(K \tan \delta)_i}$. It is assumed in the above expressions that N_q used in the downward form of bearing capacity problems is also valid for the reversed form.

4.3 EXPERIMENTAL RESULTS

4.3.1 Pushing installation into loose and dry sand

A series of pushing installation tests were performed prior to moment loading tests. It is worth pointing out that the interest of determining the maximum vertical load V_o experienced by the foundation has its roots in the critical state soil mechanics interpretation of triaxial tests, where the maximum load is analogous to the preconsolidation pressure.

In the laboratory, the vertical load V' was monitored throughout every test at an interval of half a second for a penetration rate of $\dot{h} = 0.5$ mm/s. When lid contact occurred the vertical stepper motor of the *VMH* loading rig was stopped. However, it is difficult to stop the installation exactly at the lid contact or contact load V_c , and in the best case a small increase over V_c was obtained. On the contrary, if the penetration is stopped before lid contact, there will be uncertainty of whether the skirt penetrated completely or not. As a consequence, there was always a difference between V_c and V_o . To analyse the data V_o should rigorously be adopted as the maximum value of the vertical load experienced by the foundation. Nevertheless, the analysis is more consistent if an intrinsic property of the foundation as the *contact* vertical load V_c is considered instead of random values of V_o . They were in average around 30% larger than V_c (Tables 4.1 and 4.2). As a result, the values of V_c and h_c will be adopted in the subsequent analyses.

Load-penetration curves are shown in Figures 4.7(a) and 4.7(b), where it is possible to observe the variation of V' with h as well as V_c and V_o . Figures 4.8(a) and 4.8(b) show two normalisations for the previous plots: $\frac{V'}{V_c}$ and $\frac{V'}{\gamma_d(2R)^3}$. These normalisations prove to be very effective in unifying results from different soil densities and was possible to include both in the same plot because V_c and γ_d (or V_c and R_d) can be correlated as

Table 4.1: Pushing installation tests of caisson A in dry, loose Leighton Buzzard sand

Test	γ' kN/m ³	R_d %	v	V_c N	h_c mm	V_o N	h_o mm	V_t N	h_t mm
FV1_1_1	15.16	20	1.714	473	143.7	726	145.2	-55	142.7
FV15_2_1	15.05	16	1.727	482	144.4	606	145.7	-55	144.6
FV26_3_1	15.37	28	1.692	575	143.2	728	145.0	-56	143.4
FV27_3_1	15.37	28	1.692	558	144.3	822	145.9	-	-
FV29_3_1	15.37	28	1.691	554	143.7	868	145.5	-	-
FV30_4_1	15.52	34	1.675	665	134.7	904	136.4	-56	134.7
FV31_4_1	15.50	33	1.677	654	135.2	925	136.3	-	-
FV32_4_1	15.24	23	1.706	561	143.5	844	145.5	-	-
FV33_4_1	15.24	23	1.706	541	144.5	651	145.4	-	-
FV34_5_1	15.18	21	1.713	546	145.0	705	146.2	-51	143.6
FV35_5_1	15.34	27	1.695	595	145.2	817	146.6	-52	143.5
FV36_5_1	15.37	28	1.691	613	143.7	774	145.5	-52	143.5
FV37_5_1	15.37	28	1.691	613	143.3	870	145.2	-52	143.4
FV57_10_1	15.60	37	1.666	721	141.2	975	143.4	-	-
FV58_10_1†	15.60	37	1.666	729	141.7	2388	146.4	-61	145.0
FV60_10_1	15.60	37	1.666	677	142.3	802	143.7	-55	140.2
FV61_10_1	15.60	37	1.666	695	143.7	934	144.6	-64	143.2
FV81_14_1	15.85	46	1.640	726	139.5	786	141.3	-47	130.0
FV82_14_1	15.85	46	1.640	784	141.4	906	142.5	-53	134.2
FV84_14_1	15.85	46	1.640	795	141.4	983	143.0	-60	139.5
FV85_15_1	15.99	50	1.626	783	141.2	1013	142.6	-48	128.9
FV86_16_1	15.11	18	1.721	458	146.3	798	148.8	-	-
FV87_16_1	15.11	18	1.721	461	145.6	703	148.1	-59	146.6
FV88_16_1	15.11	18	1.721	503	144.3	884	147.4	-57	144.2
FV89_16_1	15.11	18	1.721	478	143.8	693	147.6	-58	146.0
FV90_17_1	15.03	15	1.730	463	145.9	751	147.9	-51	143.0
FV91_17_1	15.03	15	1.730	468	146.0	670	147.7	-	-
FV92_17_1	15.03	15	1.730	491	145.6	667	147.0	-	-
FV93_17_1	15.03	15	1.730	473	144.3	791	147.3	-	-
FV94_18_1	15.00	14	1.733	445	146.5	663	148.0	-	-
FV95_18_1	15.00	14	1.733	456	145.6	690	147.9	-	-
FV97_18_1	15.00	14	1.733	465	144.0	676	146.6	-	-
FV99_19_1	15.01	14	1.732	430	143.2	645	148.6	-	-
FV100_19_1	15.01	14	1.732	496	145.0	650	147.5	-	-
FV101_19_1	15.01	14	1.732	473	144.5	661	147.0	-53	145.1
FV107_21_1	14.96	12	1.738	460	145.2	586	146.9	-	-
FV108_21_1	14.96	12	1.738	483	143.7	602	145.9	-	-
FV109_21_1	14.96	12	1.738	487	143.4	526	145.1	-	-
FV111_22_1	15.23	23	1.707	557	145.3	745	149.2	-62	145.1
FV113_22_1	15.23	23	1.707	530	147.8	759	150.2	-	-
FV116_22_1	15.23	23	1.707	573	144.4	708	147.6	-	-
FV118_22_1	15.23	23	1.707	538	145.2	700	147.9	-	-
FV121_23_1	15.10	18	1.722	521	145.8	756	149.6	-55	144.7
FV123_23_1	15.10	18	1.722	534	145.4	638	148.5	-47	136.1
FV125_23_1	15.10	18	1.722	560	145.7	790	148.9	-51	137.9
FV127_23_1	15.10	18	1.722	530	144.1	747	148.5	-43	128.9
FV130_24_1	15.29	25	1.700	582	145.4	764	148.4	-61	144.5
FV132_24_1	15.17	21	1.714	513	147.2	735	150.8	-58	148.2
FV134_24_1	15.17	21	1.714	528	145.5	707	147.8	-62	145.9
mean	15.23	23	1.708	558	144.3	780	146.2	-55	141.8
st deviation	0.27	10	0.030	98	2.8	247	3.2	5	5.2

†vertical loading tests until rig capacity reached

Table 4.2: Pushing installation tests of caisson B in dry, loose Leighton Buzzard sand

Test	γ' kN/m ³	R_d %	v	V_c N	h_c mm	V_o N	h_o mm	V_t N	h_t mm
FV38_6_1	15.27	24	1.702	540	199.7	696	202.0	-75	200.5
FV40_6_1	15.27	24	1.702	608	198.5	792	200.8	-70	198.7
FV41_6_1	15.33	27	1.696	653	198.4	728	200.7	-68	199.1
FV42_6_1	15.27	24	1.702	557	197.9	681	200.1	-60	197.0
FV45_7_1	15.35	27	1.694	676	197.4	777	198.8	-68	198.3
FV46_7_1	15.35	27	1.694	663	198.1	817	200.0	-78	198.4
FV47_7_1	15.35	27	1.694	624	197.8	770	199.7	-74	198.4
FV48_7_1	15.40	29	1.688	700	196.8	853	199.3	-74	197.2
FV49_8_1	15.37	28	1.692	623	197.7	688	198.8	-77	198.7
FV50_8_1	15.37	28	1.692	676	197.7	852	199.6	-76	197.0
FV51_8_1	15.37	28	1.692	655	199.0	778	200.5	-80	199.6
FV52_8_1	15.37	28	1.692	668	197.6	819	199.6	-80	197.9
FV53_9_1	15.46	32	1.681	695	196.3	938	198.6	-81	198.4
FV54_9_1	15.46	32	1.681	724	195.9	897	198.6	-80	196.6
FV55_9_1	15.46	32	1.681	640	197.2	790	199.3	-75	199.3
FV56_9_1	15.46	32	1.681	698	195.6	910	198.3	-78	196.8
FV101_19_2	15.10	18	1.722	483	197.7	653	200.5	-53	196.6
FV102_20_1	15.00	14	1.733	428	202.4	606	205.6	-67	204.7
FV103_20_1	15.00	14	1.733	417	202.9	535	204.7	-	-
FV110_22_1	15.10	18	1.722	443	203.2	518	205.2	-72	191.4
FV112_22_1	15.00	14	1.733	433	203.0	500	204.6	-67	202.0
FV117_22_1	15.10	18	1.722	469	203.1	578	204.6	-71	-
FV119_22_1	15.23	23	1.707	557	198.7	799	201.7	-	-
FV120_23_1	15.05	16	1.727	421	203.6	567	205.8	-	-
FV122_23_1	15.10	18	1.722	443	204.4	563	206.4	-74	206.8
FV124_23_1	15.10	18	1.722	467	202.2	575	204.4	-64	198.7
FV126_23_1	15.10	18	1.722	459	200.4	581	203.5	-71	204.2
FV129_24_1	15.11	18	1.721	465	201.6	559	203.1	-81	194.4
FV131_24_1	15.11	18	1.721	460	201.8	629	204.8	-65	203.2
FV133_24_1	15.11	18	1.721	467	200.5	629	203.8	-68	201.2
FV135_24_1	15.11	18	1.721	470	201.4	650	204.8	-69	203.0
mean	15.23	23	1.708	553	199.7	700	202.0	-72	199.4
st deviation	0.16	6	0.018	107	2.6	127	2.7	7	3.4

shown in Figures 4.9(a) and 4.9(b). The mean error in the estimation of $\frac{V_c}{\gamma_d(2R)^3}$ using a linear regression are 0.031 ± 0.008 (Figure 4.9(a)) and 0.15 ± 0.05 (Figure 4.9(b)), for a 95% confidence level for the mean and assuming an infinite number of measurements.

To evaluate the theoretical predictions with the experimental results, test FV81_14_1A was chosen as a representative example. In the calculations a peak angle of friction ϕ'_{peak} was estimated using the procedure suggested by Bolton (1986). Using a direct shear apparatus Lings and Dietz (2005) determine interface friction angles δ between 10.8° and 13.3° for a medium sub-rounded sand with relative densities between 23% and 78% and under a normal stress of 25 kPa. The surface to which they sheared the sand corresponded to a

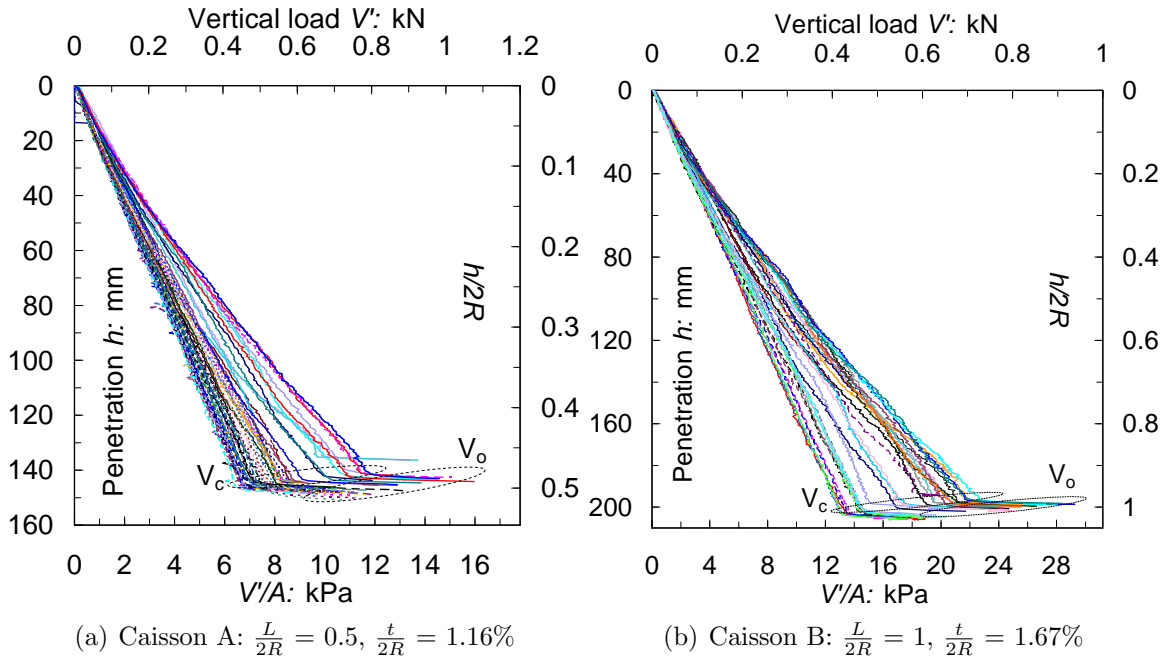


Figure 4.7: Pushing installation tests

material with a maximum roughness R_{max} of $3.85 \mu\text{m}$. A value $R_{max} = 4 \mu\text{m}$ was found for a dural plate (Chapter 2), and a value of R_{max} of the same order of magnitude was assumed to hold for the aluminium caissons A and B. Therefore, a compromise value of $\delta = 12.5^\circ$ is adopted.

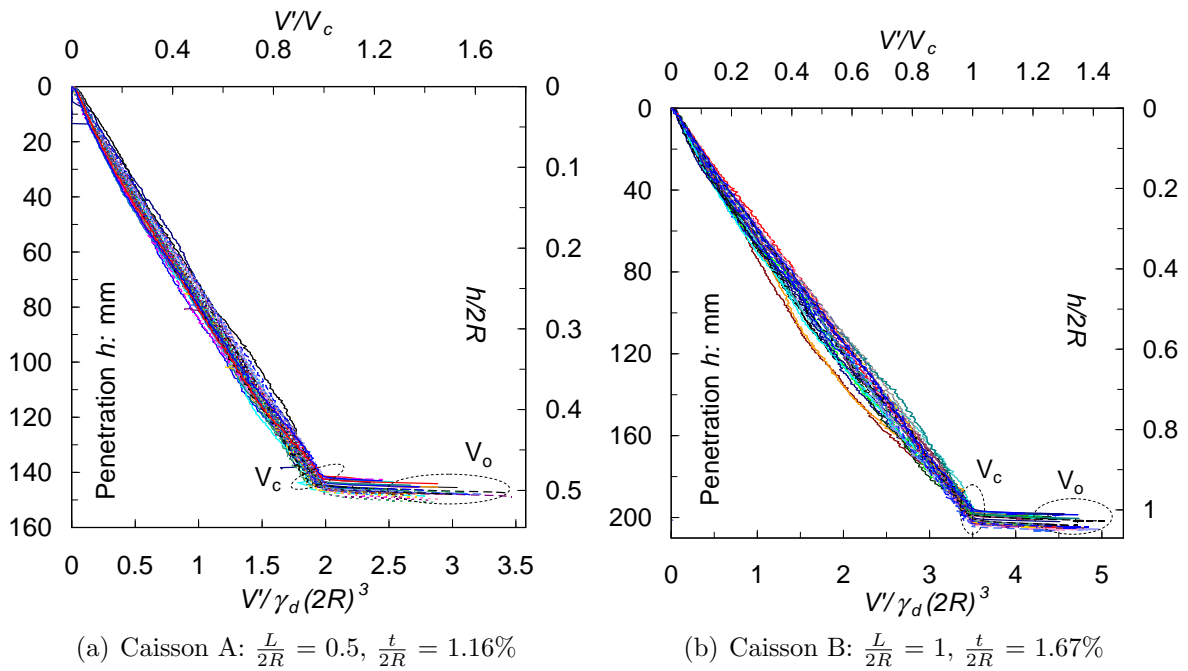


Figure 4.8: Normalised results of the pushing installation tests showing V_c and V_o

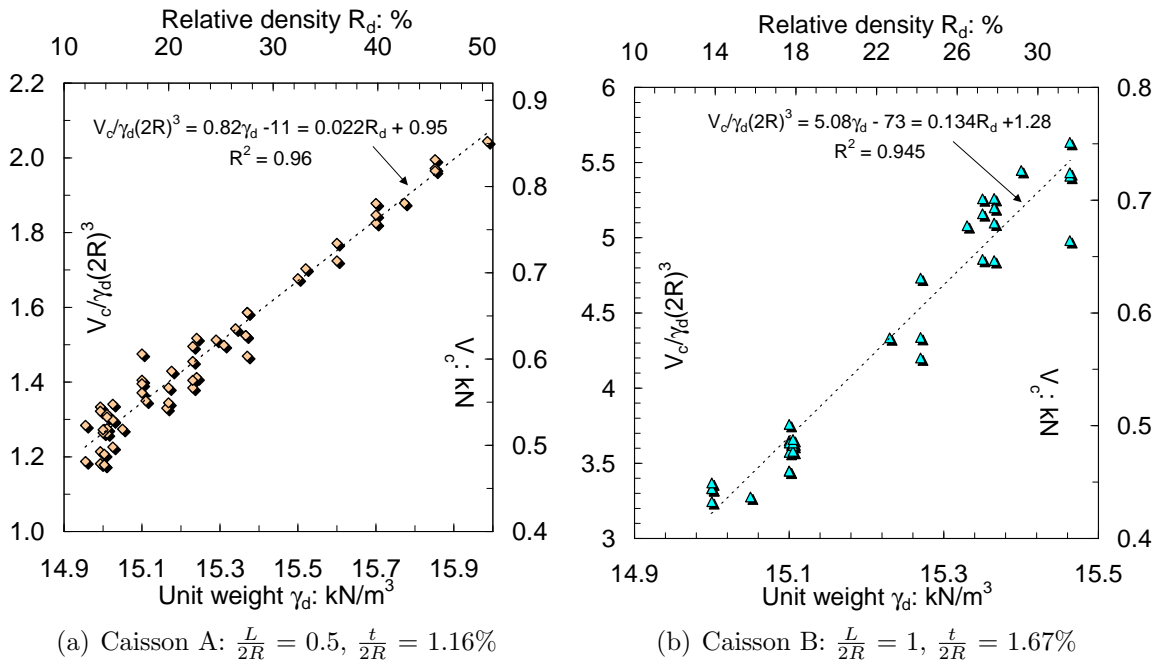


Figure 4.9: Relationships between the contact vertical load V_c and the soil unit weight γ_d and the relative density R_d

It can be observed in Figure 4.11(a) that the prediction obtained is poor when a linear stress distribution is considered ($\sigma'_{v\ geostatic}$ in Figure 4.10(a)). The frictional forces are equal $F_i = F_o$ since a similar friction parameter $K \tan \delta$ was used inside and outside. The exponential stresses shown in Figure 4.10(a) increase over the geostatic after 20 mm of penetration, which is the effect of considering soil arching. This results in a better prediction of V' as Figure 4.11(b) demonstrates. The value of m can be changed to increase

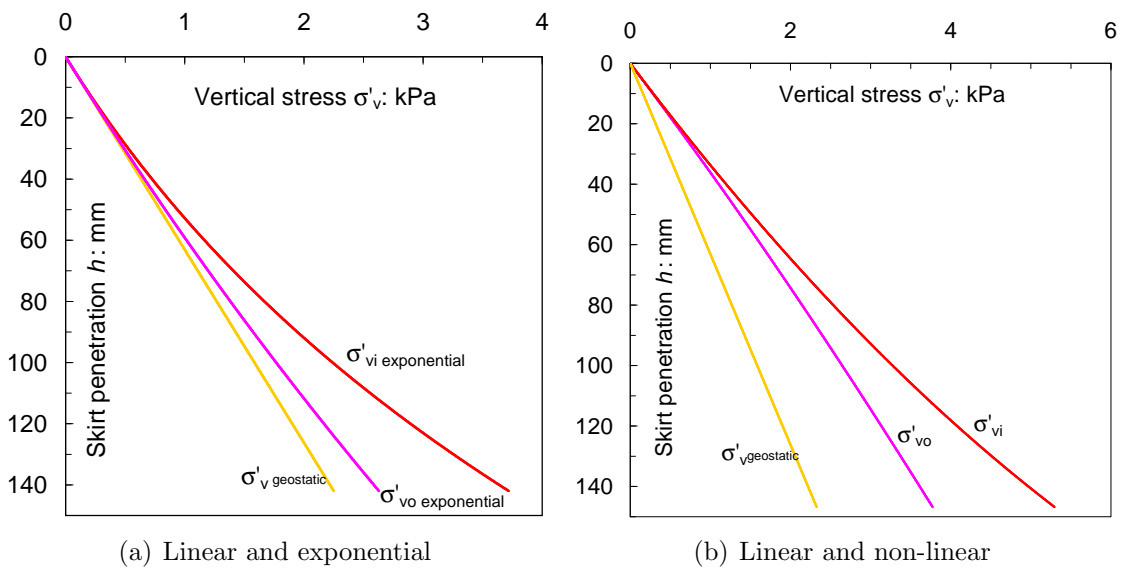


Figure 4.10: Vertical stress distributions

σ_{vo} , but the prediction of V' will not significantly improve.

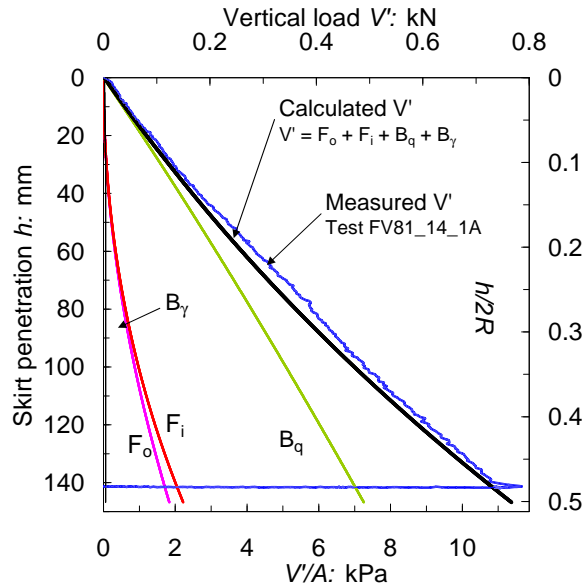
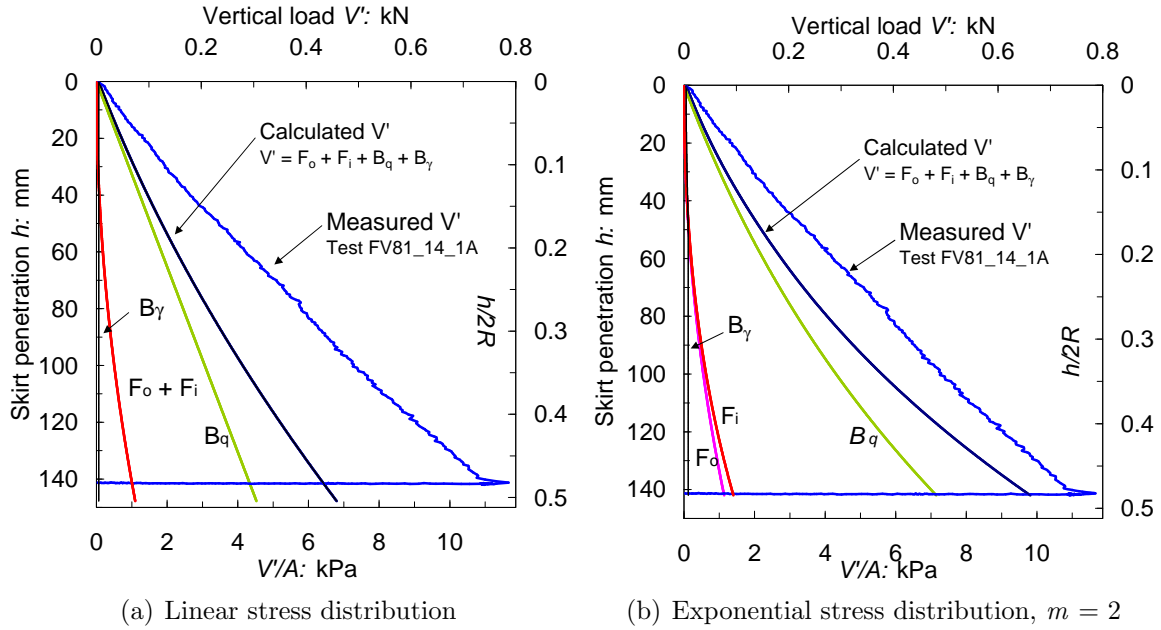


Figure 4.11: Measured and calculated load-penetration response assuming the following parameters: $\gamma_d = 15.85 \text{ kN/m}^3$, $\phi'_{peak} = 36.8^\circ$ and $\delta = 12.5^\circ \Rightarrow K \tan \delta = 0.47$

Higher non-linear stresses were obtained when the soil arching was taken for a radius linearly varying with depth at a rate of $f_i = f_o = 1$. Figure 4.10(b) shows that the vertical stresses inside and outside the caisson increase over the geostatic from the onset of the penetration and again $\sigma'_{vi} > \sigma'_{vo}$. Figure 4.11(c) shows that using the non-linear stresses led to a good agreement between the measured and calculated V' . The values of f_i or f_o could be slightly changed to improve the prediction, however, the intention here is to show the convenience of increasing non-linearly the stresses according to the formulation

presented in section §4.2.2. It is worth pointing out that in this example the chosen value of N_γ was irrelevant (in the three stress distributions) since the surcharge and friction components are substantially higher than the soil weight component.

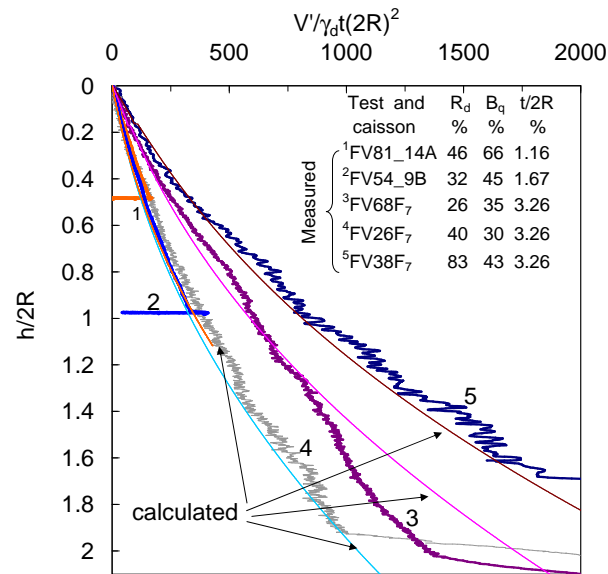


Figure 4.12: Measured and calculated normalised load-penetration curves for three different caissons assuming non-linear stresses with $f_i = f_o = 1$. In test FV54.9B the parameter values adopted were: $\gamma_d = 15.46 \text{ kN/m}^3$, $\phi'_{peak} = 34.7^\circ$ and $\delta = 14^\circ \Rightarrow K \tan \delta = 0.49$

Figure 4.12 compares installation curves of tests carried out with caisson F_7 (Chapter 3) in loose and dense Leighton Buzzard sand and loose Dogs Bay sand, with installation curves of tests carried out with caissons A and B. Note that owing to the large influence of the surcharge component B_q (especially in tests with caissons A and B), the normalised vertical load should include the thickness ratio to achieve similarity. Using the dimensionless relationship: $\frac{V'}{\gamma_d (\frac{t}{2R})(2R)^3} = \frac{V'}{\gamma_d t(2R)^2}$, the installation curves of three different caissons compare relatively well for loose Leighton Buzzard sand (tests FV81.14A, FV54.9B and FV26F₇). The tests in very loose calcareous sand (FV68F₇) and in dense Leighton Buzzard sand have higher normalised vertical loads due to the higher angles of friction. For the former the higher value of $\phi'_{peak} = \phi'_{cs}$ is due to the angularity of the grains, whilst for the silica sand is due to soil dilation. Calculated curves using non-linear stresses show that a reasonable good prediction can be achieved. The values of unit weight and peak angle of friction for the tests with caisson F_7 are presented in Chapter 3; a value of $\delta = 12.5^\circ$ was adopted.

4.3.2 Drained pullout tests

Models developed for the study of shallow foundations do not include tensile capacity, for instance, Model B and Model C described in Chapter 1. However, from Figures 4.13(a) and 4.13(b) it can be observed that fully drained pullout tests of caissons A and B exhibited tensile capacity due to friction developed on the skirt. Values of maximum tensile loads V_t and displacements h_t are listed in Tables 4.1 and 4.2. Pullout tests were carried out under a rate of $\dot{h} = 2$ mm/s, but with different load histories (monotonic and/or cyclic rotational or translational tests). Only test FV58_10_1A was carried out exclusively to explore the vertical load capacity, but because the caisson was more deeply embedded due to the larger V_o applied the maximum tensile load V_t was slightly higher. It

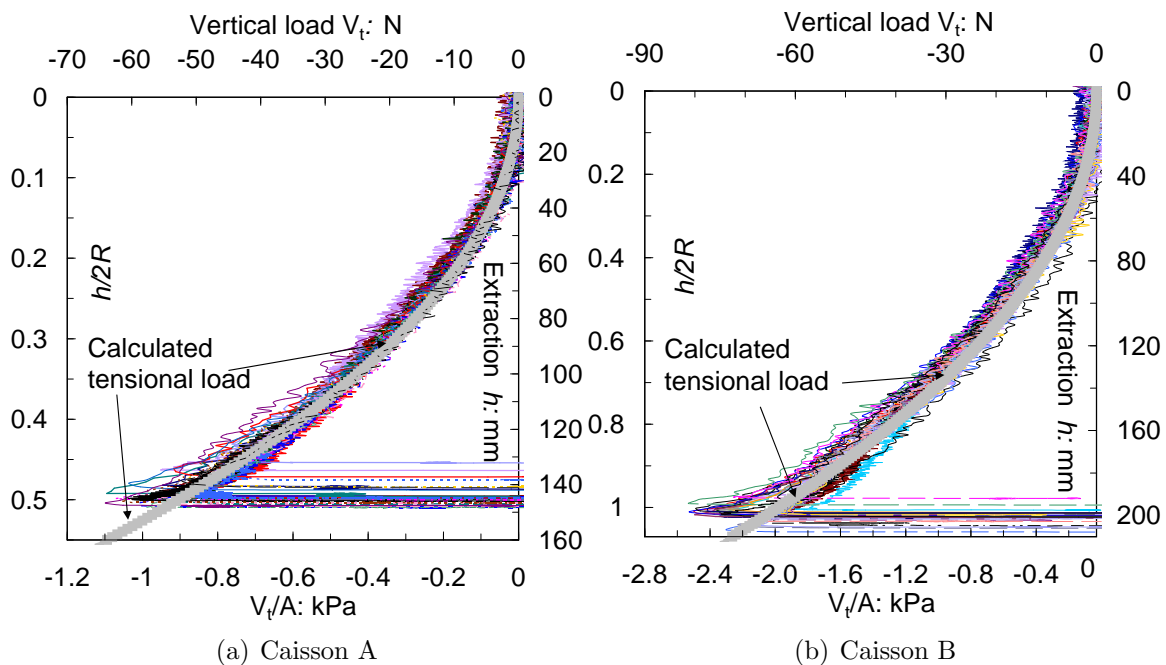


Figure 4.13: Measured and calculated drained pullout curves assuming: $\gamma_d = 15.2$ kN/m³, $\phi'_{cs} = 33^\circ$ and $\delta = 18^\circ \Rightarrow K_A \tan \delta = 0.18$

can be concluded that, independent of the load history, a very small mobilised extraction ($h = h_o - h_t$) is required to trigger the maximum tensile capacity. After the maximum tensile capacity is reached the tensile load decreases with further extraction of the caisson. The calculated pullout-extraction curves using equation (4.4) are shown in Figures 4.13(a) and 4.13(b). The calculation of V_t depends strongly on the value of $K_A \tan \delta$ adopted. The parameter values assumed attempt to represent an average of all tests. The prediction

agrees with the measured curves in spite of the soil disturbance caused by shearing during installation and subsequent moment loading. The disturbance was diminished since the soil was always in a loose state.

4.3.3 Pushing installation into dense saturated sand

Before studying suction assisted installation, it is felt important to investigate pushing installation under saturated conditions. This will allow a comparison between both installation methods and also with those test results in dry and loose sand.

It is necessary to clarify that the use of V' does not refer to an effective load as if it were an extension of the principle of effective stresses by Terzaghi. The use of the dash, as before, must be interpreted as the submerged weight of the whole structure plus appurtenances. The effective stresses are transmitted only through the soil skeleton, whereas loads on the caisson foundation can be related by equilibrium.

Table 4.3 summarises soil and conditions of the tests performed with caissons C and A, where D_f corresponds to the height of fluid above the mudline, t_p is the total time required to install the caisson and \dot{h} is the constant penetration rate at which both caissons were pushed into the ground. Measured and calculated load-penetration curves are shown in Figures 4.14(a) and 4.14(b) for two groups of similar tests, which allowed for only one calculation for each caisson. The calculation procedure developed in section §4.2.2 for non linear stresses was used to estimate V' as the sum of $F_i + F_o + B_q + B_\gamma$. Figures 4.14(a) and 4.14(b) show clearly that the major contribution is done by the surcharge component B_q , which increased even more for the larger caisson A. On the other hand the weight component B_γ is practically negligible (it is next to left ordinate axis) despite the greater than twofold increase in the thickness ratio $\frac{t}{2R}$ for caisson A. Finally, it can be observed that a very good agreement exists between the theory and the experimental results for both caissons. A relevant implication of this is that values of V_o can be predicted properly by this theory, which is crucial for a successful application of hyperplasticity theories.

Table 4.3: Data and parameters for load-penetration calculations of pushing installation tests

Test and caisson	γ' kN/m ³	R_d %	ϕ' °	δ °	$K\tan\delta$	D_f mm	\dot{h} mm/s	t_p min	h_o mm	V_o N
FV2_4_1C†	9.76	74	40.5	17	0.75	60	0.5	3	87	258
FV3_4_1C†	9.48	64	37.2	0	0	121	0.016	105	98	28
FV6_3_1C	9.70	75	44.1	15	0.76	130	0.5	3.2	97	403
FV7_1_1C	9.66	74	44.1	15	0.76	130	0.5	3.3	101	414
FV7_5_1C	9.66	74	44.1	15	0.76	122	0.5	3.3	102	422
FV7_2_1A	9.66	74	44.1	14	0.70	130	0.4	5.5	131	1715
FV7_4_1A	9.66	74	44.1	14	0.70	136	0.2	11.4	136	1537
FV8_2_1A	9.88	81	44.1	14	0.70	128	0.2	10.6	126	1641

†tests in oil-saturated Baskarp Cyclone sand, remainder tests in water-saturated Redhill sand

For example, V' was calculated as approximately 0.4 kN for caisson C and as 1.6 kN for caisson A (Table 4.3 shows V_o values obtained directly from the tests).

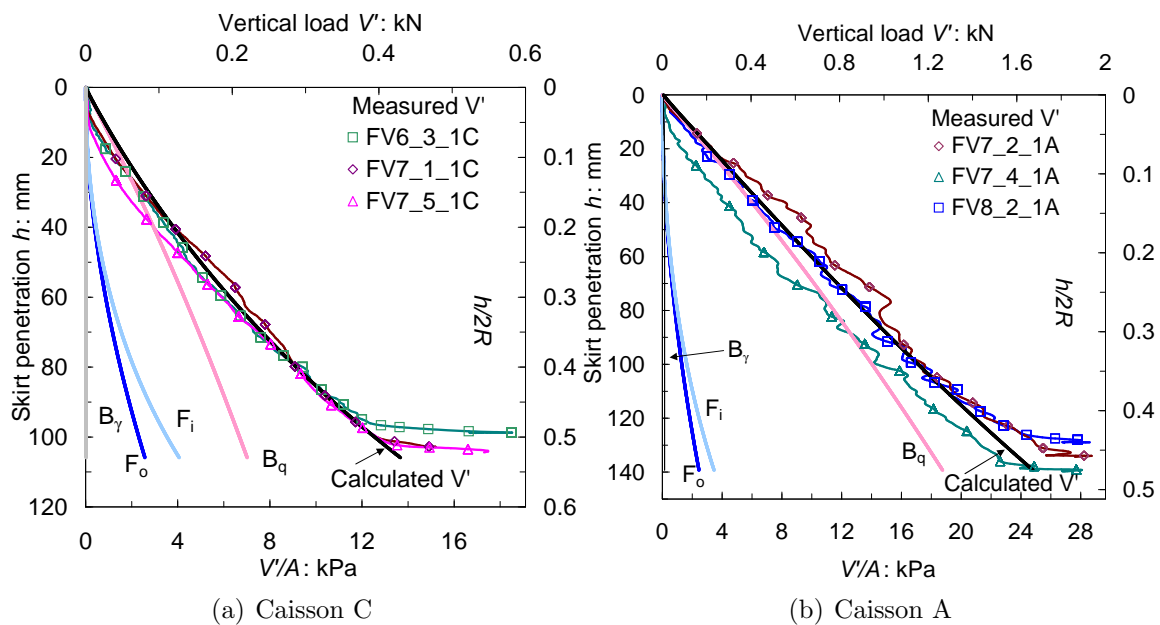


Figure 4.14: Measured and calculated load-penetration curves of pushing installation tests assuming $f_i = f_o = 1$, $\gamma' = 9.66$ kN/m³, $\phi'_{peak} = 44.1^\circ$, $\delta = 15^\circ$ and $14^\circ \Rightarrow K\tan\delta = 0.7$ and 0.76

Although the bleed valve was kept open during all the pushing installation tests an increase in pore pressure with penetration was observed. Figure 4.15(a) shows excess pore pressure (over the hydrostatic) recorded underneath the caisson lid. This was caused by insufficient section area of the bleed valve to compensate the rate of water flowing out the caisson with the penetration rate. However, this transient excess pore pressure increment dissipated once the installation ended. Note in Table 4.3 the very low value of V_o obtained in test FV3_4_1C. According to estimations of V_o using the theory already

presented it can be hypothesized that the only way to achieve such a low value is with frictional forces tending to zero due to $\delta \rightarrow 0$ as a result of the very low penetration rate and high viscosity fluid. As stress is expected to decrease with strain rate, it would be similarly expected that very low penetration rates would reduce friction. Moreover, it seems that a high viscosity fluid might act as a lubricant under the vertical penetration and interface conditions, which may also be a cause for the reduction of friction.

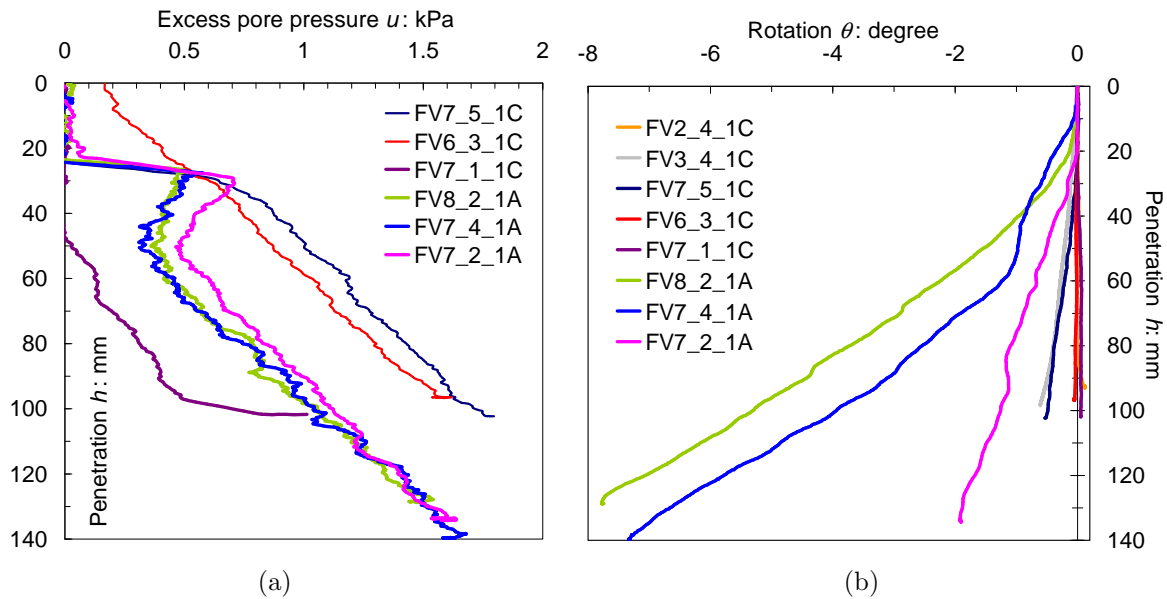


Figure 4.15: (a) Measured excess pore pressures during pushing penetration, and (b) rotation of caisson during pushing penetration. See details of the tests in Table 4.3

Figure 4.15(b) shows that caisson A rotated during penetration more than caisson C, rotating up to 8° . The negative sign in the plot is because of the counterclockwise rotation. The sign of the rotation is not important, as under this loading no rotation would be expected, and the measured rotation is just a measure of experimental variability. Rotation started once fluid flowing out of the caisson through the open vent created an upward force that due to the eccentricity caused a moment, which became larger with depth and especially for caisson A. Positive moment caused negative rotation because the program subroutine instructs the caisson to rotate opposite to counterbalance the positive increase of horizontal load H and moment M during vertical loading. This resulted in the reduction of H and M by translating and rotating the caisson in the opposite direction. Low penetration rates favoured the caisson tilting too since the counterbalance process occurs for a longer period of time. Initial penetration is caused by the structure's self-weight,

therefore, tilting can become an issue if eccentric loads act on the caisson. In the next section it will be seen that caissons penetrate straight naturally using suction, but if the caisson is initially rotated suction will not correct that inclination.

4.3.4 Suction installation results in dense sand

The theory presented in section §4.2.3 to predict the required suction to assist the installation of caissons requires experimental results for calibration and validation. Preliminary comparisons between this theory and four case records and one series of laboratory tests were presented by Houlsby and Byrne (2005b). The database used for the calculations is reproduced in Table 4.4, where values of δ have been deduced using equation (4.5) and $K \tan \delta$. The first two cases correspond to trial tests at Tenby and Sandy Haven, South Wales. The suction installation results at Tenby demonstrated the importance of determining the limits of suction-assisted penetration. The caisson could not be penetrated into the ground past 1.4 m because of piping failure. The other two cases involved caisson foundations for the jacket structures: Draupner E and Sleipner T (Tjelta, 1994; 1995). These cases correspond to much larger caissons and also to much higher vertical loads than in the trial tests. Latterly, Houlsby *et al.* (2006) add new data from suction caisson installation during field trials at Luce Bay, Scotland. The theory performs reasonably well for those cases analysed. It was concluded that for successful predictions k_f should be between 2 and 3, and $K \tan \delta = 0.54 \pm 0.09$ for unitary stress distribution factors ($f_i = f_o = 1$). An exception was the high value of $K \tan \delta$ for the trials in Luce Bay, which may correspond to a high roughness of the skirt wall δ or a compensation for not using a higher value of k_f .

Whilst Table 4.4 shows a range of data there is still a pressing need for additional studies of suction-penetration of caissons under diverse conditions, in particular different caisson geometries, soil properties and submerged weights. Furthermore, investigation of the effect of the installation method on the subsequent loading performance must also be considered. The foundation response to subsequent monotonic or cyclic lateral loading

Table 4.4: Data and parameters for suction calculations installation tests (taken from Houlsby and Byrne (2005b) and Houlsby *et al.* (2006))

Location	$2R$ m	L m	t mm	V' kN	γ' kN/m ³	ϕ' °	δ °	$K \tan \delta$	k_f
Tenby	2	2	8	10	8.5	40	11	0.48	3
Sandy Haven	4	2.5	20	100	8.5	40	11	0.48	2
Draupner E	12	6	45	6622	8.5	44	12	0.63	3
Sleipner T	15	5	45	12000	8.5	45	15	0.8	3
Laboratory	0.15	0.2	1.65	†	8.5	45	9	0.45	2.5
Luce Bay	1.5, 3	1, 1.5	8	7, 60	10.3	45	19	1	3

†45, 85, 165 ($\cdot 10^{-3}$)

will be related to whether the soil strength was modified or not during installation. Consequently, a series of installation tests using suction were planned covering a range of different caisson geometries, soils and submerged weight V' . Chapters 5, 6 and 7 are devoted to loading of caissons after installation. A summary of the parameters assumed

Table 4.5: A summary of parameters used in the calculations

Test and caisson	V' N	D_f mm	γ' kN/m ³	R_d %	ϕ °	δ °	$K \tan \delta$	k_f
FV1.2.1E†	5	46	10.25	90	43	15	0.73	2.7
FV10.4.1D	45	200	10.10	89	46.3	15	0.85	1.3
FV3.1.1C†	-4	46	9.93	80	41.5	15	0.69	2.7
FV9.4.1C	7	160	10.21	92	46.8	15	0.88	2.6
FV6.5.1C	7	115	9.70	75	44.3	15	0.78	2.8
FV9.2.1C‡	40	180	10.21	92	46.8	15	0.88	2.8
FV9.1.1C	62	185	10.21	92	46.8	15	0.88	2.8
FV9.5.1A	14	202	10.21	92	46.8	14	0.81	3.5
FV10.3.1A	16	180	10.10	89	46.3	14	0.80	3.4
FV7.3.1A	65	140	9.66	74	44.1	14	0.72	8
FV10.2.1A	62	204	10.10	89	46.3	14	0.80	3.4
FV7.1.3A	125	130	9.66	74	44.1	14	0.72	10
FV10.1.1A	117	193	10.10	89	46.3	14	0.80	3.4

†carried out in oil-saturated Baskarp Cyclone sand

‡caisson initially tilted 4°

for the suction calculations is listed in Table 4.5. The values of angle of friction have been estimated using the procedure proposed by Bolton (1986) to calculate peak friction angles. The interface angles δ have been assumed according to value ranges presented by Lings and Dietz (2005) (section §4.3.1). Additionally, Table 4.6 includes information of the suction variation with penetration $\frac{ds}{dh}$ (which is not constant, but a relatively fair constant variation can be assumed at the end of the installation), suction rate \dot{s} , penetration rate \dot{h} , time during suction application t_s , penetration by self weight h_p , final penetration h_o , estimated penetration by self weight h_{pe} and calculated V_o . The recorded

suction underneath the lid with a pore pressure transducer PPT was corrected to obtain the differential pressure (see Chapter 2 for details of the suction system used), which is the difference between the pressure in the caisson compartment and the pressure in the fluid outside the caisson at the same level, according to Figure 4.5 the corrected suction results in:

$$s = s_{ppt} - \gamma_f(D_f - L + h) \quad (4.34)$$

where γ_f is the unit weight of the fluid equal to 9.8 kN/m³ for water and 9.4 kN/m³ for the silicon oil. The range of suction applicable diminishes with D_f , but even if more suction were applied there is a maximum available suction given by:

$$s_{available} = p_a + \gamma_f D_f - p_{cav} \quad (4.35)$$

where p_a is the atmospheric pressure (≈ 101.3 kPa) and p_{cav} is the cavitation pressure (≈ 100 kPa). Therefore, the available suction relies mostly on the fluid height D_f , without which suction is very limited or maybe insufficient to install successfully a suction caisson.

Test FV10_2_1A was selected to compare the different calculations of suction presented in section §4.2.3. The measured suction-penetration curve shown in Figure 4.16(a) indicates that the suction was applied after an initial pushing penetration $h_p = 20$ mm, obtained when $V' = 62$ N (the calculated penetration for this load is $h_{pe} = 4$ mm). Subsequently, the suction commences under the constant vertical load $V' = 62$ N that caused the self weight penetration. To compare these results with other suction records the non dimensional parameters $\frac{s}{\gamma' 2R}$ and $\frac{h}{2R}$ were included in the plots. The suction calculations shown in Figures 4.16(a) and 4.16(b) correspond to: i) linear stress distribution with depth, ii) exponential stress distribution with depth based on soil arching, and iii) other non-linear increase of stresses with depth due to soil arching.

According to these calculation results the three procedures lead to an underestimation of the measured suction. The use of non-linear σ'_v gave a better prediction followed by exponential σ'_v , and linear σ'_v . A large discrepancy of V_o was obtained using the same

Table 4.6: A summary of suction installation tests

Test and caisson	$\frac{ds}{dh}$ kPa/m	\dot{s} kPa/hr	\dot{h} mm/min	t_s min	h_p mm	h_{pe} mm	h_o mm	V_o N
FV1.2.1E†	22	1.3	0.82††	106	25	4	98	217
FV10.4.1D	17	2.8	2.64	42	27	20	138	641
FV3.1.1C†	18	0.8	0.93	73	29	0	97	250
FV9.4.1C	19	$0.17e^{2.825t}$	$0.45e^{0.042t}$	50	13	2	90	414
FV6.5.1C	22	2.6	2.22	25	35	4	92	296
FV9.2.1C	22	2.8	2.29	37	16.5	13	94	443
FV9.1.1C	20	6	5.30	13	29.5	20	96	458
FV9.5.1A	26-10	1.7	$0.26e^{0.027t}$	98	12	0	128	2616
FV10.3.1A	21	1.6	$0.29e^{0.027t}$	97	13	3	119	2146
FV7.3.1A	22	4.6	3.67	30	29	7	131	1724
FV10.2.1A	20	0.6	0.18 - 0.44‡	300	20	4	135	2582
FV7.1.3A	30	8	4.33	22	46	13	123	1571
FV10.1.1A	20	0.8	0.34 - 0.62‡	215	22	8	131	2472

†oil-saturated Baskarp Cyclone sand, †† $\dot{h} = -0.63 \cdot 10^{-4}t^2 + 0.15t - 0.38$, ‡bi-linear

soil parameters for $h_o = 135$ mm, resulting in: i) 820 N, ii) 1474 N, and iii) 2582 N. Villalobos *et al.* (2005) report a similar underestimation of the suction when using the stress enhancement calculation procedure iii) for the test FV7.3.1A adopting a very high $K \tan \delta = 0.9$, $f_i = f_o = 1$ and $k_f = 1$ ($V_o = 1700$ N for $h_o = 131$ mm).

The initial pushing penetration of the skirt into dense sand rises a soil plug owing to

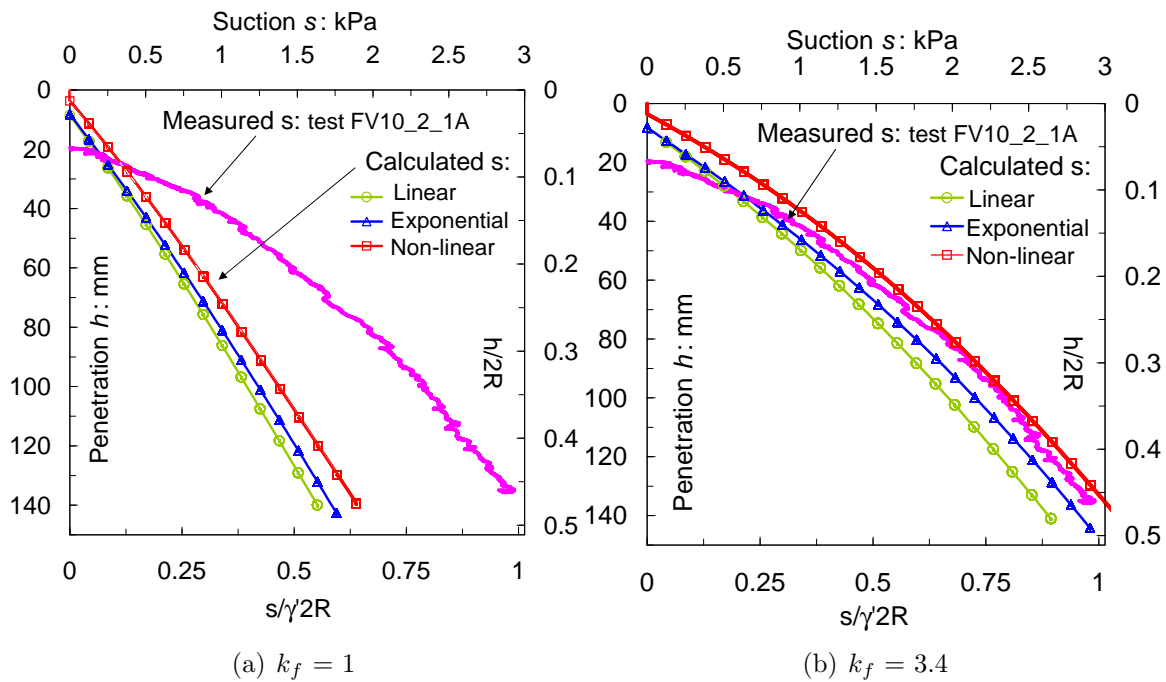


Figure 4.16: Measured and calculated suction-penetration curves assuming $V' = 62$ N, $m = 2$ for exponential, and $f_i = f_o = 1$ for non-linear stress distribution

dilative behaviour as discussed in Chapter 3. As a consequence of sand dilation an increase of specific volume occurs, hence permeability increases too if the sand is saturated according to the Kozeny-Carman equation (4.21). In the light of the experimental results this is confirmed, since the soil permeability changes due to dilation and seepage, which modifies the effective stresses during caisson penetration, and as a consequence the specific volume and in turn the permeability ratio $k_f > 1$. This qualitative experimental evidence is supported quantitatively by the suction calculation and equation (4.21), which relates the increase of permeability with specific volume. Indeed, Figure 4.16(b) shows the significant improvement of the suction estimation when a permeability ratio k_f of 3.4 is chosen. Although the use of linear or exponential distribution of stresses still underestimate the suction compared with the non-linear approach, they can be useful as preliminary estimations or as a verification of numerical results. Furthermore, for piles soil arching effects diminishes as pile diameter increases (Hight *et al.*, 1996; Lehane *et al.*, 2005). Therefore, these simpler calculation procedures may be useful. However, this needs to be investigated for suction caissons.

It was not a surprise that in calculations of the suction the surcharge force B_q was predominant whereas the influence of the weight force B_γ was negligible as in sections §4.3.1 and §4.3.3, since those calculations are based on formulations for pushing penetration. Finally, the variation of soil permeability cannot be overlooked if an accurate estimation of the suction is pursued. In Chapter 3 it was pointed out that the skirt penetration causes a soil plug heave as a result of dilative behaviour in dense sand. In consequence, soil permeability k_i increases next to the skirt wall since dilation induces the increase of void ratio, but k_o decreases due to the opposite direction of seepage.

Calculated distributions of effective vertical stress are shown in Figure 4.17 for test FV10.2.1A. Non-linear distributions of σ'_{vo} and σ'_{vi} were calculated as in the case of pushing penetration (see Figure 4.10(b)). The effect of seepage on the stresses is also reflected in Figure 4.17, where the calculated effective vertical stress $\sigma'_{vo\ seepage}$ increased whereas $\sigma'_{vi\ seepage}$ reduced with depth. Furthermore, the calculated distribution of excess

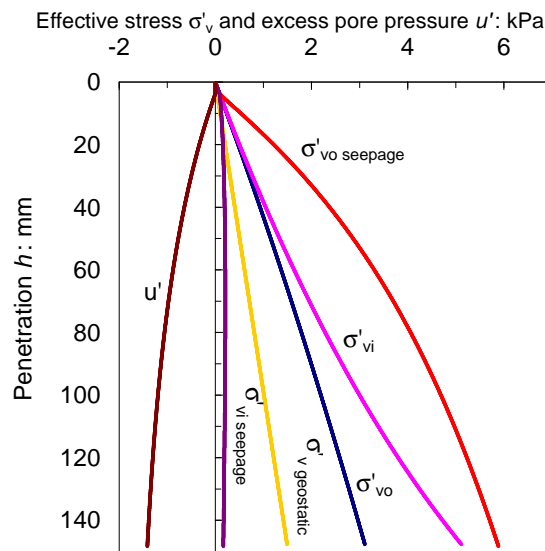


Figure 4.17: Calculated distribution of effective vertical stresses with and without seepage, showing also calculated distribution of excess pore water pressure u' at the tip of the caisson (test FV10.2.1A)

pore water pressure u' at the tip of the caisson as penetration occurs is plotted in Figure 4.17. Because the calculation of u' includes the pressure factor a , the distribution of u' is not linear since a varies non linearly with depth. Note the drastic reduction of σ'_{vi} to $\sigma'_{vi seepage}$ explains why installation under low net vertical load is possible.

Measured and calculated suction were compared for three different values of submerged weight V' as shown in Figure 4.18(a) for caisson A and in Figure 4.18(b) for caisson C. The calculated suction reduces when V' is increased, reproducing the same trend observed in the measured suction. Test FV9.2.1C was carried with the caisson tilted 4° . However, the suction did not straight the caisson up during penetration. The use of suction does not rotate or translate the caisson as may occur during pushing penetration. Calculated hydraulic gradients, using equation (4.13), are opposite in direction yet clear differences in magnitude are found as shown in Figures 4.19(a) and 4.19(b). Whilst i_o causes a flow downwards and can be larger than one, i_i causes a flow upwards and has a high initial increase that continues asymptotically. This asymptote corresponds to the critical hydraulic gradient $i_c = \frac{\gamma'}{\gamma_f} = 1.03$, hence $i_i < 1$. A high i_o is beneficial because it strengthens the sand, buffering for instance the spread of an initial piping condition. On the other hand, i_i is also beneficial in the sense that allows the skirt to penetrate under

a much lower vertical load. However, i_i is limited by the critical hydraulic gradient i_c , otherwise piping failure may occur and further penetration may not be possible. It is worth noting that the increase of V' reduces the hydraulic gradient inside the caisson i_i , so reducing the risk of piping failure as well. Figures 4.19(a) and 4.19(b) show that at small penetrations the downward hydraulic gradient i_o is much greater than the upward hydraulic gradient i_i until a maximum value is reached. During subsequent penetration i_o diminishes to values close to i_i at the end of penetration. In the theory this is directly related to the pressure factor a . Experimentally, it was found that initially the suction increases causing small penetration, but once a certain level of suction was reached much larger penetration occurs at a lower (and approximately constant) increase of the suction with penetration. Those approximately constant values of $\frac{ds}{dh}$ are shown in Table 4.6.

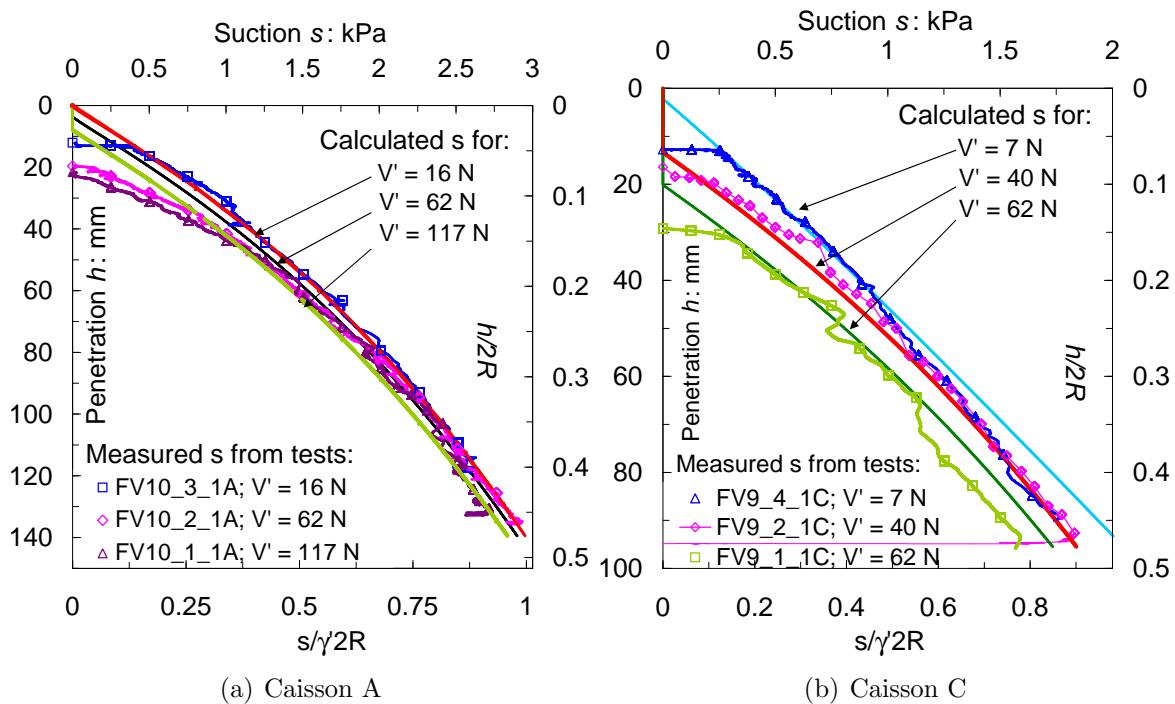


Figure 4.18: Measured and calculated suction-penetration curves using non-linear stress distribution and $k_f > 1$

Figure 4.20(a) shows the suction applied to caissons E and D, which differed only in the skirt length L as presented in Chapter 2. Nevertheless, caisson E was installed in a very fine oil-saturated sand under a low vertical load $V' = 5$ N, and caisson D was installed in a fine water-saturated sand under a higher vertical load $V' = 45$ N. Owing to these differences two patterns of suction variation with depth appeared. For the former an

initial high increment of suction occurred, whilst for the latter a lower and relatively constant increment of suction with depth occurred. However, once the initial high increment of suction diminished both curves were almost parallel. For caisson E a higher suction increment was needed in order to start the caisson penetration as a consequence of the

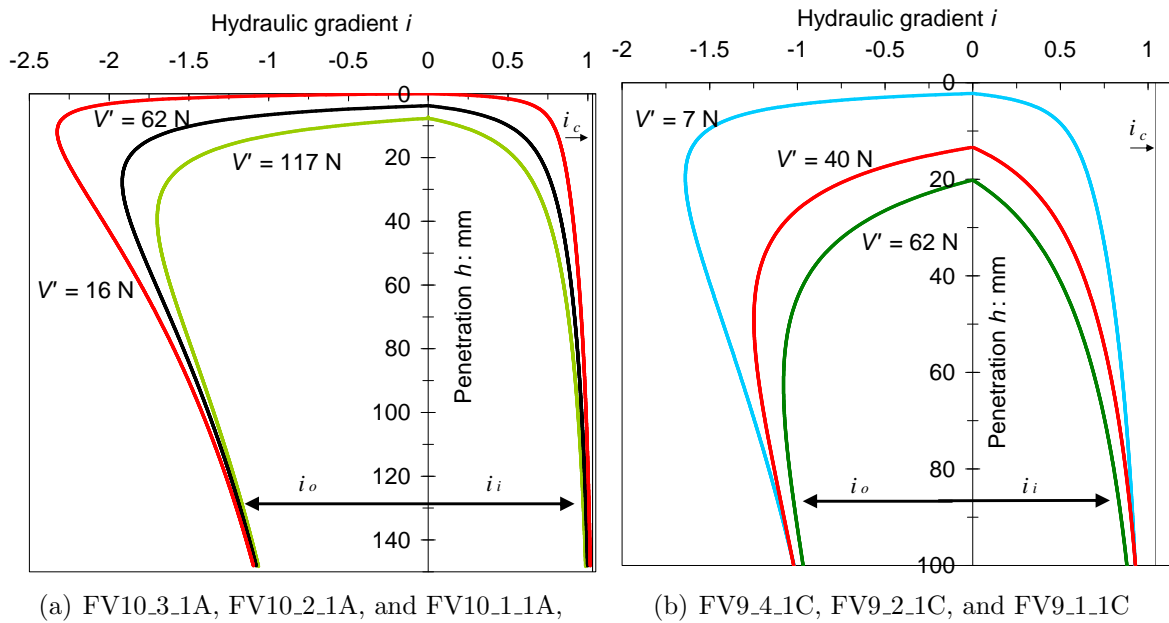


Figure 4.19: Calculated average hydraulic gradients, showing critical hydraulic gradient i_c using equation (4.13)

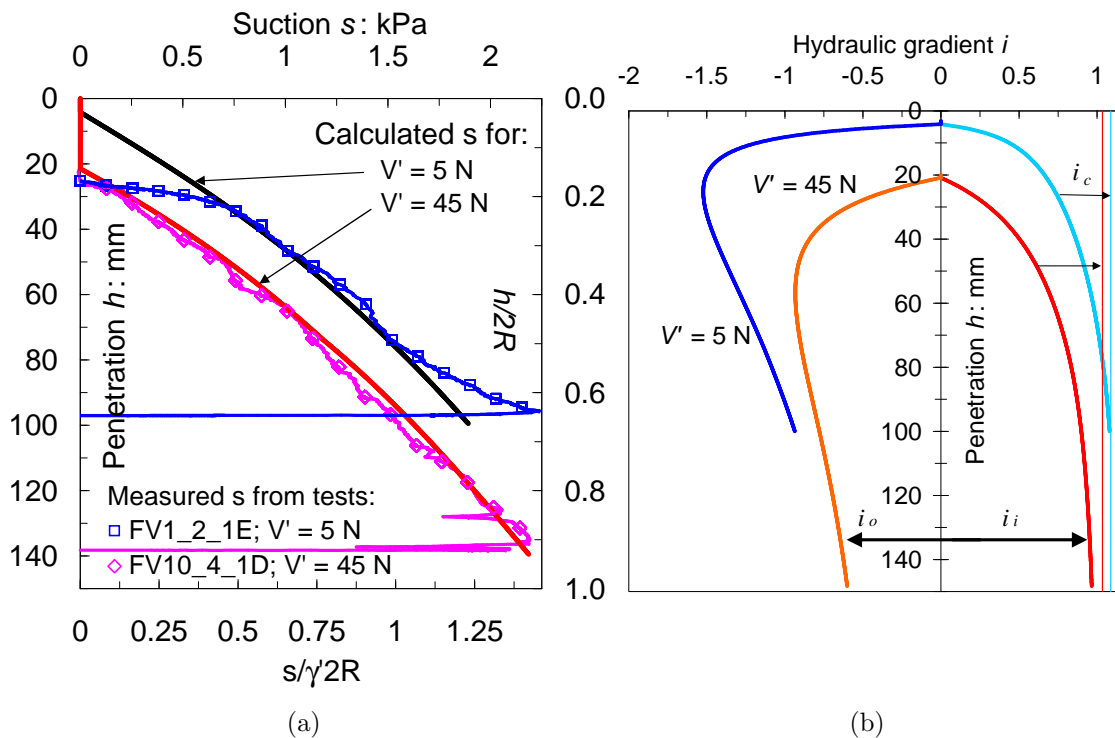


Figure 4.20: (a) Measured and calculated suction-penetration curves, and (b) calculated hydraulic gradients outside and inside the caisson, showing critical hydraulic gradient i_c

low soil permeability caused by the oil permeant. In other words, to create enough upwards seepage forces to reduce the soil strength. To achieve this an increase of pore fluid pressure was required to cause the reduction of effective stresses at the tip. An equivalent finding by Tran *et al.* (2004) indicates that the suction increases with penetration rate. However, the increase of the suction with the reduction of permeability or with the increase of penetration rate, although consistent, have not been yet explained by theory. Once the flow regime was developed the increment of suction *stabilised*, for that reason both curves end up with similar slopes. This *stabilisation* or steady state flow regime requires more suction for caisson E because it is not only being penetrated under a lower vertical load, but also into a soil with a permeability three orders of magnitude lower than that for caisson D. (In Figures 4.18(a) and 4.18(b) the difference in the measured suction curves was only due to different V' , because the sand and the permeant were the same). It can also be observed that the measured suction for caisson E increased at a higher rate after a penetration of 75 mm. This indicates the presence of a much denser sand layer that forces a higher suction to be applied in order to progress. This sample was around three years old and probably for that reason there was this increase of density with depth.

The purpose of the following series of tests was to investigate the caisson installation under very low vertical loads as well as higher penetration rates. Figure 4.21(a) shows that installation by suction was possible even under a tensile load V' of -4 N in oil-saturated Baskarp Cyclone sand (test FV3_1_1C). Installation under negative V' is not relevant to field but it was included for completeness. A second test shown in Figure 4.21(a) corresponds to the installation in water-saturated Redhill sand under a low load V' of 7 N (test FV6_5_1C). Contrary to Figure 4.20(a), where both measured curves were distant, in Figure 4.21(a) both measured curves are almost similar once suction stabilisation was reached. Because the values of V' were similarly low, there was a compensation between the differences in soil permeabilities and the suction rate \dot{s} . Not surprisingly, for the less permeable soil \dot{s} and \dot{h} were lower than for the more permeable soil (Table 4.6). This was also reflected in the time needed to install the caisson, three times more for the less permeable soil.

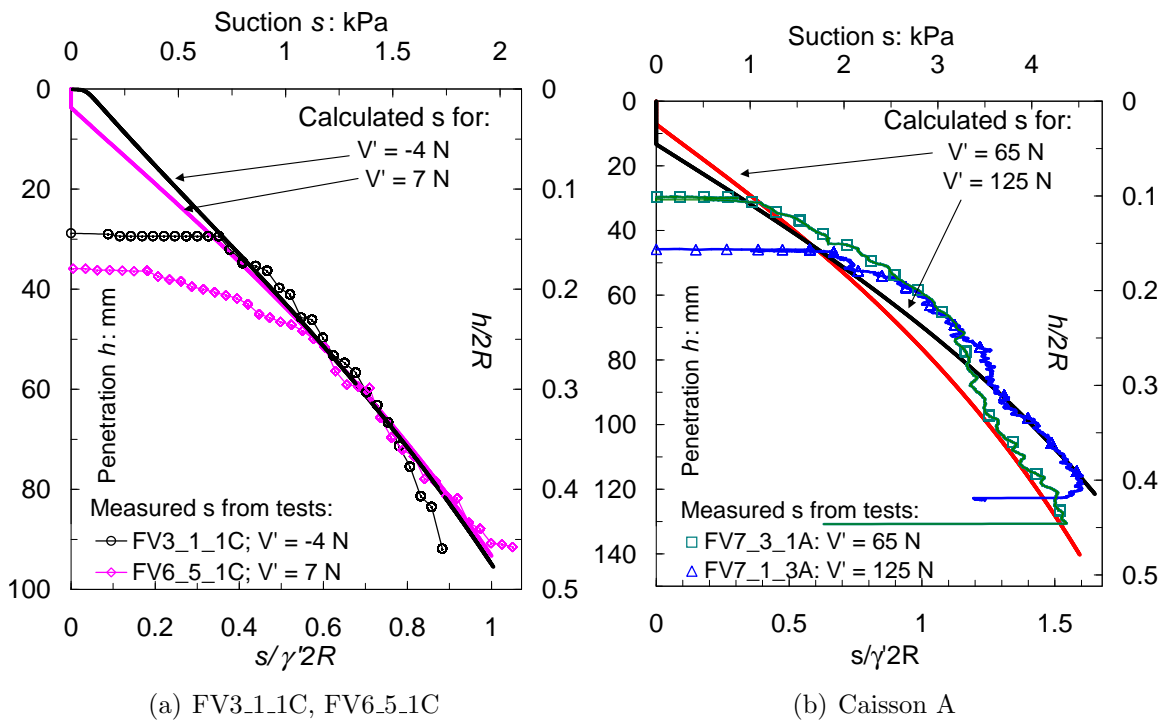


Figure 4.21: Measured and calculated suction-penetration curves for higher penetration rates

An almost twofold increase of the applied suction can be observed in Figure 4.21(b) when comparing with similar tests shown in Figure 4.18(a). The comparison is also valid with other tests in terms of $\frac{s}{\gamma'2R}$, usually less than one, now reaches a maximum value of 1.6. For example, tests FV7.3.1A and FV10.2.1A have relatively similar V' and R_d (65 N, 74%, and 62 N, 89%), but for the doubled suction applied an increase of ten times the rate of penetration \dot{h} was obtained. The same occurred comparing tests FV7.1.3A and FV10.1.1A. Furthermore, when the suction was doubled an increase of twenty times the penetration rate was found in tests carried out by Tran *et al.* (2004) in water-saturated silica sand ($2R = L = 100$ mm, $t = 0.5$ mm, $V' = 2.6$ N and $R_d = 92\%$). Therefore, the suction increment causes penetration rate effects. The underestimation of suction in the test FV7.3.1A by Villalobos *et al.* (2005) reveals that in part it was due to rate effects because the calculated suction in Figure 4.21(b) used a k_f value of 8 (Table 4.6). It is assumed that expressions (4.20) and (4.22) hold despite the fact that the pore pressure factor a parameters was estimated for a range of k_f between 1 and 5. The model does not consider rate effects and a high value of k_f results as an attempt to fit the data. Further work is needed to include rate effects in the calculations. Figure 4.22(a) shows that higher suction rate increases substantially the outside hydraulic gradient i_o and Figure 4.22(b)

shows that this results in high stresses outside the caisson.

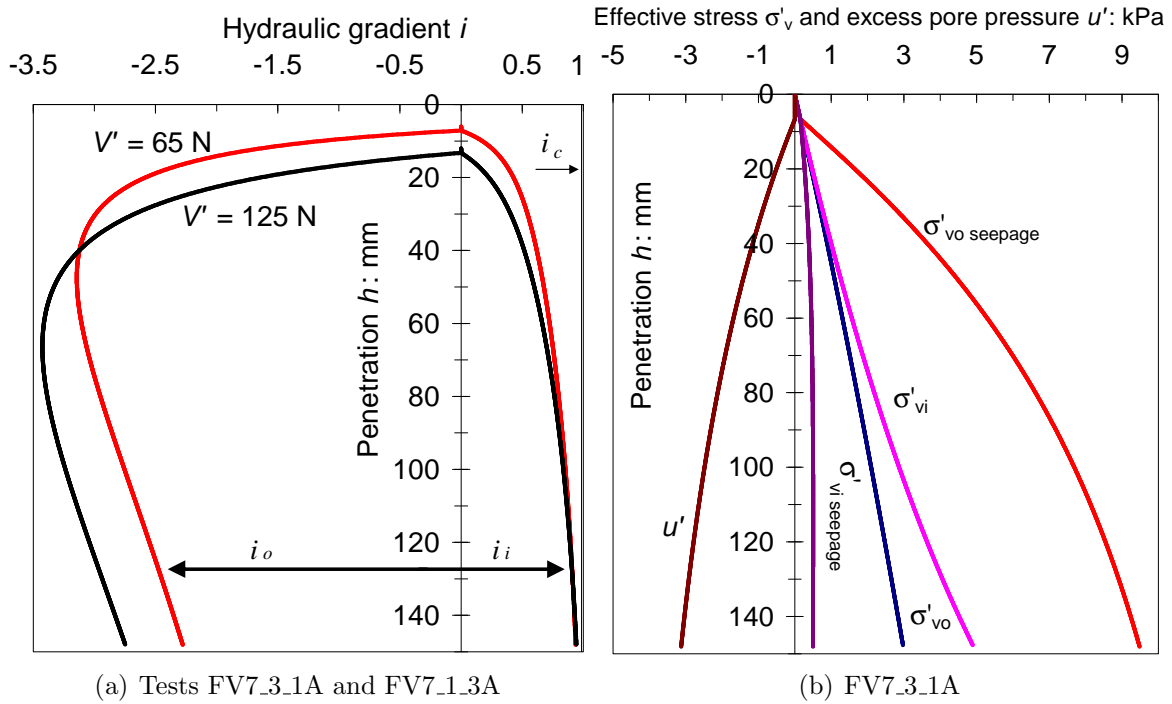


Figure 4.22: (a) Calculated hydraulic gradients, and (b) calculated effective vertical stresses and excess pore water pressures at the caisson tip

Limits to suction installation were determined using the expressions from section §4.2.4. Hydraulic gradients have already been shown in Figures 4.19(a), 4.19(b), 4.20(b) and 4.22(a) and compared against the critical hydraulic gradient i_c . Table 4.7 coalesces three criteria to evaluate the limit to the applied suction: i) hydraulic gradient $i_i < i_c$, ii) the safety factor to inverse bearing capacity failure $\frac{\sigma'_{vi} N_q}{\sigma'_{vo}} < 1$, and iii) penetration $h_{crit} > L$. Only in test FV7.3.1A a local piping occurred at a penetration of 43 mm, however, after reapplying the suction the test continued without further interruption. In general, around the outside of the caisson a settlement of the sand in the form of a wedge occurred as a result of densification or rearrangement of fine particles. This was particularly visible in test FV10.4.1D. Therefore, criteria i) and ii) were in agreement with the experimental results. In criterion iii) equation (4.28) overestimates the critical penetration, whereas equation (4.31) underestimates the critical penetration.

A comparison between two tests with the same caisson and sand conditions, but installed by pushing and by suction is shown in Figure 4.23. For the suction installation test the

Table 4.7: Limits to suction installation

Test and caisson	i_c	$i_{i\ max}$	$\frac{\sigma_{vi} N_q}{\sigma'_{vo}}$	h_{crit} (4.28) mm	h_{crit} (4.31) mm
FV1_2.1E†	1.09	1.07	1	135	64
FV10_4.1D	1.03	0.96	19	211	130
FV3_1.1C†	1.09	1.03	4	157	70
FV9_4.1C	1.04	0.99	7	173	83
FV6_5.1C	0.99	0.93	5	173	84
FV9_2.1C	1.04	0.91	17	209	118
FV9_1.1C	1.04	0.87	24	229	138
FV9_5.1A	1.04	1.02	2	242	113
FV10_3.1A	1.03	1.00	4	250	115
FV7_3.1A	0.99	0.94	2	259	129
FV10_2.1A	1.03	0.99	5	292	141
FV7_1.3A	0.99	0.90	4	272	144
FV10_1.1A	1.03	0.99	5	331	167

vertical load V' was kept constant at 60 N, and the curve labelled $V' + S$ represents the net vertical load due to the constant 60 N plus the pressure differential on the caisson lid in terms of force. It is clear that there is a significant reduction of the net vertical load using suction, reflected in the difference between the suction curve and the pushing curve. That difference between these curves represents the beneficial effects of the hydraulic gradients set up within the soil due to the suction.

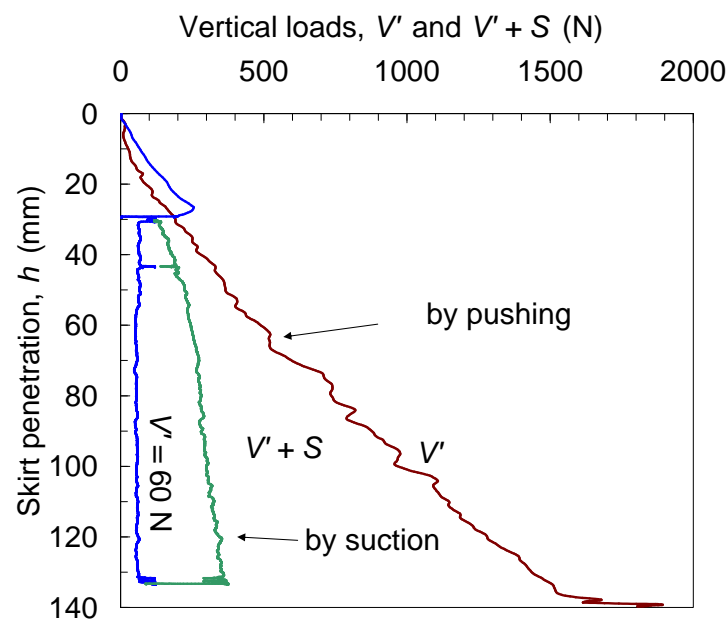


Figure 4.23: Comparison between pushed installation and suction installation for the 293 mm diameter caisson

4.4 CONCLUSIONS

From the experimental and analytical work carried out to study the installation of caissons by pushing and by suction the following conclusions can be drawn.

An expression to evaluate the lateral earth pressure against a frictional wall (not smooth) is suggested. Interface friction angles were correlated by means of the wall maximum roughness. In this way the parameter $K \tan \delta$ could be evaluated and not back calculated.

The pushing installation method was used to simulate a condition of self-weight penetration. In the field extremely large self-weights would be normally necessary to install fully a prototype caisson. The use of suction can supply the vertical load over the self weight available to completely install a caisson. With the assistance of suction there is a considerable reduction in the net force required to penetrate a caisson into dense sands due to the hydraulic gradients created by the application of suction. Pushing installation was extensively used in the laboratory owing to simplicity, especially when subsequent monotonic or cyclic loading tests were planned. These results were extremely useful for the parameter calibration and general assessment of the installation theory. It was found that for the thickness ratios and aspect ratios used the surcharge force was the most relevant followed by the friction forces in terms of the calculation of the vertical load and the suction. The end bearing component is practically negligible.

Caisson verticality must be carefully controlled during pushing penetration. Tests results demonstrated that a caisson can increasingly tilt with depth if the resultant vertical force is not centred. When suction was applied, the caisson penetration was straight and no tilting or translation was observed in the vertical plane measured. However, if the caisson is tilted the suction application can not straighten it up.

Under similar conditions, less suction was required when the submerged self weight increased. In addition, not only the caisson self weight, but also the permeability influences

the suction which generates seepage. It was found that the permeability ratio was a very decisive parameter in the determination of the suction. A range of values between 2 and 3 were previously suggested by Houlsby and Byrne (2005b), but in this study a wider range was necessary to predict appropriately the experimental results. In tests with high penetration rates as a result of high suction rates values of the permeability ratio between 8 and 10 were used to estimate the measured suction. Therefore, there is a rate effect that needs to be accounted for to calculate the required suction in the case of applied suction rates which are of one order of magnitude higher in conjunction with low values of V' . More research is needed to study the interaction between suction rate and penetration rate.

A study of the critical suction or critical penetration must be done to assess the adequacy of the caisson design. It was found that the maximum hydraulic gradient i_i compared with the critical hydraulic gradient i_c and the safety factor to the inverted bearing capacity are useful options to evaluate the limits to the suction. Critical penetration was overestimated when calculated with linear stress distribution, whereas the critical penetration was underestimated when non-linear stress distribution was adopted.

Chapter 5

MOMENT LOADING CAPACITY OF CAISSONS IN DRY SAND

Abstract

This chapter presents and analyses experimental results obtained from combined loading tests on model scale caissons. Combined moment and horizontal loading tests conducted with low constant vertical load are covered broadly to explore the shape and size of the caisson yield surface and the corresponding vectors of incremental plastic displacements. A major purpose of this investigation was to provide the information necessary to construct hyperplasticity formulations within the framework of force resultant models. It has been found that caissons can resist moment and horizontal loads under tension. The experimental results indicate that a yield surface and a flow rule formulation derived from hyperplasticity theory can be applied to modelling the results described here.

5.1 A SIMPLE MODEL

A simple model based on force equilibrium is a useful way of giving insight and understanding in soil-footing interaction problems. Figure 5.1 depicts the external forces applied to a caisson at the load reference point LRP as well as the reacting internal stresses and lateral earth pressures. It is assumed that the enclosed soil plug moves with

the caisson and as a result does not interact with the caisson. Then, the shear stresses represent the external friction between the caisson and the soil next to the wall and across the base. End bearing stresses around the caisson rim are included in the total vertical stresses σ'_v at the base. Assuming that σ'_v is uniformly distributed as a consequence of the soil plug weight and V' is a simplification. Because it may be arguable that a triangular distribution would appear when large moments are transmitted to the tip level overlapping the stresses due to soil plug weight and V' . In that case σ'_v should be considered as an average value. It is also assumed that the caisson rotates without lateral displacement around a point exactly under the LRP at a distance z_m . This point of rotation is referred to as the *metacentre*.

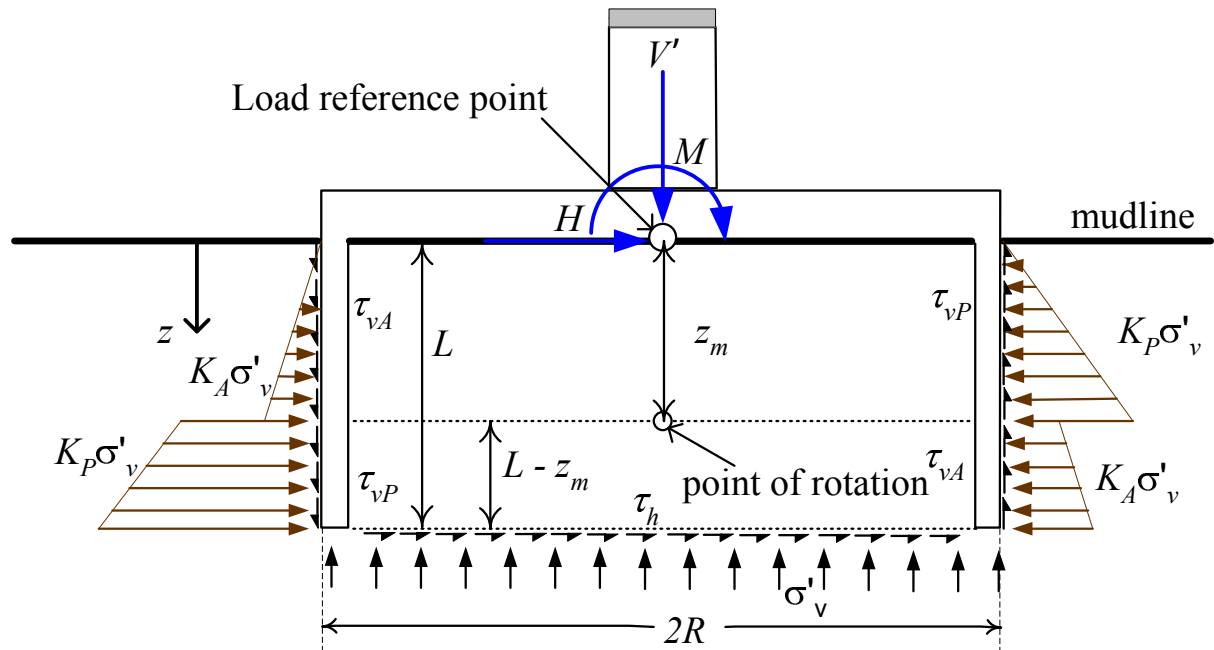


Figure 5.1: Simplified model of soil-footing interaction mechanism for a caisson with an aspect ratio of $\frac{L}{2R} = 0.5$ under a planar system of combined loading

The inclusion of the vertical load V' extends the analysis carried out by Byrne (2000) using M and H . The equations of force equilibrium that include the applied loading system (V', M, H) and the reaction forces due to friction and earth lateral pressure can be expressed as follows:

$$V' = \sigma'_v \pi R^2 + F_v \quad \text{with} \quad F_v = 2R\gamma' L \tan \delta K(2z_m - L) \quad (5.1)$$

$$H = 2R\gamma'K \left(z_m^2 - \frac{L^2}{2} \right) - F_h \quad \text{with} \quad F_h = \tau_h \pi R^2 = \sigma'_v \tan \phi' \pi R^2 \quad (5.2)$$

$$M = \frac{2R\gamma'K}{3} (L^3 - 2z_m^3) + F_h L + f(F_v) R \quad \text{with} \quad f(F_v) = \frac{(K_A + K_P)[(L - z_m)^2 + z_m^2]}{LK(2z_m - L)} F_v \quad (5.3)$$

At the base σ'_v includes the geostatic pressure of the soil plug and stresses transmitted by the vertical load V' , F_v is the resultant of vertical frictional forces along the skirt, K is the difference between the passive and active lateral earth pressure coefficients $K = K_P - K_A$, F_h is the resultant of horizontal frictional forces caused by the shear stresses at the base, where ϕ' is the soil-soil interface angle of friction. It is assumed that the resultant lateral earth pressures (and shear stresses) act along the skirt over a perimeter equal to the diameter of the caisson $2R$. From equation (5.2) the horizontal load is proportional to the square of the caisson skirt length, whereas from equation (5.3) the moment is proportional to the cube of the caisson skirt length. If frictional forces on the skirt are neglected and

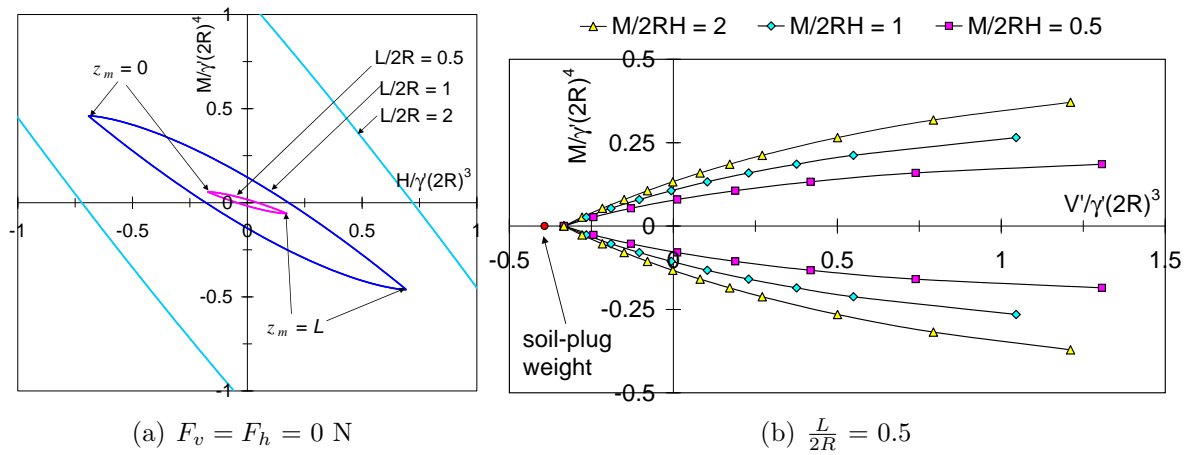


Figure 5.2: (a) Load envelopes in the normalised moment and horizontal load plane for three caisson aspect ratios $\frac{L}{2R}$, and (b) load envelopes in the normalised moment and vertical load plane for three load ratios $\frac{M}{2RH}$

equations (5.2) and (5.3) are merged z_m can be eliminated to obtain a load envelope, also referred to as interaction diagram, in which a state of loading on the envelope corresponds to a condition of limit equilibrium; outside the envelope static equilibrium is not possible. This load envelope can be expressed by:

$$\left[\frac{1}{2} - \frac{3(M - F_h L - f(F_v)2R)}{4R\gamma'KL^3} \right]^2 - \left[\frac{H + F_h}{2R\gamma'KL^2} + \frac{1}{2} \right]^3 = 0 \quad (5.4)$$

Three load envelopes were calculated using equation (5.4) and plotted in a normalised moment and horizontal load plane as shown in Figure 5.2(a). All the frictional forces have been neglected, so that the caisson response is independent of the vertical load V' and equation (5.4) holds for any value of V' . As a result of that an enormous increase in lateral load and moment load resistance with the caisson aspect ratio $\frac{L}{2R}$ is observed. Figure 5.2(a) illustrates that as the metacentre moves along the centre of the caisson from $z_m = 0$ to the bottom where $z_m = L$, similarly z_m moves from top to bottom of the load envelope. To include the effect of V' on the caisson resistance frictional forces were included in the calculations. The weight of the soil plug and V' are implicit in the calculation of σ'_v in F_h . Figure 5.2(b) shows the increase of the normalised moment load with the normalised vertical load. Therefore, the increase of V' triggers frictional forces that have a beneficial effect on the caisson moment resistance.

5.2 THEORETICAL FRAMEWORK

From the simple model presented above more sophisticated models can be constructed, assuming failure mechanisms plasticity models can be developed. A different approach recently taken is to derive constitutive models from thermodynamics. This approach is referred as hyperplasticity. In hyperplasticity the elements of the constitutive model arise from the thermodynamic laws instead of adding *ad hoc* elements to construct a model.

The present study is intended to provide experimental information to construct hyperplasticity models by means of determining for instance the yield surface and a flow rule. In order to obtain practical results hyperplastic models necessitate accurate values of the model parameters. Thus the determination of these parameters from laboratory tests was an important objective of this investigation. The advance in theoretical modelling necessitates of advances in physical modelling as well to make possible that a mathematical theory has useful applications in geotechnical engineering.

5.2.1 Elasticity

In hyperplasticity theory the elastic behaviour occurs inside and on the yield surface as assumed traditionally in plasticity. An elastic load-displacement relationship can be presented in a displacement controlled form as follows:

$$\begin{Bmatrix} V' \\ M \\ H \end{Bmatrix} = \begin{Bmatrix} K_V & 0 & 0 \\ 0 & K_M & K_{MH} \\ 0 & K_{MH} & K_H \end{Bmatrix} \begin{Bmatrix} w \\ \theta \\ u \end{Bmatrix} \quad (5.5)$$

where K_V , K_M , K_H and K_{MH} are the stiffness coefficients given by:

$$\begin{aligned} K_V &= 2GRk_v; & K_M &= GR^3k_m - 8GR^2dk_{mh} + 2GRd^2k_h; \\ K_H &= 2GRk_h; & K_{MH} &= 4GR^2k_{mh} - 2GRdk_h \end{aligned} \quad (5.6)$$

R is the footing radius, d is the distance between the assumed LRP and the point where the combined loads are applied as pointed out in Chapter 2 (d is zero if the loads are applied on the LRP); w , θ and u are the elastic vertical, rotational and horizontal displacements. If the LRP is located at the elastic metacentre, the matrix in (5.5) becomes diagonal ($K_{MH} = 0$) and coupling of moment and horizontal load does not occur (Bell, 1991; Houlsby, 2003). This is because the moment applied in the elastic metacentre causes pure elastic rotation of the caisson and *vice versa* the elastic horizontal load applied at the elastic metacentre causes only translation of the caisson. Numerical analyses carried out recently by Doherty and Deeks (2003) provide the dimensionless stiffness coefficients k_v , k_m , k_h and k_{mh} for assessing the elastic behaviour of skirted footings at different embedments. A Poisson' ratio of 0.2 was assumed, which is appropriate for a wide range of sands. Moreover, four caisson aspect ratios were considered, $\frac{L}{2R} = 0.25, 0.5, 1$ and 2 . Additionally, an α parameter that accounts for the type of shear modulus G distribution with depth as well as a rigid caisson were considered. Latterly, Doherty *et al.* (2005) extend the analysis to the case of flexible caissons, which can introduce significant reduction of the stiffness coefficients for low caisson thickness ratios $\frac{t}{2R}$ and even more if the soil is very stiff. Assuming a constant shear modulus G , the elastic displacement components

for the planar case can be derived as follows:

$$\begin{Bmatrix} w \\ \theta \\ u \end{Bmatrix} = \begin{Bmatrix} \frac{1}{K_V} & 0 & 0 \\ 0 & \frac{K_H}{D} & -\frac{K_{MH}}{D} \\ 0 & -\frac{K_{MH}}{D} & \frac{K_M}{D} \end{Bmatrix} \begin{Bmatrix} V' \\ M \\ H \end{Bmatrix} \quad (5.7)$$

where

$$D = K_M K_H - K_{MH}^2 \quad (5.8)$$

From the elastic stress wave propagation problem it is well known that the elastic shear modulus is related to the shear wave velocity v_s and the density ρ of the medium of propagation by $G = \rho v_s^2$. Measurements of shear wave velocities in sand (Hardin and Richart, 1963; Ishihara, 1993) have demonstrated that even under small strain amplitudes G has a non-linear dependency on the current level of stresses. Moreover, G was found to be a function of the specific volume v and grain angularity. These findings have led to the use of the following general expression of G assuming isotropic stress conditions (Schnaid, 1990; Houlsby *et al.*, 2005; Mitchell and Soga, 2005; Kelly *et al.* 2006):

$$\frac{G}{p_a} = A f(v) \left(\frac{\sigma'_v}{p_a} \right)^n \quad (5.9)$$

where σ'_v is a representative effective stress that represents the current stress level, p_a is the atmospheric pressure adopted as a reference stress, n and A are constants that can be related to grain angularity and $f(v)$ is a function of the specific volume v . Kelly *et al.* (2006) assume a mean effective stress as the effective vertical stress at a depth aR below the caisson as:

$$\sigma'_v = \frac{V'}{\pi R^2} + \gamma'(L + aR) \quad (5.10)$$

Equation (5.9) was used by Houlsby *et al.* (2005) in the derivation of a hyperelastic formulation. It was found that a pressure exponent $n = 0.5$ gives a good representation of shear strain contours when compared with experimental results. Values of the constant A and expressions of the function $f(v)$ for different soils can be found in Mitchell and Soga (2005).

5.2.2 Yield surface

Changes in the loading of a footing can cause the surrounding soil to yield. The combination of these loadings can be used to define a yield surface if plastic irreversible displacements of the footing occur. Mathematically, yield is expressed by means of yield surfaces. Yield surface formulations for flat footings date from the works by Butterfield and Ticof (1979) and Butterfield and Gottardi (1994). Subsequently, yield functions were proposed by Martin (1994) to construct Model B as well as Gottardi *et al.* (1999) and Cassidy (1999) to construct Model C.

Recently, an expression of the yield surface for caisson footings has been proposed by Nguyen-Sy and Houlsby (2005). This new formulation differs from the yield function used by Cassidy (1999) since it includes the possibility for tensile vertical loads. The yield function can be expressed in a reduced form as follows:

$$y = t^2 - \beta_{12}^2 (\nu_1 + t_o)^{2\beta_1} (1 - \nu_2)^{2\beta_2} = 0 \quad (5.11)$$

The horizontal and moment loads are expressed through t in the form of an eccentric ellipse, where for the planar case t is given by:

$$t = \sqrt{h^2 + m^2 - 2emh} \quad (5.12)$$

where e is the eccentricity of the ellipse. Considering the isotropic hardening case the dimensionless horizontal and moment loads are given by the following expressions:

$$h = \frac{a_H \chi_H + (1 - a_H)H}{h_o V_o} \quad m = \frac{a_M \chi_M + (1 - a_M)M}{2Rm_o V_o} \quad (5.13)$$

The dimensionless vertical loads ν_1 and ν_2 are given by:

$$\nu_1 = \frac{a_{V_1} \chi_V + (1 - a_{V_1})V'}{V_o} \quad \nu_2 = \frac{a_{V_2} \chi_V + (1 - a_{V_2})V'}{V_o} \quad (5.14)$$

χ_V , χ_M and χ_H are the dissipative generalised vertical, moment and horizontal loads, which are related to the dissipation function d by means of the partial derivative $\chi_i = \frac{\partial d}{\partial \alpha_i}$, where α_i are internal variables that represent irreversible behaviour and play the role of plastic displacements under certain conditions (Collins and Houlsby, 1997). It is worth mentioning that in kinematic hardening models for instance, $\sigma_{ij} - \chi_{ij}$ plays the role of a ‘back stress’, where the kinematics comes from the definition established with the internal variable α_{ij} for the generalised stress $\bar{\chi}_{ij}$ (Puzrin and Houlsby, 2001). On the other hand, σ_{ij} represents the true loads V' , M and H , and a_{V_1} , a_{V_2} , a_M and a_H are “association factors”. However, depending on their values they are able to describe non-associativity as well. a_{V_1} and β_1 deal with low vertical loads, whereas a_{V_2} and β_2 deal with the higher V values. The yield surface maximum dimension is defined by α (in a dimensionless $m - \nu$ or $h - \nu$ plane or at $V' = \alpha V_o$ in a $M - V'$ plane):

$$\alpha = \frac{\beta_1 - \beta_2 t_o}{\beta_1 + \beta_2} \quad (5.15)$$

Furthermore, according to equations (5.11) and (5.12) at the point α the intersection of the yield surface with the m and h axes are simultaneously maximums. These maximum intersection points are referred to as m_o and h_o . The tension parameter t_o is defined by:

$$t_o = \frac{|V_{tmax}|}{V_o} \quad (5.16)$$

where V_{tmax} is the load of maximum tension or also referred to as the pullout capacity. V_o represents a pre-consolidation load, commonly the largest load experienced by the caisson during installation. Both loads (V_{tmax}, V_o) correspond to the cases of pure vertical load and they define the size of the yield surface. The parameter β_{12} is given by:

$$\beta_{12} = \beta_1^{-\beta_1} \beta_2^{-\beta_2} \left(\frac{\beta_1 + \beta_2}{t_o + 1} \right)^{\beta_1 + \beta_2} \quad (5.17)$$

5.2.3 Flow rule

In hyperplasticity theory the dissipation function gives origin to the yield function and the flow rule (Collins and Houlsby, 1997). Therefore, there is no need to define a plastic potential function. This is a significant difference with the work hardening plasticity theory implemented for instance in Model B and Model C. The flow rule defines the direction of the irreversible displacement increments. The traditional division between elastic and plastic as reversible and irreversible is not necessarily true because of the dependency of stiffness on the internal variable in coupled materials. However, an associated flow rule in generalised load space holds always and plastic displacement increments are obtained according to:

$$\dot{\alpha}_i = \lambda \frac{\partial y}{\partial \chi_i} \quad (5.18)$$

where λ is a positive scalar multiplier that accounts for the magnitude of the velocity vectors. The α_i components are known generically as internal state variables and are related with irreversible processes, for this reason they are related with χ_i by means of the dissipation function.

The non-associated flow rule can be expressed in hyperplasticity as:

$$\begin{pmatrix} \dot{\alpha}_V \\ \dot{\alpha}_M \\ \dot{\alpha}_H \end{pmatrix} = \lambda \begin{pmatrix} \frac{\partial y}{\partial \chi_V} \\ \frac{\partial y}{\partial \chi_M} \\ \frac{\partial y}{\partial \chi_H} \end{pmatrix} \quad (5.19)$$

Once the derivatives are obtained in true load space the internal variable increments have the following expressions:

$$\dot{\alpha}_V = \lambda \frac{\partial y}{\partial \chi_V} = \lambda \frac{2\beta_{12}^2}{V_o} (\nu_1 + t_o)^{2\beta_1} (1 - \nu_2)^{2\beta_2} \left\{ \frac{\beta_2 a_{V_2}}{1 - \nu_2} - \frac{\beta_1 a_{V_1}}{\nu_1 + t_o} \right\} \quad (5.20)$$

$$\dot{\alpha}_M = \lambda \frac{\partial y}{\partial \chi_M} = \lambda \frac{2a_M}{2Rm_o V_o} (m - eh) \quad (5.21)$$

$$\dot{\alpha}_H = \lambda \frac{\partial y}{\partial \chi_H} = \lambda \frac{2a_H}{h_o V_o} (h - em) \quad (5.22)$$

Cassidy (1999) proposes the use of a deviatoric load $Q = V_o t$ to derive a radial displacement increment \dot{q} , that is for the consideration of the combined effect of the moment and horizontal load as well as the rotational and translational displacements, which in the incremental form results:

$$\dot{\alpha}_Q = \lambda \frac{\partial y}{\partial \chi_Q} = \frac{\lambda 2Q}{V_o^2} = \frac{\lambda}{\sqrt{1-e^2}} \sqrt{(h_o \dot{\alpha}_H)^2 + (m_o \dot{\alpha}_M)^2 + 2e(h_o \dot{\alpha}_H)(m_o \dot{\alpha}_M)} \quad (5.23)$$

The use of radial displacements can allow a more direct study of the flow rule, for instance comparing plastic vertical displacement increments with plastic radial displacement increments instead of separately with plastic rotational or plastic horizontal displacement increments.

5.3 EXPERIMENTAL RESULTS

5.3.1 Experimental procedures

The data was recorded as voltages and transformation to engineering units was carried out using relationships obtained from calibration of the instruments. The transformation was automatically implemented in the Visual Basic control program. Subsequently, the displacement raw data in engineering units - directly obtained from the tests, was corrected for the flexibility of the apparatus according to the rig flexibility matrix presented in Chapter 2. Next, loads and displacements were referred to the caisson LRP, which for both caissons tested was 10 mm below the base plate of the rig arm. Displacements w , $2R\theta$ and u were zeroed at the beginning of rotation or translation tests.

Tests were displacement controlled, the installation was done by pushing the caisson into the ground at a constant rate of $\dot{w} = 0.5$ mm/s until the underside of the lid made complete contact with the soil. Once installed, a constant rotational rate of $2R\dot{\theta} = 0.005$ mm/s or 0.01 mm/s was applied to the caisson (see Tables 5.1 and 5.3). For translational tests a constant horizontal velocity of $\dot{u} = 0.01$ mm/s was applied. In both cases a feedback control subroutine allowed for V' and $\frac{M}{2RH}$ to be kept constant during rotational or

translational tests. The reader should refer to Chapter 2 for details of the apparatus and its control, caisson dimensions and soil used as well as Chapter 4 for information of the installation tests carried out before the caissons were subjected to the combined loading tests.

5.3.2 Constant vertical load tests

To map out a yield surface in force space (V' , $\frac{M}{2R}$, H) and to determine the corresponding displacements (w , $2R\theta$, u) a series of combined loading tests under low vertical loads were performed. Information on each test is given in Tables 5.1 and 5.2 for caisson A and in Table 5.3 for caisson B. Plotted load-displacement and displacement-displacement curves from test FV1_1_1A to test FV65_11_1A are contained in Villalobos *et al.* (2003b).

Examples of test results using caisson A under a vertical load $V' = 0$ N, but different loading ratios are plotted in Figures 5.3(a), (b), (c) and (d). From plots (a) and (b) yield points were determined and from plots (c) and (d) velocity vectors were determined. The meaning as well as the methods to determine yield points and flow vectors will be explained in section §5.4.

It is possible to see a clear pattern in the curves shown in Figures 5.3(a) and 5.3(b). Initially, the curves are steep (steeper in the $H - u$ curve) which could be seen as linear within a very reduced range of displacement $2R\theta$ (0, 0.2) mm and u (0, 0.05) mm. The load-displacement response progresses after this narrow range of displacement reducing drastically the initial slope until a second ‘almost’ linear response is reached at a much wider range of displacements $2R\theta$ (0.8, 1.7) mm and u (0.3, 0.8) mm. Broadly speaking, the entire response can be interpreted as an initial stiff response predominantly elastic and a final much softer response where plastic displacements occur. There is evidently a transition response in between. It is clear from Figure 5.3(c) that the loading ratio $\frac{M}{2RH}$ does not affect the displacement curves $u - 2R\theta$. The same observation is not totally true for the displacement curves $w - 2R\theta$ shown in Figure 5.3(d), since the test FV26_3_1

Table 5.1: Summary of the tests undertaken using caisson A

Test	V' N	$\frac{M}{2RH}$	$\frac{K_{mi}}{\frac{N}{mm}}$	$\frac{K_{hi}}{\frac{N}{mm}}$	$\frac{M_y}{2R}$ N	H_y N	$2R\theta_y$ mm	u_y mm	$\frac{K_{mf}}{\frac{N}{mm}}$	$\frac{K_{hf}}{\frac{N}{mm}}$	$\frac{\delta u^P}{2R\delta\theta^P}$	$\frac{\delta w^P}{2R\delta\theta^P}$
FV130.24.2	-48	0.30	42	181	5.6	18.2	0.51	0.29	2	15	0.44	-1.21
FV84.14.2	-29	0.28	198	460	11.9	40.3	0.35	0.26	3	20	0.51	-0.55
FV85.15.2	4	0.28	283	597	19.1	64.8	0.50	0.35	2	16	0.52	-0.54
FV86.16.1	2	0.29	102	581	14.3	48.6	0.57	0.35	2	10	0.53	-0.50
FV87.16.1	23	0.28	142	631	18.2	60.4	0.60	0.32	2	13	0.51	-0.45
FV88.16.2	51	0.28	306	745	23.6	78.7	0.63	0.52	2	12	0.53	-0.40
FV89.16.1	100	0.28	756	1326	29.0	94.4	0.56	0.48	2	13	0.57	-0.27
FV82.14.2	-29	0.54	235	1088	16.4	29.6	0.45	0.20	4	16	0.46	-0.53
FV26.3.2†	0	0.53	40	534	18.4	33.6	0.60	0.25	4	15	0.46	-0.57
FV35.5.2†	20	0.53	40	350	25.6	45.1	0.78	0.31	3	13	0.49	-0.44
FV34.5.2†	52	0.54	82	680	33.1	58.4	0.81	0.30	3	13	0.49	-0.39
FV33.4.1	101	0.54	204	774	38.8	73.4	0.60	0.34	3	11	0.49	-0.24
FV30.4.2†	99	0.53	151	1269	43.3	75.6	0.69	0.26	4	18	0.50	-0.32
FV99.19.3	-54	1.03	34	50	6.1	6.1	0.54	0.21	3	6	0.41	-0.60
FV60.10.2	-39	1.03	63	109	11.9	10.9	0.29	0.10	10	22	0.44	-0.51
FV61.10.2	-28	1.04	215	246	18.3	17.6	0.47	0.19	5	12	0.40	-0.49
FV27.3.2†	1	1.05	56	298	25.2	23.1	0.74	0.25	4	9	0.44	-0.44
FV57.10.2	21	1.05	218	266	32.5	30.1	0.37	0.18	10	25	0.45	-0.41
FV1.1.2†	51	1.04	628	287	39.1	37.4	0.56	0.30	4	10	0.44	-0.28
FV31.4.2†	103	1.04	166	461	51.9	48.8	0.64	0.32	5	12	0.47	-0.25
FV81.14.2	-29	2.02	122	73	22.0	10.8	0.54	0.25	6	8	0.42	-0.48
FV15.2.2†	-1	2.06	67	130	26.5	12.0	0.65	0.20	5	8	0.44	-0.42
FV36.5.2†	20	2.05	79	170	35.6	17.0	0.70	0.22	6	7	0.41	-0.38
FV37.5.2†	49	2.05	118	170	45.3	22.3	0.64	0.27	7	7	0.43	-0.30
FV29.3.2†	101	2.06	320	151	54.7	27.6	0.60	0.32	7	8	0.40	-0.17
FV32.4.2†	99	2.05	200	170	54.9	26.4	0.64	0.26	7	9	0.41	-0.09
FV100.19.3	-44	-1.93	195	-158	11.5	-6.0	0.29	0.15	5	-7	0.43	-0.50
FV92.17.3	-29	-1.93	221	-150	33.2	-16.3	0.48	0.20	5	-9	0.41	-0.44
FV107.21.2	0	-1.91	145	-228	36.0	-16.7	0.64	0.14	9	-20	0.30	-0.30
FV90.17.2	22	-1.93	193	-180	45.3	-23.9	0.56	0.21	11	-18	0.32	-0.25
FV92.17.2	50	-1.92	165	-181	56.4	-29.5	0.65	0.23	12	-20	0.32	-0.15
FV94.18.2	101	-1.93	229	-175	61.3	-33.0	0.44	0.22	16	-24	0.31	0.04
FV132.24.2	-48	-0.94	114	-232	16.8	-19.3	0.37	0.16	12	-38	0.31	-0.38
FV91.17.3	-29	-0.96	434	-224	42.2	-48.1	0.44	0.29	11	-31	0.34	-0.36
FV108.21.2	2	-0.95	188	-329	40.2	-45.9	0.44	0.17	21	-95	0.23	-0.20
FV91.17.2	20	-0.95	131	-391	51.2	-56.3	0.55	0.17	22	-103	0.22	-0.14
FV99.19.2	21	-0.96	343	-250	46.0	-55.0	0.42	0.24	18	-90	0.23	-0.21
FV93.17.2	50	-0.95	154	-427	68.2	-71.0	0.76	0.20	17	-97	0.22	-0.02
FV95.18.2	99	-0.96	185	-650	68.8	-85.3	0.62	0.18	23	-125	0.15	0.06
FV94.18.3	-48	-0.47	58	-409	20.7	-34.3	0.45	0.02	21	190	-0.26	-0.31
FV109.21.2	0	-0.47	280	-499	61.0	-124.3	0.48	0.11	28	158	-0.46	-0.18
FV97.18.2	0	-0.47	129	-1111	59.3	-130.0	0.70	0.00	26	133	-0.45	-0.45
FV118.22.2	21	-0.47	206	-740	60.9	-148.8	0.47	0.09	42	184	-0.42	-0.07
FV123.23.2	50	-0.46	278	-571	79.4	-164.0	0.67	0.01	26	168	-0.43	-0.04
FV100.19.2	50	-0.47	127	-909	73.3	-152.0	0.78	0.04	26	133	-0.40	0.10
FV101.19.2	101	-0.46	135	-606	80.5	-172.0	0.76	0.08	29	125	-0.36	0.18
FV134.24.2	-47	-0.23	-304	-6061	12.2	-52.3	-0.26	-0.14	-7	53	0.64	0.76
FV113.22.2	0	-0.22	284	-872	28.0	-119.8	0.06	-0.02	-72	100	3.18	1.69
FV121.23.2	51	-0.22	105	-827	31.0	-145.7	0.24	0.24	286	149	-3.25	-0.48
FV111.22.2	1	-0.07	250	-2222	5.8	-83.5	-0.17	-0.11	-2	50	0.66	0.56
FV116.22.2	22	-0.07	-285	-2500	7.8	-108.0	-0.19	-0.11	-3	57	0.84	0.52
FV125.23.2	53	-0.07	48	-1538	8.8	-126.5	-0.03	-0.09	-5	71	0.96	0.47

† $2R\theta = 0.005$ mm/s

Table 5.2: Summary of the tests undertaken using caisson A

Test	$\frac{M_i}{2R}$ N	H_i N	$2R\theta_i$ mm	u_i mm	$\frac{M_m}{2R}$ N	H_m N	$2R\theta_m$ mm	u_m mm	$\frac{M_f}{2R}$ N	H_f N	$2R\theta_f$ mm	u_f mm
FV130.24.2	3	8	0.12	0.05	7	22	0.98	0.38	9	29	1.79	0.81
FV84.14.2	7	23	0.05	0.05	14	47	0.70	0.45	16	55	1.63	0.87
FV85.15.2	10	27	0.04	0.05	21	71	0.84	0.52	23	78	1.68	0.93
FV86.16.2	7	22	0.07	0.04	16	52	0.87	0.49	17	57	1.81	0.96
FV87.16.2	11	37	0.09	0.06	20	65	0.98	0.50	21	70	1.73	0.96
FV88.16.2	14	46	0.05	0.06	25	83	0.83	0.55	26	89	1.72	1.02
FV89.16.2	18	50	0.03	0.04	31	103	0.91	0.59	32	110	1.72	1.14
FV82.14.2	8	10	0.04	0.01	20	36	0.80	0.43	23	42	1.70	0.78
FV26.3.2†	12	15	0.27	0.03	21	38	0.74	0.40	24	44	1.81	0.77
FV35.5.2†	20	33	0.40	0.08	26	51	0.84	0.53	29	54	1.81	0.82
FV34.5.2†	24	36	0.30	0.06	35	62	1.09	0.40	38	68	1.80	0.86
FV33.4.2†	25	46	0.13	0.06	40	77	0.80	0.50	44	82	1.87	0.91
FV30.4.2†	28	35	0.20	0.03	45	81	0.93	0.40	48	90	1.73	0.86
FV99.19.3	2	2	0.08	0.05	8	8	0.89	0.41	10	10	1.75	0.73
FV60.10.2	9	8	0.15	0.08	14	12	0.34	0.16	18	17	0.81	0.36
FV61.10.2	8	8	0.03	0.03	22	21	0.83	0.38	28	25	1.84	0.71
FV27.3.2†	18	11	0.32	0.04	27	26	1.07	0.44	30	29	1.71	0.73
FV57.10.2	20	20	0.12	0.09	35	33	0.44	0.21	39	37	0.82	0.42
FV1.1.2†	14	23	0.03	0.08	42	40	0.86	0.39	45	43	1.64	0.78
FV31.4.2†	26	26	0.16	0.06	55	52	1.00	0.40	59	56	1.65	0.76
FV81.14.2	9	5	0.08	0.06	27	13	1.07	0.43	32	16	1.78	0.75
FV15.2.2†	19	6	0.27	0.05	30	14	0.99	0.31	33	16	1.63	0.70
FV36.5.2†	25	9	0.33	0.06	39	19	0.10	0.37	43	21	1.74	0.67
FV37.5.2†	33	13	0.30	0.08	50	24	1.00	0.40	54	26	1.65	0.70
FV29.3.2†	28	16	0.10	0.11	60	30	1.00	0.45	65	32	1.70	0.73
FV32.4.2†	27	16	0.14	0.10	60	28	1.12	0.36	64	31	1.73	0.74
FV100.19.3	5	-3	0.02	0.02	15	-6	0.60	0.20	20	-10	1.72	0.75
FV92.17.3	19	-6	0.10	0.04	36	-18	0.70	0.30	41	-21	1.67	0.68
FV107.21.2	17	-10	0.13	0.04	44	-19	1.19	0.19	50	-25	1.73	0.53
FV90.17.2	20	-14	0.11	0.07	55	-27	1.05	0.31	61	-32	1.72	0.56
FV92.17.2	35	-21	0.23	0.12	64	-33	0.97	0.35	73	-37	1.73	0.58
FV94.18.2	45	-27	0.20	0.16	67	-36	0.66	0.30	81	-42	1.59	0.55
FV132.24.2	5	-7	0.05	0.03	25	-28	0.85	0.32	36	-37	1.74	0.56
FV91.17.3	12	-34	0.03	0.15	48	-53	0.70	0.40	58	-60	1.60	0.61
FV108.21.2	16	-31	0.10	0.10	52	-55	0.80	0.24	69	-71	1.65	0.42
FV91.17.2	33	-44	0.24	0.11	63	-66	0.93	0.24	78	-82	1.61	0.38
FV99.19.2	15	-51	0.05	0.20	58	-59	0.85	0.27	73	-75	1.60	0.48
FV93.17.2	30	-57	0.20	0.13	80	-80	1.15	0.26	89	-94	1.69	0.40
FV95.18.2	32	-82	0.16	0.16	82	-88	0.96	0.19	96	-100	1.62	0.29
FV94.18.3	10	-14	0.18	0.03	31	-64	0.84	-0.08	49	-101	1.67	-0.30
FV109.21.2	26	-55	0.09	0.11	76	-156	0.73	0.05	88	-189	1.18	-0.15
FV97.18.2	24	-54	0.20	0.05	75	-160	1.04	-0.10	91	-191	1.66	-0.36
FV118.22.2	25	-55	0.13	0.07	80	-180	0.76	0.03	99	-208	1.18	-0.15
FV123.23.2	17	-57	0.08	0.10	100	-206	1.08	0.04	109	-239	1.48	-0.19
FV100.19.2	40	-80	0.30	0.08	85	-185	1.00	-0.07	101	-214	1.66	-0.32
FV101.19.2	49	-44	0.37	0.07	90	-209	0.94	-0.21	111	-236	1.66	0.24
FV134.24.2	6	-21	-0.02	0.00	16	-73	-0.57	-0.38	19	-86	-1.05	-0.65
FV113.22.2	22	-32	0.08	0.35	32	-154	0.05	-0.27	37	-170	-0.04	-0.40
FV121.23.2	31	-39	0.24	0.05	31	-185	0.24	-0.09	41	-209	0.27	-0.27
FV111.22.2	3	-40	0.00	-0.02	7	-97	-0.35	-0.09	8	-114	-0.86	-0.60
FV116.22.2	6	-43	-0.03	0.01	9	-124	-0.35	-0.24	10	-140	-0.70	-0.56
FV125.23.2	4	-43	0.03	0.03	10	-148	0.11	-0.22	11	-166	-0.36	-0.48

† $2R\dot{\theta} = 0.005$ mm/s

Table 5.3: Summary of the tests undertaken using caisson B

Test	V' N	$\frac{M}{2RH}$	K_{mi} $\frac{N}{mm}$	K_{hi} $\frac{N}{mm}$	$\frac{M_y}{2R}$ N	H_y N	$2R\theta_y$ mm	u_y mm	K_{mf} $\frac{N}{mm}$	K_{hf} $\frac{N}{mm}$	$\frac{\delta u^p}{2R\delta\theta^p}$	$\frac{\delta w^p}{2R\delta\theta^p}$
FV131.24.2	-49	0.30	65	326	8.3	21.6	0.45	0.35	3	13	0.86	-0.55
FV42.6.2†	0	0.54	289	250	17.2	32.5	0.18	0.26	14	24	0.93	-0.40
FV45.7.2	0	0.57	320	250	21.9	38.8	0.22	0.29	13	24	0.92	-0.34
FV38.6.2†	21	0.54	315	350	22.4	40.3	0.23	0.27	11	21	0.92	-0.28
FV46.7.2	21	0.57	763	410	25.2	44.1	0.17	0.25	16	29	0.95	-0.32
FV47.7.2	50	0.57	756	501	29.1	51.3	0.18	0.25	16	28	1.01	-0.21
FV48.7.2	101	0.56	1256	426	34.4	59.6	0.17	0.27	17	30	1.04	-0.06
FV102.20.3	-57	1.05	256	176	24.3	20.9	0.44	0.35	8	10	0.86	-0.61
FV40.6.2†	1	1.06	170	250	24.8	24.5	0.24	0.20	21	23	0.84	-0.27
FV49.8.2	1	1.07	850	651	31.9	28.0	0.18	0.21	23	20	1.18	-0.36
FV41.6.2†	21	1.06	543	352	27.6	25.8	0.16	0.20	22	24	0.76	-0.22
FV50.8.2	21	1.02	431	151	35.4	33.8	0.20	0.30	22	22	0.93	-0.28
FV51.8.2	52	1.07	1352	190	40.7	39.0	0.18	0.30	25	25	0.98	-0.17
FV52.8.2	101	1.07	2002	241	45.1	42.7	0.15	0.30	24	22	0.99	-0.04
FV129.24.2	-49	2.08	168	169	24.5	10.4	0.45	0.32	10	6	0.81	-0.46
FV53.9.2	1	2.08	756	136	35.9	16.3	0.16	0.20	30	18	0.90	-0.30
FV54.9.2	19	2.08	896	236	43.9	19.1	0.20	0.20	30	18	0.97	-0.25
FV55.9.2	51	2.08	1000	351	42.5	18.6	0.15	0.16	30	18	0.92	-0.11
FV56.9.2	103	2.07	1100	166	52.9	24.2	0.17	0.26	31	18	0.94	0.01
FV124.23.2	21	-0.70	756	-333	102.0	-140.0	0.21	-0.26	115	222	-0.62	-0.25
FV135.24.2	-46	-0.46	1215	-1111	30.0	-65.0	-0.08	-0.08	-26	45	1.21	0.83
FV117.22.2	2	-0.46	-4000	-644	48.6	-98.0	-0.05	0.01	-81	92	1.91	0.80
FV122.23.2	20	-0.44	3333	-649	55.0	-112.0	-0.04	0.03	-66	81	1.88	0.80
FV133.24.2	-46	-0.20	-100	1326	7.3	-34.1	-0.16	-0.16	-8	33	0.98	0.73
FV112.22.2	1	-0.21	-356	-1538	14.6	-68.0	-0.14	-0.13	-10	38	1.24	0.53
FV126.23.2	22	-0.21	-1200	-1326	16.6	-80.0	-0.12	-0.10	-12	45	1.24	0.50
FV110.22.2	2	-0.06	-90	2600	3.4	-63.7	-0.19	-0.20	-1	28	1.03	0.43
FV120.23.2	22	-0.05	-35	14500	4.1	-71.1	-0.27	-0.21	-1	26	1.15	0.45

$$\dagger 2R\dot{\theta} = 0.005 \text{ mm/s}$$

separates from the other test curves after $2R\theta > 0.6$ mm of rotation has occurred.

Figures 5.4(a), (b), (c) and (d) show examples of test results using caisson B and a loading ratio of $\frac{M}{2RH} = 1$ over a range of vertical loads. Although caisson B was rotated half of the total rotation applied to caisson A (except test FV102.20.3), a similar type of load-displacement response is observed in Figures 5.4(a) and (b). It is worth noting in these figures the increase of moment load capacity as well as lateral load capacity with the increase of vertical load. It is remarkable that the caisson rotated under very high tension load ($V' = -57$ N) still has a significant moment and lateral load resistance. In the displacement curves shown in Figure 5.4(c) the magnitudes of u and $2R\theta$ are similar, contrarily to the displacement curves shown in Figure 5.3(c), where the magnitude of u was around half of $2R\theta$. Furthermore, Figure 5.4(d) shows that there is a reduction in

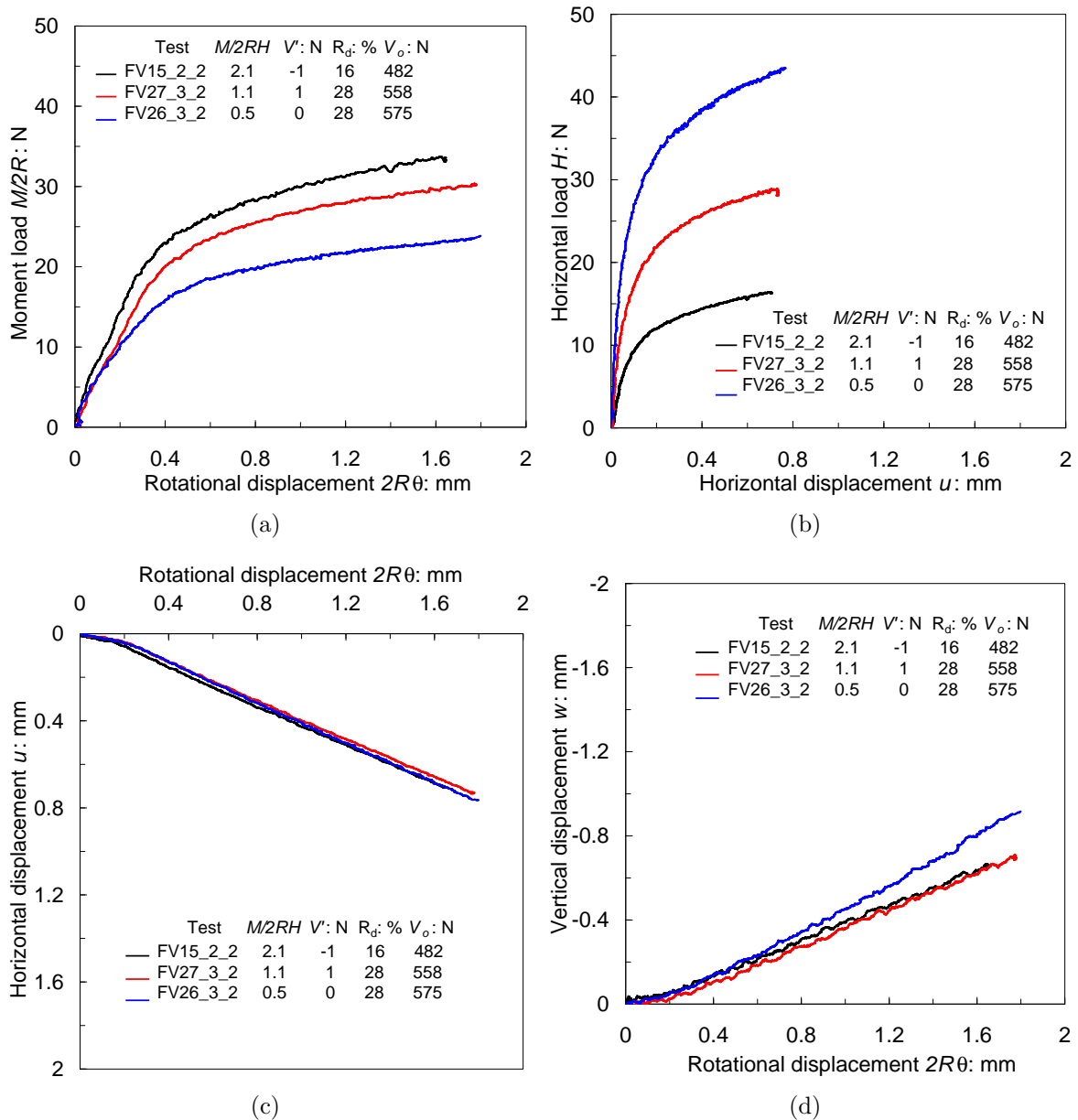


Figure 5.3: Rotational tests using caisson A under constant vertical load $V' = 0$ N at different ratios of $\frac{M}{2RH}$

the caisson uplift when the vertical load increases. During the rotation under tension the caisson uplift was the highest, as would be expected.

Another group of tests using caisson A under zero vertical load is shown in Figures 5.5(a) and 5.5(b), but for negative loading ratios $\frac{M}{2RH}$. Tests with $\frac{M}{2RH} = -1.9$ and -1 were conducted as before, *i.e.* under rotational displacement control. As a result of the large increase in the magnitude of horizontal displacements and hence horizontal loads, rotational displacement controlled tests were not well suited for the range of loading ratios of

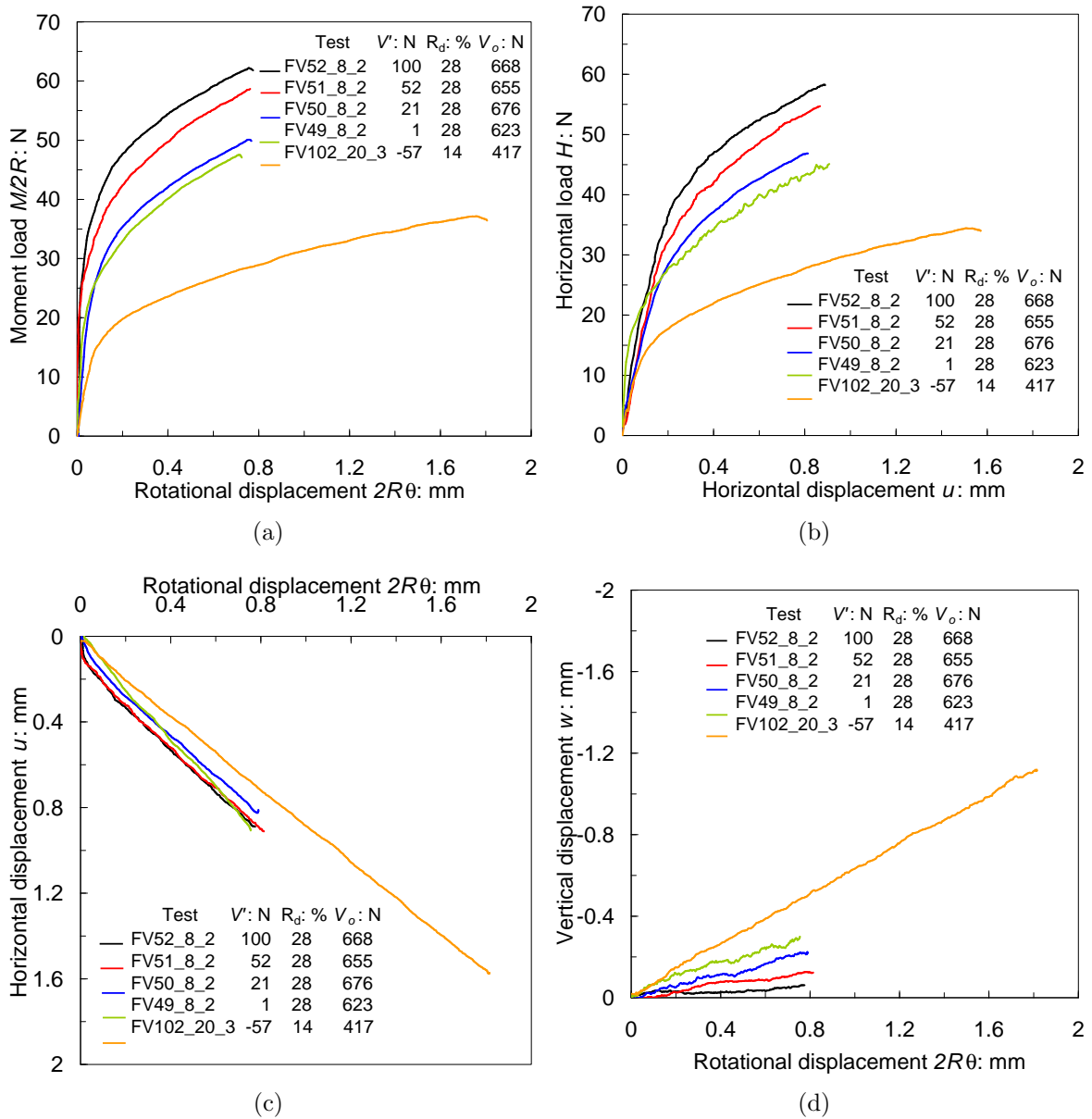


Figure 5.4: Rotational tests using caisson B under a constant load ratio of $\frac{M}{2RH} = 1$ at different vertical loads V'

$0 > \frac{M}{2RH} > -1$. This was because this type of test put the caisson in a loading condition close to pure sliding. For these tests the horizontal displacement was controlled instead of the rotational displacement. The response pattern followed by the caisson in the tests with negative $\frac{M}{2RH}$ can be interpreted as before, but for the test under $\frac{M}{2RH} = -0.5$ the pronounced initial stiff response and final softer response are harder to delimit. Changes in the displacement directions from positive to negative are observed in three tests. Figure 5.5(c) shows how the displacement curves $u - 2R\theta$ vary anticlockwise as the loading ratio $\frac{M}{2RH}$ changes from -1.9 to -0.1, giving evidence of a great displacement ratio gradient. The displacement ratio gradient is the variation of a displacement with respect to the variation

of another displacement, for example $\frac{\delta u}{2R\delta\theta}$. This gradient will be considered in subsequent sections to study the flow rule using the values of plastic displacement summarized in Tables 5.1 and 5.3. Under $\frac{M}{2RH} = -0.2$ the caisson rotates less than 0.1 mm, returning at the end at the initial position. Notwithstanding that the tests with $\frac{M}{2RH} = -0.2$ and -0.1 switched the rotation direction, Figure 5.5(d) shows that they have similar magnitudes of w as the other tests that did not switch rotation direction.

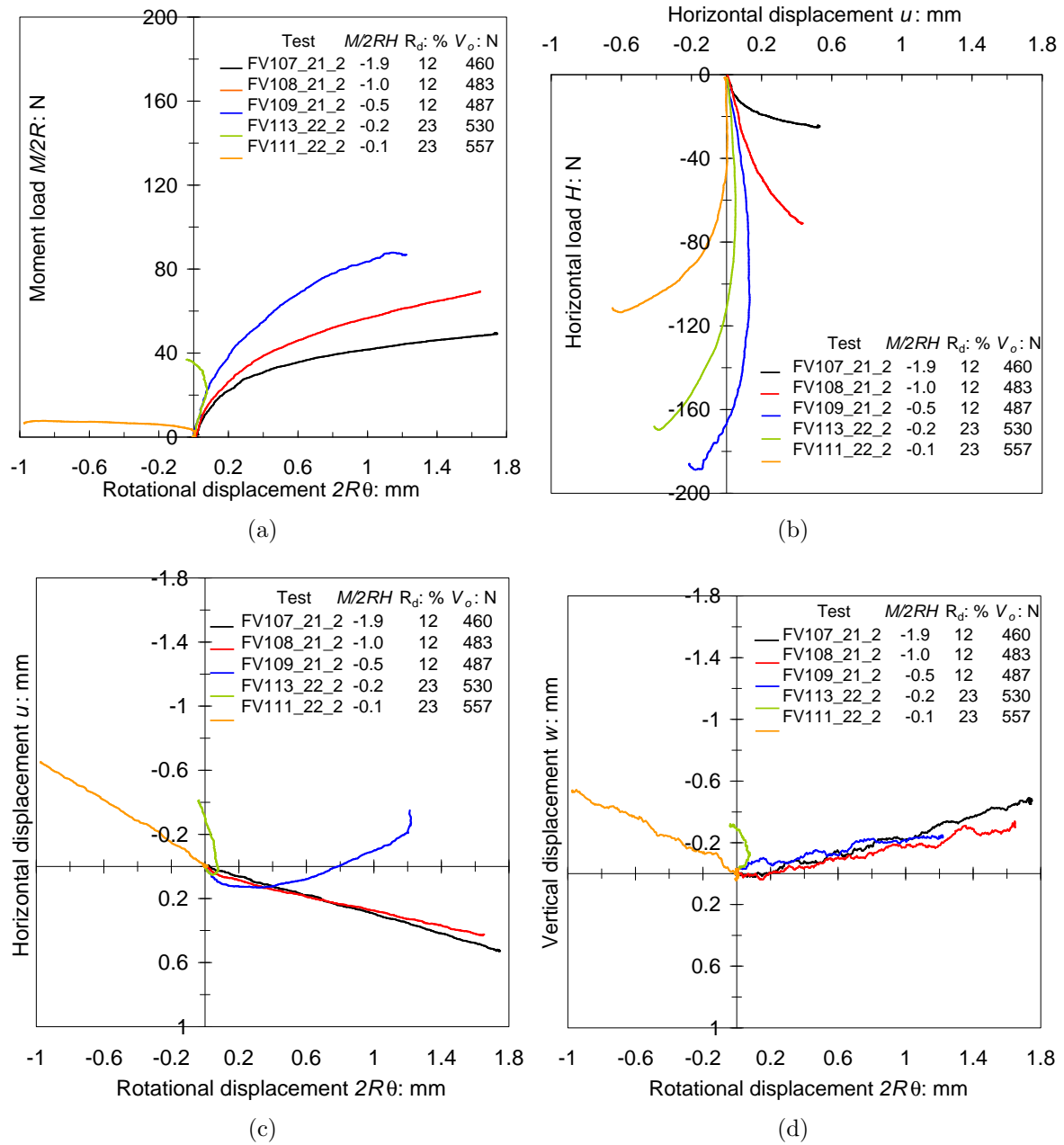


Figure 5.5: Rotational and translational tests using caisson A under a constant vertical load $V' = 0$ N at different ratios $\frac{M}{2RH}$

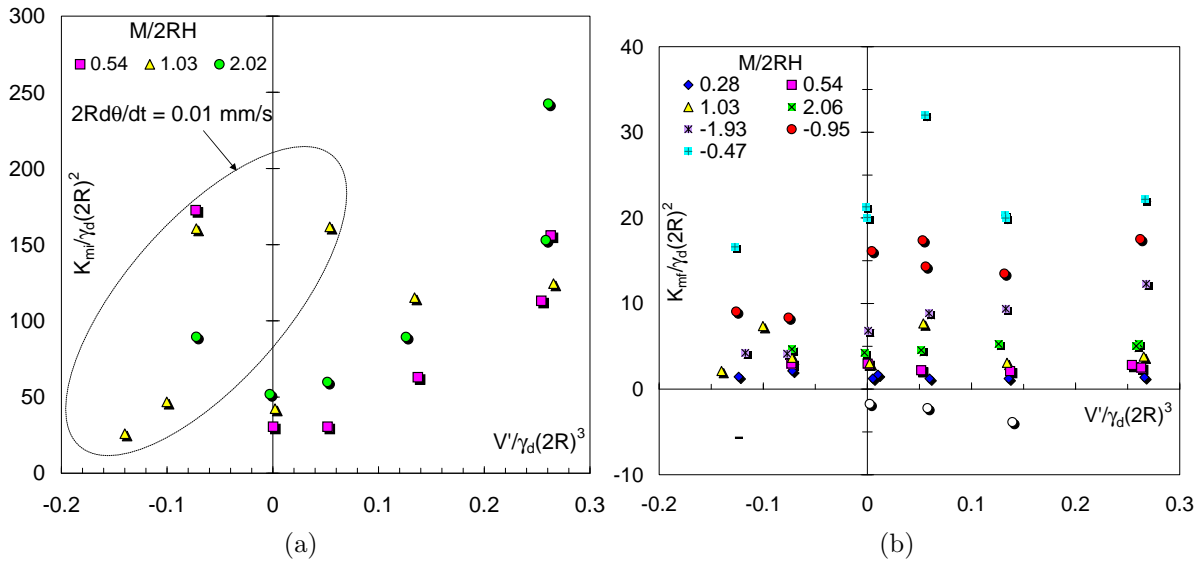


Figure 5.6: (a) Initial moment stiffness K_{mi} for caisson A. The encircled left side of the plot corresponds to tests under $2R\dot{\theta} = 0.01$ mm/s, the other points correspond to $2R\dot{\theta} = 0.005$ mm/s, and (b) final moment stiffness K_{mf} for caisson A

The difference in the rotational velocity $2R\dot{\theta}$ applied to the caisson has an effect on the initial load-displacement response. The initial slopes of the $\frac{M}{2R} - 2R\theta$ and $H - u$ curves changed according to $2R\dot{\theta}$ (see Tables 5.1 and 5.3). Figure 5.6(a) shows that the normalised foundation initial moment stiffness K_{mi} increased when the rotational velocity changed from $2R\dot{\theta} = 0.005$ mm/s to 0.01 mm/s. However, it will become apparent later that this rate difference does not influence noticeably the determination of yield points and the yield surface. On the other hand, Figure 5.6(b) shows that there is little influence on the final moment stiffness of the foundation K_{mf} either from the rotational velocity or from the vertical load. However, an influence of the loading ratio can be seen.

5.4 ANALYSES OF THE RESULTS

5.4.1 Yield surface

Yield is a gradual process where irreversible deformation occurs. Because soil is not a continuum but a particulate material this is a broad definition. It has been found that irreversible deformations start to develop at early stages where for instance in sandy soils shear strains are as small as 0.002% (Chaudhary and Kuwano, 2003; Mitchell and Soga, 2005). In practical terms, yield can be understood as the transition from a load-

displacement state with small magnitudes of irreversible deformation to another state with large magnitudes of irreversible deformation. Although the latter definition narrows the range for a definition of yield, it is not sufficient to link yield with a unique loading state.

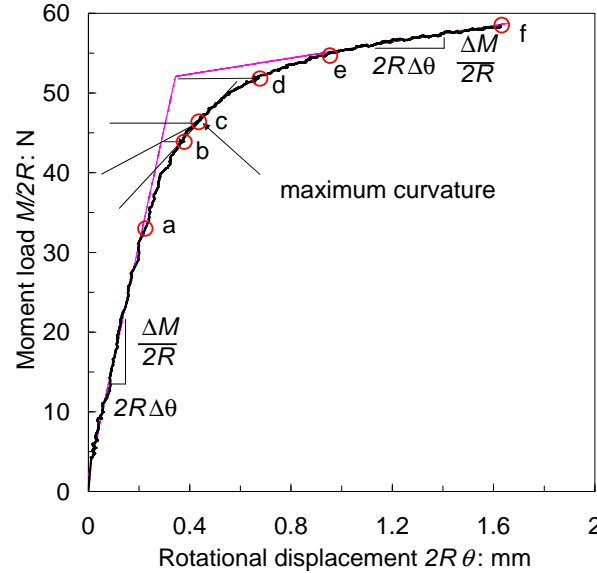


Figure 5.7: Five criteria for the determination of the yield point (test FV31.4.2A)

In order to visualise a yield point determination Figure 5.7 shows an example of a $\frac{M}{2R} - 2R\theta$ response with circles indicating the gradual progress of yield according to five criteria. The first criterion (a) establishes that yield occurs at the end of a linear response, *i.e.* when the ratio between the moment load variation $\frac{\Delta M}{2R}$ and the rotational displacement variation $2R\Delta\theta$ is not longer constant and commences to reduce. The second criterion (b) corresponds to the procedure used in consolidation analysis to determine the preload of a soil sample in oedometer tests (Terzaghi, 1943; Poorooshasb *et al.*, 1967). The third criterion (c) defines yield as the point of maximum curvature on the $\frac{M}{2R} - 2R\theta$ curve (McDowell, 2002). The fourth criterion (d) determines yield as the intersection of the two straight lines that fit the experimental curve at the beginning and at the end of the curve (Graham *et al.*, 1982). To obtain the displacement associated to the yield load the intersection point must be translated to the curve as illustrated in Figure 5.7. The fifth criterion (e) is the inverse of the first criterion in the sense that yield occurs when a linear response commences, resulting in a constant ratio between $\frac{\Delta M}{2R}$ and $2R\Delta\theta$, and lowest during the loading process. Finally the sixth circle (f) is not a criterion, but the final

loading state once the test has finished.

Values of yield points obtained according to criteria (a), (d), (e) and the final circle (f) are summarised in Tables 5.1 and 5.2. Figures 5.8(a), (b), (c), (d), (e) and (f) show these yield points plotted in a normalised plane of moment load *versus* normalised horizontal load. Criteria (b) and (c) are less reliable since they involve determination by eye or by a ‘best’ curve fit, leading to a scale dependency. Observing these yield point plots for each vertical load V a pattern of progression is visible from state (a) to state (f), showing a yield surface expansion. In addition, this expansion in each group of yield points shows that the initial state (a) separates clearly from states (d), (e) and (f) which are relatively close to each other in the first and third quadrants; they are further apart in the second and fourth quadrants (when $\frac{M}{2R}$ and H have opposite sign). A comparison between Figure 5.8(c) and the plot for $\frac{L}{2R} = 0.5$ in Figure 5.2(a) shows similarities in shape and inclination, considering the absence of friction assumed in the calculations ($F_h = 0$), which reduces the size and squats the yield surface.

Figures 5.9(a), (b), (c) and (d) show the evolution of yield points with V' and $\frac{M}{2RH}$. These plots confirm that criterion (d) is more suitable to interpret yield due to irreversible plastic displacements. This criterion proved to be consistent and repeatable in determining yield points as pointed out in an earlier study by Byrne *et al.* (2003). Less favourable cases exist for the range $-2 \leq \frac{M}{2RH} \leq -0.2$ in the second and fourth quadrants where criterion (d) gives a lower boundary of the yield surface, but (d) still is close to the medium and final states than to the initial state.

A rational and repeatable procedure that minimises personal influences was implemented following Graham *et al.* (1982) to determine yield points using criterion (d). This method was used due to its simplicity and the consistency of the results. The least square error method was used to fit the data employing a bilinear function with a slope discontinuity at $x = c$ where x is the displacement. For a planar analysis x can represent w (as used in Chapter 3 for the determination of yield points in vertical loading tests of caissons in

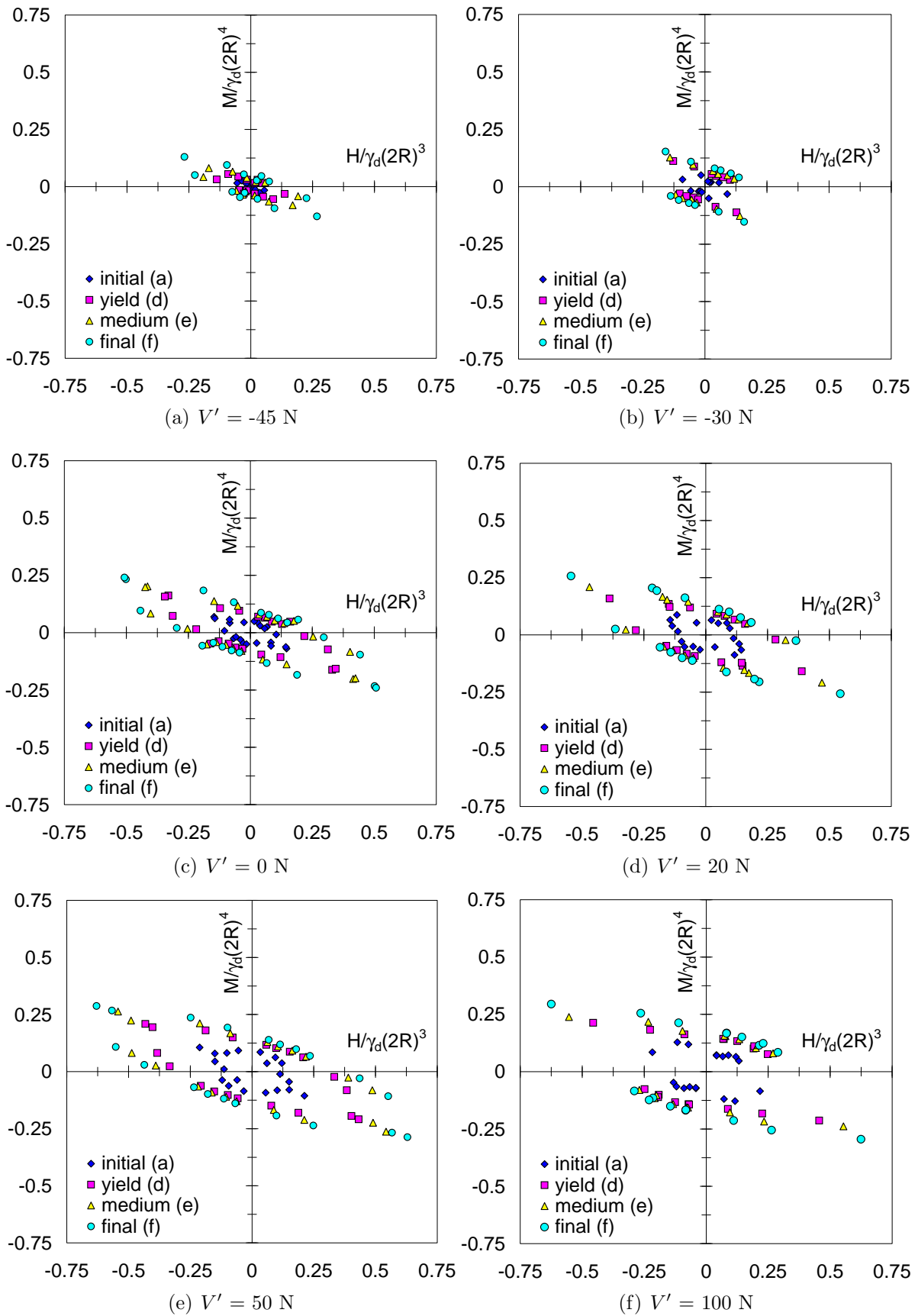


Figure 5.8: Variation of yield points along loading for caisson A in the plane of moment load and horizontal load (V' is an average nominal value, for exact values of V' see Table 5.1)

loose sand), $2R\theta$, and u . The displacement x at c does not have a physical meaning; it is used only to find the load y at yield.

$$y = y_o + ax \quad \text{for } x < c; \quad y = y_o + ax + (b - a)[x - c] \quad \text{for } x \geq c \quad (5.24)$$

Where y_o is the initial load at $x = 0$, a and b are the slope of the initial and final linear sections equal to $\frac{\Delta M}{(2R)^2 \Delta \theta}$ in a moment load-rotational displacement curve and $\frac{\Delta H}{\Delta u}$ in a lateral load-translational displacement curve. The values of these slopes are summarised in Table 5.1 as K_{mi} and K_{hi} for the initial linear section and K_{mf} and K_{hf} for the final

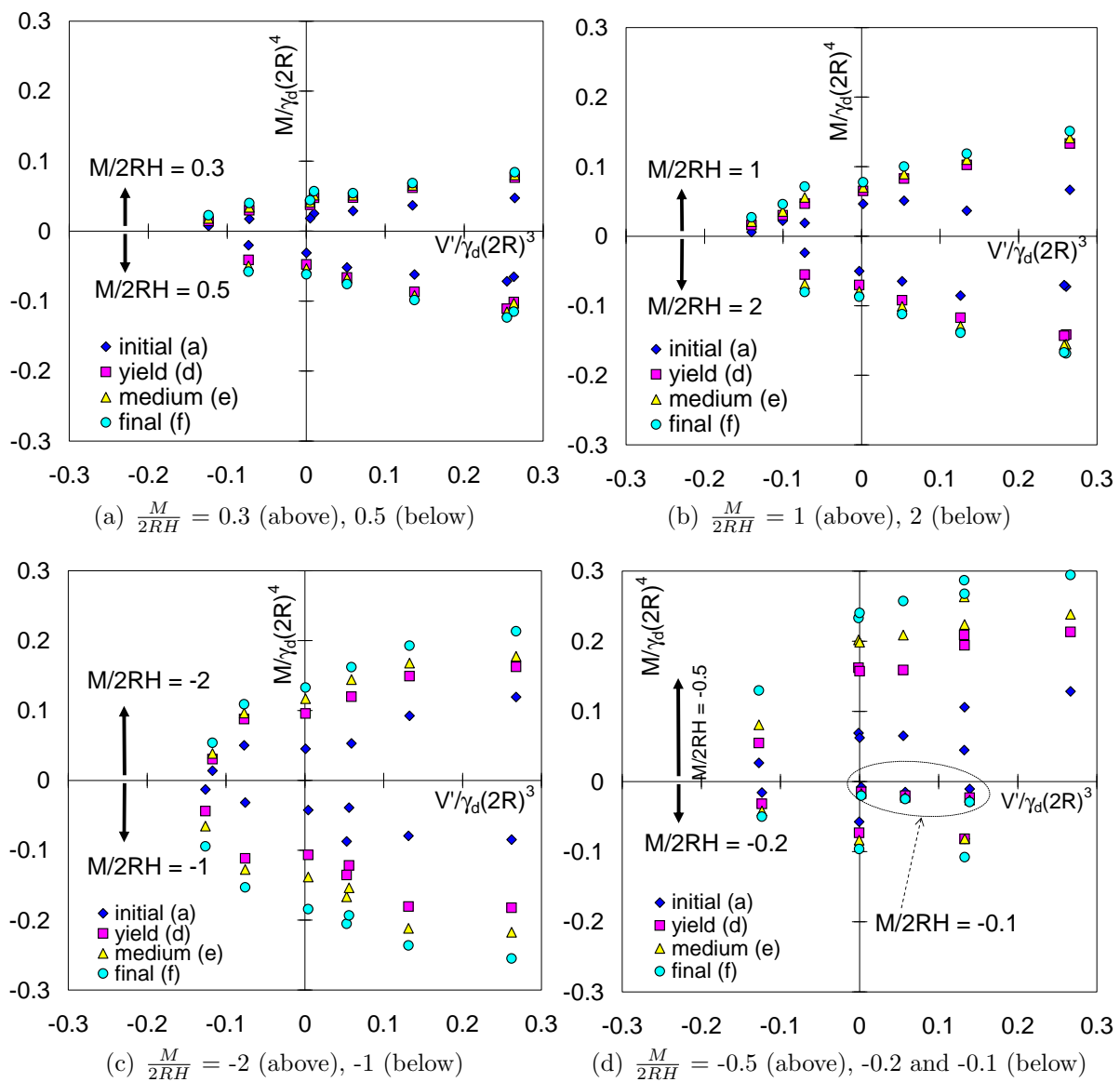


Figure 5.9: Variation of yield points along loading for caisson A in the plane of moment load and vertical load ($\frac{M}{2RH}$ is an average nominal value, for exact values of $\frac{M}{2RH}$ see Table 5.1)

linear section. In general the initial foundation stiffness is much larger than the final stiffness and it increases with the soil density and the vertical load. This is not the case for the final stiffness, where there is no influence of the vertical load, but the loading ratio $\frac{M}{2RH}$ influences the final response instead as shown in Figure 5.6(b).

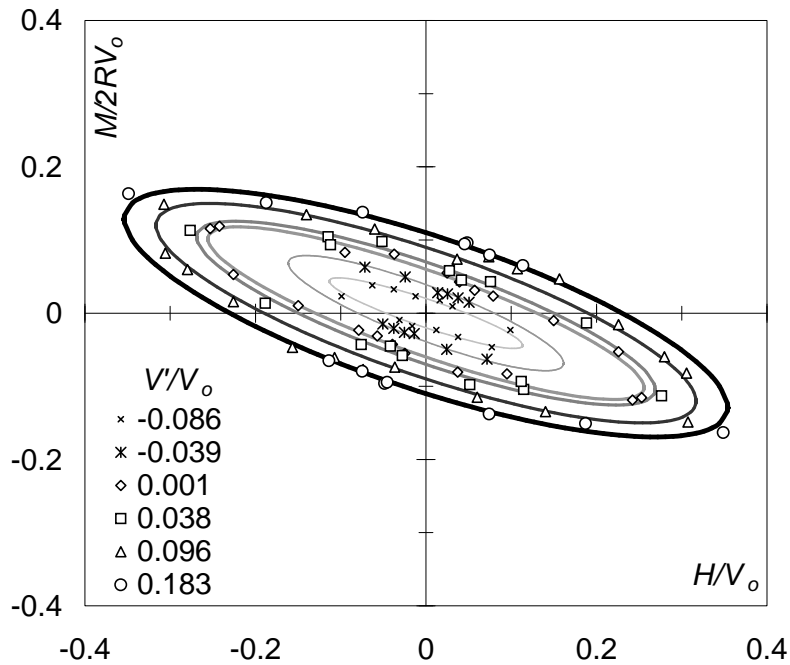


Figure 5.10: Yield points (d) determined from experiments using caisson A in the normalised $\frac{M}{2RV_o} - \frac{H}{V_o}$ plane and expression (5.25) fitted

The yield points obtained using the two straight lines method were normalised by V_c to interpret the results according to the hyperplasticity theory. Subsequently, yield points were plotted in a plane of nondimensional moment load and horizontal load $\frac{M}{2RV_c} - \frac{H}{V_c}$, assuming that V_c gives a better representation of V_o as discussed in Chapter 4. The nought subscript o is used henceforth to keep the same nomenclature used in the theoretical formulation. Figure 5.10 shows that the normalised yield points form non-symmetric ellipses in the $m - h$ plane ($\frac{M}{2RV_o} - \frac{H}{V_o}$) for different values of $\nu = \frac{V'}{V_o}$; the ellipses are rotated according to the eccentricity e , which from the figure it seems to be the same for all the ellipses. It is worth noting that the maximum combined loading capacity is found when m and h have different sign at the ellipse apices. On the other hand, the minimum loading capacity occurs when m and h are positive, which not only corresponds to the main loading on a foundation, but also controls the design. There are also in Figure 5.10 fitted curves constructed using equation (5.11), but reduced to the planar case, resulting

in:

$$y = \left(\frac{H}{h_i V_o} \right)^2 + \left(\frac{M}{2Rm_i V_o} \right)^2 - 2e \frac{H}{h_i V_o} \frac{M}{2Rm_i V_o} - 1 = 0 \quad (5.25)$$

where h_i and m_i represent the intersection of each ellipse with the axis $\frac{H}{V_o}$ and $\frac{M}{2RV_o}$ respectively, and e is the eccentricity of each ellipse. Values of the parameters m_i , h_i and e were determined using the least square error method; they are presented in Tables 5.4 and 5.5. Yield points were normalised as mentioned before by the respective V_o obtained from each test, but for the fit analysis an average value was used for each of the vertical loads V' shown in Tables 5.4 and 5.5. An increase of h_i and m_i with the normalised vertical load $\frac{V'}{V_o}$ was found previously by Martin (1994) for spudcan tests in clay. Indeed, Figures 5.11(a) and 5.11(b) show clearly this trend for both caissons. In addition, two fitted curves to the data were obtained by means of the following two equations:

$$h_i = \frac{H_i}{V_o} = h_o \left[\frac{(\beta_1 + \beta_2)^{\beta_1 + \beta_2}}{\beta_1^{\beta_1} \beta_2^{\beta_2} (t_o + 1)^{\beta_1 + \beta_2}} \right] \left(\frac{V'}{V_o} + t_o \right)^{\beta_1} \left(1 - \frac{V'}{V_o} \right)^{\beta_2} \quad (5.26)$$

$$m_i = \frac{M_i}{2RV_o} = m_o \left[\frac{(\beta_1 + \beta_2)^{\beta_1 + \beta_2}}{\beta_1^{\beta_1} \beta_2^{\beta_2} (t_o + 1)^{\beta_1 + \beta_2}} \right] \left(\frac{V'}{V_o} + t_o \right)^{\beta_1} \left(1 - \frac{V'}{V_o} \right)^{\beta_2} \quad (5.27)$$

Equations (5.26) and (5.27) proposed by Martin (1994), but without the tension parameter t_o , introduce the parameters β_1 and β_2 which play two roles. Firstly they shift the maximum normalised moment load m_o or the maximum horizontal load h_o from the middle along the normalised vertical load axis whilst keeping the same peak values by means of β_{12} (expression (5.17) shown in square brackets in (5.26) and (5.27)). Secondly, the tangent at the edges of the yield surface, *i.e.* at $t_o = \frac{V_t}{V_o}$ and $\frac{V'}{V_o} = 1$ can be changed from the parabolic case when $\beta_1 = \beta_2 = 1$. For the particular case of $\beta_1 < 1$ and $\beta_2 < 1$ the tangent increases, which can provide a better fit to the data. Figure 5.11(a) also highlights in a circle the parameter α which corresponds to the point in the normalised vertical load axis where the peaks m_o and h_o are located, also shown in circles. Although a visual observation of the ellipses does not clearly indicate a difference in inclination of the ellipse axes, a variation of the eccentricity with $\frac{V'}{V_o}$ was found as shown in Figures 5.12(a), and 5.12(b) where linear and parabolic best fit curves are included.

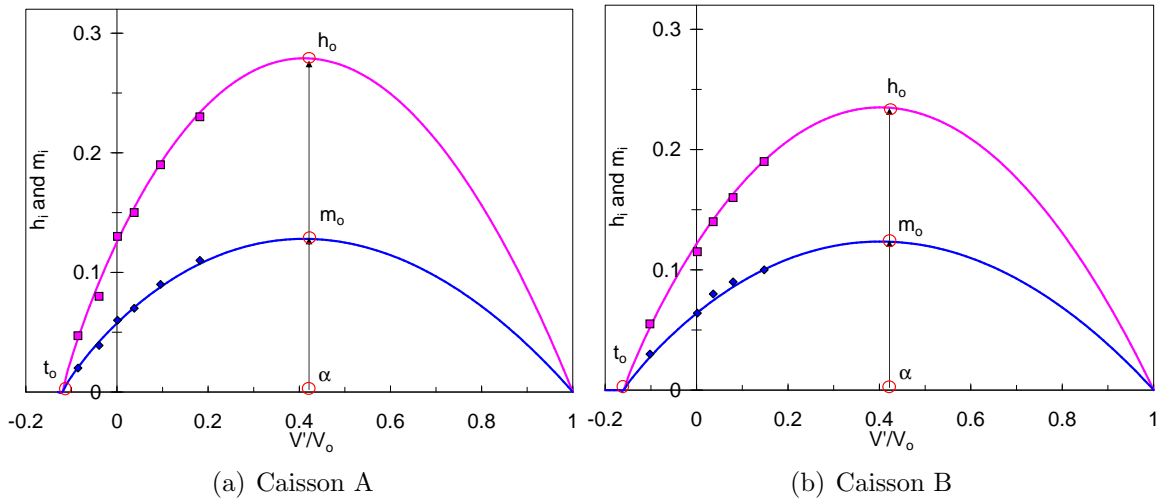
A better fit is obtained with a parabolic equation instead of a linear fit, as can be ob-

Table 5.4: Intersection and eccentricity parameters: h_i , m_i and e (caisson A)

V' : N	V'/V_o	V_o : N	V_o st dev: N	h_i	m_i	e
-47	-0.086	548	71	0.047	0.020	-0.91
-29	-0.039	734	58	0.080	0.039	-0.87
1	0.001	553	103	0.130	0.060	-0.86
21	0.038	561	81	0.150	0.070	-0.83
51	0.096	531	35	0.190	0.090	-0.80
100	0.182	552	86	0.230	0.110	-0.76

 Table 5.5: Intersection and eccentricity parameters: h_i , m_i and e (caisson B)

V' : N	V'/V_o	V_o : N	V_o st dev: N	h_i	m_i	e
-49	-0.102	484	54	0.055	0.030	-0.92
1	0.002	563	101	0.115	0.064	-0.83
21	0.036	572	117	0.140	0.080	-0.83
51	0.080	640	14	0.160	0.090	-0.79
102	0.148	689	16	0.190	0.100	-0.75


 Figure 5.11: Intersection points h_i and m_i as a function of the normalised vertical load $\frac{V'}{V_o}$

served in Figures 5.12(a) and 5.12(b), for that reason the parabolic expressions were used in subsequent calculations. Another reason for choosing parabolic equations is because they allow the variation of e , as found by Martin (1994), for higher values of ν , so extrapolation of e using the above parabolic equations is possible, which is not the case when using linear equations. Values of the parameter obtained from the best curve fits using the experimental results are summarised in Table 5.6. Figure 5.13 shows the normalised yield points projected in the $\frac{M}{2RV_o} - \frac{V'}{V_o}$ plane with the best fit curves using equation (5.11)

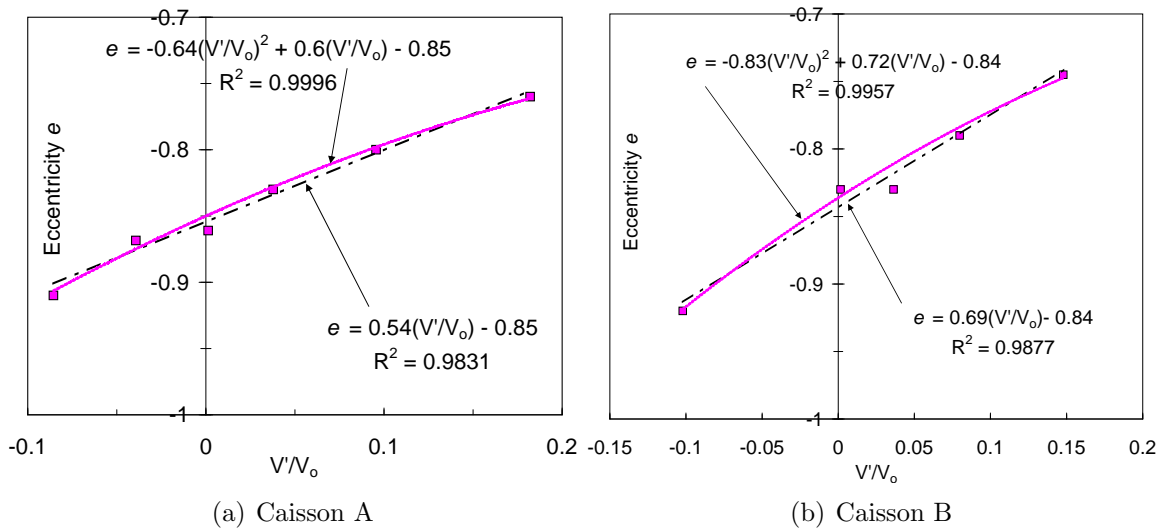


Figure 5.12: Eccentricity as a function of the normalised vertical load $\frac{V'}{V_o}$

in the following form and the parameter values listed in Table 5.6:

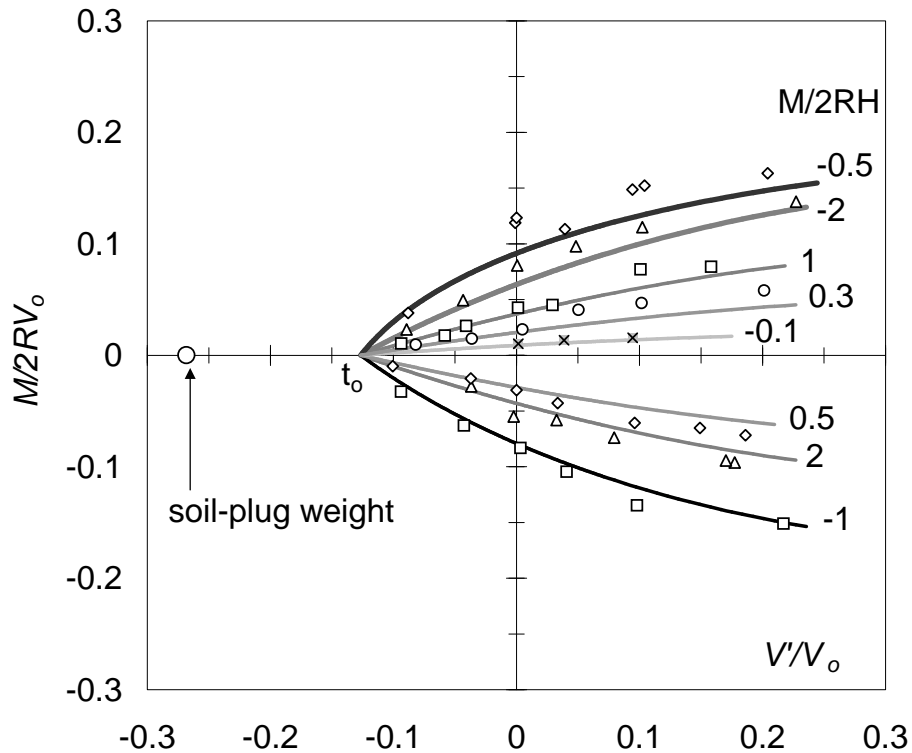
$$y = \left(\frac{H}{h_o V_o} \right)^2 + \left(\frac{M}{2Rm_o V_o} \right)^2 - 2e \frac{H}{h_o V_o} \frac{M}{2Rm_o V_o} - \beta_{12}^2 \left(\frac{V'}{V_o} + t_o \right)^{2\beta_1} \left(1 - \frac{V'}{V_o} \right)^{2\beta_2} = 0 \quad (5.28)$$

Expression (5.28) captures too the trend followed by the experimental yield points in the $m - \nu$ plane with the fitted parameters. However, the yield surface slightly under predicts the yield points. The values of $t_o = 0.12$ and 0.16 obtained from the best fit of the data are larger than the value obtained from the pullout tests ($t_o \approx 0.10$ and 0.12 , see Chapter 4). It seems that the caisson installation reduces the tension capacity due to the rearranging of grains sheared during the skirt penetration. The soil plug weight has been included as a circle in the $\frac{V'}{V_o}$ axis because of the potential application to caisson dimensioning. A view of the yield surface in three dimensions is shown in Figure 5.14 for low vertical loads and for intervals of 50 N along the vertical load axis.

Moment capacity tests carried out with caisson B were intended to investigate the effect that a different caisson geometry causes on the determination of a yield surface. Although the series of tests were not as numerous as for caisson A (see Table 5.3), it was sufficient to define the type of variation of the model parameters. Following the same criterion and procedures to determine yield points and yield surface parameters the set of values obtained for caisson B is also shown in Table 5.6 ($\frac{L}{2R} = 1$, $\frac{t}{2R} = 1.67\%$). How-

Table 5.6: Parameters suggested for the yield surface and flow rule expressions

Parameter	$\frac{L}{2R} = 0.5$	$\frac{L}{2R} = 1$	$\frac{L}{2R} = 1$
Thickness ratio, $t/2R$: %	1.16	1.67	1.16
Eccentricity of yield surface (average), e	-0.84	-0.87	-0.87
Contact vertical load (average), $V_c \Rightarrow V_o$: N	580	590	512
Maximum pure pullout load (average), V_t : N	-70	-94	-82
Tension factor, t_o	0.12	0.16	0.16
Dimension of yield surface (horizontal), h_o	0.279	0.235	0.300
Dimension of yield surface (moment), m_o	0.128	0.124	0.145
Curvature factor for yield surface (low V'), β_1	0.89	0.93	0.96
Curvature factor for yield surface (high V'), β_2	0.99	0.99	0.99


 Figure 5.13: Normalised yield points in the $\frac{M}{2RV_o} - \frac{V'}{V_o}$ plane and expression (5.28) fitted for caisson A

ever, a direct comparison of these parameters with the ones obtained for caisson A is not possible because the scaling does not match for the caisson wall thickness t . Villalobos *et al.* (2005) point out that V_o is, amongst other parameters, a function of t and because of that m_o and h_o obtained for both caissons cannot be directly compared.

An option to compare both caissons without the bias of the thickness, is for example instead of repeating the testing, to recalculate V_o for caisson B as presented in Chapter 4, but with the same thickness ratio of caisson A ($\frac{t}{2R} = 1.16$), which means to adopt t

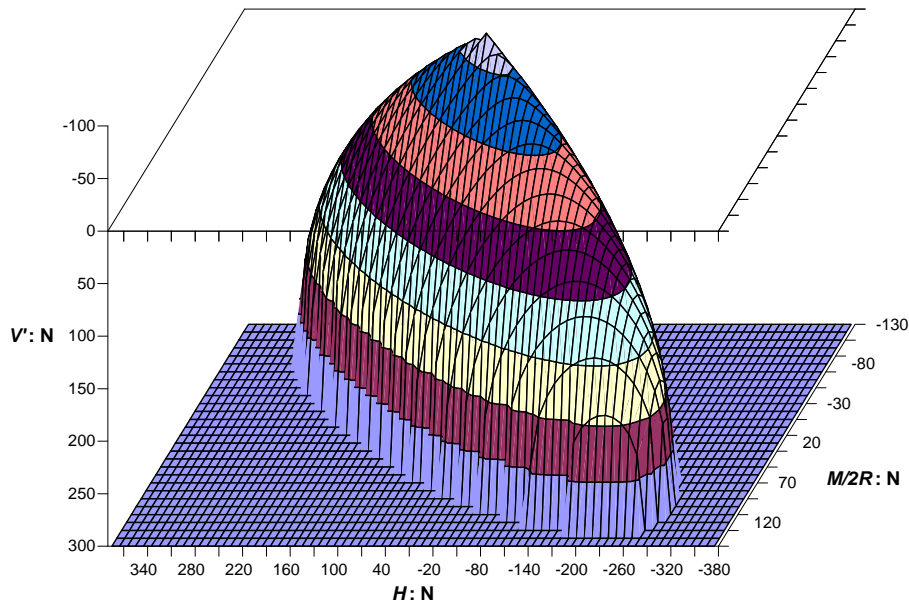


Figure 5.14: A 3D view of the yield surface for caisson A, showing the side of low vertical loads = 2.4 mm instead of 3.4 mm. Recalculate means that V_o is first calculated to calibrate the installation model parameters ($K \tan \delta$) using the installation test results for caisson B and subsequently V_o is recalculated for $t = 2.4$ mm. A parallel line was found to the previously determined relationship between V_o and γ_d (or $V_c - \gamma_d$ as shown in Chapter 4), which corroborates that V_o is a linear function of t . The results obtained from this exercise are shown in the last column of Table 5.6.

Figure 5.15(a) shows the range of values of the eccentricity e obtained in this study compared with previous values obtained for caissons with different aspect ratios. For aspect ratios from 0 to 0.5 a significant variation of eccentricity occurs according to the three sources of data. The results obtained in this study are shown in Figure 5.15(a) as average values (in circle) with the bars representing the variation which is a function of the vertical load ratio. It is clear that for caisson aspect ratios between 0.5 and 1 e tends to a fairly constant value.

The values of m_o and h_o as a function of the caisson aspect ratio are plotted in Figure 5.15(b). There are two values of m_o and h_o obtained in this study for $\frac{L}{2R} = 1$ due to a variation in thickness ratio, as presented in Table 5.6. Additionally, Figure 5.15(b)

shows values of m_o and h_o from the work of Cassidy (1999) and Byrne (2000). In spite of the scatter, both sets of h_o and m_o follow roughly similar trends (removing the point h_o for $\frac{L}{2R} = 0.66$). The scatter can be the result of differences in soil densities, whilst Cassidy and Byrne used dense sands, in the present study a loose sand was used. Moreover, the values of m_o and h_o obtained in this study correspond to yield surfaces that did not expand much further after installation. On the contrary, Byrne (2000) penetrated the caisson footings further after they were completely installed to simulate pre-loading as in jack-ups applications. Pre-loading implies higher values of V_o with which m_o and h_o are determined. However, these two reasons should be covered because V_o scales for the soil density and the shape of the yield surface is independent of its size. Therefore, a possible reason of the scatter should be sought in the caisson thickness ratio and in the mathematical formulation of the yield surface used.

The thickness ratio has a clear influence on the resulting values of m_o and h_o as observed in Figure 5.15(b) for the caisson with aspect ratio of one. Byrne (2000) did not include the tension capacity of caissons in the analysis, assuming a yield surface formulation as proposed by Butterfield and Gottardi (1994) for flat footings and also adopted by Martin (1994) for the study of spudcan footings. In the yield surface formulation presented here

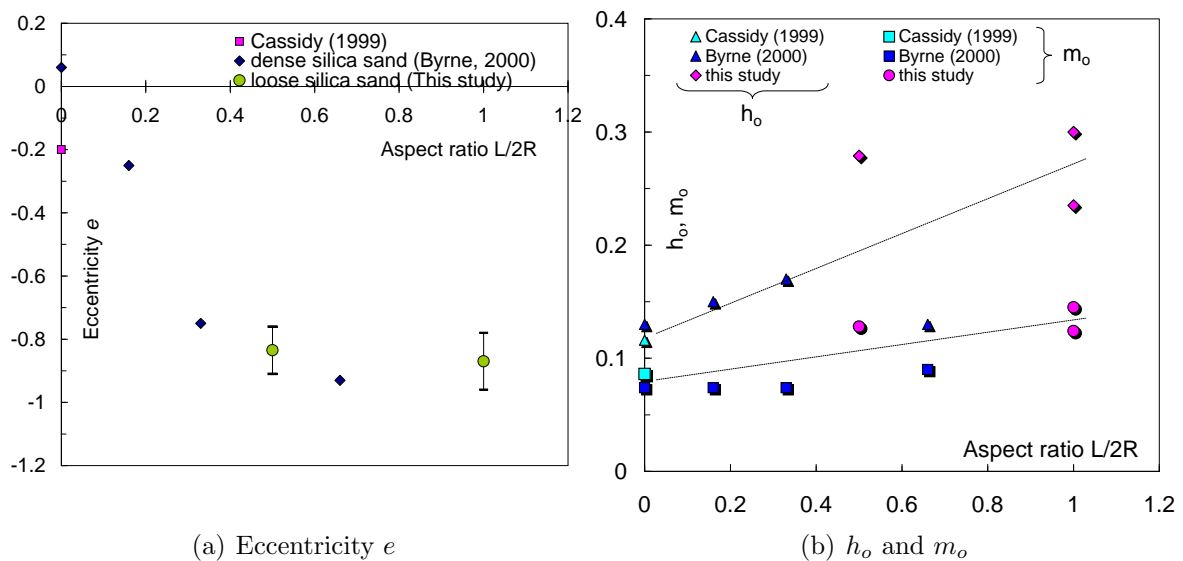


Figure 5.15: Data with $\frac{L}{2R} = 0$ by Cassidy (1999); $\frac{L}{2R} = 0, 0.16, 0.33$ and 0.66 by Byrne (2000) and $\frac{L}{2R} = 0.5$ and 1 from this study

the parameter t_o accounts for the tension capacity.

5.4.2 Discussion

In section §5.2.1 the issue of decoupling elastic moment and elastic horizontal loads raised the existence of an elastic metacentre. A decoupling between plastic moment and plastic horizontal loads also occurs if the LRP is located at the plastic metacentre according to Houlsby (2003). Moreover, Houlsby (2003) points out that the parameters of the yield surface expression m_o , h_o and e change with the movement of the LRP. In spite of locating the LRP always at the caisson lid (see Figure 5.1) the issue of coupling is still present. The values of m_o and h_o represent a maximum of the intersection between the yield surface and the axes m and h respectively. But these intersection points are not really comparable for caissons with different aspect ratios since the eccentricity is different (Figure 5.15(a)). Consequently, load decoupling is necessary for an appropriate comparison of the data. This is achieved by eliminating the eccentricity from the yield surface expression. The expression for the location of the plastic metacentre can be derived as:

$$\frac{z_m}{2R} = -e \frac{m_o}{h_o} \quad (5.29)$$

h_{om} changes with the eccentricity as follows:

$$h_{om} = \frac{h_o}{\sqrt{1 - e^2}} \quad (5.30)$$

However, m_o does not change, hence $m_{om} = m_o$ and Figure 5.15(b) still is valid. The variation of the metacentre-diameter ratio $\frac{z_m}{2R}$ with the caisson aspect ratio is shown in Figure 5.16(a). Using Cassidy's data and this study $\frac{z_m}{2R}$ increases asymptotically instead of linearly when using Byrne's data. Figure 5.16(b) shows the same h_o data presented in Figure 5.15(b) but referred to the metacentre as h_{om} . A better defined trend is found compared with the values of h_o in Figure 5.15(b), revealing that the use of a plastic metacentre improves the analysis. However, again Byrne's data follow a linear trend rather than a more asymptotic trend as the rest of the data.

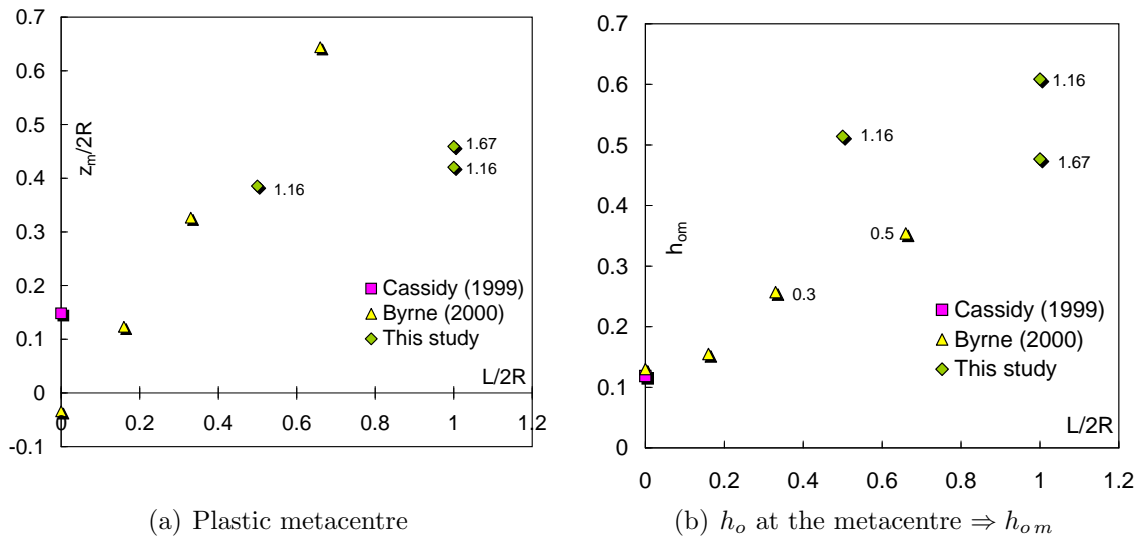


Figure 5.16: Data with $\frac{L}{2R} = 0$ by Cassidy (1999); $\frac{L}{2R} = 0, 0.16, 0.33$ and 0.66 by Byrne (2000), and $\frac{L}{2R} = 0.5$ and 1 by this study, showing $\frac{L}{2R}$ next to data points

5.4.3 Flow rule

The study of footing displacements is extremely important in geotechnical engineering since foundation designs are not only controlled by ultimate limit states, but also by displacements. Alternatively, stresses and loads are calculated from strains or displacements. In hyperplasticity theory as well as in classical plasticity theory the flow rule is the mathematical tool that allows modelling of incremental plastic displacements at yield. Therefore, the testing of caissons was intended to provide the information required to calibrate and validate the flow rule for hyperplasticity theory. With this objective, incremental plastic displacements at yield have been determined by subtracting the elastic components from the measured total displacements. The plastic displacement increments were obtained subtracting the measured displacements to estimated elastic displacements using equation (5.7) as follows:

$$\begin{Bmatrix} \dot{w}^p \\ \dot{\theta}^p \\ \dot{u}^p \end{Bmatrix} = \begin{Bmatrix} \dot{w} \\ \dot{\theta} \\ \dot{u} \end{Bmatrix} - \begin{Bmatrix} \frac{1}{K_V} & 0 & 0 \\ 0 & \frac{K_H}{D} & -\frac{K_{MH}}{D} \\ 0 & -\frac{K_{MH}}{D} & \frac{K_M}{D} \end{Bmatrix} \begin{Bmatrix} \dot{V} \\ \dot{M} \\ \dot{H} \end{Bmatrix} \quad (5.31)$$

where D is given by equation (5.8) and K_V , K_H , K_M and K_{MH} are the stiffness coefficients (see equation (5.6)), the shear modulus G is implicit in the stiffness coefficients.

The values of G adopted were firstly based on the expressions presented in section §5.2.1 and secondly slightly adjusted based on the results (initial part of the load-displacement response). Values of G between 0.5 MPa and 2 MPa were used in the calculations. The resulting magnitude of elastic displacements represented a very small proportion of the total displacements. Straight lines were fitted to determine plastic displacement increments as the ratios of $\frac{\dot{u}^p}{2R\dot{\theta}^p}$ and $\frac{\dot{w}^p}{2R\dot{\theta}^p}$. These straight lines could be fitted even in cases when the plastic displacements changed drastically from an initial positive direction to a negative direction. This occurred for negative load ratios $\frac{M}{2RH}$ between -0.5 and -0.1 (see Figure 5.5(c), although in this figure total displacements are shown, the plastic displacements do not considerably differ).

Figure 5.17 depicts the same yield surface previously shown in Figure 5.10 but with arrows on each yield point that represent the velocity vectors. They represent the incremental plastic displacement directions in the $\frac{M}{2RV_o} - \frac{H}{V_o}$ plane; only three vertical load ratios $\frac{V}{V_o}$ are shown for clarity. There are two sets of arrows, the black arrows were obtained from the experiments and the grey arrows are normal to the yield surface which represents the case of an associated flow rule.

The flow rule has been expressed by the following relationship between $2R\dot{\theta}^p$ and \dot{u}^p :

$$\frac{2R\dot{\theta}^p}{\dot{u}^p} = \frac{a_M h_o(m - eh)}{a_H m_o(h - em)} \quad (5.32)$$

An associated flow rule is achieved with expression (5.32) when the association factors a_M and a_H are equal. Figure 5.18 shows measured and calculated results plotted in the π plane as $\tan^{-1} \frac{\dot{u}^p}{2R\dot{\theta}^p}$ versus $\tan^{-1} \frac{M}{2RH}$ using $a_M = a_H$ in (5.32). Then, it is clear that an associated flow rule is able to capture the measured results in this plane. This reaffirms previous findings by other researchers. For instance, Martin (1994) confirms the hypothesis of normality to the yield surface in the $\frac{M}{2RV_o} - \frac{H}{V_o}$ plane for experimental results with spudcan footings in clay. In addition, Gottardi *et al.* (1999) reveal that an associated flow rule captures adequately test results using a circular flat footing on sand. It is also

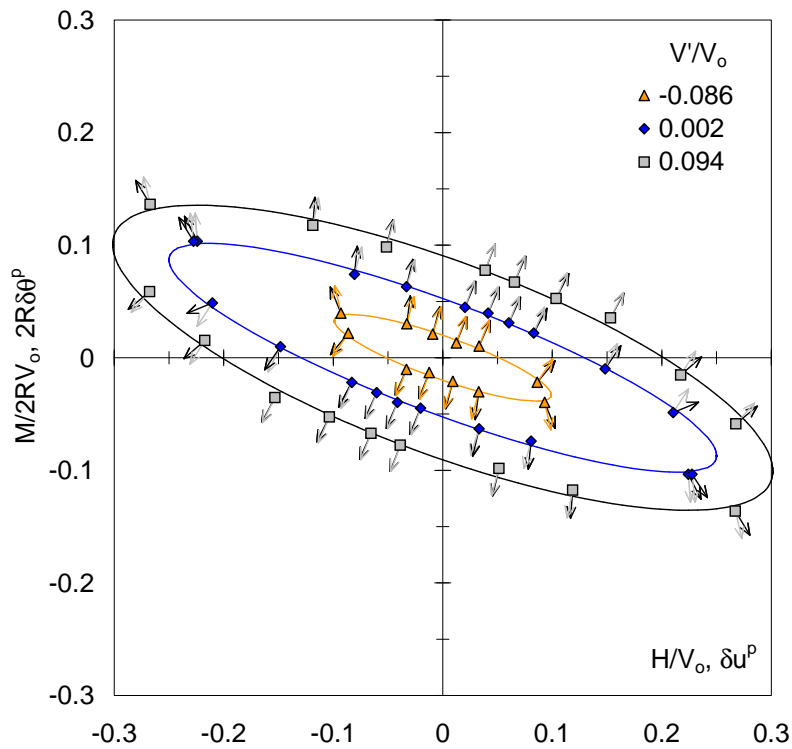


Figure 5.17: Yield points with incremental plastic displacement vectors obtained from tests (in black) and normal vectors (in grey) for caisson A (taken from Villalobos *et al.*, 2004b)

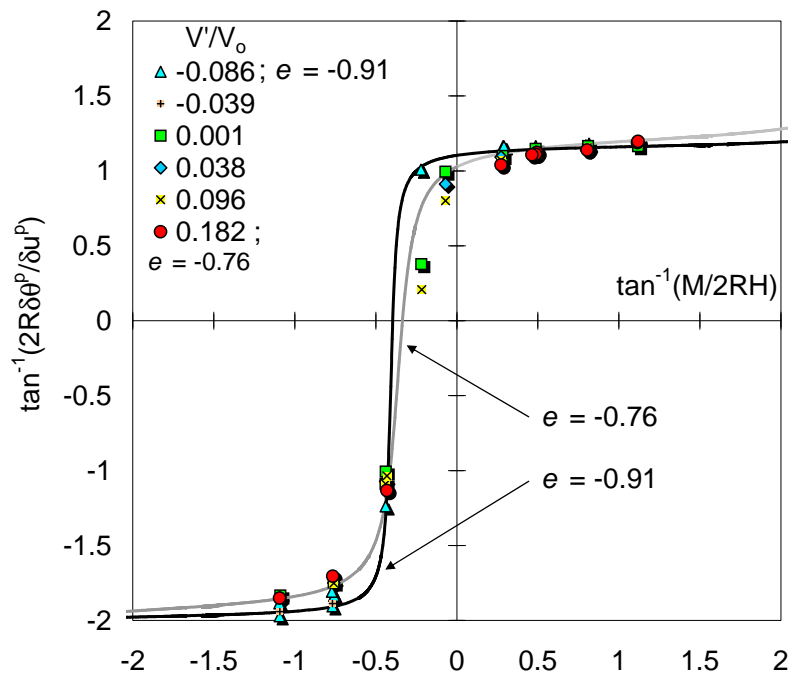


Figure 5.18: Experimental and theoretical predictions of incremental plastic displacement ratios in the π plane for caisson A

interesting to observe in Figure 5.18 the improvement of the flow rule prediction using the variation of the eccentricity for the two extreme cases of vertical load ratio.

An expression was developed to transform the measured results in terms of the ratios $\frac{\dot{w}^p}{2R\dot{\theta}^p}$ and $\frac{\dot{w}^p}{2R\dot{\theta}^p}$ into the ratio between \dot{w}^p and the radial displacement increment \dot{q}^p (equation (5.23)), resulting in:

$$\frac{\dot{w}^p}{\dot{q}^p} = \frac{\dot{w}^p}{2R\dot{\theta}^p} \sqrt{\frac{1 - e^2}{\left(h_o \frac{\dot{w}^p}{2R\dot{\theta}^p}\right)^2 + m_o^2 + 2eh_o m_o \frac{\dot{w}^p}{2R\dot{\theta}^p}}}} \quad (5.33)$$

To compare the above flow rule obtained from the experiments with the theoretical flow rule, the following expression was deduced:

$$\frac{\dot{w}^p}{\dot{q}^p} = \frac{\beta_{12} (\nu_1 + t_o)^{\beta_1} (1 - \nu_2)^{\beta_2} \left\{ \frac{\beta_2 a_{V_2}}{1 - \nu_2} - \frac{\beta_1 a_{V_1}}{\nu_1 + t_o} \right\} \sqrt{\frac{1}{h_o^2} + \left(\frac{1}{m_o} \frac{M}{2RH} \right)^2} - \frac{2e}{h_o m_o} \frac{M}{2RH}}{\frac{a_H}{h_o \sqrt{1 - e^2}} \left(\frac{1}{h_o} - \frac{e}{m_o} \frac{M}{2RH} \right) \sqrt{h_o^2 + \left(m_o \frac{2R\dot{\theta}^p}{\dot{w}^p} \right)^2 + 2eh_o m_o \frac{2R\dot{\theta}^p}{\dot{w}^p}}} \quad (5.34)$$

where the ratio $\frac{2R\dot{\theta}^p}{\dot{w}^p}$ is given by 5.32. Figure 5.19 shows measured velocity vectors in the $Q - V'$ plane for three cases of $\frac{M}{2RH}$ ratios. Strong non normality is clearly observed as the velocity vectors seem to point almost vertical and parallel to the Q axis.

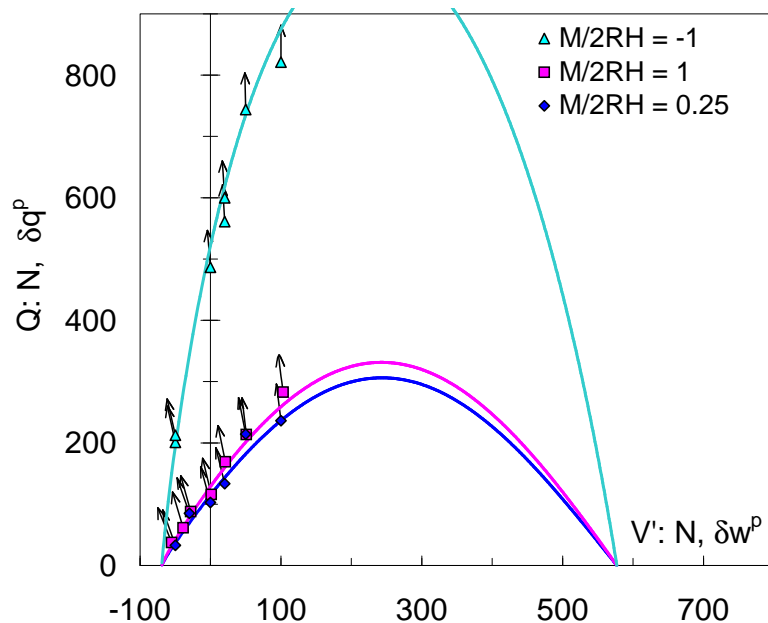


Figure 5.19: Experimental radial plastic displacement increments for three $\frac{M}{2RH}$ using caisson A

Figure 5.20 depicts the π plane $\tan^{-1} \frac{\dot{w}^p}{\dot{q}^p} - \frac{V'}{V_o}$ including the experimental results using expression 5.33 and theoretical curves obtained with equation (5.34). Five set of association factors were used to represent the data. In general the data follow a similar trend

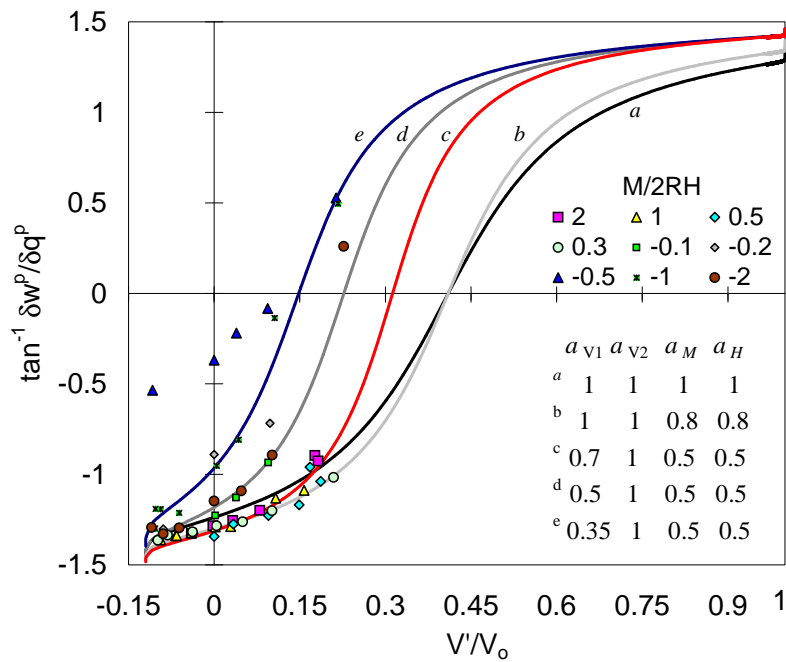


Figure 5.20: Experimental and theoretical predictions of incremental plastic displacement ratios in the π plane with variation of the association factors for caisson A

for positive load ratios which reflects a constant decreasing of the caisson uplift with $\frac{V'}{V_0}$, deviating for negative load ratios where a drastic reduction in uplift and even caisson settlement occur. An associated flow rule is obtained when $a_{V_1} = a_{V_2} = 1$. Figure 5.20 also shows that a non-associated flow rule is obtained with variations of a_{V_1} below unity, in this case, whilst keeping $a_{V_2} = 1$. The association factor $a_{V_2} = 1$ is a compromise due to the lack of results from this study for high vertical loads. In order to determine caisson response with accuracy it is necessary to carry out a parametric study to evaluate which set of association factors provides the best prediction.

5.4.4 Validation

An assessment of the hyperplastic model using the parameters already obtained is necessary to evaluate the performance of the model against experimental results. The simple case of a single yield surface and isotropic hardening is used for an initial validation. Test FV1.1.2A was chosen and the soil properties and test parameters for this test are summarised in Tables 4.1 and 5.1. Additionally, the following parameters as previously determined (Table 5.6) were used: $m_o = 0.279$, $h_o = 0.128$, $e = -0.84$ and $t_o = 0.12$. The chosen sets of association factors were those of b and c shown in Figure 5.20, where the

only constraint was that a_M and a_H should be equal to give an associative flow rule in the $M - H$ plane.

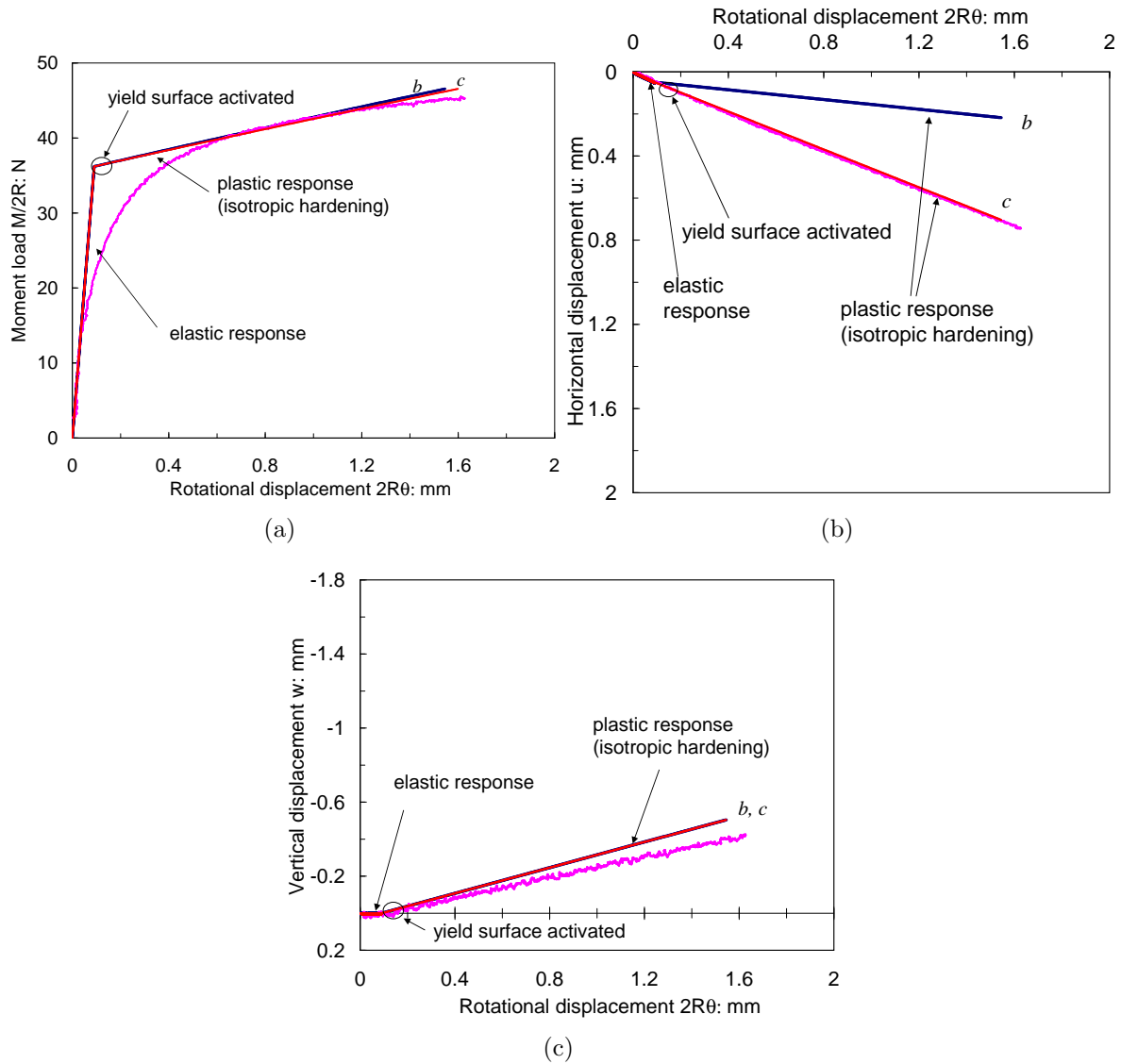


Figure 5.21: Measured and calculated response for caisson A under the load ratio $\frac{M}{2RH} = 1$ at constant vertical load $V' = 50$ N

An elastic shear modulus $G = 1$ MPa was used in the calculations. Figure 5.21(a) shows the measured and calculated $\frac{M}{2R} - 2R\theta$ response, noting immediately the poor modelling of the transition between ‘elastic’ and ‘fully plastic’ response. Initially the load path proceeds inside the yield surface resulting in a pure elastic response until the yield surface is reached. Then, yield occurs and further increase in the moment load causes the expansion of the yield surface. There is a good prediction of the measured vertical displacement w as shown in Figure 5.21(c), although it is slightly overestimated. However, Figure 5.21(b) shows that the theory gives a better prediction of the measured horizontal displacement

u using the set of association factors c instead of b (Figure 5.20). It is worth mentioning that the theoretical calculations are more sensitive to the association factors than any other parameter. Moreover, the parameter selection does not follow the sequence and magnitudes proposed by Nguyen-Sy (2006) following the results from Model B and Model C, where $a_{V1} = 0.297$, $a_H = a_M = 0.7$, and $a_{V2} = 1$. This selection of association factors for flat footings and spudcan footings in sand and clay follows the sequence: $0 < a_{V1} \leq a_H, a_M \leq a_{V2} \leq 1$. Whilst a value of $a_{V1} > a_H, a_M$ was used in the previous example. From this particular example, caisson foundations seem to deviate from the pattern of association factors for spudcan and flat footings.

5.5 CYCLIC COMBINED LOADING TESTS

5.5.1 Introduction

The cyclic nature of the maritime and environmental loadings was pointed out in Chapter 1. For this reason, an important issue in this investigation was to study the response of caisson footings under repeated loading. The purpose of the experiments was not to reproduce exactly the offshore cyclic loadings during storm events, but to identify important patterns of foundation behaviour that contribute towards modelling and design. In particular, it has been demonstrated that the hyperplasticity theory is suitable to modelling the cyclic behaviour of soils (Puzrin and Houlsby, 2001; Einav, 2005; Nguyen-Sy, 2006).

In practical terms, cyclic moment loading tests can be seen as a continuation of monotonic tests, where instead of applying a one-directional rotation or translation, several rotations of increasing amplitude are applied by simultaneously switching the direction. Byrne (2000) concludes that no major differences exist between monotonic and cyclic tests in terms of $\frac{M}{2R} - 2R\theta$ response (using smaller model caissons in a very dense oil-saturated Baskarp cyclone sand). Furthermore, no rate effect was found even though monotonic tests were performed at a much slower rate than the cyclic tests. However, there was not

a clear conclusion about the vertical displacements caused by cyclic loading. In addition, symmetrical loading tests were mostly preformed, whilst the environmental forces normally have a predominant direction. It was important to explore loading cases where the rotational displacements are not completely recovered.

A series of 45 combined loading tests were performed in the laboratory for the investigation of cyclic response of caisson foundations. Test information is summarized in Tables 5.7 and 5.8, where the minimum moment load $\frac{M_{min}}{2R}$ was obtained in the first cycle, whereas the maximum $\frac{M_{max}}{2R}$ in the tenth cycle (otherwise indicated). The net or total vertical displacement during each test is w_t , where a negative value corresponds to upward movement and positive to settlement. In the majority of the tests caissons were

Table 5.7: Summary of cyclic tests undertaken using caisson A

Test	V' N	$\frac{V'}{\gamma_d(2R)^3}$	V_o N	R_d %	γ_d kN/m ³	$\frac{M}{2RH}$	$\frac{M_{min}}{2R}$ N	$\frac{M_{max}}{2R}$ † N	w_t mm
FV127_23.3	-30	-0.08	550	18	15.10	1	5, -6	18 ⁹ , -19	-16.8
FV108_21.3	3	0.01	483	12	14.96	2	18, -15	36 ⁸ , -36	-6.3
FV78_13.2	4	0.01	750	41	15.73	1	15, -17	38 ⁶ , -36 ⁷	-7.6
FV81_14.3	4	0.01	726	46	15.85	0.5	23, -8	31 ⁵ , -28 ⁷	-8.2
FV85_15.3	4	0.01	783	50	15.99	0.25	18, -8	24 ⁶ , -21 ⁶	-9
FV86_16.3	2	0.01	458	18	15.11	0.25	16, -8	18 ⁶ , -18	-7.8
FV111_22.3	3	0.01	557	23	15.23	-0.1	-2, 1	10, -10	-2.6
FV113_22.3	6	0.02	530	23	15.23	-0.25	5, -8	44, -47	-0.3
FV73_12.2	31	0.08	830	46	15.87	1	22, -22	54, -52	-2.8
FV82_14.3	27	0.07	784	46	15.85	0.5	24, -7	40 ⁹ , -36	-4
FV87_16.3	19	0.05	461	18	15.11	0.25	17, -8	22 ⁸ , -21	-4
FV90_17.3	13	0.03	463	15	15.03	-2	17, -14	66, -60	-2.5
FV79_13.2	54	0.14	730	41	15.73	1	22, -21	56, -57	-1.7
FV83_14.3	51	0.13	730	46	15.85	0.5	31, -6	46, -44	-1.5
FV88_16.3	59	0.15	503	18	15.11	0.25	23, -9	31, -30	-1
FV77_13.2	43	0.11	906	41	15.73	-1	10, -10	123, -114	-0.3
FV80_13.2	110	0.28	821	41	15.73	1	30, -26	73, -72	-0.2
FV84_14.3	101	0.25	795	46	15.85	0.5	25, -9	58, -56	0.1
FV89_16.3	100	0.26	478	18	15.11	0.25	25, -8	36, -36	0.8
FV109_21.3	193	0.51	487	12	14.96	2	24, -39	89, -90	3.2
FV104_20.3	182	0.48	480	12	14.95	1	26, -21	77, -76	3.2
FV107_21.3	185	0.49	460	12	14.96	0.25	23, -19	45, -45	3.4
FV105_20.3	283	0.75	480	12	14.95	1	22, -25	92, -93	3.6
FV106_21.3	385	1.02	460	12	14.96	0.5	26, -29	88, -89	4.2
FV130_24.3	2	0.00	582	21	15.17	1	20	41	-1.3
FV132_24.3	3	0.01	513	21	15.17	1	16	38	-1.4
FV121_23.3	11	0.03	521	18	15.10	0.25	17	22 ⁷	-2.9
FV123_23.3	9	0.02	534	18	15.10	0.25	8, -8	23 ¹³ , -22 ¹⁷	-10
FV125_23.3	17	0.04	560	18	15.10	0.25	17, -15	26 ¹⁵ , -26 ¹⁵	-7.7
FV136_24.3	11	0.03	540	21	15.17	-0.5	-35	-151	-0.05
FV134_24.3	47	0.12	528	21	15.17	-0.25	-19	-66	-0.2

†numbers up indicate cycle at which M_{max} was reached

Table 5.8: Summary of cyclic tests undertaken using caisson B

Test	V' N	$\frac{V'}{\gamma_d(2R)^3}$	V_o N	R_d %	γ_d kN/m ³	$\frac{M}{2RH}$	$\frac{M_{min}}{2R}$ N	$\frac{M_{max}}{2R}$ N	w_t mm
FV124_23.3	-2	-0.02	467	18	15.10	2	19, -38	65, -68	-4.9
FV102_20.3	3	0.02	428	12	14.95	1	26, -25	59, -55	-5
FV120_23.3	-1	-0.01	421	18	15.10	0.5	24, -16	36, -38	-6.2
FV128_23.2	6	0.05	540	18	15.10	0.25	12, -15	28, -29	-5.7
FV110_22.3	0	0.00	443	23	15.23	-0.1	-1, 1	-6, 6	-2
FV112_22.3	-3	-0.03	433	23	15.23	-0.25	-7, 4	-24, 24	-1.9
FV115_22.2	19	0.15	600	23	15.23	1	27, -31	64, -63	-2.3
FV117_22.3	46	0.36	469	23	15.23	1	34, -24	62, -65	0.6
FV126_23.3	95	0.75	459	18	15.10	2	43, -33	89, -88	2.9
FV119_22.3	85	0.67	557	23	15.23	1	35, -33	75, -76	1.6
FV122_23.3	89	0.70	443	18	15.10	0.5	27, -27	56, -53	1.9
FV133_24.3	20	0.16	467	21	15.17	-0.25	-15.8	-31.4	-1.2
FV135_24.3	17	0.13	470	21	15.17	-0.5	-34.4	-113.7	-0.7
FV129_24.3	48	0.37	465	21	15.17	1	30, -19	73, -64	0.1

rotated symmetrically with respect to the centre of the caisson. A preliminary analysis of these experiments was carried out by Villalobos (2004). However, a few tests shown at the bottom of Tables 5.7 and 5.8 were not symmetrically rotated, also referred to as one-way cyclic loading tests. The whole series of tests is reported by Villalobos *et al.* (2004a). This section presents representative tests and draws relevant conclusions from the analysis of all the tests.

5.5.2 Cyclic moment-rotation response

A computer controlled *VMH* loading rig was used to carry out the testing, using caissons A and B and a dry, loose, white Leighton Buzzard sand (see Chapter 2 for details). Tests were conducted holding a low vertical load whilst a cyclic rotational or lateral displacement of increasing amplitude was applied until a maximum displacement. In this section it is not intended to reproduce a loading path resembling field conditions, but to find foundation response patterns which can be incorporated in the modelling.

Figure 5.22(a) shows a test with ten rotational cycles applied to caisson A at a rate of $2R\dot{\theta} = 0.02$ mm/s. The same test is shown in Figure 5.22(b), but in a $H - u$ plot, where it is observed that u increases less than $2R\theta$ in each cycle. Figures 5.23(a) and 5.23(b) shows another test with ten rotational cycles, but applied to caisson B; in this

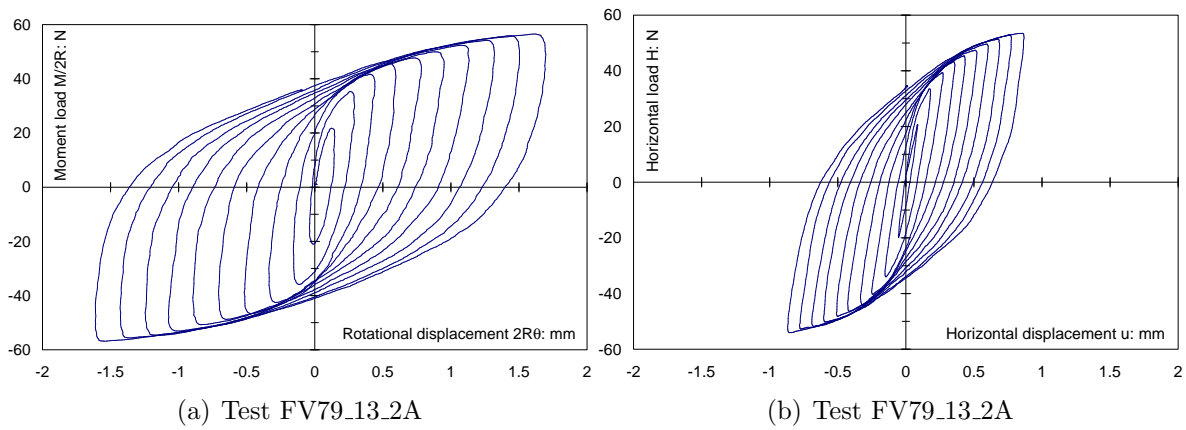


Figure 5.22: Cyclic rotational response under constant vertical load $V' = 54$ N at $\frac{M}{2RH} = 1$

case u is similar to $2R\theta$. As a consequence, a larger area is enclosed by the cycle loops. Another important feature of these results is that the response is hysteretic and stiffness degradation during each cycle is observed.

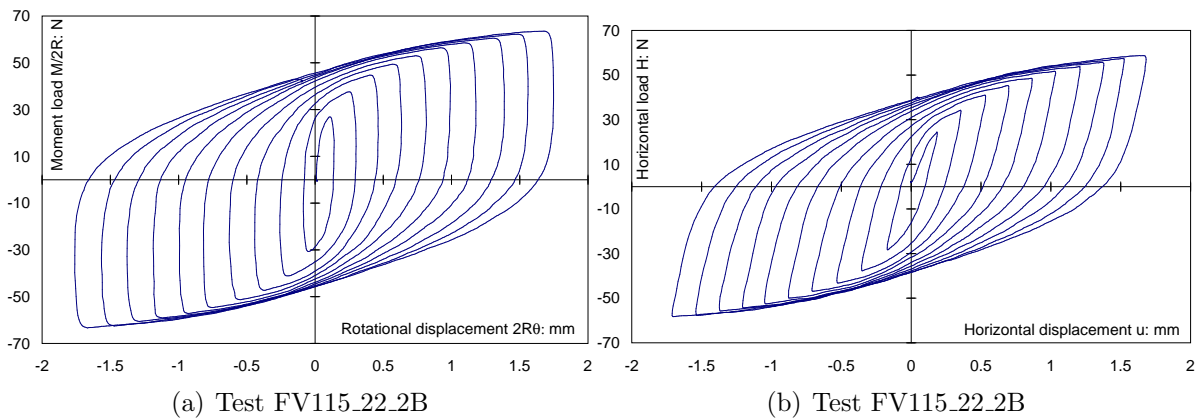


Figure 5.23: Cyclic rotational response under constant vertical load $V' = 19$ N at $\frac{M}{2RH} = 1$

Hysteresis is a phenomenon observed in soils that experience cyclic loading. Therefore, a foundation cyclically loaded naturally manifests this phenomenon. In a load-displacement curve hysteresis is recognised as loops where the loading and unloading curves do not coincide, albeit sharing the points of load reversal. Masing (1926) indicated that the property of pure kinematic hardening allows the prediction of unloading and reloading response once the initial loading curve is known. The first Masing rule states that the tangent slope of the reloading curves is identical to the tangent slope of the initial curve. The second Masing rule states that the shape of unloading and reloading curves is the same as that of the doubled initial curve. Figure 5.24 confirms that the first and second Masing rule (for test FV79_13.2A) are obeyed.

To compare different cyclic loading tests peak load values and displacements at peak in each cycle were obtained as shown in Figure 5.25. Knowledge of these peak values allows a ‘backbone’ curve to be defined, which is used in modelling to generate cyclic loops. The importance of obeying the Masing rules has favourable modelling implication since knowing the initial loading any subsequent unloading-reloading can be reproduced. In addition, the backbone curve can be reproduced symmetrically during positive and negative loads. Figure 5.25 shows that experimentally symmetry is fairly achieved.

The minimum and maximum ‘peak’ moment capacity listed in Tables 5.7 and 5.8 are normalised and plotted in Figures 5.26(a) and 5.26(b) as functions of the normalised vertical load and the load ratio. It is clear that independent of the load ratio the maximum moment capacity increases with the vertical load. However, the increase of the minimum moment capacity obtained in the first cycle with the vertical load is less pronounced and reach a threshold. These figures show only results from positive load ratios, the few data for negative load ratios showed lower values of minimum peak moment capacity and higher maximum peak moment capacity. Moreover, higher moment capacity was obtained for the caisson with aspect ratio of one. Therefore, the normalised moment should include the aspect ratio (or skirt length L) to compare results from different caissons.

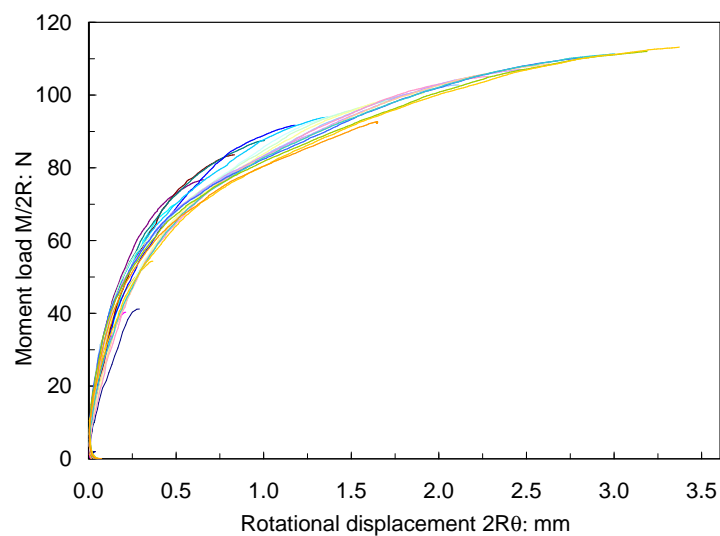


Figure 5.24: Proof of the first and second Masing rule (test FV79_13.2A)

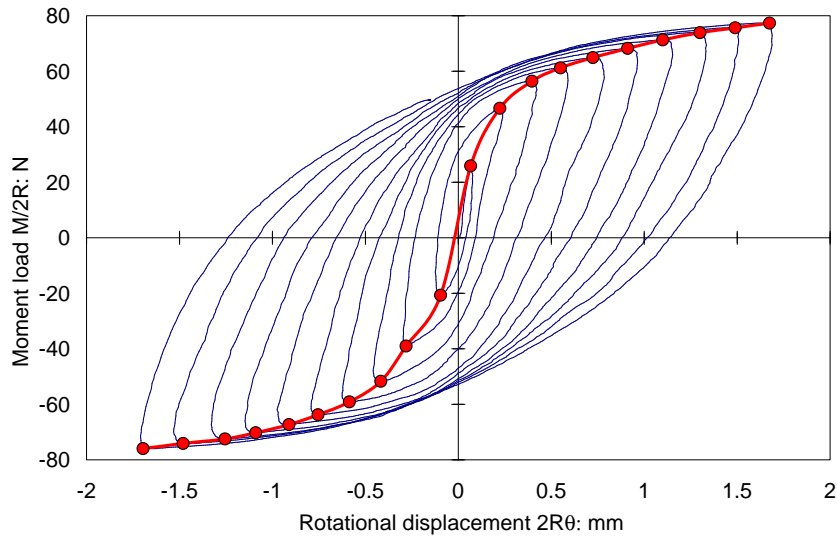


Figure 5.25: Backbone curve of test FV104_20.2A showing peak points

Tests with increasing constant vertical loads from -50 N to 200 N, for a loading ratio $\frac{M}{2RH} = 1$ are shown in Figure 5.27(a) as the dimensionless quantity $\frac{M}{\gamma_d(2R)^4}$ and θ in radians. There is an asymptotic moment resistance at the end of the tests with $V' = -50$ N and 0 N. On the other hand, the remainder of the tests show an increase in their moment resistance after each cycle. For clarity only two monotonic tests have been plotted together with the cyclic tests for comparison. Byrne’s (2000) conclusion is confirmed since no great difference is observed between monotonic and cyclic curves. This is not very surprising since the test history is identical, *i.e.* a series of cycles with monotonically increasing

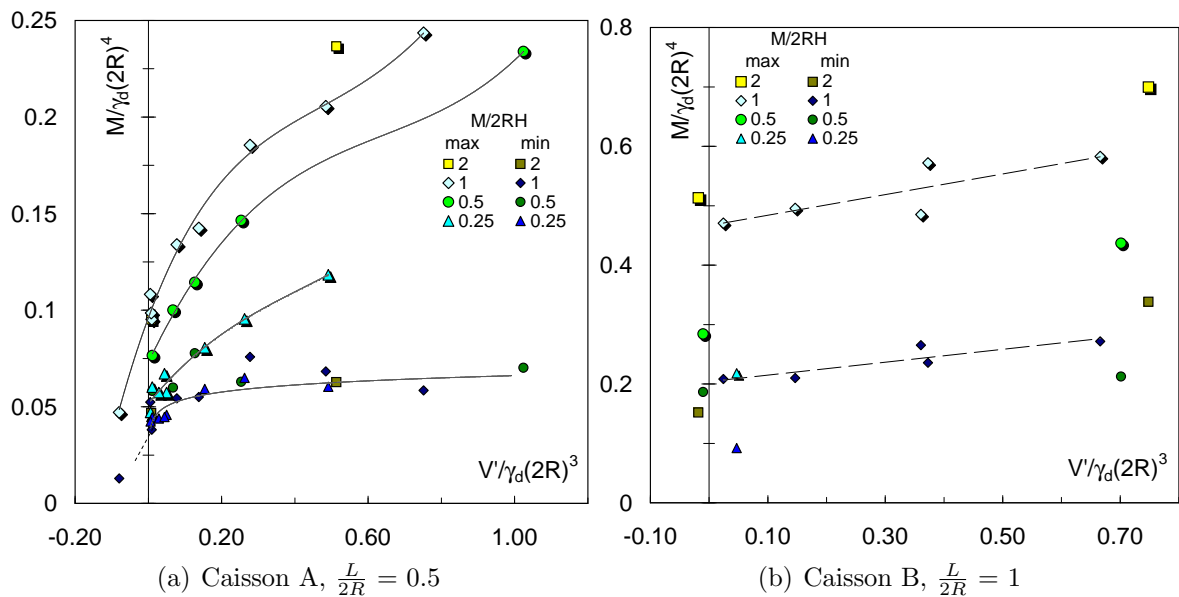


Figure 5.26: Variation of the normalised moment capacity (minimum and maximum peaks) with the normalised vertical load and with the load ratio

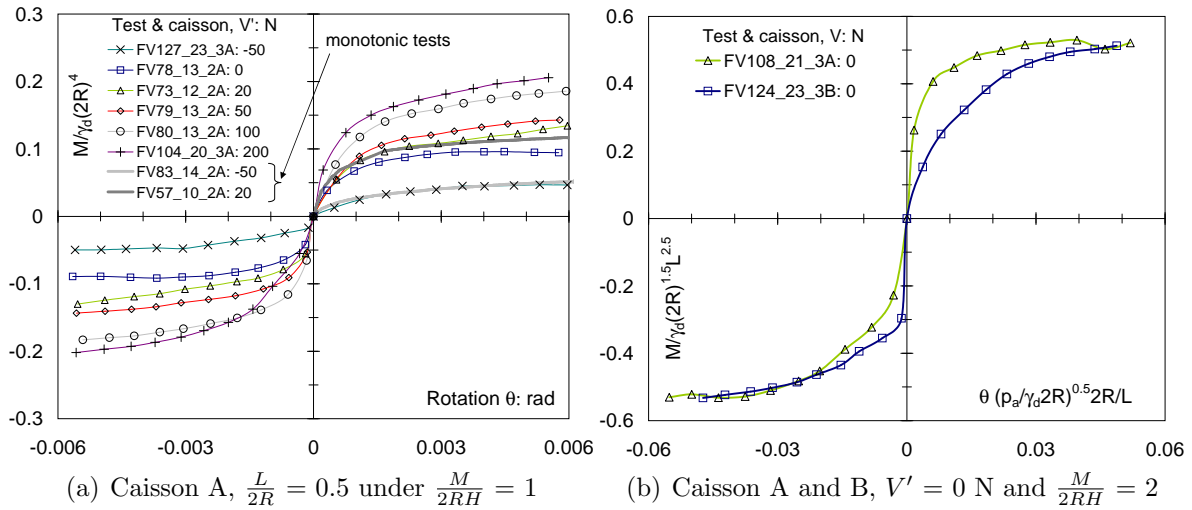


Figure 5.27: Peaks of cyclic moment load versus rotational displacement comparing (a) different constant vertical loads. Note the presence of two monotonic tests, and (b) curves from caissons A and B

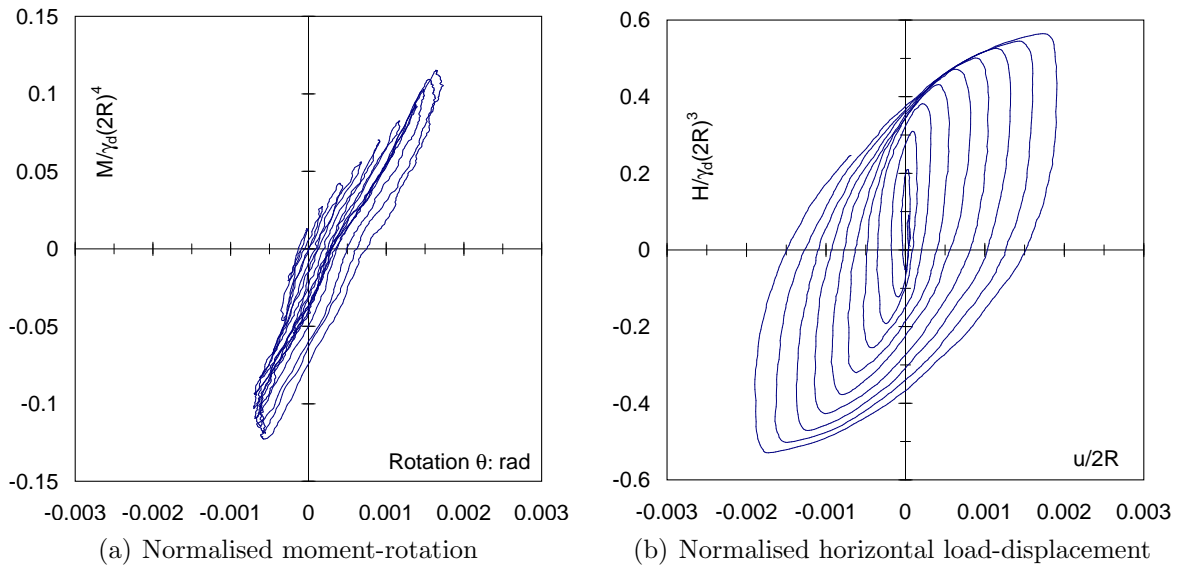


Figure 5.28: Test FV113.22_3A cycled under $M/2RH = -0.25$ and $V' = 6$ N

amplitude, such that virgin soil is always yielding at the end of a new loading or reverse cycle. Therefore, it is not surprising that the peaks fall close to the backbone curve for a single one-way rotation. Furthermore, an even more relevant conclusion for caisson design is the favourable effect of the increase of V' on the caisson moment capacity. Figure 5.27(b) compares the cyclic response of caissons with different aspect ratios. The scaling expressions used and shown in the figure were found to better capture the effect of the skirt length. Strictly, in section §5.1 the moment was found to be a function of L^3 , but in view of the experimental results a better agreement was achieved scaling by $L^{2.5}$ instead.

Differences appear at the beginning of the cyclic tests and more significant to the right hand side mostly due to disturbance of the sand sample by a previous monotonic tests. But in the left hand side a better agreement is found.

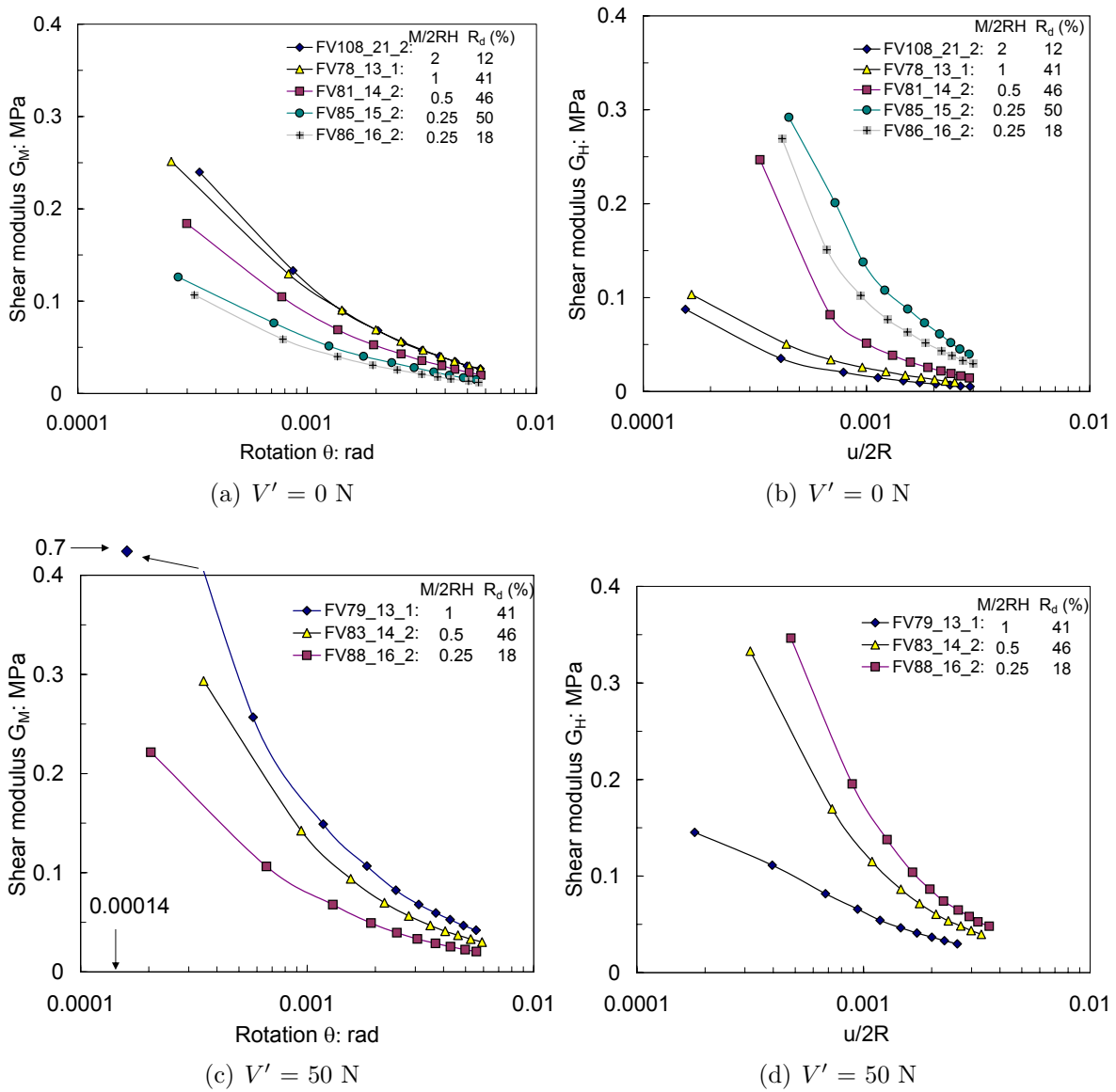


Figure 5.29: Secant shear modulus variation with rotation and horizontal displacement

Figure 5.28(a) shows a lateral cyclic tests with a much higher horizontal load than moment load as well as having opposite directions. Under these conditions no open loops were developed during cycling. However, the $H - u$ response possesses hysteresis as it can be observed in Figure 5.28(b).

The degradation of the foundation stiffness is caused by the appearance of plastic displacement. From soil dynamics studies the variation of shear stiffness with the shear

strain is well known. However, the curves found in the technical literature are not directly applicable to problems of soil-footing interaction. The values of G were obtained using equations (5.5) and (5.6), where G can be expressed as a function of the caisson radius, moment and horizontal load, rotation and horizontal displacement and dimensionless stiffness coefficients. Two expressions for G can be deduced, one depending on the moment and the other depending on the horizontal load. Since a secant modulus was calculated peak loads and the corresponding displacements were taken as shown in Figure 5.25. Figures 5.29(a) and (c) are examples of secant shear moduli G obtained from cyclic $\frac{M}{2R} - 2R\theta$ curves as a function of the footing rotation. Figures 5.29(b) and (d) show secant shear moduli G obtained from cyclic $H - u$ curves as a function of the normalised lateral displacement $\frac{u}{2R}$. These figures show clearly the reduction of the secant shear modulus after each cycle. The initial plateau well known in soil dynamics to appear for very small deformations corresponds to the elastic G . However, larger values of G were not captured from the measurements. Values of G that correspond to elastic response were estimated as between 0.5 MPa and 2 MPa.

5.5.3 Non-symmetric moment loading tests

The symmetry in the loading regime is an idealization that assists as a starting point in the calibration and validation of numerical models. Moreover, the offshore loading regime is not symmetric and loads are more likely to be predominant in one direction. Tests were performed to generate non-symmetrical cyclic response instead of applying symmetrical rotations or lateral displacements (by adding to the current unloading-reloading rotations the previous unloading-reloading rotations plus the initial rotation). Figure 5.30(a) compares the response of a non-symmetric test with a symmetric test. Peaks of both tests follow a similar trend, at least until both curves are comparable. In addition, the tenth cycle loop of the symmetrical test is overlapped exactly at the tenth cycle of the non-symmetrical test. Both tenth cycle loops coincide in the unloading, but not in the reloading where they are close each other in the initial part, albeit they differ at the end of the reloading. The fact that rotation after $2R\theta = 1.6$ mm is not experienced by the

symmetrical test influences the response in reloading but not in unloading.

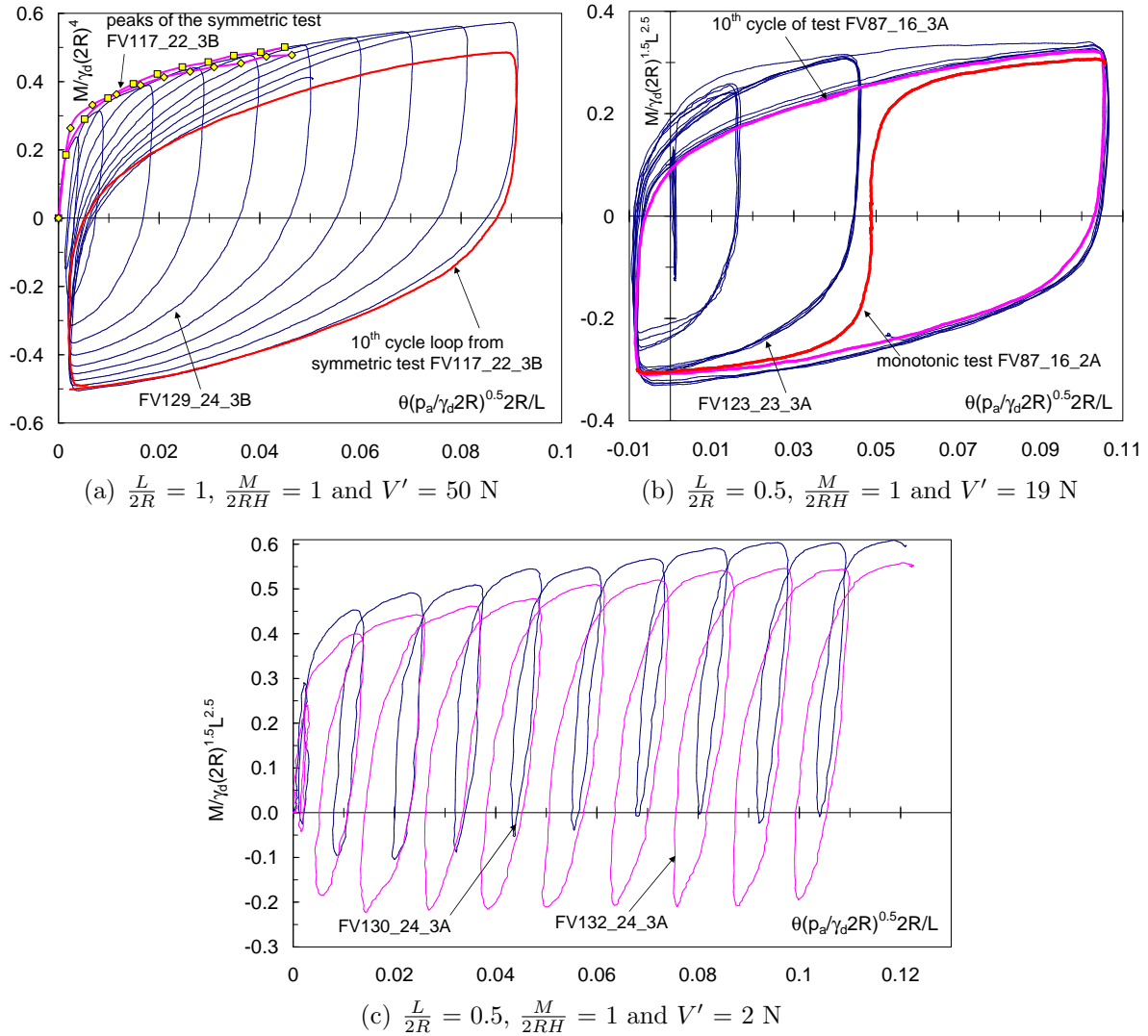


Figure 5.30: (a) Non-symmetric test FV129_24_3B comparing with peaks and tenth cycle loop of symmetric test FV117_22_3B, (b) non-symmetric 17 cycles test FV123_23_3A comparing with tenth cycle loop of symmetric test FV87_16_3A and with monotonic test FV87_16_2A, and (c) one-way cyclic loading tests FV130_24_3A and FV132_24_3A

A 17 cycles test (in groups of 3, 4, 5 and 5 cycles) was performed to investigate the effect of repeating cycles under the same amplitude. Figure 5.30(b) shows that no significant difference in the load-displacement response is found in cycles with the same amplitude. Moreover, Figure 5.30(b) compares this test with another two tests under similar conditions, but different loading regimes. Test FV87_16_2A corresponds to monotonic loading and test FV87_16_3A to symmetric cyclic loading. To compare the last five cycles of the non-symmetric test with the tenth cycle of the symmetric test and the monotonic test the curves were overlapped and for the latter the negative moment load replicated. The

monotonic test can be used as backbone curve not only for a symmetric cyclic response, but also for the non-symmetric cyclic response.

Figure 5.30(c) illustrates the case of unloading to a constant rotation smaller than the next reloading rotation. As a consequence the caisson tilts steadily after each cycle without passing through the origin as shown in Figures 5.30(a) and 5.30(b). Two tests are shown in Figure 5.30(c), the unloading rotation magnitude being the only difference. As a result of the shorter rotation amplitude the caisson moment capacity is higher than that shown in Figure 5.30(b), and compares fairly well with the results shown in Figure 5.30(a). A monopod caisson foundation of an offshore wind turbine is more likely to be under this type of loading regime. Therefore, if a caisson undergoes a series of extreme events as the last nine cycles shown in Figure 5.30(c) large irrecoverable rotations should be expected. It is important then to avoid this detrimental irrecoverable deformation of the foundation. To this end, the caisson foundation response should not occur beyond the first cycle shown in Figure 5.30(c). To ensure this the caisson design should restrict any reduction of foundation stiffness that could cause large irrecoverable rotations.

5.5.4 Cyclic vertical displacement response

In the above section it has been demonstrated that the moment capacity of a caisson is independent of the loading regime for similar rotation amplitudes for a small number of cycles, *e.g.* 10 cycles. Kelly *et al.* (2006) scale the cyclic moment load and rotational displacement response to compare results from displacement controlled laboratory tests and load controlled field trials. However, Byrne (2000) and Kelly *et al.* (2006) do not show the effect of monotonic and cyclic loading on the vertical displacement response.

The total vertical displacement w_t listed in Tables 5.7 and 5.8 is plotted in Figures 5.31(a) and 5.31(b) as a function of the normalised vertical load $\frac{V'}{V_o}$ and the load ratio $\frac{M}{2RH}$. It can be observed clearly a transition of the caisson movement from upward to downward. The change from uplift to settlement occurs at $\frac{V'}{V_o} = 0.13$ for caisson A and at 0.10 for

caisson B. For the normalisation $\frac{V'}{\gamma_d(2R)^3}$ the transition was found to be at 0.25 and at 0.35 respectively. The values of 0.13 and 0.1 are lower than those extrapolated from the monotonic moment tests ($\frac{V'}{V_o} \approx 0.3$, see Figure 5.20). The implication of this transition are discussed in the following with examples of test results.

Figure 5.32 shows the evolution of the vertical displacement w with the rotational displacement $2R\theta$ for three tests with similar characteristics, but performed under different vertical loads V' (20 N, 100 N and 200 N). For the test under $V' = 20$ N the caisson's upward movement is steady with negligible recovery. The final uplift of caisson A monotonically rotated (test FV27.3.2A) was less than 0.8 mm (see Figure 5.3(d)). Whilst the total uplift of caisson A cyclically rotated under $V' = 20$ N shown in Figure 5.32 is almost 3 mm. This reveals that the caisson upward movement obtained in a monotonic loading can be totally different from that obtained in a cyclic loading.

From Tables 5.1 and 5.2 test FV31.4.2A had a final uplift under $V' = 100$ N of $w_f \approx \frac{\delta w^p}{2R\delta\theta^p} \cdot 2R\theta_f = -0.25 \cdot 1.65 = -0.4$ mm. This compares very well with the final uplift observed in Figure 5.32 for the test under $V' = 100$ N. After an initial small uplift the caisson rocks following the same trajectory in each cycle returning always to the same

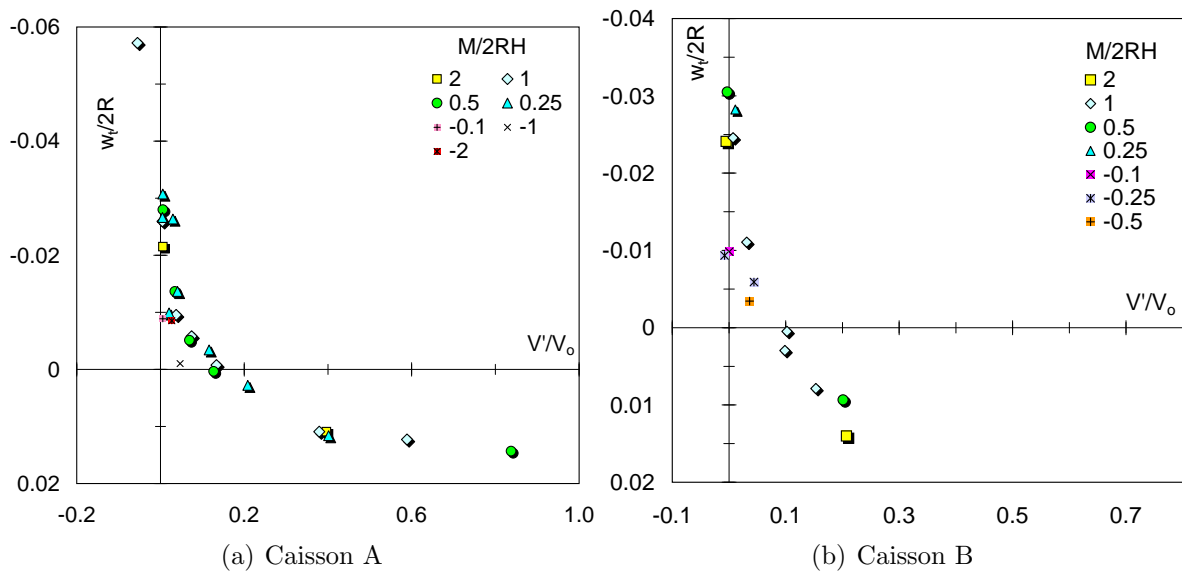


Figure 5.31: Variation of the total vertical displacement with the normalised vertical load $\frac{V'}{V_o}$ and load ratio $\frac{M}{2RH}$

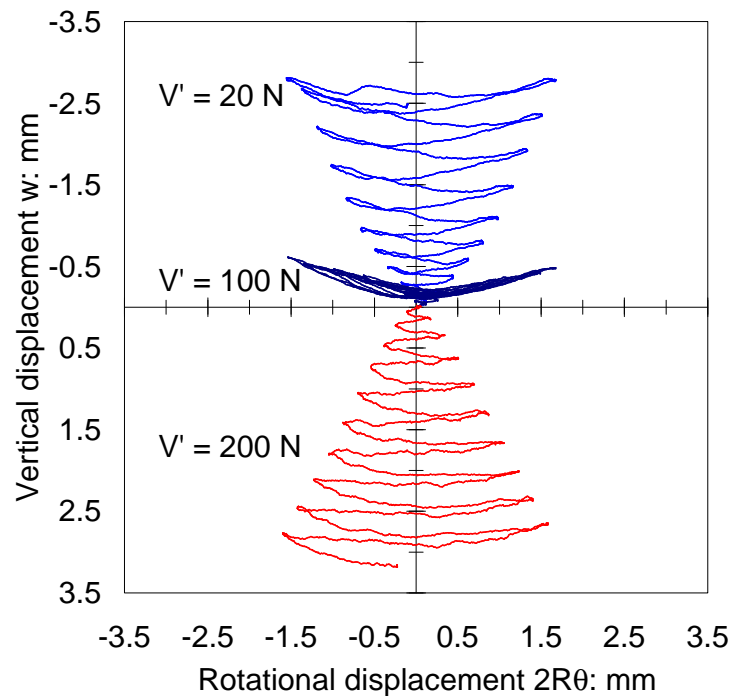


Figure 5.32: Ten cycles tests under $\frac{M}{2RH} = 1$. Test FV73_12_2A, $V' = 20$ N; test FV80_13_2A, $V' = 100$ N; test FV104_20_3A, $V' = 200$ N

point in the center. This absence of net vertical movement after each cycle has important implications in modelling, since it gives evidence of the parallel point. The parallel point derives its name from the fact that a velocity vector located in the parallel point has no vertical displacement component, therefore the velocity vector becomes parallel to the deviatoric load or radial displacement axis. Due to the zero increment of the plastic vertical displacement the yield surface size does not change. Furthermore, the parallel point establishes the boundary between heave and settlement of the footing (Cassidy, 1999), and the loading regime does not influence the caisson vertical movement response.

The third test carried out under $V' = 200$ N shows the steady settlement of the caisson during each cycle. Although no monotonic test was performed at $V' = 200$ N, it is believed that the final w will not reach more than a 1 mm if the slope of the first cycle shown in Figure 5.32 were followed. The effect of V' on the development of heave or settlement is also illustrated in Figure 5.33(a), where the w values correspond to reversals coinciding with the peak moment loads (Villalobos, 2004). Figure 5.33(b) shows that for caisson B the parallel point is located at a vertical load of about 50 N (test FV129_24.3B,

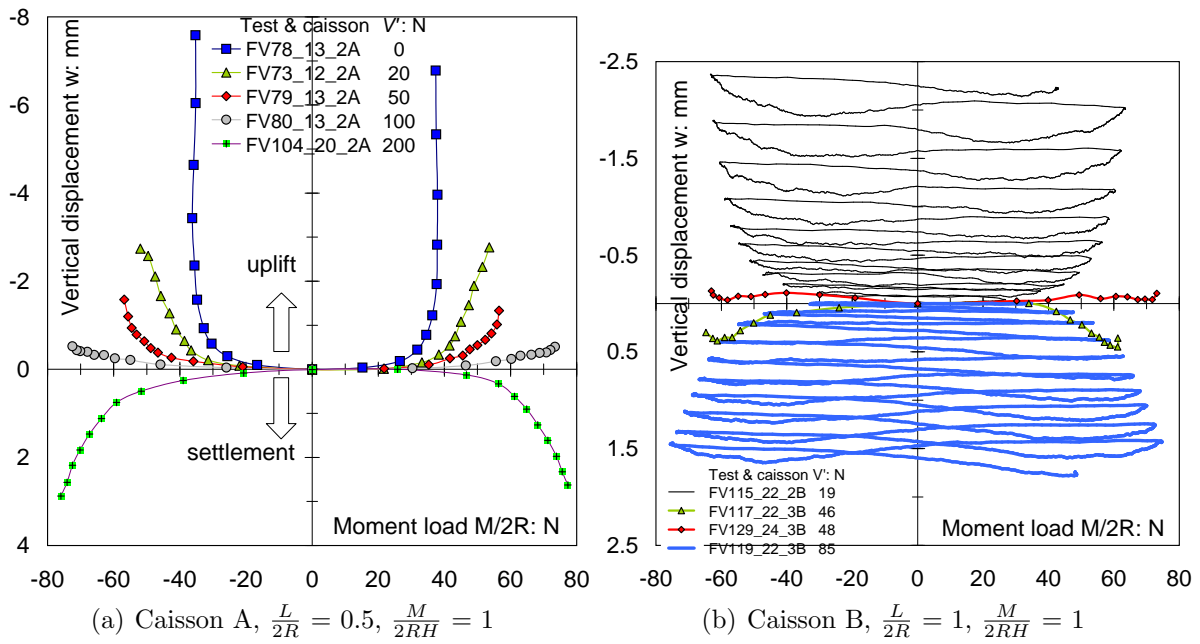


Figure 5.33: Vertical displacement *versus* moment load showing peaks and curves

$V' = 48$ N). Figures 5.34(a) and 5.34(b) show the vertical displacement of two tests for the last four and three cycles respectively. The trajectory of the curves follows the sequence illustrated by the arrows, although non-symmetry is visible in Figure 5.34(a) due to the non symmetric loading. Unloading and reloading reproduce the same trajectories but for opposite moment loads. A caisson rocking with increasing amplitude of rotation and far from the parallel point increases its net vertical displacement after each cycle.

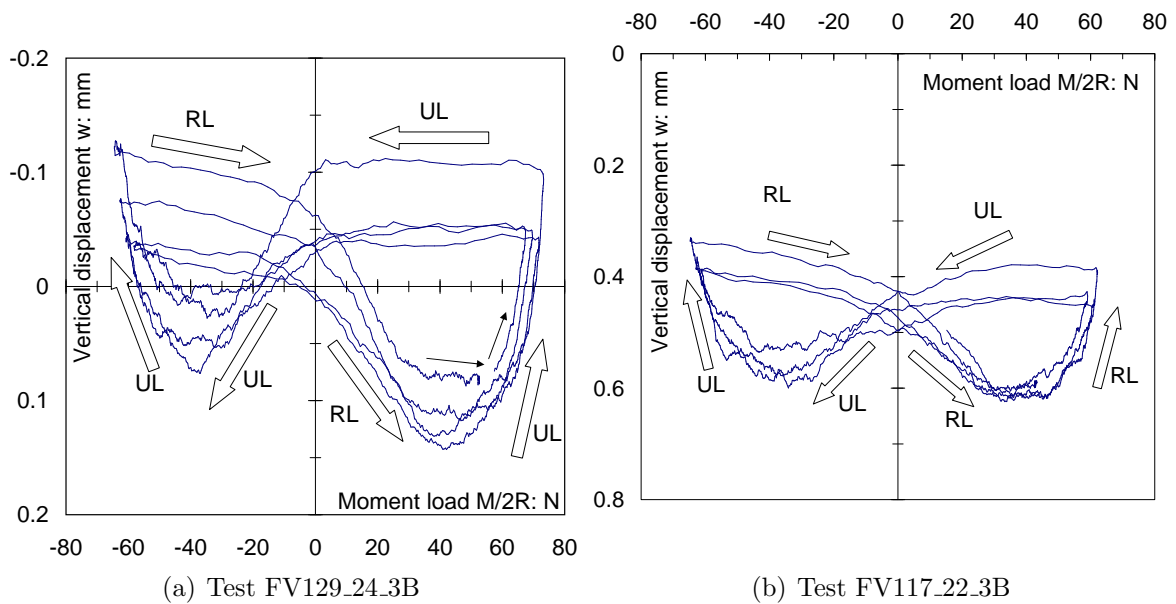


Figure 5.34: Vertical displacement *versus* moment load showing trajectories under reloading RL and unloading UL

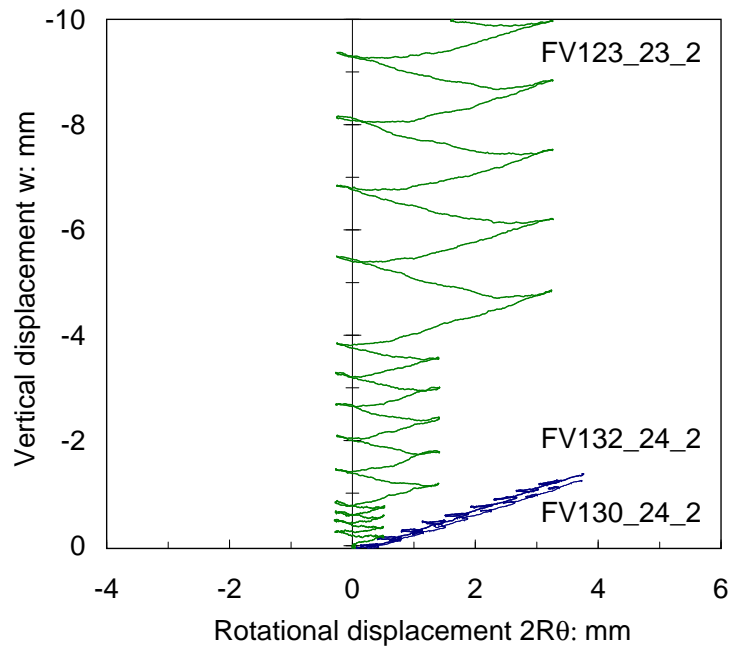


Figure 5.35: Vertical displacement *versus* rotational displacement for tests FV130.24.2, FV132.24.2 and FV123.23.2 with caisson A under $\frac{M}{2RH} = 1$ and $V' = 0$ N

However, if the amplitude of rotation is kept constant, but the caisson increases its tilt in each cycle as shown in Figure 5.30(c) the vertical displacement response resembles a monotonic loading regime. Figure 5.35 shows that despite the large rotation suffered by the caisson under $V' = 0$ N the net vertical displacement is less than -1.5 mm, much less than the -7 mm reached in test FV78.13.2A (Figure 5.33(a)). As mentioned before, this type of loading is more likely to be encountered offshore, therefore, large caisson uplifts due to large rotation amplitudes are less probable to occur under low V' .

5.6 CONCLUSIONS

A series of drained monotonic and cyclic rotational and translational tests under constant vertical load were carried out using model caissons in loose, dry sand. A combined loading system was applied to caissons of two different aspect ratios to study their behaviour. The results obtained allow expressions for the yield surface and flow rule to be established within hyperplastic models.

5.6.1 Monotonic moment capacity

The highest foundation resistance was found for moment and horizontal loads applied in opposite directions for a load ratio around -0.5. However, for design purposes the worst loading condition was found for moment and horizontal loads having the same direction of application. In order to investigate a wider loading spectrum it was necessary to study various load ratios.

Moment test results proved that the moment resistance is a function of the vertical load and the caisson aspect ratio. Caisson uplift was observed in tests with low vertical load, diminishing with the increase of the vertical load.

Rotational and translational tests were performed on caissons, including the application of tension loads. It is concluded that a caisson can resist moment loads even under such unfavourable conditions. This evidence was incorporated within the yield surface expression by means of the tension parameter t_o .

The yield surface formulation can capture appropriately the measured yield points at low vertical loads by including the tension parameter t_o . In addition, the caisson thickness ratio was found to affect the yield surface parameter values. The use of the plastic metacentre decouples the moment and horizontal loads, which eliminates the eccentricity bias when comparing the yield surface dimension parameter h_o .

Related to the flow rule, it was found that an associated flow rule can describe incremental rotational and horizontal displacements, but a non-associated flow rule was necessary for the appropriate description of vertical displacement increments. Additional tests would be required in case of studies with high vertical loads to determine the parameter a_{V_2} and also the yield surface parameter β_2 .

5.6.2 Cyclic moment capacity

From the analysis of cyclic moment loading, it was possible to note more clearly the effect of the vertical load on the moment capacity. A higher moment resistance was obtained when the vertical load was increased in a similar way as with monotonic loading. However, the caisson upward movement was found not to be comparable with that obtained from monotonic tests. A much larger uplift of the caisson was observed for very low vertical loads. However, the caisson reached a transition state where no further uplift occurred and settlement developed instead. This transition state was referred as the parallel point and was found to be at values of $\frac{V'}{V_o} = 0.13$ and 0.10 for caisson aspect ratios of 0.5 and 1 respectively. However, results from the monotonic moment loading tests suggest a value of $\frac{V'}{V_o} \approx 0.3$.

Cyclic tests proved to obey the Masing's rules, which has important implications in modelling. In addition, monotonic tests can be used to construct a backbone curve according to comparisons with cyclic tests under similar conditions. Stiffness degradation during each cycle was observed. The secant shear modulus G diminished with the increase in rotation and horizontal displacement respectively.

Further investigation is necessary to include the effect of caisson installation by suction on the monotonic and cyclic moment response. In particular, the study of partially drained and undrained conditions to assess how the pore fluid pressure may affect or not the caisson loading response.

From the yield surface determined multiple yield surfaces of different sizes can be generated to model monotonic or cyclic behaviour. A preliminary study using a hyperplastic model with one yield surface and isotropic hardening showed that the modelling of the incremental response was sensitive to the association factors. Further parametric studies are necessary to calibrate and validate hyperplastic models.

Chapter 6

MOMENT LOADING OF CAISSONS IN SATURATED SAND

Abstract

This chapter focuses on the study of monotonic and cyclic moment loading of suction caisson foundations installed into saturated sands. Firstly, a water-saturated sand was used to study drained conditions. Results of moment capacity tests under low vertical load from caissons installed by pushing and by suction are presented and compared. Caissons installed by suction had lower moment capacity than caissons installed by pushing. Furthermore, it was observed that more uplift occurred in caissons installed by pushing than in caissons installed by suction. However, no substantial differences in foundation stiffness and plastic deviatoric displacement increments were found. Secondly, a series of moment loading tests in oil-saturated sand were performed to study the effect of undrained and partially drained conditions. It was found that the caisson moment capacity was drastically reduced under undrained conditions due to large pore pressure build-ups. The caisson moment capacity under partially drained conditions was found to be similar to that under drained conditions due to the presence of suction, especially under tensile or very low vertical loads. The caisson vertical movement observed was small compared with results under drained conditions.

6.1 EXPERIMENTS IN WATER-SATURATED SAND

6.1.1 Load paths

It has been pointed out in Chapters 3 and 4 that the loading experienced by the soil due to the caisson installation can influence the in-service performance. The results shown in Chapter 5 correspond to caissons installed into dry sand by pushing. The aim of this chapter is to study the performance of caissons installed by suction due to the importance that this installation method may have on the subsequent loading response. Before presenting the experimental results it is useful to show a simple conceptual analysis of the load paths followed by a caisson installed using the two different methods.

Possible load paths in a pushed installation, including subsequent moment loadings, are illustrated in Figure 6.1. It is assumed that drained conditions prevail, however, excess pore pressures (not featured in the figure) can appear even under slow penetration rates ($\dot{h} < 1$ mm/min) in soils with very low permeability ($k < 2 \cdot 10^{-7}$ m/s). The sign of the excess pore pressures developed will depend on the initial specific volume and stress level. For example, in a dense sand the excess pore pressures will be negative, resulting in the short term in the increase of the shear strength and stiffness. Therefore, the penetration resistance will be higher in a dense sand, but higher resistance will imply a better performance once installed and subjected to combined loads during operation.

Figure 6.1(c) depicts the load-penetration curve during pushed installation, also called self-weight or jacking installation. The final caisson penetration at $V_c = V_o$ is prior to subsequent unloading at $V_3 > V_2 > V_1$, resulting in the maximum vertical load which establishes the size of the yield surface, as shown in dashed lines in Figure 6.1(a). Because the unloading reaches a very low value of V_3 compared with V_o , the yield surface contracts due to relaxation. A moment loading event under constant V_3 generates the $\frac{M}{2R} - 2R\theta$ and $w - 2R\theta$ curves as depicted in Figure 6.1(b). The $\frac{M}{2R} - 2R\theta$ curve is at the top, resulting in the highest yield point $\frac{M_y}{2R}$, whilst the $w - 2R\theta$ curve is at the bottom, resulting in zero vertical displacement. Since no vertical movement occurs the resultant flow vector is

parallel to the $\frac{M}{2R}$ and H axis, which is denoted as the parallel point as depicted in Figure 6.1(a). The hardening shown in the $\frac{M}{2R} - 2R\theta$ curves is illustrated in Figure 6.1(a) as an isotropic expansion of the internal yield surface to the external yield surface (dashed line). According to Byrne and Houlsby (2001) this hardening should be attributed to the deviatoric displacements since no vertical displacement occurred.

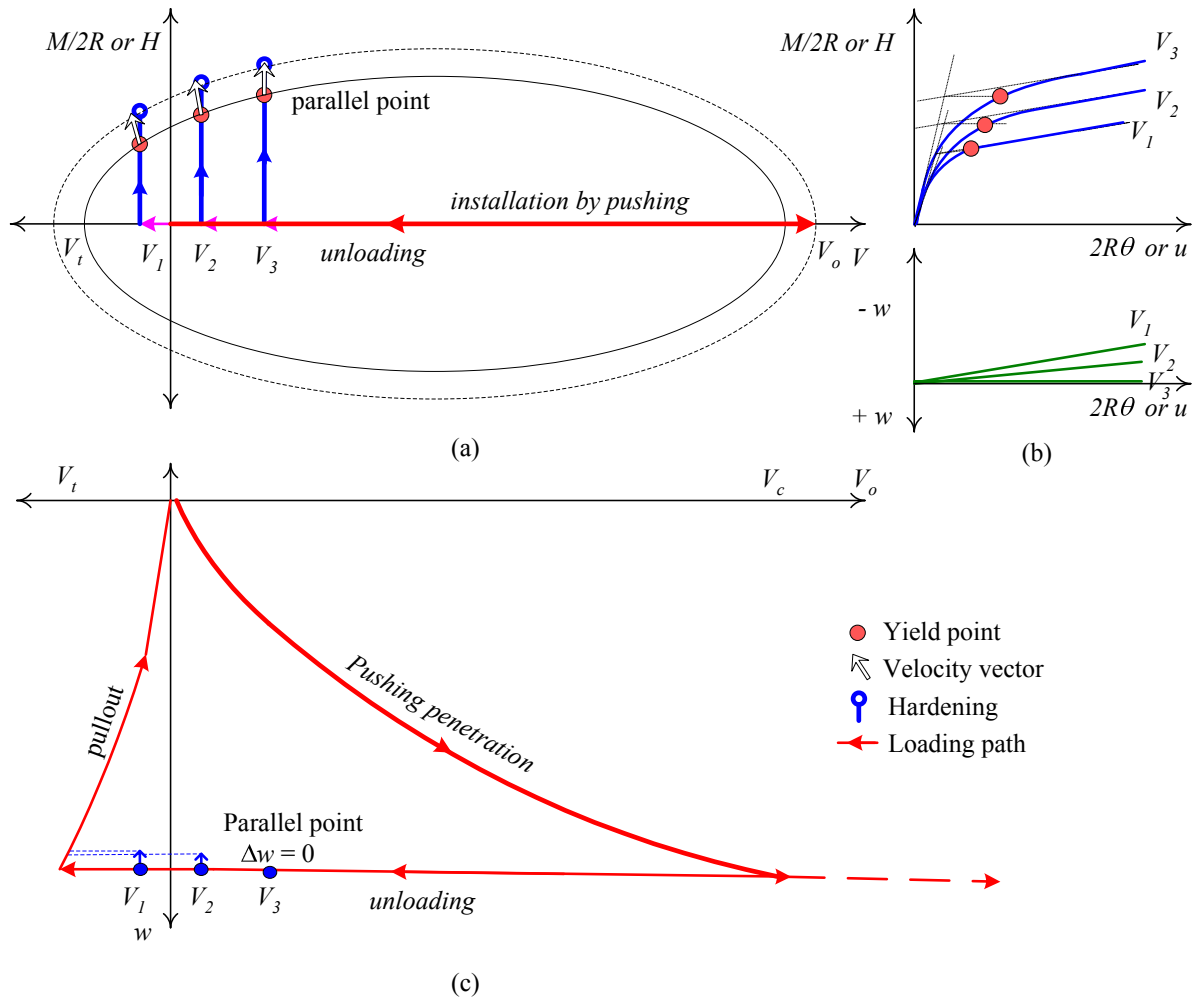


Figure 6.1: Pushing installation: (a) load paths for monotonic moment loading events under low vertical load and the resulting yield surface, (b) load-displacement curves and vertical-rotational displacement curves, and (c) installation curve, including unloading and pullout

Unloading to $V_2 < V_3$ and the subsequent moment loading event under constant V_2 results in a lower moment capacity with a reduced value of $\frac{M_y}{2R}$. The $w - 2R\theta$ curve for V_2 shows an upward movement of the caisson, resulting in the tilted flow vector on the yield point in Figure 6.1(a). The deviatoric displacements contribution to the hardening is evident since negative vertical displacement (caisson upward movement) generates softening, *i.e.* the contraction of the yield surface.

The last example illustrates the case of unloading to a tensile load V_1 , followed by a moment loading event under the constant tension V_1 . The $\frac{M}{2R} - 2R\theta$ curve and $\frac{M_y}{2R}$ value are the lowest and the $w - 2R\theta$ curve is the highest which represents the largest caisson uplift. The hardening assumed based on experimental evidence becomes smaller.

It is important to note that in the pushed installation unloading and the subsequent moment loading event at constant V' is analogous to a triaxial test of a soil sample that is normally consolidated to $p' = p'_o$, unloaded to a certain overconsolidation ratio $\frac{p'}{p'_o}$ and then sheared at a constant σ'_v . The displacement flow vectors at yield in the footing correspond to the strain flow vectors at yield in the triaxial test. This analogy was first established by Houlsby and Martin (1992) following the work by Tan (1990).

Possible load paths followed by a caisson installed by suction are illustrated in Figure 6.2. The moment loading events are exactly the same as for the pushing installation. However, the $\frac{M}{2R} - 2R\theta$ and $w - 2R\theta$ curves as well as the $\frac{M_y}{2R}$ values are not necessarily identical to those obtained in the pushed installation examples. The load-penetration curve is definitely different since the initial pushed penetration stops at a value that represents the applied self weight (for example V_2 or V_3). Subsequently, the caisson penetrates assisted by the suction applied inside the caisson compartment. Therefore, V_o becomes a function not only of the vertical displacement, but also of the suction, which defines a surface in the (V_o, w, s) space. This allows penetration at low V' with high suction s , but when s reduces V_o increases. In analogy with a triaxial test the foundation is in a normally consolidated condition since V_o has not been experienced by the foundation.

The fluid flow taking place owing to the suction is responsible for the reduced penetration resistance. This is caused by the gradient of excess pore pressures within the soil, which reduces the effective stresses and hence the soil strength. As a consequence, the resulting yield surface is smaller, since at the end of a suction installation V_o is smaller than that at the end of a pushed installation. However, the small yield surface starts to

grow as long as the flow regime ceases. Note that for the suction installed caisson the yield surface will significantly expand due to excess pore pressure dissipation.

Despite the complex changes in effective stresses that occur during the suction assisted penetration, once the combined loading is applied, the caisson can be assumed to have ‘recovered’ the potential bearing capacity V_o corresponding to the final penetration of a pushed installation (shown in Figure 6.2(c) as the V_o curve with $s = 0$). Whether the recovery is complete or partial will depend mainly on the time given to the excess pore pressures to dissipate. The hypothesis of complete recovery of V_o assumes that modifications in the soil index and mechanical properties due to the suction installation do not affect the value of V_o . The validity or not of this hypothesis and its consequences on the

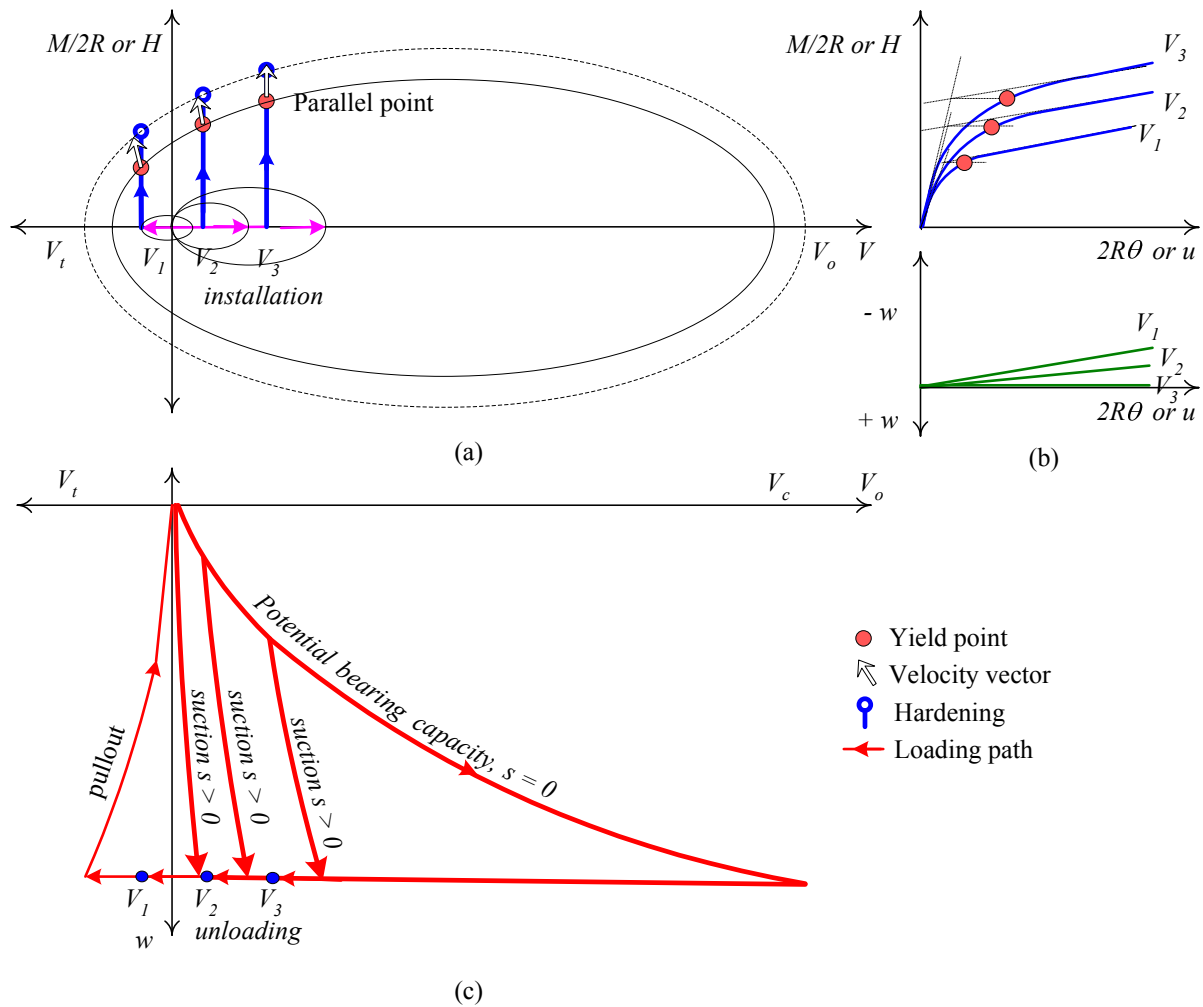


Figure 6.2: Suction installation: (a) load paths for monotonic moment loading events under low vertical load and the resulting yield surface, (b) load-displacement curves and vertical-rotational displacement curves and (c) installation curve, including potential bearing capacity

subsequent caisson response was investigated and presented subsequently.

6.1.2 Response of caissons installed by pushing and by suction

The use of dry sands has the advantage of easier and faster sample preparation than if the sand were saturated. This allows a larger number of tests to be carried out at different densities. To mitigate the effects of scale, the tests beds were chosen to be relatively loose as discussed in Chapter 2. However, using pushed installation by applying increasing vertical loads is different from the procedure that has to be used in the field, *i.e.* the suction assisted installation method. The different installation techniques may impose different stress paths on elements of soil around the caisson, which in turn affect the caisson load path as described above. Therefore, it is necessary to carry out experiments similar to those in the dry sand, but on caissons installed by suction, to observe if there are any fundamental differences in foundation behaviour.

In a fully saturated ground the resistance of shallow foundations is reduced since in general the effective unit weight of a submerged soil is about half that of a dry soil. Because of submergence, the bearing capacity of shallow foundations (section §3.2) may become significantly smaller, even assuming that N_γ does not reduce due to saturation (Ausilio and Conte (2005) suggest a reduction of 40% for $\phi' = 20^\circ$, 30° , and 40°). Moreover, influence of the water flow through the soil may add seepage forces to the gravity forces. However, this component may increase or decrease the bearing capacity depending on whether positive or negative excess pore water pressure is developed.

The moment loading tests are similar to those reported by Byrne *et al.* (2003) and Villalobos *et al.* (2004), and consist of rotation and translation of the footing at a specified load ratio $\frac{M}{2RH}$ and constant V' . The submerged vertical load V' was directly obtained from the rig load cell, *i.e.* without subtracting the excess pore pressure or the suction underneath the lid multiplied by the lid section area sA (refer to sections §4.3.3 and §7.1.2 for discussions about the definition of V').

According to the scaling rule $n_t = n^{\alpha-2}$ determined from expression (6.7), the time of dissipation of any excess pore pressure is one thousand times faster in the laboratory when compared with a caisson one hundred times larger in the field. If $\alpha = 0$ implies that no attempt of considering stress level is made, which scales the time of dissipation to ten thousands times faster agreeing with the consolidation dimensionless time equation (6.6). Tests were carried out at a rotational velocity $2R\dot{\theta} = 0.01$ mm/s to obtain drained conditions as in the dry sand tests. Using this rotational velocity, water as the pore fluid, sand type and caisson sizes a fully drained condition is obtained. To verify this, a non-dimensional footing velocity used by Finnie (1993) for studying spudcan footings in calcareous soils suggests that for the following expression:

$$v_n = \frac{vL}{c_v} \quad (6.1)$$

from which an undrained footing response is obtained for $v_n > 10$ and a drained footing response is obtained for $v_n < 0.01$. The caisson skirt length L is taken as the relevant dimension for drainage since the caisson is laterally loaded (for this series of tests the caissons have $L = R$). Taking the Redhill sand coefficient of consolidation $c_v = 0.19$ m²/s (Kelly *et al.*, 2004) results in a non-dimensional footing velocity v_n of $5 \cdot 10^{-6}$. Despite some differences between Finnie's test conditions (R as the relevant dimension, soil type, density, vertical loading instead of rotational) drained conditions are deduced. Although offshore loading conditions can induce partially or even undrained conditions, the study of drained conditions provides a reference to compare the caisson moment resistance. Moreover, results from both installation methods can be more difficult to interpret for partially drained conditions. The study of the combined loading of suction caissons in undrained and partially drained conditions will be presented in section §6.2.

Table 6.1 summarises the data from moment loading tests, and further data about initial conditions can be found in Chapter 4 (V_o , initial R_d and γ' , *etc.*). The test label FV6_5_2CS refers to the sample 6, site 5, test 2 within site 5, caisson C and installation

Table 6.1: Summary of moment capacity tests in Redhill sand

Test	V' N	K_{mi} $\frac{N}{mm}$	K_{hi} $\frac{N}{mm}$	$\frac{M_y}{2R}$ N	H_y N	K_{mf} $\frac{N}{mm}$	K_{hf} $\frac{N}{mm}$	$\Delta u'$ kPa	G MPa	$\frac{\delta u^p}{2R\delta\theta^p}$	$\frac{\delta w^p}{2R\delta\theta^p}$
FV6_5_2CS	5.5	146	89	6.5	5.0	5	12	-0.35	2.5	0.444	-0.376
FV7_5_2CP	6	120	120	14.1	12.9	2	4	-0.2	2.5	0.529	-0.436
FV6_2_2CS	40	120	85	12.0	11.1	5	9	-0.16	2.5	0.515	-0.110
FV6_3_2CP	40	197	204	24.1	21.7	4	9	-0.25	3.0	0.503	-0.281
FV6_8_2CS	60	197	120	17.7	16.3	5	9	-0.06	3.0	0.534	-0.046
FV7_1_2CP†	60	250	250	29.0	27.0	4	7	0.4	3.5	0.528	-0.273
FV8_1_2AS	10	181	253	14.8	15.1	6	17	-0.4	2.5	0.314	-0.400
FV8_2_2AP	10	220	220	33.6	32.7	4	6	-0.45	2.5	0.583	-0.575
FV7_3_2AS	60	340	350	30.9	27.7	13	33	-0.34	2.5	0.453	-0.276
FV7_4_2AP	60	240	260	41.5	40.3	7	15	-0.42	2.5	0.459	-0.496
FV7_1_4AS	120	647	406	40.2	39.0	16	42	-0.2	4.0	0.385	-0.119
FV7_2_2AP	120	652	290	55.4	50.8	15	33	-0.36	4.0	0.544	-0.288

All tests carried out at $\frac{M}{2RH} = 1$, †air valve open

by suction S. The parameter values were determined following the procedures presented in Chapter 5. Figures 6.3(a) and 6.3(b) show for the two different installation methods the $\frac{M}{2R} - 2R\theta$ curves and $H - u$ curves of caisson C under a constant $V' = 40$ N and load ratio $\frac{M}{2RH} = 1$. It is clear from these figures that the installation method has a strong effect on the load-displacement behaviour. The load-displacement curves have been interpreted by fitting linear expressions to the initial elastic and final plastic components of the curve (Chapter 5). The intersection of the lines represents a yield point. The yield points and the fitted straight lines are shown on the figures, and the values of the yield loads and the initial and final stiffness are collected in Table 6.1. In terms of yield it was found that suction installation reduces the yield loads as can be observed in Figure 6.4(a). This reduction is more pronounced for caisson C, possibly as a consequence of the smaller thickness ratio.

The displacements paths are shown in Figures 6.3(c) and 6.3(d), where the elastic component of the total displacement has been subtracted to obtain the plastic displacement. Values of the shear modulus G used and the ratios obtained between plastic horizontal and rotational displacement increments $\frac{\delta u^p}{2R\delta\theta^p}$ and between plastic vertical and rotational displacement increments $\frac{\delta w^p}{2R\delta\theta^p}$ are summarised in Table 6.1. The vertical displacement variation during the caisson rotation is shown in Figure 6.3(d). Whilst $\frac{\delta u^p}{2R\delta\theta^p}$ values from suction and push installed caissons are very similar, values of $\left| \frac{\delta w^p}{2R\delta\theta^p} \right|$ are larger for cais-

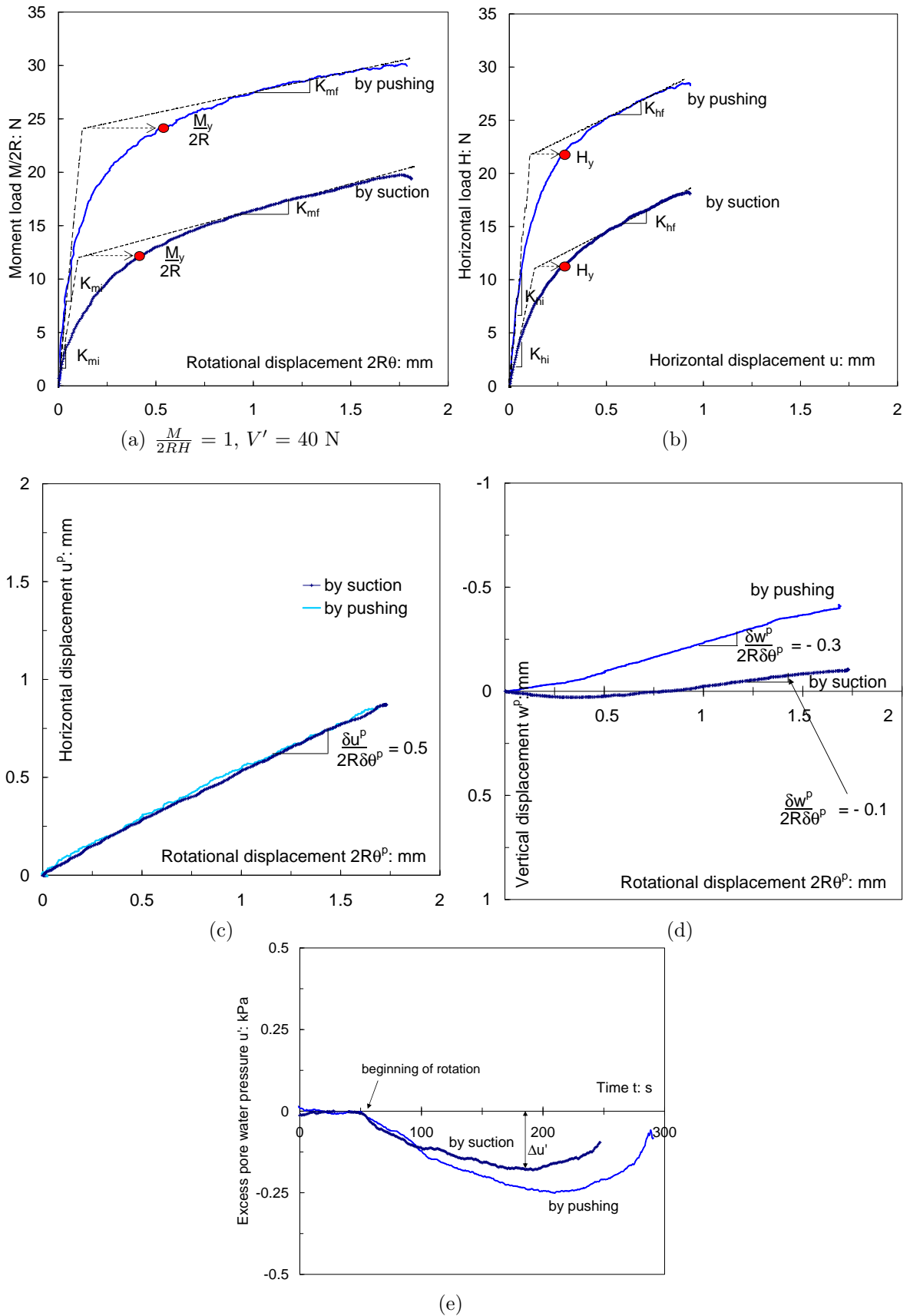


Figure 6.3: Comparison between the response of a caisson installed by suction, test FV6.2_2CS and by pushing, test FV6.3_2CP

sons push installed as can be observed in Table 6.1 and Figure 6.4(b). This indicates that suction installed caissons experience a lower magnitude of uplift compared with caissons installed by pushing. Moreover, the parallel point is reached for the caissons installed by suction at a value of $\frac{V'}{V_o} \approx 0.16$, which is close to value obtained for cyclic tests in dry sand. Although from Figure 6.4(b) the point of intersection of the pushing data with the $\frac{V'}{V_o}$ axis is less evident, it is likely a value of $\frac{V'}{V_o} \geq 0.3$, closer to value obtained from monotonic tests in dry sand.

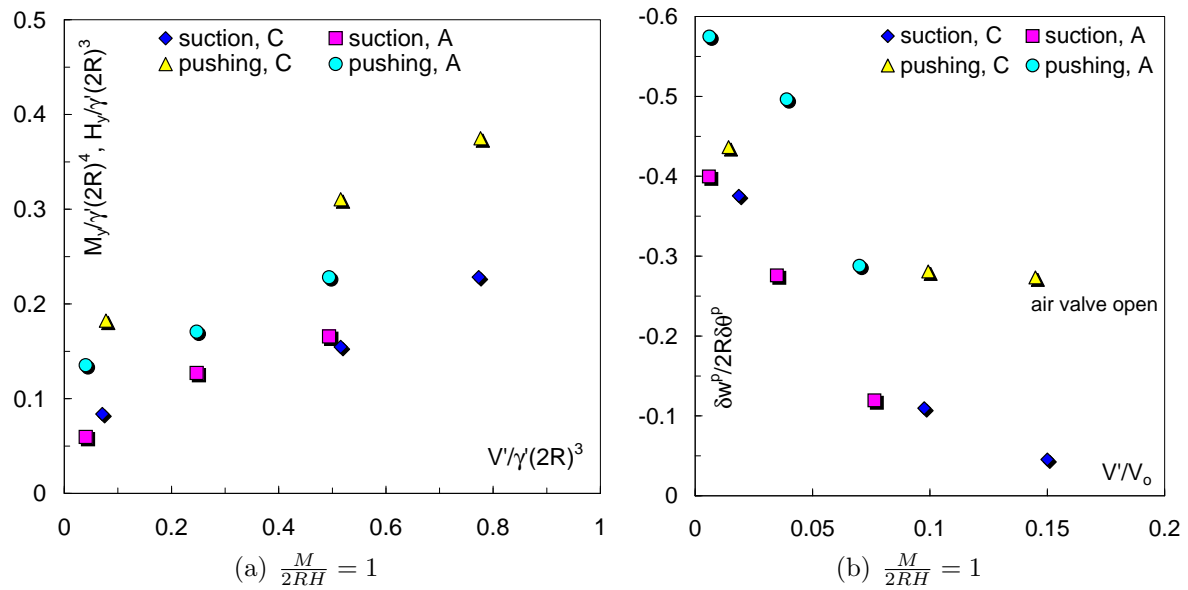


Figure 6.4: (a) Normalised yield loads as a function of $\frac{V'}{\gamma'(2R)^3}$, (b) plastic increment ratio between vertical and rotational displacements as a function of $\frac{V'}{V_o}$

The excess pore pressure variation in excess of the hydrostatic pressure $\Delta u'$ measured underneath the caisson lid is shown in Figure 6.3(e) for both moment capacity tests. Negative values of u' were caused by the upward movement of the caisson, being slightly higher for the caisson push installed due to the larger uplift. Note that at the end of the tests a considerable percentage of the suction generated under the caisson lid has dissipated. Although u' underneath the caisson lid does not necessarily represent the variation u' around the caisson skirt, it can be interpreted as a reference for further analysis.

6.1.3 Foundation stiffness

The straight lines fitting the initial and final slopes of the load-displacement curves represent the foundation stiffness. Dimensionless expressions of the foundation stiffness

were obtained dividing the normalised load by the normalised displacement (equation (6.4)) as proposed by Kelly *et al.* (2006a), resulting in:

$$\frac{K_m}{(\gamma' p_a)^{0.5} (2R)^{1.5}}; \quad \frac{K_h}{(\gamma' p_a)^{0.5} (2R)^{1.5}} \quad (6.2)$$

Figures 6.5(a) and 6.5(b) show that there is no consistent difference between results from both installation methods. In Figure 6.5(a) is hard to differentiate the data, and in Figure 6.5(b) the pushing data is in between the suction data showing a separation between data from caisson A and C. For caisson A the dimensionless value of K_{hi} is higher for the suction case, in contrast to the case for caisson C. It is worth pointing out that the initial stiffness determined for push installed caissons covered a larger range of load for a same displacement than for suction installed caissons. In other words, the initial linear response is larger for the caissons installed by pushing than for the caissons installed by suction. The final foundation stiffness determined at the end of the load-displacement curves are plotted in Figures 6.5(c) and 6.5(d) using the normalisations in (6.2). An enormous reduction in stiffness occurs as a consequence of progressive yielding. In Figure 6.5(c) no considerable difference is observed between suction points and pushing points, although slightly higher values for suction points appear. In Figure 6.5(d) suction points are located above the pushing points (except for one point), but again no systematic difference can be established. In conclusion, foundation stiffness was not significantly affected by the installation method.

6.1.4 Yield surface and velocity vectors

The yield loads $\frac{M_y}{2R}$ summarised in Table 6.1 were initially used to trace the yield surface in the $\frac{M}{2R} - V'$ plane for low vertical loads as illustrated with squares in Figure 6.6. Also, calculated yield surfaces are shown in Figure 6.6 using the expression (5.43), which is reproduced here:

$$y = \left(\frac{H}{h_o V_o} \right)^2 + \left(\frac{M}{2R m_o V_o} \right)^2 - 2e \frac{H}{h_o V_o} \frac{M}{2R m_o V_o} - \beta_{12}^2 \left(\frac{V'}{V_o} + t_o \right)^{2\beta_1} \left(1 - \frac{V'}{V_o} \right)^{2\beta_2} = 0 \quad (6.3)$$

in which $h_o, m_o, t_o, e, \beta_1$ and β_2 are the parameters that define the shape of the yield surface and $\beta_{12} = \beta_1^{-\beta_1} \beta_2^{-\beta_2} (\frac{\beta_1 + \beta_2}{t_o + 1})^{\beta_1 + \beta_2}$. The values of these parameters can be found in Table 5.6. These values were determined from a series of moment loading tests performed with caisson aspect ratios of 1 and 0.5 in dry sand. It is then not surprising that the calculated yield surface gives a good prediction of the experimental yield points for the pushing method. On the other hand, the yield loads are reduced by the suction application. Therefore, the calculated yield surface does not give a good prediction for the suction installation case. A second yield surface was calculated exactly as before, but including the lower tensile load. Nevertheless, the experimentally obtained yield loads are still overestimated. Also shown on Figure 6.6 are the directions of the plastic displacement increment vectors. The installation method had also an effect on the flow vectors. For

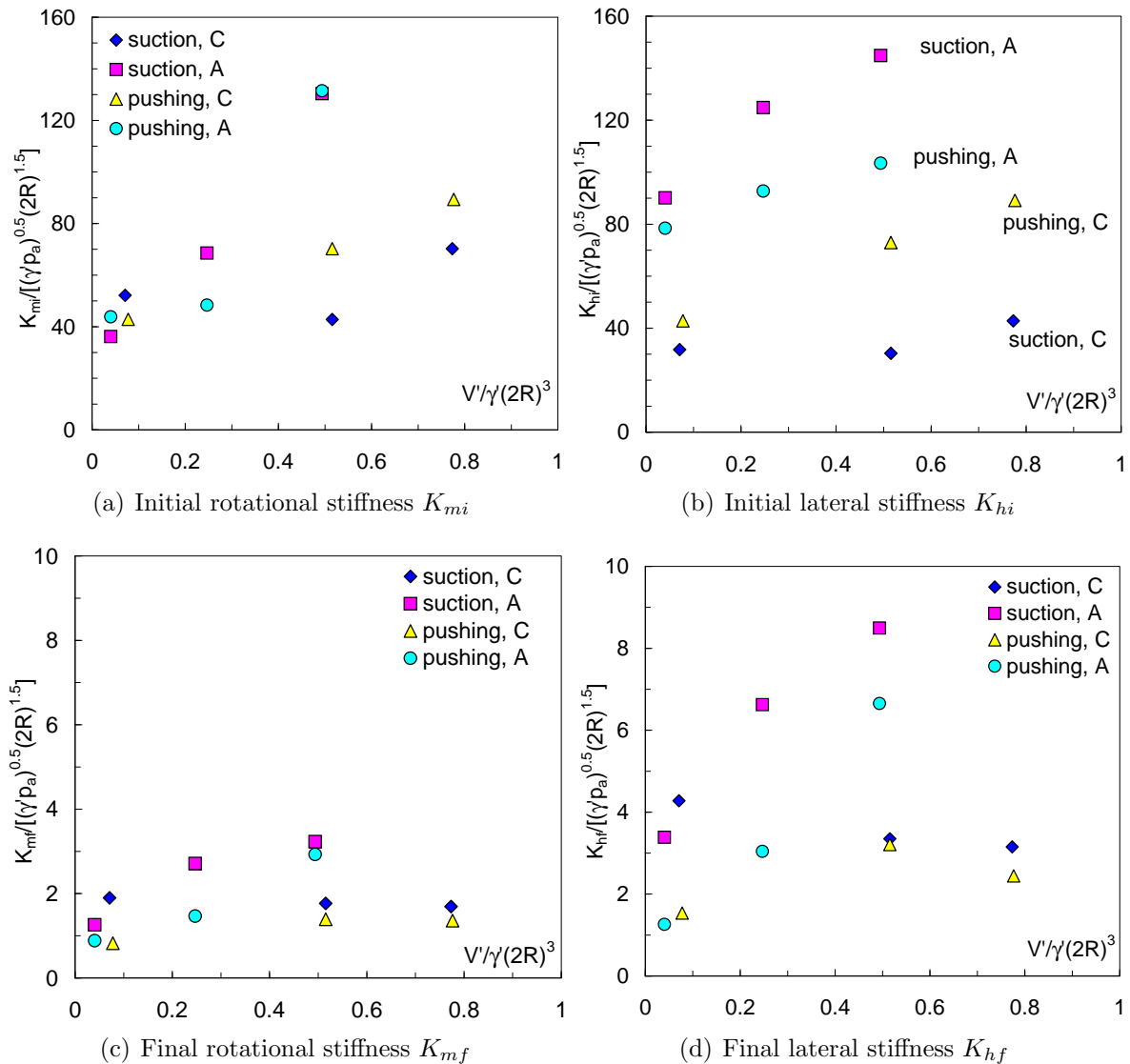


Figure 6.5: Normalised foundation stiffness

example, different directions can be observed for $V' = 40$ N and 60 N (see Figure 6.4(b) to compare the vertical and rotational ratio of plastic displacement increments for all the tests).

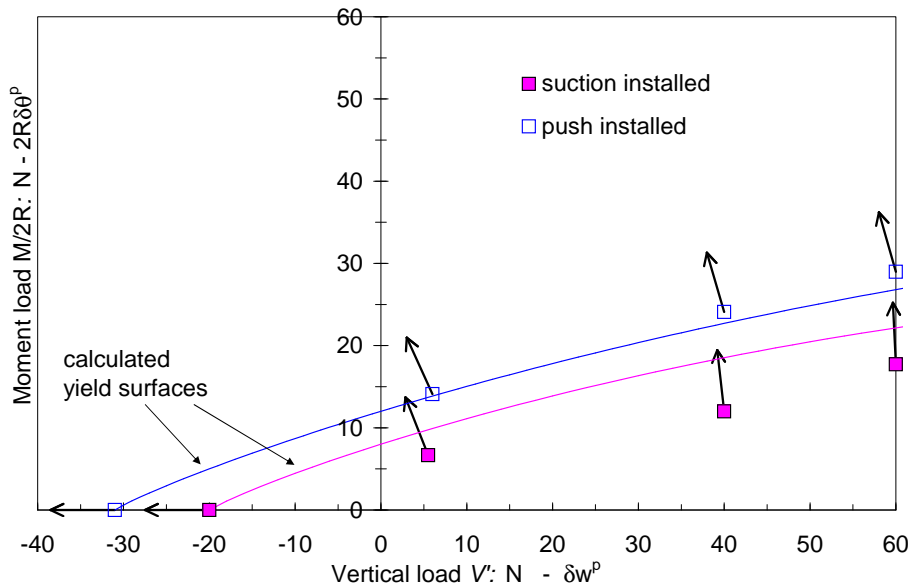


Figure 6.6: Yield points, velocity vectors and calculated yield surfaces comparing the installation method for caisson C

Results from both caisson diameters can be presented together by normalising with respect to V_o , the maximum applied vertical load. Figure 6.7 shows the normalised experimental yield points and the calculated yield surfaces. Equation (6.3) has been included in this plot with a value of $t_o = 0.064$ for the smaller footing and 0.040 for the larger footing. It is necessary to use different values of t_o in this plot because the tensile capacity scales with $2RL^2$ (equation §4.4) whilst the V_o value scales principally with $2RtL$ as discussed in section §4.3. Since the two footings have the same value of aspect ratio $\frac{L}{2R}$ but different value of thickness ratio $\frac{t}{2R}$ their tensile capacities differ on the normalised plot. However, the normalisation by V_o merges the two curves shown in Figure 6.6 for caisson C, thus suction or pushing installation has only a minor effect on the normalised curve. In more detail, however, the yield surfaces presented in Figure 6.7 serve as lower bounds for the moment capacity in the case of a caisson installed by pushing. On the other hand, it represents an upper bound for a suction installed caisson. The differences are thought to be due to disturbance in the installation process due to suction.

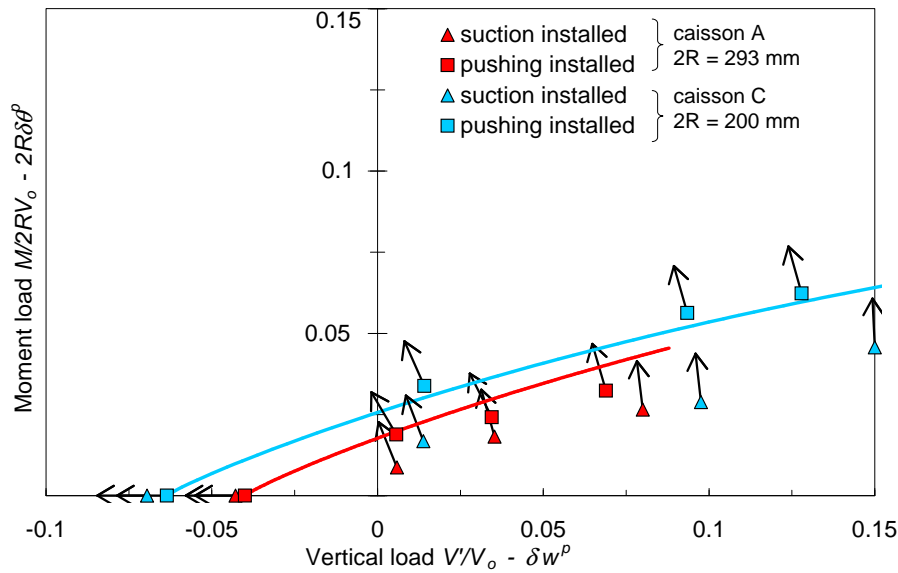


Figure 6.7: Velocity vectors, normalised yield points and calculated yield surfaces for caissons installed by pushing and by suction

The flow vectors obtained from suction installed caissons had a smaller component in the w -direction compared with the velocity vectors obtained from push installed caissons (see last column in Table 6.1). In other words, there was less uplift during the rotation of a caisson when the suction was used. This possibly implies that the soil is looser after a suction installation, and therefore dilates less when sheared.

6.1.5 Swipe tests of caissons installed by suction

Constant V' tests are analogous to critical state soil mechanics interpretation of drained triaxial testing (Martin, 1994). This analogy was first established by Tan (1990) for the case of undrained triaxial testing, from which he deduced the load path of a ‘side-swipe’ test. The zero specific volume change corresponds to zero vertical displacement. As a consequence, the yield surface obtained from swipe tests of footings is analogous to the yield locus of Modified Cam Clay model. A swipe test can also be compared with an undrained simple shear test; since no dilation is allowed the normal load is free to vary during shearing.

Swipe tests are used to trace the yield surface along different load paths and constant V' tests are conducted as probe tests to verify one point of the yield surface already traced

by a swipe test (Tan, 1990; Martin, 1994; Gottardi *et al.*, 1999; Byrne, 2000). Swipe tests have the advantage that only one swipe event is required to trace a part of the yield surface that would take several probe tests to achieve. To illustrate this, load paths of swipe tests are sketched in Figure 6.8 (compare with Figure 6.2). The fact that swipe tests are carried out under constant vertical displacement makes the flow rule analysis more complex. In this section swipe events were performed to assess the results from previous constant V' tests. Additionally, swipe tests allowed for the insertion of data not covered by the constant V' tests.

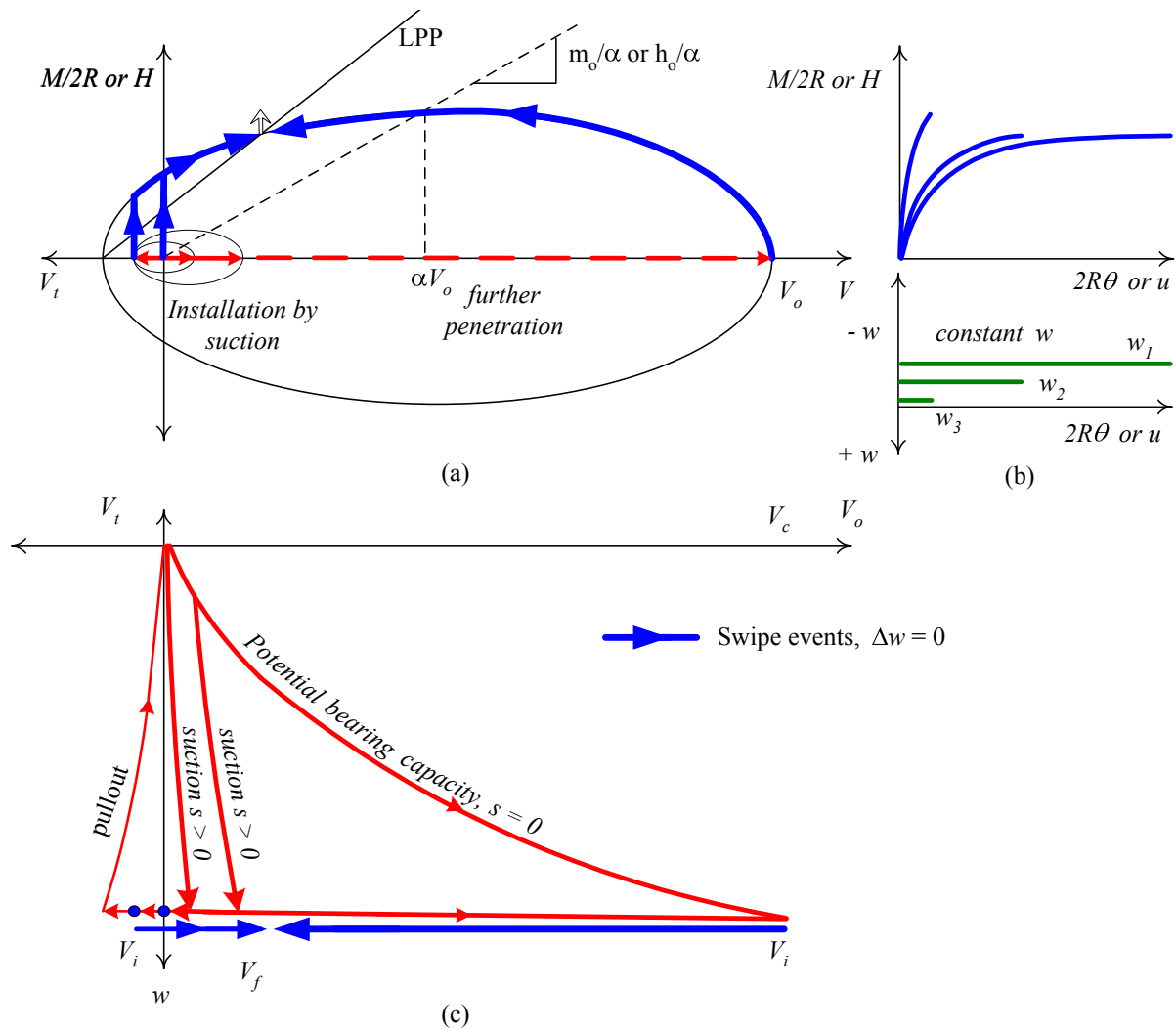


Figure 6.8: Suction installation: (a) load paths followed in swipe tests showing the line of parallel points LPP, (b) load-displacement curve and the resultant constant vertical displacement curve, (c) installation curve, including unloading and pullout

Rotational swipe tests were performed on caissons installed by suction. Details of the swipe tests are summarised in Table 6.2. Figure 6.9 shows normalised moment-rotation

Table 6.2: Summary of swipe tests in Redhill sand of caissons installed by suction

Test	V'_i N	V'_f N	$\frac{M}{2RH}$	$2R\theta_t$ mm	h_f mm	V_o N	$\frac{\delta u^p}{2R\delta\theta^p}$
FV10.1.2A	-27	365	1	4.8	133	2400	0.542
FV9.3.3C	-5	24	1	2	99.7	480	0.501
FV9.3.4C	-1	87	1	5	100	480	0.451
FV9.4.4C	-10	140	1	10	91	420	0.484
FV9.1.2C	420	180	-1	0.7	98.8	450	-0.282

curves obtained from the swipe tests, where a wide range of applied rotational displacement $2R\theta_t$ can be observed. Note the much stiffer response of the swipe event starting close to V_o (test FV9.1.2C) compared with the other tests starting close to V_t . Figure 6.10 shows results from the swipe tests together with yield points from the constant V' tests (Figure 6.7) in the deviatoric-vertical load plane normalised by V_o (axes not scaled). The deviatoric load Q was introduced in section §5.2.4 and $\frac{Q}{V_o}$ corresponds to the square root of the three first terms in equation (6.3). The curve of test FV10.1.2A progresses very close to the yield points obtained in the constant V' tests for caissons installed by suction (the triangular points). Test FV10.1.2A was conducted immediately after the suction installation.

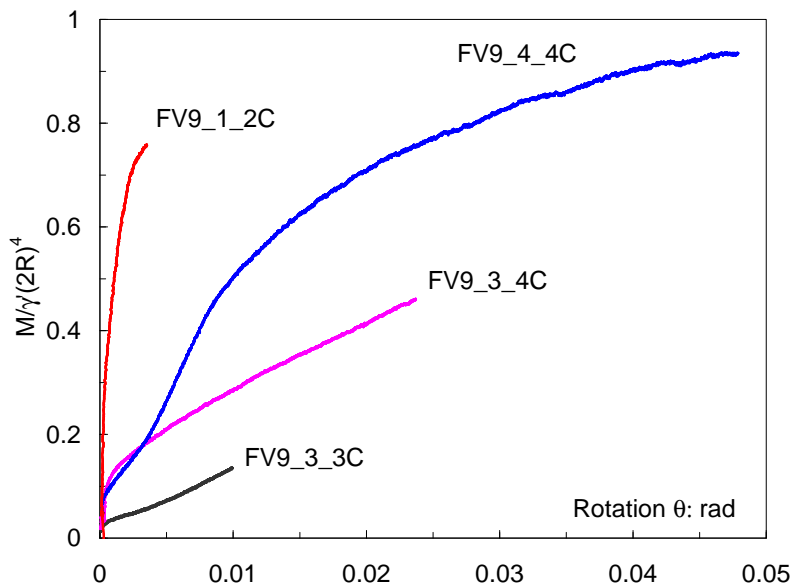


Figure 6.9: Normalised moment-rotation curves from swipe tests

Three other swipe tests using caisson C were also performed starting from low V' . The curve of test FV9.3.3C follows the triangular yield points along its short path. In addition, the curve of test FV9.3.4C initially follows the triangular yield points but from

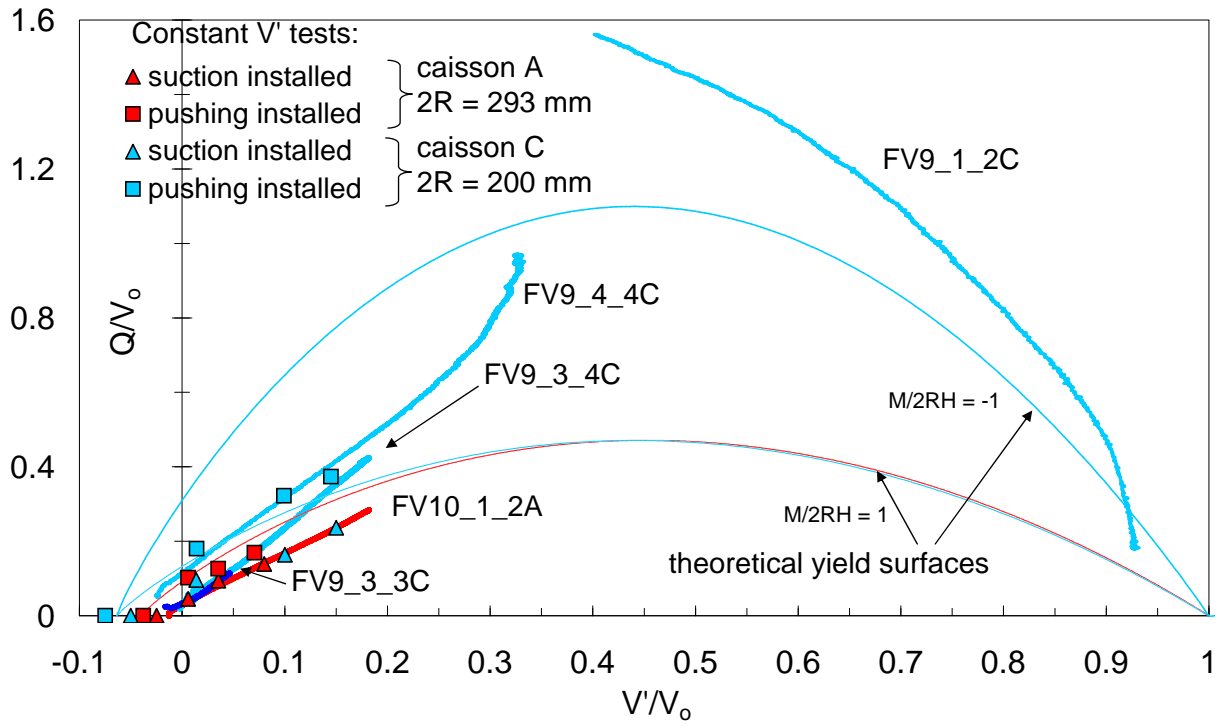


Figure 6.10: Swipe tests in the normalised deviatoric and vertical load plane comparing with results from constant V' tests and calculated yield surfaces for $\frac{M}{2RH} = 1$ and -1

half way through follows a steeper path close to the square yield points that represent caissons installed by pushing. The curve of test FV9_4_4C has higher moment capacity following clearly the square points. A reason for this disparity may be due to disturbance (densification) of the sand sample after a previous test (the last number 3 or 4 represents a second or third test in the same site after installation). Time between the end of the suction and the beginning of the rotation may induce an ageing effect, which causes recovery of the soil strength lost during the suction installation. Another reason can be the effect of the skirt wall thickness as commented previously in Figure 6.4(a). For a thicker skirt wall, more soil is disturbed during penetration, which reduces the influence of the installation method.

To be applicable to offshore loading conditions of wind turbines, swipe tests were carried out for low vertical loads as for the constant V' tests. However, swipe test FV9_1_2C was performed to explore the yield surface from V' close to V_o . This is equivalent to the application of a very large vertical load on the caisson after the suction installation. The moment-rotation curve of this test in Figure 6.9 shows that large moment loads were

obtained at small rotations. Because this test was carried out under a load ratio of -1, another yield surface was calculated, which underestimates that tracked by the swipe event. A load ratio of -1 can represent for instance the case where the wind blows in opposite direction to tidal currents. Note that a curved yield surface was traced by this swipe event. Conversely, the yield surface shape traced by the low vertical load swipe events can be approximated by straight lines. These lines might seem to represent a steady load state or lines of parallel points LPP in analogy with the critical state line CSL (Tan, 1990). However, from Figure 6.9 a convergence of moment loads as rotation progresses under fixed vertical movement is not possible to observe.

It is worth pointing out that a variation of the initial value of V_o occurs during a swipe event when V' diminishes (Gottardi *et al.*, 1999; Byrne, 2000; Martin and Houlsby, 2001). Although the vertical displacement remains constant, the elastic vertical displacement is negative and as a consequence appears an identical positive plastic vertical displacement. This increase in the plastic vertical displacement induces an increase in V_o . To account for this increase the elastic vertical stiffness of the foundation K_v^e and the plastic vertical stiffness of the foundation K_v^p should be assessed. K_v^e can be obtained from the caisson unloading-reloading response. For caisson C the order of magnitude of K_v^e was around 1600 N/mm. Whilst K_v^p was in the order of 10 N/mm before the caisson lid made full contact with the sand ($h < L$), and around 100 N/mm when the caisson lid is in full contact with the sand ($h \geq L$). However, for these stiffness values a negligible variation of V_o is obtained as $\frac{K_v^p}{K_v^e} \ll 1$.

6.1.6 Cyclic loading tests under constant vertical load

The purpose of carrying out cyclic moment loading tests was to investigate the effect of different soil conditions and caisson geometries on the cyclic response of suction caissons. To this end, this section will continue the analysis performed in section §5.5. To compare appropriately results from different soil conditions and caisson geometries normalised quantities will be extensively used. For that reason, prior to exploring the

experimental results, the dimensionless quantities used to scale loads and displacements will be reviewed.

The dimensionless quantity of the moment $\frac{M}{\gamma'(2R)^4}$ or horizontal load $\frac{H}{\gamma'(2R)^3}$, can be compared only if similarity of $\frac{V'}{\gamma'(2R)^3}$, $\frac{L}{2R}$ and $\frac{M}{2RH}$ is achieved. From results of moment loading tests, the yield points in the moment-vertical load plane were found to follow a linear relationship for low vertical loads. Figure 6.11 shows for four load ratios the straight lines fitted. In the straight line $y = a + bx$ shown in Figure 6.11, a is the intersection with the ordinate, b is the slope and the intersection with the abscissa corresponds to the maximum dimensionless tensile load $\frac{V_t}{\gamma'(2R)^3} = -0.2$, so that $\frac{a}{b} = 0.2$. From this linear relationship is possible to compare results at yield from different $\frac{V'}{\gamma'(2R)^3}$ and similar $\frac{M}{2RH}$ or vice versa. For example, data with load ratio of -1 can be multiplied by $\frac{y_1}{y_{-1}}$ to compare with data having a load ratio of 1 and similar value of $\frac{V'}{\gamma'(2R)^3}$. Extrapolations to scale different vertical loads and load ratios are limited to $\frac{V'}{\gamma'(2R)^3} < 0.3$ and $\frac{L}{2R} = 0.5$.

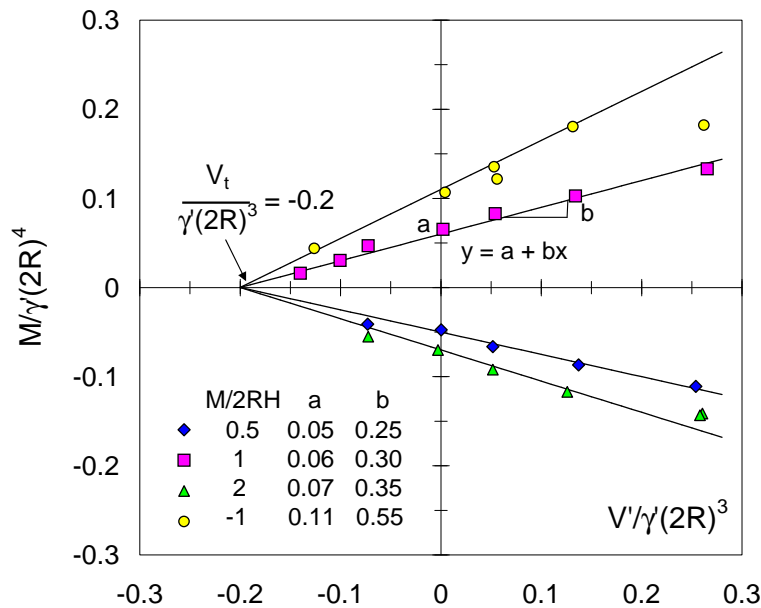


Figure 6.11: Straight lines fitted to the yield points for caissons with $\frac{L}{2R}$, showing two set of information above the abscissa and two below for clarity

A dimensionless displacement quantity that allows for comparisons from different sand unit weights and caisson diameters is suggested by Kelly *et al.* (2006a). For the vertical displacement w , the rotational displacement $2R\theta$ and the horizontal displacement u ,

dimensionless quantities can be expressed as follows:

$$\frac{w}{2R} \left(\frac{p_a}{2R\gamma'} \right)^{0.5}; \quad \theta \left(\frac{p_a}{2R\gamma'} \right)^{0.5}; \quad \frac{u}{2R} \left(\frac{p_a}{2R\gamma'} \right)^{0.5} \quad (6.4)$$

Expressions in (6.4) were derived by Kelly *et al.* (2006a) from the elastic load-displacement relationship (5.9) and the exponent 0.5 comes from the elastic shear modulus in equation (5.14), which attempts to account for the stress level.

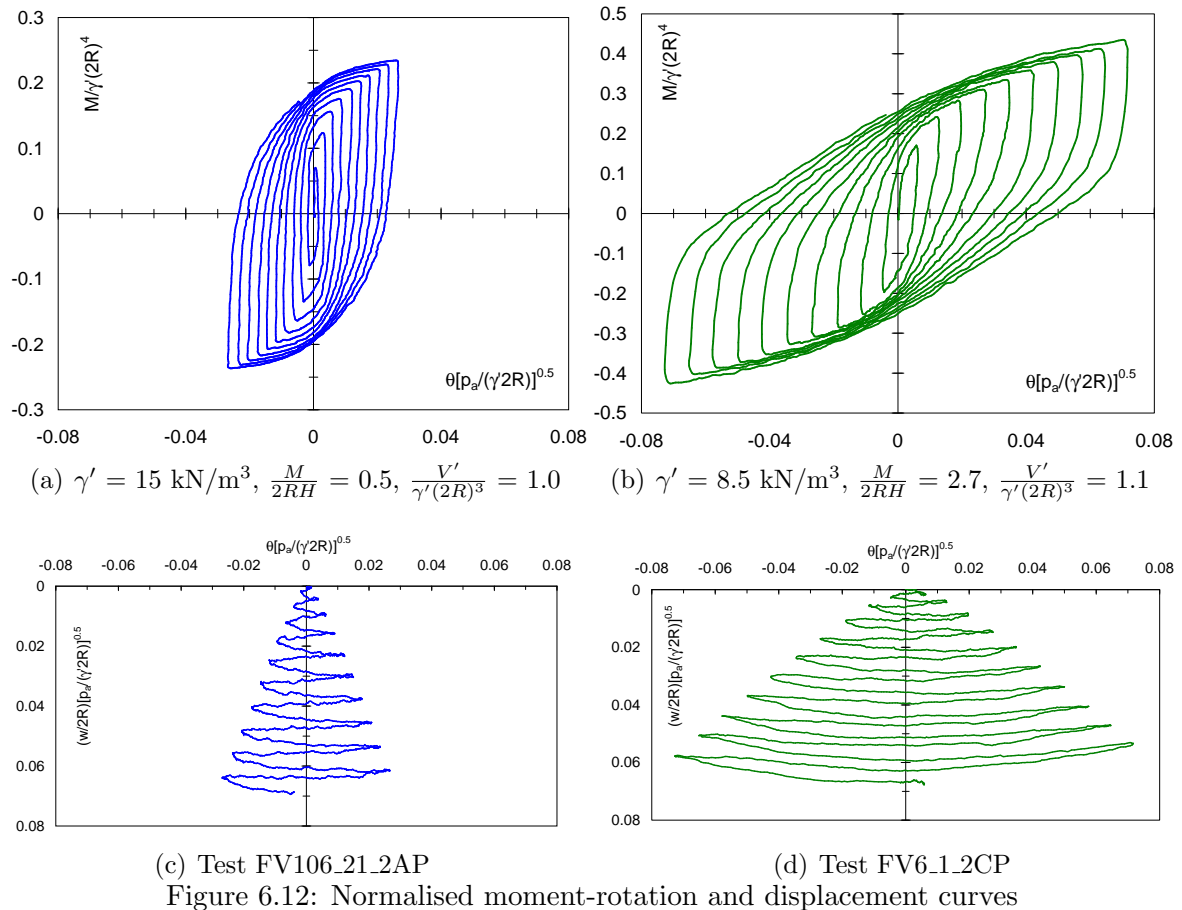
The results from cyclic moment loading tests in a saturated Redhill sand will be presented and compared with results from loose dry Leighton Buzzard sand shown in section §5.5. For details of the cyclic moment tests in saturated sand see Table 6.3 and for the tests in dry sand see Tables 5.7 and 5.8. The majority of the tests were carried out in dense sands since in several of the offshore wind farm sites around the UK coasts dense sands are expected to be found. In addition, results in dense sands are useful to compare with previous results in loose sands by assessing dimensionless expressions.

Table 6.3: Summary of cyclic moment loading tests

Test	$V'_{average}$ N	$\frac{V'}{\gamma'(2R)^3}$	V_o N	R_d %	γ' kN/m ³	$\frac{M}{2RH}$	w_t mm
FV9_3_2CS	8	0.1	500	92	10.21	1	-4
FV9_2_2CS	42	0.5	443	92	10.21	1	2.7
FV6_1_2CP	73	1.1	122	26	8.47	2.7	1.8
FV6_4_3CS	100	1.2	420	92	10.21	1.1	1.1
FV9_5_2AS	15	0.06	2616	92	10.21	1	-7.3
FV7_3_3AS	60 - 200	0.25 - 0.82	1724	74	9.663	1.1	0.4

Test FV6_1_2C was carried out in a loose water-saturated Redhill sand, whereas test FV106_21_2A was carried out also in a loose but dry Leighton Buzzard sand. Both tests had a similarly high value of $\frac{V'}{\gamma'(2R)^3}$, but different $\frac{M}{2RH}$ values. Figures 6.12(a) and 6.12(b) show the normalised moment-rotation curves for both tests, which can be compared when the normalised rotations are similar (second and tenth cycles respectively in Figure 6.12(a)). It is observed a stiffer response of the caisson in dry sand than for the caisson in saturated sand. The amplitude of rotation applied to both caissons was the same, but due to the different soil and caisson geometry, the normalised or comparable rotation, was more than double for the smaller caisson. It is worth noticing in Figures

6.12(c) and 6.12(d) that regardless the differences between both tests a similar normalised cyclic vertical displacement w was obtained. This would be expected for caissons with similar normalised vertical load, showing that the effect of submergence which affects the unit weight is covered appropriately by the normalisations for these particular conditions. Note that settlement occurs on the unloading parts of each cycle.



Henceforward, tests in saturated sand will correspond only to dense samples. A comparison of hysteresis loops from a test in saturated sand with backbone curves from tests in dry sand is now presented. Figures 6.13(a) and 6.13(b) show normalised cyclic load-displacement curves obtained from test FV9_5_2AS and two backbone curves from tests FV73_12_2AP and FV78_13_2AP (carried out in a loose and dry Leighton Buzzard sand), where $\frac{M}{2R}$ is interchangeable with H because the tests were conducted at $\frac{M}{2RH} = 1$. The moment backbone curves of tests FV78_13_2AP and the test in dense saturated sand are fairly close, leading to a good agreement between normalised moment capacity, but not so good agreement for the normalised rotation. Broadly similar dissipation of energy is caused by the unloading-reloading cycles for both tests. For a caisson with aspect ratio

of 0.5 the hysteresis loops are less open, so less energy is dissipated. The horizontal load backbone curves do not compare so well as with the moment curves.

Figure 6.13(c) shows that the caisson uplift was significant in the saturated sand as that observed in test FV78_13_2AP, which had a smaller value of $\frac{V'}{\gamma'(2R)^3} = 0.01$. The V' values that appear in Tables 5.7, 5.8 and 6.3 are an average of fluctuations or variations as shown in Figure 6.13(d) in the form of uniform pressure $\frac{V'}{A}$ underneath the caisson lid. Moreover, suction appears as a consequence of the upward movement following the $\frac{V'}{A}$ fluctuation. Note that there are two peaks and two troughs in the pore pressure response in each cycle. This phenomena is related with the vertical displacement of the caisson.

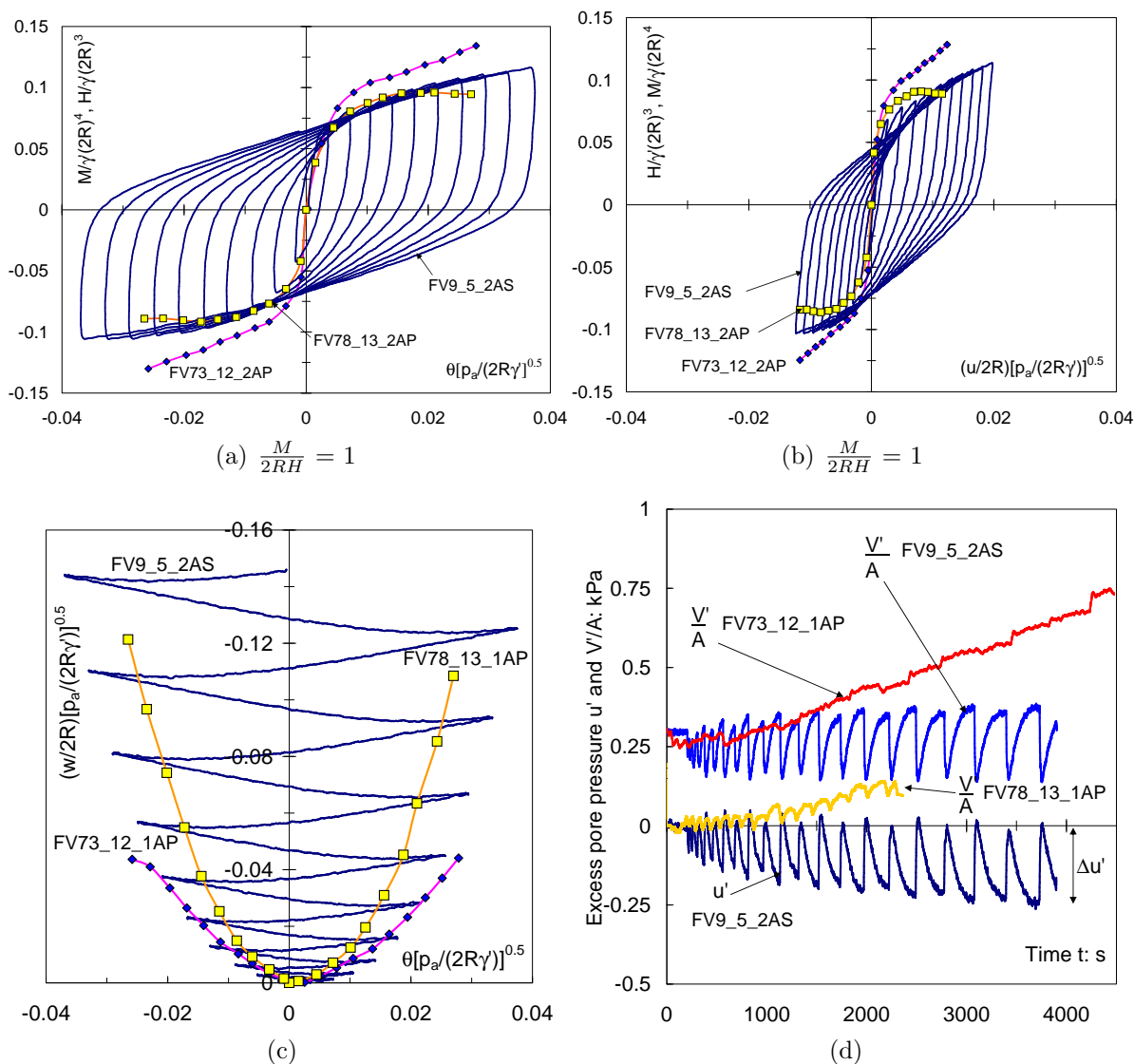


Figure 6.13: Comparison of normalised backbone curves, normalised vertical displacement curves, excess pore pressure and vertical uniform pressure underneath the lid

A non-symmetric one-way cyclic rotation test was conducted at $\frac{M}{2RH} = 1$ and is compared in Figure 6.14(a) with a similar type of test as those described in section §5.5.2, but at a different value of $\frac{V'}{\gamma'(2R)^3}$. Surprisingly the normalised moment loads are comparable when the rotations are similarly scaled, despite the large difference in the value of $\frac{V'}{\gamma'(2R)^3}$. As expected the caisson under very low $\frac{V'}{\gamma'(2R)^3}$ had upward movement, whereas the caisson under high $\frac{V'}{\gamma'(2R)^3}$ exhibited settlement.

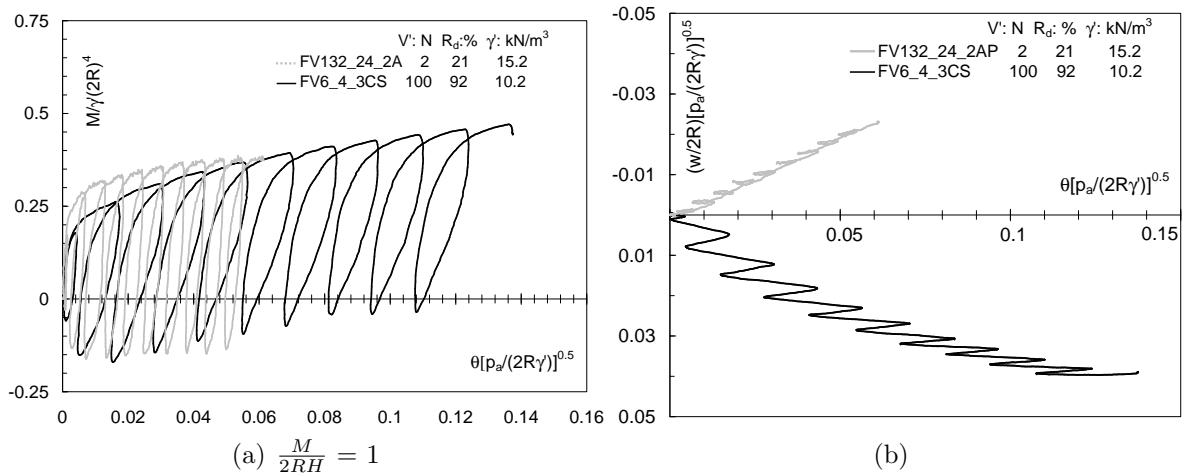


Figure 6.14: Comparison between two one-way cyclic rotation tests

It is also important to consider results from field tests (if available) to understand whether or not similar foundation response patterns are reproduced in the laboratory. Figures 6.15(a) and 6.15(b) show the moment-rotation curve and the vertical-rotational displacement curve respectively obtained in a field trial at Luce Bay by Houlsby *et al.* (2006) using a caisson 3 m diameter and 1.5 m skirt length. Kelly *et al.* (2006a) have compared the field moment resistance with laboratory tests especially programmed to scale $\frac{V'}{\gamma'(2R)^3}$ and $\theta[p_a/(\gamma'2R)]^{0.5}$. According to Kelly *et al.* a reasonable agreement occurred only when in the laboratory the caisson was installed by pushing and subsequently rotated under small rotations ($\theta[p_a/(\gamma'2R)]^{0.5} < 0.01$). Caissons installed by suction did not reach more than half of the moment resistance of the caisson installed by pushing due to strong sand disturbance during suction installation. Furthermore, a difference in hysteresis loop shape for higher normalised rotation was attributed to gapping in the field not observable in the laboratory tests.

A cyclic moment-rotation curve was obtained in the laboratory without the particular intention of replicating the field trial results and unlike Kelly *et al.*'s tests the caisson was installed by suction. Figure 6.15(a) shows this curve with the typical shape of hysteresis loops previously found. The normalised moment was amplified by a factor of 1.2 to scale the difference between $\frac{V'}{\gamma'(2R)^3} = 0.15$ in the field and 0.098 in the laboratory (following Figure 6.11, $\frac{y_{0.15}}{y_{0.098}} = \frac{0.06+0.3 \cdot 0.15}{0.06+0.3 \cdot 0.098} = 1.2$). It can be observed that the rotation scales relatively well, however, the moment resistance for large rotations is much lower than that in the field as also observed by Kelly *et al.*. It is important to realise that in the field CPT records showed a strong increase of cone resistance with depth (in the first 3 m). As shown in Figure 5.1, the caisson moment resistance is a function of the lateral earth pressure along the caisson wall. Therefore, a larger stress level with depth increases the caisson moment response.

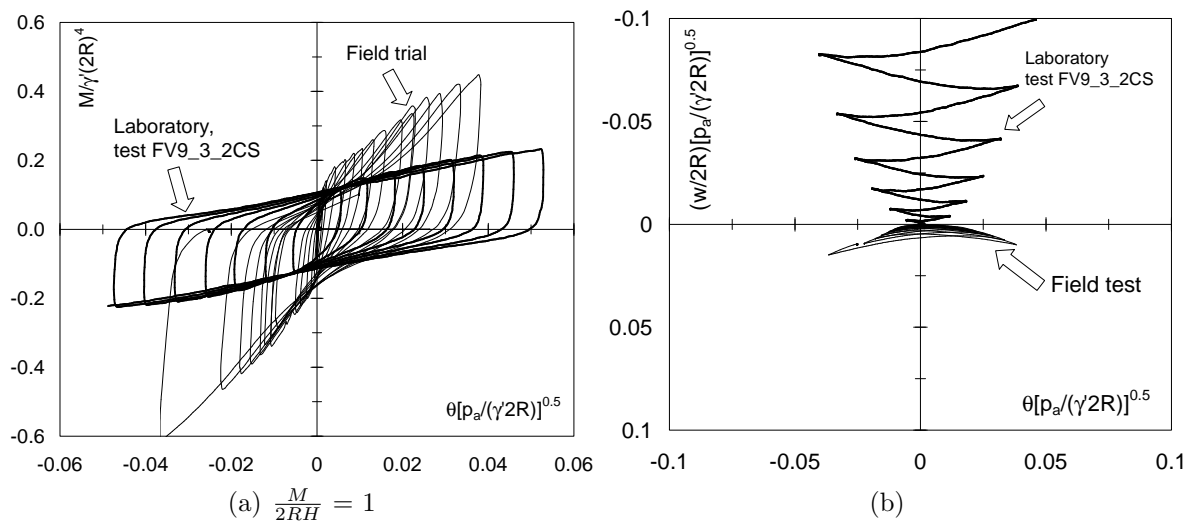


Figure 6.15: Comparison between results from the laboratory and from the field, where $2R = 3$ m, $V' = 42.4$ kN, $R_d = 80\%$, $\gamma' = 10.3$ kN/m³ (taken from Houlsby *et al.*, 2006)

Figure 6.15(b) compares the normalised vertical displacement. Whilst the caisson in the laboratory moved upwards significantly, the caisson in the field rocks with very little settlement. The high stress level induces large frictional forces on the wall that restrain the vertical movement of the caisson.

A final example represents the case of a cyclic moment loading event conducted without holding constant V' nor w , but the load ratio $\frac{M}{2RH} = 1.1$. It is observed in Figures

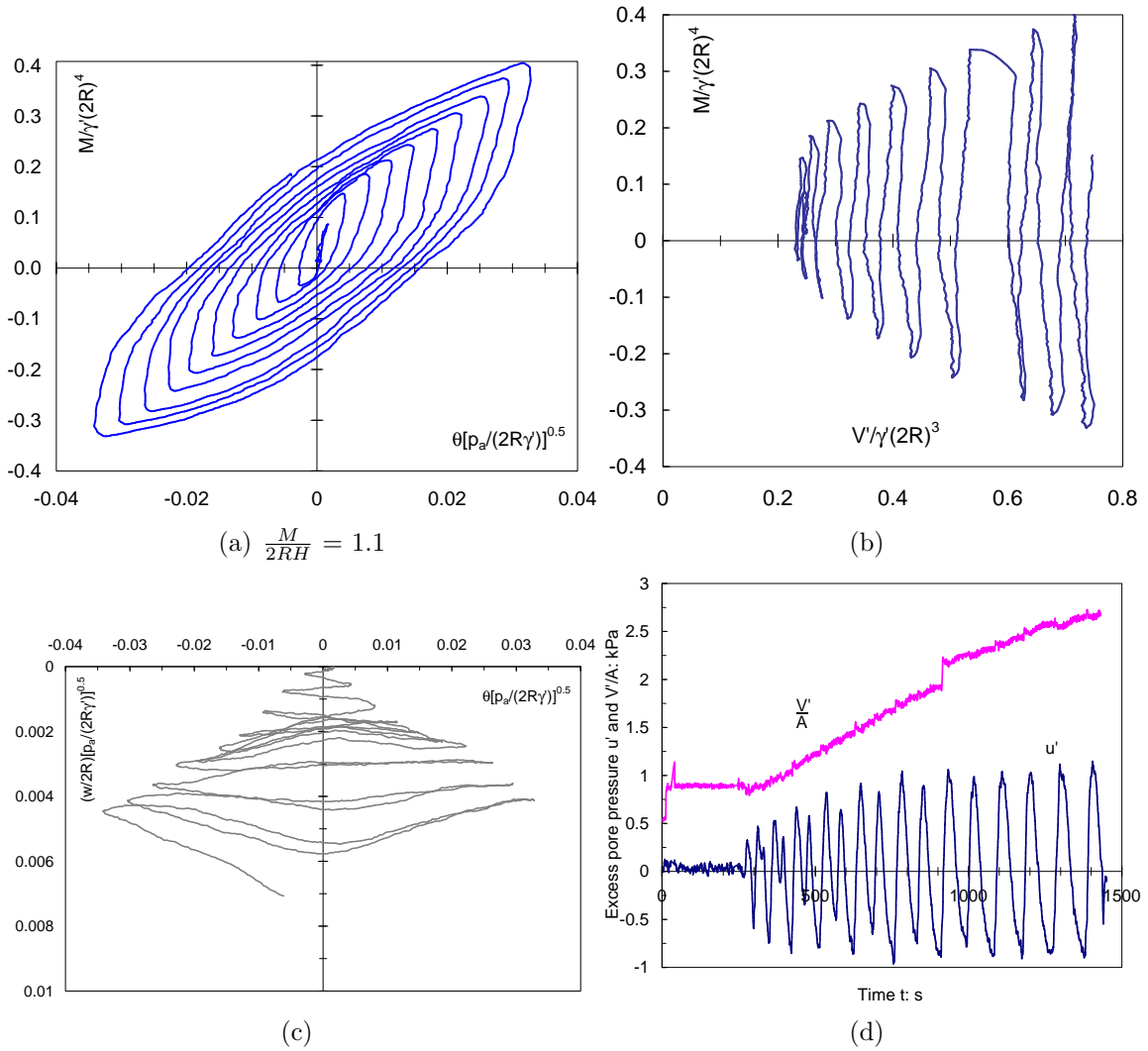


Figure 6.16: Results from test FV7_3_3AS, where only the load ratio is constant

6.16(a) and 6.16(b) that despite the pore pressure variation, the steady increase of V' during cycling causes considerable enhancement of the moment resistance. Figure 6.16(c) shows that the first three small amplitude cycles cause a noticeable settlement of the caisson. There is virtually no settlement in the next four cycles of larger amplitude, but

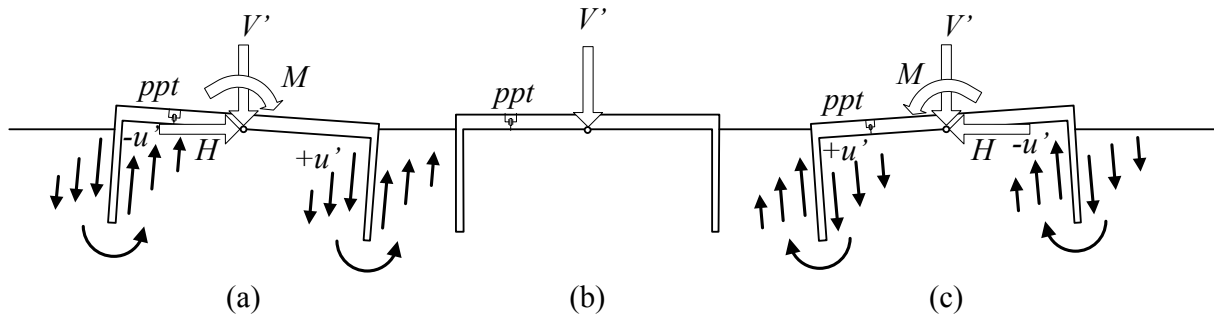


Figure 6.17: Cyclic flow caused by the cyclic rotation of the caisson

settlement occurs again in the last three largest amplitude cycles. The evolution of the excess pore pressure u' and V' (from 60 N to 200 N) can be seen in Figure 6.16(d), where $\frac{V'}{A}$ is the uniform pressure underneath the lid. The peaks values of u' stabilizes around a value of ± 1 kPa in spite of the steady increase of V' . The positive and negative values of u' are related to the position of the pore pressure transducer PPT. Whilst on one side of the lid settlement is occurring, on the other side uplift is occurring. This interesting feature of the variation of u' gives insight into the flow directions taking place around the caisson during the cyclic moment loading. According to the negative or positive values of u' the flow is assumed to be as shown in Figure 6.17. This indicates that a cyclic flow regime occurs during cycling. From the lifted side of the caisson water enters the caisson, whereas at the compressed side water leaves the caisson. A transition condition without flow occurs during unloading when the moment and horizontal loads become zero.

6.1.7 Cyclic swipe tests of suction caissons

The motivation of this part of the investigation relies on the fact that cyclic swipe events can represent a loading condition where moment and horizontal load vary with the vertical load. The fact that waves apply vertical loads as well as horizontal loads gives a physical interpretation of cyclic swipe tests in offshore problems. A wave train

Table 6.4: Summary of cyclic swipe tests of caissons installed by suction in Redhill sand

Test	V'_i N	V'_f N	V_o N	$\frac{M}{2RH}$	h mm	$\frac{\delta u^p}{2R\delta\theta^p}$
FV10.2.2AS	-25	535	2472	1	138	0.68
FV10.3.2AS	-31	150	2146	1	118	1.06
FV10.3.3AS	-26	494	2146	0.98	118	1.07
FV10.4.2DS	-23	145	641	0.48	138	-2.40
FV10.4.3DS	-22	180	641	0.52	138	-2.42

same sand sample: $R_d = 89\%$, $\gamma' = 10.1$ kN/m³

induces pressure oscillation on the seabed, then the difference between this pressure and the pressure underneath a skirted footing resting in the seabed will induce a fluctuation of the vertical load. The wave-induced pressure oscillation has a downward maximum at the peak, compressing the footing and an upward maximum at the trough, pulling out the footing. These pressures are not negligible since maximum pressures may range between 1 kPa and 6 kPa according to Sassa and Sekiguchi (2001) from a study of wave-induced

liquefaction of sand beds. In practical terms 1 kPa would induce a variation of the vertical load for caisson A of approximately $V'_{weight} \pm 67$ N. Note that if the bleed valve is open the pressure difference is drastically reduced and such a vertical load fluctuation is minimal.

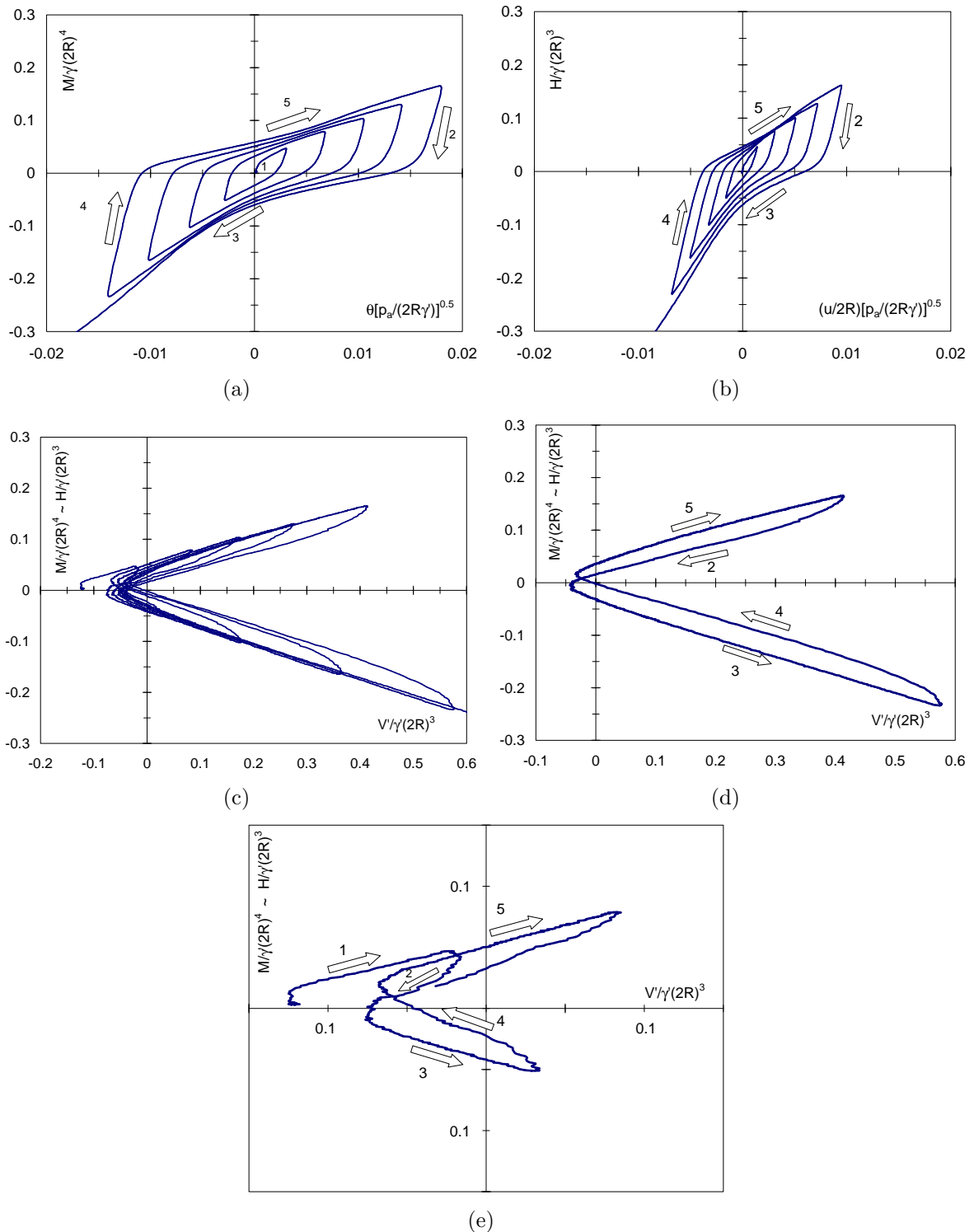


Figure 6.18: Cyclic swipe test FV10.2.2AS showing details of initial and final load path

Table 6.4 summarises details of the cyclic swipe tests performed. For example, in test

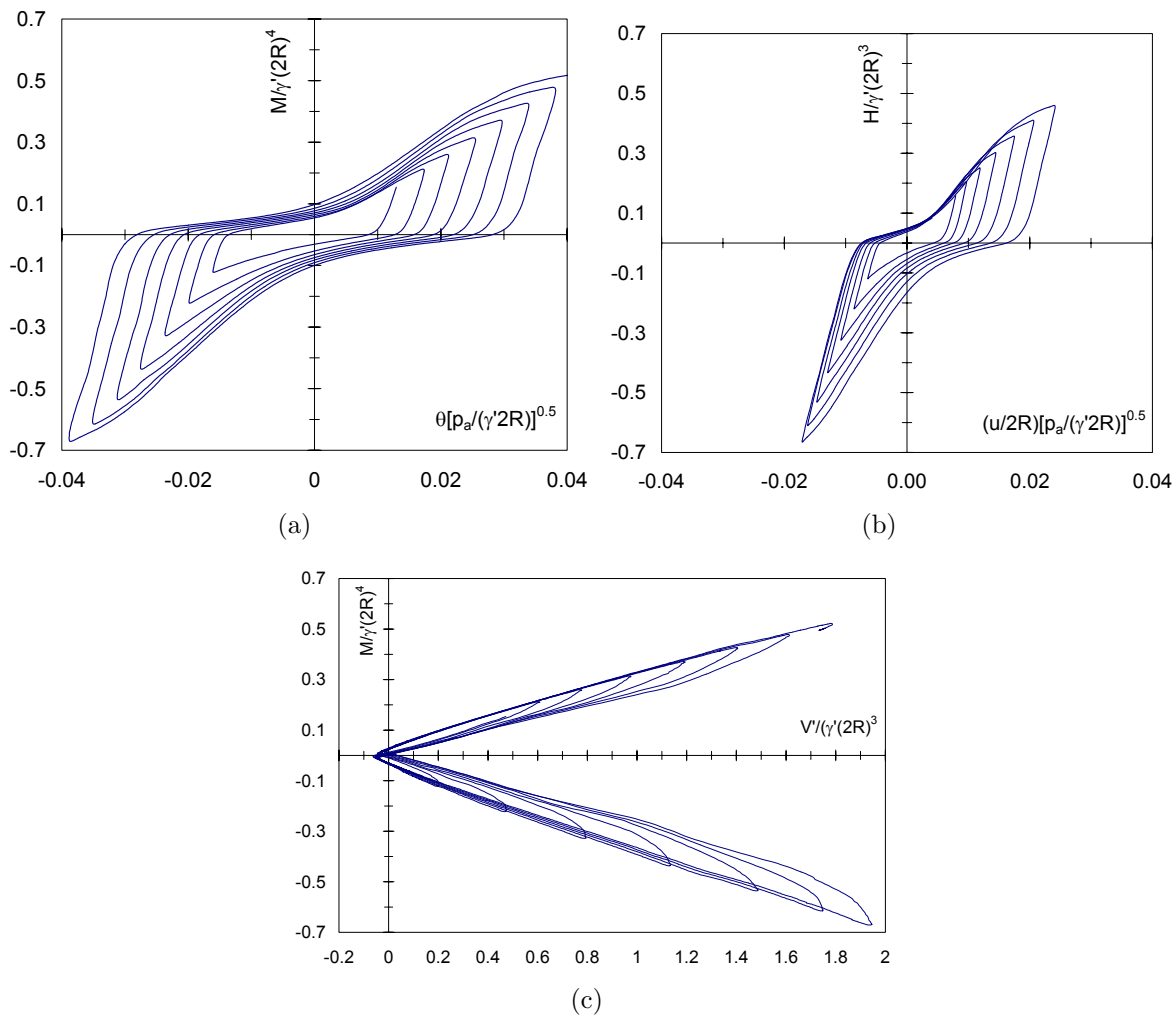


Figure 6.19: Cyclic swipe test FV10.3-3AS

FV10.3.2AS the caisson was installed by suction under a constant $V' = 16$ N until a final penetration $h = 118$ mm, following immediately a cyclic swipe event under increasing amplitudes at $\frac{M}{2RH} = 1$ (from $V'_i = -31$ N and keeping the caisson penetration constant at 118 mm). Figures 6.18(a) and 6.18(b) show the normalised curves of $\frac{M}{2R} - 2R\theta$ and $H - u$, where it can be observed that the hysteresis loops are slightly flattened on top and at the bottom (arrows 3 and 5). This shape of the reloading and unloading curves becomes most visible for the largest rotation amplitude cycles. This is a consequence of the V' variation as shown in Figure 6.18(c). Figures 6.18(d) and 6.18(e) depict the first and final cycles respectively, in which arrow 1 corresponds to the first loading, arrows 2 and 3 unloading and arrows 4 and 5 reloading. As a consequence of the fixing of the caisson in the vertical direction during rotation and translation V' increases with the rotation amplitude. This causes the moment and horizontal load to increase too. However, at every reversal

V' returns to a value close to the initial V' . Figures 6.18(d) and 6.18(e) show that the normalised value of V' at reversal is around -0.05. Due to the drastic reduction of V' the cyclic loop tends to close in the middle of unloading and in the middle of reloading. The hysteresis loop shape is hence different from that obtained previously in constant V' tests. The pore pressure observed was negligible because, despite the caisson rotation, the vertical fixity does not induce significant pore pressure variations underneath the lid.

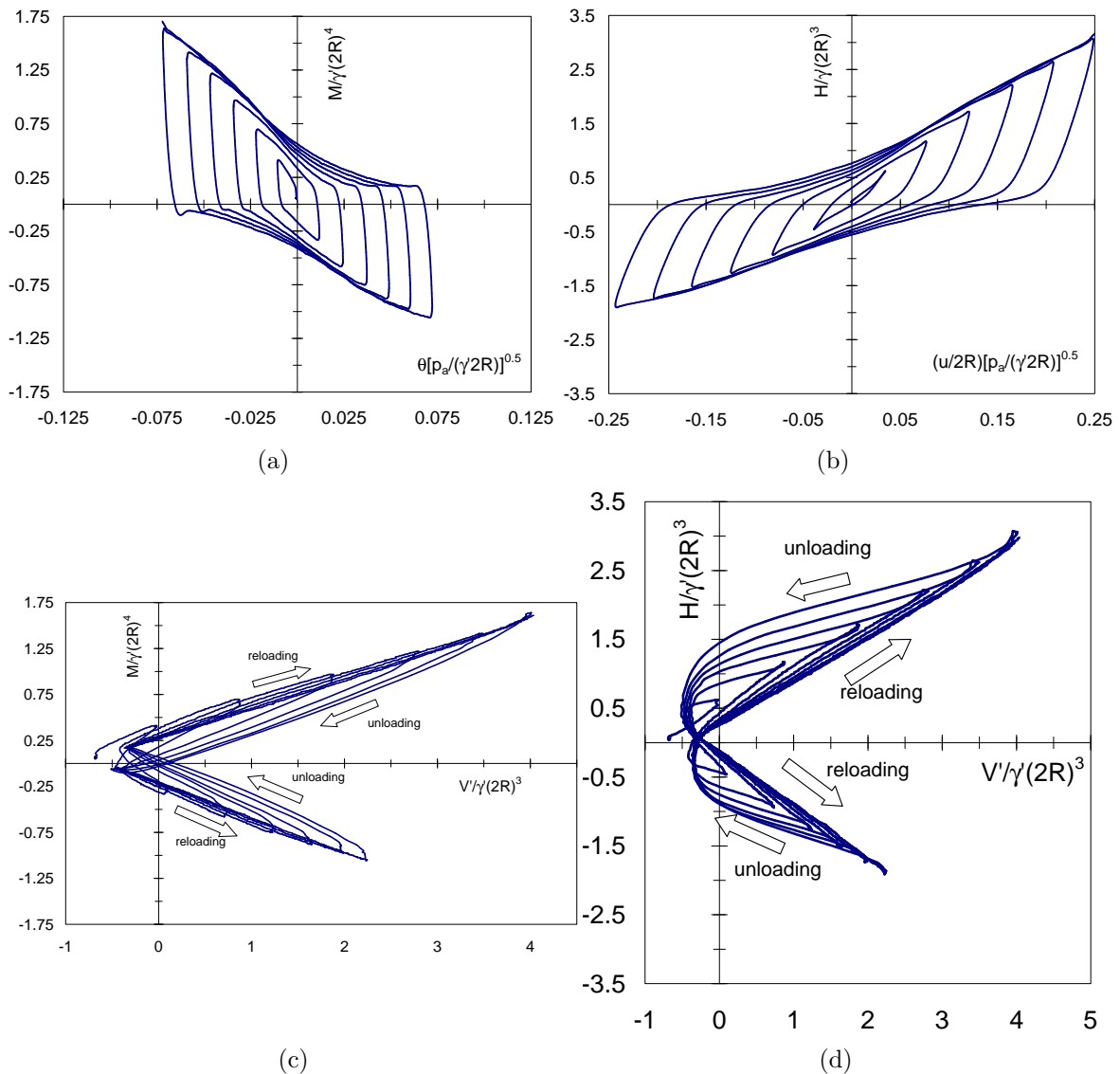


Figure 6.20: Cyclic swipe test FV10.4.2DS

A similar test but for larger rotation amplitudes is shown in Figures 6.19(a) and 6.19(b), where the characteristic shape of the hysteresis loops is clear. This test resembles the field moment-rotation response. However, in the field trial this loop shape was associated

with gapping, whereas in these tests is attributed to the strong vertical load fluctuation. If gapping occurred, they were not visible. Figure 6.19(c) shows that the response in the normalised moment-vertical load plane follows the same trend shown in Figure 6.18(c) for increasing values of vertical load. A slight curvature during reloading at the top (arrow 5) and during unloading at the bottom (arrow 3) can be observed. As before no excess pore water pressure was observed.

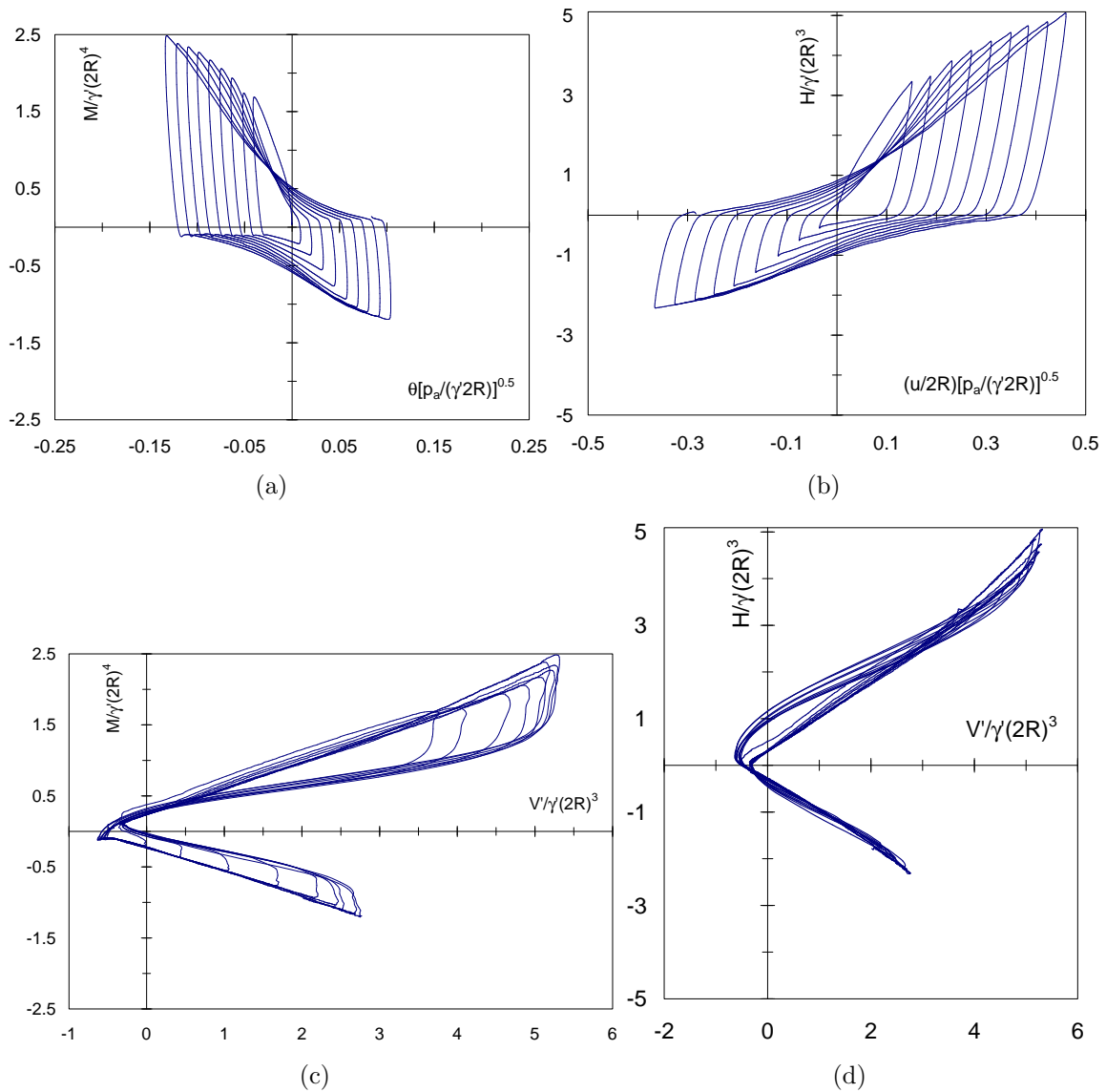


Figure 6.21: Cyclic swipe test FV10.4.3DS

Cyclic swipe tests were also performed using caisson D ($2R = 150$ mm and $\frac{L}{2R} = 1$) under a load ratio $\frac{M}{2RH} = 0.5$. In Chapter 5 it was found that the moment capacity increases with the aspect ratio. This can be confirmed looking at Figures 6.20(a) and 6.20(b), where normalised load-displacement curves are shown. Moreover, it is interesting to observe that

the normalised horizontal displacement is 3.5 times larger than the normalised rotation and the direction of rotation and horizontal displacement are opposite. Both issues are the contrary to what was shown in Figures 6.18(a) and 6.18(b) or in Figures 6.19(a) and 6.19(b). Again, the characteristic shape of the hysteresis loops with large rotation amplitude is observed. Additionally, a more pronounced asymmetry is observed after each cycle. Comparing Figures 6.20(c) and 6.20(d), different load paths during reloading and unloading are observed.

Figures 6.21(a) and 6.21(b) show that test FV10_4_3DS extends the cycling further, showing more pronounced asymmetry in the load-displacement curves and more difference in the magnitude of normalised rotation and horizontal displacement. However, the unloading curves shown in Figure 6.21(d) are not following the same trend as in Figure 6.20(d).

6.2 EXPERIMENTS IN OIL-SATURATED SAND

Monotonic moment loading tests of suction caissons in water-saturated sand did not cause a significant variation of the excess pore pressure u' . When variations of pore pressure were measured, for instance in cyclic loading tests, no noticeable effects on the caisson response were observed. In addition, dissipation of u' occurred quickly due to the high soil permeability. It was deduced that fully drained conditions were prevalent in the water-saturated sand tests. However, offshore loading conditions can be partially drained or even undrained. Therefore, it was considered important to study the moment loading response of suction caissons in events where u' can become a relevant parameter.

Scaling laws in the form of scale factors are useful in the study of physical geotechnical modelling, since relationships involving representative physical quantities can link prototype conditions with model conditions in the laboratory.

6.2.1 Scaling laws in partially drained physical models

The purpose of this section is to illustrate the effects of the use of a silicon oil as a pore fluid 100 times more viscous than water. Scaling relationships will be used to compare the relative effect of using water or oil. This will allow the scaling of time when studying partially drained phenomena.

The loading of a soil in the presence of fluid in the soil pores introduces a transfer effect between the soil grains and the fluid. In soil mechanics this loading transfer phenomenon is referred as consolidation (Terzaghi, 1943). From the normalisation of the one dimensional consolidation equation the following dimensionless time expression appears:

$$T_v = \frac{c_v t}{H^2} \quad (6.5)$$

where the coefficient of consolidation can be written as $c_v = \frac{k}{m_v \gamma_{fluid}}$; m_v is the coefficient of volume compressibility, which can be obtained from standard oedometer tests as the inverse of the stiffness in a load-settlement curve, referred to as the constrained modulus M_o . The soil permeability k is related to the absolute or specific permeability K , and the viscosity of the fluid μ as presented in Chapter 2. Therefore, the dimensionless time can also be expressed as:

$$T_v = \frac{K M_o t}{\mu H^2} \quad (6.6)$$

Introducing scale factors for the physical quantities in (6.6) it is possible to scale the consolidation time from the prototype to a model or *vice versa*. Muir Wood (2004) introduces the following expression:

$$n_t = \frac{n_\mu n_L^2}{n_G} \quad (6.7)$$

where the physical quantities correspond to diffusion time n_t , fluid viscosity n_μ , length n_L and soil stiffness n_G . Muir Wood (2004) also points out that expression (6.7) can also be derived from the analogy between the flow volume (according to the Darcy's law equal to $kiAt$, permeability, hydraulic gradient, area, time) and the strain volume (ϵV , strain,

volume), both caused by a change in stress. Then (6.7) can be applied for any problem involving diffusion time where consolidation is one possible phenomenon. For a model n times smaller than the prototype the length scales linearly as $n_L = 1/n$; n_G is the stiffness quantity that represents the variation of stress level between the geotechnical model in the laboratory and the prototype. A compromise is assumed by adopting the relationship for G in equation 5.9, where $G \propto \sigma^\alpha$ (n has been used before, but to not confuse with the scaling n term α is used instead), hence $n_G = 1/n^\alpha$. If the same fluid is used in the model and the prototype $n_\mu = 1$, on the contrary $n_\mu = \frac{\mu_{\text{model fluid}}}{\mu_{\text{prototype fluid}}}$. If the prototype fluid is water, $\mu_{\text{prototype fluid}} \approx 1 \text{ mm}^2/\text{s}$, then an option appears to increase the drainage time in sandy soils by increasing the fluid viscosity. Choosing in this particular case the model viscosity as the length scale n the diffusion time gives:

$$n_t = n^{\alpha-1} \quad (6.8)$$

For sands $\alpha \approx 0.5$, thus assuming for instance a model 100 times smaller as well as a model fluid 100 times more viscous the diffusion time becomes ten times faster. To determine the velocities in the laboratory that correspond to the velocities in the field a similar analysis can be carried out in terms of the soil permeability n_k instead of the viscosity n_μ , resulting in the diffusion time as $n_t = \frac{n_L^2}{n_k n_G}$. From this expression the diffusion time can be obtained using the parameters for the model and the prototype as follows (Kelly *et al.*, 2006b):

$$\frac{t_m}{t_p} = \frac{k_p}{k_m} \left(\frac{2R_p}{2R_m} \right)^{2-\alpha} \quad (6.9)$$

Expression (6.9) will be used in the next section to interpret the experimental results in terms of the response of a prototype caisson.

6.2.2 Moment loading tests

The procedure to prepare low permeability Baskarp cyclone sand samples using sili-con oil was described in Chapter 2. The suction assisted installation was carried out as described in Chapter 4. When the caisson penetration had finished the bleed and fluid

Table 6.5: Summary of moment loading tests in oil-saturated sand using caissons C

Test	$\frac{M}{2RH}$	$2R\frac{d\theta}{dt}$ mm/s	h mm	V' N	$\frac{V'}{A}$ kPa	u'_i kPa	$\Delta u'_i$ kPa	$\Delta u'_f$ kPa
FV2.2.2S	1.3	0.01	100	20	0.6	0.0	0.7	0.7
FV2.3.2S	1.4	0.005	100	50	1.6	0.0	1.5	1.3
FV2.4.2P	1.4	0.004	92.6	50	1.6	0.0	0.6	0.6
FV3.1.9S	1.0	0.0007	107.5	50	1.6	-1.0	0.4	0.2
FV3.1.5S	1.5	0.04	105.9	100	3.2	1.8	0.9	0.4
FV3.1.7S	1.0	0.007	107.2	100	3.2	1.8	0.9	0.6
FV3.1.4S	1.5	0.007	105.6	100	3.2	1.8	0.9	0.7
FV3.1.6S†	1.6	0.007	106	200	6.4	1.8	2.2	2.2
FV3.1.3S	1.6	0.007	105.4	200	6.4	2.2	1.7	1.7

Test	K_{mi} N/mm	K_{hi} N/mm	$\frac{M_y}{2R}$ N	H_y N	K_{mf} N/mm	K_{hf} N/mm	G_M MPa	$\frac{\delta u^p}{2R\delta\theta^p}$	$\frac{\delta w^p}{2R\delta\theta^p}$
FV2.2.2S	3	1	0.8	1.2	1	1	-	0.479	-0.009
FV2.3.2S	2	2	0.6	0.6	2	2	-	0.558	0.040
FV2.4.2P	51	20	4.0	2.2	0.4	0.4	1.0	0.817	0.014
FV3.1.9S	550	600	8.5	8.1	15	17	6.5	0.932	-0.025
FV3.1.5S	48	10	2.8	0.3	10	8	0.7	0.916	-0.005
FV3.1.7S	308	200	10.5	9.0	9	9	3.5	0.936	-0.012
FV3.1.4S	100	30	2.6	0.9	7	5	2	0.945	0.020
FV3.1.6S†	200	100	12.6	7.1	10	6	3	0.935	0.101
FV3.1.3S	200	120	9.1	5.0	4	3	3	1.018	0.022

†cyclic test

valves were closed. Once the suction was stopped the recovery of a hydrostatic condition underneath the caisson lid was almost instantaneous. However, a pore fluid pressure above or below the hydrostatic pressure can be easily induced by changes in the vertical load, different from that used during the installation. Because the dissipation takes 100 times longer for the silicon oil than for water, the initial excess pore pressure u'_i did not always dissipate completely as shown in Table 6.5.

The use of silicon oil in a very fine and dense sand reduces considerably the soil permeability making the loading rate a very important parameter. The tests were displacement controlled with the rotational displacement rates $2R\frac{d\theta}{dt}$ listed in Table 6.5. The initial test conditions were very similar, *e.g.* $\frac{M}{2RH}$, $R_d = 64\%$ for sample 2 and 80% for sample 3, and installation by suction (except test FV2.4.2CP, push installed). A second series of tests was carried out with slower rotation rates (Table 6.6). Selected tests from both series are shown on Figure 6.22(a), from which the dramatic effect of the rotation rate $2R\frac{d\theta}{dt}$ on the caisson moment-rotation response is clear.

The moment capacity is very small for the tests with $2R\frac{d\theta}{dt} = 0.01$ mm/s and 0.005 mm/s. Figure 6.22(b) shows that underneath the caisson lid the fluid has taken the loading instead of the soil grains. Although there is no measurements of u' around the caisson skirt, this lack of moment resistance is an indication of a loss of soil strength at the points where the soil was loaded by the caisson. However, the single measurement of u' appears to capture a general pattern of response. In addition, the foundation stiffness is drastically diminished ($K_{mi} = 2 - 3$ N/mm; $K_{hi} = 1 - 2$ N/mm) and as a consequence, a reduction in resistance is observed no matter the amount of rotation applied. Undrained loading conditions were reached under these relatively high rotation rates. This proved to be detrimental to the suction caisson moment response.

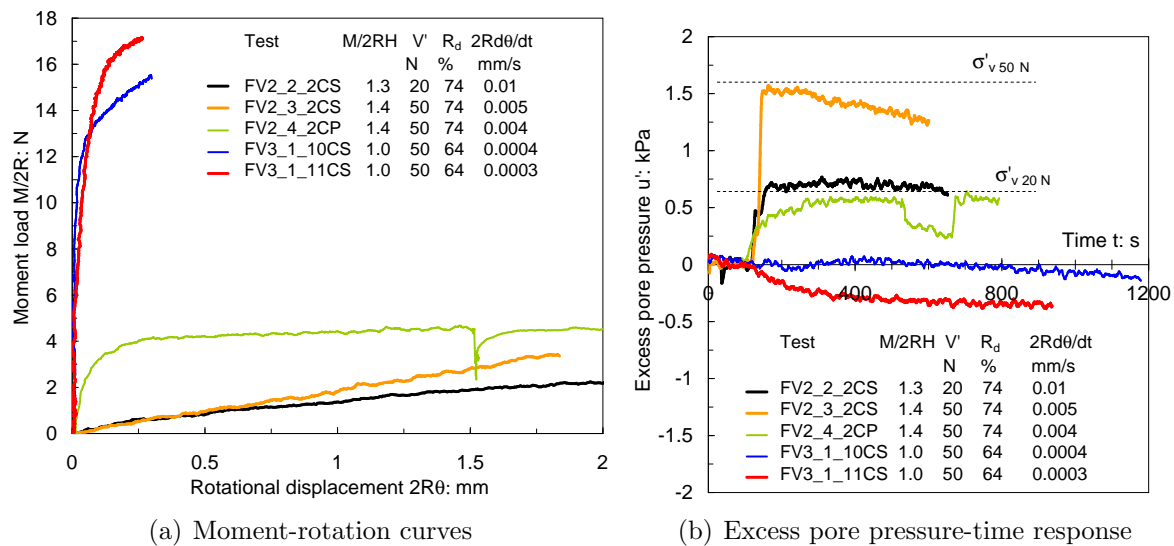


Figure 6.22: Moment loading tests showing effect of rate on the caisson moment capacity

Test FV2_4_2CP was carried out under $2R\frac{d\theta}{dt} = 0.004$ mm/s, but the caisson was pushed into the ground instead of being installed by suction. This difference in installation method has an effect on the initial foundation stiffness response ($K_{mi} = 51$ N/mm; $K_{hi} = 20$ N/mm). However, as can be observed in Figure 6.22(a) there is not a significant improvement in the moment resistance. This can be also attributed to the build up of u' shown in Figure 6.22(b).

Tests conducted at one order of magnitude less of rotational velocity, shown also in Figures 6.22(a) and 6.22(b), presented a much better moment response. At these rates more

time for the same rotation is allowed, leading to a ‘partially’ drained condition. Indeed, test FV3.1.10CS performed under $2R\frac{d\theta}{dt} = 0.0004$ mm/s shows a substantial recovery of the foundation response ($K_{mi} = 850$ N/mm; $K_{hi} = 400$ N/mm; $\frac{M_y}{2R} = 13$ N). This was a consequence of the partially drained conditions underneath the caisson lid which are highly likely to have occurred in the soil loaded by the caisson skirt too. Figure 6.22(a) shows another test with also a very slow rotational velocity $2R\frac{d\theta}{dt} = 0.0003$ mm/s with an even better moment response. Although the foundation stiffness was reduced, a slightly higher moment resistance was obtained ($K_{mi} = 400$ N/mm; $K_{hi} = 160$ N/mm; $\frac{M_y}{2R} = 16$ N). Negative values of u' shown in Figure 6.22(b) reflect the beneficial effect of the suction.

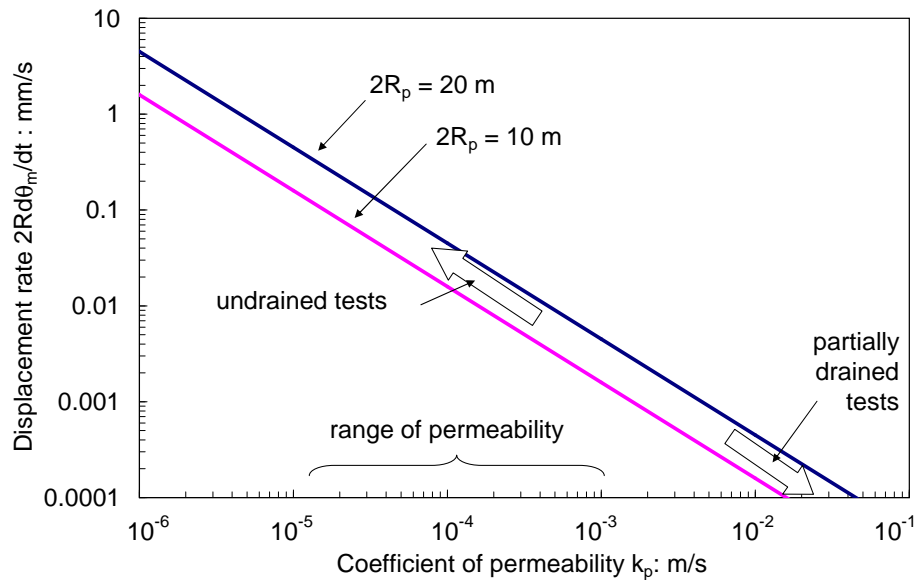


Figure 6.23: Rotational velocity of the model caisson as a function of the field permeability and prototype caisson diameter

To interpret these test results in terms of drainage conditions in the field, estimations of the scaling of rotational velocity is attempted with expression (6.9). In this expression the dissipation time is a function of the permeability and the caisson diameter. Assuming for the model a coefficient of permeability $k_m = 1.8 \cdot 10^{-7}$ m/s (Chapter 2), and for the field diameters $2R_p$ of 10 m and 20 m, $\alpha = 0.5$, and a diffusion time $t_p = 10$ s as the period of an extreme wave, the diffusion time t_m can be determined. The rotational velocity $2R\dot{\theta}$ of a model caisson of 0.2 m diameter can be obtained dividing a common rotational displacement $2R\theta_m = 0.25$ mm by the diffusion time t_m . Figure 6.23 shows the rotational

velocity varying with the field permeability k_p for two caisson diameters. For the likely range of permeability encountered in the field (bracketed in the figure) the rotational velocities of the model caisson results higher than 0.001 mm/s representing an undrained condition in the field. Therefore, only for very permeable soils and small caissons a better moment capacity would be expected. In conclusion, for extreme conditions the moment capacity of a prototype is small according to the model caisson test results.

The effect of letting the bleed valve open (Figure 2.13) during the caisson rotation is shown in Figures 6.24(a) and 6.24(b), where the two slowest tests shown in Figures 6.22(a) are included and compared with test FV3_1_16CS. The open bleed valve test shows a slightly lower moment capacity, but a similar u' variation is observed. Whilst no variations in vertical displacements was observed in the two former tests with closed bleed valve, the caisson with open bleed valve exhibited uplift, as shown in Figure 6.24(c).

The moment capacity of caissons installed by suction was significantly reduced as pointed out in section §6.1.2. These moment loading tests were carried out immediately after the installation (around 10 minutes). Figure 6.25(a) shows the results from moment loading tests conducted around 48 hours after the suction installation. Only a minor difference exists between the moment capacity of the caisson installed by suction and by pushing. The improvement in the caisson response was not caused by the suction, since no suction was recorded during the moment loading tests. This suggests that time plays an important role in the recovery of the strength lost by the soil during the penetration. Figure 6.25(b) shows that the vertical movement was very small and there was no significant effect on w from the installation methods.

Although the main interest of this research is the study of moment loading of caissons under low vertical load, it is important to know whether the rate effect modifies or not the response under higher constant V' . Figures 6.26(a), (b) and (c) show the moment-rotation response under a much higher constant vertical load ($V' = 200$ N) for cyclic and monotonic tests. The initial caisson response is very similar for the three tests in terms of

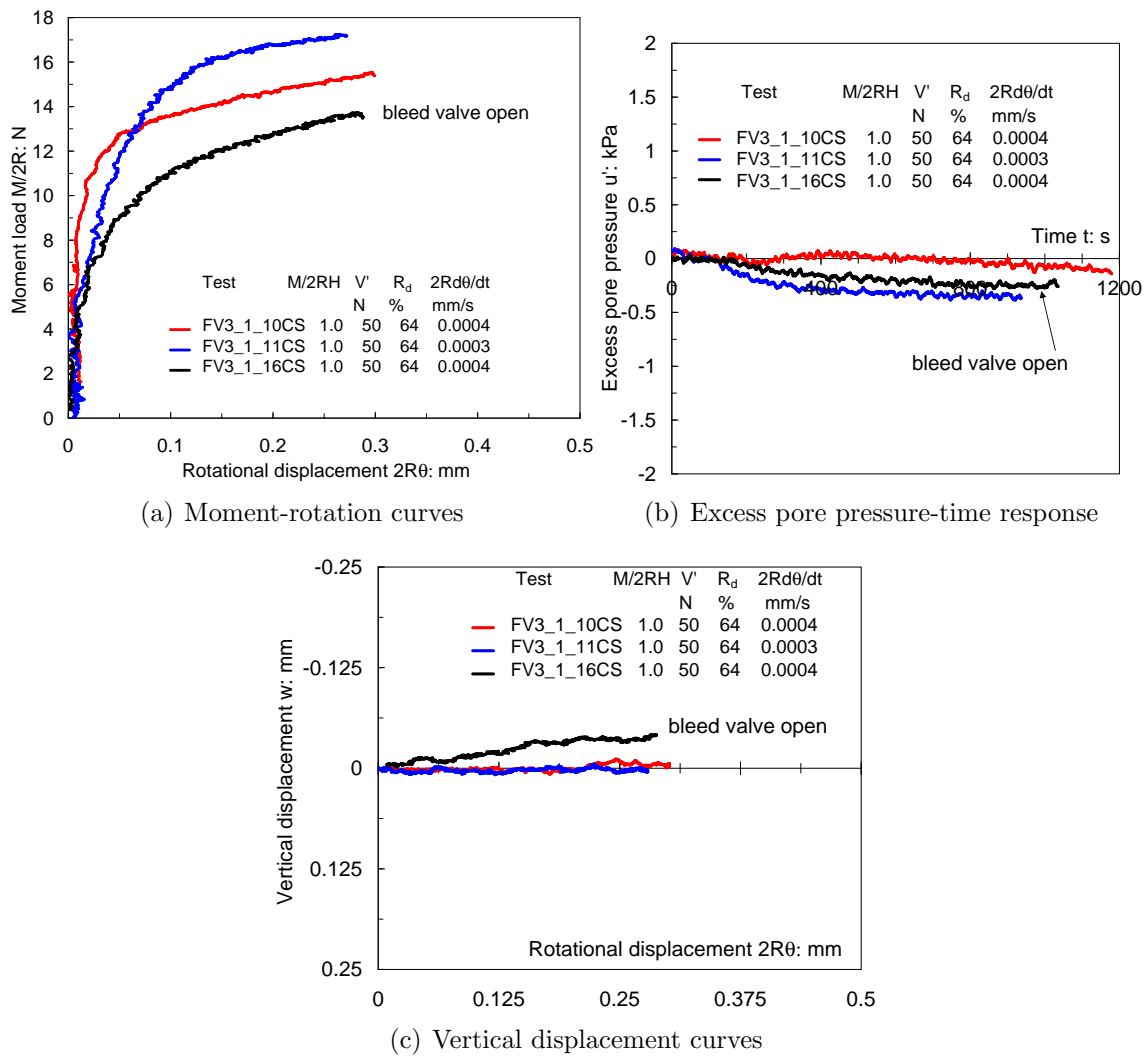


Figure 6.24: Effect of the bleed valve open on the caisson response

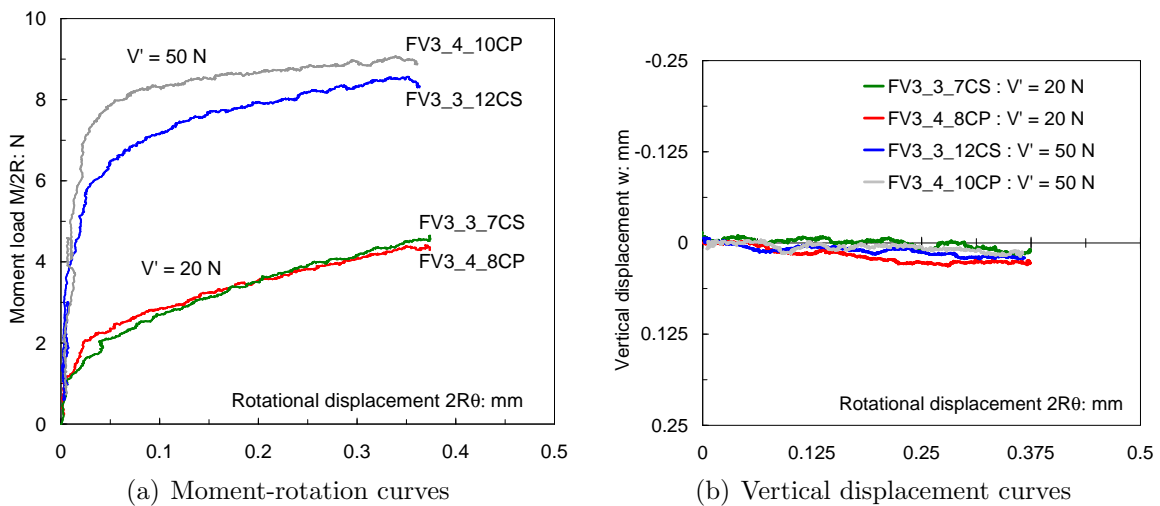


Figure 6.25: Comparison of moment capacity of a caisson installed by pushing and by suction

normalised moment, $\Delta u'_i$ and total w_t . However, the subsequent response differs specially for the cyclic tests. The excess pore pressure increases and a cyclic fluctuation $\Delta u'_{cyclic}$

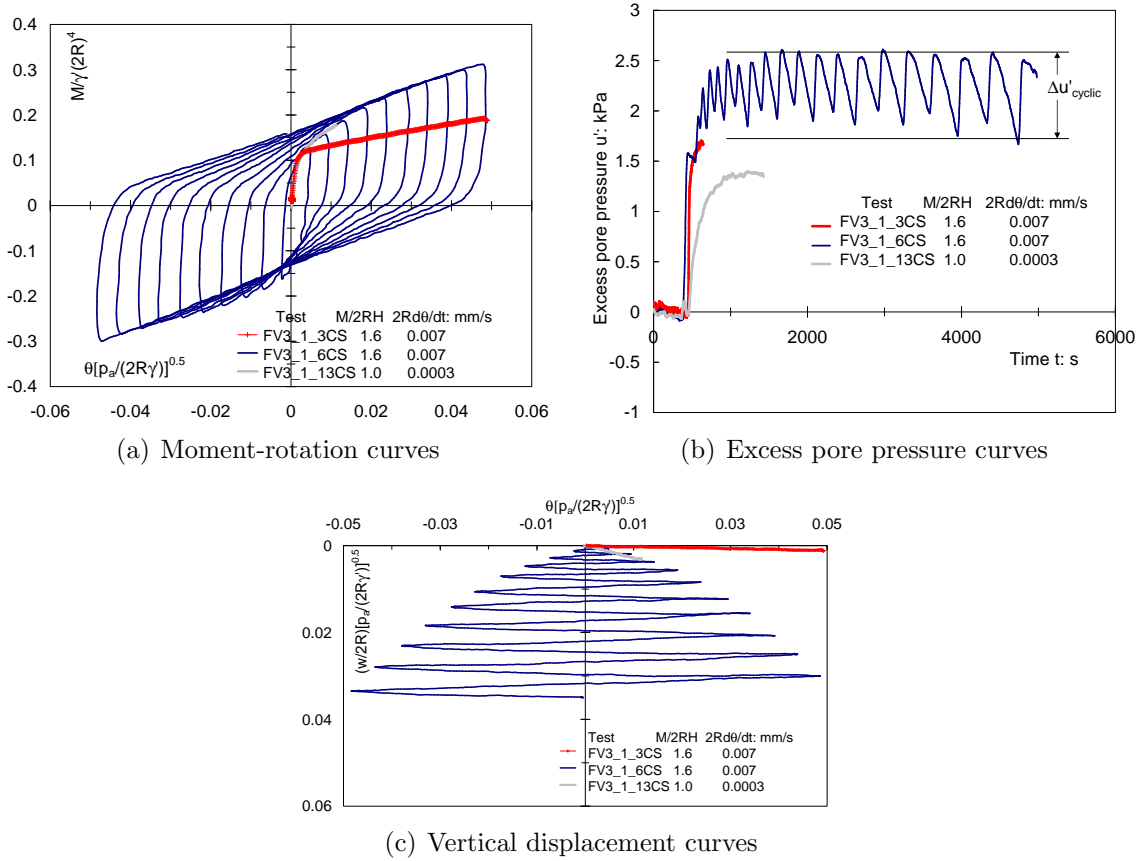


Figure 6.26: Monotonic and cyclic response of a caisson under a very high value of $\frac{V'}{\gamma'(2R)^3} \approx 2.5$ occurs as well as a much larger caisson settlement (see Figures 6.26(b) and 6.26(c)). However, the level of u' reached did not appear to be a detrimental to the monotonic nor to the cyclic moment response.

6.2.3 Yield points

In the previous section it was found that unless a large V' is applied, high rotational velocities cause an unfavourable undrained response of the caisson foundation. Furthermore, high rotational velocities are more representative of the field condition for a certain range of permeability values. To generate fluid draining in the soil loaded by the caisson, it was necessary to rotate the caisson at a velocity $2R\frac{d\theta}{dt}$ between 0.0003 and 0.0004 mm/s. This allowed the identification of yield in the moment-rotation curves. To study partially drained conditions a second series of tests was performed, thereby yield loads $(\frac{M_y}{2R}, H_y)$ were determined as defined in section §5.4, and are presented in Table 6.6.

Table 6.6: Summary of constant V' moment loading tests installed by suction

Test	h mm	V' N	$\frac{V'}{A}$ kPa	u'_i kPa	$\Delta u'_i$ kPa	$\Delta u'_f$ kPa
$\frac{M}{2RH} = 1$						
FV3_3.19C	97	-11	-0.4	-0.4	-0.1	-0.3
FV3_2.5C	106.2	-10	-0.3	-0.3	-0.1	-0.6
FV3_2.2C	106.1	20	0.6	0.0	-0.4	-0.3
FV3_3.9C	95.9	20	0.6	0.0	0.0	-0.3
FV3_1.14C	108.1	30	1.0	0.0	-0.8	-0.8
FV3_1.10C	107.6	50	1.6	-1.0	0.1	-0.1
FV3_1.11C	107.6	50	1.6	-1.0	-0.3	-0.4
FV3_1.12C	107.6	100	3.2	0.0	-0.4	-0.2
FV3_3.10C	96	48	1.5	0.0	0.5	0.5
FV3_1.16C [†]	108.7	50	1.6	0.6	0.0	-0.2
FV3_2.3C	106.1	50	1.6	0.1	0.2	0.3
FV3_2.4C	106.3	100	3.2	0.2	0.8	0.7
FV3_3.21C	105	100	3.2	0.7	0.4	0.4
FV3_2.6C	106.5	150	4.8	0.0	1.5	1.8
FV3_1.13C	107.8	200	6.4	1.1	1.4	1.4
FV3_1.15C	108.2	250	8.0	3.3	1.2	1.2
FV3_3.27C	107.7	250	8.0	0.0	0.6	0.9
FV3_3.31C	109	1000	31.8	0.0	1.2	1.0
FV3_3.32C	110.5	2000	63.7	-0.8	0.5	0.8
$\frac{M}{2RH} = 0.5$						
FV3_3.18C	97	-10	-0.3	-0.5	-0.2	-0.2
FV3_3.4C	95.5	1	0.0	0.0	0.0	-0.3
FV3_3.6C	95.6	9	0.3	0.0	0.0	-0.3
FV3_3.7C	95.7	20	0.6	0.0	0.0	-0.2
FV3_3.12C	97.2	48	1.5	-0.5	0.5	0.0
FV3_3.20C	104.5	100	3.2	0.4	1.4	1.5
FV3_3.26C	107.5	248	7.9	1.0	0.4	0.5
FV3_3.30C	108.2	500	15.9	0.5	0.6	0.5
$\frac{M}{2RH} = -2$						
FV3_2.7C	106.5	50	1.6	0.0	-0.2	-0.4
FV3_3.13C	97.4	50	1.6	0.0	0.5	0.5
FV3_3.23C	105	100	3.2	0.0	0.2	0.6
FV3_1.8C [†]	107.3	100	3.2	0.0	1.3	0.8
FV3_3.28C	107.8	250	8.0	0.0	0.0	0.3
$\frac{M}{2RH} = -0.5$						
FV3_3.15C	97.6	49	1.6	0.0	0.3	0.6
FV3_2.8C	106.5	50	1.6	0.0	0.3	0.0
FV3_3.24C	105.4	100	3.2	0.0	0.5	0.5
FV3_3.29C	107.9	250	8.0	0.0	0.0	0.0
$\frac{M}{2RH} = -0.25$						
FV3_2.9C	106.6	50	1.6	0.0	0.2	0.3
FV3_3.16C	98	50	1.6	0.0	0.7	0.9
FV3_3.25C	105.6	99	3.2	0.0	0.1	0.8

[†] $\frac{M}{2RH} = -1.5$, [‡]bleed valve open

Normalised plots showing the yield points as a function of the difference $V' - u'A$ were constructed. Measured values of u' are restricted to only the location of the pore pressure transducer. It is believed that during the caisson rotation u' varies across the lid. The inclusion of u' attempts to account the level of excess pore fluid pressure underneath the

Table 6.7: Summary of constant V' moment loading tests (continuation Table 6.6)

Test	K_{mi} N/mm	K_{hi} N/mm	$\frac{M_y}{2R}$ N	H_y N	K_{mf} N/mm	K_{hf} N/mm	G MPa	$\frac{\delta u^p}{2R\delta\theta^p}$	$\frac{\delta w^p}{2R\delta\theta^p}$
$\frac{M}{2RH} = 1$									
FV3.3.19C	90	60	1.7	1.5	5	10	1.5	0.54	0.01
FV3.2.5C	70	90	2.4	2.7	12.5	15	1	0.71	-0.12
FV3.2.2C	220	120	6.8	6.6	2	3.5	3	0.72	-0.06
FV3.3.9C	222	70	4.6	4.9	8	9	3.5	0.81	0.02
FV3.1.14C	350	200	9.2	9.0	9	10	5	0.90	-0.09
FV3.1.10C	850	400	12.8	12.6	10	11	10	0.88	-0.01
FV3.1.11C	400	160	15.8	15.5	7	8	3	0.98	-0.03
FV3.1.12C	280	400	14.5	15.0	24	18	5	1.07	0.11
FV3.3.10C	270	180	6.8	6.4	6	9	3.5	0.76	0.09
FV3.1.16C [†]	350	180	10.9	10.5	11	12	5	1.01	-0.16
FV3.2.3C	350	180	8.7	8.7	2.5	3	5	0.74	0.07
FV3.2.4C	200	150	6.8	6.9	12.5	15	3	0.84	0.14
FV3.3.21C	300	180	5.7	5.4	15	21	4	0.70	0.43
FV3.2.6C	350	290	10.5	10.6	12.5	13	4.5	0.84	0.21
FV3.1.13C	280	200	9.6	8.8	15	15	4	1.10	0.31
FV3.1.15C	180	130	9.8	8.5	19	19	2.5	1.31	0.46
FV3.3.27C	1000	300	28.0	28.1	19	21	12	0.83	0.07
FV3.3.31C	320	520	23.8	18.7	80	65	6.5	1.30	0.31
FV3.3.32C	1220	420	41.5	35.7	150	105	15	1.65	0.49
$\frac{M}{2RH} = 0.5$									
FV3.3.18C	50	60	1.0	1.8	4	10	1	0.75	-0.03
FV3.3.4C	180	190	2.2	4.1	5	13	3	0.80	0.04
FV3.3.6C	180	190	4.4	8.6	4	8	3	0.85	0.02
FV3.3.7C	222	100	2.2	5.0	7	15	3.5	0.81	0.05
FV3.3.12C	470	770	7.1	13.7	5	12	6.5	0.79	0.06
FV3.3.20C	150	250	6.3	11.8	5	14	2.5	0.83	0.15
FV3.3.26C	500	1420	13.2	25.6	25	45	6.5	1.05	0.23
FV3.3.30C	400	420	23.0	45.9	40	60	6.5	1.39	0.36
$\frac{M}{2RH} = -2$									
FV3.2.7C	350	-65	10.5	-5.2	18	-13	4.5	0.79	-0.07
FV3.3.13C	300	-80	8.6	-4.4	11	-8	3.5	0.59	0.05
FV3.3.23C	300	-50	9.5	-5.0	15	-12	3.5	0.69	0.46
FV3.1.8C [†]	48	-40	2.3	-2.0	12	-9	0.7	0.91	0.00
FV3.3.28C	1200	-85	40.8	-22.3	50	-50	12	0.58	0.03
$\frac{M}{2RH} = -0.5$									
FV3.3.15C	300	-220	12.8	-26.4	11	-80	3.5	0.29	0.11
FV3.2.8C	130	-175	13.7	-28	22	-220	1.5	0.30	0.13
FV3.3.24C	500	-220	16.0	-35.2	22	-100	4	0.43	0.54
FV3.3.29C	2200	-263	38.3	-69.0	60	400	17.5	-0.36	0.01
$\frac{M}{2RH} = -0.25$									
FV3.2.9C	230	-400	10.4	-42	22	26	1.5	-3.79	0.05
FV3.3.16C	300	-250	9.2	-40.5	22	19	3.5	-4.45	0.41
FV3.3.25C	300	-357	16.2	-72.0	32	40	2	-3.94	1.71

[†] $\frac{M}{2RH} = -1.5$, [‡]bleed valve open

caisson lid. In Table 6.6 a value of initial excess pore pressure u'_i is included to account for non dissipated pore pressures at the beginning of the moment loading test. The variation in excess pore pressure caused by the caisson rotation above or below u'_i is $\Delta u'$. In general the value of $\Delta u'$ was fairly constant during the caisson rotation, but to account

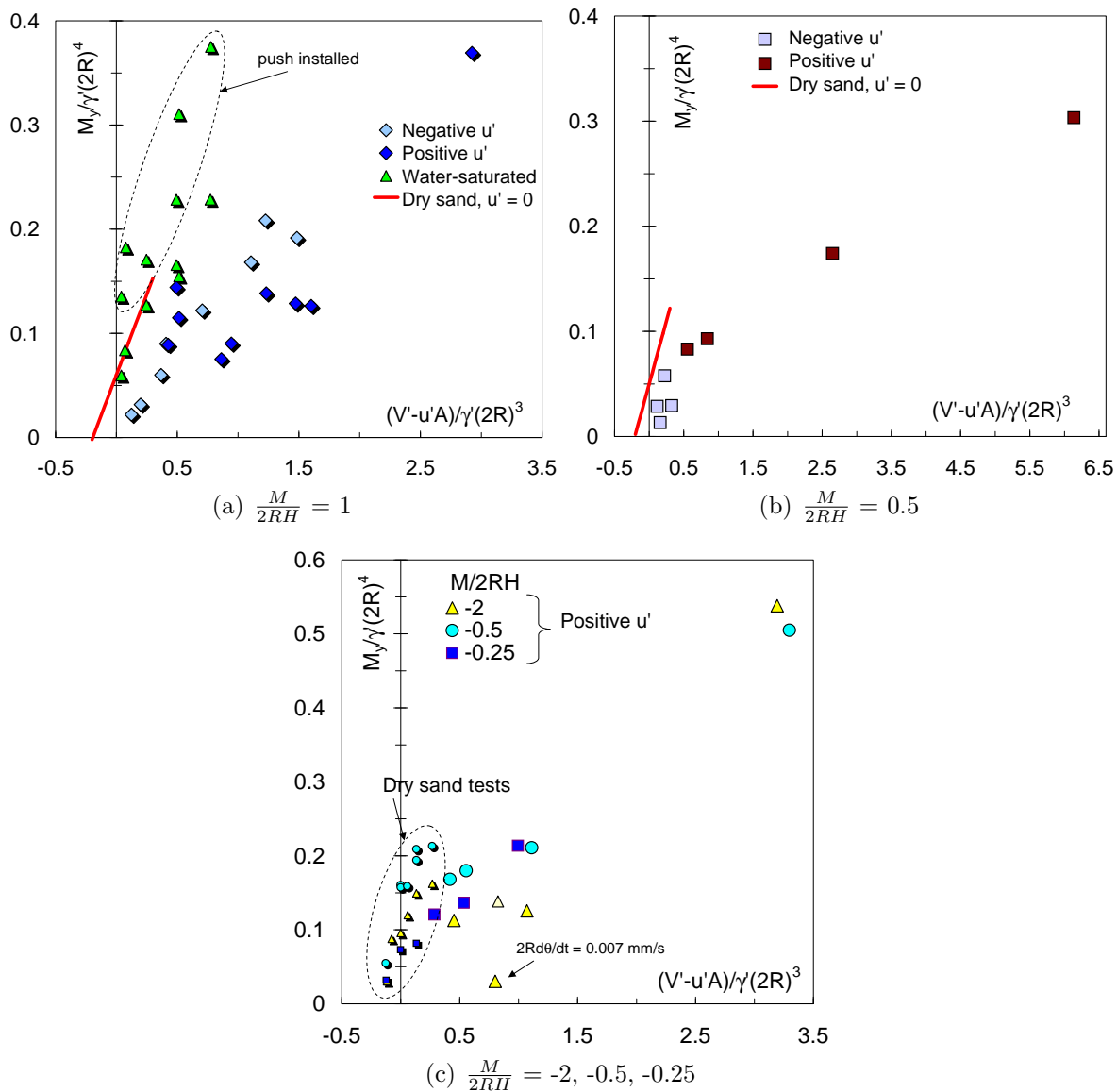


Figure 6.27: Comparison of the moment capacity between partially drained and drained tests

for a possible variation a final value of pore pressure variation $\Delta u'_f$ (assuming $u'_i = 0$) was considered. In the following figures the excess pore pressure u' is taken as the maximum sum of $u'_i + \Delta u'$ or $u'_i + \Delta u'_f$.

Yield points of tests conducted at $\frac{M}{2RH} = 1$ are shown in Figures 6.27(a). Results from partially drained oil-saturated sand tests can be compared with drained test results from loose dry sand (line) and from water-saturated sand (triangular yield points). A similar plot for $\frac{M}{2RH} = 0.5$ is shown in Figure 6.27(b) and for $\frac{M}{2RH} = -2, -0.5, -0.25$ in Figure 6.27(c). It can be observed that the yield points from water-saturated sand tests follow the trend of the results from the dry tests. Yield loads from the oil-saturated tests, asso-

ciated with negative values of u' , represent the presence of suction during rotation. These yield points are slightly moved towards the right from the trend follow by the drained tests, owing to the inclusion of the suction in the normalised vertical load. Whilst, positive u' values, generated by increasing values of normalised V' , shift the yield loads to the left. In view of these plots, the caisson moment capacity was reduced by the build up of u' in comparison with that obtained from drained tests.

An example of the yield points projected on the $\frac{M_y}{2RV_o} - \frac{H_y}{V_o}$ plane is shown in Figure 6.28 where results of tests with $V' = 50$ N from oil-saturated sand are compared with results from the tests in dry sand for $V' = 100$ N since both V' scale as $\frac{V'}{V_o} \approx 0.2$. It can be observed the favourable effect of negative u' on the caisson lateral capacity, which is reflected in the increasing values of $\frac{M_y}{2R}$ and H_y .

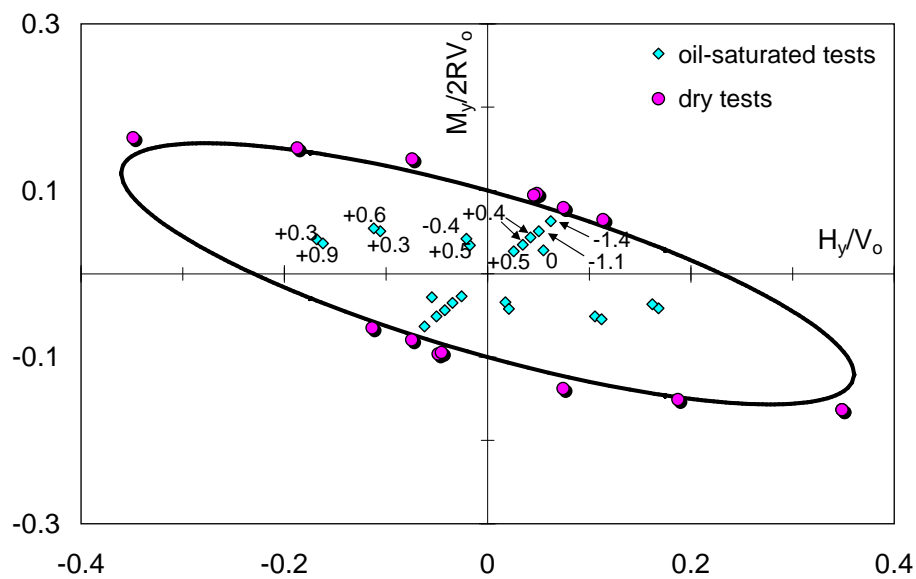


Figure 6.28: Comparison between the yield surface and yield points determined in drained condition and in partially drained conditions. Numbers next to the points indicate the maximum u' in kPa

6.2.4 Foundation stiffness

The moment capacity can be significantly reduced if not enough suction is developed or an even more unfavourable condition if positive u' build up occurs. It is important to assess the foundation stiffness before a yield condition occurs. Values of the initial and

final foundation rotational and lateral stiffness are presented in Table 6.7 as K_{mi} , K_{mf} , K_{hi} and K_{hf} . Comparisons, in terms of a normalised K_{mi} (Kelly *et al.*, 2006a), are shown in Figure 6.29(a) between results obtained in the partially drained oil-saturated tests and drained test results from dry and water-saturated sands. There is scatter in the data, but it is clear that the normalised stiffness from partially drained test follows the trend of the normalised stiffness from drained tests. It is worth noting that the foundation stiffness was even higher when suction appeared.

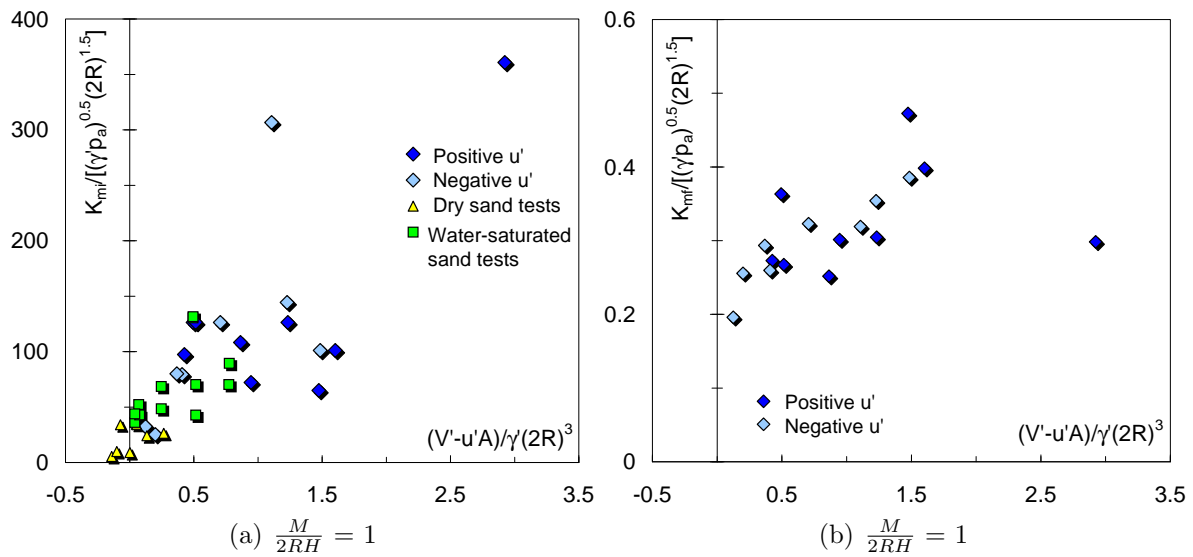


Figure 6.29: Comparison of the normalised foundation stiffness between partially drained tests and drained tests

As previously pointed out, K_{mf} is practically independent of V' and also independent of the excess pore pressure as can be observed in Figure 6.29(b). Values of normalised K_{mf} from the drained tests are not shown because they are much higher (see Figure 6.5(c)). This is evidence that a gradual process of yield leads to a state where the foundation response is the same, no matter the combined loading applied or even the pore fluid pressures developed.

6.2.5 Vertical displacement

The previous analysis of the effect of u' on the resultant moment load at yield is in fact a consequence of the displacements experienced by the caisson and in particular of the vertical displacement w . Figures 6.30(a) and 6.30(b) shows the ratio between the plastic

vertical displacement increment and the plastic rotational displacement increment $\frac{\dot{w}^P}{2R\dot{\theta}^P}$ varying with $\frac{V'-u'A}{V_o}$.

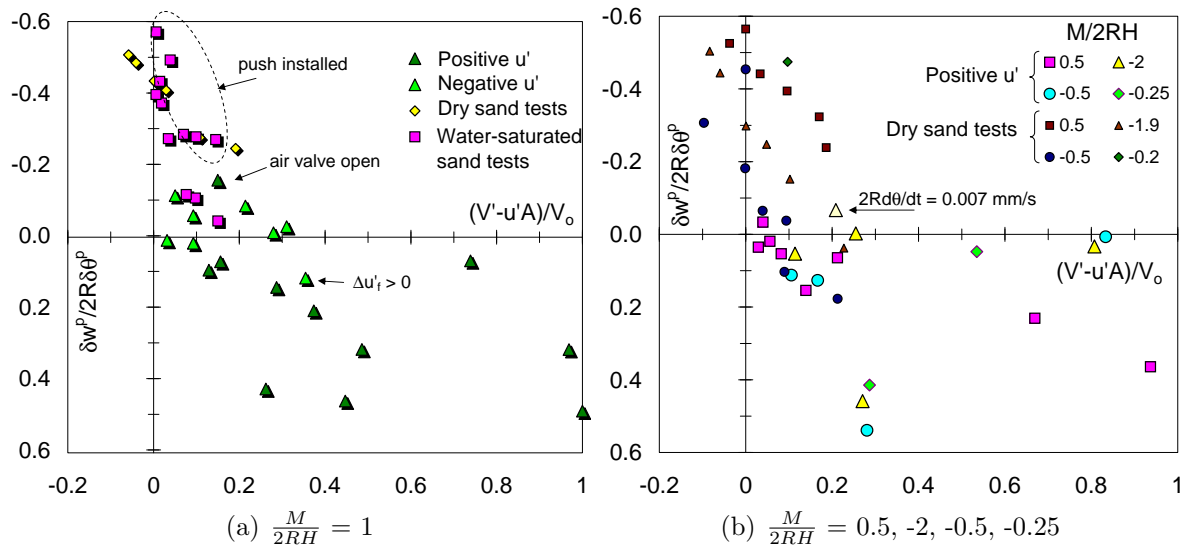


Figure 6.30: Comparison of the normalised plastic vertical displacement between partially drained tests and drained tests

The suction generation during loading reduces the caisson upward movement, whereas positive u' induces settlements increasing with the vertical load. There is scatter in the partially drained data, which is believed to be due to the pore pressure transducer location. Therefore, it is difficult to identify the parallel point, but rather a range of $\frac{V'-u'A}{V_o}$ values between 0.05 and 0.3. Further experiments are required to determine the u' variation across the caisson lid during moment loading.

6.3 CONCLUSIONS

With the purpose of investigating the moment response of suction caissons under drained, partially drained and undrained conditions, two main groups of tests were performed, one in water-saturated sand and the other in oil-saturated sand.

6.3.1 Experiments in water-saturated sand

From experiments comparing caissons installed by suction and by pushing was found that the moment resistance of a suction caisson depends on the method of installation. The yield loads determined from suction installed caissons were approximately half of

those determined from pushing installed caissons for the case of low thickness ratio $\frac{t}{2R} = 0.5\%$. Less difference was found for $\frac{t}{2R} = 1.2\%$. The suction installation method causes a fluid flow regime around the caisson that disturbs the soil, reducing the shear strength of the soil inside the caisson. The initial foundation stiffness was significantly reduced for the case of suction installation only for the caisson with lower thickness ratio.

The ratio of plastic deviatoric displacement increments was found to be independent of the installation method. However, the ratio of plastic vertical and rotational displacement increments was reduced when the suction was used. In other words, more uplift was observed in pushing installed caissons than in suction installed caissons.

The yield surface expression was applied successfully to two different size suction caissons after normalisation by V_o , but requires different values of t_o to account for the different thickness ratios.

Comparisons between results from laboratory cyclic tests and results from field trials showed the importance of the level of stresses on the lateral earth pressure, when assessing moment capacity and vertical displacements. Difference in the shape of the hysteresis loops for large rotation was observed due to gapping for the caisson in the field trial.

Cyclic swipe events can be used as an approach to reproduce offshore wave loading, where the vertical load varies simultaneously with the moment and horizontal loads. Masing's rules were not obeyed in these tests.

6.3.2 Experiments in oil-saturated sand

To study undrained and partially drained conditions moment loading tests of suction caissons were carried out in an oil-saturated sand. For a plausible range values of soil permeability in the field, it was found that the high rotational velocity tests in the laboratory which caused undrained conditions are representative of the field conditions. Undrained

conditions had a detrimental effect on the moment response of suction caissons under low vertical load.

In partially drained tests the presence of suction during combined loading under low vertical loads improves the moment capacity and reduces almost completely the caisson uplift. However, in $V' - u'A$ plots the caisson resistance appears reduced in comparison with drained test results. Positive excess pore pressures induced settlements increasing with the vertical load.

It was assumed an uniform excess pore pressure distribution from measurement in one location underneath the caisson lid. Further experiments with measurements at several locations are required to determine the excess pore pressure distribution across the caisson lid during monotonic and cyclic moment loading.

Chapter 7

SUCTION CAISSONS IN CLAY

Abstract

A testing programme to study the response of a suction caisson with an aspect ratio of one in heavily overconsolidated clay was conducted. Firstly, installation of the caisson by pushing and by suction, as well as the maximum pullout capacity was studied. Secondly, three series of cyclic vertical loading tests, which are relevant to applications for multi-caisson foundations, were performed. It was found that, before failure, the caisson installed by suction had less upward movement than the caisson installed by pushing for increasing cyclic load amplitudes around a mean vertical load $V_m = 0$ N. This is attributed to the different pore water pressure variation developed and measured underneath the caisson lid, since both series of tests were performed under identical conditions. Thirdly, monotonic and cyclic moment loading tests, which are relevant to applications for monopod caisson foundations, were performed in the form of swipe events and constant vertical load events. In the cyclic tests hysteresis loop constriction appeared as a consequence of gapping, reducing the moment capacity and increasing caisson uplift when experiencing tensile load. Results from monotonic tests permitted the parameters of a mathematical expression for the yield surface to be determined. It was found that the yield surface had different shape and size depending on the ratio between the caisson load history and bearing capacity $\frac{V_o}{V_u}$. An associated flow rule was defined to suit the ratio $\frac{V'_o}{V_o}$. However, variations with the $\frac{V_o}{V_u}$ ratio were found.

7.1 INSTALLATION AND PULLOUT CAPACITY

7.1.1 Introduction

Suction caisson response in clayey soils has been studied more widely than for sands. Research has concentrated mostly on suction caissons as anchors, and in normally consolidated soils for a variety of offshore deep water structures, where caisson aspect ratios are commonly higher than three. Information on this application can be found in Andersen *et al.* (1993), Clukey *et al.* (1995), El-Gharbawy (1998), Andersen and Jostad (1999), House (2002), Colliat and Dendani (2002) and Aubeny *et al.* (2003) among others. Latterly, the proceedings of the conference “Frontiers in Offshore Geotechnics” held in Perth, Australia in 2005 included a state-of-the-art keynote paper by Andersen *et al.* and a section dedicated to suction caissons in deepwater developments. However, very little research of foundations for offshore wind turbines in clay has been carried out. Therefore, this study emerges as a natural and rational response to a necessity in this area of geotechnical engineering.

Recent studies by House (2002), Rauch *et al.* (2003) and Chen and Randolph (2004) have demonstrated that there is not a substantial difference (as in sands) between the net vertical load required to install caissons (with $\frac{L}{2R} \geq 4$) into normally consolidated clay by pushing (V') and by suction ($V' + |S|$). However, it is not yet clear the effect that the different installation methods have on the caisson response to subsequent loading. Although, installations by pushing were mostly chosen owing to the simplicity in the use of the *VMH* loading rig, one suction installation test was performed. This allowed comparisons with theoretical estimations of the suction, as well as to assess if the net vertical load is indeed independent of the installation method. Furthermore, comparisons of subsequent short term vertical cyclic response were established.

Caisson D (diameter and skirt length $2R = L = 150$ mm, aspect ratio $\frac{L}{2R} = 1$, and skirt thickness $t = 1$ mm), shown in Figure 2.8(e), was selected for the testing programme in heavily overconsolidated kaolin clay specimens. Properties, details of the preparation

and set-up conditions of the clay specimens are presented in Chapter 2. Natural over-consolidated clays are the product of a number of geological processes such as glaciation, ground water level changes, *etc.* This type of soil is encountered in the offshore seabed at some of the sites released by Crown Estates and is commonly referred to as stiff or hard clay.

7.1.2 Penetration resistance

The vertical load required (without suction) to penetrate a caisson into a purely cohesive soil can be obtained from equilibrium of the acting and reacting forces involved. The frictional resistance inside and outside the caisson are calculated using adhesion factors α_i and α_o . The end bearing is calculated using the cohesion bearing capacity coefficient N_c for deep plane strain (strip footing). As a result, the submerged vertical load V' needed to penetrate a caisson a depth h can be expressed as follows:

$$V' = \alpha_o \bar{s}_u 2\pi R_o h + \alpha_i \bar{s}_u 2\pi R_i h + 2\pi R t (\gamma' h + s_u N_c) \quad (7.1)$$

where \bar{s}_u is the average undrained shear strength amidst the mudline and the caisson tip, s_u is the undrained shear strength at the caisson tip, R_o , R and R_i are the outside, mean and inside caisson radii, and t is the skirt wall thickness (see Figure 4.2 for suction caisson outline). House (2002) and Chen and Randolph (2004) adopted a value of $N_c = 7.5$. However, N_c varies with depth between 7 and 12; for that reason a value of 9 is considered more appropriate.

The suction required to assist the installation of a caisson into clay a depth h can be derived from equation (7.1), resulting in the following expression:

$$s = \frac{1}{\pi R_i^2} [\alpha_o \bar{s}_u 2\pi R_o h + \alpha_i \bar{s}_u 2\pi R_i h + 2\pi R t (\gamma' h + s_u N_c) - V'] \quad (7.2)$$

where the suction s has been added as the contributing force $S = s\pi R_i^2$ to the left hand side of (7.1). It is necessary to clarify that V' does not correspond to the subtraction

$V' = V - S$. The subtraction $V'_e = V' - S$, where the subscript e stands for ‘effective’, emulates Terzaghi principle of effective stresses. Once full penetration is achieved, care should be taken in the interpretation of V'_e values, since values of s correspond to one point, which can be assumed uniformly distributed underneath the caisson lid. However, it has been shown in Chapter 6 that for instance, during caisson rotation s can vary substantially across the caisson lid.

7.1.3 Pushing and suction installation test results

House (2002) employing equation (6.1) with t as the relevant dimension instead of $2R$ (as originally suggested for calcareous sand by Finnie (1993)) found that in NC kaolin clay undrained conditions correspond to dimensionless footing velocities $v_n > 10$, whilst fully drained conditions will be reached for $v_n < 0.1$. In this study penetration of the caisson skirt into the ground by pushing was conducted at a rate \dot{h} of 0.5 mm/s. Then, since $v_n = 1.6$, it is deduced that partially drained conditions occur, assuming vertical flow with a value of $c_v = 0.3 \text{ mm}^2/\text{s}$ for a vertical pressure $p' = 200 \text{ kPa}$ (de Santa Maria, 1988).

Figure 7.1(a) shows all the pushing load-penetration curves $V' - h$, in addition to the curve $(V' + |S|) - h$ of test FV7_1S, which was installed by suction assistance after 30 mm of pushing penetration. This initial pushing penetration followed the curves of tests FV2_1 and FV6_1 due to the proximity of s_u values. Note that between 30 mm and 60 mm $(V' + |S|) - h$ reduces the rate of increase with penetration as a result of the starting and fluctuation of the suction. However, after 60 mm of penetration the curve of test FV7_1S undoubtedly follows again in between the pushing penetration curves of tests FV2_1 and FV6_1. Therefore, it can be concluded that the caisson penetration resistance is independent of the installation method in heavily overconsolidated kaolin clay, as previously found in NC kaolin clay and in high aspect ratio caissons by House (2002), Rauch *et al.* (2003) and Chen and Randolph (2004).

Differences observed in the curves shown in Figure 7.1(a) are due to the different val-

ues of s_u and V_c (contact vertical load at full penetration). Thus, those differences can be reduced normalising V' (and $V' + |S|$) by V_c or by $s_u(2R)^2$ as shown in Figure 7.1(b).

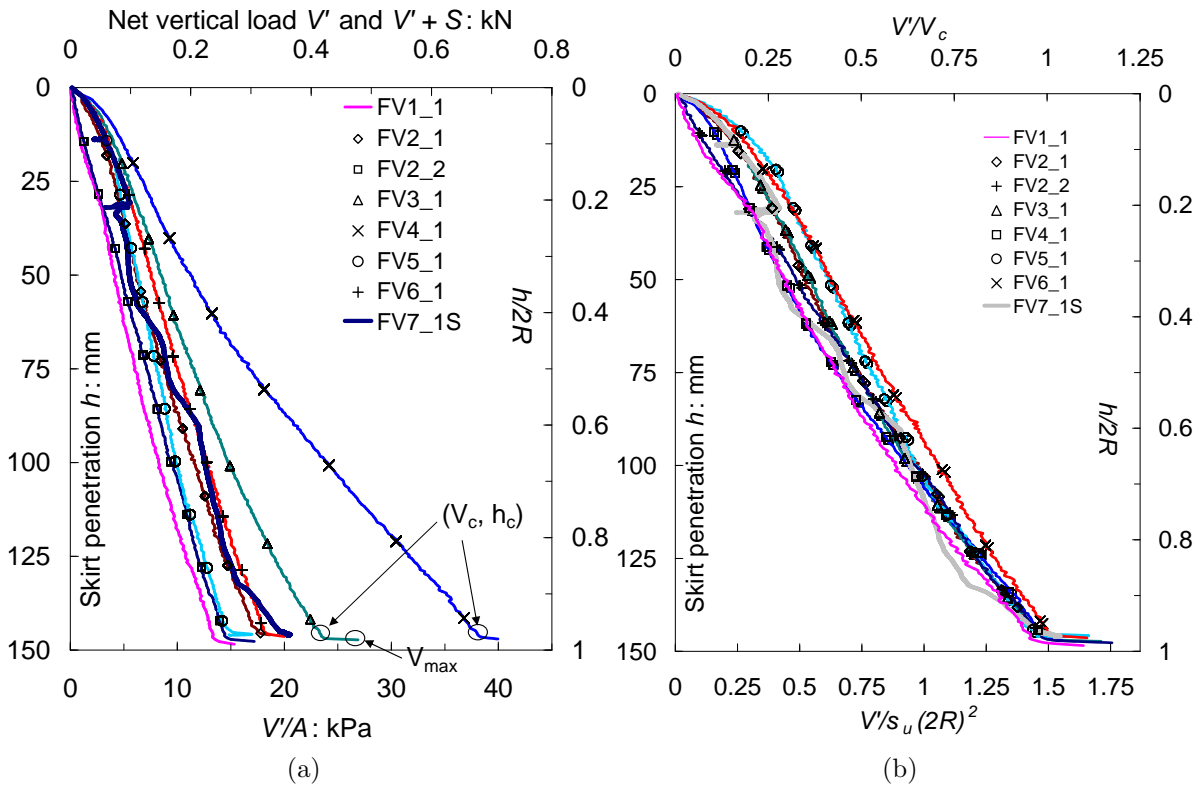


Figure 7.1: (a) Load-penetration curves, (b) Normalised load-penetration curves

From the load-displacement curves shown in Figure 7.1(a), values of contact vertical load V_c , contact penetration h_c , V_{max} , and back-calculated values of adhesion $\alpha_i = \alpha_o$ were obtained and are summarized in Table 7.1. It is worth pointing out that differences between the values of h_c and $L = 150$ mm (4 mm in average) are due to internal soil-plug upheaval, which is caused by the soil displaced inwards by the skirt penetration. Surprisingly, the inwards flow caused by the suction did not induce more upheaval than that obtained in the pushing tests. If only inwards movement occurred the soil volume displaced by the skirt penetrating would result in a heave of 4 mm (with 1 mm wall thickness). This suggests that the volume occupied by the penetrating skirts may be fully displaced inwards, indicating the existence of a non-symmetrical shear failure mechanism. This demonstrates that the plug-heave represents a tiny 2.7% of the caisson length L . In caissons with higher $\frac{L}{2R}$ heave can be totally different, for instance House (2002) reported cases for $\frac{L}{2R} > 8$ (in NC kaolin) where the plug-heave percentage was as high as 30% or 40%.

Table 7.1: Parameter values obtained from the installation test results

Test	V_c N	h_c mm	V_{max} N	$\alpha_{io}\dagger$	s_u kPa
FV1_1	248	148	500	0.35	7.3
FV2_1	316	146	998	0.47	8.1
FV2_12	260	147	1089	0.42	7.3
FV5_1	271	145	301	0.55	6.1
FV3_1	417	146	478	0.50	10.2
FV6_1	321	145	417	0.48	8.4
FV4_1	682	147	1082	0.60	13.2
FV7_1‡	353	145	353	0.40	9.8

†back calculated using $N_c = 9$

‡installation by suction, $\alpha_{io} = 0.5$ assumed for the initial pushing installation

Normalisations by s_u and V_c are shown in Figure 7.1(b) because a linear relationships was found between s_u and V_c . The values of s_u were obtained from shear vane measurements carried out after each test in non disturbed sites at depths of 25 mm and 125 mm (Table 2.5). Whilst, V_c values were obtained directly from the load-displacement curves (Table 7.1). Figure 7.2 shows that the results of s_u at 125 mm depth are more consistent than the obtained at 25 mm, since (discarding test FV5_1) more scatter occurred for measurements close to the surface. This is confirmed by the higher value of the coefficient of determination R^2 (closer to 1) of the fitted curve. The value of s_{u125} assumed as s_u at the tip gives hence more consistent values for normalisation by the clay strength.

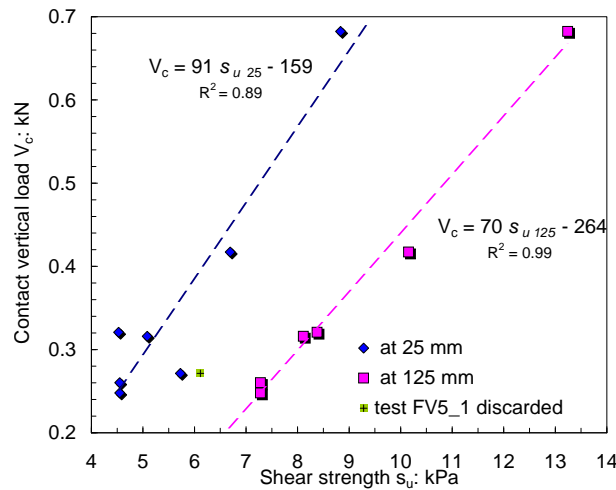


Figure 7.2: Relationships between V_c , measured in caisson installation tests, and s_u , measured at two depths: close to the surface and close to the caisson tip

The equations (7.1) and (7.2) were use to fit the load-penetration curves by back-analysing a theoretical adhesion factor, assumed to be equal inside and outside the caisson skirt ($\alpha_{io} = \alpha_i = \alpha_o$). Figure 7.3(a) shows that the values of α_{io} obtained correlated reason-

ably well with s_u and hence with V_c . The expression that best fit the results is:

$$\alpha = 0.0275s_u + 0.23 \quad (7.3)$$

It is important to mention that (7.3) is restricted to the particular conditions of the testing, namely $\frac{L}{2R} = 1$ and a heavily OC clay. The API RP2A (1993) (quoted by Kolk and van der Velde, 1996) established expressions for axial capacity of fully installed driven piles in clay (after full consolidation). For clays with plasticity index of $I_p > 20\%$, α can be obtained as follows

$$\begin{aligned} \alpha &= \frac{1}{2} \left(\frac{s_u}{\sigma'_v} \right)^{-0.5} & \text{for } \frac{s_u}{\sigma'_v} \leq 1.0 \\ \alpha &= \frac{1}{2} \left(\frac{s_u}{\sigma'_v} \right)^{-0.25} & \text{for } \frac{s_u}{\sigma'_v} > 1.0 \end{aligned} \quad (7.4)$$

Although (7.4) has been found to be adequate for piles in heavily OC clays (Kolk and van der Velde, 1996), resulting values of α between 0.22 and 0.26 are too conservative to be applied for caissons. This reveals that direct extrapolations from pile design may lead to wrong predictions in suction caisson analyses. Conversely, Andersen and Jostad (1999, 2002) suggest that the reduction of s_u along the skirt due to penetration is caused by clay remoulding. On the grounds that by definition the clay sensitivity is a measure of the remoulded state, they define that α is the inverse of the sensitivity S_t , as defined by Terzaghi (1943), in the following form:

$$\alpha = \frac{C_t}{S_t} = C_t \frac{s_{u(\text{remoulded})}}{s_{u(\text{peak})}} \quad (7.5)$$

where C_t is the thixotropy strength ratio which accounts for the capacity of a remoulded clay to return to its undisturbed state after a certain time interval (Skempton and Northey, 1952). For kaolin clay C_t is close to unity, for other clays refer to Skempton and Northey (1952) and Andersen and Jostad (2002). Equation (7.5) gives an initial value of α , which is obtained immediately after installation, hence before any dissipation of excess pore pressures. Figure 7.3(b) shows $\alpha - \Theta$ curves obtained from shear vane tests. The ma-

majority of these tests were stopped around 60° of rotation, after a peak value was reached. However, three vane tests carried out in sample 6 continued further until a remoulded condition (assumed as residual) was reached after more than 360° of rotation. It can be observed that a value of α around 0.4 can be obtained directly from the plot for a depth of 125 mm (slightly lower than the back-calculated 0.48), and around 0.25 for a depth of 25 mm.

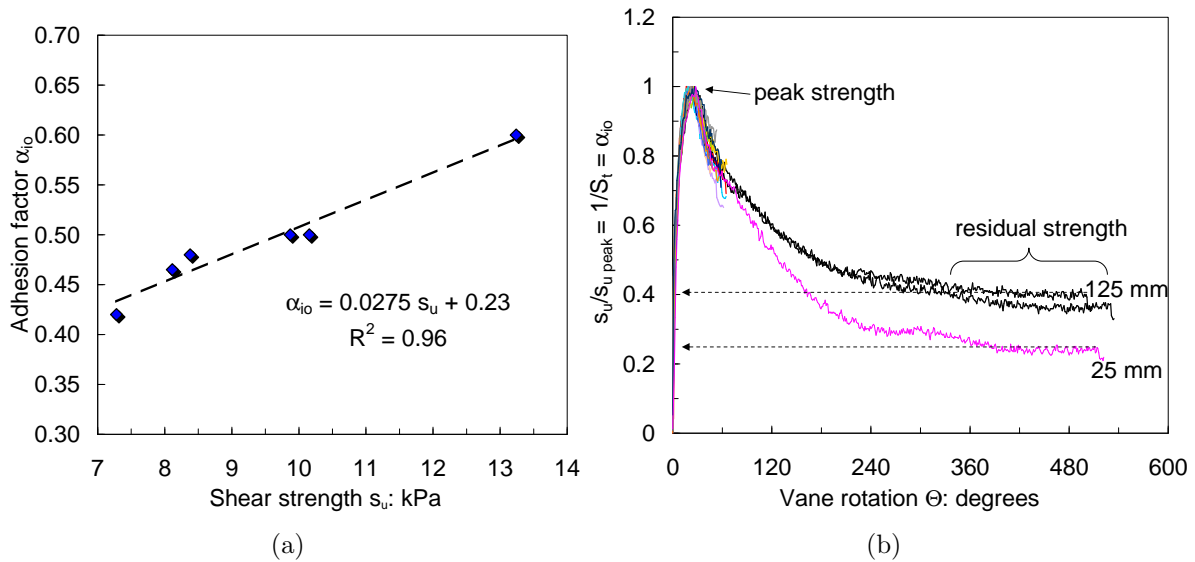


Figure 7.3: (a) Relationship between the adhesion factor and the shear strength $\alpha - s_u$, and (b) adhesion factor as the inverse of the sensitivity $\alpha = \frac{s_{u(remoulded)}}{s_{u(peak)}} = \frac{1}{S_t}$ versus vane rotation Θ

With the back-calculated α values an estimation of the caisson penetration resistance with depth using equation (7.1) is presented in Figure 7.4(a) for test FV2_1. It can be observed that between 5 mm to 60 mm of penetration the calculated V' is lower than the measured value of V' . This is due to the lower shear strength assumed in the idealized distribution for that range of penetration. However, the predicted curve is fairly close to the measured curve after that initial layer was penetrated.

Figure 7.4(b) shows the measured and calculated suction-penetration curve obtained in test FV7_1. To account for the variation of strength with depth in the same plot the suction appears normalised by $\frac{s}{\rho 2R}$, where the shear strength gradient $\rho = \frac{ds_u}{dz}$ was assumed constant and equal to 23 kPa/m. This is a very high value compared with values around 1 kPa/m reported for NC clay by Chen and Randolph (2004). In OC clays much

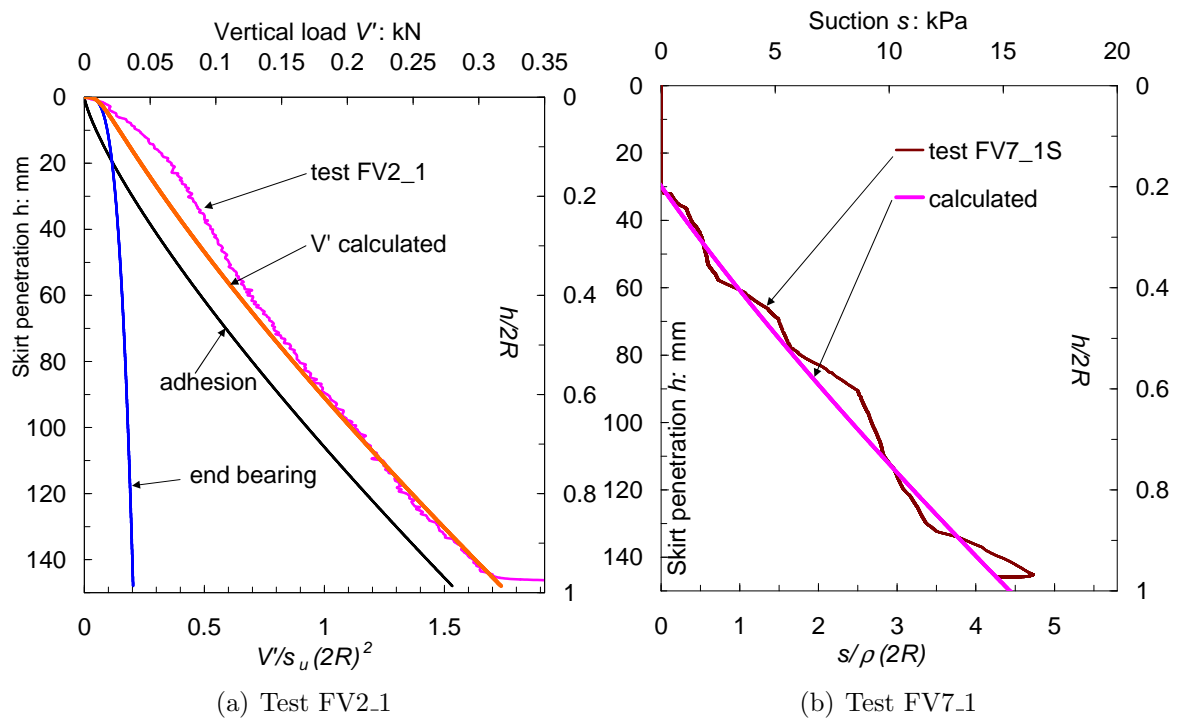


Figure 7.4: Measured and calculated (a) load-penetration curve, and (b) suction-penetration curve ($\rho = \frac{ds_u}{dz}$)

higher values of ρ can be observed near the surface. Valuable comparisons with field values can be obtained by means of the quantity $\frac{\bar{s}_u}{\rho 2R}$. The application of suction introduced a reduction of the back-calculated α value from 0.5 (pushing) to 0.4. In the long term the dissipation of excess pore pressures after the caisson suction installation in a NC clay induces horizontal consolidation, therefore, a horizontal coefficient of consolidation c_h should be used in the analysis (Cao *et al.*, 2002). For instance, calculation examples of α as a function of the dissipation time is presented by Andersen and Jostad (2002) for different type of clays.

7.1.4 Pullout capacity

The tensile capacity of a suction caisson with the compartment fully sealed, *i.e.* valves closed, and assuming a reversed bearing capacity failure can be expressed by (House, 2002):

$$V_{pullout} = W + (N_c s_u - \sigma_{v tip}) \pi R^2 + \alpha_o \bar{s}_u 2\pi R_o h \quad (7.6)$$

where $V_{pullout}$ represents the pullout capacity, W represents the submerged weight of the caisson plus the total soil-plug weight and plus the weight of the water column above the caisson lid. N_c is the reverse bearing capacity factor, σ_{vtip} is the total stress at the caisson tip, α_o is the outside adhesion factor and \bar{s}_u is an average undrained shear strength. Equilibrium of the axial forces of the soil-plug allows the calculation of the suction developed under the caisson lid according to Fuglsang and Steensen-Bach (1991) (quoted by House, 2002) as follows:

$$s = \alpha_i \bar{s}_u \frac{2h}{R_i} - N_c s_u \quad (7.7)$$

where α_i is the inside adhesion factor. Using (7.6) N_c can be obtained from experiments, assuming for instance that α_o does not change in the short term, *i.e.* the time interval for the pullout event is not long enough for consolidation to occur. In long term pullout events α_o in equation (7.6) may probably increase from installation values. This consolidation effect is more pronounced in NC clays as revealed by Watson (1999) and House (2002) in centrifuge tests, where days, weeks and even years of consolidation time were simulated.

Pullout tests using caisson D were performed at a rate of 2 mm/s (limited by the maximum rate of the loading rig). Taking the diameter as the relevant dimension gives a value of $v_n = 250$, which is high enough for a fully undrained condition to be assured. The pullout test FV3_8 was performed after a swipe event from $V' = 0.45$ kN to 0.18 kN and a series of five moment loading events at constant $V' = 100$ N, from which practically no vertical displacement was observed (see Tables 7.3 and 7.4). The resulting maximum pullout load recorded was -1.8 kN with a maximum pore load of -1.5 kN ($u' = -85$ kPa) after a caisson extraction of 27 mm. Pore load is the pore pressure multiplied by the interior sectional area of the caisson lid. It was observed that the soil around the caisson sunk during extraction, implying that the soil-plug inside the caisson lost the contact with the soil at the base causing a reversed bearing capacity failure mechanism.

The response in terms of pressure $\frac{V'}{A}$ and u' versus extraction h is shown in Figure 7.5(a),

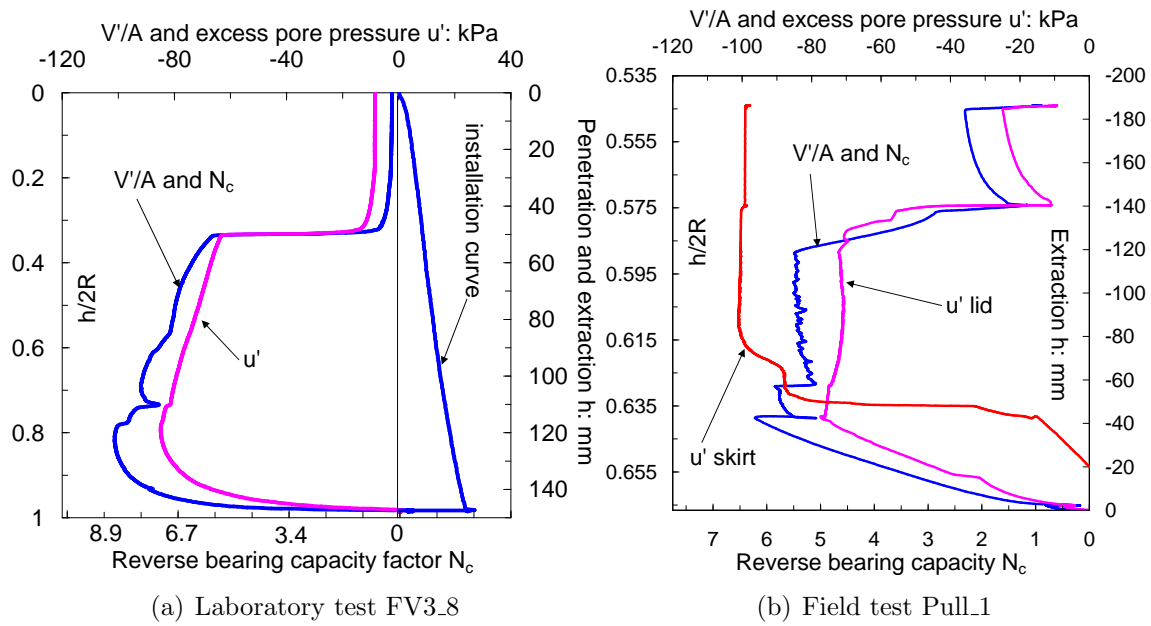


Figure 7.5: Pullout test curves: (a) laboratory and (b) field (from Houlsby *et al.*, 2005)

including the installation curve and the unloading caused by the swipe test. Figure 7.5(a) also shows in the bottom abscissa the variation of N_c calculated with equation (7.6) assuming $\alpha_o = 0.5$ (obtained from the installation). The maximum value of N_c (at the maximum pullout load) was 8.6, which is lower than the theoretical lower bound solution of $N_c = 9.3$ determined by Martin (2001) for a caisson with identical aspect ratio, smooth skirts, but in a NC soil. A smooth condition agrees with observations after the caisson extraction, as it was found that the external skirt was very clean.

Results from large scale pullout tests carried out by Houlsby *et al.* (2005) with a caisson 1.5 m diameter and skirt length of 1 m are shown in Figure 7.5(b), where it can be seen that u' was measured close to the tip and reaches the highest value. The maximum value of N_c obtained was 6.4 using an adhesion factor $\alpha = 0.2$ as suggested by the same authors. Martin's (2001) lower bound solution for an aspect ratio of 0.67 and for rough and smooth skirts give values of 10.1 and 9.3 respectively. Although similarities exist between $\frac{V'}{A}$ and u' , measured in the laboratory and measured in the field, there is a pronounced disparity in extraction, $\frac{h}{2R} \approx 0.65$ in the laboratory, whereas $\frac{h}{2R} \approx 0.1$ in the field. The load-controlled mode applied in the field seems to be the cause for the much lower pullout capacity and extraction. In load-controlled tests it is difficult to reach and hold loads

close to failure. For that reason lower capacities are obtained without the possibility of having post failure softening.

7.2 CYCLIC VERTICAL LOADING TESTS

7.2.1 Introduction

The investigation of vertically cycled caissons is pertinent for multiple-caisson foundations for offshore wind turbines, since the tensile capacity controls the response. It is assumed that there is sufficient separation amongst the footings to reduce to a minimum any interaction effect. Therefore, the analysis of a single suction caisson is appropriate. Previous studies by El-Gharbawy (1998) and House (2002) have concentrated on cycling around high negative mean vertical loads (cyclic pullout) as well as aspect ratios relevant for anchoring applications ($\frac{L}{2R} \geq 3$). In this study, three series of tests with escalating sequences of 10 cycles per load packet were planned. The first series considered increasing load packets around the $V' = V_c$, load reached by the caisson after the pushing installation. In the second series the increasing cycling was carried out around $V' = 0$ N, after unloading from the V_c value reached in the pushing installation. The third series was a repetition of the second, but employing suction instead of pushing to install the caisson, hence unloading from $V' + |S|$. In this form assessment of the effect of the installation method on the caisson cyclic response can be made. To this end, evaluation of the stiffness degradation, displacement and pore pressure variations were pursued.

Before analysing the test results, it is important to look at the load, displacement and pore pressure variation with time during a cyclic event. Pseudo-load-controlled tests were conducted by means of a feedback subroutine with a specified loading history. Examples of sinusoidal loading history inputs with a period of 12 seconds (0.08 Hz) are shown in Figures 7.6(a) and 7.6(b) as $\frac{V'}{A}$. Extreme waves have long periods, typically between 7 s to 13 s (Kühn, 2002). Byrne (2000) found in dense oil-saturated sand that for frequencies between 0.3 Hz and 0.03 Hz there is very little influence on the caisson response as long

as a failure condition is not approached. El-Gharbawy (1998) showed that in NC clay cyclic pullout close to the long term failure (drained capacity) caused the same 13 mm of displacement after: 300 cycles at 20 Hz, 2000 cycles at 2 Hz, or 10000 cycles at 0.2 Hz. These findings imply that there is a frequency effect for higher frequencies than those considered by Byrne (2000), but for cyclic pullout loads close to failure.

Tests were in reality displacement-controlled, since to achieve a specified loading history the stepper motor moves up or down the caisson attached to the rig arm until the target load is reached within a certain tolerance. It can be observed in Figures 7.6(a) and 7.6(b) that $\pm\Delta V'$ peaks of the first cycles are slightly below of the remaining peaks. This shows the effect of low gain values introduced at the beginning of the test in the feedback control subroutine; once the gain was increased $\pm\Delta V'$ peak values were closer to the nominal targets. However, even with the increase of the gain during cycling the target nominal $\pm\Delta V'$ peaks were never accurately achieved. This subtle detail did not cause any effect on the results obtained.

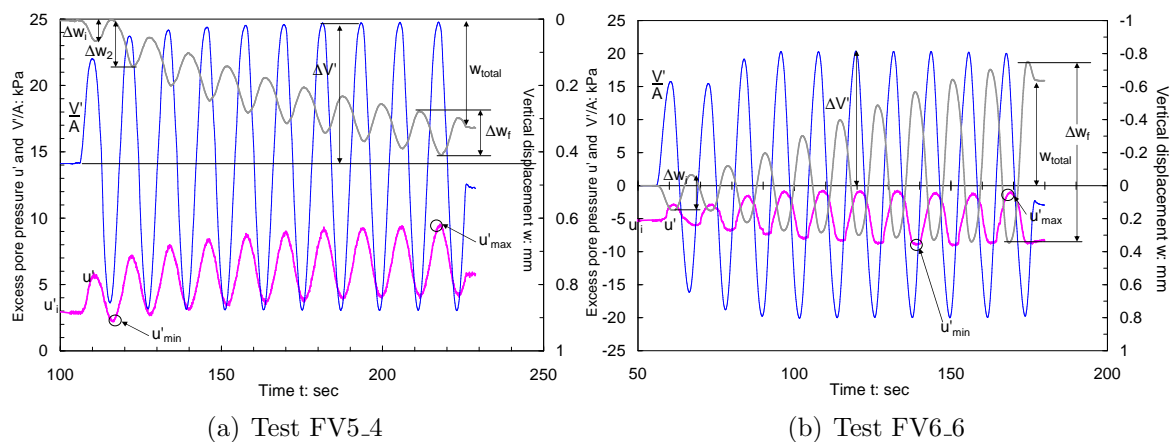


Figure 7.6: Loading history applied (as average pressure over the lid area $\frac{V'}{A}$), displacement w , and excess pore pressure u' response, showing characteristic parameters used in the analysis

Figure 7.6(a) shows the displacement variation Δw in each cycle, but because $\Delta w_2 \approx \Delta w_f$ a common value $\Delta w = \Delta w_f$ was collected for the entire cycling event (ignoring Δw_i which corresponds to the initial half cycle). Conversely, in test FV6_6 it is not possible to claim uniformity of Δw for all the cycles since Δw is indeed varying cycle after cycle as can be clearly observed in Figure 7.6(b). To simplify the analysis, initial and final values of Δw_i

and Δw_f were collected. Additionally, it was important to account for the total or net vertical movement w_t of the caisson at the end of each cyclic event. A maximum and a minimum excess pore pressure value (u'_{max} , u'_{min}) during a cycling event was considered an appropriate indication of the range of variation of u' . The variation of u' in test FV5.4 occurs mainly above the initial value u'_i , whereas in test FV6.6 u' varies around u'_i . Values of u'_{max} and u'_{min} are able to capture these variations.

7.2.2 Results of cyclic loading around $V_m = V_c = 250$ N

In the first series of tests, immediately after the installation by pushing, the caisson was cyclically loaded by a series of eight loading packets of 10 cycles each. Increasing cyclic amplitudes $\pm\Delta V'$ from ± 47 N for the first packet to up to ± 560 N for the last packet were applied around a mean vertical load $V_m = V_c = V_o = 250$ N, *i.e.* the load required to penetrate the caisson into the ground V_c was at the same time the maximum pre-load V_o experienced by the caisson at $h_c = 145$ mm. The load-displacement curves of the whole sequence of cyclic events are presented in Figure 7.7(a) adopting two nor-

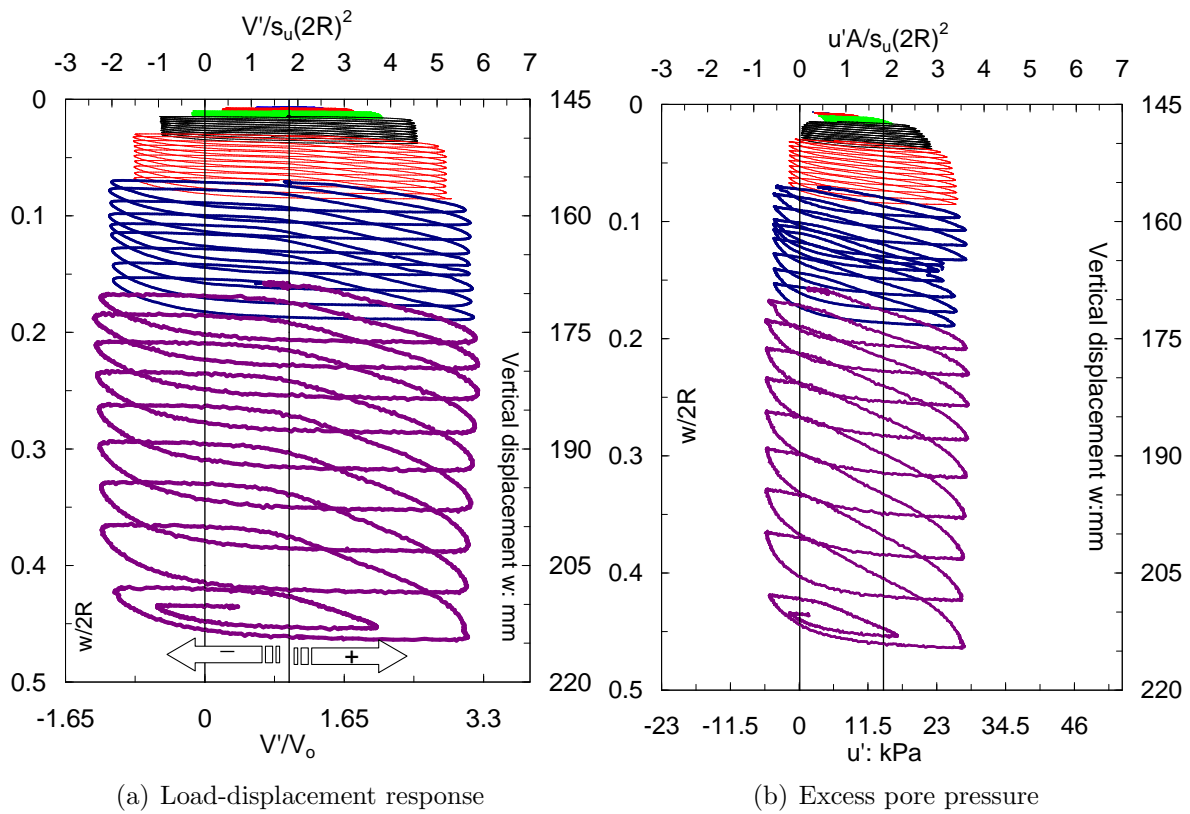


Figure 7.7: Series of cyclic vertical loading events FV5 under $V_m = 250$ N

malisations: strength s_u and ‘pre-load’ V_o , which are related by the relationship stated in Figure 7.2. Variation of s_u with depth has not been taken into account since its profile is fairly constant as can be seen in Figure 2.4(b) (Tank 2).

Figure 7.7(b) shows the variation with depth of u' and also the normalised excess pore load $U' = u'A$, where A is the cross sectional area of the caisson πR_i^2 . These figures allow only the inspection of events with extremely large displacements corresponding to the last two or three loading packets, where the caisson reached a settlement almost half of its length L . Note that there is no sign of settlement attenuation in these large displacement cycles. It is also worth observing that the positive build-up of pore water pressure accounts for almost half of $\frac{V'}{A}$.

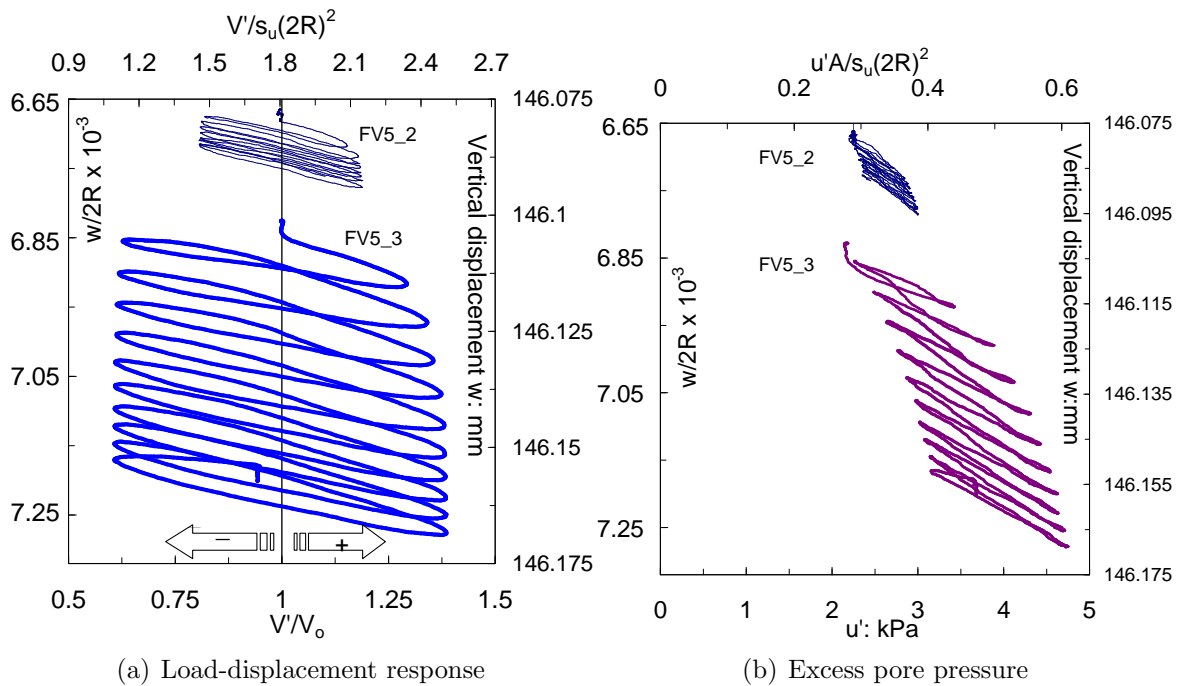


Figure 7.8: Tests FV5_2 and FV5_3 under $\Delta V' = \pm 50$ N and ± 100 N

Figures 7.8(a) and 7.8(b) show the load-displacement curves of tests FV5_2 and FV5_3, corresponding to the first two loading packets, *i.e* the lowest $\pm \Delta V'$ applied, which in turn resulted in the smallest displacement variations measured. The high resolution of the short LVDTs ($1 \mu\text{m}$) allowed refined displacement measurements as shown in the figures. The entire cyclic loading induced irrecoverable settlements and little build-up of pore water pressure. It is worth highlighting that the rate of settlement attenuates after

each cycle as can be clearly observed in the second loading packet, which may tend in the long term to a state where only very small settlements occur (cyclic shakedown). Furthermore, it is important to point out that this type of ‘small’ load-displacement response will be more often experienced by a caisson in a tetrapod foundation, but for periods probably lower than 12 s.

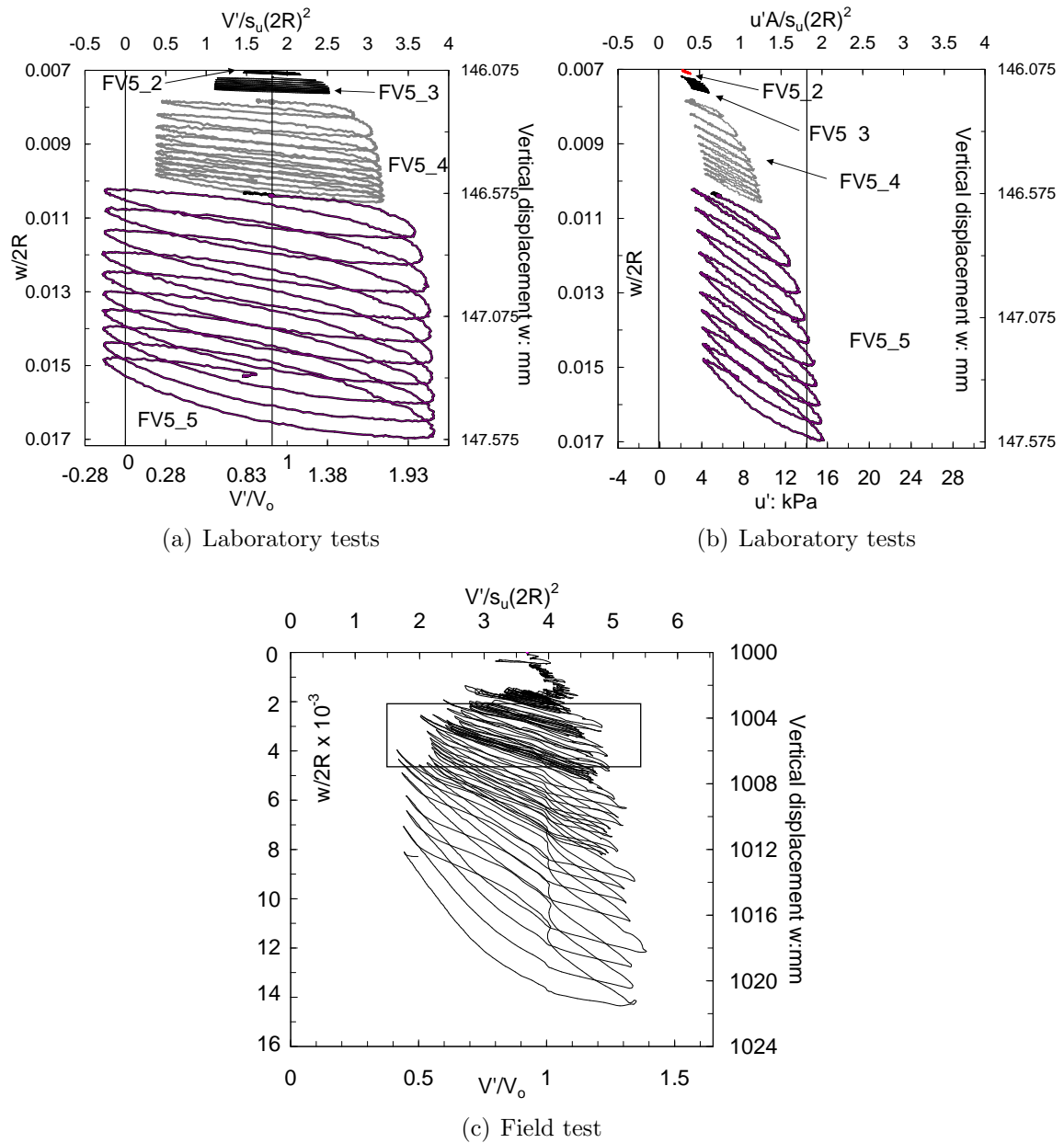


Figure 7.9: Normalised curves obtained in the laboratory and in the field site at Bothkennar (taken from Houlsby *et al.*, 2005)

The next tests FV5_4 and FV5_5, shown in Figures 7.9(a) and 7.9(b), exhibit a substantial increase in settlement compared with the previous lower $\Delta V'$ tests FV5_2 and FV5_3. Moreover, excess pore water pressure variations are more significant, reaching values that

account for approximately half of the load pressure $\frac{V'}{A}$. An attempt to compare these results with results obtained in large scale tests is pursued in the following. Houlsby *et al.* (2005) carried out lateral cyclic loading tests with a caisson of 1.5 m diameter and an aspect ratio of 0.67. A vertical load-displacement response was obtained since a constant load ratio $\frac{H}{V'}$ was attempted whilst loading laterally. It was not possible to keep $\frac{H}{V'}$ constant due to difficulties in the simultaneous control of two hydraulic jacks, leading to a complex load path. Figure 7.9(c) shows the vertical load-displacement curve obtained with the large caisson. Notwithstanding the test condition disparities, the framed part of the field curve shown in Figure 7.9(c) has a resemblance to the curve of test FV5_4, since in both cases $\frac{\Delta V'}{V_o} \approx \pm 0.5$ and $\frac{\Delta w}{2R} \approx 0.002$. However, the lateral loading in the large caisson reduced drastically the vertical response by approximately a factor of three when interpreted as the normalised secant stiffness $\frac{K_v}{2R s_u}$.

7.2.3 Results of cyclic loading around $V_m = 0$ N

The second and third series of cyclic tests were carried out to investigate the response of cyclic loading around $V' = 0$. The former was conducted immediately after the caisson was installed by pushing and the latter immediately after the caisson was installed by suction. Figures 7.10(a) and 7.10(b) show the load-displacement curves for the whole sequence of cyclic tests, where is only possible to observe large displacements caused by the largest $\pm \Delta V'$. A totally different load-displacement response was obtained compared with the response shown above (cycling around $V_m = V_c$). There are also differences between the curves shown in Figures 7.10(a) and 7.10(b), revealing that the installation method has an effect on the short term cyclic response. On one hand, a gradual increase of displacement with cyclic loading occurred in the pushing installation case (increasing degradation due to softer response), leading to failure for $\Delta V' = \pm 505$ N. On the other hand, the suction installation induced a much stiffer response for values of $\Delta V'$ beyond ± 505 N until sudden large displacements occurred for $\Delta V' = \pm 744$ N.

Figures 7.10(c) and 7.10(d) reveal that totally different excess pore water pressure vari-

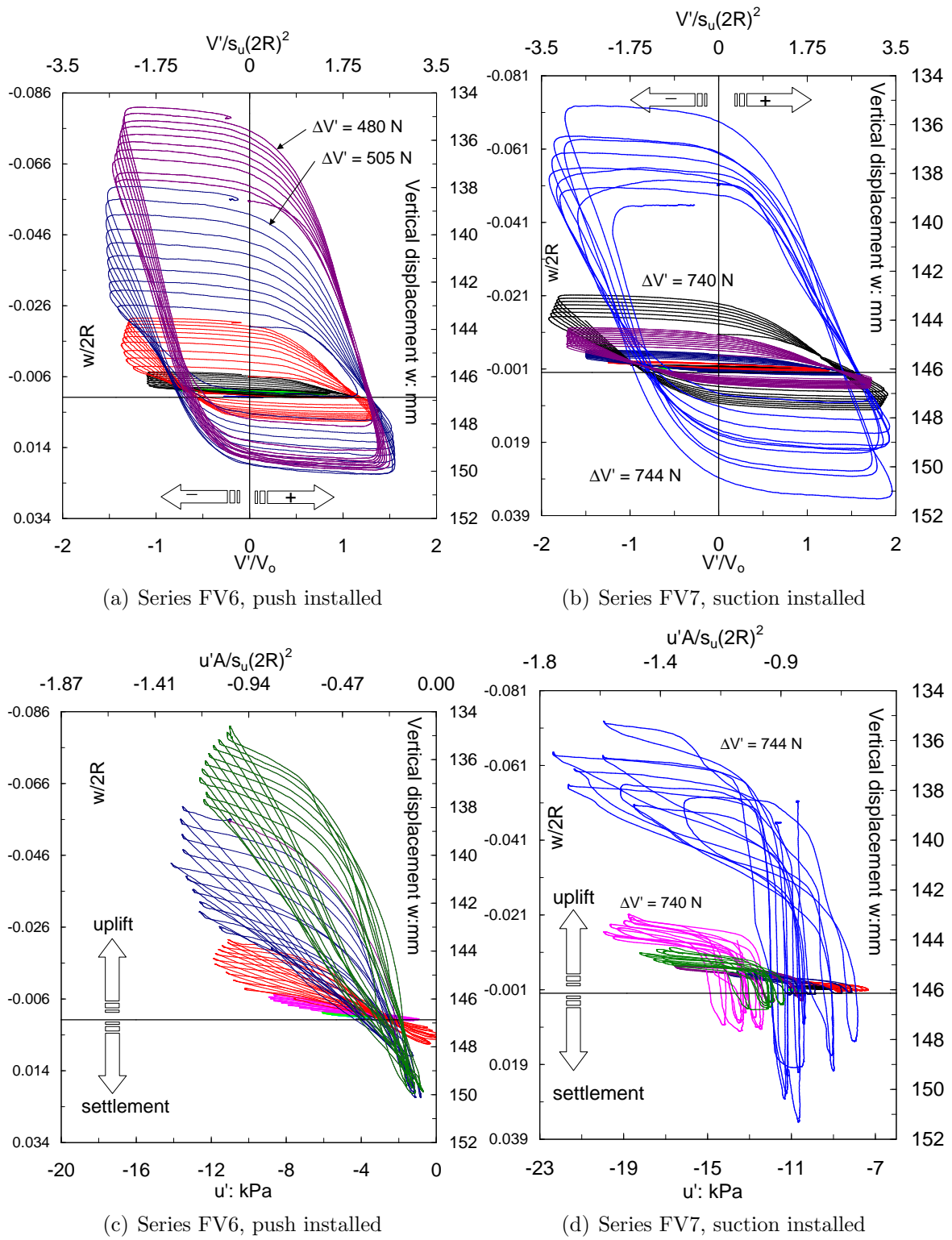


Figure 7.10: Sequence of vertical loading events FV6 and FV7 under $V_m = 0$ N showing: (a), (b) load-displacement response and (c), (d) pore pressure-displacement response

ations were found in these tests compared with the cycling tests around $V_m = 250$ N. Whilst only negative values were measured in the former (even under compression loads), predominant positive values were measured in the latter, although negative values were

measured under the presence of high tensile loads (Figure 7.7(b)). This is evidence of the fact that the development of excess pore water pressure is directly related to the caisson vertical movement. As a result, for cycling around $V' = 250$ N permanent settlement generated positive excess pore pressure and during cycling around $V' = 0$ N predominant upward movement generated exclusively suction. The uplift was, however, not permanent since the caisson moves up and down passing through the initial position ($\frac{w}{2R} = 0$) in each cycle.

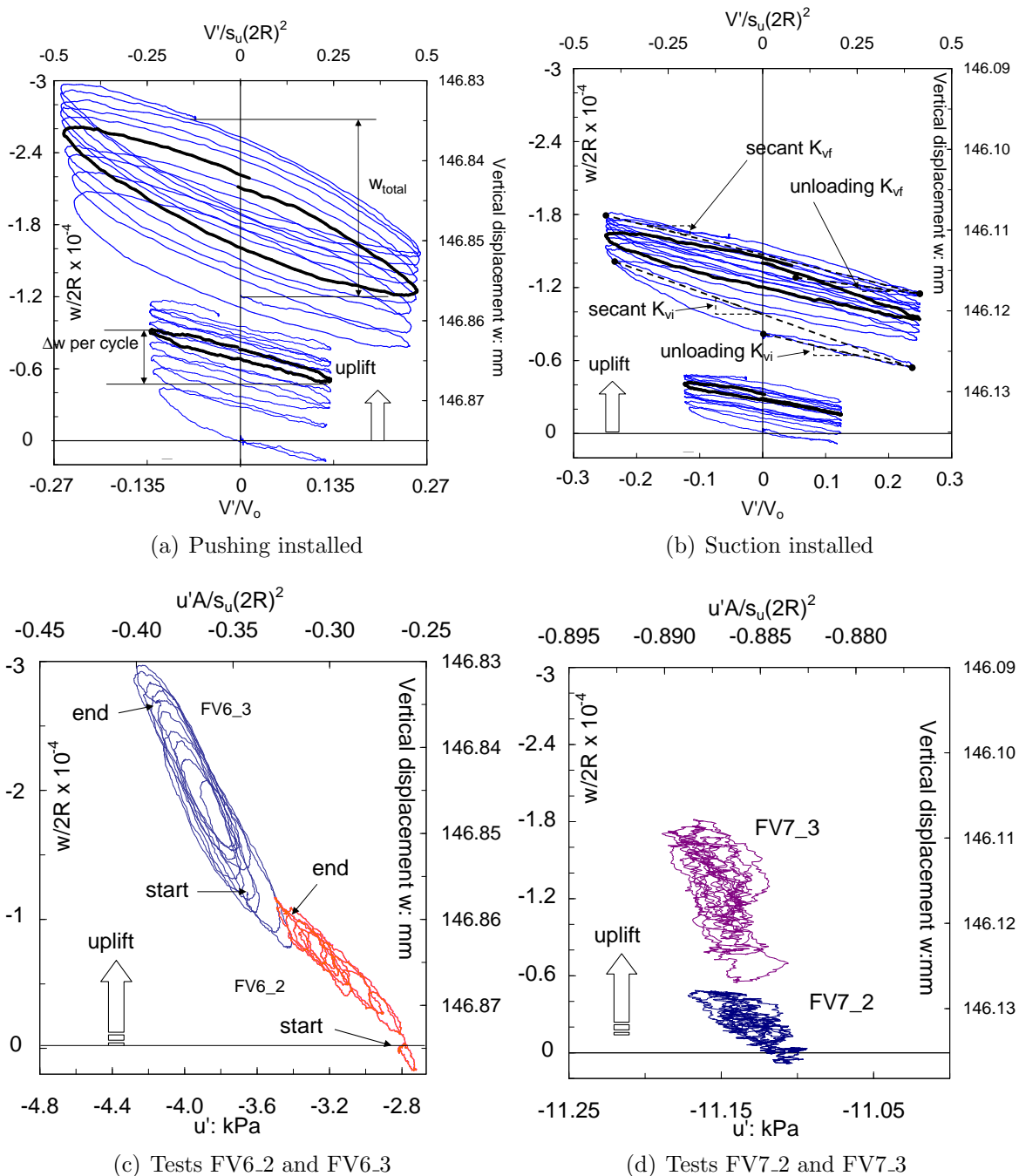


Figure 7.11: Small displacement response showing curves of normalised load-displacement and excess pore load and excess pore pressure variation with displacement

The first two series of loading tests had very small displacements under the application of the nominal values of $\Delta V' = \pm 50$ N and ± 100 N, for that reason they are not visible in Figures 7.10(a) and 7.10(b). As mentioned before, it is of fundamental importance to study the range of small displacements since they represent the expected foundation serviceability condition, with large displacements to be encountered in sporadic loading events. Previously it was found that for the same nominal load amplitudes ($\Delta V' = \pm 50$ N and ± 100 N) irrecoverable settlements occurred when cycling around $V_m = 250$ N. Figures 7.11(a) and 7.11(b) show that now a permanent uplift occurs when the same cyclic load amplitude is applied around $V_m = 0$ N. It is important to highlight that displacements of the caisson installed by pushing were higher than displacements of the caisson installed by suction. An explanation for this difference can be found in the higher suction during the loading. The suction varied with the vertical movement of the caisson as can be observed in Figure 7.11(c). On the contrary, no suction variation is observed in Figure 7.11(d), where $u' = u'_i = -11$ kPa, value that represents a great percentage of the maximum suction applied during the installation ($s \approx 16$ kPa).

7.2.4 Comparison of displacements and excess pore pressure

This and the next section attempt to find patterns of the caisson behaviour as a function of the displacement variation Δw occurring in each cycle. Table 7.2 summarizes the values of the parameters to be compared.

Figure 7.12(a) shows clearly the increase of vertical displacement with vertical load in the semi-log plot. For the series of tests FV5 there was very little variation of Δw within each loading packet of cycles (Figure 7.6(a) shows an example), for that reason the points of the first cycle are merged with the points of the last cycle. Conversely, for the series FV6 and FV7 this was not the case in all the tests, for instance, there were tests where in the last cycle Δw was larger than for the first cycle as shown in Figure 7.6(b). The points for the series FV5 follow a fairly straight line in the semi-log plot, which is followed closely by the series FV7, except for the last packet. However, the series FV6 follows this

Table 7.2: Parameters of the series of cyclic vertical loading tests

Test	$\pm\Delta V'$ N	Secant		Unloading		$\Delta w \dagger$ mm	w_{total}	u' kPa		
		K_{vi} N/mm	K_{vf} N/mm	K_{vi} N/mm	K_{vf} N/mm			initial	min	max
FV5_2	47	20591	16249	17953	13898	0.015	0.01	2.25	2.25	3
FV5_3	96	18453	12316	16025	14347	0.032	0.06	1.9	1.9	4.5
FV5_4	187	5295	3841	11490	5874	0.14	0.4	3	2.2	9.4
FV5_5	280	2794	1815	7862	5377	0.37	0.9	5.3	3	15.3
FV5_6	380	1362	646	4629	3266	1.45	3.4	6.3	0	21.7
FV5_7	460	563	344	3648	3133	3.3	8	5.9	-2.1	26
FV5_8	530	284	209	2937	1786	7.6	17.4	5	-4.3	27.8
FV5_9	560	198	140	963	1458	14.36	45.5	4.8	-5.6	28
FV6_2	45	9409	16722	19135	22615	0.009	-0.02	-2.8	-3.6	-2.7
FV6_3	90	9100	8596	14469	17162	0.023	-0.02	-3.7	-4.3	-3.3
FV6_4	180	5491	4248	15310	16280	0.07→0.09	-0.07	-4.25	-5.8	-3.4
FV6_5	270	3749	2178	13137	11307	0.1→0.23	-0.09	-5.2	-6.17	-2.3
FV6_6	360	2684	653	18284	7296	0.2→1.06	-0.66	-5	-8.9	-0.7
FV6_7	450	611	198	5301	5738	1.3→3.7	-2.3	-7.5	-11.8	0.3
FV6_8	505	229	83	2090	1934	3.9→11.7	-5.4	-8.7	-14.1	-0.85
FV6_9	480	87	58	1508	1379	10.3→14.5	-3.57	-11	-12.5	-0.7
FV7_2	46	21190	26690	29636	25140	0.010	-0.01	-11	-11.1	-11
FV7_3	92	13402	18854	22413	24666	0.016	-0.01	-11	-11.1	-11
FV7_4	186	10926	9685	20272	22437	0.042	-0.02	-11.2	-11.2	-10.8
FV7_5	275	8145	6231	18211	17725	0.09	-0.01	-11	-11	-10.4
FV7_6	385	6312	4554	16707	16062	0.14→0.17	-0.02	-10.6	-10.8	-8.6
FV7_7	480	3729	2468	8539	9746	0.28→0.39	-0.08	-9	-10.7	-7.1
FV7_8	580	2057	1154	6757	6106	0.6→0.99	-0.37	-9	-14	-8.2
FV7_9	660	1008	539	5588	4627	1.43	-0.96	-11.9	-18.2	-10.5
FV7_10	740	501	294	4133	3328	3.26→5.31	-1.6	-15	-20	-12
FV7_11	744	160	115	2584	1689	9.78→33	-2.5	-10.6	-22.3	-7.9

†initial and final range of vertical displacement per cycle

line in the first four loading packets after which the first cycle points deviate slightly and the last cycle points deviate even more, following a different line.

The difference between the maximum and minimum excess pore pressure normalised by s_u is shown in Figure 7.12(b) as a function of $\log \frac{\Delta w}{2R}$, but for more clarity, Δw is now presented as the average between the first and last cycle. The maximum difference was found in the series FV5 ($V_m = 250$ N), whereas the lowest differences corresponded to the suction installed caisson for $V_m = 0$ N. The excess pore pressure difference between the series FV6 and FV7 were related to the initial excess pore pressure u'_i . For the suction installed caisson $u'_i = -11$ kPa (test FV7.2), giving evidence of the recent maximum suction applied ($s \approx 16$ kPa) to install the caisson. Not surprisingly, u' has not yet been dissipated due to the short time elapsed. During cyclic loadings with small $\frac{\Delta w}{2R}$ ($< 10^{-3}$), u' did not move away from u'_i , but when larger Δw were caused $\Delta u'$ increased significantly with Δw

from u'_i . No excess pore pressure accumulation was observed since at the beginning of every cyclic loading event $u' \approx u'_i = -11$ kPa. Conversely, for the push installed caisson u' at the beginning of every cyclic loading event varied after each series of cycling events from -2.8 kPa for FV6_2 to -11 kPa for FV6_9. This short term excess pore pressure response needs confirmation with long term results, *i.e.* when excess pore water pressure generated during installation has been mostly dissipated.

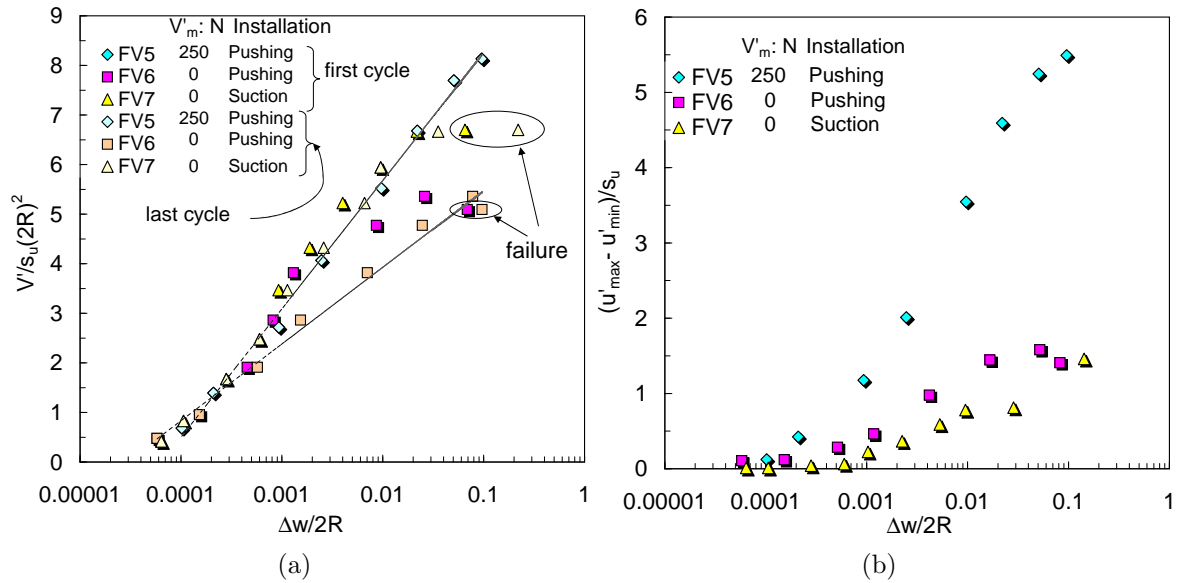


Figure 7.12: (a) Normalised load *versus* displacement variation per cycle and (b) normalised range of pore pressure variation *versus* average displacement variation

7.2.5 Comparison of caisson foundation stiffness

Normalised secant and unloading stiffness, determined as illustrated in Figure 7.11(b), are shown in Figures 7.13(a) and 7.13(b), respectively. Including initial and final stiffness (K_{vi} , K_{vf}) to reveal whether there exists or not degradation within the cycles at the same constant load amplitude $\pm \Delta V'$.

It can be observed that for all the series the secant stiffness shows a clear decrease with displacement (or load amplitude). Series FV5 presents also a stiffness decrease within each 10 cycles of loading. On the contrary, the series FV6 and FV7 have an initial stiffness lower than the final stiffness for the cycling loading with $\Delta V' = 46$ N. This only reveals that a weak initial response occurred (larger uplift during unloading than settle-

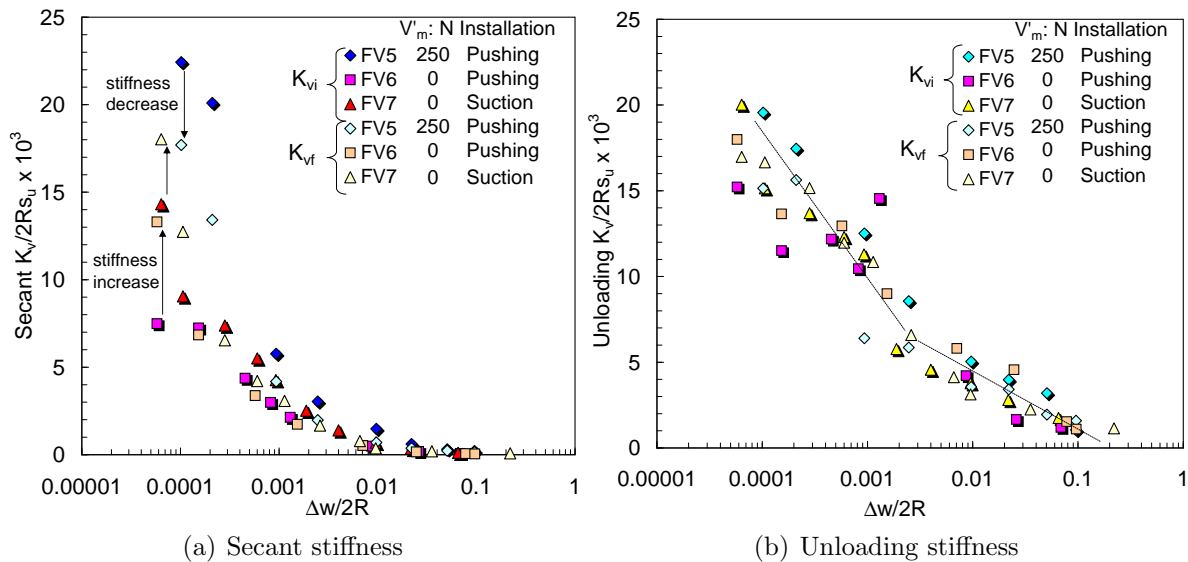


Figure 7.13: Normalised initial and final vertical stiffness plotted against normalised displacement variation per cycle

ment during initial loading) which is recovered immediately at the second cycle, as shown in Figures 7.11(a) and 7.11(b). Conversely, in Figure 7.13(b) is observed that the normalised unloading stiffness does not show a strong reduction at small displacements as in the secant stiffness ($6 \cdot 10^{-6} < \frac{\Delta w}{2R} < 3 \cdot 10^{-4}$), but a more regular decrease along the whole range of Δw that could be reduced to a bilinear relationship in the semi-log plot.

7.3 MOMENT CAPACITY

7.3.1 Introduction

Combined loading of suction caisson foundations in clay has been mainly studied analytically (Bransby and Randolph, 1998; Taiebat and Carter, 2000; Gourvenec and Randolph, 2003). Although some researchers have focused on experimental studies, attention has been paid to foundations for heavy offshore structures such as oil rigs, or as mentioned before to suction anchors in deep water applications such as floating structures. One of the few studies for the former was reported by Cassidy *et al.* (2004), where swipe tests were carried out in a drum centrifuge to compare the moment response of a spudcan footing and a suction caisson ($\frac{L}{2R} = 0.5$) in a soft NC clay. For the latter, where lateral loading is applied through a chain connected to a padeye, more work has been

done (e.g. House, 2002; Clukey *et al.*, 2003; Aubeny and Murff, 2005). The possibility of using suction caisson foundations for offshore wind turbines has led to this study since the geometry of monopod caisson foundations, water depths, turbine weight and load paths are totally different to other previous applications.

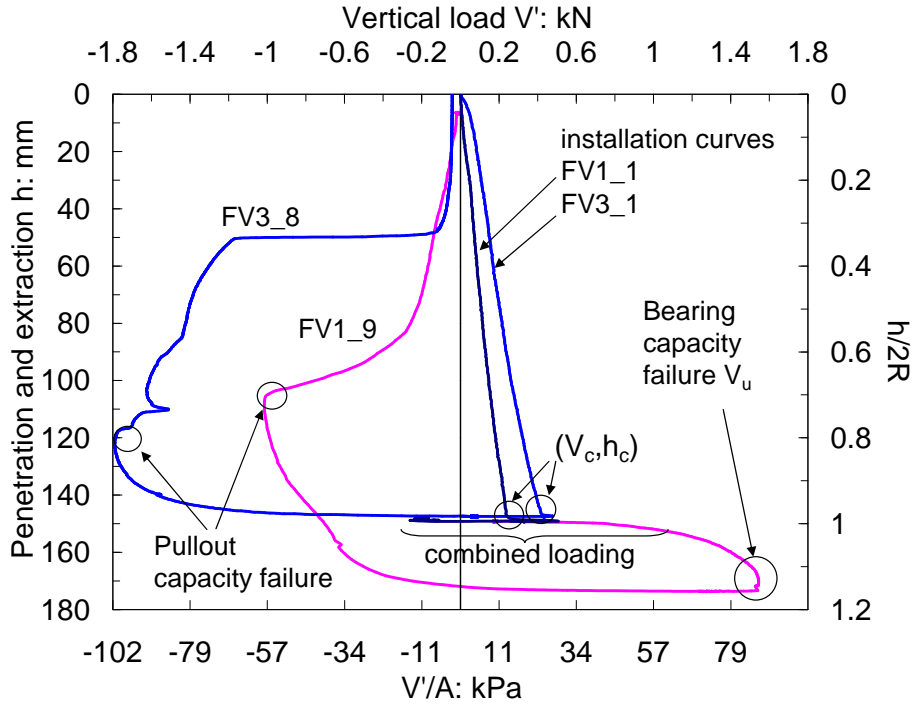


Figure 7.14: Installation, combined loading, bearing capacity failure and pullout

The experimental strategy included monotonic and cyclic swipe events as well as moment loading tests at constant V' , using caisson D ($2R = 150$ mm, $\frac{L}{2R} = 1$) tested in heavily OC kaolin clay. Before analysing the test results it is useful to review the global context of the combined loading with respect to the vertical loading. Figure 7.14 shows the pushing installation curves of tests FV1.1 and FV3.1 studied in section §7.1, where V_c and h_c are as in Figure 7.1(a) and V_u is the ultimate bearing capacity. After installation combined loading events can be conducted straightaway, or further penetration, or tensile loading can be applied before any subsequent combined loading. Any of these possibilities may have important effects on the caisson response depending on the variation of w , the vertical displacement after installation. It is worth noting that although a bearing capacity failure occurs around $V_u = 1.5$ kN at 169 mm of penetration (test FV1.9), serious reduction of vertical stiffness started from 1 kN. Therefore, any incursion beyond that level of vertical load and penetration (> 152 mm) could have detrimental effects on the caisson

moment response.

Additionally, Figure 7.14 shows the pullout response following the bearing capacity failure, and the pullout response shown in Figure 7.5(a) for comparison. The reduced pullout capacity after failure compared with the pullout capacity after installation agrees with previously reported results by Byrne and Cassidy (2002). The pullout capacity reduces from 1.8 kN to 1 kN after 67 mm of extraction, but it still represents two third of V_u . Finally, in order to determine the size of the yield surface and normalise the loads, the maximum value of V' experienced under a particular value of h , *i.e.* V_o will be used.

7.3.2 Swipe test results

Swipe tests are an efficient way to obtain information of the shape and size of the yield surface. For that reason, mapping out of the yield surface was attempted by swiping from the tensile side and from the compressional side (analogous to the Cam Clay critical state terminology from the dry side of critical and from the wet side of critical). The former represents an OC condition for the foundation with an $OCR = \frac{V_o}{V'}$, whereas the latter represents a NC condition for the foundation. Swipe tests were described in section §6.1.5 for caissons installed by suction into sand. Table 7.3 summarizes the values of excess pore pressure u' underneath the caisson lid (initial u'_i , initial and final variation $\Delta u'_i$ and $\Delta u'_f$ with respect to u'_i), initial and final foundation secant stiffness K_{mi} , K_{hi} , K_{mf} and K_{hf} , yield loads $\frac{M_y}{2R}$ and H_y , shear modulus G (back-calculated from the moment caisson response using the expressions of elastic behaviour presented in section §5.2.2), and plastic displacement increment ratios. Complementary information can be found in Table 7.1 (*e.g.* s_u , V_c and V_{max}).

It can be seen in Table 7.3 that the tests were carried out with the load ratio usually $\frac{M}{2RH} = 1$. This represents a condition where wind forces are similar to wave and current forces. Conversely, jack-up rigs have a higher $\frac{M}{2RH} \approx 2.5$ (Cassidy *et al.*, 2004). They found a considerable moment and lateral capacity under tensile vertical loads and a max-

Table 7.3: Summary of swipe tests

Test	V'_i N	V'_f N	V_o N	h mm	$\frac{M}{2RH}$	$2R\theta_t$ mm	u'_i kPa	$\Delta u'_i$ kPa	$\Delta u'_f$ kPa
FV4.2	-563	268	682	147.1	1.01	3.3	0	0	0
FV4.5	-250	-16	650	142.9	0.43	-5.8	-0.4	1	0.8
FV1.2	-190	25	250	148.2	1.02	3.9	0	0	0
FV3.2	450	183	474	147.3	1.03	3.4	5.3	2.7	-3.3
FV6.13	645	423	750	185.6	1.05	2.6	9.6	0	0.8
FV2.2	878	506	900	147.7	1.06	3.7	34	0	-11
FV2.7	899	633	900	148.8	0.65	4.7	18	1	8
FV2.14†	838	294	1100	153.1	1.05	± 1.75	38	-6	-16

Test	K_{mi} N/mm	K_{hi}	$\frac{M_u}{2R}$ N	H_y N	V_y N	K_{mf} N/mm	K_{hf}	G MPa	$\frac{G}{s_u}$	$\frac{\delta u^p}{2R\delta\theta^p}$	$\frac{\delta w^p}{2R\delta\theta^p}$
FV4.2	2000	400	203.8	203.2	-300	25	24	30	2266	1.057	-0.010
FV4.5	140	349	27.7	65.8	-120	-21	-55	3	227	0.940	-0.154
FV1.2	600	171	60.6	58.1	-50	10	8	8	1099	1.26	-0.083
FV3.2	1191	278	126.4	120.2	388	17	17	30	2956	1.047	0.010
FV6.13	1200	400	72.0	68.8	528	24	24	20	2387	0.964	-0.026
FV2.2	1045	311	98.3	94.2	730	15	14	15	1850	0.931	0.036
FV2.7	150	378	12.8	20.8	867	10	14	1.5	206	0.912	0.020

†cyclic swipe test

imum moment load capacity of $\frac{M}{s_u(2R)^3} \approx 0.83$. Furthermore, the interest of that study was to trace the outermost yield surface, with a size defined by $\pm V_o = \pm V_u$. As a consequence, a failure envelope for flat circular footings suggested by Taiebat and Carter (2000) was used in conjunction with upper bound solutions to obtain the moment and horizontal loads at failure M_u and H_u . In this study interest was focused on defining the yield surface with a size V_o around the installation load V_c , hence before a bearing capacity failure.

Swipes tests were carried out at a rotational velocity $2R\dot{\theta} = 0.01$ mm/s, resulting in partially drained conditions since $v_n = 5$ (< 10 , according to the criterion in section §7.1.3). Figure 7.15(a) shows the moment-rotation curves of the swipe tests where the moment load has been normalised by s_u and $2R$. Note the moment load peak in the curves of tests FV4.2, FV4.5 and less visible in test FV6.13. This reflects the effect of higher degree of overconsolidation of the clay sample and explain the high value of $\frac{s_u}{\sigma'_{vi}}$ shown in Table 2.4. Heavily OC soils tend to dilate, inducing suction. However, from Figure 7.15(c) zero variation of the pore pressure occurred during test FV4.2 and actually positive $\Delta u'$ occurred in tests FV4.5 and FV6.13, not giving evidence of soil dilation since the lid does not move vertically. Conversely, as the lid rotates it is expected that on the side that moves upwards u' will be negative and on the side that moves downwards it will

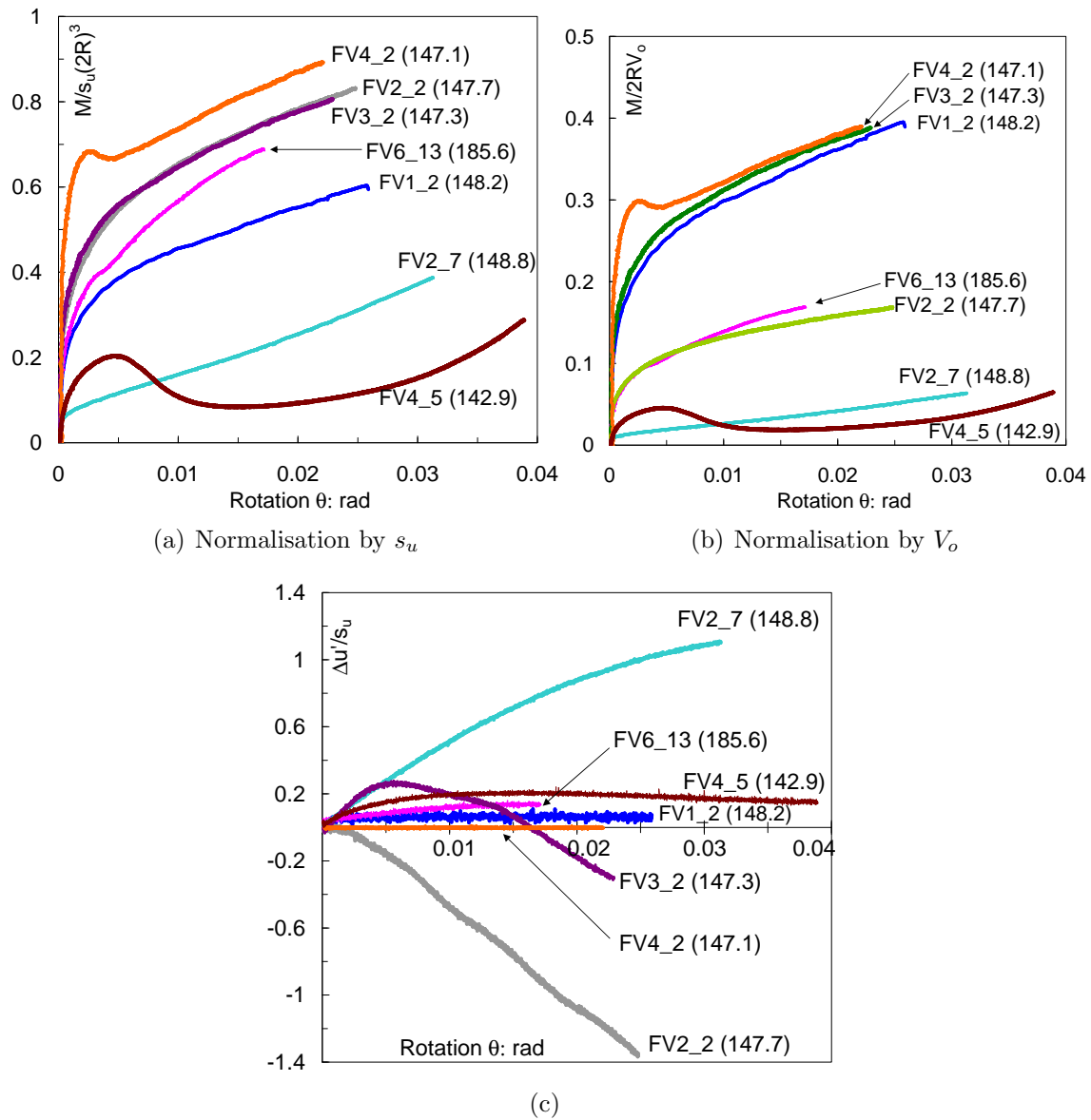


Figure 7.15: Swipe tests showing normalised moment-rotation and excess pore pressure-rotation curves (in brackets penetration h in millimetres)

be positive as shown in Figure 6.17. Therefore, there is probably a situation where the pore pressure transducer recorded positive u' because it was located under the lid side moving downwards, which compensates or prevails over the suction generated due to soil dilation. In addition, the passive lateral pressure on the loaded side induces suction due to soil dilation, but $u' > 0$ on that side of the soil-plug caused by water flowing outwards, whereas the opposite occurs on the other side.

Figure 7.15(b) shows the same curves as in Figure 7.15(a) but with the moment load normalised by V_o . In these figures the fixed caisson penetration h appears in brackets and

in millimetres, where except tests FV4_5 and FV6_13, h is between 147 mm and 149 mm. Figure 7.15(b) highlights that the normalisation by V_o creates three groups of curves. The first group above corresponds to swipe events conducted immediately after installation without further penetration or preloading. The second group in the middle shows a lower normalised moment capacity because test FV2_2 was vertically preloaded more than three times $V_c = 316$ N, approaching the value of bearing capacity failure $V_u \approx 1.5$ kN. Test FV6_13 was conducted after a series of cyclic vertical loads. Nevertheless, the strongly remoulded soil in the interface could have been sufficient to reduce the moment capacity. In the third group at the bottom the moment capacity is the lowest. Test FV4_5 presents the effects of soil disturbance as a consequence of previous moment loading events despite showing a moment load peak. Previous loading with V_o near to V_u reduced considerably the moment capacity of Test FV2_7.

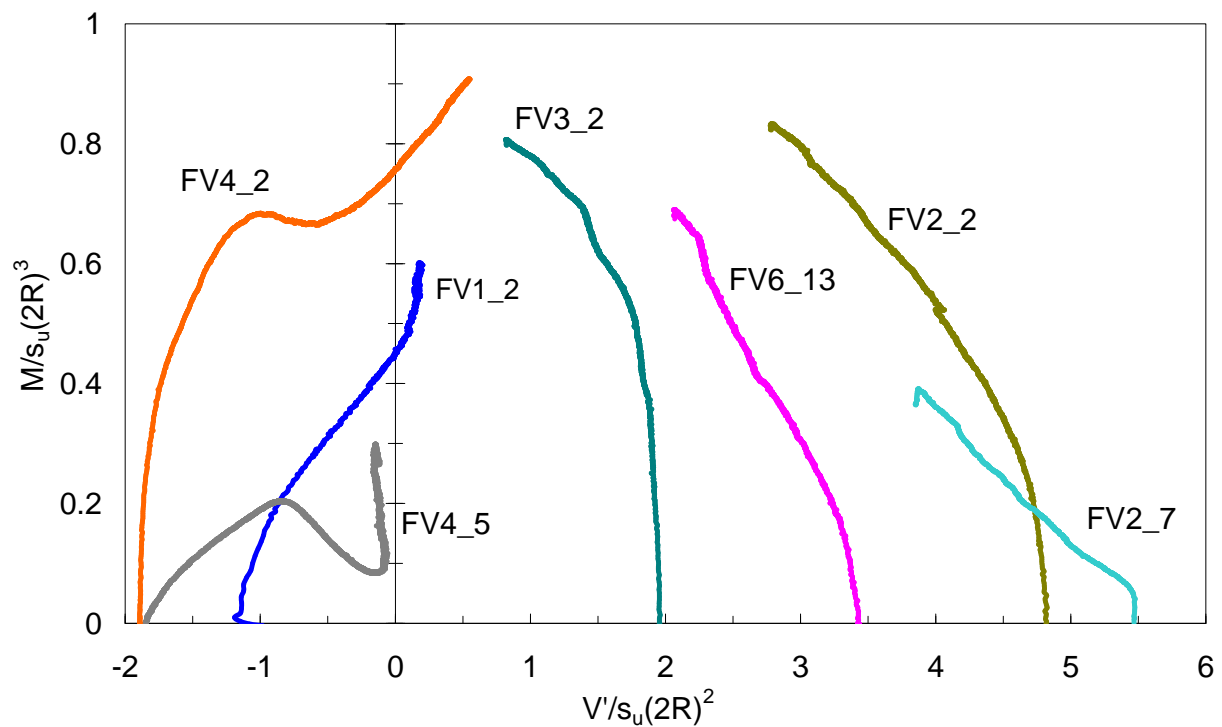


Figure 7.16: Swipe tests in the normalised moment vertical load plane

Figure 7.16 shows all the swipe tests in the strength normalised moment-vertical load plane. No moment peaks with further softening is observed in the compressive swipe tests. The shape of the yield surface traced by the swipe events can be observed as well as the increase of the size with the increase of $\left| \frac{V'}{s_u(2R)^2} \right|$. The expansion of the yield surface

towards the tension side is substantially more significant as proportion of the compressive side than in sand. This is due to the fact that in clay low permeability assures the prevalence of partially or undrained conditions, which in turn allows suction to develop even under slow loading rates. It is worth noting that an upper limit for the moment load is reached at $\frac{M}{s_u(2R)^3} \approx 0.8$, which is very close to the value reported by Cassidy *et al.* (2004). Test FV4_5 shows apart from a peak and subsequent softening previously described, a further increase of moment capacity with rotation at constant vertical load close to zero. A negative rotation was applied in this test, which returned the caisson to a centred position after positive rotations were applied in the previous three tests. It is believed that caisson contact with soil less disturbed on the opposite side as rotation progresses increased the moment capacity.

Figures 7.17(a) and 7.17(b) show the results of a cycle swipe test. A particular hysteresis loop shape appears after the fourth cycle, giving evidence of gapping. In fact, there is a point around zero rotation before which the tangential stiffness decreases and after which it increases during reloading and unloading. The cyclic swipe test FV2.14 was carried out immediately after a second installation into the same site but with the loading plane changed 90° . Full installation was completed with $V_c = 260$ N (FV2.12) and a further penetration from 147 mm to 153 mm caused V' to increase up to 1100 N, which is a value near to V_u . Despite the increase of the normalised moment capacity with rotation (and with the decrease of V'), the maximum moment capacity has reduced to a half of that obtained for instance in tests FV2.2 or FV3.2. Moreover, the loading history is reflected in the high values of u' as shown in Figure 7.17(c). Although u' dissipates cycle after cycle, the normalised pore load represents a significant percentage of the normalised vertical load.

In section §6.1.7 cyclic swipe tests of caissons in dense saturated sand starting from tension and regardless of the rotation amplitude, the vertical load always returned to a value of tensile load close to the initial V' after each cycle. On the contrary, in Figure 7.17(b) the cyclic swipe test started from a large compressive V' load where V' continu-

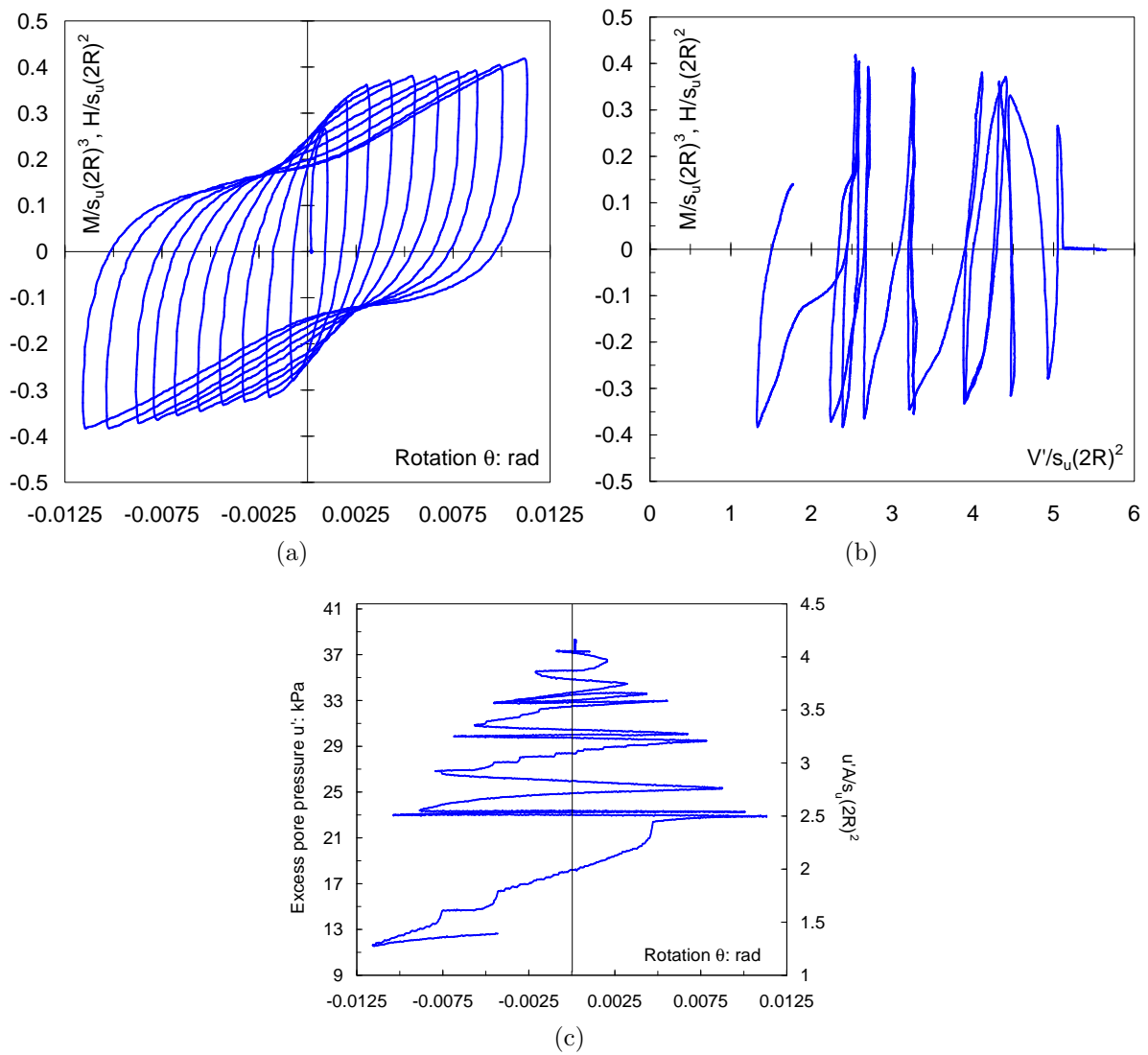


Figure 7.17: Cyclic swipe test FV2.14, $\frac{M}{2RH} = 1$, $V' = 838 \text{ N} \mapsto 296 \text{ N}$ showing normalised: (a) moment-rotation curve, (b) moment-vertical load curve, and (c) pore pressure-rotation curve

ously decreases after every cycle. It would be interesting to see if this is the case in cyclic swipe events in sand and vice versa.

7.3.3 Constant V' moment loading tests

Moment loading tests under constant V' were performed extensively for caissons in sand at various relatively low $\frac{V'}{V_0}$ values and covering a spectrum of $\frac{M}{2RH}$ values (details of experimental procedure, load path, *etc.* can be found in sections §5.3 and §6.1). A similar testing strategy to determine the yield surface and flow rule of a caisson in clay is extremely time consuming owing to the preparation of samples. Swipe tests disturb the clay sample next to caisson mostly in one direction, leaving other directions of loading

not so seriously damaged, additionally, no vertical movement occur. This offers the opportunity to perhaps obtain useful complementary data of good quality from constant V' tests in the same site.

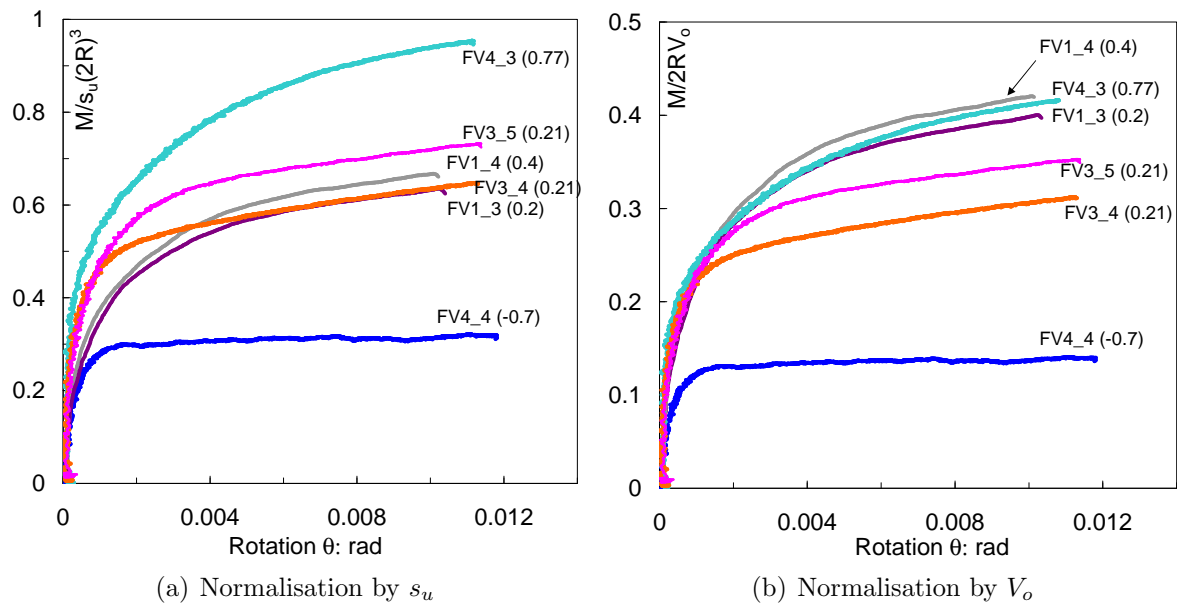


Figure 7.18: Normalised moment-rotation curves for tests with $\frac{V'_o}{V'_u} \leq 0.32$, $\frac{M}{2RH} = 1$, showing $\frac{V'_o}{V'_u}$ values in brackets

Table 7.4 collects information of the constant V' tests conducted at a rotational velocity of 0.01 mm/s, which as for the swipe tests corresponds to a partially drained condition. Moment-rotation curves of tests with low values of $\frac{V'_o}{V'_u}$ are shown normalised by s_u in Figure 7.18(a) and normalised by V_o in Figure 7.18(b); with the numbers in brackets corresponding to $\frac{V'_o}{V'_u}$. The value of V_u for series FV1 was experimentally obtained as 1.5 kN, from which a value of $N_c = 11$ was deduced and used to calculate V_u for the remaining series. It is interesting to note that the curve of test FV4_4 follows a perfect elasto-plastic response, *i.e.* an initial very stiff response mostly linear until yield occurs with the development of large plastic rotations progressing under constant moment, hence with the absence of hardening. However, for the curves above test FV4_4 hardening appears after yield instead of the perfect-plastic behaviour. These curves represent a OC condition for the foundation: $|\text{OCR}| = \frac{V'_o}{V'_u} \geq 1.3$.

The curves of plastic vertical displacement *versus* plastic rotation $\delta w^p - \delta \theta^p$ are presented in Figure 7.19(a), where two trends can be clearly identified: i) large uplift due

Table 7.4: Summary of moment loading tests under constant vertical load V'

Test	$\frac{V'_o}{V'_u}$	$\frac{V'_o}{V'_o}$	V' N	V_o N	V_u N	$\frac{M}{2RH}$	h mm	u'_i kPa	$\Delta u'_i$ kPa	$\Delta u'_f$ kPa
FV1_3	0.17	0.20	50	250	1500	1.00	148.0	0.2	0	0
FV1_4	0.17	0.40	100	250	1500	1.01	148.1	0.2	0	0.2
FV1_5	0.17	0.80	200	250	1500	1.02	148.8	0.9	6	9
FV1_6	0.17	0.40	100	250	1500	-0.40	148.5	0	1	9.5
FV1_7	0.17	0.80	200	250	1500	-1.2	149.0	8.6	1.4	7.4
FV1_8	0.17	0.80	200	250	1500	-0.77	149.0	14	1.5	1
FV3_3	0.24	0.21	100	474	2000	1.99	147.4	1.6	0	-3.2
FV3_4	0.24	0.21	100	474	2000	1.00	147.3	-0.8	0	0.7
FV3_5	0.24	0.21	100	474	2000	1.00	147.3	-2	0.2	1
FV3_6	0.24	0.21	100	474	2000	-0.99	147.4	-2	0	0.5
FV3_7	0.24	0.21	100	474	2000	-0.50	147.4	0	0	0.1
FV4_3	0.26	0.77	500	650	2500	1.01	147.0	6	-2.5	-3.5
FV4_4	0.26	-0.75	-487	650	2500	0.96	146.7	-0.4	-4	-4.3
FV6_12	0.31	0.20	100	500	1600	-0.89	154.4	0	0.1	0.25
FV7_15S	0.40	0.62	494	800	2000	1.02	151.8	0.6	0	1.2
FV7_16S	0.45	0.81	732	900	2000	1.06	154.7	4.6	0	2.4
FV7_17S	0.45	0.95	852	900	2000	1.04	156.0	8.3	0	2.2
FV2_3	0.60	0.44	400	900	1500	1.02	148.0	20	-2	-3.5
FV2_4	0.60	0.22	200	900	1500	1.01	148.0	12.4	-2.4	-6.4
FV2_5	0.60	0.11	100	900	1500	1.00	148.0	3.8	-1	-3.5
FV2_6	0.60	-0.11	-100	900	1500	0.98	147.9	-3	-2	-1.5
FV2_9	0.60	0.22	200	900	1500	0.50	149.2	14.4	-3.5	-3.5
FV2_10	0.60	0.00	3	900	1500	0.47	148.8	6	0	-1.4
Test	K_{mi} N/mm	K_{hi}	$\frac{M_y}{2R}$ N	H_y N	K_{mf} N/mm	K_{hf}	G_M MPa	$\frac{\delta u^p}{2R\delta\theta^p}$	$\frac{\delta w^p}{2R\delta\theta^p}$	
FV1_3	776	300	86.1	82.5	13	11	10	1.240	0.001	
FV1_4	776	251	87.7	85.1	16	11	10	1.264	0.121	
FV1_5	503	129	37.6	37.1	39	23	10	1.450	0.122	
FV1_6	588	-258	23.5	-69.0	-333	500	0.6	0.460	-0.310	
FV1_7	1503	-128	126.3	-80.0	120	-263	2.5	0.570	0.402	
FV1_8	800	-500	53.2	-200.0	52	179	2	0.300	-0.080	
FV3_3	2500	150	187.5	91.6	41	23	25	1.115	0.035	
FV3_4	1800	350	118.8	116.5	18	16	30	1.107	-0.008	
FV3_5	1599	450	138.8	137.3	18	16	25	1.091	0.015	
FV3_6	1750	-215	54.2	-50.0	165	-323	2.5	0.633	0.399	
FV3_7	550	-377	110.4	-190	165	328	0.5	-1.993	0.900	
FV4_3	2824	500	225.9	218.3	38	31	50	1.158	0.061	
FV4_4	1029	349	89.0	87.8	4	7	10	0.850	-0.808	
FV6_12	824	2034	51.1	-46.0	140	-606	2	0.300	0.080	
FV7_15S	800	800	38.0	36.0	25	33	10	0.760	0.330	
FV7_16S	1200	1000	38.4	36.0	28	36	20	0.730	0.610	
FV7_17S	2000	1850	47.0	48.1	22	24	30	0.675	2.019	
FV2_3	1263	404	132.8	131.4	15	13	20	0.971	0.038	
FV2_4	1370	400	143.9	140.0	12	13	20	0.943	0.001	
FV2_5	1085	312	143.9	139.1	13	15	26	0.942	0.021	
FV2_6	1500	320	106.7	106.5	-7	-8	23	0.800	-0.400	
FV2_9	700	900	59.5	118.4	12	21	12	0.940	-0.061	
FV2_10	1000	1200	38.0	78.0	98	151	18	1.007	-0.170	

S: caisson installed by suction

to the application of a tensile load (test FV4.4), and ii) very small or simply no vertical movement for $\frac{V'}{V_o} = 0.2, 0.4$ and 0.77 . Note that the concept of parallel point or parallel

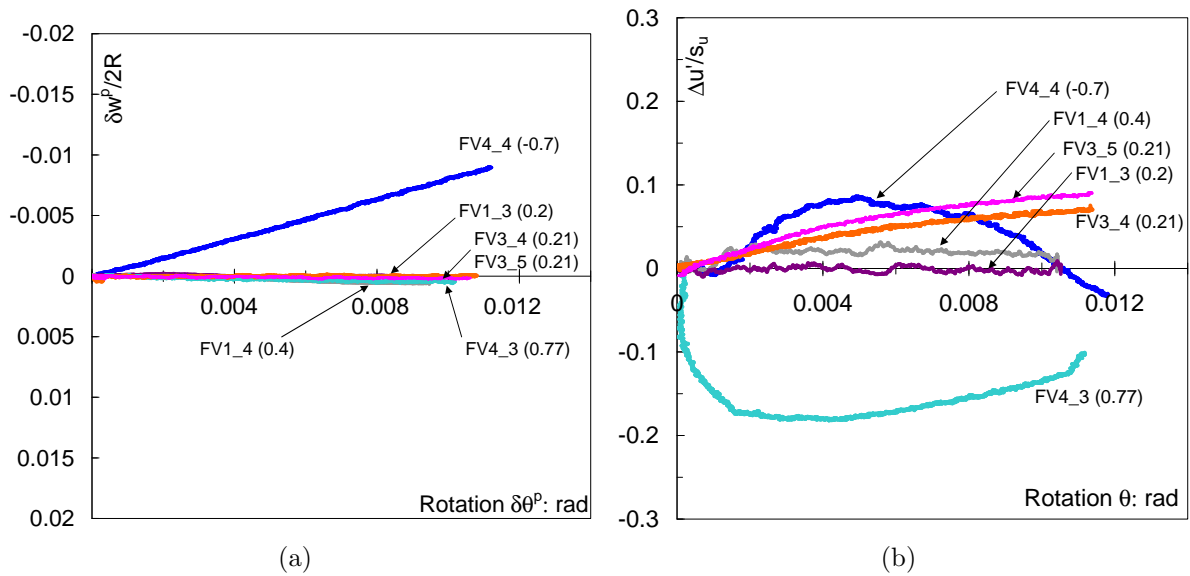


Figure 7.19: Tests with $\frac{V_o}{V_u} \leq 0.32$, $\frac{M}{2RH} = 1$ and $\frac{V'}{V_o}$ values in brackets, showing normalised: (a) plastic vertical displacement *versus* plastic rotation, and (b) excess pore water pressure variation *versus* rotation

line introduced in Chapters 5 and 6 for caissons in sand seems to apply for a range of values since in ii) $\delta w^p \cong 0$ for five tests with $0.2 < \frac{V'}{V_o} < 0.77$. In test FV4.3 the initial negative $\Delta u'$ was due to the double effect of previous inclination of the caisson caused by a swipe event and the PPT location at the rising side of the lid. Nevertheless, once those initial effects disappear the $\Delta u'$ trend switched from negative to positive due to the slight settlement of the caisson. In tests FV3.4 and FV3.5 the $u' - \theta$ curves tend to a zero absolute value of u' . In general the level of $\Delta u'$ was much higher in the swipe tests because of the larger caisson rotations and also the larger variation in V' seems to affect more than the w variation. The two trends are linked with the curves of pore water pressure variation with rotation $\Delta u' - \theta$ as shown in Figure 7.19(b) (with the exception of the initial part of tests FV4.4 and FV4.3 owing to the location of the *ppt* under the lid).

Tests with high values of $\frac{V_o}{V_u}$ are shown in Figures 7.20(a) and 7.20(b), representing a ‘normally loaded’ condition ($|\text{OCR}| \leq 1.1$). It can be observed that the order of magnitude of $\frac{M}{s_u(2R)^3}$ in these curves are fairly similar to the curves in Figure 7.18(a). Conversely, the effect of a different range of V_o values is obviously evident comparing Figures 7.20(b) and 7.18(b) since V_o is used in the normalisation of the moment load. Although larger V_o values cause an increase in the moment capacity (compare for example tests under similar

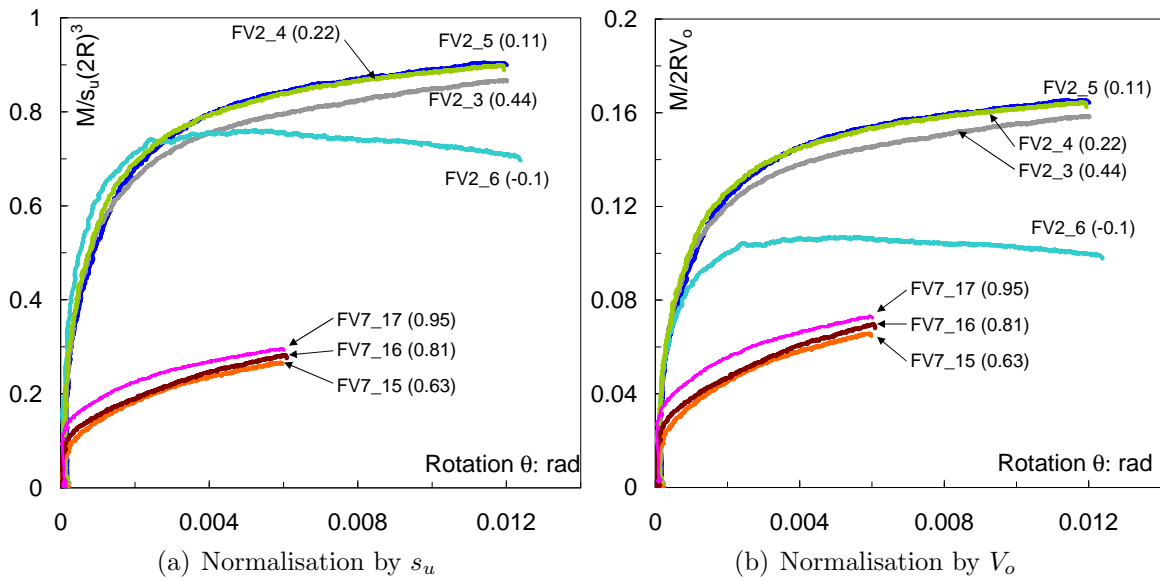


Figure 7.20: Tests with $\frac{V_o}{V_u} \geq 0.4$, $\frac{M}{2RH} = 1$ and $\frac{V'}{V_o}$ values in brackets showing normalised moment-rotation curves

$\frac{V'}{V_o}$; FV1.3 with FV2.4 and FV1.4 with FV2.3 in Table 7.4), the increase in moment load capacity does not compensate the increase of V_o , resulting in a reduction of $\frac{M}{2RV_o}$ from 0.4 to 0.16.

Three trends of plastic vertical displacement can be identified in Figure 7.21(a). The two first trends were found and described in Figure 7.19(a). The third trend corresponds

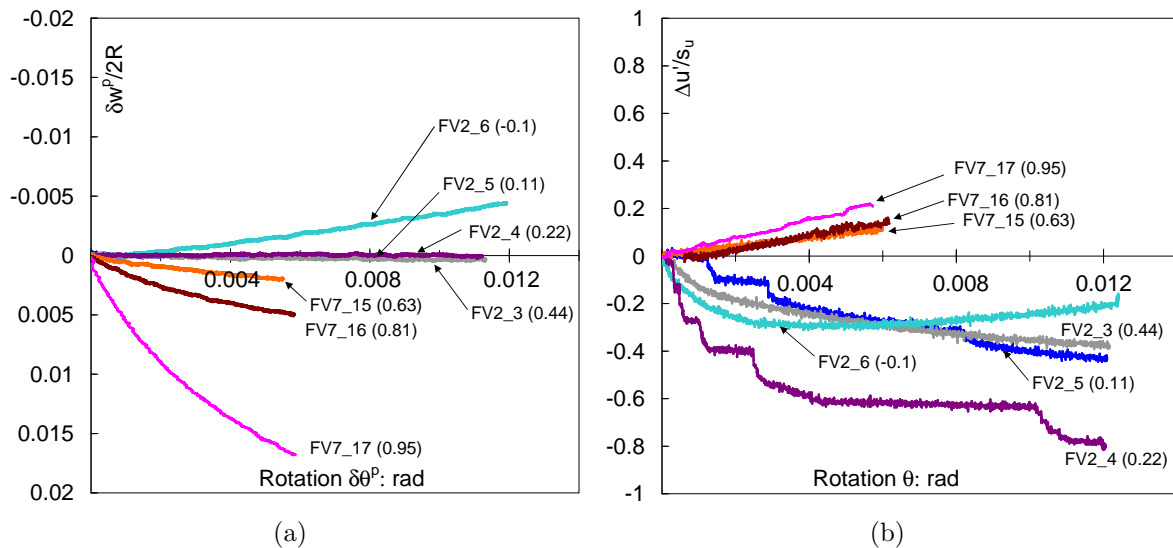


Figure 7.21: Tests with $\frac{V_o}{V_u} \geq 0.4$, $\frac{M}{2RH} = 1$, and $\frac{V'}{V_o}$ values (numbers in brackets) showing: (a) plastic vertical displacement *versus* rotation, and (b) pore water pressure variation *versus* rotation

to the increasing caisson settlement with $\frac{V'}{V_o}$. Figure 7.21(b) shows that suction appeared under the caisson lid for values of $\frac{V'}{V_o} < 0.45$. This reveals that during the caisson rotation the underside of the lid and the top of the soil plug kept in contact. Full contact during uplift is a strong assumption made in numerical analysis of undrained moment capacity of skirted footings (Gouvernec and Randolph, 2003; Gouvernec, 2003).

7.3.4 Yield surface and flow vectors

The results of constant V' tests are shown in Figure 7.22 as yield points (values listed in Table 7.4) in the normalised moment *versus* horizontal load. In the same figure two calculated yield surfaces are included based on the yield surface formulation presented in Chapter 5. Despite the lack of data for load ratios different to one, two major groups can be identified regardless of the value of $\frac{V'}{V_o}$: one group with high deviatoric load capacity forming an exterior boundary, and a second group with low deviatoric load capacity forming an interior boundary. The yield surfaces were estimated relying mainly on the few yield points with negative load ratios. The parameters h_o , m_o and e obtained from these estimations are summarized in Table 7.5. Obviously, more data for a wider variety of load ratios is required to confirm or not these tentative values. However, in the next stage of this analysis these values will be validated using a three dimensional yield surface formulation (expression (5.43) or (6.3)).

Figure 7.23 coalesces the results from swipe tests and from constant V' tests in the $\frac{M}{2RV_o} - \frac{H}{V_o}$ plane. The data is divided according to the $\frac{V_o}{V_u}$ ratio, from where two groups can be recognized as well, at least for the data with load ratio of one. Based on the values of h_o , m_o and e estimated from Figure 7.22 two yield surfaces were calculated for $\frac{V_o}{V_u} \geq 0.4$ and for $\frac{V_o}{V_u} \leq 0.32$, as shown in Figure 7.23. Table 7.5 presents the values of the parameters β_1 and β_2 determined by fitting the experimental results. In the light of these results, it appears a third group of data above the yield surface for data with $\frac{V_o}{V_u} \leq 0.32$. This reflects that larger capacities were obtained owing to higher degree of OC (samples 4 and 3 had the highest values of s_u). In addition, series of tests FV3 and FV4 had V_o

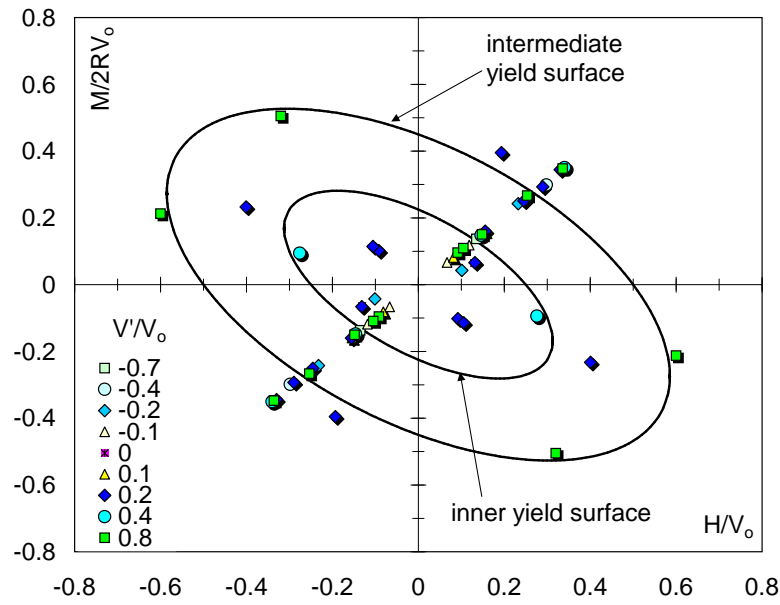


Figure 7.22: Normalised yield points in the $\frac{M}{2RV_0} - \frac{H}{V_0}$ plane and fitted yield surfaces

values much closer to V_c rather than V_u . The set of parameter values estimated for this outer yield surface are presented in Table 7.5.

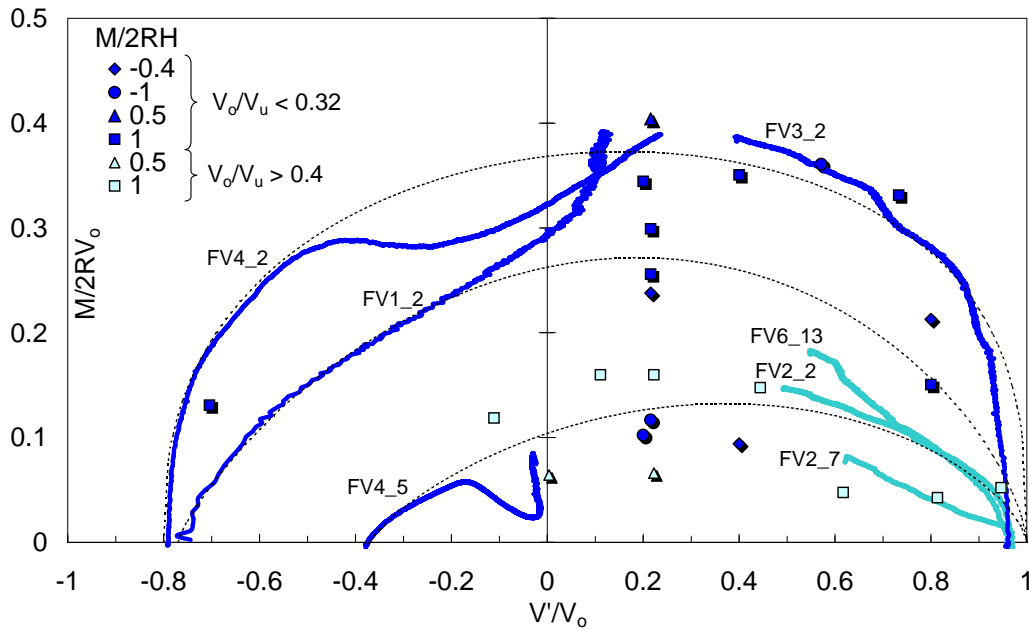


Figure 7.23: Normalised yield points in the $\frac{M}{2RV_0} - \frac{V'}{V_0}$ plane and fitted yield surfaces

The study of the flow rule follows the analysis of section §5.4.3. Associated flow has been assumed in the calculations, hence the association factors are equal $a_M = a_H$. The theoretical flow rule is compared with the experimental results in Figure 7.24(a) using the parameter values summarized in Table 7.5. Although associated flow may hold for the

Table 7.5: Parameter values of the yield surface

Yield surface for $\frac{V_o}{V_u}$	m_o	h_o	t_o	e	β_1	β_2
≤ 0.32 †	0.7	0.6	0.8	-0.5	0.4	0.35
≤ 0.32	0.5	0.45	0.77	-0.52	0.8	0.675
≥ 0.4	0.25	0.225	0.37	-0.6	0.8	0.675

†clay heavily overconsolidated with the highest values of s_u

results presented more data (with different load ratios and load histories) is required for a definitive conclusion. Experimental and theoretical predictions of the vertical plastic displacement increments are shown in Figure 7.24(b), where associated flow has been assumed, making the association factors $a_{V_1} = a_{V_2} = 1$. The study of the flow rule becomes more complex not only for the variation of the flow vector directions with $\frac{V'}{V_o}$ and $\frac{M}{2RH}$ as presented in section §5.4.3, but also due to the different load history $\frac{V_o}{V_u}$ and pore pressure variations. The development of suction can modify substantially the vertical displacement of the caisson. Some of the larger values of $\Delta u'$ are shown in Figure 7.24(b) next to each point.

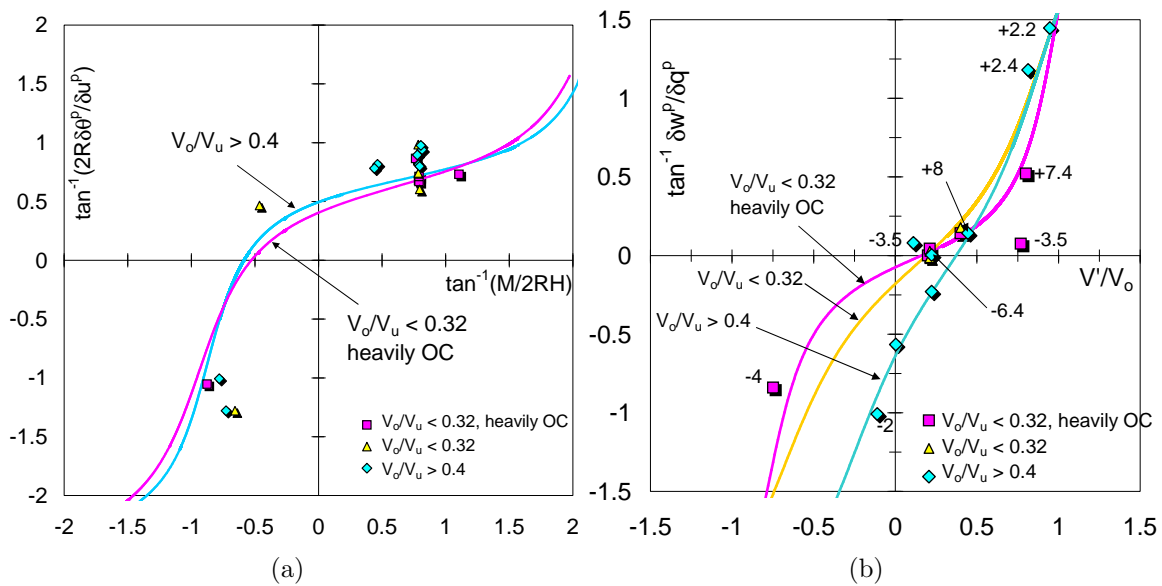


Figure 7.24: Experimental and theoretical predictions of incremental plastic displacement ratios in the π plane assuming normality (numbers in (b) refer to u' and points without numbers imply $u' \approx 0$ kPa)

7.3.5 Cyclic moment loading tests

The cyclic rotational response of suction caissons in clay is a fundamental issue owing to the cyclic nature of the offshore environmental loads as mentioned in Chapter 1. Pre-

Table 7.6: Summary of cyclic moment loading tests. Field test taken from Houlsby *et al.* (2005)

Test	2R m	$\frac{L}{2R}$	s_u kPa	V_o kN	$\frac{V'}{V_o}$	$\frac{V'}{s_u(2R)^2}$	$\frac{M}{2RH}$	w_t mm
FV7_12S	0.15	1	9.9	0.75	-0.13	-0.44	1	-5
FV6_10	0.15	1	8.4	0.5	0.20	0.45	1	-0.2
Field trial	3	0.5	14.4	200	0.21	0.33	1	5

vious research of cyclic combined loading has concentrated on suction caissons as anchors for deep water floating structures, which include eccentric vertical cyclic loading in tension leg platforms TLP (Andersen *et al.*, 1993; Clukey *et al.*, 1995) and laterally moored systems (House, 2002). Therefore, it was regarded as important to investigate the cyclic moment loading response of monopod suction caisson foundations due to the differences prevalent in offshore wind turbines as pointed out in section §7.3.1. Recently, results from cyclic moment loading tests with large scale caissons at the Bothkennar site have been reported by Houlsby *et al.* (2005) for offshore wind turbine applications. Consequently, comparisons of laboratory results with field results will be pursued.

Cyclic moment loading tests FV7_12S and FV6_10 were performed using caisson D under the soil and loading conditions listed in Table 7.6. Both tests were conducted after a series of cyclic vertical loading events, for that reason it was thought that the clay samples were not so seriously damaged in the lateral direction. Figure 7.25(a) shows the moment-rotation curve of test FV6_10 with the strength normalisation by s_u on the left hand side and the load normalisation by V_o on the right hand side of the plot. The first four cycles present the typical growing hysteresis loops with increasing rotation amplitude. But beyond the fourth cycle a hysteresis loop constriction appears added to the fact that the moment capacity stabilizes and even decreases slightly with larger rotation amplitudes. This modification in the hysteresis loop shape is not considered in the Masing rules, in which cycles are reproduced following the first loading curve. This issue may cause modifications in the modelling.

Figure 7.25(b) shows the curve response of test FV7_12S, with the caisson installed by suction and experiencing tension. It is noteworthy that the onset of a hysteresis loop con-

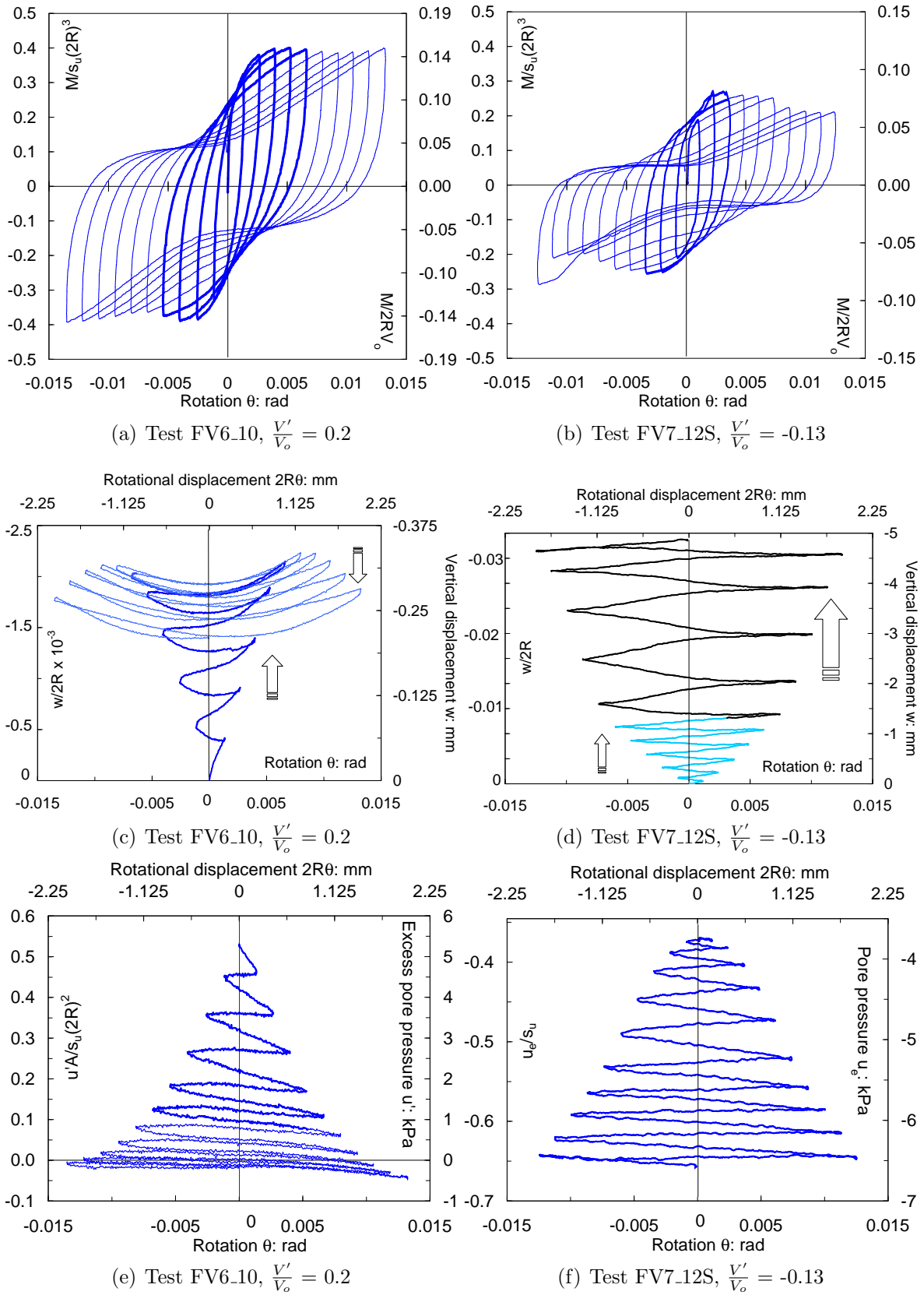


Figure 7.25: Results from two cyclic moment loading tests

striction starts earlier (third cycle) and is much more pronounced than in test FV6_10, causing a considerable moment capacity decrease. Constriction of the hysteresis loops is the result of gaps simultaneously opening and closing from top to bottom, and vice versa, next to the skirt during each rotational cycle. This phenomenon is also found when cracks appear in cyclic shear loading of reinforced concrete elements. Then the onset of gapping is an indication of foundation failure and further opening of the gaps reveals the level of damage.

The resulting vertical displacement evolution in test FV6_10 is shown in Figure 7.25(c), where the arrows indicate the direction of the vertical displacement. It is interesting to note that initially the caisson moves upwards, but when it reaches the fourth cycle the caisson rocks with a small vertical movement during three cycles. Thereafter, the caisson rocks moving downwards although it was not able to return to the initial point. This pattern of vertical displacement evolution does not agree with the monotonic tests with $\frac{V'}{V_c} = 0.2$, in which zero vertical displacement was observed. However, it is similar to the behaviour observed in test FV80_13_1B with also a caisson aspect ratio of one but in dry loose sand (section §5.5.3). This agreement leads to the same conclusion related to the transition or parallel point being reached between uplift and settlement. Conversely, Figure 7.25(d) shows that in test FV7_12 there was not a transition point since the uplift increased steadily with the amplitude of rotation due to the tensile load being applied.

Figure 7.25(e) shows the pore pressure variation during cyclic rotation in test FV6_10. A significant reduction of u' in the first four cycles from an initial value of 5 kPa to a value close to 1 kPa is seen. In the next cycles u' reduces even more although at a lower rate since the caisson is not moving upwards any more. Nevertheless, suction appears in the last three cycles. By comparison, in Figure 7.25(f) the tensile load causes the appearance of suction from the beginning and the onset of rotational cycles increases the suction even more.

In a moment *versus* vertical displacement plot the pattern followed by the curve of test

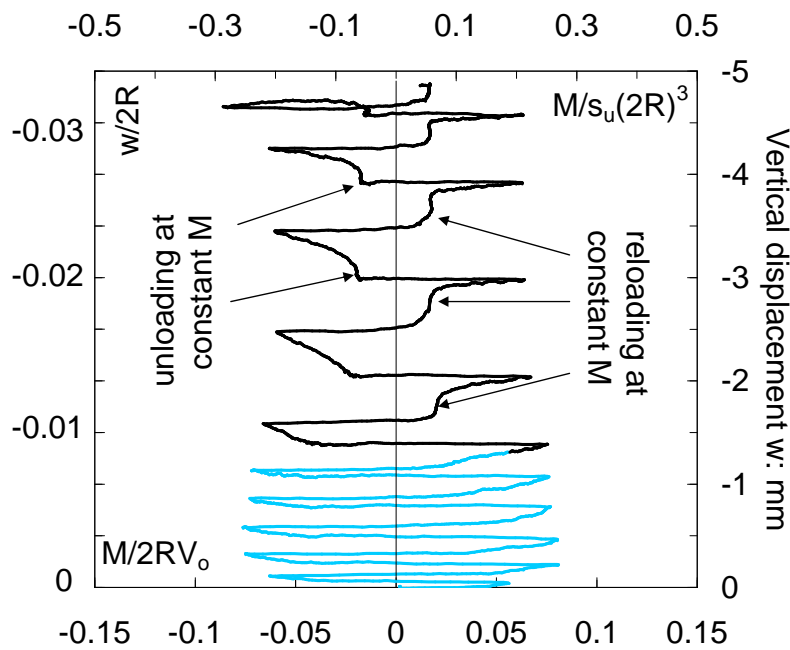


Figure 7.26: Effect of hysteresis loop constriction on the higher rate of uplift during moment reloading and unloading (test FV7_12S)

FV6_10 (not shown) in the last cycles is identical to that shown in Figure 5.34. The caisson settles smoothly during reloading and unloading, whereas uplift occurs when reaching the maximum positive and negative moment load in each cycle. Conversely, in Figure 7.26 it is clear that only uplift occurs with a pattern totally different to that mentioned above. The largest uplifts occur not near the maximum moment load, but at a lower and almost constant value which is reached during constriction or gapping. This indicates that under tension the reduction of moment capacity induced by gapping also increases the rate of caisson uplift.

Houlsby *et al.* (2005) undertook a series of large scale tests under load-controlled conditions at the Bothkennar site using a suction caisson with the dimensions and loading conditions listed in Table 7.6. The Bothkennar clay is an estuarine clay with an $OCR \leq 1.6$ (Hight *et al.*, 1992). Results from the field offer an invaluable opportunity for comparison with laboratory results. In this context, Kelly *et al.* (2006) reproduce the same normalised cyclic rotational displacement paths (and normalised V') in the laboratory to those in the field with the intention of studying effects of scale on the moment capacity. Although the purpose of the present study was not to replicate the conditions of the

Bothkennar tests, it is very interesting to see whether similar patterns and trends exist or not. Figure 7.27(a) reproduces the moment-rotation curve from the field, which can be compared with test FV6_10 owing to closeness in the normalised vertical load (although the caisson aspect ratios are different). The normalised moment capacity for the first cycles in both tests is comparable (around $\frac{M}{s_u(2R)^3} \approx 0.3$) as well as for the final cycles (around $\frac{M}{s_u(2R)^3} \approx 0.4$). This agreement reveals that the effect of higher level of stresses in the field is not as important in clay as it is in sand. In terms of the normalisation by V_o test FV6_10 exhibits less moment capacity because of the larger V_o value caused by the further penetration during the cyclic vertical loading.

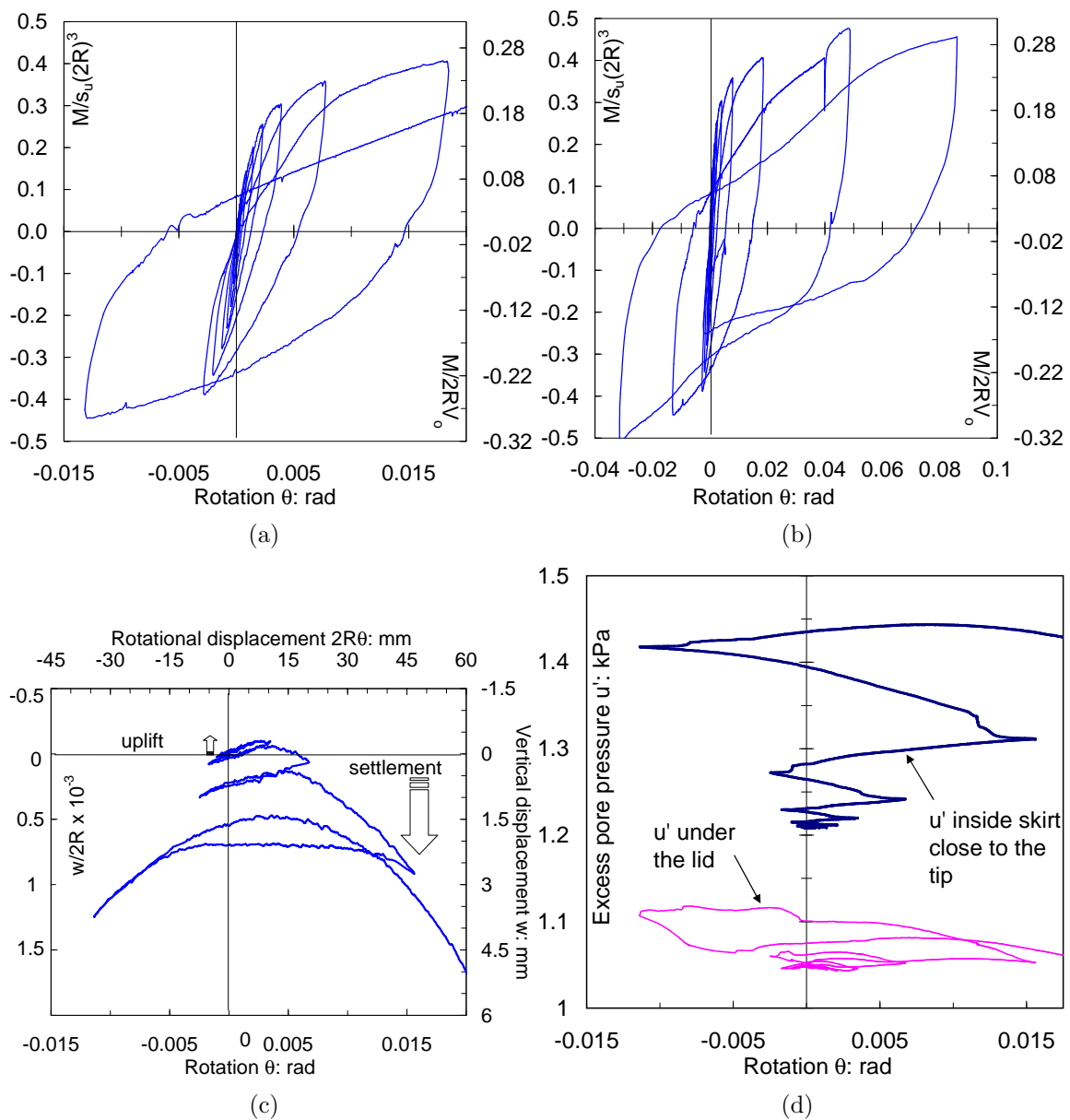


Figure 7.27: Large scale test results (adapted from Housby *et al.*, 2005)

It is worth noting the influence of the loading control mode in Figures 7.27(a) and 7.25(a). The load-controlled mode applied in the field forces the caissons to reach in each cycle an increased moment load target, to cope with that the rotation in each cycle should recover from the previous cycle. With the appearance of plastic rotations, larger rotations will develop in order to complete the cycle as it can be observed in the last cycle shown in Figure 7.27(a), where for a minor increase in moment load a very large rotation results. Even much larger rotations will develop to achieve a very small increase in moment load in the next two cycles as shown in Figure 7.27(b). Conversely, the displacement-controlled tests performed in the laboratory target rotations instead, therefore the moment load is free to increase, decrease or stay the same. The gapping response obtained in the laboratory under small rotations ($\theta \geq 0.005$ rad) also occurred in the field, but for rotations one order of magnitude less ($\theta \geq 0.04$ rad) as shown in Figure 7.27(b).

By comparing Figures 7.27(c) and 7.25(c) it can be observed that the normalised vertical displacement obtained in the field shows initially a four times smaller upward movement of the caisson than the obtained in the laboratory. Afterwards, the caisson moves downwards with the largest settlements occurring at reversals. Although the laboratory result also shows a switch from upward to downward movement, normalised settlements in the field are three times larger. In addition, in the laboratory the largest settlements occur around $\theta = 0$ rad and the minimum settlements at reversals, hence opposite to the field. Figure 7.28 depicts the rotation mechanism of the caisson in the field occurring around the centre and the rotation mechanism of the caisson in the laboratory lifting up on the edges.

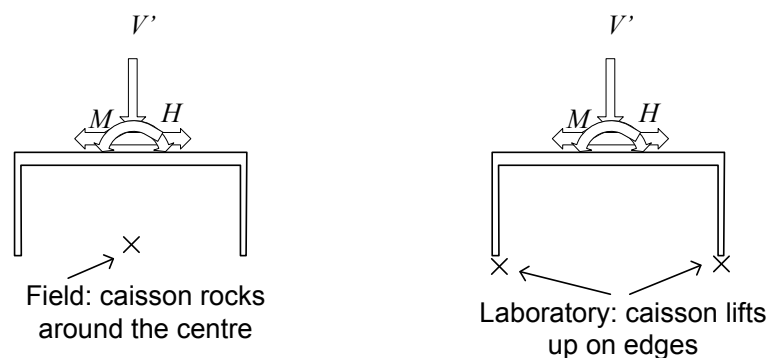


Figure 7.28: Rotation mechanisms observed in the field and in the laboratory

Figure 7.27(d) shows the variation of the pore pressure underneath the caisson lid and inside the caisson skirt near the tip. It is interesting to observe that there is a minor variation of u' under the lid, not agreeing with the laboratory results, whereas a small increase of u' develops close to the tip.

7.4 CONCLUSIONS

The results of an experimental study of suction caisson foundations in clay for offshore wind turbines have been described. This study was necessary to obtain the data to determine the parameters required to model the response of suction caisson foundations. A suction caisson with an aspect ratio of 1 was tested in heavily overconsolidated kaolin clay. This study considered three stages. Firstly, installation and pullout capacity, secondly, cyclic vertical loading, and thirdly, the monotonic and cyclic moment capacity.

7.4.1 Installation and pullout

The calculation procedure proposed by Houlsby and Byrne (2005) was used to back-analysed the inside and outside adhesion factors. Similarly, remoulded s_u values obtained from shear vane tests provided reliable values of adhesion factors as the inverse of the clay sensitivity following Andersen and Jostad (2002). This allowed the prediction of the penetration resistance for caissons installed by pushing. However, the prediction of the suction for suction assisted penetration should account for a diminished adhesion factor due to non-dissipated pore pressures. No substantial difference was found between the net vertical load required to install a caisson by pushing and by suction, agreeing with previous findings for normally consolidated kaolin clay found in the literature.

A reverse $N_c = 8.6$ was determined from a pullout test, value that is slightly lower than the lower bound solution for smooth skirts. Furthermore, an even lower $N_c = 6.4$ was determined from a large scale pullout test.

7.4.2 Cyclic vertical loading

Results of cyclic vertical loading tests are relevant for applications of multiple-caisson foundations. The cyclic vertical loading around a mean vertical load equal to the maximum installation load induced permanent settlement of the caisson, whereas the cycling around a mean vertical load equal to zero induced permanent uplifting of the caisson, although for large load amplitudes temporary settlements were observed during compressive loading.

It was found that in the short term substantial difference occurred in the vertical cyclic loading response between a caisson installed by pushing and a caisson installed by suction. The large magnitude of non dissipated pore water pressure generated during the suction installation influences the load-displacement response, diminishing substantially the amount of caisson uplift and increasing the bearing capacity failure in 50%.

7.4.3 Moment loading

Results from cyclic moment loading tests revealed hysteresis loop constriction at small level of rotation, reducing the caisson moment capacity and increasing the rate of uplifting under tensile load. This was caused by the opening and closing of gaps next to the skirt amidst the reloading and unloading. Recently, this phenomenon has been reported in the literature for large scale caisson tests, but for rotations one order of magnitude higher. Furthermore, the parallel point or transition from uplift to settlement was found to occur at the onset of the hysteresis loop constriction.

Swipe and constant V' tests were performed to determine the yield surface. It was found that the size and shape of the yield surface depend on the caisson load history and bearing capacity, expressed as the ratio $\frac{V_o}{V_u}$. For values of $\frac{V_o}{V_u} \geq 0.4$ the yield surface size was found to reduce, whilst for $\frac{V_o}{V_u} \leq 0.32$ the yield surface size increased.

The parallel point was found to extend for a wide range of $\frac{V'}{V_c}$ values, namely from 0.2 to

0.77 for low V_o and from 0.11 to 0.44 for high V_o . Despite the acceptable agreement of the associated flow assumed with the experimental results, more data is required to confirm the assumption of associated flow.

7.4.4 Discussion and recommendations

The majority of tests concentrated on $\frac{M}{2RH} = 1$ at different V' values, with only few tests with $\frac{M}{2RH} \neq 1$. As a consequence, these series of combined loading tests carried out are not sufficient to cover exhaustively other load paths needed to define accurately the size and shape of the yield surface, hence the parameters for modelling. The preparation of kaolin samples is time consuming and is not possible to obtain more than two fresh sites per specimen. Therefore, further experiments in undisturbed samples are required to increase the data base, using not only a caisson with $\frac{L}{2R} = 1$, but also including caissons with other geometries. Moreover, a study of the effect of the installation method on the caisson moment capacity is necessary. It has been confirmed that no significant difference exists, whether the caisson is installed by pushing or by suction. However, this similarity accounts only for the penetration resistance and not for the subsequent moment capacity. Furthermore, such a study should consider the case of combined loading immediately after suction installation (no dissipated pore pressures) and cases accounting for some degree of consolidation (dissipation of pore pressures).

Chapter 8

CONCLUSIONS

This thesis has presented the study of an experimental research programme of suction caisson foundations for offshore wind turbines. The results were interpreted within the framework of force-resultant plasticity models. From the analysis of the results, it was possible to estimate the parameter values needed to apply hyperplasticity formulations to the modelling of suction caissons. Conclusions and discussions of each part of this research programme have been included in the previous chapters. In this chapter the principal conclusions are summarized and suggestions for future research are proposed.

8.1 CONCLUDING REMARKS

In this investigation a variety of testing conditions were used: i) different caisson geometries, ii) five type of soils: two dry sands - loose and dense, two dense saturated sands - water-saturated and oil-saturated, and a heavily overconsolidated Kaolin clay, and iii) different loading systems and regime: pure vertical and combined loading and monotonic and cyclic loading. From these conditions valuable comparisons between tests were possible using normalised expressions, which also allow preliminary estimations of the scaling of prototype load capacity, displacements, pressures and stiffnesses.

8.1.1 Main findings

The study of monotonic vertical loading in sand revealed that once the full bearing capacity is mobilised, caisson stiffness reduced considerably, nevertheless, permanent softening did not occur as in flat footing, on the contrary, in loose sands the vertical load increased further with penetration. In dense sands hardening occurred after a sequence of peak response followed by relaxation and softening. A new formulation for the hardening law was proposed for this observed response.

The results from caisson installation tests showed considerable reduction of the net vertical load when suction was used to assist the penetration, owing to the creation of hydraulic gradients. Krynine's expression (Handy, 1985) was used to calculate the passive earth lateral pressure coefficient for caisson penetration and the active pressure for caisson drained pullout. The calculation procedure proposed by Houlsby and Byrne (2005b) to estimate the suction was found to be very sensitive to the permeability ratio, which is the soil permeability inside the caisson divided by the soil permeability outside the caisson. Good estimations of the suction were obtained with values of the permeability ratio between 2 and 4. However, for rapid penetrations of a caisson with large thickness ratio high values of the permeability ratio were required to obtain good estimations of the suction.

The yield surface was determined from moment loading tests under low constant vertical loads. A yield surface expression including tensile loads was fitted to the experimental results, which allowed the estimation of the parameters required to construct plasticity models. The flow rule formulation was derived from the yield surface expression rather than from a potential function. The flow rule was found to be associated in the plane of radial plastic displacement increments. Moment and horizontal association factors a_M , a_H were found to be identical. Conversely, a strongly non-associated flow rule was found in the radial-vertical load plane, leading to the vertical association factor a_{V_1} to be different to the other association factors. From symmetric and non-symmetric cyclic moment loading tests under constant V' it was found that Masing's rules were obeyed. However,

from cyclic swipe tests Masing's rules were not obeyed.

In the analysis of moment and lateral loading under drained, partially drained and undrained conditions the effect of the installation method has been considered. Under drained conditions and in the short term, the moment resistance of a suction caisson depends on the method of installation. However, the ratio of plastic radial displacement increments was independent of the installation method. Conversely, the suction installation reduced the caisson uplift during rotation. Under partially drained conditions the caisson resistance diminished with the build-up of excess pore pressures in comparison with that under drained conditions. However, the caisson rotational stiffness was similar to that under drained conditions. To model in the laboratory the wave periods of extreme waves, and the range of permeabilities of the seabed and prototype caisson diameters, the scaled rotation velocities applied to the caisson to induce undrained conditions were determined. Moment loading tests under low constant vertical loads simulating those conditions revealed a dramatic reduction of the caisson resistance and stiffness. Without a substantial increase of the constant vertical load, the caisson moment capacity and stiffness did not recover.

In the study of cyclic vertical loading of suction caissons in clay it was found that in the short term negative excess pore pressures, induced by suction installation, reduced the caisson uplift compared with that from a caisson installed by pushing. Cyclic moment loading showed the effect of gapping at smaller normalised rotations than in the field. The change of hysteresis loop shape due to gapping cannot be reproduced using only the Masing rules. From moment swipe and constant vertical load tests it was found that the moment capacity diminished with the increase of the ratio between the preload V_o and the ultimate bearing capacity load V_u . Since for suction caissons for offshore wind turbines this ratio is low, $\frac{V_o}{V_u} \approx 0.2$, it is expected that the caisson moment capacity will be high.

8.2 SUGGESTIONS FOR FURTHER RESEARCH

The bearing capacity of skirted footings in sand was determined using the bearing capacity factors for flat footings. Therefore, bearing capacity factors N_q and N_γ considering the geometry of skirted footings are necessary.

It was found that high values of permeability ratio were necessary to obtain a good estimations of the suction in rapid caisson penetrations. It is suggested that suction installation experiments using the same caisson aspect ratio but with different thickness ratios, soil densities as well as different penetration rates should be carried out. Calculation procedures including penetration rates related to the field would be necessary to estimate the suction.

A series of moment loading tests under high constant vertical loads is necessary to complete the analysis of the flow rule, so as to estimate the value of the association factor a_{V_2} and β_2 , which have been assumed in this study equal to 1 and 0.99 respectively.

There was not great difference between results of moment loading tests performed 48 hours after suction installation and moment loading tests of caissons installed by pushing. This proved that soil strength was recovered. It is suggested that subsequent moment loading tests should consider different consolidation times, *i.e.* after suction installation. It is well established that fine-grained soils and clays have strength properties and behaviour that change over time as a result of consolidation. The way in which the strength of the soil, disturbed by the flow induced by the suction, changes with time is not known. However, it is known that ageing effects can include the contribution of creep processes, continuous viscous rearrangement of particles (no densification as in secondary consolidation). Therefore, the effect of the suction on the soil strength should be considered in the study of caisson moment capacity.

Research that includes the long term effect of small ocean wave loading amplitude, where

the period is much lower than 12 s is required (between 2 s and 7 s). Although, this loading train has small loading amplitude, their period is closer to the period of the structure, which may induce resonance. Furthermore, it is the prevalent regime of loading offshore, which accounts for millions of cycles per year (from 1 to up to 5 millions). This unexplored condition needs experiments that consider saturated sandy and clayey soils to measure possible build-up of excess pore pressure. It is also of fundamental importance to know if the cyclic response encountered in this investigation continues for larger number of cycles or stabilizes. Vertical loading as well as combined loading should be studied.

Offshore loading of a wind turbine is three dimensional. Therefore, the extension of this study from two dimension to three dimensions is necessary to account for simultaneous loadings along different axes and the inclusion of torsion.

The effect of anisotropy has not been included in the estimation of elastic displacements, since a unique value of elastic shear modulus has been assumed in the calculations. Research to find out whether anisotropy is important or not is suggested. It would be necessary to know the sensitivity of the displacement calculations to the different shear modulus values in each direction to assess whether is worth to include different shear moduli.

In combined loading tests the vertical load has been kept constant. However, moment loading tests where the vertical load varies during rotation could be carried out. For instance, the vertical load could be reduced or increased keeping the ratio between the moment load and vertical load constant. For instance, this would reflect the combined loading occurring in a multiple caisson foundation. It would be interesting to find out whether, through different load paths with all the loads varying, the same yield surface is reached and the same flow vectors are obtained or not.

It has been found that the pore pressure is a key parameter. However, the measurement of the pore pressure at one point on the caisson lid limits the analysis, since variations across

the lid as well as along the skirt occur during caisson rotation. Therefore, it is suggested that model suction caissons be instrumented with at least two pore pressure transducers on the lid and at least two at the skirt. At the skirt the use of miniature PPT will be required. Additionally, knowing in advance the final caisson penetration PPT could be located from below within the soil to measure pore pressures during and after installation.

Further experiments are necessary in clay to confirm or not the parameter values of the yield surface and flow rule expressions presented in this investigation. In particular, experiments with load ratios different to one should be considered. The evaluation of the effect of different consolidation times on the moment response of suction caissons is also suggested.

Finally, research that integrates the experimental results with hyperplasticity formulations is necessary. It is suggested that a parametric calibration study of hyperplasticity models with experimentally obtained parameter values should be pursued to use those models with confidence in the design of suction caisson foundations for offshore wind turbines.

REFERENCES

- Aldwinckle, C. G. (1994). The installation of offshore plated foundation for oil rigs. Final Year Project Report, Department of Engineering Science, University of Oxford
- Allersma, H.G.B., Kirstein, A.A., Brinkgreve, R.B.J. and Ferres, B. (1999). Centrifuge and numerical modelling of methods to optimise the horizontal bearing capacity of suction piles. *International Offshore Mechanics and Arctic Engineering Conference OMAE*, St. Johns
- Allersma, H.G.B., Kirstein, A.A., Brinkgreve, R.B.J. and Simon, T. (1999b). Centrifuge and numerical modelling of horizontally loaded suction piles. *Proceedings of the 9th International Symposium on Offshore and Polar Engineering Conference*, Brest, 711-717
- Allersma, H.G.B., Hogervorst, J.R. and Pimouille, M. (2001). Centrifuge modelling of suction pile installation using a percussion technique. *Proceedings of the 11th International Offshore and Polar Engineering Conference ISOPE*, Stavanger, 2: 260-265
- Andersen, K., Dyvik, R., Schrøder, K., Hansteen, O. and Bysveen, S. (1993). Field tests of anchors in clay II: Predictions and interpretation. *Journal of the Geotechnical Engineering Division ASCE* **119**, No 10, 1532-1549
- Andersen, K. and Jostad, H. P. (1999). Foundation design of skirted foundations and anchors in clay. *Offshore Technology Conference*, Houston, Paper 10824
- Andersen, K. and Jostad, H. P. (2002). Shear strength along outside wall of suction anchors in clay after installation. *Offshore and Polar Engineering Conference*, ISOPE, Kitakyushu, 785-794
- Andersen, K.H., Murff, J.D., Randolph, M.F., Clukey, E.C., Erbrich, C.T., Jostad, H.P., Hansen, B., Aubeny, C., Sharma, P. and Supachawarote, C. (2005). Suction anchors for deepwater applications. *International Symposium on Frontiers in Offshore Geotechnics*, ISFOG, Perth, 3-30
- Aubeny, C. and Murff, J. (2003). Simplified limit solutions for the capacity of suction anchors under undrained conditions. *Ocean Engineering* **32**, 864-877
- Aubeny, C., Han, S. and Murff, J. (2003). Suction caisson capacity in anisotropic, purely cohesive soil. *International Journal of Geomechanics*, Vol.3, No. 2, 225-235
- Ausilio, E. and Conte, E. (2005). Influence of groundwater on the bearing capacity of shallow foundations. *Canadian Geotechnical Journal* **42**, 663-672
- Bell, R.W. (1991). The analysis of offshore foundations subjected to combined loading. *MSc thesis*, University of Oxford

- Beresford, J.M. (2003). Economic comparison and laboratory simulation of field scale tests of foundations for offshore wind energy structures. Final Year Project Report, Department of Engineering Science, University of Oxford
- Bienen, B., Byrne, B.W., Houlsby, G.T. and Cassidy, M.J. (2006). Investigating six degree of freedom loading of shallow foundations on sand. *Géotechnique* **56**, No 6, 367-379
- Bolton, M.D. (1986). The strength and dilatancy of sands. *Géotechnique* **36**, No 1, 65-78 and discussion *Géotechnique* **37**, No 2, 219-226
- Bolton, M.D. and Lau, C.K. (1993). Vertical bearing capacity factors for circular and strip footings on Mohr-Coulomb soil. *Canadian Geotechnical Journal* **30**, 1024-1033
- Boulbibane, M. and Ponter, A.R.S. (2005). Linear matching method for limit load problems using the Drucker-Prager yield condition. *Géotechnique* **55**, No 10, 731-739
- Boussinesq, J. (1878). Équilibre d'élasticité d'un solide isotrope sans pesanteur, supportant différents poids. *Compte Rendus à l'Académie des Sciences Paris* **86**, 1260-1263
- Bowden, R.K. (1988). Compression behaviour and shear strength characteristics of a natural silty clay sedimented in the laboratory. *DPhil thesis*, University of Oxford
- Bowles, J.E. (1996). *Foundation Analysis and Design*. McGraw-Hill
- Bowman, E. T., Soga, K., and Drummond, W. (2001). Particle shape characterisation using Fourier descriptor analysis. *Géotechnique* **51**, No 6, 545-554
- Bransby, M.F. and Randolph, M.F. (1998). Combined loading of skirted foundations. *Géotechnique* **48**, No 5, 637-655
- Bransby, P.L. (1973). Cambridge contact stress transducers. Report No. CUED/C-SOILS/LN2, Engineering Department, University of Cambridge
- Brinch Hansen, J. (1970). A revised and extended formula for bearing capacity. Bulletin No 28, Danish Geotechnical Institute, Copenhagen, 5-11
- British Geological Survey (2004). Seabed sediments in the Irish Sea. Walney Offshore Windfarm. Scoping Report, Consortia Dong and Statkraft
- Brown, G. A. and Nacci, V. A. (1971). Performance of hydrostatic anchors in granular soils. *Offshore Technology Conference*, Houston, Paper 1472
- Butterfield, R. and Tiof, J. (1979). Design parameters for granular soils, discussion contribution. *Proceedings 7th International Conference of Soil Mechanics and Foundation Engineering*, Brighton, Vol. 4, 259-261
- Butterfield, R. (1980). A simple analysis of the load capacity of rigid footings on granular materials. *Journée de Géotechnique*, ENTPE, Lyon, 128-134
- Butterfield, R. and Gottardi, G. (1994). A complete three-dimensional failure envelope for shallow footings on sand. *Géotechnique* **44**, No 1, 181-184
- Butterfield, R., Houlsby, G.T. and Gottardi, G. (1997). Standardized sign conventions and notation for generally loaded foundations. *Géotechnique* **47**, No 5, 1051-1054
- Byrne, B.W. (2000). Investigations of suction caissons in dense sand. *DPhil thesis*, University of Oxford

- Byrne, B.W. and Houlsby, G.T. (2001). Observations of footing behaviour on loose carbonate sands. *Géotechnique* **51**, No. 5, 463-466
- Byrne, B.W. and Cassidy, M.J. (2002). Investigating the response of offshore foundations in soft clay soils. *International Offshore Mechanics and Arctic Engineering Conference OMAE*, Oslo, paper 28057
- Byrne, B.W., Houlsby, G.T., Martin, C.M. and Fish, P.M. (2002). Suction caisson foundations for offshore wind turbines. *Journal of Wind Engineering* **26**, No 3, 145-155
- Byrne, B.W. (2003). Personal communication
- Byrne, B.W. and Houlsby, G.T. (2003). Foundation for offshore wind turbines. *Phil. Trans. of the Royal Society of London, Series A* **361**, 2909-2300
- Byrne, B.W., Villalobos, F., Houlsby, G.T. and Martin, C.M. (2003). Laboratory testing of shallow skirted foundations in sand. *Proceeding BGA International Conference on Foundations*, Newson ed., Thomas Telford, Dundee, 161-173
- Byrne, B.W. and Houlsby, G.T. (2005). Investigating six degree-of-freedom loading on shallow foundations. *International Symposium on Frontiers in Offshore Geotechnics, ISFOG*, Perth, 477-482
- Byrne, B.W. and Houlsby, G.T. (2006). Assessing novel foundation options for offshore wind turbines. *World Maritime Technology Conference*, London
- Cao, J., Audibert, J. and Al-Khafaji, Z. (2002). Excess pore pressure induced by installation of suction caissons in NC clay. *Proceedings of the Society for Underwater Technology SUT Conference*, London, 405-412
- Cassidy, M.J. (1999). Non-linear analysis of jack-up structures subjected to random waves. *DPhil thesis*, University of Oxford
- Cassidy, M.J. and Houlsby, G.T. (2002). Vertical bearing capacity factors for conical footings on sand. *Géotechnique* **52**, No. 9, 687-692
- Cassidy, M.J., Byrne, B.W. and Houlsby G.T. (2002). Modelling the behaviour of circular footings under combined loading on loose carbonate sand. *Géotechnique* **52**, No. 10, 705-712
- Cassidy, M.J., Byrne, B.W. and Randolph, M.F. (2004). A comparison of the combined load behaviour of spudcan and caisson foundations on soft normally consolidated clay. *Géotechnique* **54**, No. 2, 91-106
- Cerato, A. B. and Lutenegeger A. J. (2006). Bearing capacity of square and circular footings on a finite layer of granular soil underlain by a rigid base. *Journal of Geotechnical and Geoenvironmental Engineering* **132**, 1496-1501
- Charles S. (1994). The design and installation of plated foundation for offshore structures. Final Year Project Report, Department of Engineering Science, University of Oxford
- Chaudhary, S.K. and Kuwano, J. (2003). Anisotropic multiple yielding of dense Toyoura sand in p' -constant shear plane. *Soils and Foundations* **43** (4), 59-69
- Chen, W. and Randolph, M. (2004). Radial stress changes around caissons installed in clay by jacking and by suction. *International Offshore and Polar Engineering Conference, ISOPE*, Toulon, 493-499

- Clukey, E.C., Morrison, M.J., Garnier, J. and Corté, J.F. (1995). The response of suction caissons in normally consolidated clays to cyclic TLP loading conditions. *Offshore Technology Conference*, Houston, Paper 7796
- Clukey, E.C., Aubeny, C.P. and Murff, J.D. (2003). Comparison of analytical and centrifuge model tests for suction caissons subjected to combined loads. *International Conference on Offshore Mechanics and Arctic Engineering*, Cancún, Paper OMAE 2003-37503
- Colliat, J.L. and Dendani, H. (2002). Girassol: Geotechnical design analyses and installation of the suction anchors. *Proceedings of the Society for Underwater Technology SUT Conference*, London, 107-119
- Collins, I.F. and Houlsby, G.T. (1997). Application of thermomechanical principles to the modelling of geotechnical materials. *Proceedings Royal Society of London Series A* **453**, 1975-2001
- Coop, M.R., Sorensen, K.K., Bodas Freitas, T. and Georgoutsos, G. (2004). Particle breakage during shearing of a carbonate sand. *Géotechnique* **54**, No. 3, 157-163
- Craig, R.F. (2001). *Soil Mechanics*. Sixth edition, Spon Press
- Das, B.M. (2003). *Principles of Foundation Engineering*. Fifth edition, Thomson
- Davis, R.O. and Selvadurai, A.P.S. (1996). *Elasticity and Geomechanics*. Cambridge University Press
- De Beer, E.E. (1965). Influence of the mean normal stress on the shearing strength of sand. *Proceeding 6th International Conference of Soil Mechanics and Foundation Engineering*, Montreal **1**, 165-169
- de Nicola, A. and Randolph, M.F. (1997). The plugging behaviour of driven and jacked piles in sand. *Géotechnique* **47**, No. 4, 841-856
- de Santa Maria, P.E.L. (1988). Behaviour of footings for offshore structures under combined loads. *DPhil thesis*, University of Oxford
- Dean, E.T.R., James, R.G., Schofield, A.N., Tan, F.S.C. and Tsukamoto, Y. (1992). The bearing capacity of conical footings on sand in relation to the behaviour of spudcan footings of jackups. *Proceedings of the Wroth Memorial Symposium, Predictive Soil Mechanics*, Oxford, 230-253. London, Thomas Telford
- Deng, W. and Carter, J.P. (2000). A theoretical study of the vertical uplift capacity of suction caissons. *International Offshore and Polar Engineering Conference*, ISOPE, Seattle, 342-349
- Department of Trade and Industry (2003). Energy White Paper; our energy future - creating a low carbon economy. DTI, London. Available at www.dti.gov.uk/files/file10719.pdf
- Doherty, J.P. and Deeks, A.J. (2003). Elastic response of circular footings embedded in a non-homogeneous half-space. *Géotechnique* **53**, No. 8, 703-714
- Doherty, J.P., Houlsby, G.T. and Deeks, A.J. (2005). Stiffness of flexible caisson foundations embedded on nonhomogeneous elastic soil. *Journal of Geotechnical and Geoenvironmental Engineering ASCE* **131**, No. 12, 1498-1508
- Dyvik, R., Andersen, K., Hansen, S.B. and Christophersen, H.P. (1993). Field tests of anchors in clay I: Description. *Journal of the Geotechnical Engineering Division*, ASCE,

- Edwards, D.H., Zdravkovic, L. and Potts, D.M. (2005). Depth factors for undrained bearing capacity. *Géotechnique* **55**, No 10, 755-758
- Einav, I. (2005). Energy and variational principles for piles in dissipative soil. *Géotechnique* **55**, No 7, 515-525
- El-Gharbawy, S.L. (1998). The pullout capacity of suction caisson foundations for tension leg platforms. *PhD thesis*, University of Texas at Austin
- Erbrich, C.T. and Tjelta, T.I. (1999). Installation of bucket foundations and suction caissons in sand - Geotechnical performance. *Offshore Technology Conference*, Houston, Paper 10824
- Evans, K.M. (1987). A model study of the end bearing capacity of piles in layered calcareous soils. *DPhil thesis*, University of Oxford
- Feld, T., Rasmussen, J.L. and Sørensen, P.H. (1999). Structural and economic optimization of offshore wind turbine support structure and foundation. *International Offshore Mechanics and Arctic Engineering Conference OMAE*, New Foundland
- Feld, T. (2001). Suction buckets, a new innovative foundation concept, applied to offshore wind turbines. *PhD thesis*, Aalborg University
- Ferguson, M. (1998). Support structure concepts for offshore wind turbines. *Proceedings of the twentieth British Wind Energy Association Conference*, BWEA, Cardiff
- Finnie, I.M.S. (1993). Performance of Shallow Foundations in Calcareous Soil. *PhD thesis*, University of Western Australia
- Flemming, W.G.K., Weltman, A.J., Randolph, M.F. and Elson, W.K. (1994). *Piling engineering*. Blackie & Sohn Ltd
- Fuglsang, L.D. and Steensen-Bach, J.O. (1991). Breakout Resistance of Suction Piles in Clay. *Proceedings of the International Conference Centrifuge 91*, Ko and Mclean eds, Balkema, Rotterdam, 153-159
- Georgiadis, M. and Butterfield, R. (1988). Displacements of footings on sand under eccentric and inclined loads. *Canadian Geotechnical Journal* **23**, 199-212
- Goodman, L.J., Lee, C.N. and Walker, F.J. (1961). The feasibility of vacuum anchorage in soil. *Géotechnique* **11**, No. 4, 356-359
- Gottardi, G. and Butterfield, R. (1993). On the bearing capacity of surface footings on sand under general planar loads. *Soils and Foundations* **33**, No. 3, 68-79
- Gottardi, G. and Butterfield, R. (1995). The displacement of a model rigid surface footing on dense sand under general planar loading. *Soils and Foundations* **35**, No. 3, 71-82
- Gottardi, G., Houlsby, G.T. and Butterfield, R. (1999). The plastic response of circular footings on sand under general planar loading. *Géotechnique* **49**, No. 4, 453-470
- Gourvenec, S. (2003). Alternative design approach for skirted footings under general combined loading. *Proceeding BGA International Conference on Foundations*, Newson ed., Thomas Telford, Dundee, 341-349
- Gourvenec, S. and Randolph, M. (2003). Effect of strength non-homogeneity on the

- shape of failure envelopes for combined loading of strip and circular foundations on clay. *Géotechnique* **53**, No 6, 575-586
- Gourvenec, S., Randolph, M. and Kingsnorth, O. (2006). Undrained bearing capacity of square and rectangular footings. *International Journal of Geomechanics* **6**, 147-157
- Graham, J., Pinkney, R.B., Lew, K.V. and Trainor, P.G.S. (1982). Curve-fitting and laboratory data. *Canadian Geotechnical Journal* **19**, 201-205
- Gue, S.S. (1984). Ground heave around driven piles in clay. *DPhil thesis*, University of Oxford
- Handy, R.L. (1985). The arch in soil arching. *Journal of the Geotechnical Engineering Division*, ASCE, **111**, No 3, 302-318
- Handy, R.L. (2004). Anatomy of an error. *Journal of Geotechnical and Geoenvironmental Engineering* **130**, No. 7, 768-771
- Hardin, B.O. and Richart, F.E. (1963). Elastic wave velocities in granular soils. *Journal of the soil mechanics and foundation division* ASCE, Vol. **89**, No. SM1 33-65
- Helfrich, S. C., Brazill R. L., and Richards, A. F. (1976). Pullout characteristics of a suction anchor in sand. *Offshore Technology Conference*, Houston, Paper 2469
- Hight, D.W., Bond, A.J. and Legge, J.D. (1992). Characterization of the Bothkennar clay: an overview. *Géotechnique* **42**, No. 2, 303-347
- Hight, D.W., Lawrence, D.M., Farquhar, G.B., Milligan, G.W.E., Gue, S.S. and Potts, D.M. (1996). Evidence of scale effects in the end bearing capacity of open-ended piles in sand. *Offshore Technology Conference*, Houston, Paper 7975
- Hjiaj, M., Lyamin, A. and Sloan, S. (2004). Bearing capacity of a cohesive-frictional soil under non-eccentric inclined loading. *Computers and Geotechnics* **31**, No. 6, 491-516
- Hjiaj, M., Lyamin, A. and Sloan, S. (2005). Numerical limit analysis solutions for the bearing capacity factor N_γ . *International Journal of Solids and Structures* **42**, 1681-1704
- Honjo, Y. and Amatya, S. (2005). Partial factors calibration based on reliability analyses for square footings on granular soils. *Géotechnique* **55**, No 6, 479-491
- Houlsby, G.T. (1981). A study of plasticity theories and their applicability to soils. *PhD thesis*, University of Cambridge
- Houlsby, G.T. and Martin, C.M. (1992). Modelling of the behaviour of foundations of jack-up units on clay. *Proceedings of the Wroth Memorial Symposium, Predictive Soil Mechanics*, Oxford, 339-358. London, Thomas Telford
- Houlsby, G.T. and Byrne, B.W. (2000). Suction caisson foundations for offshore wind turbines and anemometer masts. *Journal of Wind Energy* **24**, No. 4, 249-255
- Houlsby, G.T. and Puzrin, A.M. (2000). A thermomechanical framework for constitutive models for rate-independent dissipative materials. *International Journal of Plasticity* **16**, No. 9, 1017-1047
- Houlsby, G.T. and Byrne, B.W. (2001). Discussion on: Sieffert, J.-G. and Bay-Gress, Ch. (2000). Comparison of European bearing capacity calculation methods for shallow foundations. *Proceedings of the ICE, Geotechnical Engineering*, **143**, 65-74, *Geotechnical*

- Houlsby, G.T. and Cassidy, M.J. (2002). A plasticity model for the behaviour of footings on sand under combined loading. *Géotechnique* **52**, No. 2, 117-129
- Houlsby, G.T. (2003). Modelling of shallow foundations for offshore structures. BGA *International Conference on Foundations*, Newson ed., Thomas Telford, Dundee, 11-26
- Houlsby, G.T. and Byrne, B.W. (2005a). Design procedures for installation of suction caissons in clay and other materials. *Proceedings of the ICE, Geotechnical Engineering* **158**, No. 2, 75-82
- Houlsby, G.T. and Byrne, B.W. (2005b). Design procedures for installation of suction caissons in sand. *Proceedings of the ICE, Geotechnical Engineering* **158**, No. 3, 135-144
- Houlsby, G.T., Kelly, R.B., Huxtable, J. and Byrne, B.W. (2005a). Field trials of suction caissons in clay for offshore wind turbine foundations. *Géotechnique* **55**, No 4, 287-296
- Houlsby, G.T., Amorosi, A. and Rojas, E. (2005b). Elastic moduli of soils dependent on pressure: a hyperelastic formulation. *Géotechnique* **55**, No 5, 383-392
- Houlsby, G.T., Kelly, R.B. and Byrne, B.W. (2005c). The tensile capacity of suction caissons in sand under rapid loading. *International Symposium on Frontiers in Offshore Geotechnics*, ISFOG, Perth, 405-410
- Houlsby, G.T., Kelly, R.B., Huxtable, J. and Byrne, B.W. (2006). Field trials of suction caissons in sand for offshore wind turbine foundations. *Géotechnique* **56**, No 1, 3-10
- House, A. (2002). Suction caisson foundations for buoyant offshore facilities. *PhD thesis*, University of Western Australia
- House, A. R. and Randolph, M. F. (2001). Installation and pull-out capacity of stiffened suction caissons in cohesive sediments. 11th *International Offshore and Polar Engineering Conference* ISOPE, Stavanger, 2: 574-580
- HR Wallingford (2004). Scour assessment of suction caisson founded wind turbines. Project report: Future energy solutions, the application of suction caissons foundations to offshore wind turbines. DTI
- Ibsen, L.B., Schakenda, B. and Nielsen, S.A. (2003). Development of the bucket foundation for offshore wind turbines, a novel principle. *Proceeding US Wind Energy Conference*, Boston (in 'Foundation Engineering Papers', no. 20, 1398-6465, paper no. R0308)
- Ibsen, L.B., Liingaard, M. and Nielsen, S.A. (2005). Bucket foundation, a status. *Copenhagen offshore wind conference and exhibition*
- Ishihara, K. (1996). *Soil behavior in earthquake geotechnics*. Clarendon Press, Oxford
- Jardine, R., Chow, F., Overy, R. and Standing, J. (2005). *ICP Design Methods for Driven Piles in Sands and Clays*. Thomas Telford
- Johnson, K. (1999). Partially drained loading of shallow foundations. Final Year Project Report, Department of Engineering Science, University of Oxford
- Kelly, R.B., Byrne, B.W., Houlsby, G.T. and Martin, C.M. (2003). Pressure chamber testing of model caisson foundations in sand. *Proceeding BGA International Conference on Foundations*, Newson ed., Thomas Telford, Dundee, 421-431

- Kelly, R.B., Byrne, B.W., Houlsby, G.T. and Martin, C.M. (2004). Tensile loading of model caisson foundations for structures on sand. *International Offshore and Polar Engineering Conference*, ISOPE, Toulon, 638-641
- Kelly, R.B., Houlsby, G.T. and Byrne, B.W. (2006a). A comparison of field and laboratory tests of caisson foundations in sand and clay. *Géotechnique* **56**, No. 9, 617-626
- Kelly, R.B., Houlsby, G.T. and Byrne, B.W. (2006b). Transient vertical loading of model suction caissons in a pressure chamber. *Géotechnique*, **56**, No. 10, 665-675
- Kim, Y., Kim, S., Park, J., Kim, S., Kim, H. and Kim, K. (2001). A centrifuge study of suction pile installation in sand. 11th *International Offshore and Polar Engineering Conference* ISOPE, Stavanger, 2: 615-619
- Kobayashi, S. (2005). Hybrid type rigid plastic finite element analysis for bearing capacity characteristics of surface uniform loading. *Soils and Foundations* **45**, No 2, 17-27
- Kühn, M. (2002). Offshore wind farms. *Wind Power Plants: Fundamentals, design, construction and operation*, Gasch and Twele eds., 365-384
- Kumar, J. (2003). N_γ for rough strip footing using the method of characteristics. *Canadian Geotechnical Journal* **40**, No. 3, 669-674
- Larsen, P. C. (1989). Suction anchors as an anchoring system for floating offshore constructions. *Offshore Technology Conference*, Houston, Paper 6029
- Lau, C.K. (1988). Scale effects in tests on footings. *PhD thesis*, University of Cambridge
- Lee, J., Salgado, R. and Kim, S. (2005). Bearing capacity of circular footings under surcharge using state-dependent finite element analysis. *Computers and Geotechnics* **32**, No. 6, 445-457
- Lee, J. and Salgado, R. (2005). Estimation of bearing capacity of circular footings on sand based on cone penetration test. *Journal of Geotechnical and Geoenvironmental Engineering* **131**, No. 4, 442-452
- Lehane, B.M., Gaudin, C. and Schneider, J.A. (2005). Scale effects on tension capacity for rough piles buried in dense sand. *Géotechnique* **55**, No. 10, 709-719
- Lings, M.L. and Dietz, M.S. (2005). The peak strength of sand-steel interfaces and the role of dilation. *Soils and Foundations* **45**, No. 6, 1-14
- Luzzani, L. and Coop, M.R. (2002). On the relationship between particle breakage and the critical state of sands. *Soils and Foundations* **42**, No. 2, 71-82
- Mangal, J.K. (1999). Partially drained loading of shallow foundations on sand. *DPhil thesis*, University of Oxford
- Martin, C.M. (1994). Physical and numerical modelling of offshore foundations under combined loads. *DPhil thesis*, University of Oxford
- Martin, C.M. and Houlsby, G.T. (1999). Jackup units on clay: structural analysis with realistic modelling of spudcan behaviour. *Offshore Technology Conference*, Houston, Paper OTC 10996
- Martin, C.M. and Houlsby, G.T. (2000). Combined loading of spudcan foundations on clay: laboratory tests. *Géotechnique* **50**, No. 4, 325-337

- Martin, C.M. and Houlsby, G.T. (2001). Combined loading of spudcan foundations on clay: numerical modelling. *Géotechnique* **51**, No. 8, 687-699
- Martin, C.M. (2001). Vertical bearing capacity of skirted circular foundations on Tresca soil. *Proceedings 15th International Conference on Soil Mechanics and Geotechnical Engineering*, Istanbul, Vol. 1, 743-746
- Martin, C.M. (2003). User guide for ABC - Analysis of Bearing Capacity. Report No. OUEL 2261/03, Department of Engineering Science, University of Oxford
- Martin, C.M. (2003b). New software for rigorous bearing capacity calculations. *International BGA Conference on Foundations*, Newson ed., Thomas Telford, Dundee, 581-592
- Martin, C.M. (2004). Discussion of "Calculations of bearing capacity factor N_γ using numerical limit analyses" by Ukritchon *et al.* *Journal of Geotechnical and Geoenvironmental Engineering* **130**, No. 10, 1106-1107
- Martin, C.M. (2005). Exact bearing capacity calculations using the method of characteristics. *Proc. 11th International Conference of IACMAG*, Turin, Vol. 4, 441-450
- Masing, G. (1926). Eigenspannungen und Verfestigung beim Messing. Proceedings of the 2nd International Congress of Applied Mechanics, Zurich
- McCarthy, D.F. (1998). *Essentials of Soil Mechanics and Foundations. Basic Geotechnics*. Fifth edition, Prentice Hall
- McDowell, G.R. (2002). On the yielding and plastic compression of sand. *Soils and Foundations* **42**, No. 1, 139-145
- Meyerhof, G.G. (1951). The ultimate bearing capacity of foundations. *Géotechnique* **2**, No 4, 301-332
- Meyerhof, G.G. (1963). Some recent research on the bearing capacity of foundations. *Canadian Geotechnical Journal* **1**, 16-26
- Mitchell, J.K. and Soga, K. (2005). *Fundamentals of soil behavior*. Third edition, John Wiley & Sons, New Jersey
- Montrasio, L. and Nova, R. (1997). Settlements of shallow foundations on sand: geometrical effects. *Géotechnique* **47**, No 1, 49-60
- Muir Wood, D. (2004). *Geotechnical modelling*. London, Spon Press
- Ngo-Tran, C.L. (1996). The Analysis of Offshore Foundations Subjected to Combined Loading. *DPhil thesis*, University of Oxford
- Nguyen-Sy, L. and Houlsby, G.T. (2005). The theoretical modelling of a suction caisson foundation using hyperplasticity theory. *International Symposium on Frontiers in Offshore Geotechnics*, ISFOG, Perth, 417-423
- Nguyen-Sy, L. (2006). The theoretical modelling of circular shallow foundations for offshore wind turbines. *DPhil thesis*, University of Oxford
- Nova, R. and Montrasio, L. (1991). Settlements of shallow foundations on sand. *Géotechnique* **41**, No 2, 243-256
- Nova, R. and di Prisco, C. (2003). The macro-element concept and its application in geotechnical engineering. *Proceeding International Symposium FONDSUP 2003*, J.-P.

Magnan and N. Droniuc eds., Paris, Presse ENPC,1, 389-396

Nutt, N.R.F. (1993). Development of the cone pressuremeter. *DPhil thesis*, University of Oxford

Office of Public Sector Information (2002). The Renewables Obligation Order 2002. Statutory Instrument 2002 no. 914, London. The Stationery Office. Available at www.opsi.gov.uk/si/si2002/20020914.htm

Osman, A.S. and Bolton, M.D. (2005). Simple plasticity-based prediction of the undrained settlement of shallow circular foundations on clay. *Géotechnique* **55**, No 6, 435-447

Ovesen, N.K. (1979). The use of physical models in design. *Proceedings 7th International Conference of Soil Mechanics and Foundation Engineering*, Brighton, Vol. 4, 318-323

Poorooshasb, H.B., Holubec, I. and Sherbourne, A.N. (1967). Yielding and flow of sand in triaxial compression: Part I. *Canadian Geotechnical Journal* **4**, No 4, 376-388

Poulos, H.G. and Davis, E.H. (1974). *Elastic solutions in soil and rock mechanics*. Wiley, New York

Prandtl, L. (1920). Über die Härte plastischer Körper. *Nachrichten Gesellschaft Wissenschaft, Göttingen, math.-phys. Klasse*, 74 - 85

Przewłócki, J. (2005). A stochastic approach to the problem of bearing capacity by the method of characteristics. *Computers and Geotechnics* **32**, No. 5, 370-376

Puzrin, A.M. and Houlsby, G.T. (2000). A Thermomechanical Framework for Rate-Independent Dissipative Materials with Internal Functions. *International Journal of Plasticity* **17**, 1147-1165

Puzrin, A.M. and Houlsby, G.T. (2001). Fundamentals of Kinematic Hardening Hyperplasticity. *International Journal of Solids and Structures* **38**, No. 21, 3771-3794

Puzrin, A.M. and Houlsby, G.T. (2003). Rate Dependent Hyperplasticity with Internal Functions. *Journal of the Engineering Mechanics Division* **129**, No. 3, 252-263

Rao, S. N., Ravi, R. and Ganapathy, C. (1997). Pullout behaviour of model suction anchors in soft marine clay. *International Offshore and Polar Engineering Conference, ISOPE, Honolulu* 740-744

Randolph, M.F., Leong, E.C. and Houlsby, G.T. (1991). One-dimensional analysis of soil plugs in pipe piles. *Géotechnique* **41**, No 4, 587-598

Randolph, M.F., O'Neill, M.P., Stewart, D.P. and Erbrich, C.T. (1998). Performance of suction anchors in fine-grained calcareous soils. *Offshore Technology Conference, Houston*, OTC paper 8831

Randolph, M.F. and House, A.R. (2002). Analysis of suction caisson capacity in in clay. *Offshore Technology Conference, Houston*, OTC paper 14236

Rauch, A.F., Olson, R.E., Luke, A.M. and Mecham, E.C. (2003). Measured response during laboratory installation of suction caissons. *International Offshore and Polar Engineering Conference, ISOPE, Honolulu*, 780-787

Reissner, H. (1924). Zum Erddruckproblem. *Proceedings 1st International Congress on Applied Mechanics, Delft*, 295-311

- Richards, N.P. and Barton, M.E. (1999). The Folkestone Bed sands: microfabric and strength. *Quarterly Journal of Engineering Geology*, **32** 21-44
- Roscoe, K.H. and Schofield, A.N. (1957). The stability of short pier foundations in sand. *Discussion. British Welding Journal*, 12-18
- Salgado, R., Lyamin, A.V., Sloan, S.W. and Yu, H.S. (2004). Two- and three-dimensional bearing capacity of foundations in clay. *Géotechnique* **54**, No 5, 297-306
- Sanham, S.C. (2003). Investigation into the installation of suction assisted caisson foundations. Final Year Project Report, Department of Engineering Science, Oxford University
- Sassa, S. and Sekiguchi, H. (2001). Analysis of wave-induced liquefaction of sand beds. *Géotechnique* **51**, No 2, 115-126
- Schnaid, F. (1990). A study of the cone pressuremeter test in sand. *DPhil thesis*, University of Oxford
- Senpere, D. and Auvergne, G.A. (1982). Suction anchor piles - a proven alternative to driving or drilling. *Offshore Technology Conference*, Houston, OTC paper 4206
- Sentenac, P., Lynch, R. J., and Bolton, M.D. (2001). Measurement of a side-wall boundary effect in soil columns using fibre-optics sensing. *International Journal of Physical Modelling in Geotechnics* **4**, 35-41
- Sills, G. and Bartholomeeusen, G. (2001). Consolidation and strength measurements on Dibden Bay soil. Report SM18101, Department of Engineering Science, University of Oxford
- Skempton, A.W. and Northey, R.D. (1952). The sensitivity of clays. *Géotechnique* **3**, No 1, 30-53
- Smith, M.G. (1993). A laboratory study of the Marchetti dilatometer. *DPhil thesis*, University of Oxford
- Smith, C. C. (2005). Complete limiting stress solutions for the bearing capacity of strip footings on a MohrCoulomb soil. *Géotechnique* **55**, No 8, 607-612
- Sowers, G.F. (1979). *Introductory soil mechanics and foundations: geotechnical engineering*. Fourth edition, New York, Macmillan Publishing
- Sparrevik, P. (2002). Suction pile technology and installation in deep waters. *Offshore Technology Conference*, Houston, paper 14241
- Steensen-Bach, J.O. (1992). Recent model tests with suction piles in clay and sand. *Offshore Technology Conference*, Houston, Paper 6844
- Taiebat, H.A. and Carter, J.P. (2000). Numerical studies of the bearing capacity of shallow foundations on cohesive soil subjected to combined loading. *Géotechnique* **50**, No 4, 409-418
- Tan, F.S.C. (1990). Centrifuge and numerical modelling of conical footings on sand. *PhD thesis*, University of Cambridge
- Terzaghi, K. (1943). *Theoretical soil mechanics*. New York, John Wiley & Sons
- Terzaghi, K. and Peck, R. (1967). *Soil Mechanics in Engineering Practice*. New York, John Wiley & Sons

- Ticof, J. (1977). Surface footing on sand under general planar loads. *PhD thesis*, University of Southampton
- Tjelta, T.I., Guttormsen, T.R. and Hermstad, J. (1986). Large-scale penetration test at deepwater site. *Offshore Technology Conference*, Houston, Paper 5103
- Tjelta, T.I. (1994) Geotechnical aspects of bucket foundations replacing piles for the Europipe 16/11-E jacket. *Offshore Technology Conference*, Houston, Paper 7379
- Tjelta, T.I. (1995) Geotechnical experience from the installation of the Europipe jacket with bucket foundations. *Offshore Technology Conference*, Houston, Paper 7795
- Tomlinson, M.J. (1999). *Foundation design and construction*. Sixth edition, Longman
- Tran, M.N., Randolph, M.F. and Airey, D.W. (2004). Experimental study of suction installation of caissons in dense sand. *International Conference on Offshore Mechanics and Arctic Engineering*, Vancouver, Paper No OMAE2004-51076
- Tran, M.N., Randolph, M.F. and Airey, D.W. (2005). Study of sand heave formation in suction caissons using particle image velocimetry (PIV). *International Symposium on Frontiers in Offshore Geotechnics*, ISFOG, Perth, 259-265
- Tsukamoto, Y. (2005). Evaluating superposition errors in bearing capacity factors from Sokolovski's method of characteristics. *Soils and Foundations* **45**, No 3, 161-165
- Uesugi, M. and Kishida, H. (1986). Frictional resistance at yield between dry sand and mild steel. *Soils and Foundations* **26**, No. 4, 139-149
- Ukritchon, B., Whittle, A.J. and Klangvijit, C. (2003). Calculations of bearing capacity factor N_γ using numerical limit analyses. *Journal of Geotechnical and Geoenvironmental Engineering* **129**, No. 6, 468-474
- Vesic, A. S. (1975). Bearing capacity of shallow foundations. In *Foundation Engineering Handbook*, Winterkorn, H.F. and Fang, H.Y. eds., Van Nostrand, New York, 121-147
- Villalobos, F., Byrne, B.W., Houlsby, G.T. and Martin, C.M. (2003a). Bearing capacity tests of scale suction caisson footings on sand: Experimental data. Report FOT0005/1, Department of Engineering Science, University of Oxford
- Villalobos, F., Byrne, B.W., Houlsby, G.T. and Martin, C.M. (2003b). Moment loading tests of scale suction caisson footings on sand: Experimental data. Report FOT015/1, Department of Engineering Science, University of Oxford
- Villalobos, F.A. (2004). An experimental study of cyclically loaded monopod suction caisson foundations for offshore wind turbines. *Eighth Young Geotechnical Engineer's Symposium*, BGA, Birmingham
- Villalobos, F., Byrne, B.W., Houlsby, G.T. and Martin, C.M. (2004a). Cyclic moment loading tests of suction caisson footings on sand: Experimental data. Report FOT020/1, Department of Engineering Science, University of Oxford
- Villalobos, F.A., Houlsby, G.T. and Byrne, B.W. (2004b). Suction caisson foundations for offshore wind turbines. *Proceedings 5th Chilean Conference of Geotechnics (Congreso Chileno de Geotecnia)*, SOCHIGE, Santiago
- Villalobos, F.A., Byrne, B.W. and Houlsby, G.T. (2005). Moment loading of caissons installed into saturated sand. *International Symposium on Frontiers in Offshore Geotech-*

nics, ISFOG, Perth, 411-416

Wang, M. C., Demars, K.R. and Nacci, V.A. (1977). Breakout capacity of model suction anchors in soil. *Canadian Geotechnical Journal* **14**, 246-257

Watson, P.G. (1999). Performance of skirted foundations for offshore structures. *PhD thesis*, University of Western Australia

Whittle, A.J., Germaine, J.T. and Cauble, D.F. (1998). Behavior of miniature suction caissons in clay. *Offshore site investigation and foundation behaviour '98*, SUT, London, 279-300

Wroth, C.P. (1984). The interpretation of in situ soil tests. *Géotechnique* **34**, No 4, 449-484

Zeevaert, L. (1983). *Foundation engineering for difficult subsoil conditions*. Second edition, van Nostrand Reinhold

Ziegler, H. (1977). *An introduction to Thermodynamics*. North Holland, Amsterdam

Ziegler, H. (1983). *An introduction to Thermodynamics*. Second edition, North Holland, Amsterdam

Zhu, D., Lee, C. and Law, K. (2003). Determination of bearing capacity of shallow foundations without using superposition approximation. *Canadian Geotechnical Journal* **40**, 450-459

Zhu, M. and Michalowski, R.L. (2005). Shape factors for limit loads on square and rectangular footings. *Journal of Geotechnical and Geoenvironmental Engineering* **131**, No.2, 223-231

Index

- absolute permeability, 31
- adhesion, 226
- adhesion factor, 224
- anchorage system, 18
- arching, 84, 95, 101
- arching effect, 82
- association factors, 17, 129, 153
- atmospheric pressure, 110

- backbone curve, 22, 168, 195
- bearing capacity, 59
 - reversed failure, 96
 - inverse, 118
 - potential, 179
 - surcharge component, 103
- behaviour
 - partially drained, 29
 - undrained, 29
- bleed valve, 54, 201, 211
- boundary conditions, 45, 46
- boundary effects, 47
- breakage of particles, 30

- caisson uplift, 188
- Cam Clay critical state model, 15
- cavitation, 22, 110
- coefficient
 - of consolidation, 206
 - of volume compressibility, 206
- coefficient of permeability, 31
- cohesion bearing capacity coefficient, 224
- collapse, 14, 66
- consolidation time, 206
- constant V' tests, 188
- constrained modulus, 206
- contact load, 66, 97
- contact penetration, 59
- control algorithm, 52
- Coulomb failure criterion, 84
- CPT approach, 21
- critical hydraulic gradient, 94, 113, 118
- critical penetration, 118

- critical state condition, 68
- critical state line, 192
- CSSM critical state soil mechanics, 34
- cumulative displacement, 22
- cyclic flow regime, 200

- Darcy's law, 89, 206
- deep failure mechanism, 46
- deep plane strains, 224
- deep water structures, 223
- deviatoric load, 170, 190
- differential pressure, 82
- diffusion time, 206, 210
- dilatancy, 60
- dilation, 69, 71, 103
- dilative behaviour, 70, 112
- dimensionless footing velocity, 225
- dimensionless time, 206
- displacement
 - deviatoric, 26
- drained behaviour, 29

- effective load, 105
- elastic behaviour, 16, 126
- elastic metacentre, 126
- elastic shear modulus, 127
- end bearing, 224
- equipotential, 89
- erosion, 83
- excess pore pressure, 91
- extraction, 232
- extraction rate, 22

- failure, 60, 66
 - general shear, 64
 - local shear, 64, 68
 - punching, 64, 68
- field trials, 23
 - Bothkennar, 24
 - Frederikshavn, 24
 - Luce Bay, 24, 108, 197
 - Sandy Haven, 108
 - Tenby, 108

- floating structures, 19
- floating units, 18
- flow channel, 89
- flow parameter F , 89
- flow rate, 88
- flow rule, 152
 - associated, 153
 - non associated, 155
- flow vectors, 188
- fluid valve, 54
- force-resultant model, 15, 17
- foundation
 - stiffness, 184
 - cellular, 19
 - driven piles, 9
 - elastic vertical stiffness, 192
 - gravity base, 12
 - lateral stiffness, 218
 - monopile, 9
 - monopod caisson, 26
 - multiple caissons, 22, 26
 - pile, 19
 - plastic vertical stiffness, 192
 - rotational stiffness, 218
 - secant stiffness, 24
 - stiffness, 23, 209, 217
 - stiffness degradation, 21
 - tripod pile, 12
- frequency, 23
 - turbine natural, 24
- gain, 52
- gapping, 24, 197, 204
- general shear failure, 14
- geostatic stress, 82
- geotechnical model, 207
- hardening, 60, 70, 76
- hardening law, 15, 17
- heat transfer analogy, 92
- heave, 70
- hold subroutine V' , 52
- hold subroutine w , 52
- hydraulic gradient, 19
- hyperplasticity, 25
- hysteresis, 161
 - loop, 195
 - loop constriction, 259
 - loops, 202
- hysteretic, 161
- increment of suction, 115
- incremental displacement, 22
- installation, 59
 - by pushing, 26, 180
 - by suction, 26
- interface angle of friction, 67
- interface friction angle, 84
- irreversible deformation, 139
- isotropic hardening, 25
- jacket structures
 - Draupner E, 108
 - Sleipner T, 108
- kinematic hardening, 25
- Kozeny-Carman equation, 93
- lateral capacity, 21
- lid contact, 97
- limit depth of penetration, 95
- lines of parallel points, 192
- load envelope, 124
- load-controlled mode, 232
- loading rate, 16, 21, 208
- macro-element framework, 15
- Masing behaviour, 22
- Masing hysteretic behaviour, 25
- Masing's rules, 161
- maximum lateral displacement, 47
- maximum rotational displacement, 47
- maximum roughness, 43
- metacentre, 123, 125
 - elastic, 151
 - plastic, 151
- minimum lateral displacement, 47
- mixed isotropic-kinematic hardening, 25
- mobilised angle of friction, 69
- mobilised volume of soil, 45
- model
 - continuous hyperplasticity, 25
 - hyperplasticity, 25
 - kinematic hardening, 129
 - multiple yield surfaces, 25
 - work-hardening plasticity, 25
- Model B, 16
- Model C, 17
- modified Cam Clay, 25
- mooring, 18
- negative pressure, 82

- net vertical displacement, 171
- net vertical load, 91, 119
- non-dimensional footing velocity, 181
- non-symmetrical tests, 166
- normal compression line, 34
- normalised roughness, 43

- OCR overconsolidation ratio, 34
- oedometer test, 206
- offshore cyclic loading, 158
- offshore wind farm, 4
 - cost, 12
 - seabed sediments, 8
- offshore wind turbines, 223
- one-way cyclic loading, 167

- packing of grains, 60
- parallel line, 15
- parallel point, 15, 170, 177, 219
- partially drained, 16, 210
 - oil-saturated tests, 218
- peak friction angle, 66
- peak load, 60
- penetration by self weight, 109
- penetration rate, 23, 26, 109
- peristaltic pump, 53
- permeability, 88, 206
 - absolute, 206
- permeability ratio, 20, 89, 117
- piping, 54, 94
 - local, 118
- piping failure, 23, 83, 108
- plastic potential, 15
- plastic stiffness, 78
- pore pressure build up, 27
- post failure, 60
- preconsolidation load, 97
- preconsolidation pressure, 97
- pressure factor, 19, 90, 117
- probe tests, 189
- pullout, 104
 - rapid, 22
 - rate, 22
- pump, 53
- pump cavitation, 54
- pure kinematic hardening, 161
- pushed installation, 180
- Pyke's rules, 22

- radial displacement, 170

- rate effects, 117
- relaxation, 60, 70, 79
- reloading and unloading curves, 202
- rig flexibility matrix, 51
- rotational velocity, 211

- sand
 - Baskarp, 31
 - Dogs Bay, 30, 66
 - Leighton Buzzard, 30, 66
 - Redhill, 33
 - Western Australia, 68
- scale effects, 180
- scaling
 - laws, 205
 - time, 206
- sealing, 82
- secant shear modulus, 166
- seepage, 92, 112
- seepage forces, 116, 180
- sensitivity, 228
- serviceability, 23
- shaft friction, 84
- shear strength ratio, 34
- shear stress, 84
- sideswipe tests, 15, 188
- silicon oil, 31, 206
- silos effect, 82
- skin friction, 84
- softening, 60, 70, 79
- soil plug, 59
- soil plug heave, 23, 68, 74, 112
- soil-footing interaction, 17
- soil-skirt interface, 84
- Speswhite kaolin clay, 33
- steady flow, 89
- steady load state, 192
- steady state flow regime, 116
- stiffness degradation, 21, 161, 165
 - unloading, 22
- stress distribution
 - exponential, 94, 95, 110
 - linear, 91, 101, 110
 - non-linear, 94, 110
- stress distribution factors, 108
- stress level, 198, 207
- structure-foundation interaction, 11
- submerged caisson, 82
- submerged load, 83

- submergence, 180
- suction, 23, 82
 - critical, 24, 94
 - duration, 109
 - limits, 82, 118
 - rate, 109
 - variation with penetration, 109
- suction caisson, 18
 - concrete, 19
 - installation, 26
 - multiple, 11
 - tetrapod, 11
 - tripod, 11
- suction percussive technique, 54
- suction pile, 19
- surcharge, 70
- swipe tests, 188
 - cyclic, 200
 - rotational, 189
- syringe pump, 53

- tensile capacity, 104
- tension leg platform, 19
- torsional load, 18
- transient response, 22

- ultimate bearing capacity, 21, 59
- ultimate resistance, 23
- undrained footing response, 181
- undrained shear strength, 35, 224
- unloading-reloading line, 34

- velocity vector, 170
- vertical displacement
 - cumulative, 22
 - incremental, 22
 - plastic increment, 219
- verticality, 82
- viscosity, 206
 - absolute, 31
 - dynamic, 31
 - kinematic, 32

- wave train, 200
- wave-induced pressure, 200
- work-hardening plasticity model, 15, 17

- yield, 14, 66, 68
- yield load, 66, 182
- yield surface, 15
 - cigar shaped, 15

- expansion, 16
- shape, 16, 186
- size, 16
- tensile capacity, 26